

Open Research Online

The Open University's repository of research publications and other research outputs

Thermal infrared and optical observations of near-Earth asteroids.

Thesis

How to cite:

Wolters, Stephen D (2006). Thermal infrared and optical observations of near-Earth asteroids. PhD thesis The Open University.

For guidance on citations see [FAQs](#).

© 2006 Stephen D. Wolters

Version: Version of Record

Copyright and Moral Rights for the articles on this site are retained by the individual authors and/or other copyright owners. For more information on Open Research Online's [data policy](#) on reuse of materials please consult the policies page.

oro.open.ac.uk

Thermal Infrared and Optical Observations of Near-Earth Asteroids

A Thesis Submitted for the Degree of
Doctor of Philosophy

Stephen D. Wolters
September 2005

Planetary and Space Sciences Research Institute
The Open University, U.K.

Date of submission: 20 Sept 2005
Date of award: 28 Feb 2006

ProQuest Number: 13917301

All rights reserved

INFORMATION TO ALL USERS

The quality of this reproduction is dependent upon the quality of the copy submitted.

In the unlikely event that the author did not send a complete manuscript and there are missing pages, these will be noted. Also, if material had to be removed, a note will indicate the deletion.



ProQuest 13917301

Published by ProQuest LLC (2019). Copyright of the Dissertation is held by the Author.

All rights reserved.

This work is protected against unauthorized copying under Title 17, United States Code
Microform Edition © ProQuest LLC.

ProQuest LLC.
789 East Eisenhower Parkway
P.O. Box 1346
Ann Arbor, MI 48106 – 1346

Contents

List of Figures	v
Abstract	ix
Acknowledgements	xi
1 Introduction	1
2 General Introduction to Asteroid Science	5
2.1 Introduction.....	5
2.2 Main Belt Asteroids	5
2.2.1 Origin of the Asteroid Belt.....	5
2.2.2 Size Distribution	7
2.2.3 Orbital Distribution	7
2.3 Asteroid Taxonomy.....	8
2.4 Near-Earth Objects.....	9
2.4.1 Introduction.....	9
2.4.2 Origin and Evolution.....	10
2.4.3 Orbital Subcategories	12
2.4.4 Taxonomy	12
2.4.5 Links to Meteorite Parent Bodies.....	14
2.4.6 Radar	15
2.4.7 Bias-corrected Population and Size Distribution	15
2.5 Asteroid Rotations.....	16
2.6 Impacts and NEA Search Programs.....	18
2.7 The Yarkovsky Effect and NEA Thermal Inertias.....	22
2.8 Binary Asteroids and Asteroid Densities	26
2.9 Spacecraft Exploration of Asteroids	28
2.9.1 Space Telescopes	29
2.9.2 Space Missions.....	31
2.9.3 Future Space Missions	33
2.10 Need for Improved Measurements of NEO Albedos and Diameters.....	35
3 Optical Observations	37
3.1 Introduction.....	37
3.2 Planning Observations	37
3.3 Observations at the Jacobus Kapteyn Telescope	39
3.3.1 Methodology	39
3.3.2 May 2001	40
3.3.3 December 2001	43
3.3.4 September 2002.....	44
3.4 Measuring NEA Magnitudes.....	47
3.4.1 Instrumental Magnitudes.....	47
3.4.2 Atmospheric Extinction	47
3.4.3 Geometrical Corrections	49
3.4.4 The <i>H</i> , <i>G</i> Magnitude System.....	50
3.5 CCD Photometry.....	51
3.5.1 The Charge-Coupled Device.....	51
3.5.2 Bias Subtraction and Flat Fielding.....	52
3.5.3 Bad Pixels, Chip Readout Errors and Cosmic Ray Hits	56

3.5.4	Aperture Photometry	58
3.5.5	Direct and Indirect Calibration Methodology.....	63
3.6	Photometric Calibration.....	65
3.6.1	May 2001	66
3.6.2	December 2001	67
3.6.3	September 2002	68
3.7	Reduction of Instrumental Magnitudes to Reduced Magnitudes	69
3.7.1	(433) Eros	72
3.7.2	(4034) 1986 PA.....	76
3.7.3	(5587) 1990 SB.....	77
3.7.4	(6455) 1992 HE	79
3.7.5	(19356) 1997 GH ₃	84
3.7.6	1998 UO ₁	86
3.7.7	(33342) 1998 WT ₂₄	87
3.7.8	(25330) 1999 KV ₄	88
3.7.9	(53789) 2000 ED ₁₀₄	90
3.7.10	2001 SE ₂₈₆	91
3.7.11	2002 HK ₁₂	92
3.7.12	2002 NX ₁₈	95
3.7.13	2002 QE ₁₅	98
3.8	Asteroid lightcurves.....	100
3.8.1	Composite Lightcurves Formed by Fourier Analysis.....	100
3.8.2	Physical Interpretation of Asteroid Lightcurves.....	107
3.9	Analysis and Discussion	111
3.9.1	(433) Eros	111
3.9.2	(4034) 1986 PA.....	114
3.9.3	(5587) 1990 SB.....	116
3.9.4	(6455) 1992 HE	118
3.9.5	(19356) 1997 GH ₃	120
3.9.6	1998 UO ₁	121
3.9.7	(33342) 1998 WT ₂₄	123
3.9.8	(25330) 1999 KV ₄	124
3.9.9	(53789) 2000 ED ₁₀₄	125
3.9.10	2001 SE ₂₈₆	126
3.9.11	2002 HK ₁₂	126
3.9.12	2002 NX ₁₈	128
3.9.13	2002 QE ₁₅	130
3.10	Summary.....	132
4	Thermal Modelling of Near-Earth Asteroids.....	133
4.1	Relating the Albedo, Diameter and Absolute Magnitude.....	133
4.2	The Radiometric Method of Diameter Determination.....	134
4.3	Thermal Models.....	138
4.3.1	Thermophysical Models	138
4.3.2	The Standard Thermal Model (STM)	141
4.3.3	The Fast Rotating Model (FRM)	143
4.3.4	The Near-Earth Asteroid Thermal Model (NEATM).....	145
4.3.5	The Modified Projected Model.....	148

5	Thermal Infrared Observations	151
5.1	Introduction	151
5.2	Using Michelle in Imaging Mode at UKIRT (March 2002)	151
5.3	Using Michelle in Spectroscopy Mode at UKIRT (September 2002)	159
5.3.1	Target Selection and Observation Planning	159
5.3.2	Observations	162
5.3.3	Sky Background Thermal Emission	166
5.4	Data Reduction using ORAC-DR	169
5.4.1	Bias Frames	169
5.4.2	Flat Field Frames	171
5.4.3	Standard Star Frames	173
5.4.4	Standard Stars: Preparing Frames for Spectrum Extraction	173
5.4.5	Standard Stars: Optimum Extraction of Spectrum	175
5.4.6	Standard Stars: Black Body Correction	178
5.4.7	Object Frames: Spectrum Extraction	179
5.4.8	Electronic Pickup Noise	181
5.4.9	Remaining ORAC-DR Processes	182
5.4.10	Optimum Extraction Window Diameter Investigation	183
5.5	Data Reduction: from ORAC-DR to Flux-calibrated and Binned Spectra	185
5.5.1	Wavelength Calibration	185
5.5.2	Black Body Profiling of Standard Star Spectrum	188
5.5.3	Flux Calibration	189
5.5.4	Binning Spectra	197
5.5.5	Notes on Individual Objects	201
5.6	Thermal Model Fitting of Infrared Fluxes	206
5.6.1	Using Optical Observations	206
5.6.2	Results	213
5.6.3	(433) Eros	224
5.6.4	(6455) 1992 HE	226
5.6.5	(66063) 1998 RO ₁	228
5.6.6	1998 UO ₁	229
5.6.7	1999 HF ₁	229
5.6.8	(53789) 2000 ED ₁₀₄	230
5.6.9	2000 GD ₂	231
5.6.10	2002 HK ₁₂	231
5.6.11	2002 NX ₁₈	231
5.6.12	2002 QE ₁₅	233
5.7	Summary	233
5.8	Discussion	234
5.8.1	Integration with Previous NEATM Fits to Thermal IR Fluxes	235
5.8.2	The Beaming Parameter	237
6	The Night Emission Simulated Thermal Model	245
6.1	Introduction	245
6.1.1	Implications of Previous Studies of NEAs Using the NEATM	245
6.1.2	Introducing the NESTM	247
6.2	NESTM Operation	248
6.3	Defining an Appropriate f Parameter	250
6.4	Testing the NESTM	252
6.4.1	Model Testing Method	252

6.4.2	Derived Diameters	259
6.4.3	Derived Beaming Parameters	268
6.5	NESTM Compared with NEATM and Radar Diameters for NEAs.....	275
6.6	Conclusions.....	283
7	Conclusions and Future Work	285
7.1	Conclusions.....	285
7.1.1	Optical Observations	285
7.1.2	Thermal Infrared Observations.....	285
7.1.3	Night Emission Simulated Thermal Model	288
7.2	Future Work.....	289
7.2.1	Optical Observations	289
7.2.2	Fitting More Thermal IR Fluxes with NESTM	291
7.2.3	Improving the NESTM.....	294
7.2.4	Improving the Thermophysical Model	296
7.2.5	Ellipsoid Approximation Thermal Model (EATM)	296
7.2.6	Further Thermal IR Observations.....	298
	References.....	301
Appendices		
A.	Fortran 90 Code for Thermal Model Fitting Program THERM	311
B.	Thermal IR Fluxes (March 2002)	339
C.	September 2002 UKIRT Log Sheets	341
D.	ORAC-DR Primitives Flowchart.....	347
E.	Thermal IR Fluxes (September 2002).....	363
F.	Fortran 90 Code for the NESTM.....	369
G.	Look-up Table for f Parameter.....	391

List of Figures

Fig. 2.1 Proper elements semimajor axis vs. eccentricity for 96944 numbered asteroids.....	8
Fig. 2.2 Diameter-limited fractional abundances of NEO taxonomic types.....	13
Fig. 2.3 The observed lightcurve amplitude vs. spin rate of near-Earth and Mars-crossing asteroids.....	17
Fig. 2.4 Cumulative population of NEAs vs. absolute magnitude from various surveys.....	19
Fig. 2.5 The Yarkovsky effect.....	23
Fig. 2.6 Mean change in semimajor axis Δa of inner main belt asteroids over their collisional lifetimes vs. their radius, for different surface thermal conductivity K	26
Fig. 2.7 Histogram showing the distribution of asteroid albedos from IRAS data.....	30
Fig. 2.8 Images of asteroids from spacecraft.....	34
Fig. 2.9 De-biased average albedos for NEOs for each taxonomic complex.....	36
Fig. 3.1 Theoretical phase curves for an object with absolute magnitude $H_V = 19.0$	50
Fig. 3.2 Raw frame taken on 28 September 2002 of (433) Eros in the V-filter at the JKT.....	53
Fig. 3.3 Bias levels for JKT V-filter observations of 2002 HK ₁₂ on the night of 25 September 2002 UT.....	54
Fig. 3.4 Normalised flat field frame for the JKT, 28 September 2002 UT.....	55
Fig. 3.5 Flat fielded and de-biased SITE2 (fast mode) CCD images of (433) Eros taken on 28 September 2002 UT at the JKT.....	59
Fig. 3.6 R-filter frame of asteroid 1998 WT ₂₄ , tracking, taken on 18 December 2001 at JKT.....	62
Fig. 3.7 Instrumental magnitudes of comparison stars and asteroid 2001 SE ₂₈₆	65
Fig. 3.8 Atmospheric extinction plots, JKT, May 2001.....	67
Fig. 3.9 Atmospheric extinction plot, JKT, December 2001.....	68
Fig. 3.10 Atmospheric extinction plots, JKT, September 2002.....	69
Fig. 3.11 Extinction plots of comparison stars observed on the same field as (433) Eros at the JKT in September 2002.....	74
Fig. 3.12 Reduced magnitudes $V(1, \alpha)$ of (433) Eros observed at the JKT in September 2002.....	75
Fig. 3.13 Reduced magnitudes $V(1, \alpha)$ for (4034) 1986 PA taken at the JKT in May 2001.....	77
Fig. 3.14 Reduced magnitudes $V(1, \alpha)$ for (5587) 1990 SB taken at the JKT in May 2001.....	79
Fig. 3.15 Observations of comparison stars observed on the same field as (6455) 1992 HE at the JKT in September/October 2002.....	81
Fig. 3.16 Reduced magnitudes $V(1, \alpha)$ for (6455) 1992 HE taken at the JKT in September/October 2002.....	83
Fig. 3.17 Observations of comparison stars observed on the same field as (19356) 1997 GH ₃ at the JKT in May 2001.....	85
Fig. 3.18 Reduced magnitudes $V(1, \alpha)$ for (19356) 1997 GH ₃ taken at the JKT in May 2001.....	86
Fig. 3.19 Reduced magnitudes $V(1, \alpha)$ for 1998 UO ₁ taken at the JKT on the night of the 25 September 2002.....	86
Fig. 3.20 Extinction plots of comparison stars observed on the same field as (33342) 1998 WT ₂₄ at the JKT on the night of 18 December 2001.....	88
Fig. 3.21 Reduced magnitudes $R(1, \alpha)$ for (33342) 1998 WT ₂₄ taken at the JKT on the night of the 18 December 2001.....	88
Fig. 3.22 Reduced magnitudes $V(1, \alpha)$ for (25330) 1999 KV ₄ taken at the JKT (tracked) in May 2001.....	90
Fig. 3.23 Reduced magnitudes $V(1, \alpha)$ for (53789) 2000 ED ₁₀₄ taken at the JKT (tracked) on the night of 1 October 2002.....	91
Fig. 3.24 Extinction plots of comparison stars observed on the same field as 2001 SE ₂₈₆ at the JKT on the night of 18 December 2001.....	92
Fig. 3.25 Reduced magnitudes $V(1, \alpha)$ for 2001 SE ₂₈₆ taken at the JKT (tracked) on the night of 18 December 2002.....	92
Fig. 3.26 Reduced magnitudes $V(1, \alpha)$ and relative magnitudes for 2002 HK ₁₂ taken at the JKT in September 2002.....	94
Fig. 3.27 Reduced magnitudes $V(1, \alpha)$ for 2002 NX ₁₈ taken at the JKT in September 2002.....	98
Fig. 3.28 Reduced magnitudes $V(1, \alpha)$ and relative magnitudes for 2002 QE ₁₅ taken at the JKT in September 2002.....	100
Fig. 3.29 Reduced magnitudes of asteroid (6455) 1992 HE observed at the JKT in the V-filter in September 2002, data for each individual night.....	101
Fig. 3.30 An asteroid's lightcurve has two maxima and minima per rotation.....	102
Fig. 3.31 Composite lightcurve of asteroid (6455) 1992 HE observed in September 2002 at the JKT for a Fourier fit $P = 2.736 \pm 0.0019$ h showing unadjusted mean magnitudes.....	106
Fig. 3.32 An asteroid lightcurve can have different amplitudes when viewed at different aspect angles.....	109
Fig. 3.33 Composite lightcurve of (433) Eros.....	112
Fig. 3.34 Composite lightcurve of (4034) 1986 PA.....	116

Fig. 3.35 Composite lightcurve of (5587) 1990 SB.....	117
Fig. 3.36 Two possible 6th order Fourier fits for (6455) 1992 HE.....	119
Fig. 3.37 Composite lightcurve of (19356) 1997 GH ₃	121
Fig. 3.38 Composite lightcurve of 1998 UO ₁	122
Fig. 3.39 Composite lightcurve of (33342) 1998 WT ₂₄	123
Fig. 3.40 Composite lightcurve of (25330) 1999 KV ₄	125
Fig. 3.41 Composite lightcurve of 2002 HK ₁₂	127
Fig. 3.42 Two possible 4th order Fourier fits for 2002 NX ₁₈	129
Fig. 3.43 Two possible 4th order Fourier fits for 2002 QE ₁₅	131
Fig. 4.1 Cartoon illustrating the reflection, absorption, and re-emission of solar radiation intercepted by an asteroid.....	134
Fig. 4.2 Residuals for different thermal model fits to 2002 NX ₁₈ 27 September 2002 UT thermal IR fluxes over a range of p_v	138
Fig. 4.3 Diagram of the Standard Thermal Model (STM).....	141
Fig. 4.4 Temperature distribution at different angles from the subsolar point using the Standard Thermal Model.....	142
Fig. 4.5 Diagram of Fast Rotating Model (FRM).....	143
Fig. 4.6 Temperature distribution at different latitudes using the Fast Rotating Model.....	144
Fig. 4.7 Diagram of the Near-Earth Asteroid Thermal Model (NEATM).....	146
Fig. 4.8 Temperature distribution at different longitudes and latitudes (0° is subsolar point) using the NEATM.....	147
Fig. 5.1 Extinction plots ($M_{inst} - M_{std}$) versus airmass χ for UKIRT 22 March 2002 UT with Michelle in imaging mode for 8.8, 10.3, 12.5 and 18.5 μm filters.....	154
Fig. 5.2 Extinction plots ($M_{inst} - M_{std}$) versus airmass χ for UKIRT 23 March 2002 UT with Michelle in imaging mode for 8.8, 10.3, 12.5 and 18.5 μm filters.....	155
Fig. 5.3 Flux-calibrated apparent thermal IR fluxes of three asteroids observed on 22 and 23 March 2002 UT at UKIRT with the Michelle instrument in imaging mode	158
Fig. 5.4 Michelle instrument spectroscopy mode bias frame	170
Fig. 5.5 Michelle instrument spectroscopy mode flat field frame	172
Fig. 5.6 Wavelength-calibrated-by estimation frame	174
Fig. 5.7 (a) “sky-subtracted” image of standard star BS 7264; (b) The group frame gm20020927_18.sdf formed by coadding all 4 pairs in the observation.	175
Fig. 5.8 Mean y-profile of gm20020927_18	176
Fig. 5.9 gm20020927_18_nsp, the raw normalised spectrum of BS 7264 observed on 27 September 2002 UT, outputted by ORAC-DR using 3 pixel window diameter optimum extraction.	177
Fig. 5.10 The group frame gm20020927_26 of frames 26-73, comprising observations of 2002 NX ₁₈ on 27 September 2002 UT at UKIRT using the lowN grating with the 4-pixel slit width.	179
Fig. 5.11 Mean y-profile of gm20020927_26, row centres for optimum spectrum extraction can be determined. The electronic pickup noise can be seen as a varying positive bias in intensity.	180
Fig. 5.12 gm20020927_26_nsp, the raw normalised spectrum of 2002 NX ₁₈ observed on 27 September 2002 UT, outputted by ORAC-DR using a 3 pixel window diameter optimum extraction.	180
Fig. 5.13 Estimated signal-to-noise ratio (S/N) for a variety of sources ranging from the faint using different optimum extraction window diameters.....	184
Fig. 5.14 Sky-arc spectra for N- and Q-band observations.....	186
Fig. 5.15 Example wavelength calibrations	187
Fig. 5.16 Normalised black body profiles for Eros ratio star BS 8560, calculated by ORAC-DR and manually calculated after wavelength calibration.....	188
Fig. 5.17 Flux-calibrated spectra of 2002 NX ₁₈ ratio stars.....	192
Fig. 5.18 Normalised counts-per-second spectra of 2002 NX ₁₈	193
Fig. 5.19 Flux-calibrated spectrum of BS 7001 calibrated directly and using a ratio star to estimate atmospheric extinction uncertainty	194
Fig. 5.20 Estimating the wavelength-dependent uncertainty due to differing atmospheric absorption between the ratio star and the asteroid, by dividing fluxes of BS 7001 found using different ratio stars.	196
Fig. 5.21 Flux-calibrated spectra of asteroids observed 27-30 September 2002 UT at UKIRT using the Michelle instrument in spectroscopy mode, binned and unbinned.	201
Fig. 5.22 N-band flux of asteroid 1998 UO ₁ with different optimum extraction row centres; the amplitude gives an indication of the electronic pickup noise.	203
Fig. 5.23 Reduced composite visual lightcurves. with arrows pointing to the rotational phase at the midpoint of the UKIRT thermal IR observations.....	210
Fig. 5.24 STM, FRM and NEATM fits to September and March UKIRT observations	220

Fig. 5.25 The relationship between phase angle (α) and fitted beaming parameters (η)..	235
Fig. 5.26 Geometric visible albedo versus diameter derived by NEATM for S- and Q-type NEAs	236
Fig. 5.27 Variation of NEATM best-fit beaming parameter η with rotation period, effective diameter and geometric albedo.....	241
Fig. 6.1 Limiting curves, reproduced from Delbó (2004), which fit the observed α - η distribution for different thermal parameters and surface roughness ..	246
Fig. 6.2 Equatorial temperatures produced by the thermophysical model	251
Fig. 6.3 f parameters for different thermal parameters Θ	252
Fig. 6.4 Surface temperatures for the thermophysical model run with $A = 0.09815$, $P = 5$ h, $r = 1$ AU. (a) $\Gamma = 200$, (b) equatorial surface temperatures.....	254
Fig. 6.5 Temperature profiles at different longitudes θ and latitudes ϕ produced by the NEATM and NESTM.....	257
Fig.6.6 Synthetic thermal IR fluxes at $10.7 \mu\text{m}$ for thermophysical model-derived surface temperatures simulating an asteroid with $r = 1.0$ AU, $P = 5$ h and 4 different thermal inertias Γ , “observed” at a range of different phase angles on the afternoon side ($+\alpha$) and on the morning side ($-\alpha$).	258
Fig. 6.7 Variation of model diameters with phase angle, observed on the afternoon side and the morning side, fitting to thermophysical model-derived thermal IR fluxes	263
Fig. 6.8 Figure reproduced from Delbó (2004) showing the variation of the NEATM η -values at different phase angles for a smooth ($\theta = 0$) asteroid surface, modelled with a thermophysical model.....	268
Fig. 6.9 Variation of model best-fit beaming parameters η at different phase angles α , fitting to thermophysical model-derived thermal IR fluxes.....	274
Fig. 6.10 Comparison of NEATM and NESTM relative error distribution with radar diameters.....	282
Fig. 7.1 Extinction plots for standards (R and I-filter) on JKT 1 October 2002, re-evaluated to exclude high airmass observations.....	289
Fig. 7.2 Best-fit beaming parameters η versus phase angle α for asteroids fitted with NEATM and the few asteroids fitted with NESTM..	294

Abstract

Increased physical characterisation of Near-Earth Asteroids (NEAs) is important for understanding their origin and evolution, the links between meteorites and their parent bodies, and for assessing the impact hazard. NEAs are also representative of small main belt asteroids.

Optical observations of 13 NEAs taken at the Jacobus Kapteyn Telescope in 2001 and 2002 are presented, from which composite lightcurves, mean magnitudes, absolute visual magnitudes, rotation periods and lightcurve amplitudes are derived. Thermal infrared photometry and spectrophotometry of 10 NEAs taken at the United Kingdom Infrared Telescope (UKIRT) in March and September 2002 are presented. The Standard Thermal Model (STM), Fast Rotating Model (FRM) and Near-Earth Asteroid Thermal Model (NEATM) have been fitted to the measured fluxes to derive geometric albedos (p_v), effective diameters (D_{eff}) and beaming parameters (η).

The NEATM assumes zero thermal emission on the night side of an asteroid, affecting the best-fit η , overestimating D_{eff} and underestimating p_v at large phase angles. The Night Emission Simulated Thermal Model (NESTM) is introduced. NESTM models the night side temperature (T_{night}) as an iso-latitudinal fraction (f) of the maximum day side temperature (T_{max} calculated for NEATM with $\eta = 1$): $T_{night} = fT_{max} \cos^{1/4} \phi$, where ϕ is the latitude. A range of f is found for different thermal parameters, which depend on the surface thermal inertia (Γ). NESTM is tested on thermal IR fluxes generated from simulated asteroid surfaces with different Γ . NESTM, NEATM and radar diameters are compared and it is found that NESTM removes a systematic bias of NEATM that overestimates asteroid diameters. From these tests, it is suggested that a version of the NESTM which assumes $\Gamma = 200 \text{ J m}^{-2} \text{ s}^{-1/2} \text{ K}^{-1}$ ($f \approx 0.6$) is adopted as a default model when the solar phase angle is greater than 45° .

Acknowledgements

*For my parents, Andrew and Susan Wolters.
Thank you for your tireless support and encouragement.*

I would like to thank all the postgrads and postdocs in the department. Special mention goes to Vic, for showing me that it is possible to write a thesis and learn dance moves simultaneously; James, for many wise words of counsel and forewarning; Andrew, for curry and Who; Mark B., for explaining CTRL-SHIFT-HYPHEN and other tricks; Adam, for helping me on my background research [especially the work of Scott (1979) and Jackson (2001, 2002, 2003)]; Mark P., for nearly improving my taste in music.

My research was supported by the Particle Physics and Astronomy Research Council. Many thanks to my Ph.D. examiners Prof. Alan Fitzsimmons and Prof. John Zarnecki (sorry the submitted thesis was so long – I didn't have time to write a short one!). I am grateful to Tom Kerr and Paul Hirst (for explaining the endless subtleties of Michelle and ORAC-DR) and the UKIRT Telescope Operators Thor Wold and Watson Varricatt. Thank you to Petr Pravec, for supplying valuable data and a very useful critique of my optical observations, and Marco Delbo', for advice on thermal model calculations and interpretations. Thank you to both of the above for your constructive reviews of my first paper, genuinely improving the quality of my research. My gratitude to Alan "the DLR one" Harris, for helping me establish the crucial relation: my NEATM = your NEATM. Thank you to Neil McBride for your immaculate observing notes and for coding advice. My thanks to John Davies, for valuable lessons – particularly that a good Mexican is worth exploring every square inch of Honolulu to find, and that getting lost on a lava field is no reason to lose your cool. Oh, and for helping with Starlink, too.

Most of all, I would like to thank my Ph.D. supervisor Dr. Simon Green, who has patiently tried to turn this ignorant soul into an astronomer. I have many happy memories of sitting in the freezing cold dome of the JKT in dense fog. Thank you for your wisdom, enthusiasm, encouragement, for explaining the obvious to my confused mind, and for helping me find a way through. Also, for making me poke lava with a stick.

Finally, to MTSHC – thank you for your kindness, support and Whedonverse indoctrination.

Stephen D. Wolters
September 2005

*There's a gap in between
There's a gap where we meet
Where I end and you begin
And I'm sorry for us
The dinosaurs roam the earth
The sky turns green
Where I end and you begin
I am up in the clouds
And I can't and I can't come down
I can watch but not take part
Where I end and where you start
Where you, you left me alone
You left me alone.
X will mark the place
Like the parting of the waves
Like a house falling into the sea
Lyrics to "Where I End and You Begin" by Radiohead*

1 Introduction

A near-Earth object (NEO) is a comet or asteroid whose perihelion is less than 1.3 AU. As of 8 August 2005, over 3500 NEOs have been discovered and the vast majority of NEOs are thought to be near-Earth asteroids (NEAs).

Upon discovery of an NEA, the only physical parameter that is measured is its brightness: it may be small and bright, or large and dark. Its diameter can only be determined if we also know its albedo. Follow-up observations are required to determine the albedo and other properties. But while there are well-funded programs to find NEAs and pinpoint their orbits, investigations of their physical properties have been relatively sparse. Only about 70 NEAs had measured diameters and albedos previous to this work.

The rotation period, pole orientation, shape constraints and phase curve can be determined from extended optical photometry. Thermal infrared spectrophotometry, combined with an appropriate thermal model and optical photometry, can be used to determine an asteroid's diameter and albedo.

The albedo can constrain an asteroid's taxonomic class. The size distribution and thermophysical properties of NEAs can help us to understand their origin and evolution. Size, shape, rotation and thermal properties can possibly distinguish the presence of extinct comets in the NEA population. The observed rotational and size distribution can be compared with the results of collisional evolution models to provide an insight into the 4.6 billion year history of the solar system. There is strong evidence that the physical properties of NEAs are representative of small main belt asteroids, which are difficult to study in detail.

Unravelling the basic properties of NEAs is vital for any cohesive preparatory program for mitigation of the impact hazard. Particularly important is their de-biased size distribution, obtained from linking albedo measurements to taxonomic classes, and their

internal structure and strength, which can be deduced from the distribution of rotation rates and lightcurve amplitudes.

NEAs are the precursor bodies of meteorites. The mineralogy of meteorites has been extensively studied in the laboratory. If we can improve our understanding of the physical properties of NEAs, we can make links between different meteorite and asteroid taxonomic types and reveal the NEA parent bodies in the main belt. For example, albedo studies of S-type NEAs have recently revealed a trend of increasing albedo with decreasing diameter, strengthening the proposed link between S-type asteroids and ordinary chondrite meteorites.

This thesis tackles the need for improved physical characterisation of NEAs on three interconnected fronts. A program of optical photometry of NEAs at the Jacobus Kapteyn Telescope (JKT) from May 2001, December 2001 and September 2002 is presented, from which rotation periods, absolute magnitudes and lightcurve amplitudes are derived. A program of thermal infrared spectrophotometry at the UK Infrared Telescope (UKIRT) in March and September 2002 is presented, from which diameters and albedos are derived; these observations were supported by quasi-simultaneous optical observations in September 2002. Finally, a new thermal model, which can derive NEA albedos and diameters more accurately at high phase angles, is developed and evaluated.

Chapter 2 gives a general background to the study of asteroids. The asteroid main belt is described and its link to the origin of the solar system is explained. There is an introduction to the asteroid taxonomy system. The origin of NEOs, how they are subdivided into orbital subcategories, their size distribution, their links to meteorite parent bodies, and their investigation by radar is discussed. An overview of asteroid rotations and binary asteroids is given. The impact hazard is discussed. The importance of the Yarkovsky effect on the evolution of NEAs and its dependence on the thermal properties of the surface is explained. A overview of space-based telescopes and spacecraft missions

is given. Finally, it is explained in more detail why there is a need for improved measurements of NEO albedos and diameters.

Chapter 3 describes our program of optical photometry. How observations are planned and carried out at the telescope is discussed. CCD aperture photometry and the process of bias subtraction and flat fielding is described. It is explained how to account for atmospheric extinction and how to calibrate observations using standard stars. It is discussed how we form composite lightcurves from Fourier analysis and physically interpret them. The results of the optical photometry at the JKT in May 2001, December 2001 and September 2002 are presented. The events and conditions of each night are summarised. The photometric calibration for each night and example extinction plots are given. The reduction of the instrumental magnitudes to reduced magnitudes for the 13 objects observed is described, and the observations for each object presented. Finally the results are analysed; rotation periods, mean magnitudes, absolute magnitudes, and lightcurve amplitudes are derived.

Chapter 4 explains the radiometric method of diameter determination, i.e. how a thermal model is fitted to thermal IR fluxes. Different thermal models are described: thermophysical models, the Standard Thermal Model (STM), the Fast Rotating Model (FRM), the Near-Earth Asteroid Thermal Model (NEATM) and the modified projected model.

Chapter 5 presents the results of thermal IR spectrophotometry at the UKIRT in March and September 2002. First the March 2002 observations, using the Michelle instrument in imaging mode: the standard star extinction plots are given, the calibration of the three objects observed is described and the reduced fluxes are presented. The bulk of the chapter is given to the September 2002 observations, using Michelle in spectroscopy mode. It is described how targets were selected and the observations were planned. The weather conditions for each night are briefly discussed. It is explained how spectra are obtained at

the telescope using chopping and nodding to remove background flux from the sky. It is described how the raw bias, flat, standard and object frames are reduced and spectra optimally extracted using ORAC-DR. The process of wavelength calibration, black body correction of the standard star frames, and the binning of spectra is explained. Notes on the reduction of the fluxes for each of the 10 objects observed are given. It is described how the JKT optical observations were used. The STM, FRM and NEATM are fitted to the thermal IR fluxes and diameters, albedos and best-fit beaming parameters are derived. Finally, the derived diameters, albedos and beaming parameters are put into context with previous results, and the phase angle dependence of the beaming parameter is discussed.

Chapter 6 introduces the Night Emission Simulated Thermal Model (NESTM), which approximates the thermal emission from the night side of an asteroid by applying a night side temperature that is a fraction f of the maximum day side temperature. The NESTM and its operation are described. It is explained how to find the appropriate value of f . The NESTM is tested by fitting it to synthetic thermal IR fluxes from simulated asteroid surfaces using a thermophysical model, and by comparing NESTM, NEATM and radar diameters.

Chapter 7 presents the conclusions of the thesis and ends with an outline of future work. The unreduced optical observations from September 2001 and April 2002 are outlined. A database of thermal IR fluxes needs to be created and fitted with NESTM. It is described how NESTM can be improved and tested with more sophisticated thermophysical models. A concept for a thermal model that approximates the shape of NEAs as an ellipsoid is presented. The priorities when making further thermal IR observations of NEAs are discussed.

2 General Introduction to Asteroid Science

2.1 Introduction

The planets formed 4.6 billion years ago from the gravitational accumulation of planetesimals, of which asteroids and comets are the remnants. By studying asteroids, we can understand the origin and evolution of the solar system and the initial conditions in the solar nebula. The population is concentrated in the Main Belt between the orbits of Mars and Jupiter (Section 2.2); the most populous part of the belt lies between 2.2 and 3.3 AU.

There are other populations of minor bodies; we concentrate on the Near-Earth Objects (NEOs, Section 2.4) in this chapter. There are also the Trojan asteroids, which librate about the L_4 and L_5 Lagrangian points 60° ahead and behind Jupiter's orbit. They may be primitive objects that represent the conditions in the solar nebula where Jupiter was formed. The Centaurs orbit in the region of the outer planets, a result of the gravitational interaction of Neptune with the inner regions of the Kuiper Belt, and have dynamical lifetimes of $\sim 10^6$ - 10^7 yr. A recent review of the physical properties of Trojans and Centaurs can be found in Barucci *et al.* (2002). Trans-Neptunian Objects (TNOs) orbit on average at a greater distance than Neptune; they include Kuiper Belt Objects (KBOs, 30-50 AU) and Scattered Disk objects [e.g. 2003 UB₃₁₃, which is almost certainly larger than Pluto (Brown *et al.*, 2005)].

2.2 Main Belt Asteroids

2.2.1 *Origin of the Asteroid Belt*

A brief summary of the origin of the asteroids is given by Peebles (2000). About 4.6 billion years ago, within the dust cloud of the solar nebula, elements with high melting points, such as iron, condensed into dust first, followed by those with lower melting points, like carbon. Closer to the Sun, temperatures remained too high for these materials to

condense, and they chemically combined with the higher-temperature elements. In the middle and outer parts of the belt the carbonaceous materials, as well as ice, were able to condense. After collisions, the dust grains were able to stick together, since they had small relative velocities.

As the planetesimals formed, they were also being heated. Some of the early asteroids formed iron cores. The asteroids in the middle part of the belt underwent lesser degrees of heating. They did not melt, but lost much of their volatile lighter elements and most of their water. Silicate grains and glass were aqueously altered into water-rich claylike particles. The outer belt asteroids may be more primitive bodies, retaining their volatiles.

The main belt is believed to have originally contained an Earth mass or more of material, while the present day belt only contains $\sim 5 \times 10^{-4}$ Earth masses (e.g. Petit *et al.*, 2002). The mass loss is explained by the dynamical depletion of main belt material via gravitational perturbations from planetary embryos and a newly-formed Jupiter that disrupted their orbits, increasing the relative velocity of the planetesimals, so that they began to fragment. Bottke *et al.* (2006) have modelled the fossilised “wavy” size distribution of the main belt (essentially deviations from the power law discussed in Section 2.2.2) with a collisional evolution code. They found that Jupiter most likely formed 3.3 ± 2.6 Myr after the onset of fragmentation in the main belt. Most of the post-accretion main belt mass was taken up by planetary embryos, and while many planetesimals with diameter greater than 200 km disrupted, few of their fragments survived the dynamical depletion event, explaining the limited presence of iron-rich M-types, olivine-rich A-types and non-Vesta V-types today.

2.2.2 Size Distribution

More than 200 000 Main Belt Asteroids (MBAs) have been discovered. (1) Ceres is the biggest object, about 900 km in diameter, and was the first asteroid to be discovered, in 1801 by Giuseppe Piazzi. (2) Pallas and (4) Vesta are about 500 km in diameter and (10) Hygiea has a diameter of about 400 km.

The number of asteroids increases as their size decreases and their size-frequency distribution is a direct consequence of their collisional evolution (Davis *et al.*, 2002). The largest asteroids are probably primordial objects whose sizes have not been significantly altered by collisions, while the rest are collisionally evolved and their size-frequency distribution can be expressed as a power law. At what size this transition occurs is debated, but it may be ~400 km diameter. An asteroid population in collisional equilibrium should eventually evolve to a size-frequency distribution with a cumulative power law slope index of -2.5 (Dohnanyi, 1969), although the slope index is not exactly this value because Dohnanyi's hypothesis assumes the effects of collisions are independent of the size of the bodies.

2.2.3 Orbital Distribution

Synthetic proper elements (quasi-integrals of motion representing the “average” parameters of motion over very long time spans) of 96944 numbered main belt asteroids calculated by Knezevic and Milani, available from the AstDys webpage (http://hamilton.dm.unipi.it/cgi-bin/astdys/astibo?proper_elements:0;main) are plotted as semimajor axis versus orbital eccentricity (Fig. 2.1). The Kirkwood gaps can be seen, which relate to orbital resonances with Jupiter (Section 2.4.2).

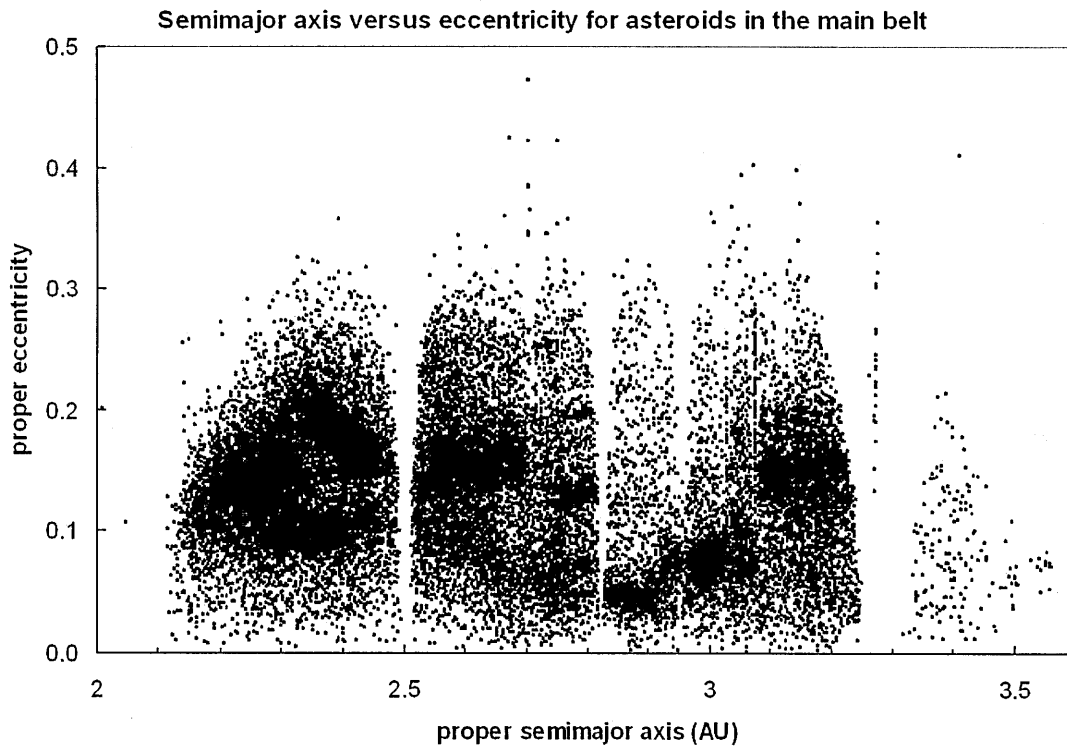


Fig. 2.1 Proper elements semimajor axis vs. eccentricity between 2 and 3.6 AU for 96944 numbered asteroids. The 3:1 mean-motion resonance with Jupiter is at ~ 2.5 AU.

Asteroid families, which can be seen as groupings of objects in Fig. 2.1 (over 60 statistically significant clusters), were first identified by Hirayama (1918). Their likely origin is as the result of catastrophic disruption of a parent body. There are approximately 25 reliable families known. More detail can be found in Zappalà *et al.* (2002) and Bendjoya and Zappalà (2002), and a summary of the results of spectroscopic campaigns to study their physical properties is given in Cellino *et al.* (2002a).

2.3 Asteroid Taxonomy

From visible spectroscopy and/or UBVRI colour photometry two common classes initially emerged. Neutrally coloured asteroids were classified as C-types and more reddish objects as S-types. There is a gradation within the main belt where S-types are more common in the inner belt and C-types in the outer [Gradie and Tedesco (1982), Gradie *et*

al. (1989)]. By 1979, two other major classes were added, E and M, which have similar reflectance and colour features, but different albedos. The letters were chosen for spectral similarities with carbonaceous (C), stony (S), enstatite (E) and metallic (M) meteorites. A major milestone in asteroid taxonomy is the Eight-Color Asteroid Survey [ECAS, Zellner *et al.* (1985)].

Observations obtained by the Infrared Astronomical Satellite derived the albedo of more than 2000 asteroids (Section 2.9.1). C-type asteroids were found to be predominantly dark, in general, with geometric albedos $p_v < 0.10$. S and M-types tend to have intermediate albedos $0.10 < p_v < 0.25$, while E-types have $0.25 < p_v < 0.60$. Zellner (1979) found that C-types dominate over all other types in the Main Belt by as much as 5:1, from a bias correction analysis. Gaffey *et al.* (2002) found that the mineralogy of asteroids across the entire S-class is diverse.

Any quoted taxonomic classes given in this work are from the system defined by Tholen (1984) and extended to include the additional designations developed by Bus (1999), Bus and Binzel (2002) and Bus *et al.* (2002). When NIR spectral data are available such that the S-class subgroups described by Gaffey *et al.* (1993) are determined, taxonomic designations are given in their system.

2.4 Near-Earth Objects

2.4.1 Introduction

A Near-Earth Object (NEO) is defined as an object having a perihelion distance $q \leq 1.3$ AU. The NEO population is composed of near-Earth asteroids (NEAs) and the nuclei of active and extinct comets. They are the precursor bodies for meteorites. If an object does not display any cometary activity, we presuppose it to be an NEA. Only about 50 short-period comets (Marsden and Williams, 1999) have $q \leq 1.3$ AU.

Currently, most groundbased observatories are incapable of measuring the detailed physical properties of MBAs at small (<5-10 km) sizes. However, NEAs can serve as a proxy for the small MBA population. There is evidence that the physical properties of NEAs and MBAs at similar sizes may be comparable. For example, Binzel *et al.* (2002) find that both reduced-lightcurve amplitudes and rotation rates are statistically indistinguishable between NEAs and MBAs below 12 km diameter. Davis *et al.* (2002) find that NEAs originating from the main belt are almost certainly at least second generation fragments resulting from catastrophic disruption of once-larger parent bodies, and so their shapes and rotations have been reworked throughout the lifetime of the Solar System. However, the crater statistics on Eros from the NEAR Shoemaker mission (Veeverka *et al.*, 2000) suggest that Eros has become effectively decoupled from the collisional environment of the Main Belt (Michel *et al.*, 1998). Therefore their shapes may be representative of MBAs at similar diameters.

The largest NEA is (1036) Ganymed, with an equivalent spherical diameter of 39 km. The second largest NEA is (433) Eros, with the approximate dimensions of a triaxial ellipsoid $13 \times 13 \times 33$ km, measured by the NEAR Shoemaker spacecraft.

Previous reviews on the physical properties of NEOs can be found in McFadden *et al.* (1989), Lupishko and Di Martino (1998), and the most recent in Binzel *et al.* (2002). An excellent updated version of the table of physical properties of NEOs given in Binzel *et al.* (2002) can be found at the European Asteroid Research Node (EARN): <http://earn.dlr.de/nea>.

2.4.2 Origin and Evolution

Since the immediate precursor bodies for meteorites are NEOs, if we can identify the sources for NEOs we can find the origin locations for meteorites. A recent detailed

summary of research on the origin and evolution of NEOs can be found in Morbidelli *et al.* (2002).

Dynamical lifetimes for NEOs are typically a few million years according to dynamical calculations (Bottke *et al.*, 2002b). Their fate is either to be ejected from the Solar System, crash into the Sun, or impact a terrestrial world. Therefore there must be sources of resupply that account for the present population.

Resonances, principally with Jupiter, can increase an asteroid's eccentricity and/or inclination so that it becomes planet-crossing. This is responsible for the gaps seen in Fig. 2.1. The ν_6 secular resonance, which lies along the inner edge of the main belt, and the 3:1 mean-motion resonance at ~ 2.5 AU, are thought to be the primary sources, with the mean time spent in the NEO region being 6.5 and 2.2 Myr respectively (Bottke *et al.*, 2002a). Other mean-motion resonances, thought to be less important sources, are 5:2 and 2:1. Chaotic diffusion drives about two asteroids larger than 5 km into the Mars-crossing region every million years (Morbidelli and Nesvorný, 1999). The main population below the ν_6 secular resonance randomly changes semimajor axis as a result of Martian encounters until they enter a resonance that is strong enough to further decrease their perihelion distance to less than 1.3 AU. Asteroids are driven into resonances from a combination of collisional evolution (catastrophic disruption or a cratering event) and the Yarkovsky effect (Section 2.7).

Comets are thought to be significant contributors to the NEO population although there is some uncertainty as to their proportion. Comets from the Kuiper Belt, including the Jupiter Family Comets, are one source. Short-period comets represent about $\sim 2\%$ of the known NEO population. Comets from the Oort cloud, including long period comets, have recently been estimated to only contribute $\sim 1\%$ of the impact hazard [Morbidelli *et al.* (2002) and references therein]. Binzel *et al.* (2002) suggest that the sum of evidence is that

comets contribute at most a few percent of the total NEO population. It is not known what fraction of NEOs that do not display a coma are extinct or dormant comet nuclei.

2.4.3 *Orbital Subcategories*

Subcategories defined by orbits, with reference to the Earth's orbit ($Q = 0.983$ AU and $q = 1.0167$ AU) are: Apollos ($a \geq 1.0$ AU, $q \leq 1.0167$ AU), Atens ($a < 1.0$ AU, $Q \geq 0.983$ AU) and Amors (1.0167 AU $< q \leq 1.3$ AU) (Shoemaker *et al.*, 1979). Amors are bodies residing just outside the orbit of Earth, Apollos and Atens are Earth-crossing asteroids, with Atens having orbits substantially inside that of Earth. Additionally there is a population inside the Earth's orbit ($Q < 0.983$ AU) called Inner-Earth Objects (IEOs) of which two have recently been discovered (2003 CP₂₀ and 2004 JG₆).

Amors and Apollos account for ~90% of currently known NEOs and roughly equal numbers have been found. Atens represent ~8% of the known NEO population. Michel *et al.* (2000) estimate that the IEO abundance is half that of the Atens.

It is possible for an NEA to move between classes since they are based on osculating orbital elements. Milani *et al.* (1989) proposed a classification indicative of long-term behaviour after studying the orbital evolution of 89 NEAs over a time span of 2×10^5 years, proposing six dynamical classes, named after the best-known and most representative object in each class: Geographos, Toro, Alinda, Kozai, Oljato and Eros.

2.4.4 *Taxonomy*

Almost all classes found in the main belt are found in the NEO population. The majority of NEAs *discovered* are S-type (~4:1). This implicates the inner belt as the main source of NEAs, even if we account for the bias factors in favour of the discovery and characterization of the higher-albedo S-type relative to C-type. Also, the decrease in

apparent brightness of the darker C-types as a function of phase angle is stronger than for S-types and NEAs are often observed at large phase angles. Luu and Jewitt (1989) used a Monte Carlo model to estimate the bias factor to be in the range of 5:1 to 6:1. Figure 2.2, using data from Stuart and Binzel (2004) (see also Section 2.4.7), shows de-biased diameter-limited fractional abundances of taxonomic complexes in NEAs. They are: A = 0.2%, C = 10%, D = 17%, O = 0.5%, Q = 14%, R = 0.1%, S = 22%, U = 0.4%, V = 1%, and X = 30%. The X-type is degenerate into E-, M-, and P-types depending on the asteroid's albedo; the large percentage of this type highlights the need for further albedo measurements of NEAs (Section 2.10).

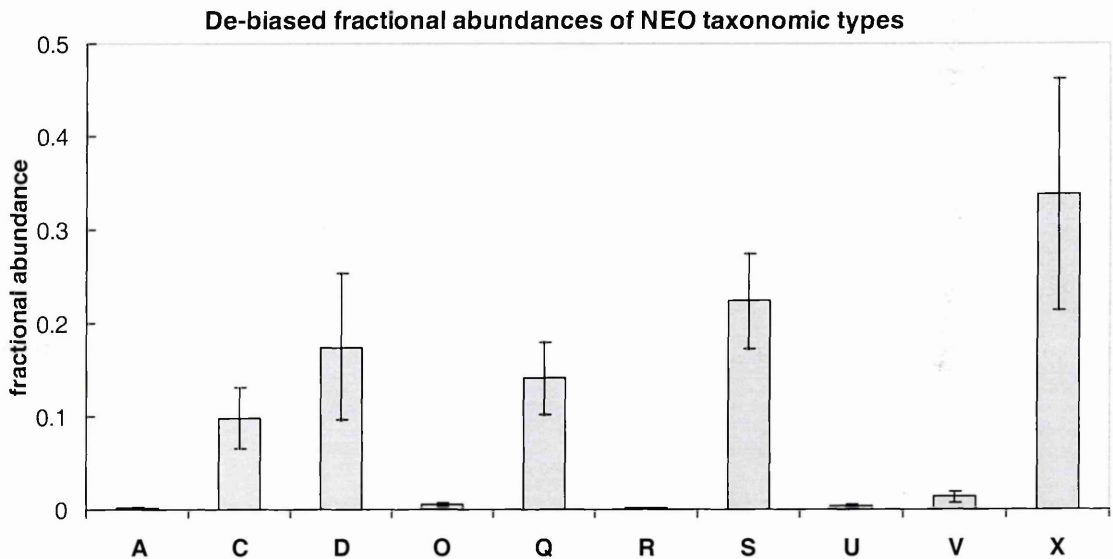


Fig. 2.2 Diameter-limited fractional abundances of NEO taxonomic types, based on data from Stuart and Binzel (2004).

D- and P-types are most common in the outer asteroid belt among the Hilda and Trojan asteroids and possibly among comet nuclei. M-types and highly differentiated olivine-rich A-types are rare. M-types have been found, e.g. (6178) 1986 DA (Ostro *et al.*, 1991), which was confirmed to be metallic from its extremely high radar albedo.

2.4.5 Links to Meteorite Parent Bodies

Links have been found between meteoritic and asteroidal taxonomic classes, tied specifically to main-belt sources. An example is E-type (3103) Eger: Gaffey *et al.* (1992) found it appeared both compositionally and dynamically related to the Hungaria family (high-inclination objects) in the inner asteroid belt and may be a source of enstatite achondrite meteorites. Cruikshank *et al.* (1991) found V-type NEAs with spectral matches to Vesta and the basaltic HED (howardite-eucrite-diogenite) meteorites.

The most common type of meteorite is the ordinary chondrite (OC) which represent ~80% (by fall statistics) of all meteorites. The Q-type asteroids have spectra most similar to laboratory spectra of ordinary chondrite meteorites [McFadden *et al.* (1984), Bus *et al.* (2002)] but only ~20% of all observed NEOs are Q-type. Clark *et al.* (2002) outline the argument that S-type asteroids are the parent bodies of ordinary chondrites. There has been observed a continuous distribution of spectral properties ranging from the spectral signature common to S-type asteroids to that of ordinary chondrites as size decreases, appearing to show a transition between S-type asteroids and OC meteorites. Space weathering, the aging of the asteroid surface due to its exposure to the space environment, would modify the reflectance spectra of fresh material to be redder, straighter, and have shallower absorption bands. It would convert the spectra of Q-type to S-type asteroids, that presumably have an older surface. Survival lifetimes against catastrophic disruption (Davis *et al.*, 2002) decrease with decreasing size. Thus, on average, as we examine smaller and smaller objects, we see younger and younger surfaces. Also, Delbó *et al.* (2003) find a trend of increasing albedo with decreasing size for S-type NEAs (Section 5.8.1). Elemental abundance measurements of S-type Eros made by the NEAR Shoemaker spacecraft [Trombka *et al.* (2000), McCoy *et al.* (2001), Cheng (2002)] found that it has almost the same elemental abundance as OC meteorites. There is evidence that does not fit this theory

though: for example Pravec *et al.* (2000a) have some spectra that suggest there are S-types among the monolithic fast-rotating asteroids, and some 5 km NEAs (with 0.5-1.0 Gyr collisional lifetimes) are Q-types.

2.4.6 Radar

NEAs are excellent targets for radar by virtue of their proximity and have been extensively observed, as described by Ostro *et al.* (2002). A model of an asteroid's shape can be determined, e.g. (6489) Golevka (Hudson *et al.*, 2000). Resolutions can be down to 10s of metres, although physical interpretation of delay-Doppler projection is complicated by “north-south ambiguity” where many points on the surface can contribute to one point on an image. Binary NEAs have also been discovered by radar (Section 2.8).

The surface roughness of an NEA can be estimated at the centimetre scale by measuring the total echo power in the two opposite circular polarizations. A large range of polarization ratios have been measured, varying from one [extremely rough, e.g. (2101) Adonis, 1992 QN, Benner *et al.* (1997)] to near zero [smooth surface, e.g. M-type (6178) 1986 DA, Ostro *et al.* (1991)].

2.4.7 Bias-corrected Population and Size Distribution

Stuart and Binzel (2004) have modelled the bias-corrected population and size distribution of NEOs, using: (i) the taxonomic distribution as measured by observational sampling (Binzel *et al.*, 2004), (ii) applied albedos associated with the taxonomic classes, (iii) observed orbital distributions and number of objects provided by the LINEAR survey [Stokes *et al.* (2000), Stuart (2001)]. The albedos came from a thermal IR radiometry program from observations at the Keck telescope, reported and combined with previous thermal IR observations of NEAs, by Delbó *et al.* (2003).

The result is a similar, but slightly updated, size distribution to that given in Fig. 2.4 (Section 2.6). The number of albedos have been increased since by Delbó (2004) (but not used by Stuart and Binzel) and the radiometry results reported in this thesis add to the gradually growing list of NEAs with measured albedos. As their number increases, the size distribution of NEAs can be further refined (Section 2.10). The bias-corrected mean geometric albedo for the NEO population is 0.14 ± 0.02 , so an asteroid of 1 km diameter would on average have an absolute magnitude $H = 17.8 \pm 0.1$, yielding 1090 ± 180 NEOs with diameters larger than 1 km.

2.5 Asteroid Rotations

The accumulation of statistics on asteroid rotations can allow us to make deductions about their physical properties and their collisional evolution. A recent review of asteroid rotations is given by Pravec *et al.* (2002b), which we summarise below.

For asteroids with diameter $D > 40$ km the distribution is close to Maxwellian, suggesting that they are collisionally evolved remnants of the original bodies of the Main Belt (Pravec and Harris, 2000). The distribution of rotation rates of NEAs and MBAs with $D < 40$ km is non-Maxwellian. For $10 < D < 40$ km the mean spin rate sharply increases as D decreases.

At $0.15 < D < 10$ km there are excesses at both slow (geometric mean spin rate $f \leq 0.8$ d⁻¹) and fast ($f \geq 7$ d⁻¹) rotations (Pravec and Harris, 2000). The cause of the fast rotation excess is not quantitatively understood. It could be a result of anisotropic thermal emission from the YORP effect (Section 2.7) or tidal forces during planetary encounters in the case of planet-crossing asteroids [Scheeres *et al.* (2000), Richardson *et al.* (1998)]. Many of the fast rotators are binary NEAs and the fast rotation is probably a clue to the mechanism of their formation (Section 2.8). It is not clear what is responsible for the slow rotation excess

although Harris (2002) hypothesises that they result from disintegration of high mass ratio (~1:5) binaries through the rapid transfer of rotational energy of the primary into the orbit of the secondary due to the irregular gravity field of the primary.

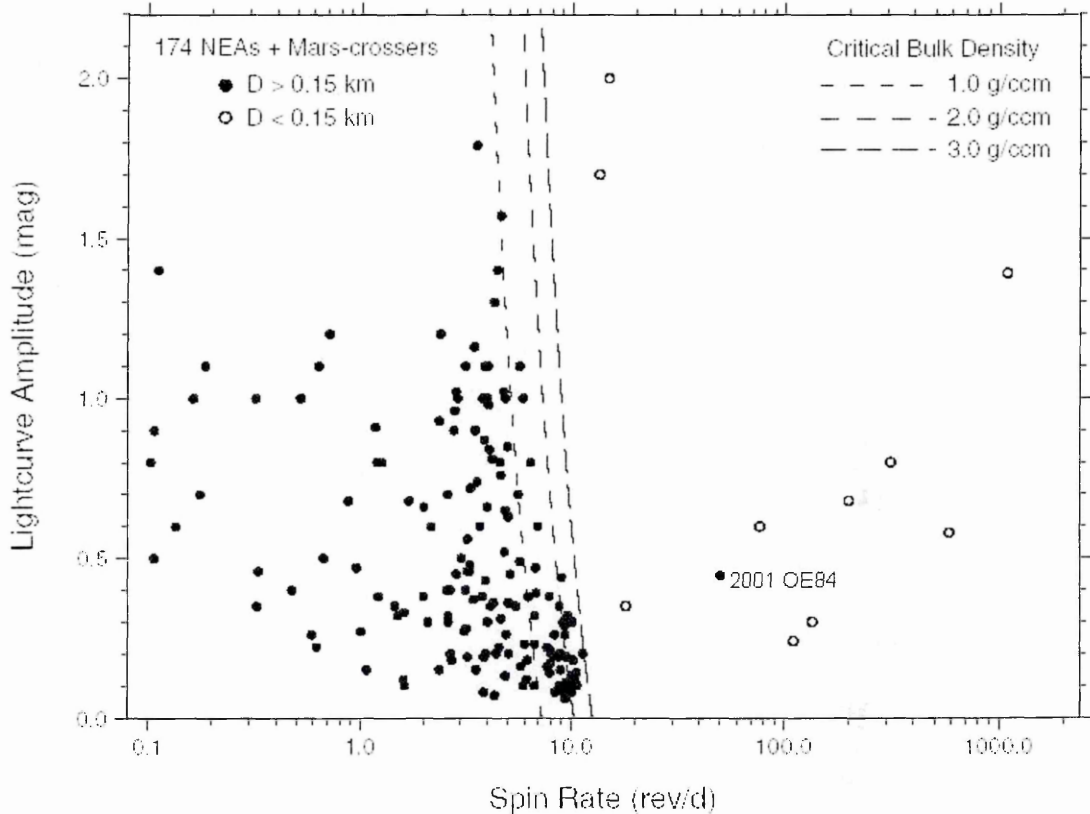


Fig. 2.3 The observed lightcurve amplitude vs. spin rate of near-Earth and Mars-crossing asteroids, reproduced from Pravec *et al.* (2002), with 2001 OE₈₄ added using the average of the lightcurve amplitudes given at <http://earn.dlr.de/nea>. The dashed curves are the approximate upper limits of spin rates of bodies held together by self-gravitation only.

In Fig. 2.3 we can see there is a “barrier” against spins faster than ~12 rotations per day and for the fastest rotators with $f > 6 \text{ d}^{-1}$ there is a trend of more spheroidal shape with increasing spin rate. This is evidence that most asteroids in this size range have negligible tensile strength and are loosely bound, gravity-dominated aggregates [“rubble-pile” or shattered interior bodies (Richardson *et al.*, 2002)], with bulk density greater than $\sim 2.5 \text{ g/cm}^3$ [Harris (1996), Pravec and Harris (2000)]. Their shattered structures are probably the result of collisions, either on themselves or their parent body (e.g. Love and

Ahrens, 1996) and they mostly gained angular momentum through collisions. There are rare asteroids that break the barrier; for example 2001 OE₈₄ has a period of 29.19 min and $D \sim 0.9$ km (Pravec and Kušnirák, 2001).

Asteroids smaller than ~ 0.15 km (absolute magnitude $H > 22$) are rotating so fast they must be coherent bodies and cannot be held together by self-gravitation. Most have periods less than 2 h. They are presumably fragments derived from catastrophic disruption of larger parent bodies. They are sometimes called “monoliths”, although their tensile strength can be very small; e.g. for the fastest known rotator 2000 DO₈ (period of 1.30 min, long axis ~ 80 m) the minimum required tensile strength is 2×10^4 Pa, $\sim 10^{-3}$ less than that of well-consolidated rock (Ostro *et al.*, 1999). The sharp transition seen in Fig. 2.3 is very distinctive. Pravec *et al.* (2000a) propose that it corresponds to the size limit of monolithic fragments from the catastrophic disruption of larger asteroids.

Asteroid lightcurves can be used to find possible candidates for extinct comets. Comets typically have axial ratios that correspond to lightcurve amplitudes 0.5-1.0 mag. [Hartmann and Tholen (1990), Luu (1994), Nelson *et al.* (2001)], while the average NEA amplitude is 0.29 mag. (Binzel *et al.*, 2002). Also, Binzel *et al.* (1992) find that slower rotations might also indicate cometary NEOs.

2.6 Impacts and NEA Search Programs

An understanding of the orbits, size distribution and physical properties of NEOs is desirable for social reasons beyond scientific curiosity: Earth-crossing asteroids (ECAs) and comets are an impact threat. NEOs are unique among natural hazards in that they have the potential for severe global consequences. Chapman and Morrison (1994) defined the threshold for a global disaster as an environmental catastrophe capable of killing 25% of the world's population. Therefore the risk ECAs present is comparable to other hazards

(e.g. volcanism) despite the lower probability of an impact. The impact hazard is calculated by combining the flux of impactors, calculated from the known size distribution of NEAs (Section 2.4.7), with the damage caused by each impact. Figure 2.4 shows the correspondence with estimates of the numbers of NEAs from various ongoing surveys with diameter (D), absolute magnitude (H), impact interval and impact energy. The greatest contemporary hazard is associated with impactors near 10^6 MT energy.

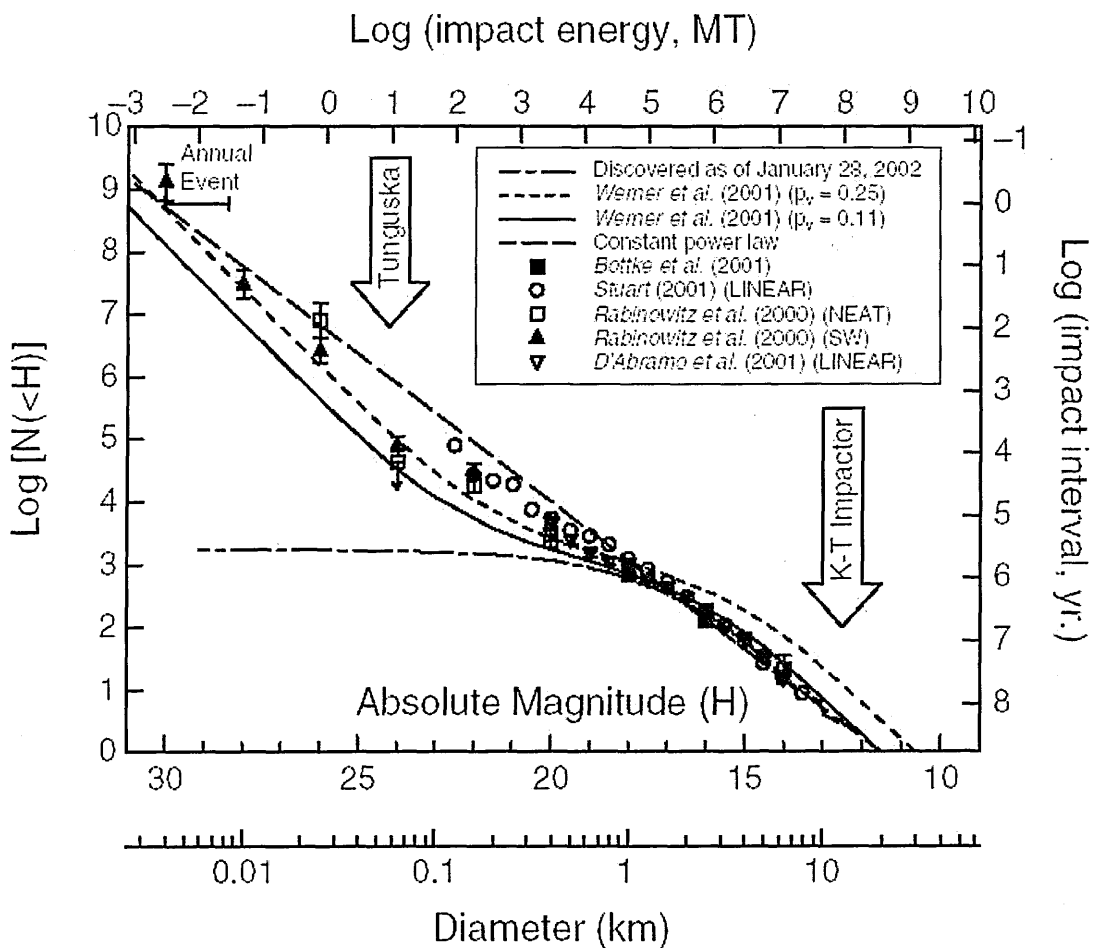


Fig. 2.4 Cumulative population of NEAs vs. absolute magnitude from various surveys [LINEAR: Stuart (2001); D'Abramo et al.(2001), NEAT, Spacewatch: Rabinowitz et al. (2000), estimated from the lunar mare crater size-frequency distribution (Werner et al., 2002), and from Bottke et al. (2002a)] with equivalent scales for diameter, impact energy, and average impact interval, reproduced from Morrison et al. (2002). The current observed rate of atmospheric impacts is plotted on the top left, and the energies of the Tunguska and K/T impacts are also indicated. The straight line is a power law that approximates the data.

A strong body of evidence exists that an impact of a 10-15 km diameter object 65 million years ago caused a mass extinction that eliminated the dinosaurs. Alvarez *et al.* (1980) inferred an impact from an Ir-enriched layer found worldwide at the Cretaceous/Tertiary (K/T) boundary, and the hypothesis was generally accepted after the identification of the Chicxulub crater [Swisher *et al.* (1992), Sharpton *et al.* (1992)]. There is increasing evidence that other extinction events were also caused by impacts, e.g. the Permian/Triassic (Becker *et al.*, 2001). However, the Ir-enriched layer is lacking at other extinction boundaries.

The energy of the K/T impact is estimated at 10^8 MT from the size of the crater. Toon *et al.* (1997) discuss the environmental effects of impacts. Since the impact occurred in a shallow sea, there were tsunamis accompanied by an initial blast. But the global effects were from a short-lived firestorm caused by the atmospheric heating of re-entering ejecta (Melosh *et al.*, 1990) and a blackout due to dust loading of the atmosphere. Toon *et al.* calculated that global dust loading occurs near 10^6 MT, although Pope (2002) has questioned the assumptions that have generally been made concerning the quantity of dust released into the stratosphere. Consequently, the threshold diameter of an asteroid that can cause a global disaster ranges from 1-4 km. Stuart and Binzel (2004) estimate that collisions of asteroids with $D > 1\text{km}$ occur every 0.60 ± 0.1 Myr on average.

In 1908, there was an impact in the Tunguska region of Siberia, estimated as having a 10-15 MT energy (~60 m diameter) when it exploded ~8 km above the ground. Numerical modelling (e.g. Chyba *et al.*, 1993) of the entry physics has shown the impactor must have been of asteroidal density to penetrate the troposphere. The Tunguska impactor is near the threshold for the atmospheric penetration of the blast effects of impacts. Stuart and Binzel (2004) estimate collisions of Tunguska scales occur every 2000-3000 years, making it a remarkable event.

At size ranges of several 100 m diameter, oceanic impacts dominate the hazard due to the generation of tsunami waves that can carry the impact energy efficiently to great distances and the concentration of human habitation near shore lines. Stuart and Binzel (2004) estimate that these regionally destructive collisions (~200 m) occur every $56\,000 \pm 6000$ yr.

The historical impact flux can be estimated by studying lunar cratering statistics. After the high flux during planetary accretion there was a general decline for the following 0.5 Gyr followed by the ~100 Myr Late Heavy Bombardment ending about 3.85 Gyr ago. Since this time, the impact rate has been lower and fairly constant, to a factor of four (Culler *et al.*, 2000), with a decrease followed by an increase in the last few hundred million years. Any possible comet showers are in little evidence, and cannot have made a large contribution.

To effectively reduce the risk by discovering and characterizing the orbit of NEAs, the Spaceguard Survey has been designed to fulfil NASA's goal of discovering 90% of NEAs greater than 1 km diameter by 2008. David Morrison's August 2005 NEO newsletter (<http://impact.arc.nasa.gov/>) assesses the progress made. Recently, the number of NEAs with $D > 1$ km ($H > 18$) discovered has started to decrease as the number left to find is reduced; since 2000 the annual totals are: 131, 91, 101, 69 and 57. As of 8 August 2005, the total number of NEOs found above this threshold is 793 (<http://neo.jpl.nasa.gov/>), while the consensus figure for the total number is about 1100, representing 73% completeness.

NEOs found on a final approach with a lead time of weeks before impact, beloved of Hollywood movies, are unlikely. A typical pattern upon discovery of a Potentially Hazardous Asteroid (PHA) is a variation (often an increase) in the probability of impact as the orbit is refined, before the probability becomes zero as Earth leaves the range of

“virtual impactors”. Any potential impactor would probably be found decades in advance. An extraordinary test case is 2004 MN₄, recently named (99942) Apophis. It has a 1 in 8000 chance of striking the Earth in 2036 depending on whether it passes through a particular “keyhole” in 2029 (when it will come within 5.7 ± 1 Earth radii). Chesley (2005) assessed the danger. Such a large asteroid (~300 m) coming this close to the Earth happens every 1500 years. Its orbit can be refined when it makes close passes in 2006 and 2013, but there will still be uncertainty due to the need to assess the Yarkovsky effect on the asteroid, which depends on its thermal inertia, shape, and rotation rate (Section 2.7), that will only be resolved in a close pass in 2021. There has been some question as to whether that would be enough lead time to prepare a mitigation mission, and whether a mission to place a radio transponder on the asteroid is required. The 2029 encounter will be a unique opportunity to study the possible abrupt alteration of Apophis’ spin state (Scheeres *et al.*, 2005).

2.7 The Yarkovsky Effect and NEA Thermal Inertias

The Yarkovsky effect is described in detail by Bottke *et al.* (2002b) and references therein, which we partly summarise here. Until recently, the “classical” asteroid evolution model held collisions and gravitational forces to be dominant. Several inconsistencies with this model and observations have become apparent, chief among these is that meteorite cosmic-ray exposure (CRE) ages less than 10 Myr are relatively rare, while the dynamical lifetimes of bodies placed in powerful resonances are a few million years. Ivan Yarkovsky noted in a pamphlet written around 1900 that the diurnal heating of a rotating object in space would cause it to experience a tiny force. Fig. 2.5 (a) shows a spherical asteroid orbiting the sun. Insolation heats up the sunward side, and the heat is reradiated into space, generally in the infrared. Because more energy and therefore more momentum (because

photons carry momentum) leaves the hotter part of the asteroid than the cooler, there is a net force in the direction away from the hotter side. Since the body has thermal inertia, there is a delay in the emission so that the afternoon side is warmer than the morning side and consequently the force not only has a component that points radially outward from the Sun, but also an along-track component. If the asteroid has a prograde rotation, this component causes a secular increase in the semimajor axis of the asteroid, while if it is retrograde there is a decrease. The magnitude of the diurnal effect depends on Sun-asteroid distance, the subsolar latitude, the size, shape, rotation rate, and surface thermal inertia.

There is also a seasonal Yarkovsky effect [Fig. 2.5 (b)]. In this case the spin axis lies in the orbital plane. When the asteroid is at A, the Sun shines most strongly on its northern hemisphere. Again there is a delay due to thermal inertia, so that the northern hemisphere is hottest at B. In the other half of the orbit, the Sun shines most strongly at C, but the southern hemisphere is hottest at D. For small orbital eccentricities, the seasonal force causes orbital decay, and it tends to circularise the orbit.

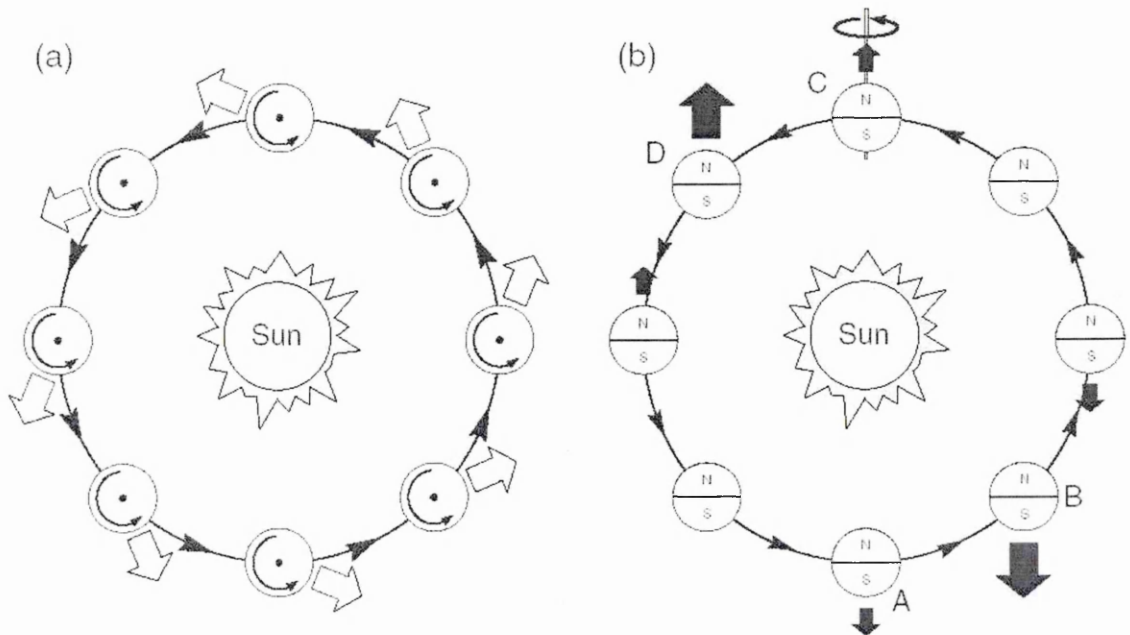


Fig. 2.5 Reproduced from (Bottke et al., 2002b). (a) The diurnal Yarkovsky effect; (b) The seasonal Yarkovsky effect.

Additionally, the Yarkovsky-O'Keefe-Radzievskii-Raddack (YORP) effect produces torques that affect the spin rate and spin axis orientation of asteroids (Rubincam, 2000). An object must have a "windmill" asymmetry for YORP to work (e.g. it has no effect on triaxial ellipsoids). The YORP effect can alter the obliquity, such that the axial torque changes sign and the object begins to spin down instead of spin up (and visa versa). YORP is strongly dependent on shape, size, distance from the Sun. Bottke *et al.* (2002b) estimate that (951) Gaspra, with $D = 12$ km and semimajor axis $a = 2.21$ AU, would go from a rotation period $P = 12$ h to 16 h in 240 million years. An observational programme to directly detect the YORP effect in the rotation of NEA 2000 PH₅ has been undertaken by Fitzsimmons (2004) and colleagues.

Farinella *et al.* (1998) realised that the Yarkovsky effect solves the CRE problem, since it is capable of slowly delivering material to powerful resonances inside the main belt, increasing the cosmic-ray exposure. Vokrouhlický and Farinella (2000) found that a combination of collisional dynamics and Yarkovsky drift is enough to efficiently supply the 3:1 and ν_6 resonances with small asteroid fragments from nearly all locations in the inner and central main belt. The semimajor axis drift is negligible for very large asteroids, but the Yarkovsky effect has a significant enough effect (relative to an asteroid's dynamical lifetime before catastrophic disruption) to deliver asteroids with $D < \sim 20$ km (Farinella and Vokrouhlický, 1999) from their parent bodies in the main belt to chaotic resonance zones capable of transferring them into Earth-crossing orbits (Section 2.4.2). Bottke *et al.* (2002a) estimate that the Yarkovsky effect causes ~ 220 asteroids with $D > 1$ km every million years to become Earth-crossing, implying that the Yarkovsky effect, rather than collisional injection, is the dominant mechanism pushing material into resonances.

To estimate the extent of the Yarkovsky effect it is crucial to have a reliable estimate of the surface thermal inertia (Γ). Farinella and Vokrouhlický (1999) calculated the average semimajor axis displacement of main belt asteroids caused by the Yarkovsky effect before undergoing catastrophic disruption (Fig. 2.6). It can be seen that it depends strongly on the surface conductivity K ($\Gamma = \sqrt{K\rho c}$, ρ = density, c = specific heat capacity), which is unknown for main belt asteroids, generally. Thermal radiometry can be used to measure Γ . Section 4.3.4 describes how fitting the Near-Earth Asteroid Thermal Model (NEATM) to thermal IR fluxes provides a measurement of the “beaming parameter” η . Spencer *et al.* (1989) found that there is a relationship between the thermal parameter Θ (Section 6.1) and η , using a simple thermophysical model (similar to that described in Section 4.3.1) assuming the asteroid is spherical and the subsolar latitude is 0° . Harris and Davies (1999) used Spencer *et al.*'s Fig. 3 to estimate Γ for (433) Eros, and found $\Gamma = 180 \text{ J m}^{-2} \text{ K}^{-1} \text{ s}^{-1/2}$ (all subsequent values are in these units) assuming the surface roughness. In my opinion, the combined effect of disregarding the asteroid's shape, pole orientation, and estimating the surface roughness, makes the resulting Γ too imprecise to be of value, and so thermal inertias are not generally reported for the asteroids observed in this thesis. In the case of Harris and Davies (1999), the problems are mitigated by Eros having a similar geometry to Spencer *et al.*'s example.

Recently however, more sophisticated thermophysical models have been applied to NEAs, modelling their known shapes and pole orientations. Mueller *et al.* (2005) found $\Gamma = 150$ for (433) Eros and $\Gamma = 350$ for (25143) Itokawa. Harris *et al.* (2005) measured $\Gamma = 180$ for (1580) Betulia and Harris *et al.* (in prep., 2006) determined $\Gamma = 150$ for (33342) 1998 WT₂₄. Thus, the average NEA surface thermal inertia appears to be considerably greater than that of (large) Main Belt asteroids: Müller and Lagerros (1998) obtained $\Gamma = 5\text{-}25$ for five MBAs using the Infrared Space Observatory (Section 2.9.1).

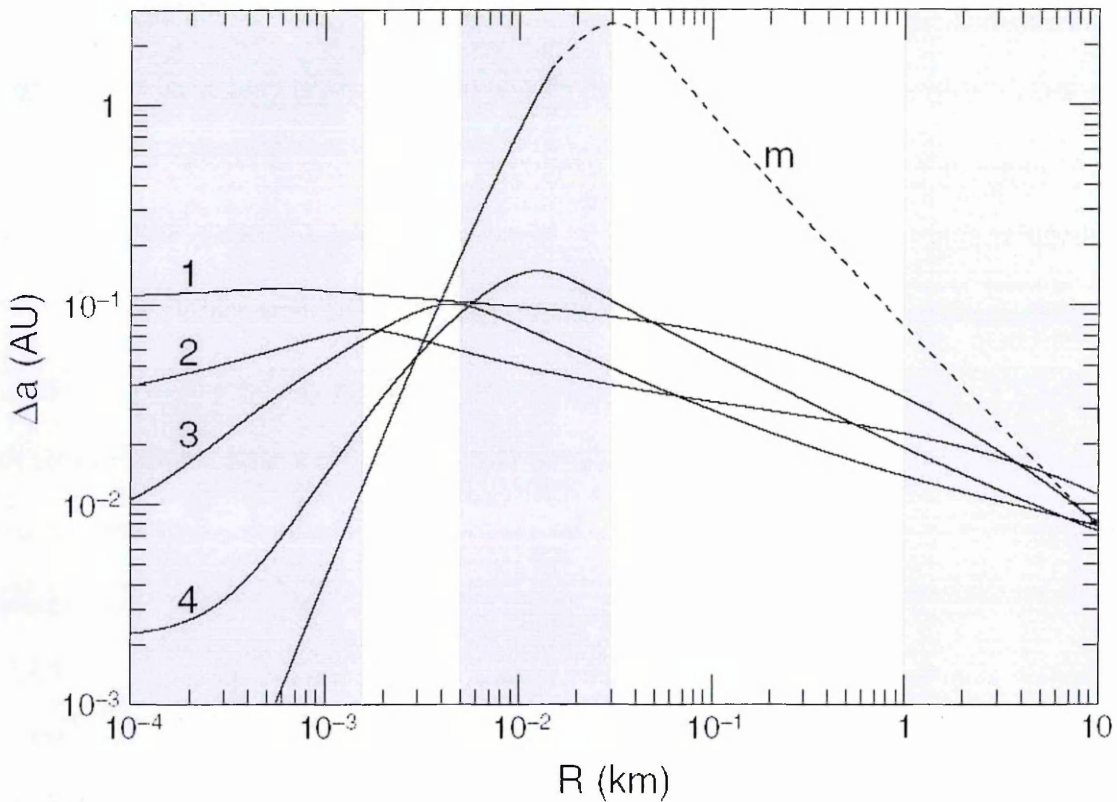


Fig. 2.6 Mean change in semimajor axis Δa of inner main belt asteroids over their collisional lifetimes vs. their radius, for different surface thermal conductivity K , reproduced from Bottke et al (2002b). Curves (1) $K = 0.002 \text{ W m}^{-1} \text{ K}^{-1}$; (2) $K = 0.02 \text{ W m}^{-2} \text{ K}^{-1}$; (3) $K = 0.2 \text{ W m}^{-2} \text{ K}^{-1}$; (4) $K = 2 \text{ W m}^{-2} \text{ K}^{-1}$ and (m) (for metal-rich) $K = 40 \text{ W m}^{-1} \text{ K}^{-1}$.

Delbó (2004) estimated that the average surface thermal inertia for NEAs was $\Gamma = 550$, using a complicated method summarised in Section 6.1.1. For an NEA with $D = 200$ m and rotation period = 5 h, at 2 AU from the Sun, Delbó estimated that the semimajor axis drift from the Yarkovsky effect is 9×10^{-4} AU/Myr.

2.8 Binary Asteroids and Asteroid Densities

The Galileo spacecraft made the first confirmed detection of an asteroid moon in 1993, discovering 1.4 km diameter Dactyl, orbiting the 31 km S-type MBA (243) Ida. The discovery rate has accelerated. As of 10 August 2005, 63 binaries have been found (<http://www.johnstonsarchive.net/astro/asteroidmoons.html>), inhabiting a variety of

dynamical populations: 24 NEAs, 23 MBAs, 1 Trojan, and 15 TNOs. Main belt and TNO binaries have been discovered because of advances in adaptive-optics telescopes and from space-based observations. Merline *et al.* (2000) discovered the first double asteroid (90) Antiope with components of nearly the same size. Recently, the first triple (main belt) asteroid has been discovered: (87) Sylvia, with its two satellites Romulus and Remus (Marchis *et al.*, 2005). A review of asteroid binaries can be found in Merline *et al.* (2002).

It is estimated that ~16% of NEAs are binaries [Pravec *et al.* (1999), Margot *et al.* (2002), Bottke and Melosh (1996a, b)] They are mostly discovered from lightcurve and radar observations. Pravec and Hahn (1997) interpret the two-period lightcurve of 1994 AW₁ as a probable binary, using a technique based on detecting brightness attenuations caused by mutual occultations/eclipses between components of the binary system superposed on the rotational lightcurve of the primary. The technique can detect binaries where the primary has an asynchronous rotation relative to the orbital period of the satellite; i.e. occultation/eclipse events occur with a different period from the rotation of the primary, hence they can be distinguished from any possible shape features. There are selection biases: the detection of close binaries is favoured, and satellites smaller than ~20% of the primary diameter are hard to detect because the brightness attenuation is less than ~0.04 mag., difficult to distinguish from changing lightcurve characteristics in different geometric conditions, for example.

The first NEA binary definitively discovered by radar is 2000 DP₁₀₇ [Ostro *et al.* (2000), Margot *et al.* (2000)]. Two distinct components are easily discriminated in delay-Doppler images and both the primary and secondary are typically resolved in range and Doppler. Most radar-observed binaries share similar characteristics: roughly spheroidal with periods near the breakup limit, secondaries with diameters roughly one-third the diameter of the primary and orbiting at a distance of a few primary radii.

The abundance of NEA binaries and the fact that half of NEA fast-rotators are thought to be binaries (Section 2.5) can be explained by the mechanism of tidal disruption [Bottke and Melosh (1996a, b)] during a close planetary encounter. The tidal disruption of ellipsoidal shattered-interior bodies (composed of equally sized chunks) was modelled by Richardson *et al.* (1998), who found that rotational spin-up causes them to shed mass, and that often the shed fragments go into orbit around the progenitor, although the secondaries were usually a lot smaller than the primary. Other possible binary asteroid creation mechanisms are reviewed in Weidenschilling *et al.* (1989) and Merline *et al.* (2002).

The detection of binary asteroids allows the precise determination of the total mass of the system, i.e. the primary and secondary bodies, from which the bulk density can be estimated. Uncertainties in the asteroids' sizes generally dominates the uncertainty in the determination of the bulk density. Therefore any improvements in the estimation of the primary's and secondary's diameter, such as from thermal radiometry (which will measure the albedo and hence the diameters of both bodies can be inferred from the ratio of their brightness), will potentially improve measurements of the bulk density. Most asteroids appear to have bulk densities well below the grain density of their likely meteorite analogues (Britt *et al.*, 2002).

2.9 Spacecraft Exploration of Asteroids

Preparatory groundbased observations are important before sending a spacecraft to an asteroid. Thermal IR radiometry can supply an asteroid's diameter, from which its mass can be more accurately estimated, providing engineers with the most likely local gravity field conditions. Optical observations can provide an asteroid's rotation rate, pole orientation and a model of its shape (Kaasalainen *et al.*, 2002), if it has been thoroughly observed at several oppositions. From these, mission parameters, such as the best orbit for

obtaining data most efficiently, can be carefully planned. Since space missions can only realistically visit a tiny fraction of the asteroids, groundbased observations are needed to put the results into context. For example, do the diameters and albedos derived using simple thermal models on groundbased observations correspond with those obtained by spacecraft? Reviews of the past, current and planned space missions are given by Farquhar *et al.* (2002) and Shevchenko and Mohamed (2005), who also review space observatories.

2.9.1 *Space Telescopes*

The first observations of asteroids from space were made by the US in 1971 using the Orbital Astronomical Observatory 2 (Caldwell, 1975). It observed the three largest main belt asteroids (1) Ceres, (2) Pallas and (4) Vesta, determining their UV albedos.

The Infrared Astronomical Satellite (IRAS) observed 3453 asteroids in 1983, enabling the diameters and albedos of 2228 asteroids to be determined (Tedesco *et al.*, 2002b) using the Standard Thermal Model (Section 4.3.2). It is the most extensive dataset of diameters and albedos available. A histogram showing the distribution of asteroid albedos is given in Fig. 2.7. Gaffey (1989) showed that the 12/25 μm flux ratios of S and M asteroids are systematically higher than for other types, but S and M-types cannot be distinguished from this ratio alone. Green *et al.* (1985a) used IRAS to search for fast-moving NEOs, discovering several comets and Apollo asteroids and measuring their diameters and albedos, including the unusual extinct cometary candidate (3200) Phaethon (Green *et al.*, 1985b).

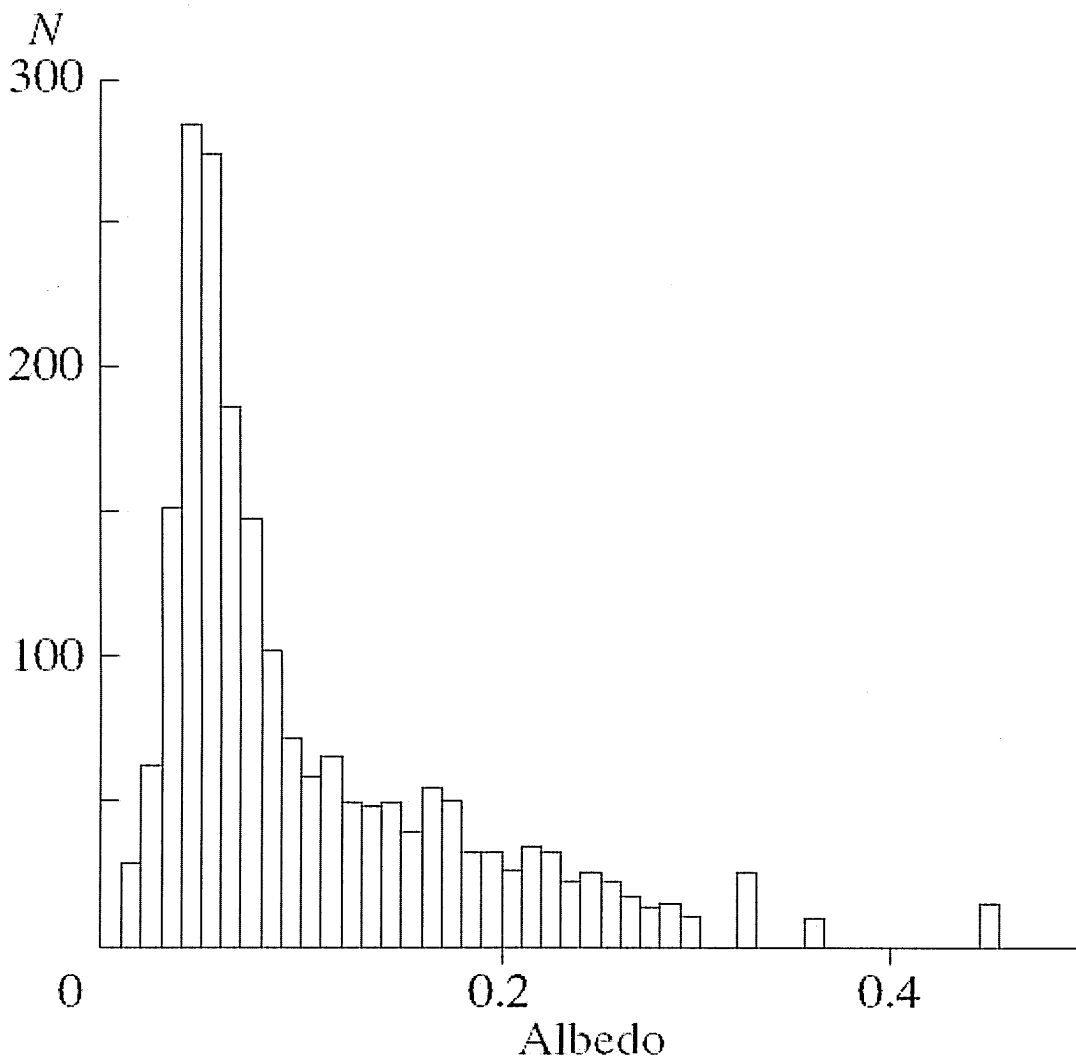


Fig. 2.7 Histogram showing the distribution of asteroid albedos from IRAS data (Tedesco *et al.*, 2002b), reproduced from Shevchenko and Mohamed (2005).

The Hubble Space Telescope (HST) has observed more than 60 asteroids (Dotto *et al.*, 2002) since it launched in 1990. It obtained high-resolution images of Ceres, mapping the albedo over the surface and finding a 250 km diameter crater, Piazzini [Landis *et al.* (1998), Parker *et al.* (2002)]; Vesta was observed in 1994, revealing a 200 km albedo spot on its surface, while detailed albedo and colour distributions showed a differentiated surface, with the western hemisphere possibly high in pyroxene [Binzel *et al.* (1997), Zellner *et al.* (1997)]. Further observations by the HST were made in 1996, revealing a 460 km crater at

the south pole presumably caused by an ancient subcatastrophic collision that resulted in the Vesta family (V-types), and the delivery of HED meteorites to Earth (Section 2.4.5).

The Infrared Space Observatory (ISO) launched by ESA in 1995 observed 40 asteroids during its three years of operation, covering 2.5-240 μm . Large MBAs were observed for subsequent use as photometric and polarimetric standards (e.g. Cohen *et al.*, 1998). The surface thermal inertias of five MBAs were measured (Section 2.7).

The Midcourse Space Experiment (MSX) launched in 1996 has observed more than 1000 asteroids in the thermal IR (6.8-10.8 μm) and in the UV. So far, albedos and diameters have been determined for 168 asteroids (Tedesco *et al.*, 2002a).

2.9.2 Space Missions

Galileo's primary mission was to study Jupiter and its moons, but it crossed the asteroid belt twice, encountering S-types (951) Gaspra on 29 October 1991 and (243) Ida on 28 August 1993 [Fig. 2.8 (a)]. Veverka *et al.* (1994) analysed the images of Gaspra, determining its size (18.2 \times 10.5 \times 8.9 km), geometric albedo ($p_v = 0.23$) and pole orientation. They also found evidence for a considerable regolith, composed mostly of olivine. The first asteroid satellite was discovered orbiting Ida (Section 2.8) and found to have a similar albedo but different colour indices. Belton *et al.* (1996) analysed the images of Ida and found its size (59.8 \times 25.4 \times 18.6 km), albedo ($p_v = 0.21$), pole coordinates, mass and bulk density ($2.6 \pm 0.5 \text{ g/cm}^3$).

The first dedicated asteroid mission was the NEAR-Shoemaker spacecraft (Near-Earth Asteroid Rendezvous) which had the primary aim of orbiting (433) Eros. Cheng (2002) gives an overview of the mission. *En route*, NEAR encountered (253) Mathilde on 26-27 July 1997 [Fig. 2.8 (b)]. Veverka *et al.* (1999) and Clark *et al.* (1999) analysed the 500 images and found its size was 66 \times 48 \times 46 km and that it had a very low albedo $p_v =$

0.036. The colour indices were similar to CM carbonaceous chondrites. Its bulk density $1.3 \pm 0.2 \text{ g/cm}^3$ is among the lowest yet found (Yeomans *et al.*, 1997). The surface had four craters exceeding the mean radius of the asteroid (Thomas *et al.*, 1999).

On 17 February 2000, NEAR began its year-long orbit of Eros, at a height of 35-50 km above the surface [Fig. 2.8 (c)]. Some of the physical properties measured, and the context they give to our optical and thermal infrared observations of Eros in 2002 are given in Sections 3.9.1 and 5.6.3. Its bulk density was determined to be $2.67 \pm 0.03 \text{ g/cm}^3$ (Yeomans *et al.*, 2000), lower than ordinary chondrite meteorites, implying that it is relatively porous. Eros appears to be a consolidated body, rather than a rubble pile, with pervasive linear structural features (Zuber *et al.*, 2000). There is various evidence for an unconsolidated regolith depth of <100 m. On 12 February 2001, NEAR landed successfully on the surface of Eros; although it was not designed to survive, it continued to transmit gamma spectrometry results from the surface (Beatty, 2001).

Stardust is the first sample return mission to a minor body; it flew by asteroid (5535) Annefrank on 2 November 2002 en route to comet 81P/Wild-2. It measured Annefrank's diameter (5 km) and albedo (0.24) (Newburn *et al.*, 2003).

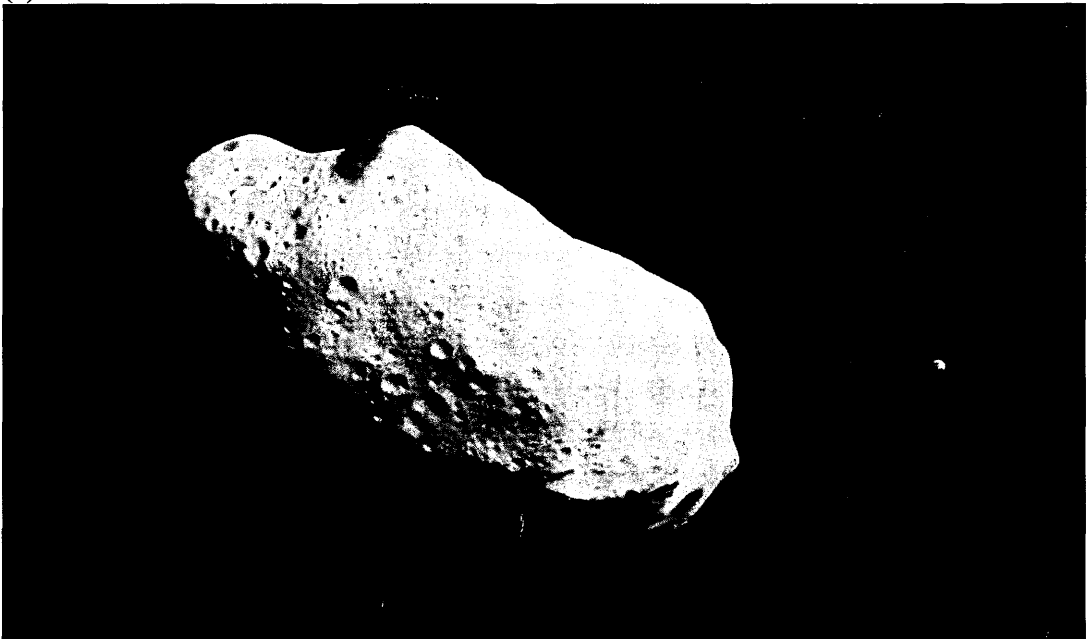
The Japanese Hayabusa spacecraft arrived at $0.3 \times 0.7 \text{ km}$ S-type NEA (25143) Itokawa on 12 September 2005. The spacecraft has retrieved spectacular images of the surface [e.g. Fig. 2.8 (d)] suggesting that Itokawa is a rubble pile, with portions of the surface that appear regolith-free and relatively uncratered. The science data from the various instruments (including near-infrared and X-ray spectrometers, and a laser altimeter) are still being analysed (<http://www.isas.jaxa.jp/e/snews/2005/1102.shtml>). Unfortunately, the mission has been plagued by technical difficulties, and hopes for successful completion of the sample return presently seem remote (<http://www.spaceflightnow.com/news/n0512/11hayabusa/>).

2.9.3 Future Space Missions

In 2007, NASA is due to launch DAWN, a mission to investigate the internal state and surface properties of Ceres and Vesta with a framing camera, a visible and infrared spectrometer, gamma ray and neutron detector and Doppler tracking (Russell *et al.*, 2005).

ESA's ambitious Rosetta mission [Hechler (1997); see also: <http://sci.esa.int/science-e/www/area/index.cfm?fareaid=13>] was launched in March 2004 and is due to encounter comet Churyumov-Gerasimenko in 2014. On the way it will encounter 10 km (2867) Steins in September 2008 and 96 km (21) Lutetia in July 2010. Rosetta will measure their shape, size, density, surface morphology and composition.

Fig. 2.8
(a)



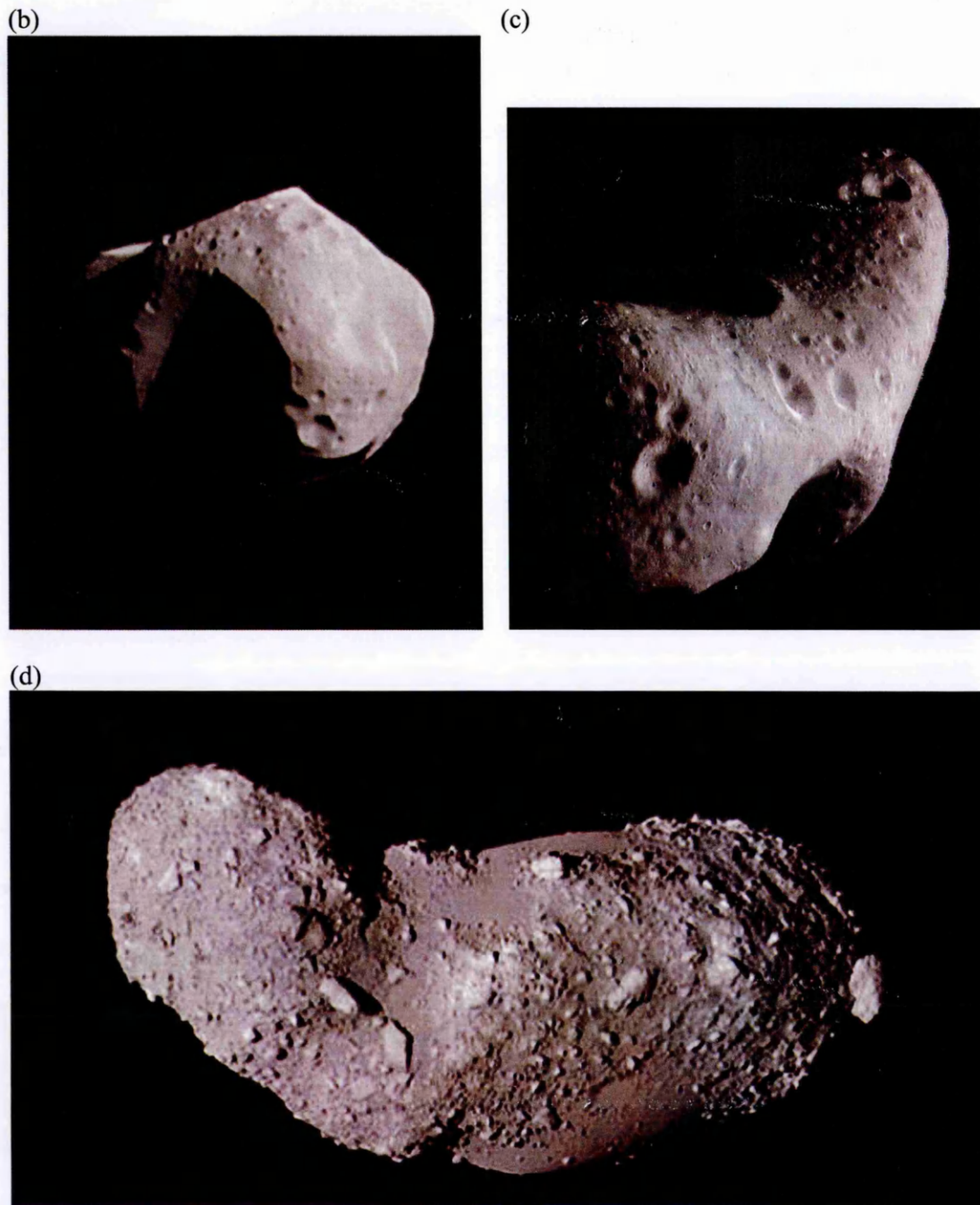


Fig. 2.8 Images of asteroids from spacecraft. (a) Ida and Dactyl in enhanced colour taken by Galileo on 28 August 1993; (b) Mosaic of Mathilde constructed from four images taken by NEAR-Shoemaker on 27 June 1997; (c) Mosaic of Eros' northern hemisphere constructed from six images taken on 29 February 2000 by NEAR-Shoemaker [(a) to (c) courtesy of NASA-JPL]; (d) Uncalibrated image of Itokawa from the Hayabusa mission (ISAS/JAXA).

2.10 Need for Improved Measurements of NEO Albedos and Diameters

Cellino *et al.* (2002b) describe the need for improved physical characterization of NEOs and how the discovery rate is vastly outstripping their investigation. As of 8 August 2005, the number of NEOs with measured diameters and albedos is about 78 (http://earn.dlr.de/nea/table1_new.html) including the eight new objects presented in this thesis (one more has derived limits) while the total number of NEOs discovered is 3496 (<http://neo.jpl.nasa.gov/>).

Improved statistics of the albedos of NEOs are needed for a more accurate derivation of their size distribution (Section 2.4.7), which is crucial for assessment of the impact hazard and for optimising survey strategies. Smaller NEOs below 1 km particularly need to be characterized; but unfortunately there is a bias against selecting small, low albedo objects, and succeeding in observing large, high albedo objects (Section 5.3.1).

As the number of NEOs with known taxonomic type increases, so does the requirement for an increase in measurements of their albedos. If an average albedo is correlated with the taxonomic type (Sections 2.3 and 2.4.4) it can be used to derive a de-biased size distribution. Stuart and Binzel (2004) have done the first study using albedo statistics from NEOs (Fig. 2.9), obtained from Delbó *et al.* (2003). However, A, R and U-types are still obtained from main-belt statistics and several values are based on very few classified objects (for example the D-type complex has one member with a measured albedo). Also, several NEAs have been found with radiometrically-derived albedos larger than the typical values for objects in their class (Harris and Lagerros, 2002).

Also, trends within taxonomic types may reveal surface processes. The majority of NEAs with measured albedos are S-types. Delbó (2004) has found a trend of increasing albedo with decreasing size among S-types and interprets it as evidence for space weathering (Section 5.8.1, Fig. 5.26). As the available data for other taxonomic types

grow, there may be other similar trends discovered. Finally, there is a large percentage of X-types among the NEO population (30%). They are degenerate into E, M or P-types in order of decreasing albedo (average 0.47, 0.14, 0.04 respectively).

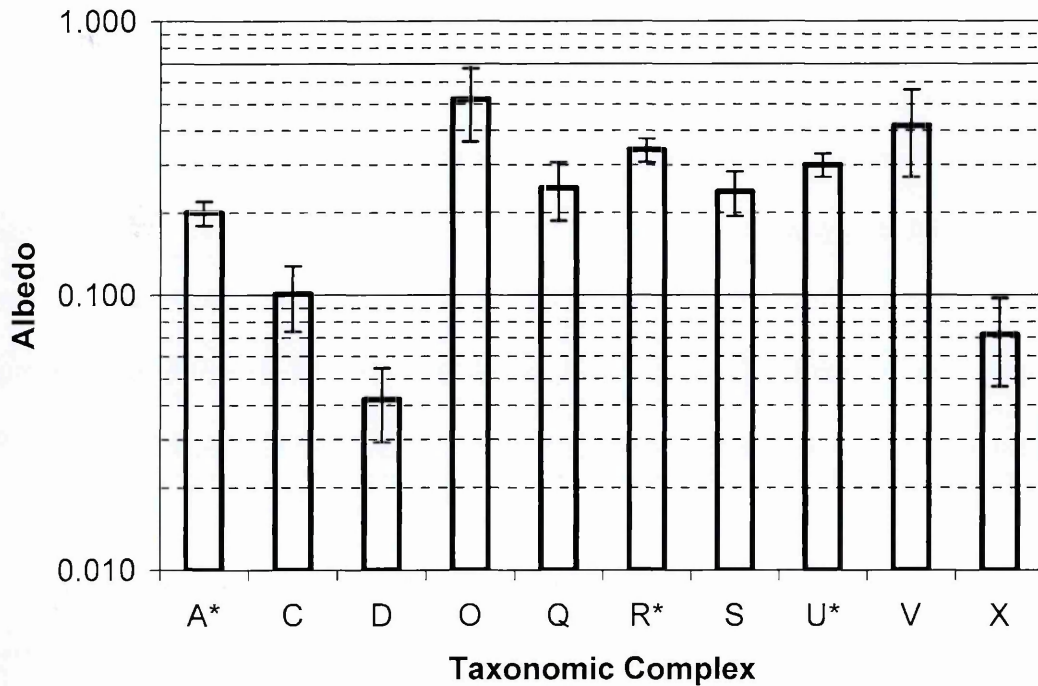


Fig. 2.9 De-biased average albedos for NEOs for each taxonomic complex, reproduced from Stuart and Binzel (2004). Complexes marked with * are based on main-belt statistics.

It is unknown what percentage of NEOs are extinct comets, and a reliable de-biased albedo survey will help reveal their number. They are expected to have low albedos; for example (20461) 1999 LD₃₁ has a retrograde orbit characteristic of a Halley-type comet and Harris *et al.* (2001) measured $p_v = 0.03 \pm 0.01$.

3 Optical Observations

3.1 Introduction

NEAs can be observed at optical telescopes using a Charge Coupled Device (CCD). Although NEAs are relatively close compared to typical astronomical distances, the objects observed typically have diameters of less than a few kilometres, and so appear as a point source in the CCD. What is measured is the asteroid's brightness in the filter being observed (its magnitude) and its variation in time. Optical observations can be combined with quasi-simultaneous observations of NEAs in the thermal infrared to provide a unique diameter and albedo. With enough observations over several nights a composite lightcurve can be formed, from which an asteroid's rotation period and limits on its shape can be derived. Lightcurves obtained at a number of apparitions allow the rotation axis orientation and shape to be determined. We observed NEAs at the 1.0 m Jacobus Kapteyn Telescope (JKT) in La Palma in May 2001, December 2001 and September 2002.

3.2 Planning Observations

As explained by Harris and Lupishko (1989), for maximum accuracy of period determination or for defining the phase relation, it is desirable to fit observations from the longest possible span of time to a single composite lightcurve. Good observing practice would be to obtain enough data over a short time span to eliminate possible ambiguity in the period determination and repeat detailed coverage often enough to evaluate deviations from strict periodicity. For main belt asteroids you can often make composite lightcurves covering the entire apparition over several months. However this is often not possible with NEAs, since their aspect (angle between the rotation axis of the body and the radius vector to the Earth) may be changing rapidly, causing the lightcurve amplitude to change

depending on the pole orientation, for example. Also, the constraints of telescope scheduling typically limit observations of an asteroid to several nights during a week.

Observing time was obtained at the JKT on the nights of 4-9 May 2001, 14-20 December 2001 and 25 September-1 October 2002 UT. On many occasions, the main goal when applying for observing time was to observe asteroids quasi-simultaneously with thermal IR observations at UKIRT. However, time was awarded on UKIRT only in September 2002. Therefore the priority for the first two observing trips was to choose NEAs most easily observable at the JKT, while for September 2002 it was to observe targets for which we had acquired, or confidently hoped to have, thermal IR fluxes.

When planning an observing trip, we first define the scientific objective, then select a list of suitable targets observable during the time allocated. The initial criterion is to select NEAs with an apparent magnitude < 17 , using the “What’s Observable” page of JPL’s Solar System Dynamics website (<http://ssd.jpl.nasa.gov/sbwobs.cgi>). From the resulting shortlist, a more detailed ephemeris was produced for each object, using JPL’s HORIZON system (<http://ssd.jpl.nasa.gov/?horizons>). Included in the ephemeris is the right ascension (RA), declination (DEC) and their corresponding rates, apparent azimuth and elevation, the object-Earth-Moon angle, and the percentage illumination of the Moon. The list of potential targets is reduced further by only including objects that have an elevation $>30^\circ$ for several hours during the night, and in the case of an observing trip with a bright Moon, $>10^\circ$ angle between the Moon and the object.

With the list of potential targets drawn up, objects can be further categorised by investigating whether they are bright enough to be observed for a short enough time that a CCD exposure can be taken without the asteroid moving more than 1.5 pixels, while still preserving a signal to noise (S/N) ratio better than 100, preferably, or 30 at a minimum. This can be done by converting the RA and DEC rates into arcsec/s rates and multiplying

by the length of arc represented by 1.5 pixels on the CCD (0.33 arcsec/pixel). This represents a maximum exposure time from which an estimated achievable S/N ratio is calculated. The S/N ratio is obtained using the SIGNAL program on the ING (Isaac Newton Group) website (<http://www.ing.iac.es/ds/signal/>, although the JKT and its instruments are no longer available). If the $S/N > 30$, then the CCD exposure can be short enough that tracking of the asteroid is not required. This has the advantage that smaller circular apertures can be used in data reduction, which makes relative photometry easier to be performed. If tracking is required, JPL Horizons can generate rates of movement in RA and DEC in arcsec/s at any required time, which must be converted to $\cos(\text{DEC}) \times d(\text{RA})/dt$ and $d(\text{DEC})/dt$ in units of arcsec/hr for the JKT Telescope Control System (TCS).

3.3 Observations at the Jacobus Kapteyn Telescope

3.3.1 Methodology

A 2048×2048 $24\mu\text{m}$ pixel SITe2 CCD was used with the V-filter in May 2001 and September 2002, while the B, V, R and I-filters were used in December 2001. There was 0.33 arcsec/pixel giving a field of view of about 10×10 arcmin. The JKT has a 1.0 m parabolic primary mirror and was used with the hyperbolic secondary mirror to form a conventional f/15 Cassegrain system.

We filled the cryostat with liquid nitrogen to keep the CCD at the correct temperature during the night. The SITe2 CCD was assigned a window to read out from, since the 2048×2048 CCD covers a greater area than the collected light is focussed onto (the windowing procedure also removes some of the area where vignetting occurs). The window used (200-1900 on the x-axis, 200-2100 on the y-axis) includes an “overscan” region which is used to determine the bias for the frame (Section 3.5.2). The CCD is operated by the instrument control system (ICS).

During the early evening, before twilight arrived, flat fields were taken (Section 3.5.2): for dome flats, several frames (typically 10) with the CCD exposed for a few seconds (around 10 s followed by the 1 min. read-out time) to lamps turned on inside the dome. When twilight arrived, this procedure was repeated, with the telescope pointing at a blank patch of sky, to produce sky flats.

The telescope pointing was fine-tuned with a seven star interactive calibration, centring the stars on a TV monitor. The telescope is focussed using a procedure on the ICS that took a series of exposures of stars at different telescope foci, shifting the telescope slightly between each exposure, all on the same frame. The frame was analysed to see which star was best focussed, i.e. which star had the smallest FWHM.

As well as observing the target objects throughout the night, standard stars are observed. These are a group of stars in one field with a known absolute photometric magnitude in each filter, from Landolt (1992). These were used later in data reduction to calibrate the measured magnitude of the target asteroid (Section 3.5.5). It is important to observe standard stars at a range of airmasses, and it is useful to use several different sets of standard stars. We had to juggle the need to observe standard stars over a range of airmasses with taking as many observations of as many targets at the highest elevation possible.

At dawn, more sky flats were taken as it became brighter. The data was read to a magnetic tape, and the log file was printed. Finally, the cryostat was refilled, and the telescope shut down.

3.3.2 *May 2001*

Observations were made in La Palma at the JKT between the nights of 4 May and 10 May 2001. The observers were S. F. Green and N. M. McBride. The NEAs observed were:

(4034) 1986 PA, (5587) 1990 SB, (19356) 1997 GH₃ and (25330) 1999 KV₄. About 10 dome flat fields and 5 sky flats were taken at the start of each night's observing.

4 May 2001

There was some cirrus and the conditions were judged not to be photometric at first. 9 s exposures of asteroid (5587) 1990 SB were taken between 21:15 and 22:34 UT, tracking at the sidereal rate, by the end of which it was judged that conditions had become photometric. Asteroid (19356) 1997 GH₃ was observed for the rest of the night (23:00 to 05:19 UT). The telescope was re-centred on the asteroid once.

5 May 2001

There was very thick cirrus, and only relative photometry was performed. Perhaps because of the cirrus, there was a problem with the focussing procedure, and so the previous night's focus was used. (5587) 1990 SB was observed for the whole night, with the telescope re-centred on the asteroid five times, so that there were six fields in total, with comparison stars overlapping between fields.

6 May 2001

There was cirrus all over the sky, very thick in places. Seeing was initially 1.9'', quickly improving to 1.6''. (5587) 1990 SB was observed in groups of 20 frames, interspersed with two 150 s exposures of asteroid (4034) 1986 PA, which was tracked. The first frame of (4034) 1986 PA did not track properly. Exposure times were reduced to 120 s. The field was shifted too much to have comparison stars overlap, unfortunately.

By 01:52 UT the clouds had mostly cleared. (5587) 1990 SB was observed, interspersed with retaken fields from the previous relative-photometry-only night, in order

to be able to calibrate comparison stars in that field and recover absolute calibration for the previous night. The seeing appeared to fluctuate between 1.4'' and 1.1''.

7 May 2001

Conditions were photometric. Initial seeing was 1.8''. (4034) 1986 PA and (25330) 1999 KV₄ were observed, tracked, in groups of four and three frames respectively. There is a problem with the JKT that it can drift when pointing to the West, so frames of (25330) 1999 KV₄ started to trail by 00:04 UT, after which only (4034) 1986 PA was observed. Seeing had changed to 1.6'' by 01:45 UT.

8 May 2001

Initial seeing was 2.4''. Humidity was >90% and the dome had to be closed. The telescope was refocused and an attempt was made on 1999 KV₄ at 21:50 UT. Seeing was still high at 2.3'', then reduced to 1.85'' at 22:01 UT. Another attempt was made to focus the telescope, more observations of (25330) 1999 KV₄ taken, then the focus reset to the previous value. Observations of (25330) 1999 KV₄ were restarted at 22:51 UT and continued to 23:21 UT, although the drives slipped and guiding was hopeless. The humidity raised above 90% again and the dome was closed. The dome was reopened at 00:09 UT but with a lot of cloud cover. The telescope was pointed to the East away from the clouds, taking continuous observations of standard star field PG1633 to assess changes in seeing, which started at 5'' and reduced to 1.8'' by 00:21 UT. At this point, humidity decreased to 17% and conditions were more stable. Observations of (4034) 1986 PA were taken, but clouds noticeably started to affect the observations from 02:27 UT onwards.

9 May 2001

Conditions were photometric. Initial seeing was 1.2'' decreasing to 1.0'' FWHM by 02:16 UT. (4034) 1986 PA and (25330) 1999 KV₄ were observed, tracking.

10 May 2001

Conditions appear to have been reasonably photometric. (25330) 1999 KV₄ (until 01:03 UT), (4034) 1986 PA and (19356) 1997 GH₃ were observed.

3.3.3 December 2001

Observations were made at the JKT with the instrument and telescope setup identical to May 2001, except that B, V, R and I-filters were used. The observing time allocated was between 14 and 18 December, but unfortunately there was unbroken cloud cover until the last night. Observers were S. F. Green, S. D. Wolters and M. D. Paton.

On the night of the 18 December 2001 there was no apparent cirrus at first, but some was seen at dawn. It was probably photometric early but then deteriorated. Seven dome flats in each filter were taken, followed by two B-filter, three V-filter and one I-filter sky flats.

Asteroid (33342) 1998 WT₂₄ was the main target. The asteroid was moving very quickly ($d(\text{RA})/dt \times \cos(\text{DEC}) = -2000$ arcsec/hr, $d(\text{DEC})/dt = -970$ arcsec/hr). 10 s exposure frames were taken (20 s for the B-filter), tracking on the asteroid. 1998 WT₂₄ was moving so quickly that new comparison stars would have to be chosen every seven frames. Initially, eight R-filter frames were taken between 20:16 and 20:36 UT, after which the sequence *R, V, R, I, R, B, R, V...* was adopted, observing in blocks of 20 frames. This pattern was repeated until 00:18 UT, after which the same observing strategy was applied to asteroid 2001 SE₂₈₆, except that it was observed in blocks of 15 frames, also tracking,

with 60 s exposures (100 s for the B-filter) until 05:32 UT. Finally, three sky flats were taken in each filter.

3.3.4 September 2002

Observations were made at the JKT with the instrument and telescope setup identical to May 2001, except that the CCD was operating in fast readout mode, between the nights of 25 September 2002 and 1 October 2002. N. M. McBride was the observer. Observations were entirely in the V-filter except for 1 October, where some *R* and *I* frames were taken.

The purpose of the run was to make supporting optical observations for the thermal IR spectra of objects observed quasi-simultaneously at the United Kingdom Infrared Telescope (UKIRT) (Chapter 5). The prioritised targets would shift from night to night depending on which objects had been successfully observed at UKIRT. Ultimately, observations of the following asteroids were made: (433) Eros, (6455) 1992 HE, 1998 UO₁, (53789) 2000 ED₁₀₄, 2002 HK₁₂, 2002 NX₁₈ and 2002 QE₁₅.

25 September 2002

The weather was clear with patchy cirrus to the West. Initial seeing was 1.3''. 10 dome flats were taken, followed by three V-filter sky flats. Asteroid 2002 NX₁₈ was observed for 67 frames between 20:14 and 23:02 UT. 2002 HK₁₂ was observed for 64 frames between 23:21 and 01:24 UT. Towards the end it became difficult to observe the asteroid, possibly due to the half-Moon, only 20° away. Then some frames of 2002 HK₁₂ were attempted while tracking. Unfortunately, the wrong dRA rate was used (×10 too small), and the asteroid could not be seen, except for the last frame (02:40 UT). Finally 1998 UO₁ was observed until astronomical twilight, tracked between 02:59 and 06:10 UT.

26 September 2002

The weather was bad, with patchy (~50%) cloud cover, so relative photometry only was performed. Seeing was 1.0''. After seven dome flats, asteroid 2002 QE₁₅ was observed between 20:26 and 00:50 UT. Then 2002 HK₁₂ was observed past astronomical twilight between 00:58 and 06:23 UT. Finally, five sky flats were taken.

27 September 2002

There was initially some thin cloud, which may have cleared by midnight. At the start of the night, five dome flats and six sky flats were taken. 2002 NX₁₈ was observed between 20:06 and 23:00 UT. Observations swapped between asteroids (433) Eros and 2002 HK₁₂ in batches of between three and five frames between 23:04 and 01:28 UT. Asteroid (6455) 1992 HE as well as the other two asteroids were observed until 04:01 UT. After 4:01 UT, (6455) 1992 HE was observed continuously until 05:42 UT, past astronomical twilight.

28 September 2002

There was thin cloud and cirrus present, conditions were not photometric. Seeing was ~1.0''. The weather appeared to clear at about 22:30 UT, but possibly worsened again around 01:00 UT. At the start of the night five dome flats and five sky flats were taken. Observations of 2002 QE₁₅ in batches of 5 frames, (433) Eros in batches of 3, and 2002 NX₁₈ in batches of between 3 and 15 were taken between 20:14 and 22:43 UT. Just (433) Eros and 2002 QE₁₅ were observed between 22:46 and 00:20 UT, both in batches of three frames. Between 00:20 and 01:30 UT only (433) Eros was observed. Then (433) Eros was observed in batches of two frames, alternating with observations of (6455) 1992 HE in batches of between three and eight frames, up until 03:21 UT. Finally (6455) 1992 HE was

observed for the rest of the night until past astronomical twilight at 05:46 UT, with the final frame taken at 05:54 UT.

29 September 2002

The weather was not clear, with thin, patchy cloud. It became thicker later, with the conditions in the last hour making observing almost impossible. Five sky flats were taken at the start of the night. 2002 NX₁₈ was observed between 20:05 and 22:55 UT. (433) Eros was then observed between 23:01 and 00:29 UT. Finally (6455) 1992 HE was observed between 01:05 and 04:27 UT.

30 September 2002

The weather was cloudy and no observations were taken.

1 October 2002

The weather appeared clear. The seeing varied between 1.5-2.0''. V, R and I-filters were used for each batch, unless noted. Five dome flats and three sky flats in each filter were taken. 2002 NX₁₈ was observed for 15 frames alternately between 20:42 and 21:15 UT. Then (53789) 2000 ED₁₀₄ was observed, tracking, for 21 frames between 21:26 and 22:20 UT. It was noticed that the asteroid passed very close to a star, and was not found on a couple of the frames. Observations of previous nights' fields in the V-filter were then taken, in order to recover the photometry for the nights that were not photometric (since it was believed that the night of 1 October was photometric).

10 frames of 2000 ED₁₀₄ tracking (V), followed by five frames of 2001 QE₁₅ and then 15 frames of 2000 ED₁₀₄ (V) between 22:58 and 00:08 UT, were taken. For the first five

frames of the second batch of 2000 ED₁₀₄ frames, the tracking did not work. Another batch of 19 frames, tracked, of 2001 ED₁₀₄ were taken between 00:25 and 01:02 UT.

Asteroid (6455) 1992 HE was observed between 01:18 and 02:06 UT for 29 frames. This was followed by two frames of previous night's fields (*V*), and then five frames of 2002 HK₁₂ between 02:14 and 02:21 UT. 6455 was observed for the rest of the night, between 02:26 and 05:37 UT.

3.4 Measuring NEA Magnitudes

3.4.1 Instrumental Magnitudes

In the standard magnitude scale, a one magnitude difference between two stars is defined as equivalent to the ratio $10^{1/2.5}$ of the flux received from both stars. The measured cumulative counts c within an aperture can be converted to an un-calibrated logarithmic measurement of the brightness, the instrumental magnitude m_{inst} :

$$m_{inst} = -2.5 \log_{10} \left(\frac{c}{gt_{exp}} \right) \quad (3.1)$$

where g is the gain (counts/photon) of the CCD and t_{exp} is the exposure time (s) in seconds. Note that the brighter the object, the lower the magnitude.

3.4.2 Atmospheric Extinction

The instrumental magnitude can be converted into the apparent magnitude, which is the magnitude of the asteroid if there were no intervening atmosphere. The instrumental magnitude must also be calibrated by the apparent magnitude zero-point for the standard Johnson UBVRI filter set, which is defined by setting the magnitude of the star Vega (α Lyrae) to zero mag.

$$\begin{aligned}
B_{app} &= b_{inst} - Z_b - k_b \chi - T_B (B - V) \\
V_{app} &= v_{inst} - Z_v - k_v \chi - T_V (B - V) \\
R_{app} &= r_{inst} - Z_r - k_r \chi - T_R (V - R) \\
I_{app} &= i_{inst} - Z_i - k_i \chi - T_I (V - I)
\end{aligned}
\tag{3.2}$$

where Z_m is the photometric zero-point of the CCD telescope system for a particular filter, k_m is the atmospheric extinction coefficient, χ is the airmass, T_M is the colour transformation coefficient, and the terms in parentheses are the apparent colour indices of the standard star. k_m compensates for scattering and absorption of the light as it passes through varying thicknesses of the atmosphere, and varies from night to night. Z_m and k_m are found for a particular filter through observations of standard stars whose magnitudes relative to Vega are known. T_M accounts for differences between JKT instrumental passbands and that of the filter set used to derive the apparent magnitudes of the standard stars: the Johnson UBVRI filter set. The transformation coefficients for our filter/CCD combination are close to zero, as determined by Green and Fitzsimmons (personal communication). Except in very photometric conditions, this is negligible compared to other uncertainties. The airmass χ can be calculated approximately from:

$$\chi = \sec(\zeta) \tag{3.3}$$

where ζ is the target's zenith angle, assuming a plane-parallel atmosphere, or, more accurately (Young, 1976):

$$\chi = \sec(\zeta) \left(1 - 0.0012 \sec^2(\zeta) \right) \tag{3.4}$$

For more detail on accounting for atmospheric extinction, including when time-variable extinction is considered, see Harris and Lupishko (1989) and references therein. See Section 3.6 for examples of standard star extinction plots.

Generally, the greatest uncertainty in the final reduced magnitude results from the extinction correction. This is estimated on each night from the spread of points on the

extinction plots, and is typically ± 0.04 mag. Relative uncertainties between magnitudes of an object taken in the same night may be much smaller.

3.4.3 Geometrical Corrections

The reduced magnitude, or the reduced visual magnitude $V(1, \alpha)$ for the V-filter, is the apparent magnitude corrected to a heliocentric and geocentric distance of 1 AU:

$$V(1, \alpha) = V_{\text{app}} - 5 \log(r\Delta) \quad (3.5)$$

where r (AU) and Δ (AU) are the heliocentric and geocentric distances respectively and V_{app} is the apparent magnitude of the asteroid in the V-filter. $V(1, \alpha)$ depends on the phase angle α of the observation, which is the Sun-asteroid-Earth angle.

We light-time corrected the observations to account for the time the light has taken to travel to Earth, and also corrected to the midpoint time of the exposure. The light-time correction is important for NEOs since they often have rapidly changing geocentric distances which introduce timing errors when folding lightcurves. If t_{frame} is the JKT frame header's recorded exposure start time in fractions of a day after 0h UT, the time associated with each measured magnitude in the frame is:

$$t(\text{day}) = t_{\text{frame}}(\text{day}) + \frac{t_{\text{exp}}(s)}{2 \times 24 \times 3600} - \frac{\Delta(\text{AU})}{173.142(\text{AU/day})} \quad (3.6)$$

3.4.4 The H, G Magnitude System

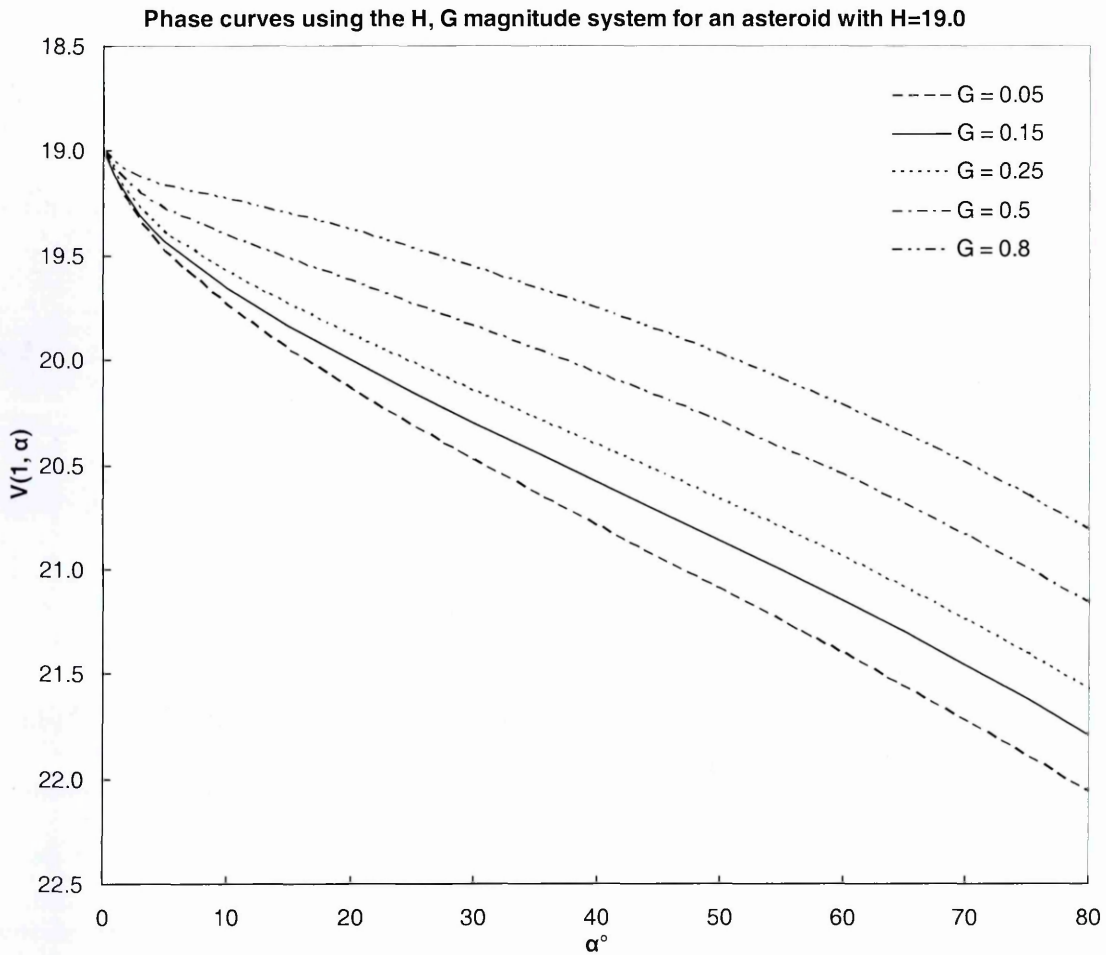


Fig. 3.1 Theoretical phase curves for an object with absolute magnitude $H_V = 19.0$ for different values of the slope parameter G . The opposition effect at low phase angles is modelled by the H, G magnitude system.

$V(1, \alpha)$ can be corrected to 0° phase angle to obtain the absolute visual magnitude H_V , via the H, G magnitude system (Bowell *et al.*, 1989) adopted by the IAU Commission 20. The phase correction, characterized by the G parameter, takes into account the so-called opposition effect, a rapid increase in brightness at low phase angles due to surface roughness features such as craters, causing reflected radiation to be preferentially scattered in a sunward direction.

The formulation is:

$$H_V = V(1, \alpha) + 2.5 \log[(1 - G)\Phi_1(\alpha) + G\Phi_2(\alpha)] \quad (3.7)$$

$$\Phi_i = W\Phi_{iS} + (1-W)\Phi_{iL} \quad (i = 1, 2)$$

$$W = \exp\left(-90.56 \tan^2 \frac{1}{2} \alpha\right)$$

$$\Phi_{iS} = 1 - \frac{C_i \sin \alpha}{0.119 + 1.341 \sin \alpha - 0.754 \sin^2 \alpha}$$

$$\Phi_{iL} = \exp\left[-A_i \left(\tan \frac{1}{2} \alpha\right)^{B_i}\right]$$

$$A_1 = 3.332 \quad A_2 = 1.862$$

$$B_1 = 0.631 \quad B_2 = 1.218$$

$$C_1 = 0.986 \quad C_2 = 0.238$$

where G is the slope parameter, which determines the gradient of the phase curve. Example phase curves are shown in Fig. 3.1.

Often G is unknown, in which case H_V can be approximated by assuming $G = 0.15$. $G \sim 0$ for steep phase curves (low-albedo bodies, generally) and $G \sim 1$ for shallow phase curves (high-albedo bodies, generally). Eq. 3.7 is valid for $0^\circ \leq \alpha \leq 120^\circ$ and for $0 \leq G \leq 1$.

3.5 CCD Photometry

3.5.1 The Charge-Coupled Device

The Charge-Coupled Device (CCD) is the most widely used and useful linear two dimensional photon detector available. The CCD consists of a grid of photosensitive silicon detectors which linearly releases electrons as more photons are incident on its surface. The accumulated charge is usually stored within metal oxide semiconductor capacitors. Typical grid sizes for an astronomical-use CCD are 1024×1024 or 2048×2048 . The charge accumulated in each pixel is transferred by manipulating the potential difference of the pixel with respect to the adjacent cells along the row into an output register which is connected to an amplifier with gain g . The charge packets are read

out one cell at a time until the entire row has been read, and then the output register moves onto the next row.

CCDs have the advantage of being highly linear and sensitive over a wide range of wavelengths, and this can hold over a large dynamical range. They have a higher quantum efficiency than other photometers (up to 90% compared to 20-30% for photomultipliers and 1-2% for photographic emulsion). Large CCDs allow a reasonable fraction of the sky to be observed at once (e.g. 10×10 arcmin. for the SITe2 CCD used at JKT) allowing easy observation of bright comparison stars at the same time as the asteroid.

Some of the weaknesses of CCDs include the fact that they must be kept cool, e.g. by liquid nitrogen, to reduce thermal noise. CCDs can take ~ 60 s to read out (depending on the size) which can be a problem if the object observed changes brightness rapidly (for example some asteroids have rotation periods of only a few minutes). There is additional readout noise introduced by the analogue-to-digital conversion.

3.5.2 Bias Subtraction and Flat Fielding

A positive voltage bias is added to each CCD pixel charge to prevent the analogue-to-digital converter (ADC) receiving a negative signal due to low-level background noise from thermal electron activity. Figure 3.2 shows a raw CCD frame before it has been bias subtracted and flat fielded. The bias level can be determined by taking a series of zero second exposure frames, if the bias is reasonably constant during the night. Additionally, a regular variation in bias can be determined, if enough frames are taken, to produce a time-dependent function. In practice, it is simpler to determine the bias level for each frame by having an overscan region, which is not exposed, in each frame.

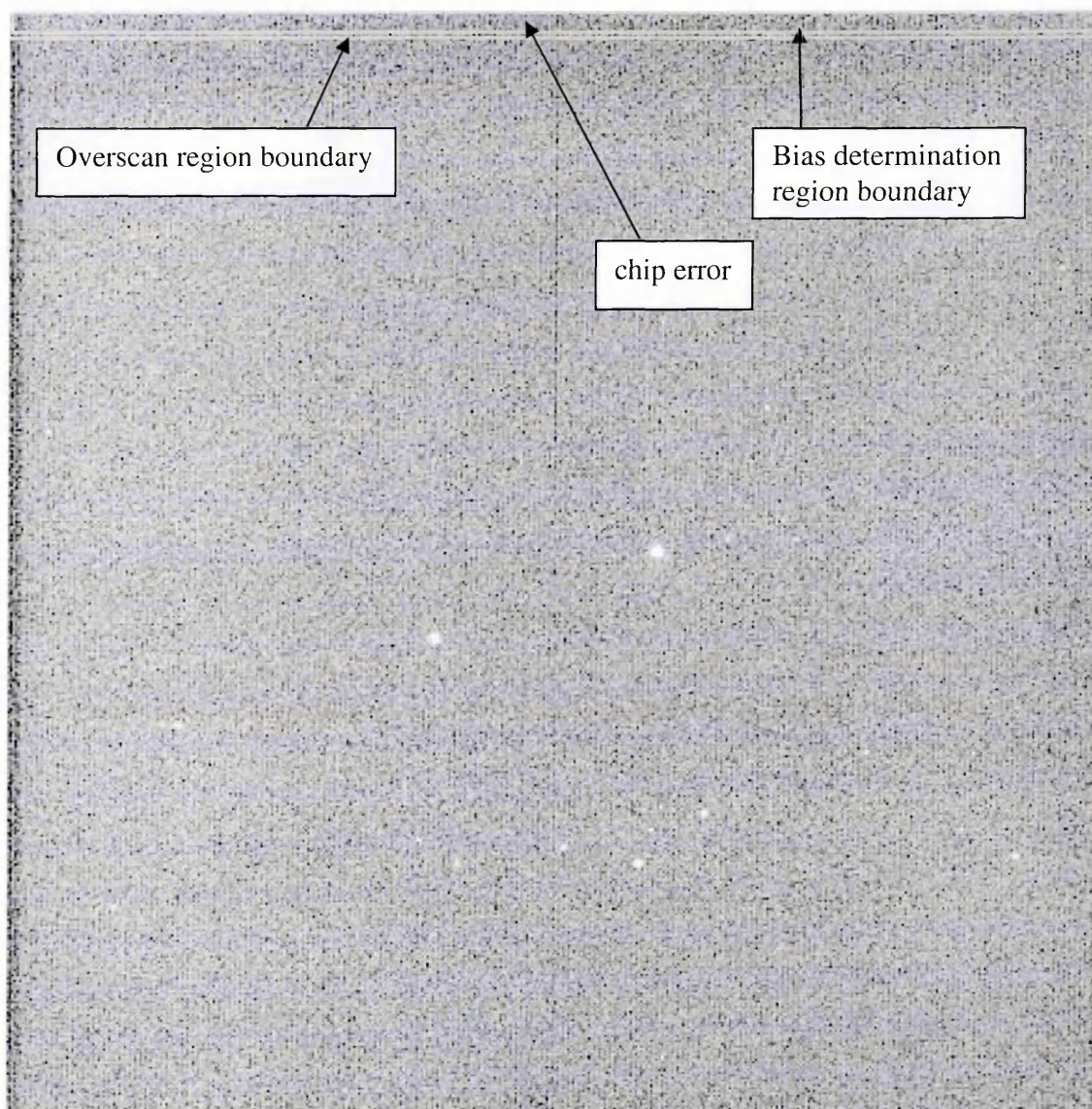


Fig. 3.2 Raw frame r256665 taken on 28 September 2002 of (433) Eros in the V-filter at the JKT, with a 10 s exposure. The frame needs to be flat fielded and de-biased before aperture photometry can be performed. The overscan region is marked by a grey rectangle, and a slightly smaller rectangle is shown, inside which the average pixel value is calculated for bias subtraction.

The bias and standard deviation (σ) are determined using the Starlink FIGARO command “istats” from a slightly smaller sub-window in the overscan region; the bias is subtracted from the whole frame using “icsub”. The bias is approximately 600 counts for the SITE2 CCD at the JKT. If the standard deviation within the window is greater than $\sim 3\%$, which it is on about 5% of frames, due to chip errors in the CCD (Section 3.5.3), the

Starlink photometry package GAIA can be used to extract the desired image region in the overscan area, then the KAPPA command “stats” can be used to calculate the mean within the region, clipped within 3σ . The standard error (σ/\sqrt{n} , where n is the number of pixels within the overscan region) indicates the accuracy of the mean value, which is typically a fraction of a count.

The bias level for the SITE2 CCD at the JKT remains fairly constant; for example, the calculated bias using the method described above for every fifth frame of asteroid 2002 HK₁₂, observed on the night of 25 September 2002 (Fig. 3.3), was 596.21 ± 0.41 . For later data reduction, when the emphasis has been on speedy bulk reduction, a simplification of the above process has been adopted, where the bias is measured for every fifth frame, and then all frames subtracted by a constant bias value. This applies to all frames subsequently reduced using MaxIM DL. The increase in uncertainty in the final photometry is negligible.

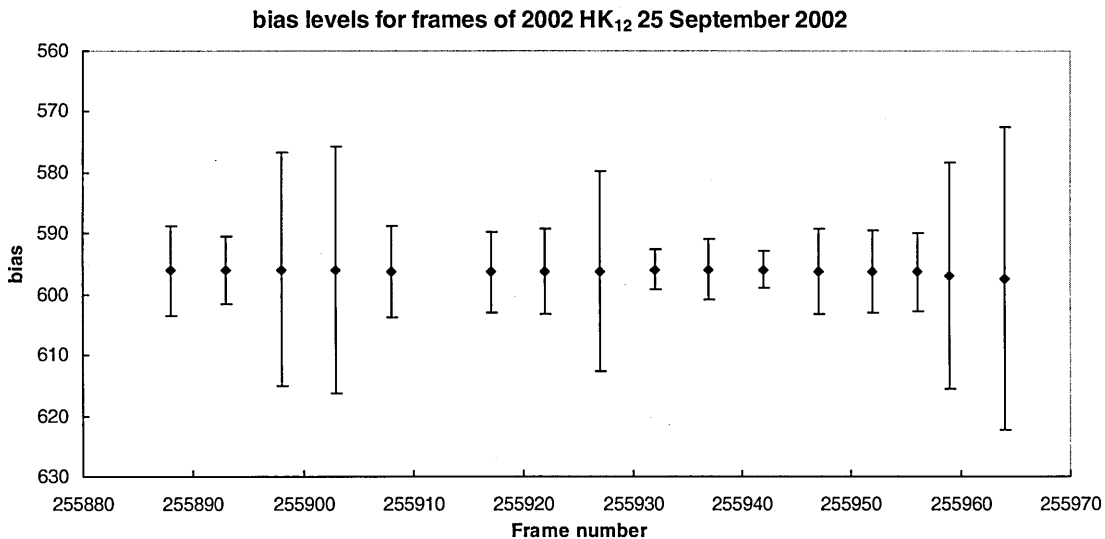


Fig. 3.3 Bias levels for JKT V-filter observations of 2002 HK₁₂ on the night of 25 September 2002 UT. Error bars represent standard deviation within the overscan region. The large scatter in some frames is probably due to cosmic rays or readout errors.

The CCD chip has pixel to pixel sensitivity variations, and there are also optical vignetting and “doughnut” shaped effects caused by dust particles within the telescope.

These are corrected for by flat-fielding: an exposure to a uniformly bright source of light. “Dome flats” are exposures to lamps inside the telescope dome, whereas “sky flats” are exposures to natural low sky light levels at twilight.

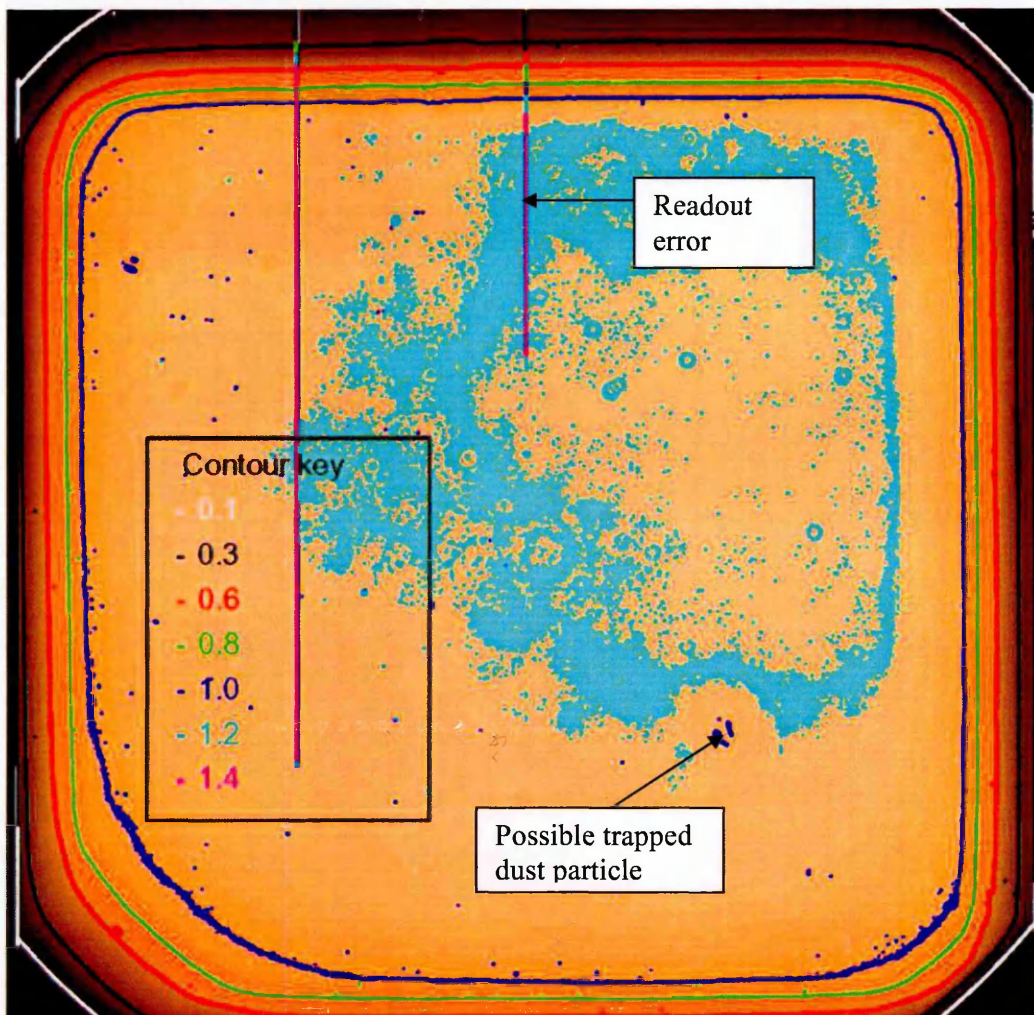


Fig. 3.4 The normalised flat field frame for 28 September 2002 UT is a combination of five dome flats with an average pixel value (not including the overscan region) of one. Some persistent artefacts, that are not removed by the recombination of the flat field frames by finding their median, include a readout error on all frames from the September run, and a dust particle, trapped either in the instrument or the telescope system. It is best to avoid measuring objects near these artefacts or near the edge (within 200 pixels) due to vignetting by the filter. With contours it can be seen how rapidly the intensity decreases towards the edge. The flat field frame cannot accurately correct for this from frame to frame.

Flat fields must be taken for every filter used due to changes in the relative pixel sensitivities with wavelength. The exposure time is varied to acquire a count level of

around 20000 ± 5000 counts, giving good S/N but not close to saturation of the CCD, where its response may be non-linear. For sky flats this means increasing the exposure time as the sky becomes darker. Typically, at least six dome flats and three sky flats will be taken for each filter. Sky flats are theoretically better than dome flats because the light source is distant and the wavelength distribution is more natural. However, the light levels in sky flats are hard to replicate from frame to frame. Often only dome flats were used, or a combination of dome and sky flats. An example flat field frame is given in Fig. 3.4.

The flat field frames are de-biased. Then the average pixel value in the exposed region of the frame is found, and the frame is divided by this value to produce a normalised flat field frame with an average pixel value of one. A median of each pixel between the frames is found, which effectively removes cosmic rays, using the FIGARO command "medsky". Before aperture photometry is carried out on any frame, it is first bias subtracted and then divided by the normalised flat field frame.

3.5.3 *Bad Pixels, Chip Readout Errors and Cosmic Ray Hits*

Cosmic ray hits can appear as a small cluster of pixels (radius 1-3 pixels) on a CCD image, with typically ~ 1000 counts greater than sky background [e.g. Fig. 3.5 (b)]. Their location is random, but the exposure time of frames is limited to reduce their number. If they appear within an asteroid or comparison star aperture, they can alter the measured brightness by several magnitudes. If a comparison star is affected, then another comparison star can be used for that frame, if the asteroid, then the correct magnitude is not recoverable and the data is taken out.

CCDs can also be affected by bad pixels, which can look similar to cosmic rays hits. Sometimes these will be clusters of pixels or short lengths of column tens of pixels long with greater counts, or sometimes zero counts. Readout errors can cause sections of

columns to be misaligned, or entire columns to have a greater or smaller intensity. Bad pixels remain in the same place from frame to frame, and readout errors can often do the same. An example can be seen in Fig. 3.5 (a).

In September 2002, the SITE2 CCD was read-out in “fast” mode, which halved the readout time to 30 s, allowing approximately 50% more frames to be observed, but a large increase in readout errors. When a cosmic ray, chip or readout error comes within the annulus of the sky background it can be removed using the “patch image” function in the Starlink photometry package GAIA to replace the error with a section of sky background (see Section 3.5.4 for a description of aperture photometry). However this is time consuming, and we used clipped means when calculating sky background levels, so this was not done often. If the common (for September 2002) readout error with a displaced column appeared inside the 6σ aperture, it appeared in most cases not to affect the measured magnitude by more than a few hundredths of a magnitude, based on its effect on constant brightness comparison stars. If the error reached the central area of the 6σ aperture (or anywhere within the 2σ aperture) the object’s measured magnitude could be compromised, and these measurements were removed.

To avoid chip and readout errors affecting the data, it is important to choose comparison stars away from regions of the CCD with these errors. However, often the choice of good comparison stars is severely limited, and the telescope’s position will shift to recentralise the asteroid or drift eastward (more so later in the night when pointing to the West), and a good comparison star will become affected by chip errors. Observing three different comparison stars can reduce these problems, and in general $<3\%$ of frames in a night would be affected. However, in the worst case in September 2002 $\sim 20\%$ of the measured magnitudes were significantly affected by chip errors.

3.5.4 Aperture Photometry

During a night's observing, CCD images of standard star fields, and fields containing the target asteroid and nearby comparison stars, are taken, as described in Section 3.3. The asteroids and stars are point-like sources of light scattered by the atmosphere, so counts can be received over regions several pixels wide, superimposed on the sky background. Sections of a typical bias-subtracted and flat-fielded CCD frame are shown in Fig. 3.5.

Aperture photometry was done using two different software packages. Most data reduction was performed using the Starlink photometry software GAIA, but reduction of 2002 HK₁₂ was done using MaxIm DL 4 for faster data reduction, albeit with a slight reduction in accuracy.

Using the Aperture Photometry tool within GAIA, virtual circular apertures of two different sizes are drawn round the target asteroid and prospective comparison stars (typically choosing three bright stars) or standard stars, depending on the type of field. The small aperture is 1.7 FWHM diameter (which we refer to as 2σ diameter, since if the object's brightness decreased from the centre as a Gaussian function, two standard deviations of the flux from the object would be included inside the aperture) and the large aperture is 5.1 FWHM diameter (6σ). The small aperture was sufficiently large to sample most of the target point spread function, but as small as possible to minimise the sky contribution, as discussed in Green and McBride (1998). The instrumental magnitudes of the asteroid obtained from the 6σ aperture were used for direct calibration into apparent magnitudes, whereas the 2σ aperture was used for relative photometry between the asteroid and comparison stars, since a smaller aperture could be used when comparing magnitudes on the same field, where the seeing will be identical.

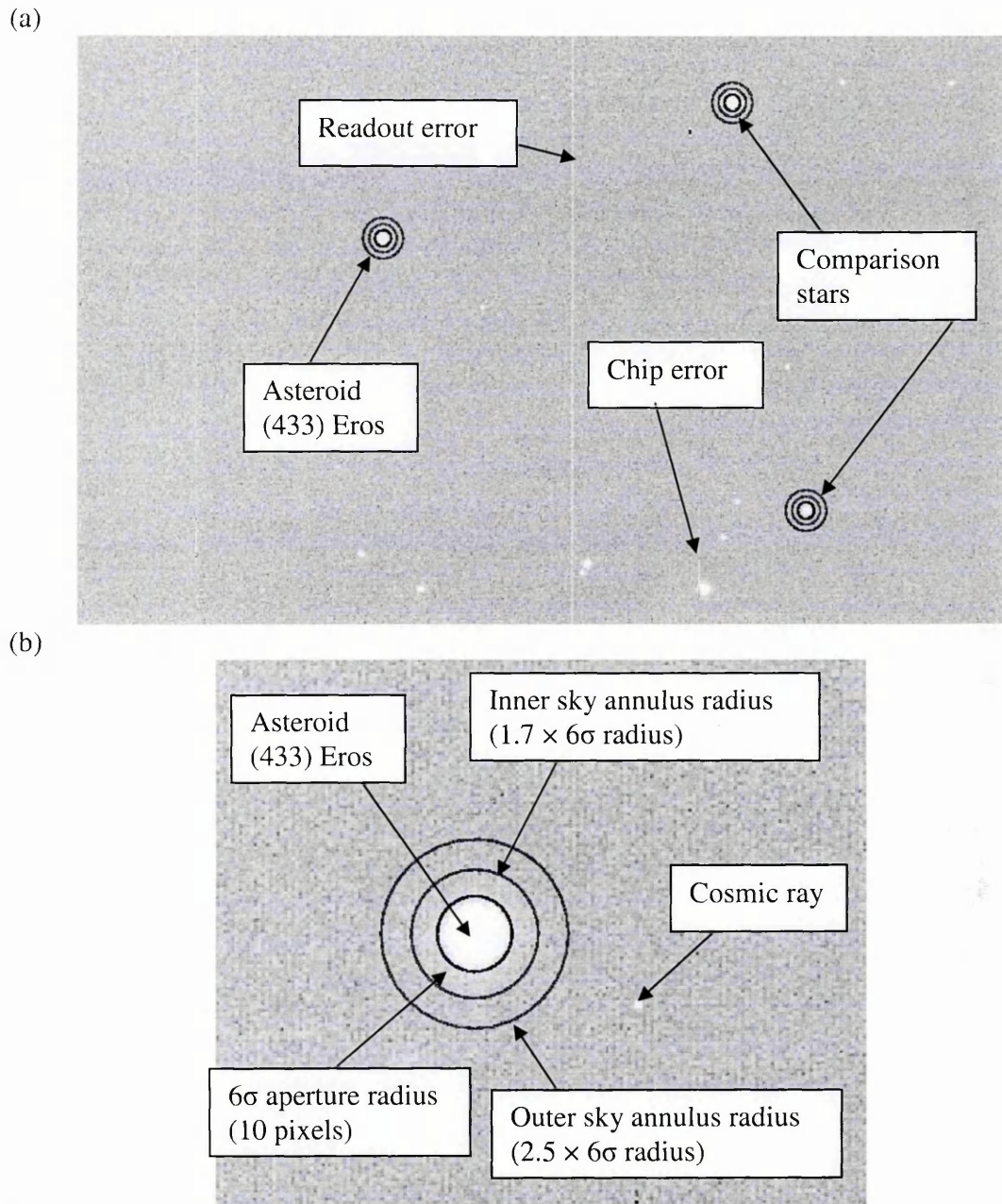


Fig. 3.5 (a) A section of a flat fielded and de-biased SITE2 (fast mode) CCD image of (433) Eros taken on 28 September 2002 UT at the JKT, frame r256665, 5 s exposure. Brighter stars in the image are good candidates for comparison stars for relative photometry. A chip error can be seen, partially covering a good potential comparison star; (b) 6σ ($1\sigma=0.425 \times \text{FWHM}$) aperture drawn around (433) Eros, with inner and outer sky background annulus at 1.7 and $2.5 \times 6\sigma$ aperture radius. A cosmic ray hit can also be seen.

The FWHM is measured using the “Pick Object” function within GAIA, a software routine which finds the FWHM within two axes, where the x-axis is defined as the direction of the longest FWHM. The FWHM can be longer in one direction, since although

the JKT attempts to track at the same constant right ascension (RA) and declination (DEC) it can drift by 1-2 pixels (the exposure times are deliberately chosen to avoid a longer drift). However, when the JKT is pointing to the West, there is a fault with the guiding system that can cause the drift to become more severe. The average FWHM is simply used to define the radius of the circular aperture. GAIA automatically calculates centroids with a maximum of nine iterations and a positional accuracy of 0.05 pixels to ensure that the maximum brightness centre is defined as the centre of the aperture.

A sky background annulus between 1.7 and $2.5 \times$ the radius of the 6σ aperture and 5.1 and $7.5 \times$ the radius of the 2σ aperture (so both apertures are the same area) is also applied. Within the annulus, all pixels outside two standard deviations of the average are rejected, the average is recalculated and subtracted from the counts in the aperture.

Also input are the exposure time t_{exp} and the photons per data unit (gain) g (e.g. 2.78 for the SITe2 CCD in fast mode), allowing an instrumental magnitude to be calculated following Eq. 3.1. Any counts above 50000 are regarded as saturated, since the CCD becomes less linear. An uncertainty for each magnitude is calculated using photon statistics inside the sky background annulus. This uncertainty will serve as a guide to the relative error between points, but not the absolute uncertainty, which is dominated by the atmospheric extinction correction.

The advantage of using MaxIM DL 4 is that it has routines which will determine the position of the asteroid and comparison stars by determining the rate of motion of the asteroid relative to the background star positions. After placing an aperture on the asteroid and three comparison stars, MaxIM DL will automatically move the apertures to follow these objects from frame to frame, and output the magnitudes. Each frame is briefly reviewed, to ensure that the process was successful, and to check for chip errors or cosmic rays that may affect the measurements. The main disadvantage is that since we are

reducing tens of frames at once, the aperture radius is constant for all frames, and not independently calculated for each frame by determining the average FWHM in the frame. Therefore, if the seeing changes drastically during a run on an object, the percentage light captured will vary. However, the effect is generally negligible for the 6σ aperture, since it contains essentially all the light from the source.

If the asteroid is moving so quickly that it is not possible to achieve adequate S/N (>30) before the asteroid has moved more than 1.5 pixels across the CCD, then the asteroid is tracked by the telescope (Sections 3.2 and 3.3). In this case, stars appear “trailed” as they move across the field during the exposure (Fig. 3.6). We continued to use circular apertures, but expanded them beyond 6σ so as to include all the light from the comparison stars (this larger aperture was used on the asteroid as well). The aperture radius was expanded by half the estimated movement of the stars across the field during the exposure (typically by 10 to 20 pixels). The 6σ aperture can continue to be used on the asteroid as well, for direct calibration (Section 3.5.3). Increasing the aperture to such large sizes causes greater uncertainty in the instrumental magnitude because it includes more sky background photons, contributing to the noise, and the likelihood of encountering chip errors, cosmic rays, or other stars within the aperture is increased. In such cases, indirect calibration is less preferable due to the necessity of using large apertures, each of which have increased noise, but in many cases it is necessary when the conditions are not photometric.

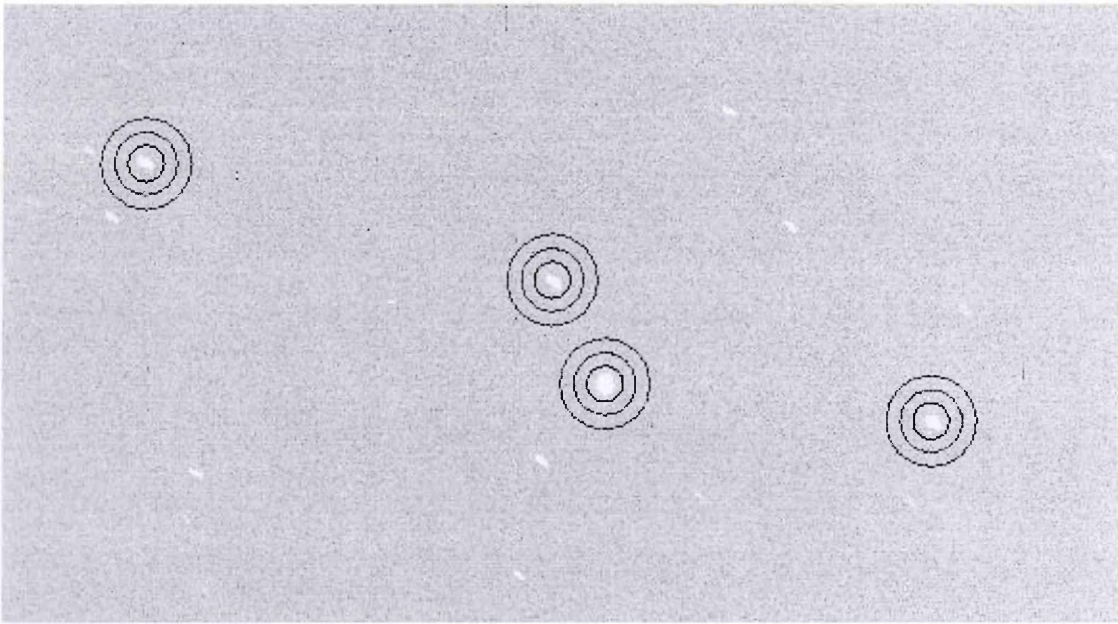


Fig. 3.6 10 s exposure frame of asteroid (33342) 1998 WT₂₄, frame 201833 taken at 20:29 UT on 18 December 2001 at JKT, using the SITe2 CCD with the R-filter. Telescope was tracking to follow the movement of the asteroid across the sky. The comparison stars are trailed across a length of 20 pixels. Larger apertures with a $6\sigma + 10$ pixel radius are used for relative photometry.

MaxIM DL works in a similar way to GAIA, except that the program will not measure instrumental magnitudes, but will only measure relative magnitudes between a comparison star and the asteroid. As will be seen, it is still possible to measure the asteroid's apparent magnitude through indirect calibration if the instrumental magnitude of the comparison star is measured. Every ten frames or so, the three comparison stars' instrumental magnitudes are measured in GAIA; after selecting one and ensuring it remains at a constant brightness relative to the other comparison stars, it is calibrated as described below.

Alternatively, we can effectively measure the asteroid's instrumental magnitude directly, and hence perform direct calibration. If the asteroid is tracked so the stars are streaked, e.g. for 1998 UO₁ in September 2002, this is the only method available. A synthetic Gaussian reference star is placed in a 32×32 pixel box in the top-left corner with a standard deviation of 1.8 pixels and a maximum intensity value of 65535. It is a trivial

matter to determine its “instrumental magnitude” which depends only on t_{exp} and g , and hence add this to the relative magnitude measured between the asteroid and the synthetic reference star to determine the asteroid’s instrumental magnitude.

The other difference with using MaxIM DL is that there is less freedom to determine the precise width of the aperture and annulus, since it can only be set at 2 pixel intervals in certain regimes. Also photon statistics are not performed on the sky background annulus, hence the magnitudes do not have measured uncertainties.

3.5.5 Direct and Indirect Calibration Methodology

Calibration can be performed directly using the values of k_m and Z_m calculated from the extinction plots for that night (Section 3.4.2), for example in the V-filter:

$$V_{ast} = v_{inst} - k_v \chi - Z_v \quad (3.8)$$

where V_{ast} is the apparent magnitude of the asteroid. If conditions are near-photometric this can produce adequate results. However, often the extinction varies throughout the night due to changing weather conditions, such as thin cirrus. More reliable calibration can be obtained through indirect calibration.

For indirect calibration, comparison stars are observed in the same field as the asteroid. We labelled the comparison stars A, B, C etc. Since the comparison star should be constant in brightness, its apparent magnitude in each frame can be calculated using Eq. 3.8, e.g. with V_{ast} replaced by V_A , and then averaged over all frames. The standard error of the comparison star apparent magnitude provides an estimate of the uncertainty contributed by this step in the calibration. If there were minor variations in extinction compared to those predicted by the derived k_v and Z_v during the night, the averaged apparent magnitude should still be reliable. But of course clouds will make the star appear too faint. If the telescope is not tracking, then the 2σ instrumental magnitudes can be used for relative

photometry (if we are using GAIA) between the asteroid and the comparison star for indirect calibration. This can increase accuracy since there is less sky background in the aperture.

The extinction calibration is acquired by adding V_A to the relative magnitude between the asteroid instrumental magnitude $v_{inst}(ast)$ and the comparison star $v_{inst}(A)$:

$$V_{ast} = V_A + v_{inst}(A) - v_{inst}(ast) \quad (3.9)$$

Frames must be carefully studied to decide what stars to use as comparison stars. It is advisable to use three comparison stars, so that plots of, e.g., $v_{inst}(A) - v_{inst}(B)$ and $v_{inst}(A) - v_{inst}(C)$ can be produced (so if the former is not constant but the latter is, it is star B that is variable and not star A) in order to ensure that the variation in their brightness is due to the weather and not to the star being variable, or some problem in the position on the CCD field (e.g. Section 3.7.4). In order to ensure continued linearity with brightness, often the comparison stars would be chosen with some dispersion in their instrumental magnitudes (for example, comparison stars of $V_{app} \sim 12, 13$ and 14 mag. would be observed, 11 th magnitude stars would saturate the CCD). Extinction plots can also be produced of the comparison stars to examine the behaviour of the atmosphere in the observed region of the sky. Choosing bright stars increases the accuracy of relative photometry. As previous comparison stars move towards the edge of the frames, three new comparison stars are chosen so that there is an overlap where both sets of comparison stars are being observed at once. The difference in magnitude between the chosen comparison star from the first set and the second is used to create a “ghost” comparison star that can be used to create a relative lightcurve.

For example, for asteroid 2001 SE₂₈₆ observed on 18 December 2001 UT in the R-filter, a new set of comparison stars was chosen at the ends of each run, so that when the telescope was moved back onto 2001 SE₂₈₆ after observing standards, the stars were still in

the field. Eventually 27 comparison stars were used, with often six stars measured in one frame. Figure 3.7 shows the instrumental magnitudes measured in the R-filter of the comparison stars and 2001 SE₂₈₆. A “ghost” comparison star is formed as a composite of stars B, D, H, J, O, U, W and Y from their relative differences in magnitude so that it appears as if O was observed constantly.

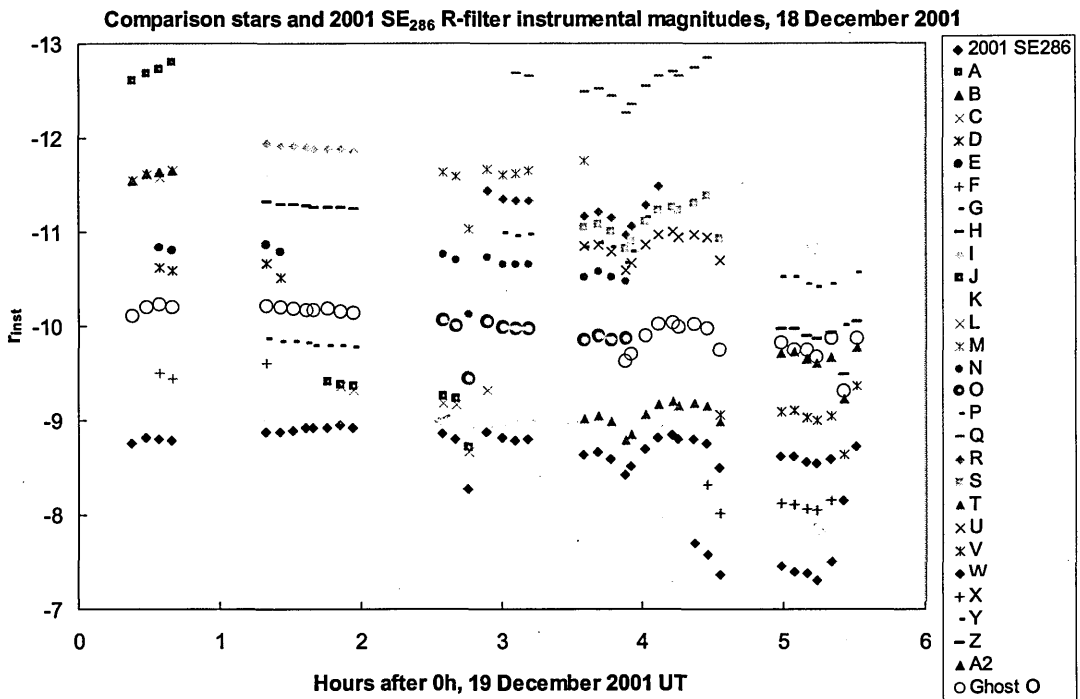


Fig. 3.7 Instrumental magnitudes of comparison stars and asteroid 2001 SE₂₈₆ observed at the JKT on the night of 18 December 2001 with 60 s exposures in the R-filter. Gaps in the data are periods when standard stars were being observed. For every run three comparison stars were observed. For as many frames as they are reasonably distant from the edge of the CCD, three more comparison stars are observed that will be in-frame on the next run. Ghost comparison star O (open circles) is formed as a composite of the overlapping relative magnitudes of the stars B, D, H, J, O, U, W and Y (all coloured red).

3.6 Photometric Calibration

The raw frames are flat fielded and de-biased as described in Section 3.5.2, and the method by which the magnitudes of the stars were measured is described in Section 3.5.4. Large 5.1 FWHM diameter (6σ) apertures were used. Atmospheric extinction correction is

described in Section 3.4.2. All standard star fields were obtained from Landolt (1992). Error bars in the extinction plots are a combination of the photon statistics and the uncertainty in the magnitude given in Landolt. A summary of the derived atmospheric extinction coefficients k and photometric zero-points Z are given in Table 3.1.

Table 3.1

Summary of derived atmospheric extinction coefficients k_v and photometric zero-points Z_v for standard stars observed at the JKT on May 2001, December 2001 and September 2002

Date	k_v	Z_v	Uncertainty	Comment
4 May 2001	0.154	-23.239	0.02	Near-solar colours adopted.
6 May 2001	0.230	-23.306	0.02	Without PG1633.
7 May 2001	0.159	-23.282	0.02	Near-solar colours adopted.
8 May 2001	0.160	-23.231	0.02	
9 May 2001	0.135	-23.253	0.02	Near-solar colours adopted.
10 May 2001	0.107	-23.094	0.02	Near-solar colours adopted.
18 December 2001	0.225	-23.427	0.04	k_r and Z_r . Used clear obs. before 23:11 UT.
25 September 2002	0.100	-22.982	0.04	
27 September 2002	0.165	-22.885	0.04	
28 September 2002	0.166	-22.882	0.04	
29 September 2002	-0.167	-22.528	0.04	Cloudy, not photometric.
1 October 2002	0.049	-22.921	0.04	May have been photometric in early night.

3.6.1 May 2001

The photometric calibrations for 4, 6, 7, 9 and 10 May 2001 were reduced by S. F. Green. Figure 3.8 shows the extinction plot for 8 May 2001, for which the standard stars were taken from the field of PG1633. All stars were used for the linear fit, from which we derive the V-filter extinction coefficient $k_v = 0.160$ and the zero-point correction $Z_v = -23.231$. The uncertainty of the photometric calibration was estimated to be 0.02 mag., from the spread of the standard stars about the linear fit.

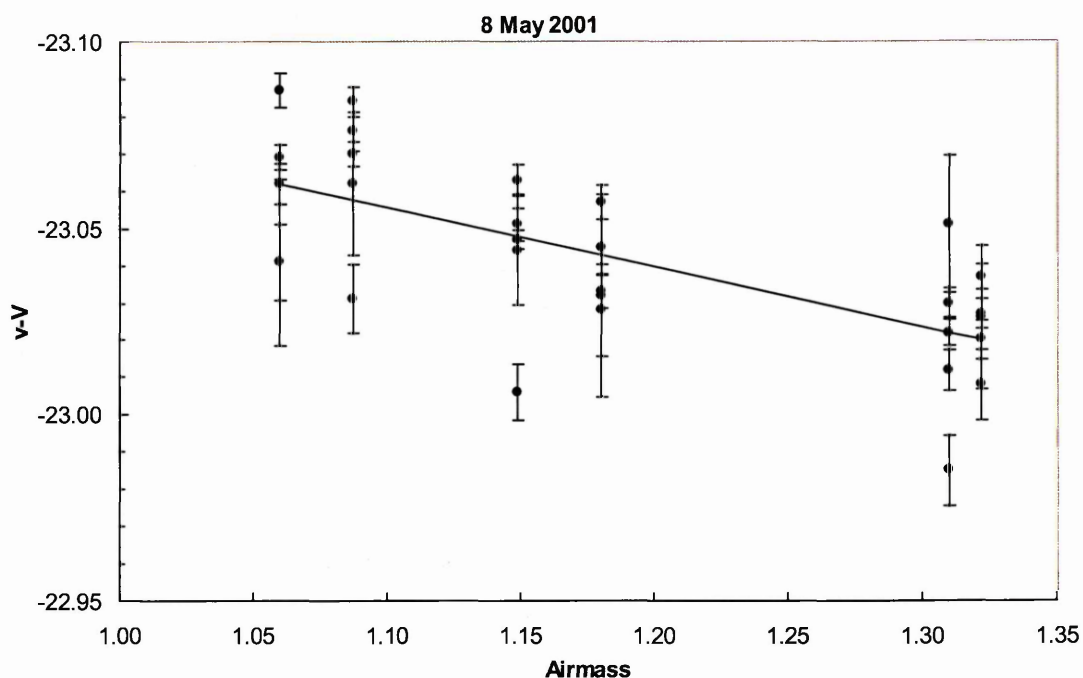


Fig. 3.8 Atmospheric extinction plots showing the difference between instrumental magnitudes (v) and apparent magnitudes (V) of standard stars versus airmass for observations at the JKT on 8 May 2001.

3.6.2 December 2001

Fig. 3.9 shows the extinction plot for 18 December 2001. The standard stars were taken from the fields of Selected Area 92 centred on star 249 (92s249), RUBIN 149 (RU 149) and PG01918+029 taken in the B, V, R and I-filters. Upon reducing the data for the night, it quickly became clear that the weather was not close enough to photometric to obtain meaningful colours $V-R$ etc., and that the standard stars after 23:11 UT are affected by cirrus. As a result, only the atmospheric extinction for the R frames was used, since asteroids (33342) 1998 WT₂₄ and 2001 SE₂₈₆ were observed mostly using that filter. Using all stars we measure $k_r = 0.050$ and $Z_r = -23.086$ (dotted line), which is not reliable due to the cirrus. Using just the stars observed during the early night, when it was clear (filled points), we measure $k_r = 0.225$ and $Z_r = -23.427$ (solid line); these values were the ones

adopted and an uncertainty of 0.04 mag. was assigned based on the spread of the standard stars about the linear fit.

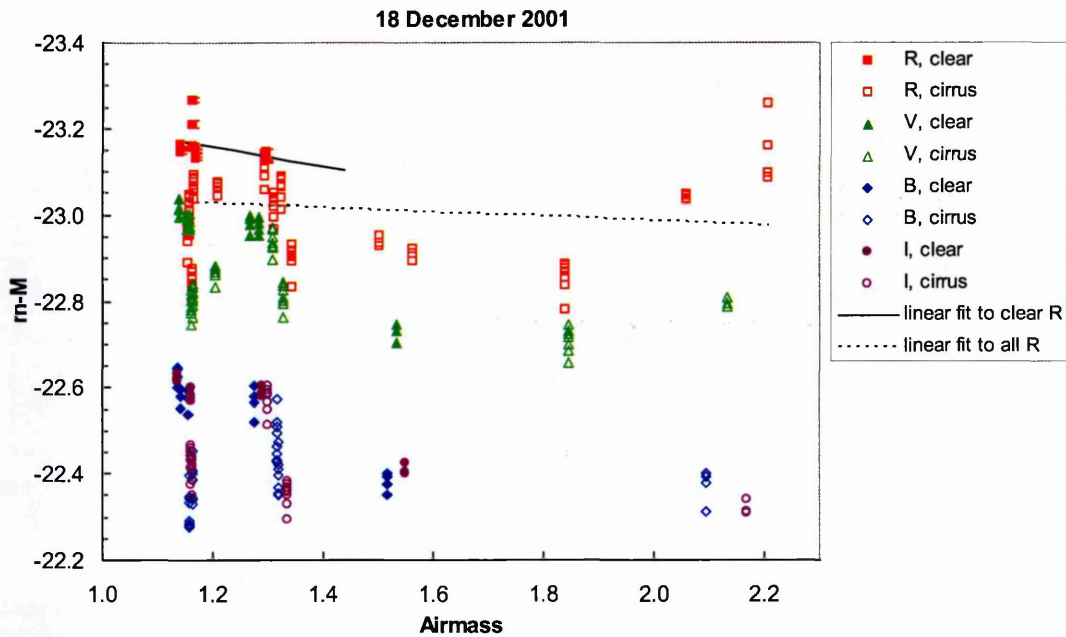


Fig. 3.9 Extinction plot for JKT 18 December 2001 showing $r-R$, $v-V$, $b-B$ and $i-I$ of standard stars versus airmass. (Filled points) are observations taken during clear weather; (open points) are observations taken when there was cirrus.

3.6.3 September 2002

Figure 3.10 shows the extinction plots for September 2002. On 25 September, three points were removed from the early night because they were half a magnitude dimmer. These were all observations of star 115420 and may have been affected by cloud. On two frames, it was not possible to measure the magnitude of 92s259 because of a chip error. For the 27 September plot, all six standard star magnitudes measured after 03:53 UT were not useable. They were all of 94s242; the first three were not measurable due to a chip error in the aperture, the last three were about half a magnitude dimmer than expected, which was probably also due to a chip error. 29 September was clearly not photometric, since the derived k_v is negative (i.e. atmospheric extinction decreases with airmass). The extinction plot (all of 115s420) ignores all observations made after 03:00 UT, by which

time the weather had worsened, so that magnitudes were 0.5-2 magnitude dimmer. On 1 October conditions may have been photometric in the early night. Stars 110sL1 and 110s362 have only had one observation made in Landolt (1992) and so are excluded since they may not be reliable. R and I-filter frames were taken for the standards also; they are not presented here since only V-filter observations of the NEAs have been reduced, due to conditions not being photometric, generally (Section 7.2.1).

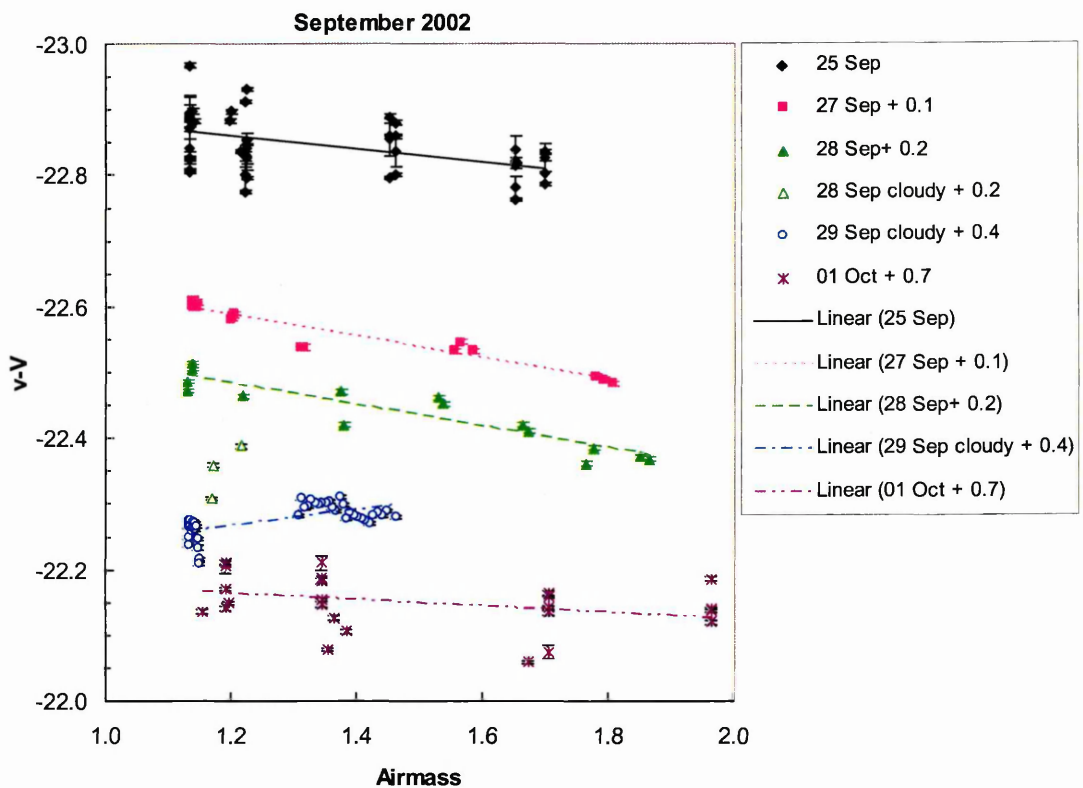


Fig. 3.10 Extinction plots for JKT September 2002 showing $v-V$ of standard stars versus airmass with arbitrary magnitudes added to different nights for clarity. The calibration of 27 and 28 September agree closely, while bad weather affected 29 September.

3.7 Reduction of Instrumental Magnitudes to Reduced Magnitudes

See Section 3.5 for a detailed description of the method used to reduce optical observations. All plots are exposure and light-time corrected. Table 3.2 shows the observational circumstances and instrument configuration.

Table 3.2 Observational circumstances and instrument configuration for asteroids observed at the JKT in May 2001, December 2001 and September 2002

Asteroid	Date (UT)	Start-End (hh:mm UT)	Start Airmass - End Airmass	Exp. time (s)	No. of frames	Tracking Y/N?	r (AU)	Δ (AU)	α°
(433) Eros	28.1 Sep. 2002	23:04 - 03:39	1.033 - 2.167	5.0 ^a	47	N	1.590	0.639	18.0
	29.0 Sep. 2002	20:37 - 03:22	1.270 - 1.995	5.0	76	N	1.588	0.640	18.6
	30.0 Sep. 2002	23:01 - 00:26	1.033 - 1.095	5.0	60	N	1.585	0.642	19.1
(4034) 1986 PA	8.1 May 2001	21:37 - 05:08	1.468 - 1.514	120.0	67	Y	1.199	0.278	41.9
	9.1 May 2001	00:24 - 05:06	1.021 - 1.550	120.0	44	Y	1.206	0.285	41.3
	10.1 May 2001	01:34 - 05:32	1.011 - 1.823	120.0	44	Y	1.212	0.291	41.8
	11.1 May 2001	22:23 - 04:48	1.217 - 1.218	120.0	21	Y	1.218	0.297	40.4
	4.9 May 2001	21:15 - 22:39	2.139 - 1.399	9.0	43	N	1.243	0.309	35.8
(5587) 1990 SB	6.1 May 2001	22:46 - 05:12	1.351 - 1.334	9.0	184	N	1.236	0.307	37.1
	7.1 May 2001	21:23 - 05:13	1.941 - 1.341	9.0	137	N	1.231	0.305	38.2
	28.2 Sep. 2002	01:31 - 05:43	1.950 - 1.924	8.0	91	N	1.353	0.444	31.5
(6455) 1992 HE	29.1 Sep. 2002	01:34 - 05:55	1.833 - 2.049	8.0	110	N	1.361	0.444	30.1
	30.1 Sep. 2002	01:06 - 04:28	1.925 - 1.606	8.0	108	N	1.368	0.444	28.7
(19356) 1997 GH ₃	2.1 Oct. 2002	01:19 - 05:34	1.677 - 1.993	7.5	49	N	1.384	0.447	25.7
	5.1 May 2001	23:00 - 05:19	1.860 - 2.345	50.0	137	N	1.377	0.373	8.0
1998 UO ₁	11.1 May 2001	22:42 - 04:42	1.762 - 2.196	50.0	66	N	1.419	0.411	5.2
	26.2 Sep. 2002	03:00 - 06:10	1.087 - 1.156	120.0	43	Y	1.201	0.337	47.2
(33342) 1998 WT ₂₄	18.9 Dec. 2001	20:29 - 23:58	1.039 - 2.085	10.0	47	Y	0.988	0.019	76
	8.0 May 2001	22:35 - 23:37	1.083 - 1.238	120.0	10	Y	1.189	0.412	54.8
(25330) 1999 KV ₄	8.9 May 2001	21:39 - 23:13	1.018 - 1.169	120.0	16	Y	1.194	0.417	54.3
	10.0 May 2001	21:12 - 01:27	1.008 - 2.038	120.0	65	Y	1.200	0.418	53.8
(53789) 2000 ED ₁₀₄	11.0 May 2001	21:02 - 01:00	1.008 - 1.755	120.0	31	Y	1.205	0.428	53.4
	2.0 Oct. 2002	21:26 - 01:03	1.037 - 2.162	10.0 ^b	40	Y ^c	1.081	0.189	60.5
2001 SE ₂₈₆	19.1 Dec. 2001	00:23 - 05:32	1.192 - 1.336	60.0	38	Y	1.121	0.146	19.2
2002 HK ₁₂	26.0 Sep. 2002	23:22 - 02:40	1.560 - 1.008	15.0	72	N	1.126	0.159	36.8
	27.2 Sep. 2002	00:59 - 06:24	1.132 - 1.365	15.0	192	N	1.133	0.165	35.0
28.1 Sep. 2002	23:17 - 03:32	1.509 - 1.007	15.0	44	N	1.139	0.169	33.5	

Table 3.2 continued.

Asteroid	Date (UT)	Start-End (hh:mm UT)	Start Airmass - End Airmass	Exp. time (s)	No. of frames	Tracking Y/N?	r (AU)	Δ (AU)	α°
2002 NX ₁₈	25.9 Sep. 2002	20:15 - 22:50	1.597 - 1.816	40.0	67	N	1.159	0.284	50.6
	27.9 Sep. 2002	20:06 - 23:01	1.615 - 1.928	36.0	83	N	1.150	0.279	52.0
	28.9 Sep. 2002	20:51 - 22:44	1.572 - 1.844	33.0	28	N	1.145	0.277	52.6
	29.9 Sep. 2002	20:05 - 22:56	1.617 - 1.938	30.0	65	N	1.141	0.274	52.3
2002 QE ₁₅	1.9 Oct. 2002	20:42 - 21:12	1.586 - 1.599	28.0	6	N	1.133	0.270	54.5
	26.9 Sep. 2002	20:26 - 00:51	1.130 - 1.979	40.0	126	N	1.135	0.427	61.3
	28.9 Sep. 2002	20:14 - 00:17	1.122 - 1.758	35.0	44	N	1.130	0.415	61.7
	2.0 Oct. 2002	23:24 - 23:32	1.507 - 1.541	28.0	3	N	1.123	0.395	62.2

Notes. ^aExcept first 12 frames exp. time = 10.0 s.

^bExcept for first frame, exp. time = 30.0 s.

^cExcept for 8 frames.

3.7.1 (433) Eros*27 September 2002 (28.1 Sep.)*

Three comparison stars were observed, labelled A, B and C (will be different stars from those similarly labelled on other nights or for other objects). C stayed at constant brightness relative to A and B (± 0.01 mag.), so it was used for indirect photometric calibration (Section 3.5.5). For seven frames, C was affected by chip errors; for those frames a star “Ghost C” was formed by cross-calibration using mostly B; its extinction plot is given in Fig. 3.11 (a) and its apparent magnitude $V = 13.27 \pm 0.04$ is derived using the filled points. The uncertainty is calculated from a combination of the standard error (σ/\sqrt{N} , where N is the number of points) of the filled points (± 0.003) and the estimated atmospheric extinction uncertainty (± 0.04 , Section 3.6), so is dominated by the extinction. Conditions were mostly photometric. Figure 3.12 (a) shows the reduced magnitudes $V(1, \alpha=18.0^\circ)$ obtained with direct calibration using 6σ apertures and the indirect calibration using 2σ and 6σ diameter apertures. Five frames where (433) Eros was in a chip error have been removed. The 6σ indirect calibration was used for the 28.1 September contribution to the composite lightcurve because (433) Eros was a bright target, so more light was captured using the larger aperture. The 2σ indirect calibration and 6σ direct calibrations produced similar results.

28 September 2002 (29.0 Sep.)

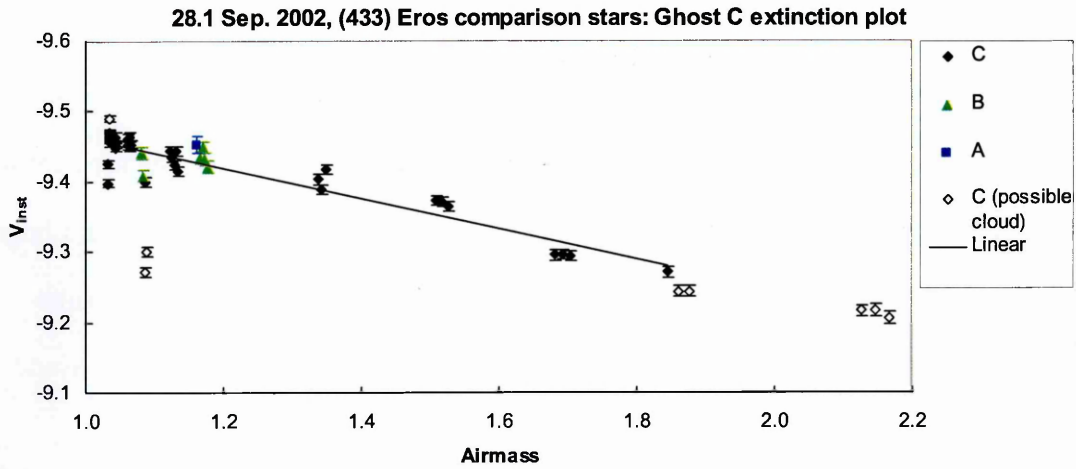
Three comparison stars were observed: A, B and C. B stayed at constant brightness relative to A and C (except when in a chip error) (± 0.01 mag.) and was used for indirect calibration. B was in a chip error for 14 frames, so “Ghost B” was formed from cross-calibration, mostly with A; its extinction plot is shown in Fig. 3.11 (b) and its derived apparent magnitude (excluding some frames in bad weather, open points) $V = 12.11 \pm 0.04$.

Conditions were mostly photometric, but there was sporadic cirrus in the early night. Figure 3.12 (b) shows the reduced magnitudes $V(1, \alpha=18.6^\circ)$ obtained with direct calibration (6σ) and indirect calibrations (2σ and 6σ). Eight frames where (433) Eros was in a chip error have been removed. The 6σ aperture indirect calibration was used for the 29.0 September contribution to the composite lightcurve because (433) Eros was a bright target. The indirect calibration (2σ) and direct calibration (6σ) produced similar results.

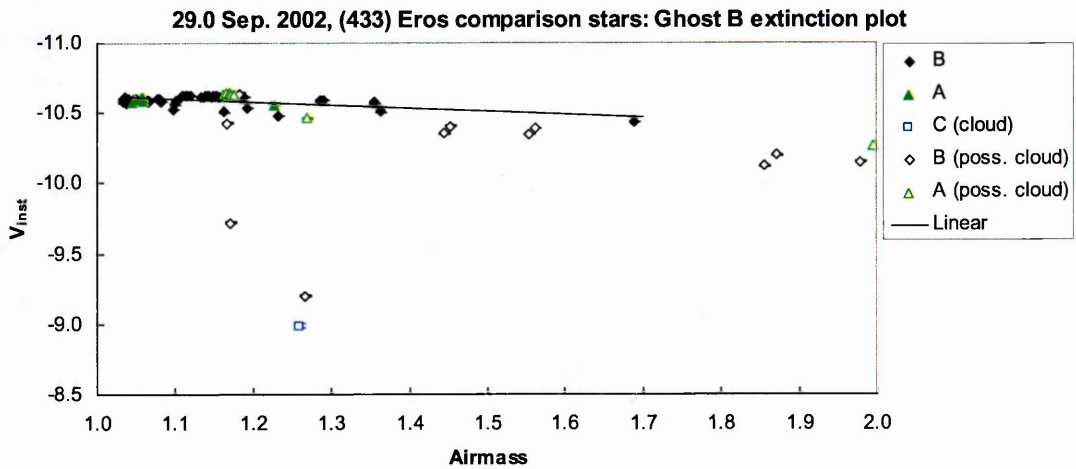
29 September (30.0 Sep.)

Three comparison stars were observed: A, B and C. C stayed at constant brightness relative to other comparison stars (± 0.02 mag.) and was used for indirect calibration. C was in a chip error for 10 frames, so “Ghost C” was formed, cross-calibrating with B; its extinction plot is given in Fig. 3.11 (c) and its derived apparent magnitude (excluding frames before 23:30 taken in bad weather) $V = 10.79 \pm 0.04$. Figure 3.12 (b) shows $V(1, \alpha = 19.1^\circ)$ obtained with direct calibration (6σ) and indirect calibrations (2σ and 6σ). One frame where (433) Eros was in a chip error has been removed. There was a sequence of five frames where (433) Eros was too close to a star to measure (around 23:50 UT). The 6σ indirect calibration was used for the 29.0 September contribution to the composite lightcurve because (433) Eros was a bright target. The conditions were not photometric, and the direct calibration is noisy. The 2σ indirect calibration produced similar results.

(a)



(b)



(c)

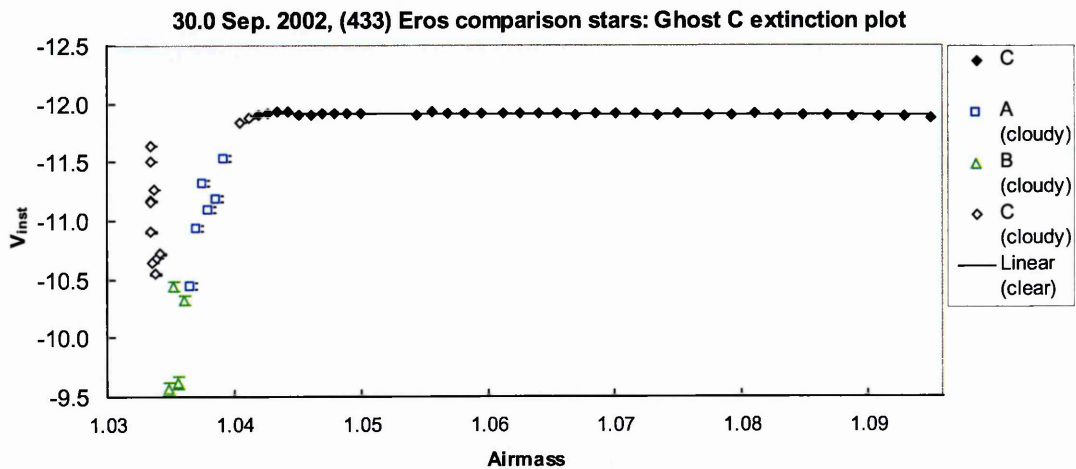


Fig. 3.11 Extinction plots of comparison stars observed on the same field as (433) Eros at the JKT in September 2002. Nights of (a) 27 Sep.; (b) 28 Sep.; (c) 29 Sep.

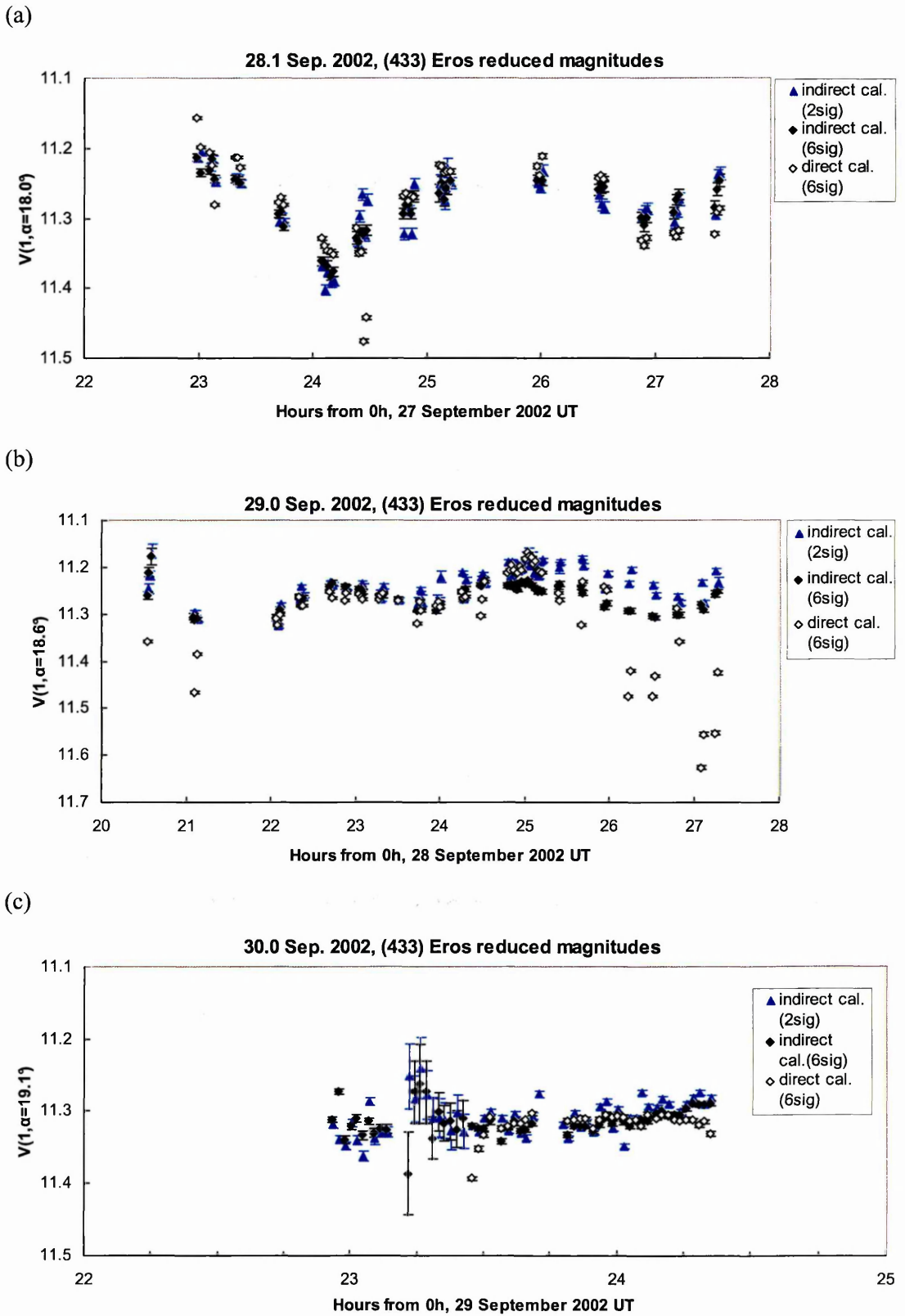


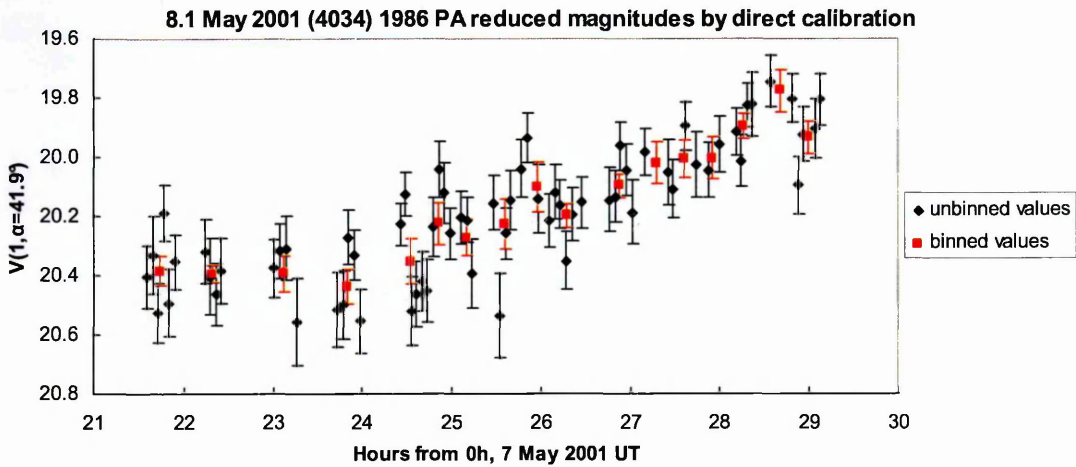
Fig. 3.12 Reduced magnitudes $V(1, \alpha)$ of (433) Eros observed at the JKT in September 2002 showing direct and indirect calibrations. Nights of (a) 27 Sep.; (b) 28 Sep.; (c) 29 Sep., some direct calibration values are outside the displayed range ($V < 13.7$).

3.7.2 (4034) 1986 PA

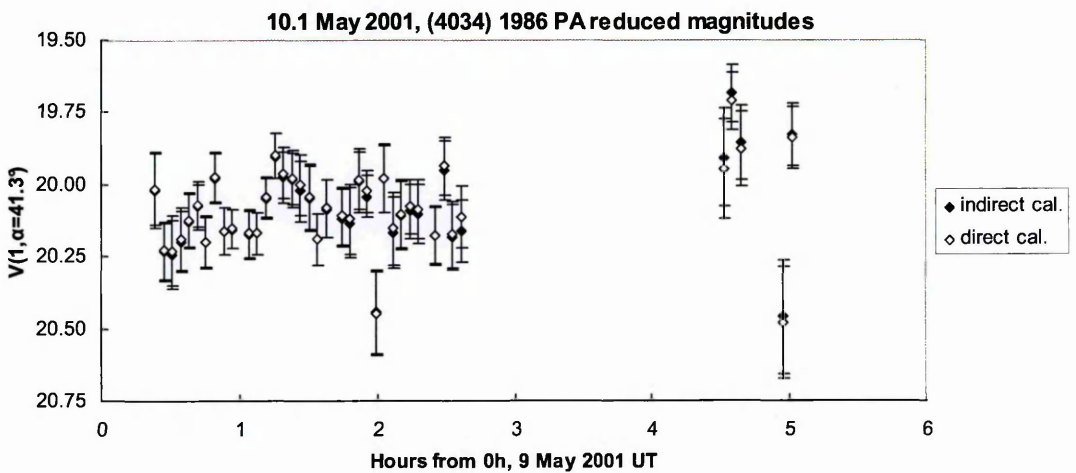
The asteroid was tracked, so only 6σ diameter apertures were observed on all nights. The reduced magnitudes obtained with direct and indirect calibration $V(1, \alpha)$ are given in Fig. 3.13. The calibrations are very similar. The direct calibration results were used to form the composite lightcurve on each night. The data for the nights of 7 and 10 May 2001 were reduced by S. F. Green. On 7 May, binned values every five frames were produced (red points), and these were used to produce the composite lightcurve.

Fig. 3.13

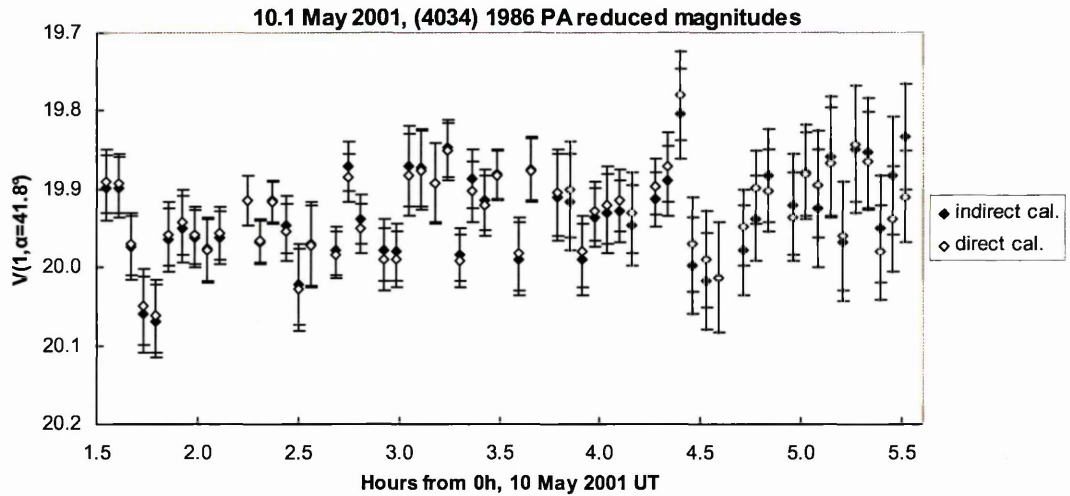
(a)



(b)



(c)



(d)

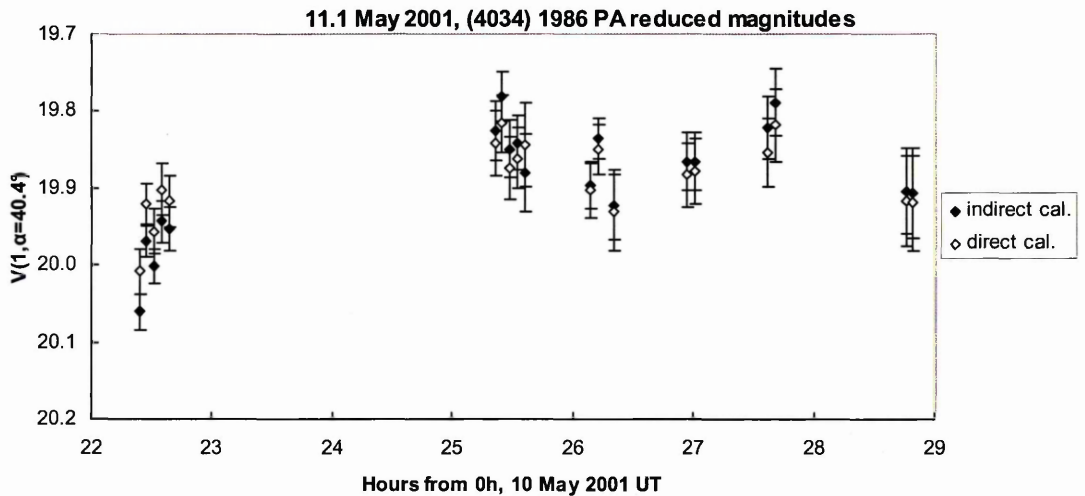


Fig. 3.13 Reduced magnitudes $V(1, \alpha)$ for (4034) 1986 PA taken at the JKT in May 2001, showing direct and indirect calibrations. Nights of (a) 7 May, (b) 8 May, (c) 9 May, (d) 10 May.

3.7.3 (5587) 1990 SB

4 May 2001 (4.9 May)

Figure 3.14 (a) shows the reduced magnitudes $V(1, \alpha = 53.8^\circ)$ obtained with direct (6σ) and indirect (2σ and 6σ) calibrations. On the first frame [outside the range of Fig. 3.14 (a)] the direct calibration is 2 mag. dimmer than the indirect calibration [note (5587) 1990 SB is at a high airmass = 2.139] but otherwise the calibrations are in good agreement with

each other. The indirect calibration using 2σ apertures was used to form the composite lightcurve.

5 May 2001 (6.1 May)

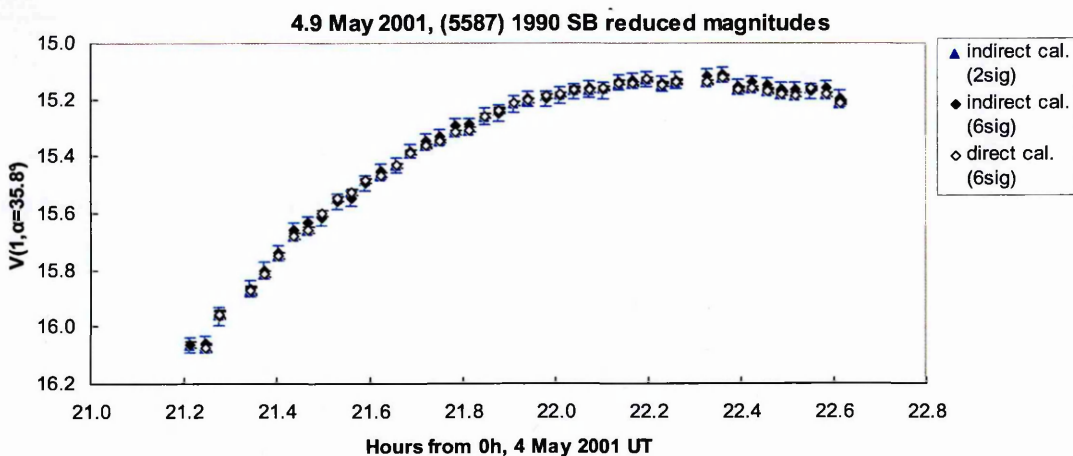
Relative photometry only was performed. However, observations of the same fields on 6 May allowed measurement of the apparent magnitude of comparison stars. Figure 3.14 (b) shows $V(1, \alpha = 37.1^\circ)$ obtained with indirect calibration using both 2σ and 6σ apertures. The 6σ calibration was used to form the composite lightcurve because (5587) 1990 SB was a bright target, so more light was captured using the larger aperture and the effect of sky noise was negligible. However, the different calibrations are similar.

6 May 2001 (7.1 May)

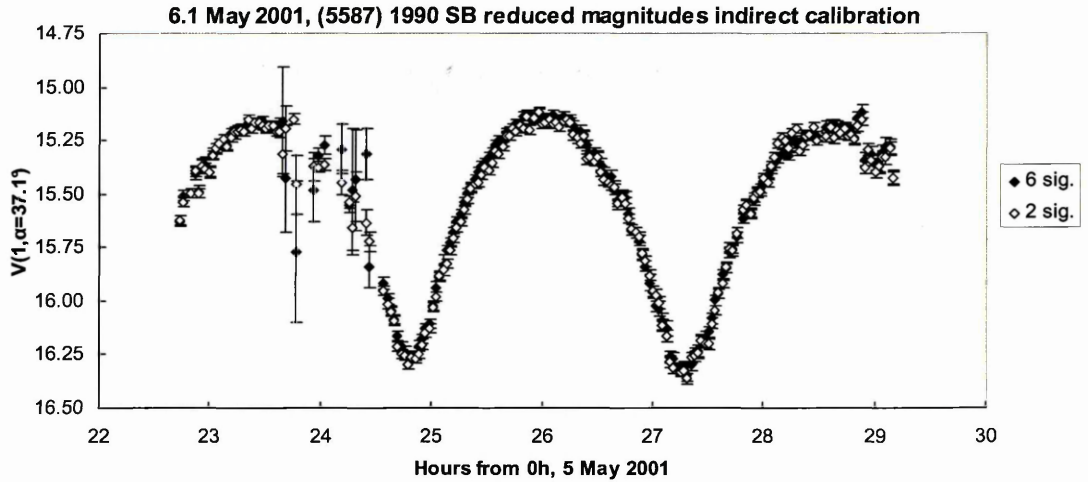
Figure 3.14 (c) shows the reduced magnitudes $V(1, \alpha = 38.2^\circ)$ obtained with direct (6σ) and indirect (2σ and 6σ) calibrations. The 6σ indirect calibration was used to form the composite lightcurve because (5587) 1990 SB was a bright target. The 2σ aperture results are similar. The direct calibration is very noisy before 01:30 UT, indicating that the atmospheric extinction was variable due to cirrus.

Fig. 3.14

(a)



(b)



(c)

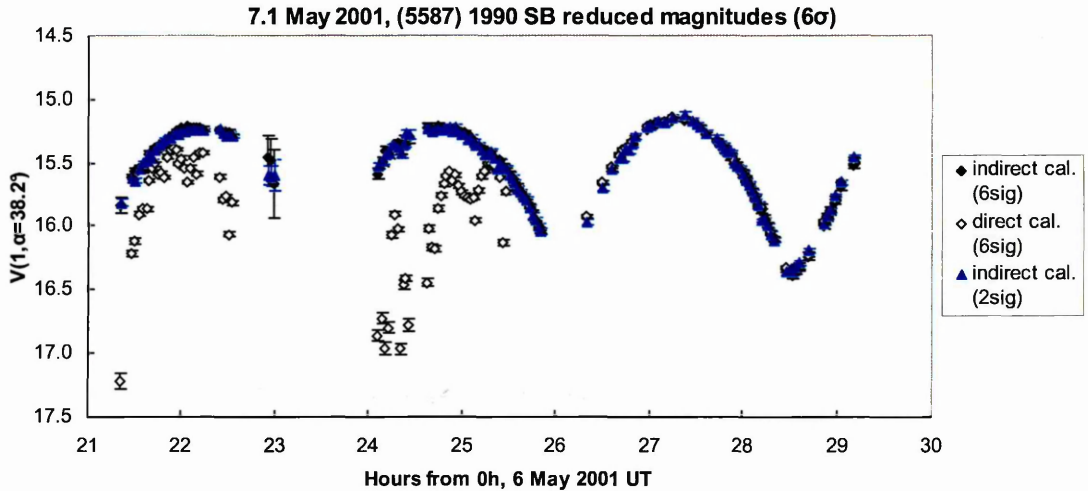


Fig. 3.14 Reduced magnitudes $V(1, \alpha)$ for (5587) 1990 SB taken at the JKT in May 2001 showing direct and indirect calibrations. Nights of (a) 4 May, (b) 5 May, (c) 6 May.

3.7.4 (6455) 1992 HE

27 September 2002 (28.2 Sep.)

Partially because the SITe2 CCD was read out in fast mode, many of the observations were affected by chip errors. Fortunately, it was judged that only (6455) 1992 HE had a chip error seriously affecting its measured magnitude on one frame, which was removed. Other frames where there was a noticeable chip error within the aperture, but where the measured magnitude seemed consistent with those previous and after it, were used. Figure

3.16 (a) shows the reduced magnitudes $V(1, \alpha = 31.5^\circ)$ obtained with direct (6σ) and indirect (2σ and 6σ) calibrations. The indirect calibration with 6σ apertures was used to form the composite lightcurve because (6455) 1992 HE was a bright target.

28 September 2002 (29.1 Sep.)

(6455) 1992 HE had noticeable chip errors within its aperture for 10 frames. These were judged to have seriously affected the measured magnitude for five frames, which were removed. Also, observations too close to the edge of the CCD, where inaccuracies in the flat field calibration were judged to have affected the measured magnitude, were made for nine frames; these were also removed.

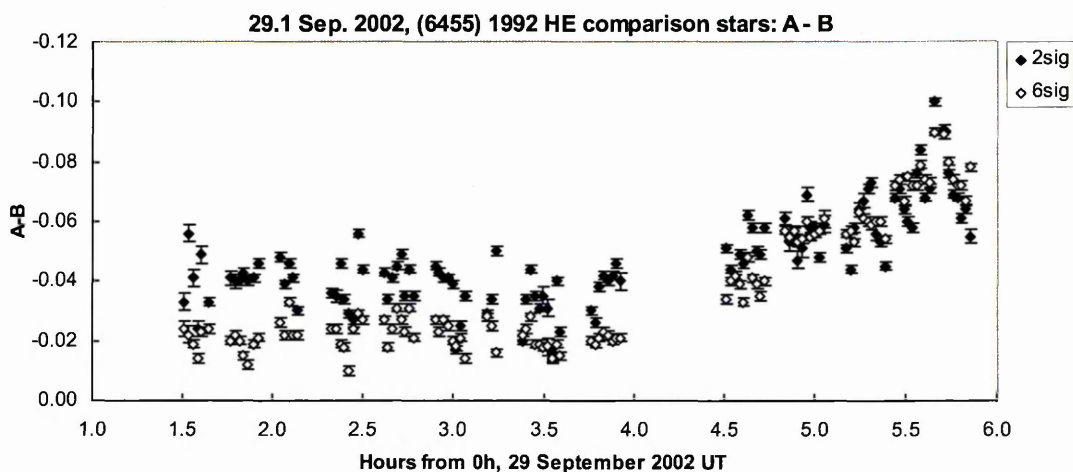
There were very limited choices for comparison stars. The only two possible comparison stars A and B, unfortunately, were both fairly close to the edge of the CCD ($x \sim 1800$, where the edge is at $x = 2100$), where uncertainties in the flat field could change their brightness as they drift East-West due to the tracking problem JKT has when pointing to the West. They were also in a portion of the CCD covered with chip errors, that we tended to avoid if possible. Figure 3.15 (a) shows their relative magnitudes using both 2σ and 6σ apertures. Note that there is a slope after 04:30 UT, i.e. the difference in brightness between the stars increases. The slope for the 2σ aperture only changes the relative magnitude by 0.02 magnitudes. Figure 3.15 (b) shows the extinction curves for these two stars. The magnitudes of both stars decrease suddenly at 1.85 airmass. Since it is a high airmass, the strange behaviour may be related to variable extinction. Star A was used for indirect calibration, a star "Ghost A" was formed which used cross-calibration to replace nine frames of A which were in chip error near the end of the night, between 05:30 and 05:41 UT, using another star D (which was 4 mag. fainter than A, and so not a good

candidate for a comparison star in general). Its derived apparent magnitude was $V = 10.15 \pm 0.04$.

Figure 3.16 (b) shows the direct (6σ) and (2σ and 6σ) indirect calibrations. Since the direct calibration is so noisy (because the conditions were not photometric) we adopted the 2σ indirect calibration, with reservations.

Fig. 3.15

(a)



(b)

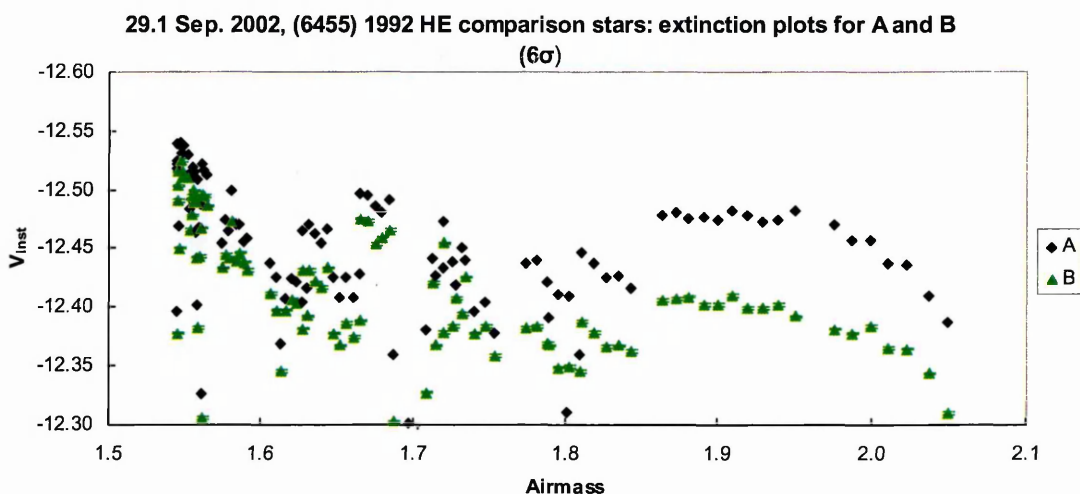


Fig. 3.15 Observations of comparison stars observed on the same field as (6455) 1992 HE at the JKT. (a) relative magnitude of stars A and B on the night of 28 September, which is not constant after 04:30 UT; (b) extinction plots for A and B on the night of 28 September.

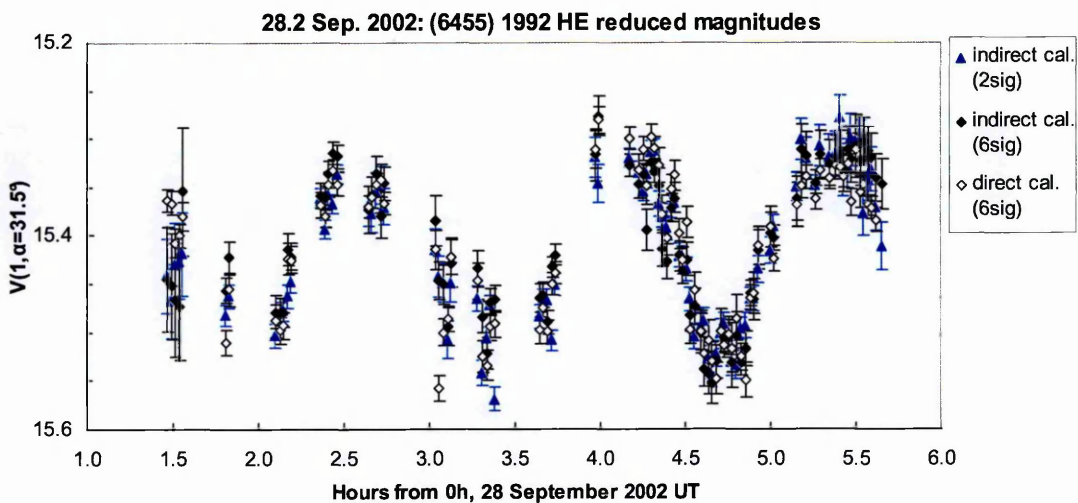
29 September 2002 (30.1 Sep.)

There were chip errors within the aperture of (6455) 1992 HE for eight frames, rendering two frames unusable. Although the weather was far from photometric (Section 3.6.3), calibration was attempted. Figure 3.16 (c) shows the direct (6σ) and indirect (2σ and 6σ) calibrations $V(1, \alpha = 28.7^\circ)$ (some direct calibration values after 03:30 UT are outside the displayed range, $V < 17.8$). Since the direct calibration is noisy, the indirect calibration with 2σ apertures was adopted.

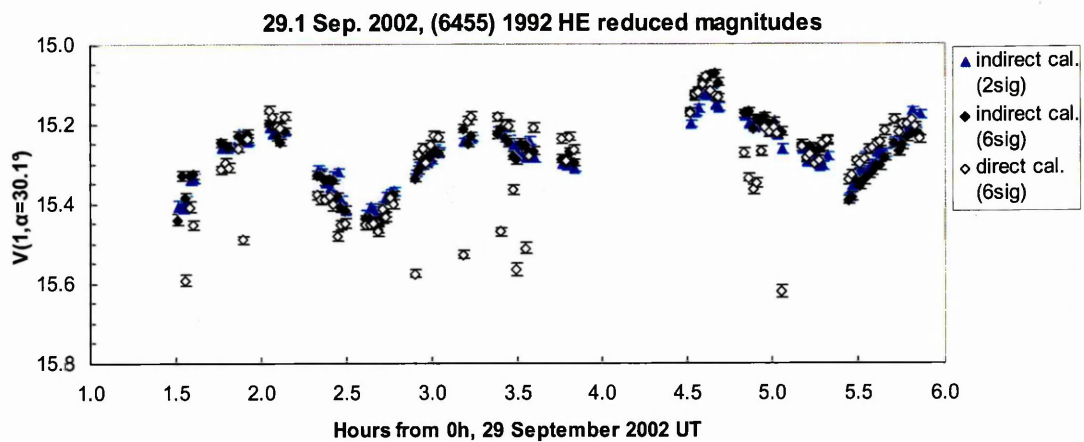
1 October 2002 (2.1 Oct.)

Six frames were removed due to chip errors within the aperture and one frame because (6455) 1992 HE was too close to a star. The direct (6σ) and (2σ and 6σ) indirect calibrations are given in Fig. 3.16 (d). The indirect calibration with 2σ apertures was determined to be the most stable, and adopted.

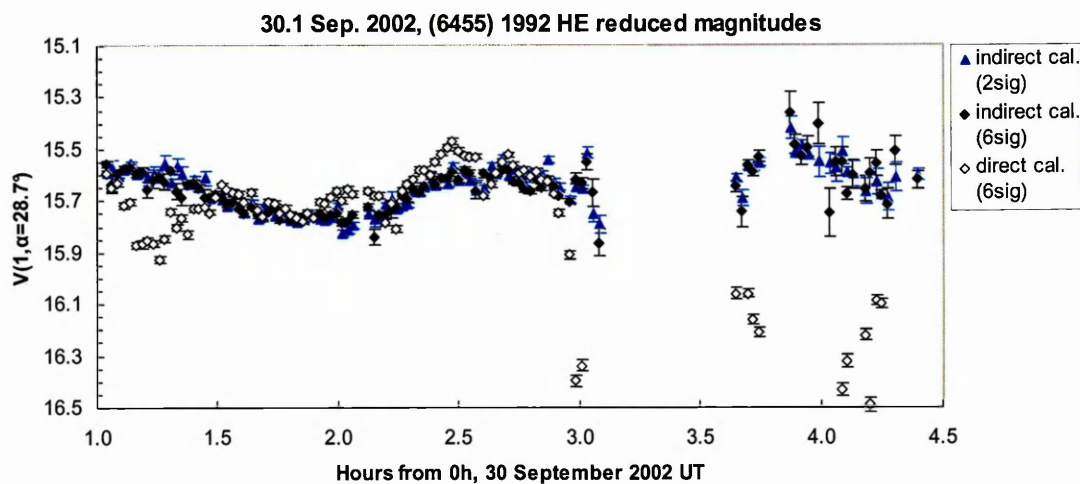
Fig. 3.16
(a)



(b)



(c)



(d)

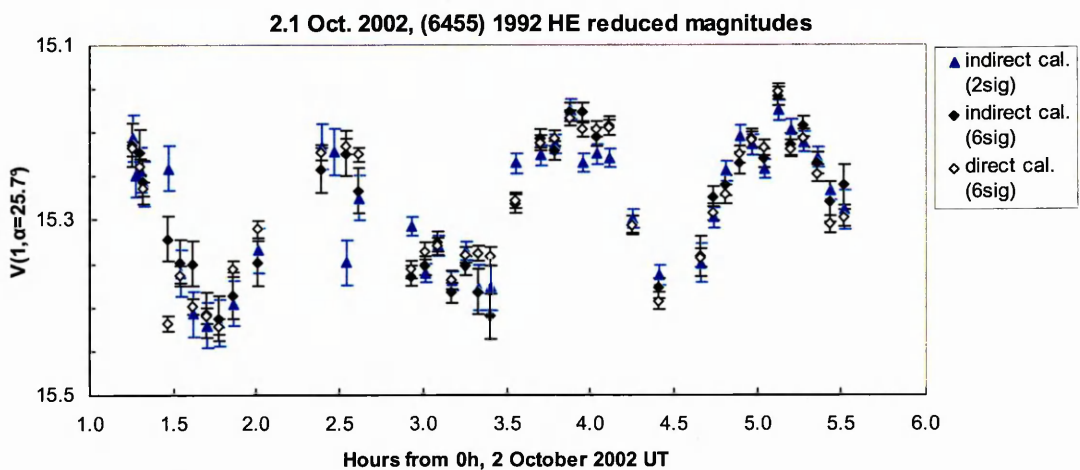
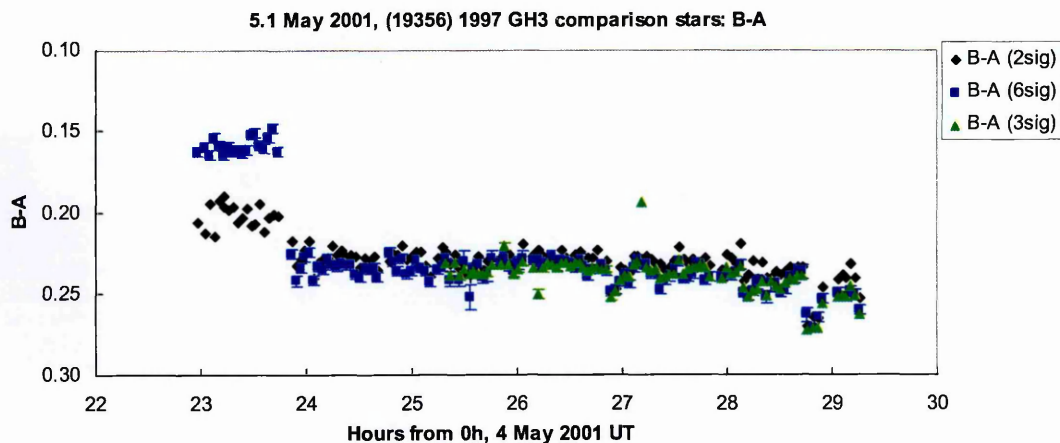


Fig. 3.16 Reduced magnitudes $V(1, \alpha)$ for (6455) 1992 HE taken at the JKT in September/October 2002, showing direct and indirect calibrations. Nights of (a) 27 September, (b) 28 September, (c) 29 September, (d) 1 October.

3.7.5 (19356) 1997 GH₃

The data were reduced by S. F. Green, S. D. Wolters and M. D. Paton. On 5.1 May comparison star B was used for indirect calibration. For the relative magnitudes B-A [Fig. 3.17 (a)] there was a shift after 23:47 UT when the field position changed. It was considered that this could be because B was near the edge of the CCD, where there could be a problem with the flat field, since it is a vignetted region where the dome and sky flats are different. It was also noticed that C-A also had a shift at the position change [Fig. 3.17 (b)]. However C-B has a constant relative magnitude, so it was determined that star B could be used as a comparison star, using the apparent magnitude determined by averaging only the values measured after 23:47 UT, $V = 12.69 \pm 0.02$. Its extinction curve can be seen in Fig. 3.17 (c), showing the same shift for observations before 23:47 UT between 1.86 and 1.56 airmass. Figure 3.18 shows the indirect (2σ and 6σ) and the direct (6σ) calibrations for 5.1 and 11.1 May 2001. The 2σ indirect calibration was adopted.

Fig. 3.17
(a)



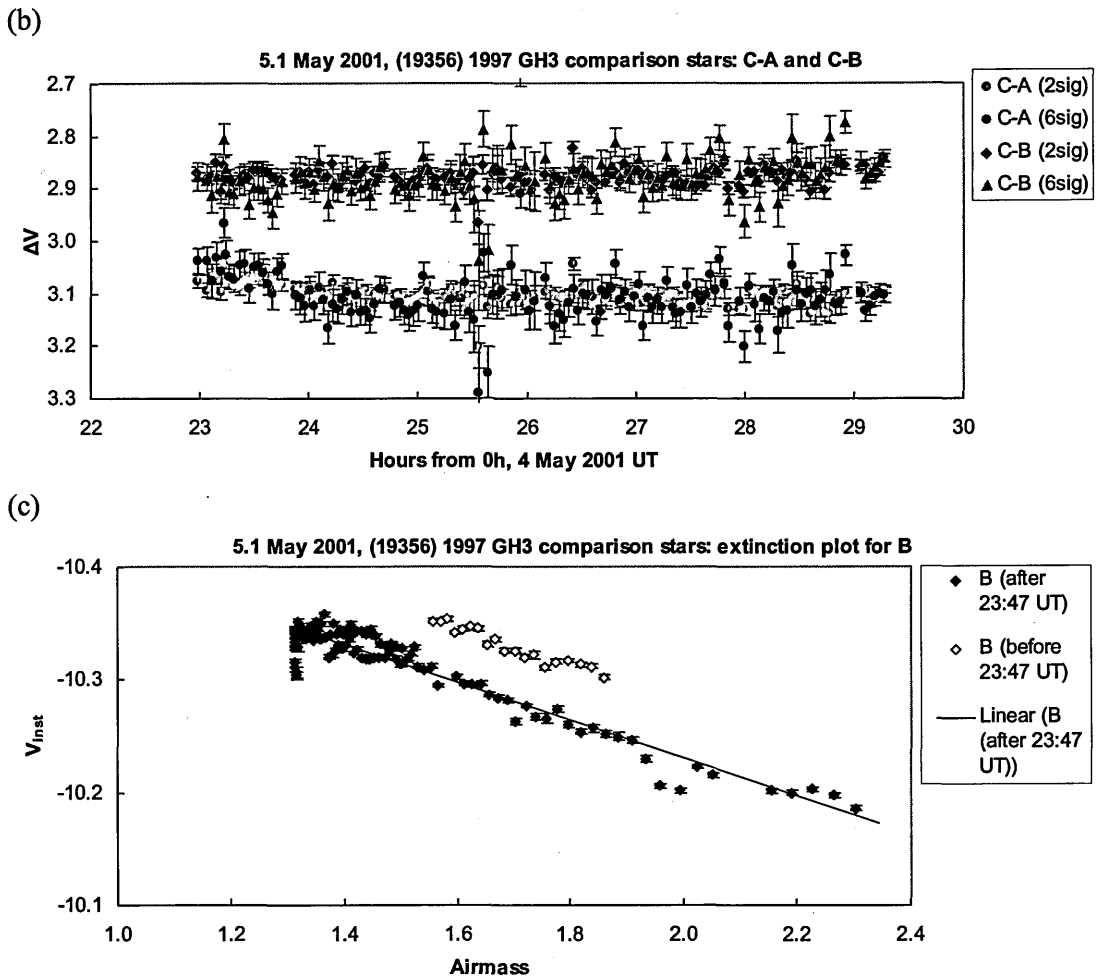
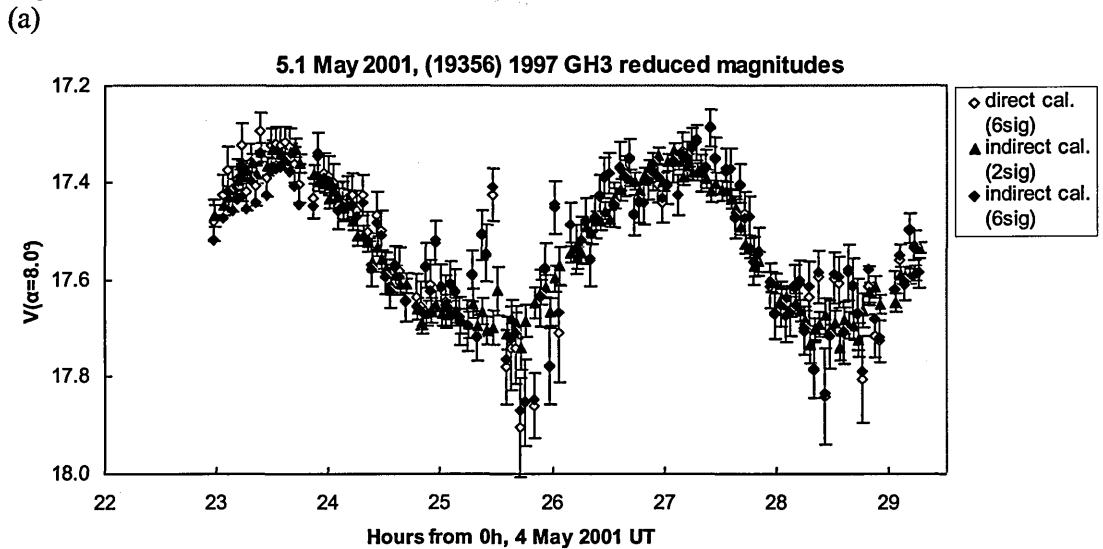


Fig. 3.17 Observations of comparison stars observed on same field as (19356) 1997 GH₃ at the JKT on the night of 4 May 2001. (a) Relative magnitudes between stars A and B; (b) relative magnitude between C and B and between C and A; (c) extinction plot of B.

Fig. 3.18



(b)

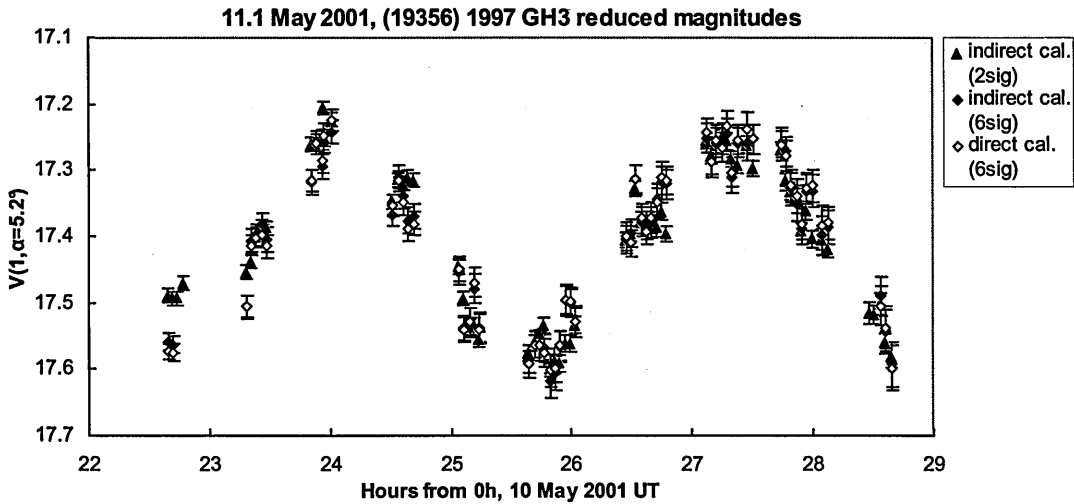


Fig. 3.18 Reduced magnitudes $V(1, \alpha)$ for (19356) 1997 GH₃ taken at the JKT in May 2001, showing direct and indirect calibrations. Nights of (a) 4 May, (b) 10 May.

3.7.6 1998 UO₁

25 September 2002 (26.2 Sep.)

The observations were tracked, so direct calibration only was performed. The conditions were fairly photometric. Three frames were removed because the asteroid was in a chip error. The resulting reduced magnitudes $V(1, \alpha = 47.2^\circ)$ are given in Fig. 3.19.

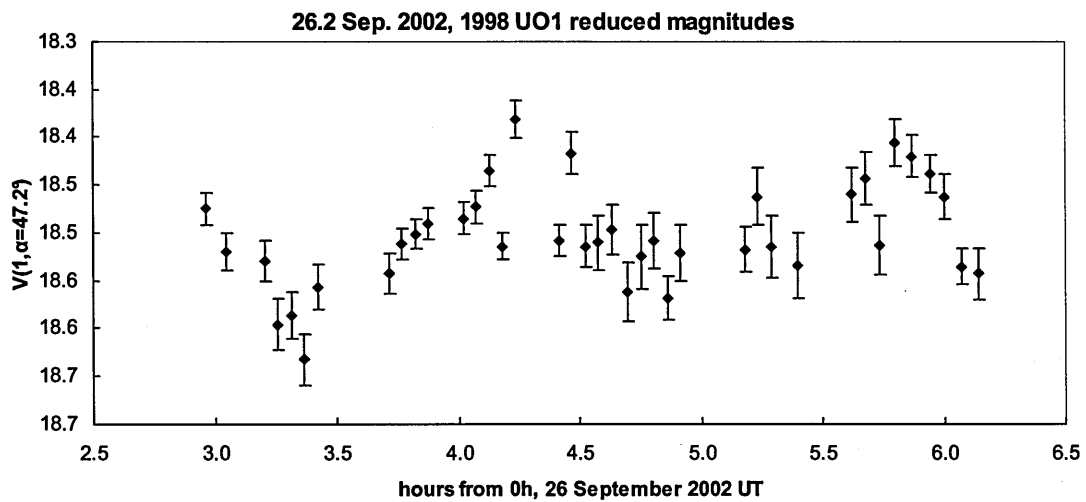


Fig. 3.19 Reduced magnitudes $V(1, \alpha)$ for 1998 UO₁ taken at the JKT on the night of the 25 September 2002, showing the direct calibration.

3.7.7 (33342) 1998 WT₂₄

18 December 2001 (18.9 Dec.)

(33342) 1998 WT₂₄ was observed in the R-filter. The asteroid was tracked, at a rate of $d(\text{RA})/dt \times \cos(\text{DEC}) = -2000$ arcsec/hr and $d(\text{DEC})/dt = -970$ arcsec/hr. Since it was moving so quickly, 33 comparison stars were observed in total (A-Z, A2-G2). Unfortunately, when the telescope was moved away and back to observe standards, there were no previously observed comparison stars in the field. As a result cross-calibration could only be done in four blocks, forming "Ghosts" C, I, R and Z. Even within these blocks, the cross-calibrations are sometimes done with only one or two frames overlapping. Their extinction plots are given in Fig. 3.20 and the derived apparent magnitudes for Ghost C, I, R and Z are, respectively: $V = 14.84 \pm 0.04$, 14.66 ± 0.05 , 12.34 ± 0.04 and 13.9 ± 0.1 . Since the stars were very trailed (even for only 10 s exposures), large radius apertures had to be applied (~30 pixels); this results in considerable noise from sky background. Therefore a direct calibration would be preferred if the conditions were photometric enough. Unfortunately, the direct calibration is very noisy after 23:00 UT, when there was cirrus. The indirect and direct (6σ) calibrations are given in Fig. 3.21. Because of the cirrus, the calibration of "Ghost Z" which was observed after 23:00 UT was very uncertain, hence the large error bars for the later indirect calibration magnitudes. The indirect calibration was adopted.

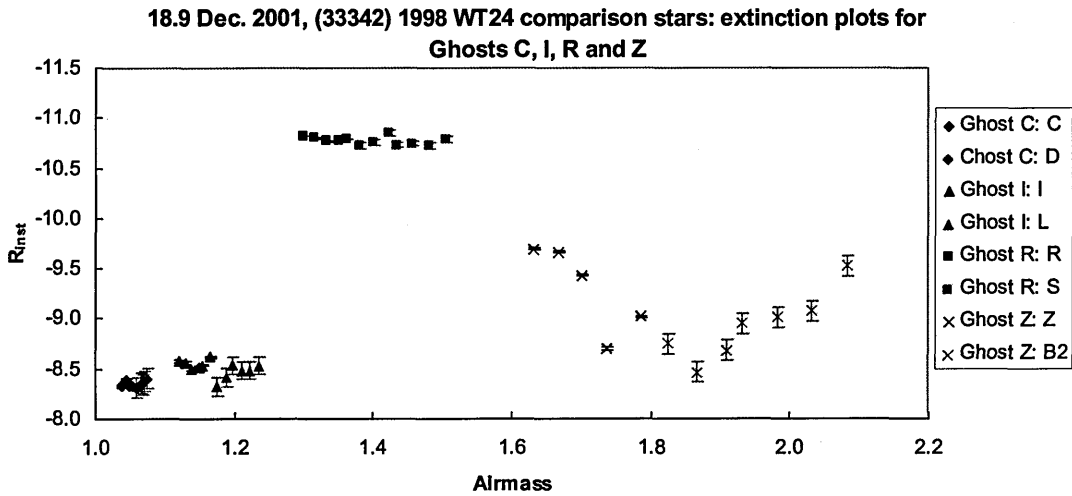


Fig. 3.20 Extinction plots of comparison stars observed on the same field as (33342) 1998 WT₂₄ at the JKT on the night of 18 December 2001.

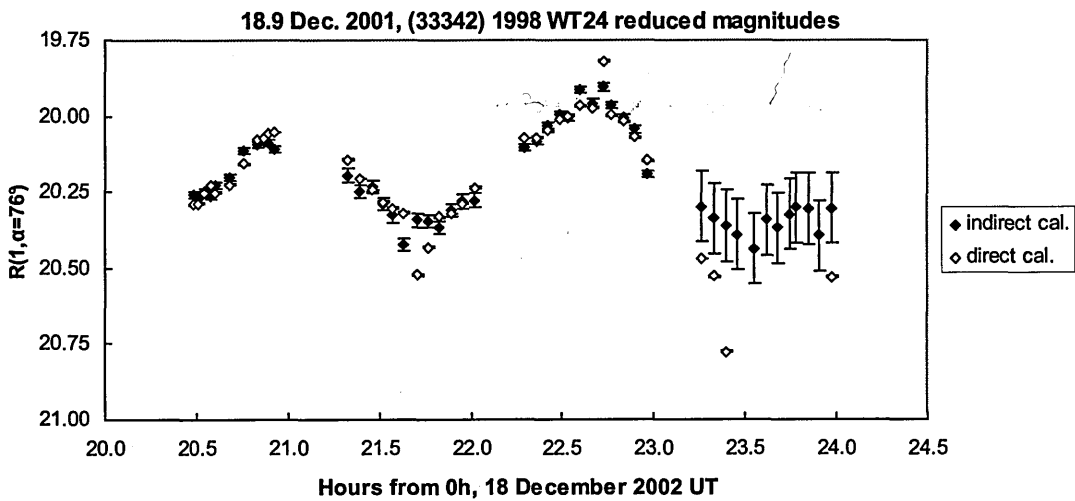


Fig. 3.21 Reduced magnitudes $R(1, \alpha)$ for (33342) 1998 WT₂₄ taken at the JKT on the night of the 18 December 2001, showing the direct and indirect calibrations. Some direct calibration values are below the displayed range ($V < 21.7$ mag.).

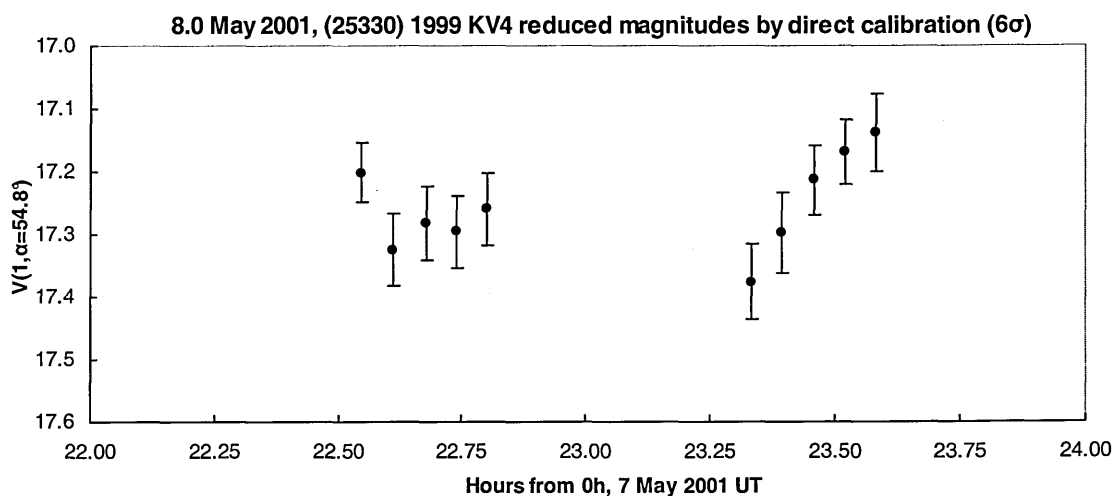
3.7.8 (25330) 1999 KV₄

The data for the nights of 7, 9 and 10 May 2001 were reduced by S. F. Green, and the direct calibrations were adopted. On 8 May 2001 (8.9 May), the asteroid was tracked and therefore comparison stars were trailed. 6σ radius apertures were applied for direct and indirect calibration. The weather was very bad during the observations (Section 3.3.2), so an indirect calibration would be preferable, even considering the large apertures that must

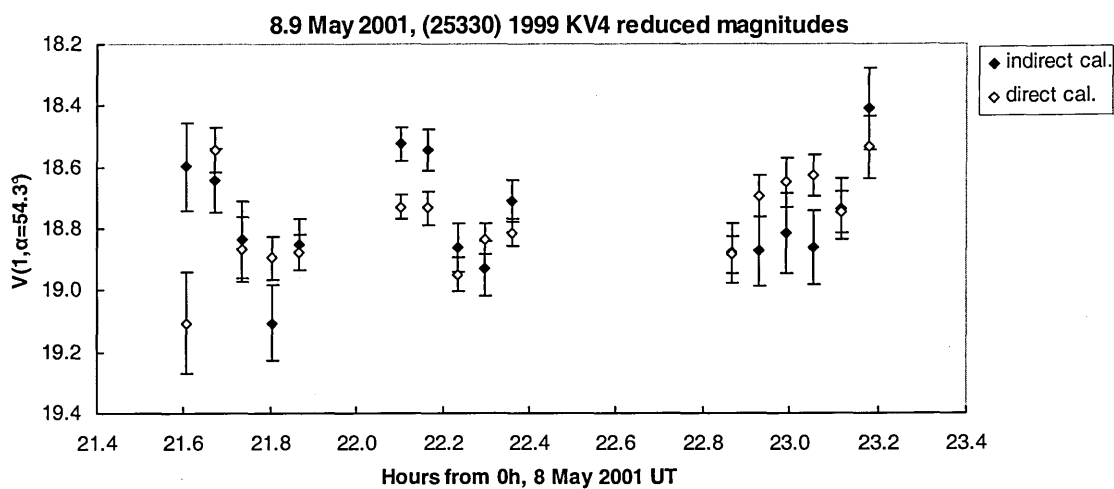
be used because of the tracking. Although the calibrations are similar, the indirect calibration was adopted. The reduced magnitudes found using direct and indirect calibrations are shown in Fig. 3.22.

Fig 3.22

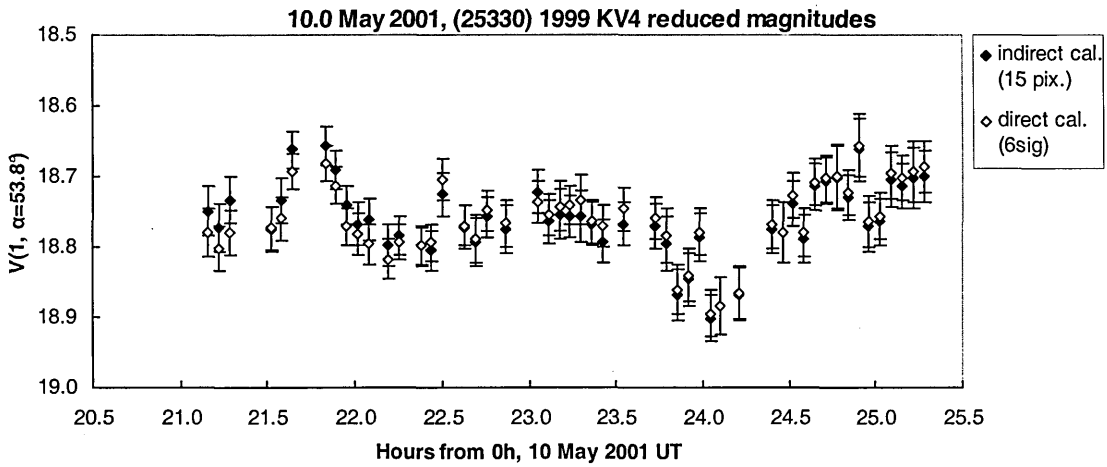
(a)



(b)



(c)



(d)

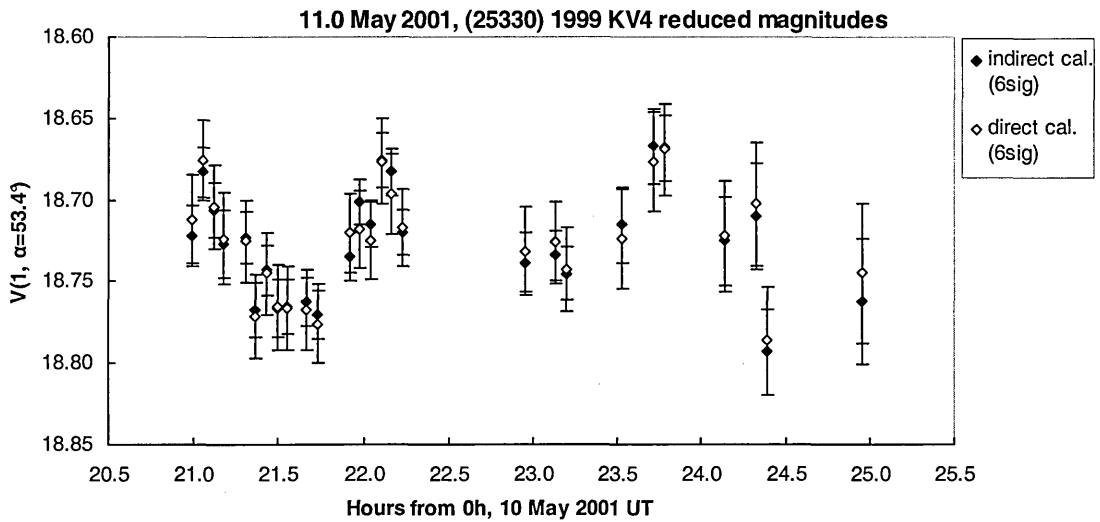


Fig. 3.22 Reduced magnitudes $V(1, \alpha)$ for (25330) 1999 KV₄ taken at the JKT (tracked) in May 2001 showing direct and indirect calibrations. Nights of (a) 7 May, (b) 8 May, (c) 10 May, (d) 11 May.

3.7.9 (53789) 2000 ED₁₀₄

1 October 2002 (2.0 Oct.)

Tracking was used; however frames 2-4 were not tracked, and on five other frames the tracking failed. 6σ apertures were used on the asteroid, while the stars were observed with 6σ apertures calculated from their own FWHM, i.e. stretched because of trailing. Four frames were lost because of a star within the asteroid's aperture. Figure 3.23 shows the

reduced magnitudes $V(1, \alpha = 60.5^\circ)$ obtained from direct and indirect calibrations. Both calibrations are similar; the direct calibration was adopted.

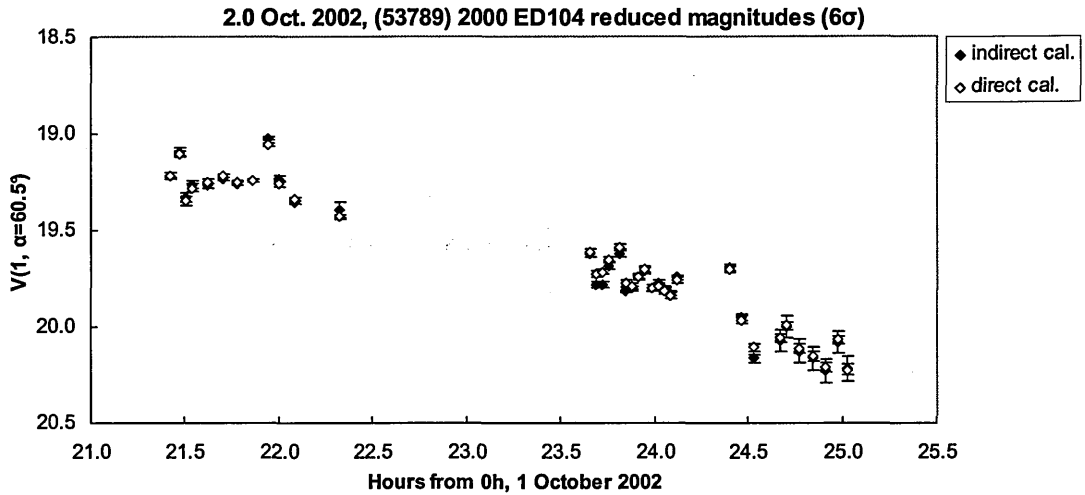


Fig. 3.23 Reduced magnitudes $V(1, \alpha)$ for (53789) 2000 ED₁₀₄ taken at the JKT (tracked) on the night of 1 October 2002, showing the direct and indirect calibrations.

3.7.10 2001 SE₂₈₆

18 December 2001 (19.1 Dec.)

2001 SE₂₈₆ was observed in the R-filter, tracking. There was thin cirrus throughout the observations (Section 3.3.3). 6σ apertures were used on the asteroid, while the stars were observed with 6σ apertures calculated from their own FWHM, i.e. stretched because of trailing. There were 27 comparison stars observed (Section 3.5.5, Fig. 3.7). “Ghost O” was formed by cross-calibrating with seven other stars; its extinction plot is given in Fig. 3.24. The overlap between comparisons was typically three frames; the uncertainty increases as cross-calibrated magnitudes are themselves cross-calibrated. The reduced magnitudes $V(1, \alpha = 19.2^\circ)$ found by indirect and direct calibration are shown in Fig. 3.25. As expected for the poor observing conditions, the direct calibration is noisier; the indirect calibration is adopted.

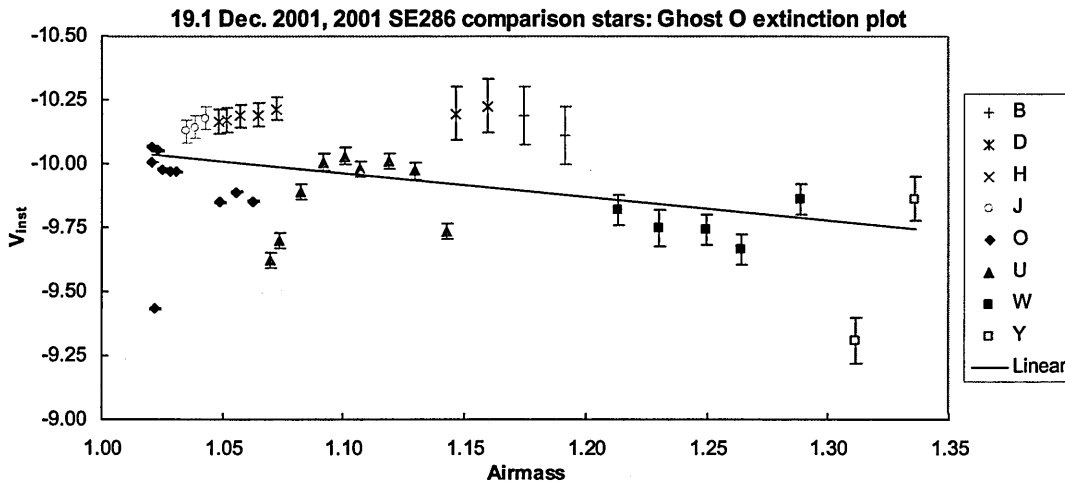


Fig. 3.24 Extinction plots of comparison stars observed on the same field as 2001 SE₂₈₆ at the JKT on the night of 18 December 2001.

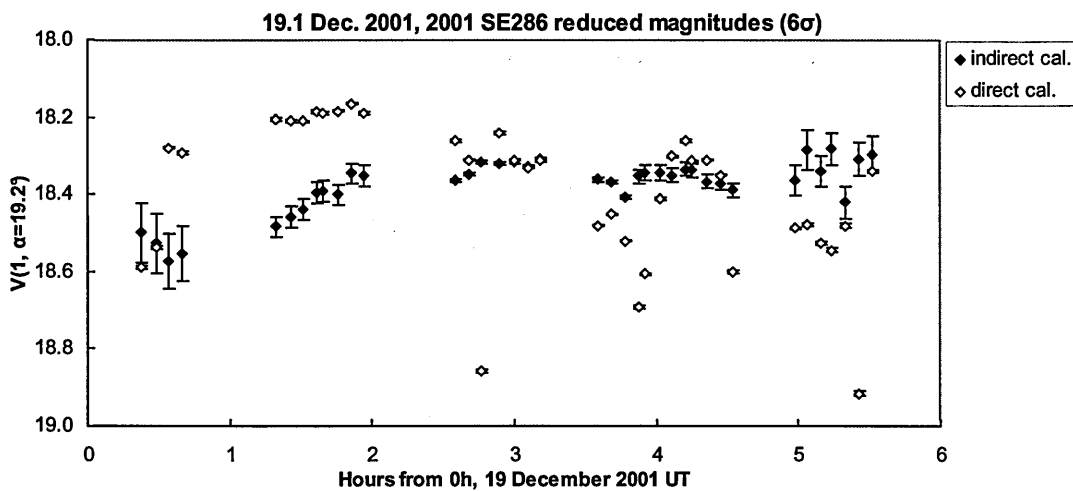


Fig. 3.25 Reduced magnitudes $V(1, \alpha)$ for 2001 SE₂₈₆ taken at the JKT (tracked) on the night of 18 December 2002, showing the direct and indirect calibrations.

3.7.11 2002 HK₁₂

The data were reduced using MaxIm DL 4. Error bars were applied by measuring the instrumental magnitude of both the asteroid and the comparison star every 10th frame using Gaia.

25 September 2002 (26.0 Sep.)

An aperture of nine pixels radius was used, which was roughly equivalent to a 6σ aperture. Conditions were not photometric. The reduced magnitudes $V(1, \alpha = 36.8^\circ)$ obtained by indirect calibration are shown in Fig. 3.26 (a).

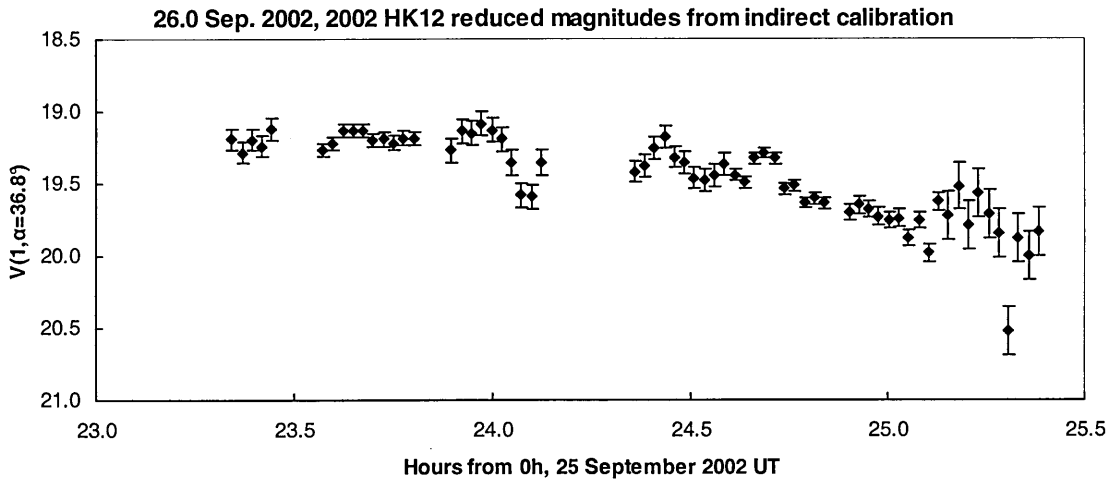
26 September 2002 (27.2 Sep.)

An 11 pixel radius aperture was used, roughly equivalent to 6σ . Conditions were not photometric, and standard stars were not observed, so photometry is relative. 16 frames were removed due to chip errors, one frame was removed due to a cosmic ray and another because the asteroid was too close to the edge of the CCD. The relative magnitudes ($V_{2002HK12} - V_A$) are shown in Fig. 3.26 (b). The weather was cloudy between 03:13 and 04:00 UT [unfilled diamonds in Fig. 3.26 (b)], but all the values were adopted for the 27.2 Sep. contribution to the composite lightcurve.

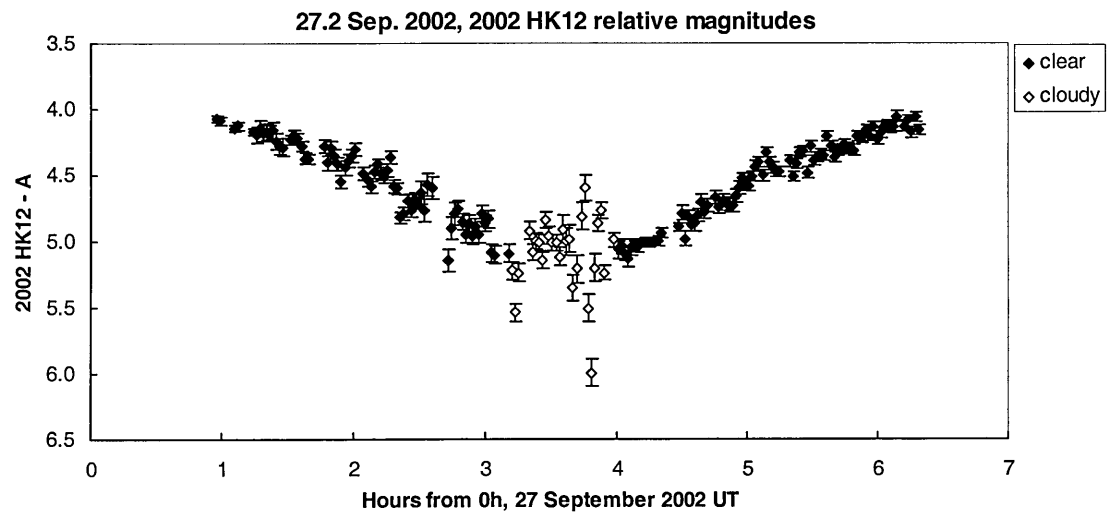
27 September 2002 (28.1 Sep.)

A 15 pixel radius aperture was used. One frame was removed due to a chip error. Conditions were fairly photometric, but there may have been occasional cirrus. The derived reduced magnitudes $V(1, \alpha = 33.5^\circ)$ are shown in Fig. 3.26 (c).

(a)



(b)



(c)

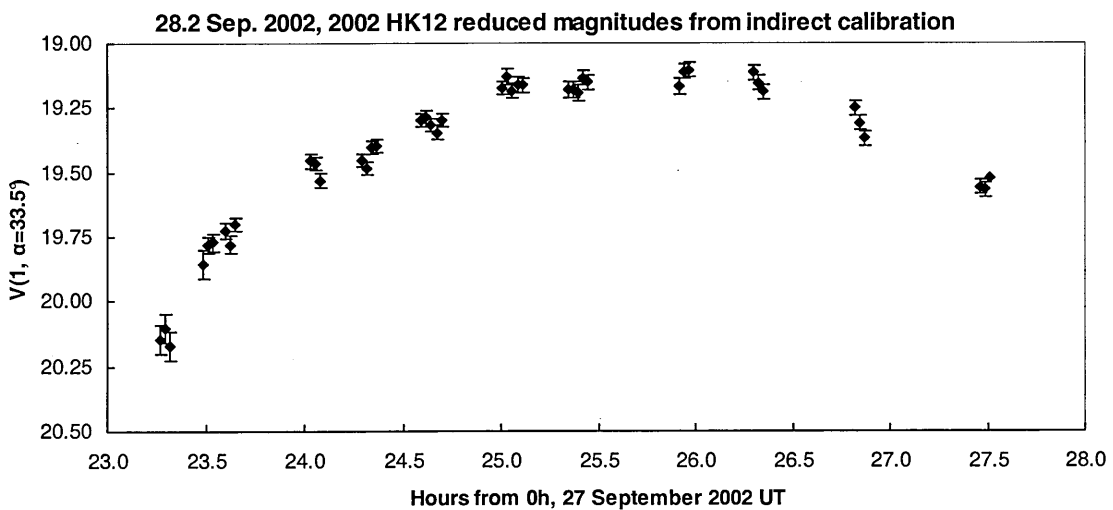


Fig. 3.26 Reduced magnitudes $V(1, \alpha)$ and relative magnitudes for 2002 HK₁₂ taken at the JKT in September 2002. Nights of (a) 25 September, (b) 26 September, (c) 27 September.

3.7.12 2002 NX₁₈

25 September 2002 (25.9 Sep.)

Seven frames were lost due to chip errors. 2σ and 6σ apertures were used. Conditions appeared to be fairly photometric. The reduced magnitudes $V(1, \alpha = 50.6^\circ)$ obtained from (6σ) direct and (2σ and 6σ) indirect calibration are shown in Fig. 3.27 (a). All three calibrations are very similar. The indirect calibration using 2σ apertures was adopted.

27 September 2002 (27.9 Sep.)

The asteroid and comparison stars were observed using 2σ and 6σ apertures. Eight frames were removed because the asteroid was too close to a star (only seven using 2σ apertures) and one frame due to a cosmic ray. Conditions appeared to be reasonably photometric. Reduced magnitudes $V(1, \alpha=52.0^\circ)$ obtained using indirect (2σ and 6σ) and direct (6σ) calibrations are given in Fig. 3.27 (b). The calibrations are similar; the indirect calibration using 2σ apertures was adopted.

28 September 2002 (28.9 Sep.)

Six and three frames were removed as a result of chip errors and being too close to a star respectively. The conditions were affected by thin cirrus. Reduced magnitudes $V(1, \alpha = 52.6^\circ)$ obtained using indirect (2σ and 6σ) and (6σ) calibrations are given in Fig. 3.27 (c). Three direct calibration values are outside the displayed range ($V < 21.6$). The direct calibration is noisier than the indirect calibration due to the cirrus. The indirect calibration using 2σ apertures was adopted.

29 September 2002 (29.9 Sep.)

Two frames were removed as a result of chip errors within the aperture, while for the last frame the weather was so cloudy it was impossible to measure the asteroid's magnitude. Reduced magnitudes $V(1, \alpha=52.3^\circ)$ obtained using indirect (2σ and 6σ) and direct (6σ) calibrations are given in Fig. 3.27 (d). Eight direct calibration values are outside the displayed range ($V < 21.9$). The 2σ and 6σ indirect calibrations are similar, and the direct calibration is noisy as a result of the cirrus. The indirect calibration using 2σ apertures was adopted.

1 October 2002 (1.9 Oct.)

Only six frames in the V-filter were taken. Comparison stars were only observed over a short range of airmasses (1.59-1.60) so we cannot tell whether the conditions were clear. Reduced magnitudes $V(1, \alpha = 54.5^\circ)$ obtained using indirect (2σ and 6σ) and direct (6σ) calibrations are given in Fig. 3.27 (e). The indirect calibration using 2σ apertures was adopted.

Fig. 3.27
(a)

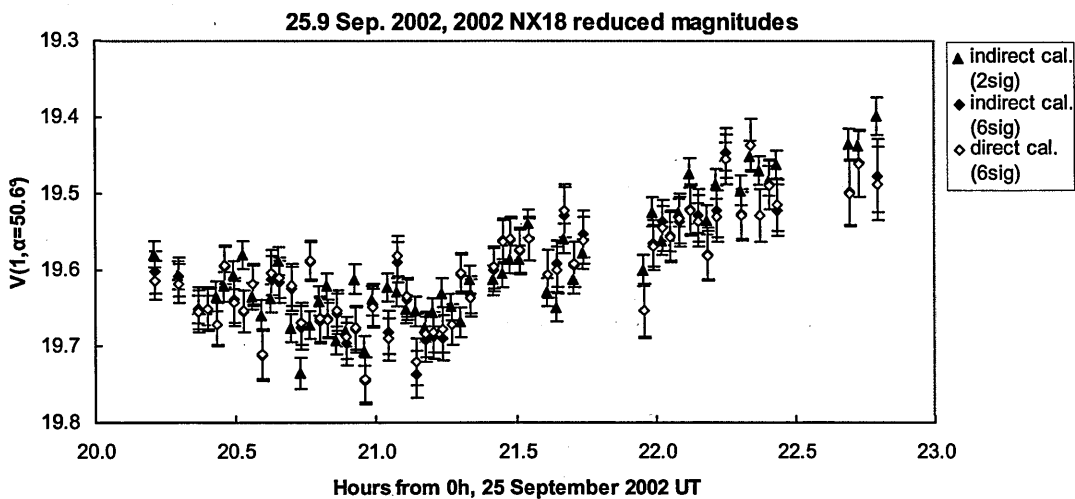
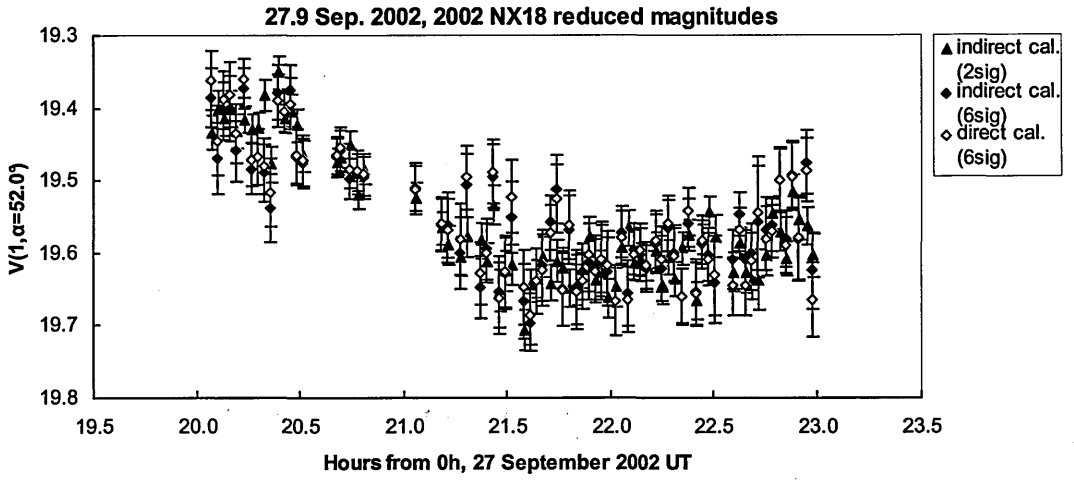
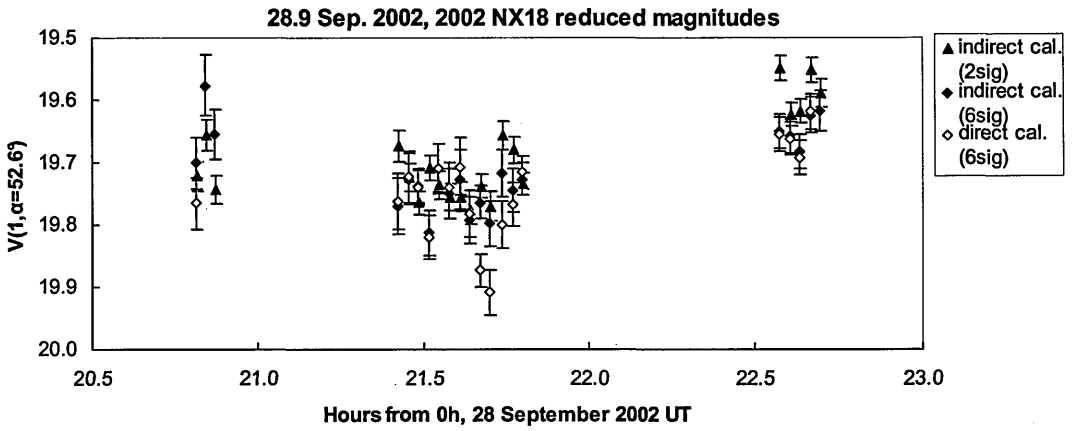


Fig. 3.27 continued.

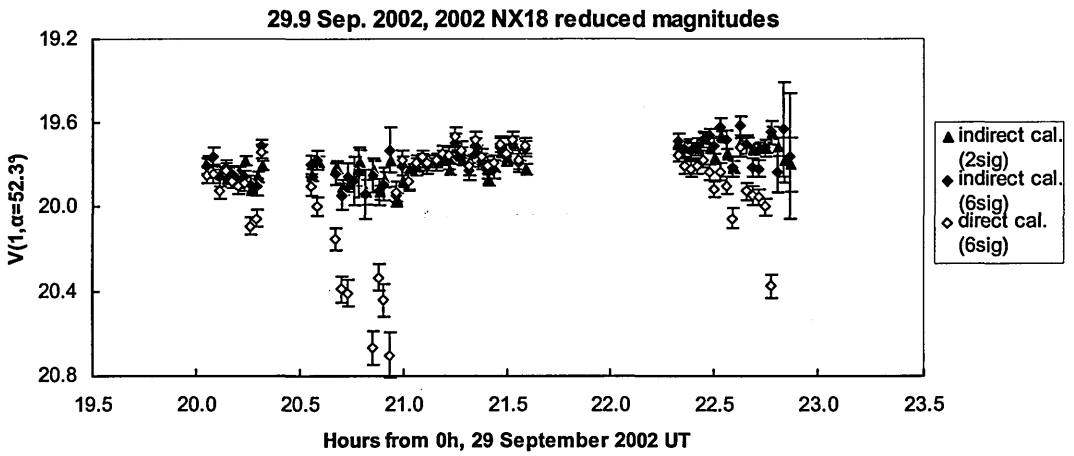
(b)



(c)



(d)



(e)

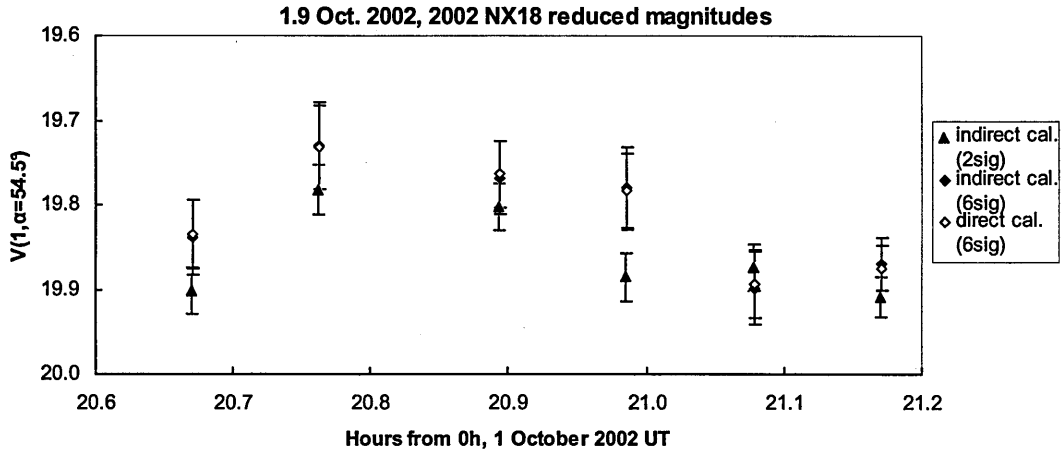


Fig. 3.27 Reduced magnitudes $V(1, \alpha)$ for 2002 NX₁₈ taken at the JKT in September 2002, showing direct and indirect calibrations. Nights of (a) 25 September, (b) 27 September, (c) 28 September, (d) 29 September, (e) 1 October.

3.7.13 2002 QE₁₅

26 September 2002 (26.9 Sep.)

There was intermittent cirrus throughout the observations and only relative photometry was performed. The relative lightcurve, obtained with 2σ and 6σ apertures, is shown in Fig. 3.28 (a). The 2σ lightcurve is less noisy and was adopted.

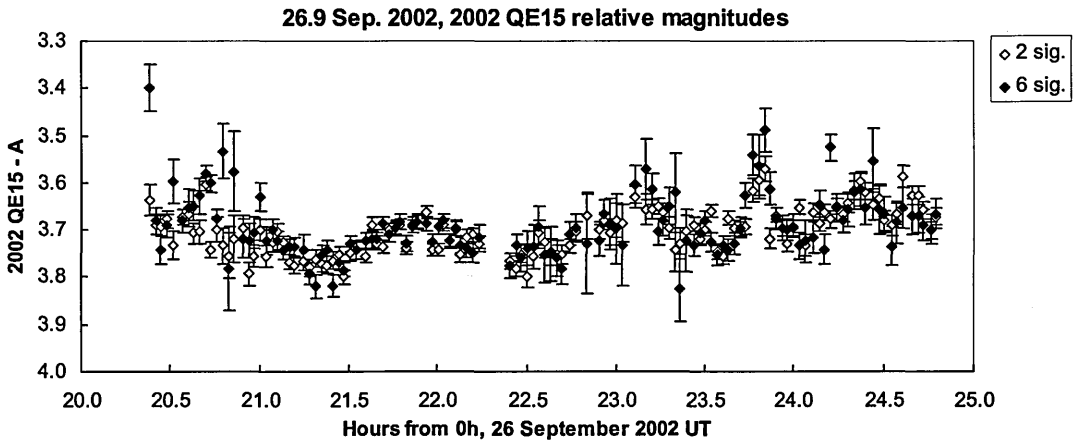
28 September 2002 (28.9 Sep.)

Two frames were removed as a result of a cosmic ray inside the aperture and another two because another star was inside the aperture. There was sporadic cirrus. Reduced magnitudes $V(1, \alpha = 61.7^\circ)$ obtained using indirect (2σ and 6σ) and (6σ) direct calibrations are given in Fig. 3.28 (b). One indirect calibration value is outside the displayed range (20.7 h, $V = 19.9$ mag.). The indirect calibration using 2σ apertures was adopted.

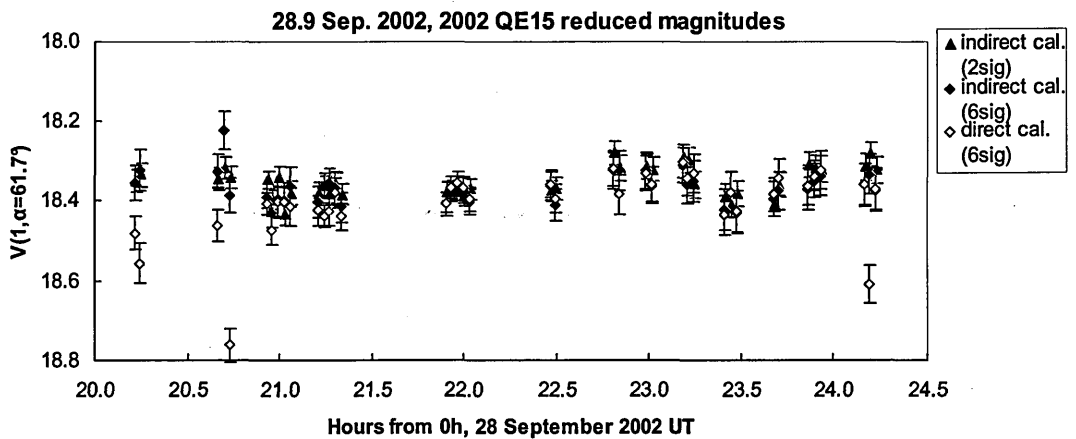
1 October 2002 (2.0 Oct.)

Only three frames were taken in the V-filter. Comparison stars were only observed over a short range of airmasses (1.51-1.54) so we cannot tell whether the conditions were clear. Reduced magnitudes $V(1, \alpha = 62.2^\circ)$ obtained using indirect (2σ and 6σ) and direct (6σ) calibrations are given in Fig. 3.28 (c). The indirect calibration using 2σ apertures appears to be consistently 0.05 mag dimmer than the other calibrations. This may be due to a background object in the 6σ aperture, although, since there were only three frames, it may be due to random photon noise. The direct calibration was the best we can do for so few observations, and was adopted.

Fig. 3.28
(a)



(b)



(c)

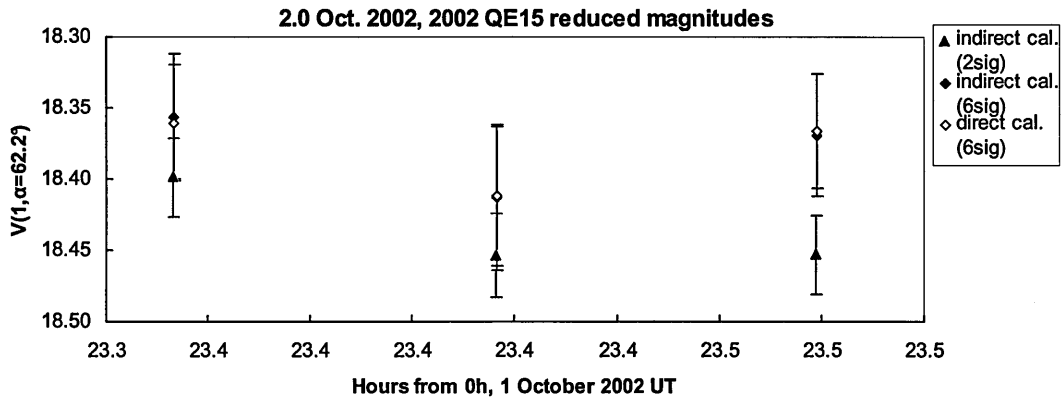


Fig. 3.28 Reduced magnitudes $V(1, \alpha)$ and relative magnitudes for 2002 QE₁₅ taken at the JKT in September 2002, showing direct and indirect calibrations. Nights of (a) 26 September, (b) 28 September, (c) 1 October.

3.8 Asteroid lightcurves

3.8.1 Composite Lightcurves Formed by Fourier Analysis

The observations of all three runs can be analysed to produce composite lightcurves, if enough observations have been taken, from which an asteroid's synodic rotation period can be determined. Figure 3.29 shows a typical sequence of reduced magnitudes $V(1, \alpha)$ taken over several nights, in this case asteroid (6455) 1992 HE observed at the JKT on the nights of 27-29 September and 1 October 2002 (c.f. Fig. 3.16). The data for each night, in the form of days after an arbitrarily defined zero-point (0h 25 September 2002 UT) $t(n)$, reduced magnitudes $V(1, \alpha)(n)$, and magnitude uncertainty $E(n)$ if available, are read into a Fortran program "rawtofal" written by N. M. McBride. The phase angle α is input for the start and end of the night's observations, and also a phase parameter G (we assume $G = 0.15$ if not known). The program calculates a magnitude correction for each point to the centre time, compensating for the change in magnitude due to the change in α (code written by S. F. Green), utilizing Eq. 3.7, assuming a linear extrapolation between the start and end α . An asteroid's phase angle rarely changes greatly during a single night's observation, and so this correction could be neglected in most cases, if desired. For

example, on the night of 27 September, the phase angle of (6455) 1992 HE changed from 31.69° to 31.43° , causing an outlier observation to be altered by only 0.004 mag. The program also prepares the text file to be in the correct format for the Fourier fitting program.

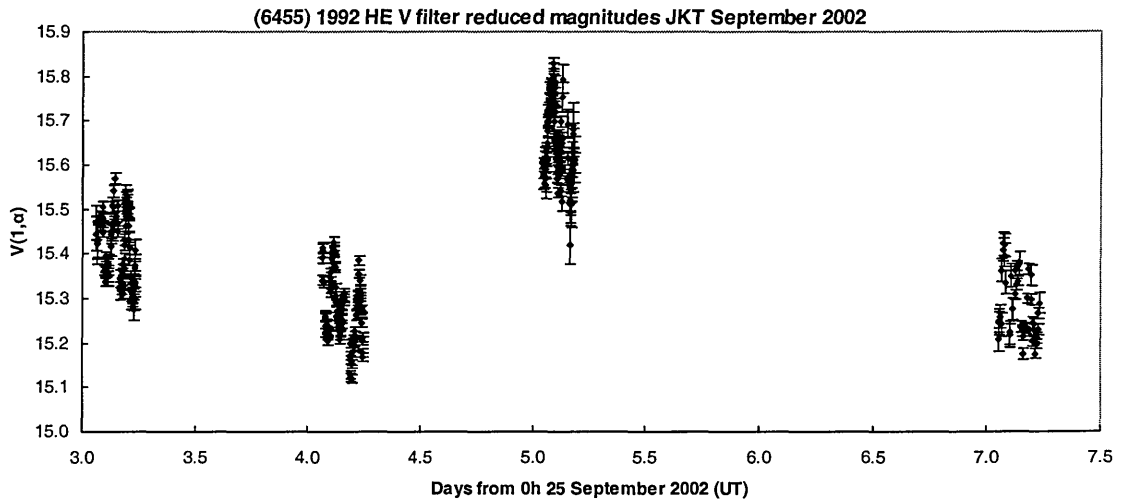


Fig. 3.29 Reduced magnitudes of asteroid (6455) 1992 HE observed at the JKT in the V-filter in September 2002, in days from 0h 25 September 2002 UT (midnight on the night of 24 September 2002). Data in this format is fed to the Fourier fitting program. It can be seen that the brightness varies by a few tenths of a magnitude from night to night, as the extinction correction varies in accuracy depending on weather conditions, and the asteroid's phase angle has changed. On the night of 27 September the conditions were reasonably photometric.

As an asteroid rotates, variations in its shape and albedo cause the observed brightness to alter (Fig. 3.30). Typically, albedo variations are of much lower order and are often not detectable, hence an asteroid lightcurve usually has two extrema per rotation as the maximum surface area on both sides is presented to the observer. The amplitude of the lightcurve will also depend on the phase angle and on the asteroid's pole orientation. Observing asteroids at different apparitions (different viewing geometries) can allow us to determine the pole orientation and determine the shape in detail, as discussed in Section

3.8.2. Observations at one apparition can still allow determination of the asteroid's rotation period, and a limit on its shape by assuming it to be an ellipsoid.

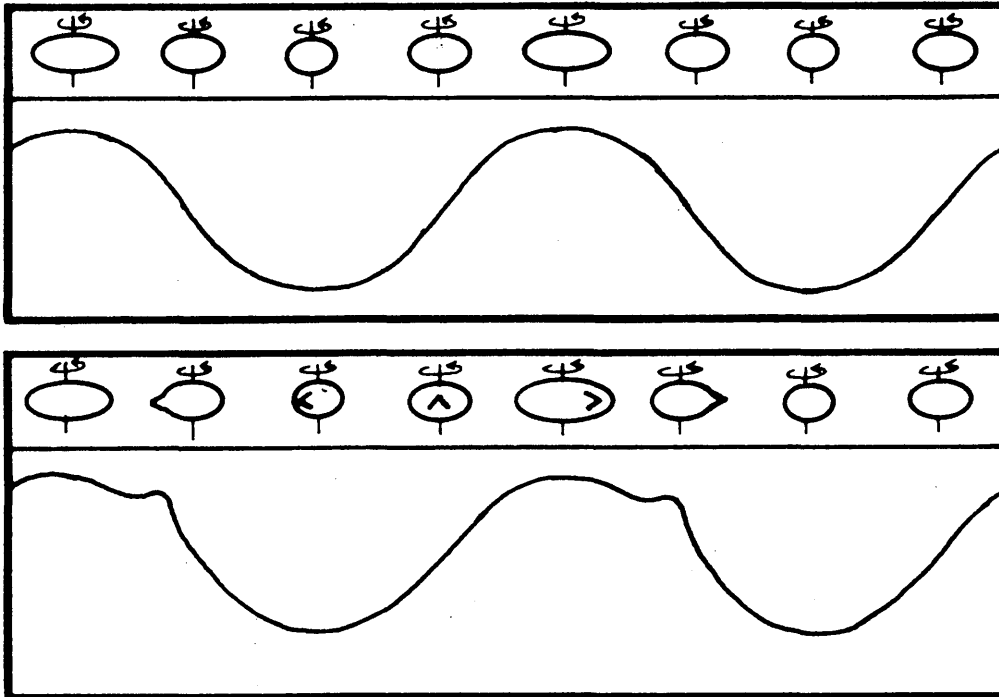


Fig. 3.30 An asteroid's lightcurve has two maxima and minima per rotation. More complex topography of the surface beyond an ellipsoid, or variations in albedo, can add higher order harmonics to a composite lightcurve. Figure reproduced by permission of S. F. Green.

Often it is not possible to cover the complete lightcurve on one night but we can superimpose coverage on successive nights to form a composite lightcurve. The data is read into a Fortran program "falc" written by A. W. Harris (JPL) which uses a Fourier analysis fitting procedure. Following Harris and Lupishko (1989), the lightcurve is represented by:

$$V(\alpha, t) = \bar{V}(\alpha) + \sum_{l=1}^n \left[S_l \sin \frac{2\pi l}{P}(t - t_0) + C_l \cos \frac{2\pi l}{P}(t - t_0) \right] \quad (3.10)$$

where $V(\alpha, t)$ is the reduced magnitude at phase angle α and time t , $\bar{V}(\alpha)$ is the mean absolute magnitude at phase angle α , S_l and C_l are Fourier coefficients, P is the rotation

period, and t_0 is an arbitrarily chosen zero-point time [0h 25 September 2002 for (6455) 1992 HE].

The function is fitted with a linear least-squares procedure for various n and over a range of P . Russell (1906) calculated the amplitudes of the harmonic coefficients which result from large-scale variations in either the surface curvature or albedo. Russell found that even for unit variations in curvature or albedo the 10th harmonic should have an amplitude of only 0.005 mag. and by the 20th harmonic the amplitude would be only 0.0008 mag. Therefore a 10th degree fit should be sufficient to define the lightcurve of an asteroid to <0.01 and a 20th degree fit would define the curve to 0.001 mag. amplitude. In practice, Harris and Lupishko (1989) state that no terms exceeding a few thousandths of a magnitude are found above the 10th order. They find that a composite lightcurve of about 50 well-spaced data points should suffice to define the lightcurve down to the noise level.

However, to make meaningful physical interpretations of the harmonic coefficients obtained, for example the presence of odd harmonics which can be interpreted as evidence for albedo variations, there must be no gaps in coverage greater than one half cycle of the highest frequency present. If this condition is not met, the Fourier analysis can only be regarded as a curve-fitting tool, but will still be of value for defining the period or light level of maximum and minimum brightness, so long as the relevant part of the lightcurve is not within the gap.

We found that a time-efficient methodology with the JKT observations was to use degree $n = 4$ as default for data for which we expect to have significant gaps in the composite lightcurve, or be poorer quality due to weather or too few observations, and $n = 6$ for more complete data sets. Generally, the quality of the data was not good enough to make physically meaningful interpretations of higher order harmonics. The range of periods searched are $P = 0.01$ h to ~ 100 h (less if the best solutions have been found or

more if the asteroid appears to be a slow rotator, i.e. if the brightness very gradually changes during a night's observation), going from 0.01 to 0.1 h in increments of 0.01 h, and the rest in 0.1 h increments. The best five or so periods with smallest errors ΔP , derived from the residuals of the linear least-squares fitting, are narrowed down by using 0.01 h and then 0.001 h increments.

Table 3.3 shows the five smallest ΔP for (6455) 1992 HE for a Fourier fit with $n = 6$. All five solutions have very small ΔP , so without further investigation any could be correct. Note however that the $P = 5.471$ h and $P = 8.208$ h solutions are multiples of the $P = 2.736$ h solution. But for the $P = 5.471$ h solution there are four extrema per rotation while the $P = 2.736$ h solution has two extrema (Section 3.9.4, Fig. 3.36), and hence it is the most physically plausible solution (although we must be careful with low amplitude lightcurves where albedo variation or complex shapes could add an extremum).

Table 3.3

The five best Fourier fits for (6455) 1992 HE observed in September 2002 with degree $n = 6$

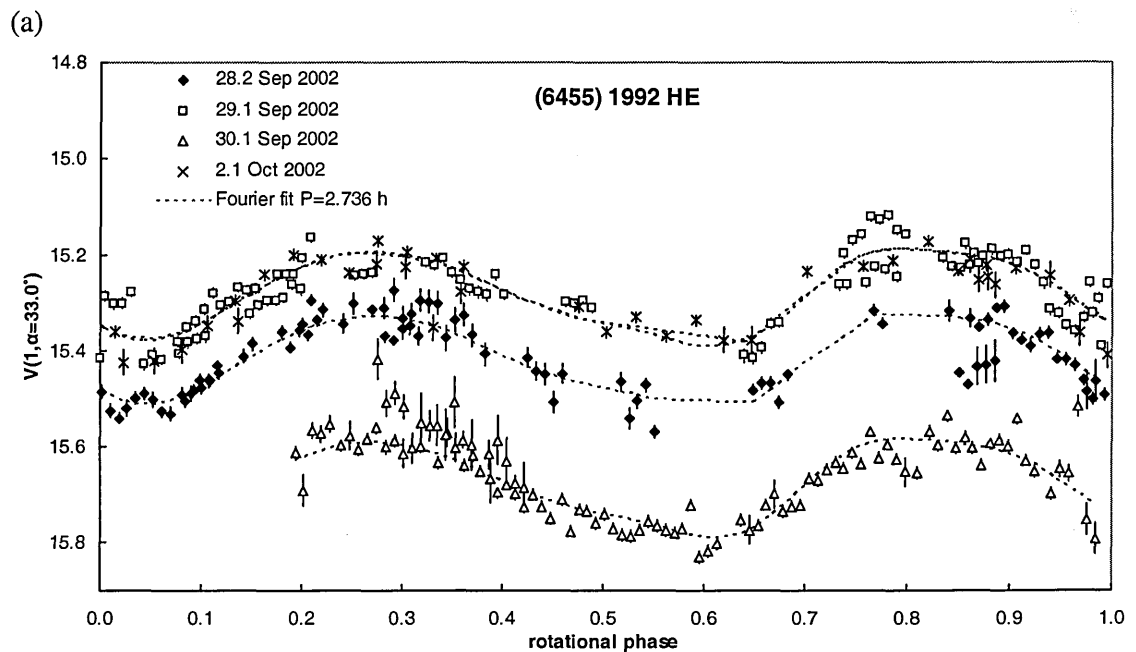
P (h)	ΔP (h)
2.736	0.0019
5.471	0.0017
6.157	0.0018
7.753	0.0016
8.208	0.0017

The uncertainty in the period, output by "falc", is the uncertainty implied by the residuals of the least squares fit.

The Fourier analysis program allows the fitting procedure to freely adjust the fitted magnitude at the boundary between different nights [Fig. 3.31 (a)]. For a chosen solution, the mean magnitude $\bar{V}(\alpha)$ is calculated for each night. "Falc" outputs the fitted magnitude and also the rotational phase for each observation, which is the fraction of a period completed after the number of completed periods since t_0 have been subtracted. For example, if an observation occurred at 6h 25 September 2002 UT, six hours after t_0 , its

rotational phase would be $6 \text{ h} / 2.736 \text{ h} - 2 = 0.193$. In this way, a composite lightcurve of observations from different nights is formed.

A particular night is chosen as the most photometric and the mean magnitudes adjusted to the $\bar{V}(\alpha)$ of this night to form an adjusted lightcurve (or an average of the mean magnitudes of the photometric nights is used if one cannot be chosen). The “mean magnitudes” of the other nights are not physically meaningful if we do not regard the night to be photometric. Although the reduced magnitudes are calculated by default, we label a night’s mean magnitude $\bar{V}(\alpha)^*$ if it is not photometric, and it can be regarded as a relative lightcurve only. The uncertainty of the derived $\bar{V}(\alpha)$ is equivalent to the uncertainty in the photometric calibration for the chosen night, which is dominated by the accuracy of the extinction correction. The phase angle α of the composite lightcurve is the midpoint α of the chosen night. For (6455) 1992 HE, the mean magnitudes are adjusted to the night of 27 September 2002 [Fig. 3.31 (b)].



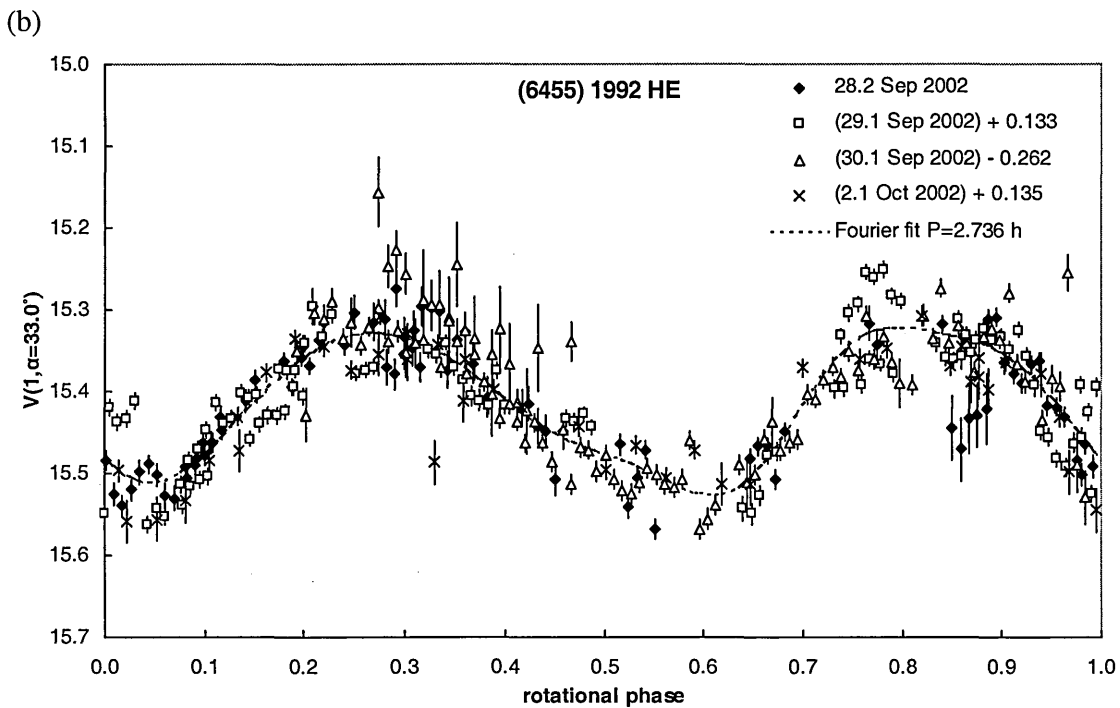


Fig. 3.31 Composite lightcurve of asteroid (6455) 1992 HE observed in September 2002 at the JKT for a Fourier fit $P = 2.736 \pm 0.0019$ h, $n = 6$. (a) Mean magnitudes $\bar{V}(\alpha)$ unadjusted, the values for each night are $\bar{V}_{28.2 \text{ Sep.}}(\alpha) = 15.42$, $\bar{V}_{29.1 \text{ Sep.}}(\alpha)^* = 15.28$, $\bar{V}_{30.1 \text{ Sep.}}(\alpha)^* = 15.68$, $\bar{V}_{2.1 \text{ Oct.}}(\alpha) = 15.28$; (b) $\bar{V}(\alpha)$ adjusted to that of 28.2 September 2002 UT, $\bar{V}(1, \alpha = 33.0^\circ) = 15.42 \pm 0.02$. The precise parameters for the fit are $\bar{V}(\alpha) = 15.4169$, and $S_1, C_1, S_2, C_2, \dots, S_6, C_6$ are: $-0.0082, -0.0205, 0.0602, 0.0687, 0.0068, 0.0190, 0.0039, -0.0079, 0.0098, 0.0039, -0.0079, 0.0098, 0.0039, -0.0014, 0.0028$.

Sometimes there is not sufficient lightcurve coverage to find a unique solution for the period. This is particularly likely if the asteroid is faint and/or has a low lightcurve amplitude. An example is 2002 NX₁₈ observed at the JKT in September 2002 (Section 3.9.12, Fig. 3.42). Since there are gaps in the coverage, the lightcurve amplitude is small (0.23 mag., so it is hard to identify extrema) and the asteroid is faint (increasing the relative uncertainty of each measured magnitude as evidenced by the error bars), there are several different possibilities for the correct period.

3.8.2 Physical Interpretation of Asteroid Lightcurves

The derived mean visual reduced magnitude $\bar{V}(\alpha)$ from the adjusted composite lightcurve can be converted to an absolute magnitude H_V in the H, G system via Eq. 3.7. The uncertainty of the conversion is increased if the phase parameter G is unknown, increasing as α becomes larger. For (6455) 1992 HE, G is known to be 0.34 ± 0.1 (Pravec, personal communication, 2003) and $V(1, \alpha = 33.0^\circ) = 15.42 \pm 0.02$. Eq. 3.7 is evaluated using $G = 0.24$ and $G = 0.44$ to determine the limits of H_V . H_V is found to be 14.32 ± 0.24 . For an object where G is unknown we assume the range of possible G to be $0.15^{+0.25}_{-0.15}$ which would cover most asteroids; it can be further narrowed if the asteroid's taxonomic type is known (Bowell *et al.*, 1989). Since NEAs are often observed at high phase angles the uncertainty in H_V can be greater than 0.5 mag.

If observations were carried out in the R-filter, then H_R can be estimated (by assuming $G_R = 0.15$ if not known). If V-filter measurements were available on the same night and the conditions are reasonably photometric, H_R could be corrected to H_V by subtracting $V-R$. Unfortunately, for December 2001 JKT observations this is not the case. However, we can assume $V-R = 0.45 \pm 0.1$. This range covers most of the known values for the colour index in asteroids (Pravec *et al.*, 1998).

In the absence of thermal IR observations, an asteroid's diameter can be estimated from H_V by assuming its geometric albedo $p_v = 0.14$, using the bias-corrected mean albedo derived in Stuart and Binzel (2004). The possible range is large: NEOs have been found with p_v between 0.023 and 0.63 (Binzel *et al.*, 2002). The factor of 27 variation in albedo corresponds to more than a factor of five range in possible diameter of an NEO with a given absolute magnitude. If its taxonomic type is known, then the mean p_v can be altered appropriately from values in Stuart and Binzel (2004). The asteroid's diameter D is related to p_v as described in Section 4.1:

$$D(\text{km}) = \frac{10^{-H_v/5} 1329}{\sqrt{p_v}} \quad (3.11)$$

We can define the lightcurve amplitude from the second harmonic of the Fourier fit to the composite lightcurve (Pravec *et al.*, 1996), which we refer to as the “peak-to-valley” amplitude A_{fit} .

$$A_{fit} = 2\sqrt{C_2^2 + S_2^2} \quad (3.12)$$

We can also define a “manually” measured amplitude A_{man} of the observed lightcurve extrema which allows comparison with data given by other researchers. For example, for (6455) 1992 HE (Fig. 3.36), $A_{fit} = 0.183$ and $A_{man} = 0.21$.

The amplitude can be used to constrain the asteroid’s shape. If we assume the asteroid is a triaxial ellipsoid with axes a , b and c ($a \geq b \geq c$) rotating about the c axis (the most dynamically stable solution, and so typically a good approximation) the lightcurve amplitude may be given by (Binzel *et al.*, 1989):

$$A(\theta) = 2.5 \log\left(\frac{a}{b}\right) - 1.25 \log\left(\frac{a^2 \cos^2 \theta + c^2 \sin^2 \theta}{b^2 \cos^2 \theta + c^2 \sin^2 \theta}\right) \quad (3.13)$$

where θ is the aspect angle (the angle between observer’s line of sight and asteroid spin vector). Figure 3.32 shows a cartoon of an asteroid in orbit about the Sun observed from two different aspect angles. If an asteroid is viewed at an equatorial aspect ($\theta = 90^\circ$, A), then the second term in Eq. 3.13 is zero and the lightcurve would have its maximum possible amplitude as the projected surface area changes from πac to πbc . If an asteroid is viewed pole-on ($\theta = 0^\circ$, B), then no change in projected surface area is seen and the expected amplitude is zero.

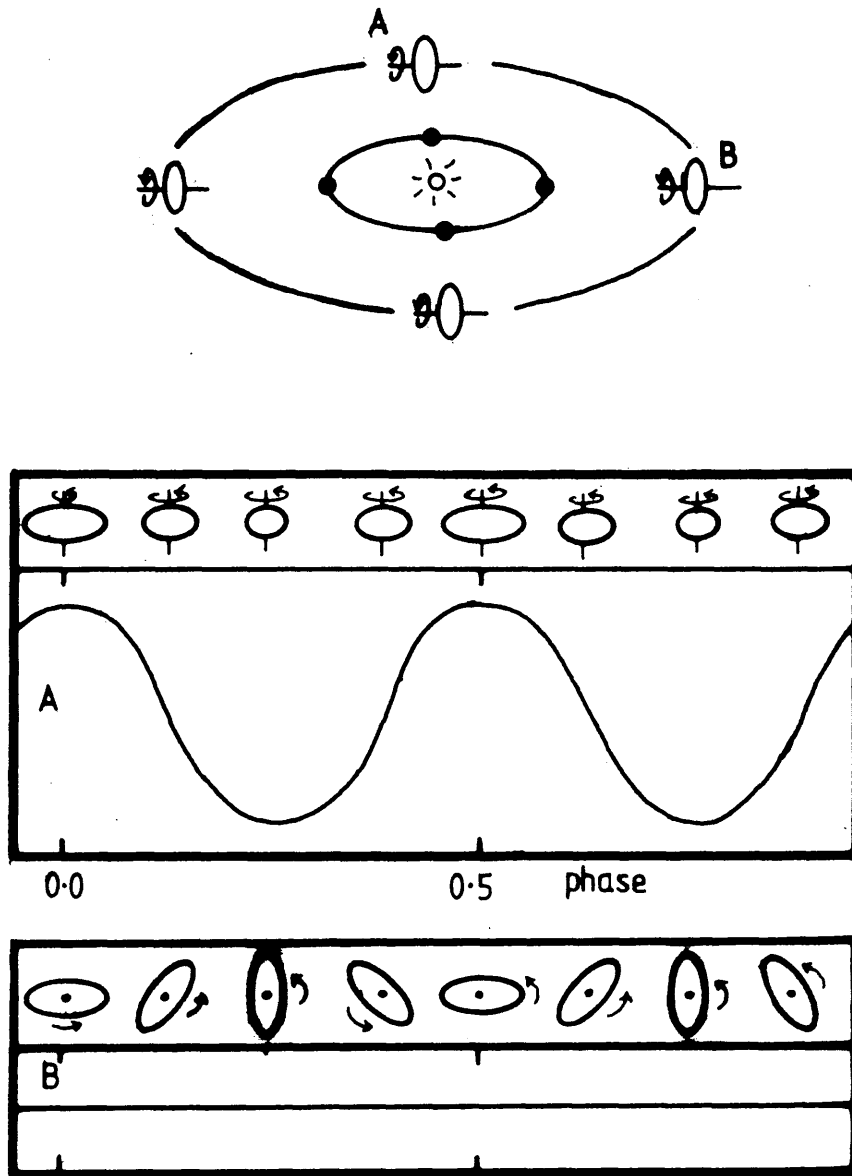


Fig. 3.32 An asteroid lightcurve can have different amplitudes when viewed at different aspect angles. In position A the asteroid is observed with the line of sight at 90° to the pole orientation, i.e. the aspect angle $\theta = 90^\circ$. The lightcurve amplitude is at its maximum. In B, the asteroid is viewed "pole-on" and $\theta = 0^\circ$. Figure reproduced by permission of S. F. Green.

Hence, if we have no information on θ at all we can assume it is equatorial to define the minimum ratio between a and b :

$$\frac{a}{b} > 10^{0.4A} \tag{3.14}$$

For (6455) 1992 HE, using $A = 0.21$, we derive $a/b > 1.2$.

If the asteroid has been observed from several oppositions, then it may be possible to measure a , b , and c and determine the pole orientation. Different methods are described in Magnusson *et al.* (1989) and references therein. More detailed shape models from optical observations can be determined using techniques such as lightcurve inversion which utilizes all available photometric data in the analysis, not just parameters like amplitudes or epochs of lightcurve features (Kaasalainen *et al.*, 2002, and references therein).

The measured lightcurve amplitude depends on the phase angle of observation. This is known as the amplitude-phase effect. Zappalà *et al.* (1990) analysed the amplitude phase relation (APR) using geometrical and laboratory models and a real asteroid dataset. They found that the slope m of the APR turns out to be function of the amplitude at 0° phase angle $A(0^\circ)$ only:

$$A(0^\circ) = A(\alpha)/(1 + m\alpha) \quad (3.15)$$

From the asteroid dataset, they determined that for a general asteroid $m = 0.018$. They were able to determine values of m for different taxonomic types. They found $m(S) = 0.030$, $m(C) = 0.015$ and $m(M) = 0.013$. However, the assumption of a linear APR is only valid for $\alpha < 40^\circ$, and for larger values you can overestimate the actual amplitude at 0° . But previous authors have applied this correction to NEAs observed at high phase angles (e.g. Binzel *et al.*, 2002), and we will apply the same correction to amplitudes measured in Section 3.9.

The primary goal of all September/October 2002 JKT observations was to produce optical observations to complement thermal IR observations (Section 5.6.1). Ideally, enough observations would be taken to create a composite lightcurve, from which the absolute visual magnitude H_V at the midpoint of the time of the UKIRT thermal IR observations can be determined. If a unique composite lightcurve cannot be formed, then we can find limits of the asteroid's lightcurve amplitude.

3.9 Analysis and Discussion

3.9.1 (433) Eros

(433) Eros is the second largest NEA [after (1036) Ganymed] and the first NEA to be discovered, by the German astronomer Gustav Witt, on 13 August 1898. It is probably the most studied NEA, or even asteroid in general, particularly after the NEAR Shoemaker spacecraft orbited it from 14 February 2000, eventually landing on the asteroid on 12 February 2001 (Cheng, 2002).

Eros is an Amor and an S-type asteroid (e.g. Tholen, 1989); we follow the taxonomic classification scheme of Bus and Binzel (2002) throughout. It has a rotation period of 5.270 h and its lightcurve amplitude can range from 0.04-1.49 mag. depending on viewing geometry (e.g. Campa, 1938). Its absolute magnitude is $H_V = 10.30 \pm 0.05$ (Erikson *et al.*, 2000). A good overview on what the NEAR Shoemaker mission has discovered about Eros can be found in Sullivan *et al.* (2002). A triaxial ellipsoid fit of $34.4 \times 11.2 \times 11.2$ km is found from the Multispectral Imager (Veeverka *et al.*, 2000) which is in good agreement with previous lightcurve and radar studies [Zellner (1976), Mitchell *et al.* (1998)]. The Radio Science results of Yeomans *et al.* (2000) give a bulk density of 2.67 ± 0.03 g/cm³.

As part of the NEAR Radio Science investigation, Konopliv *et al.* (2002) found an incredibly accurate spin state solution of: rotation period $P = 5.27025527 \pm 0.00000003$ h, pole right ascension and declination $\alpha = 11.363 \pm 0.001^\circ$, $\delta = 17.232 \pm 0.001^\circ$.

The 28.1, 29.0 and 30.0 September reduced magnitudes were Fourier fitted with a 6th order solution (Fig. 3.33). The derived best-fit synodic rotation period solution was $P = 5.249 \pm 0.001$ h.

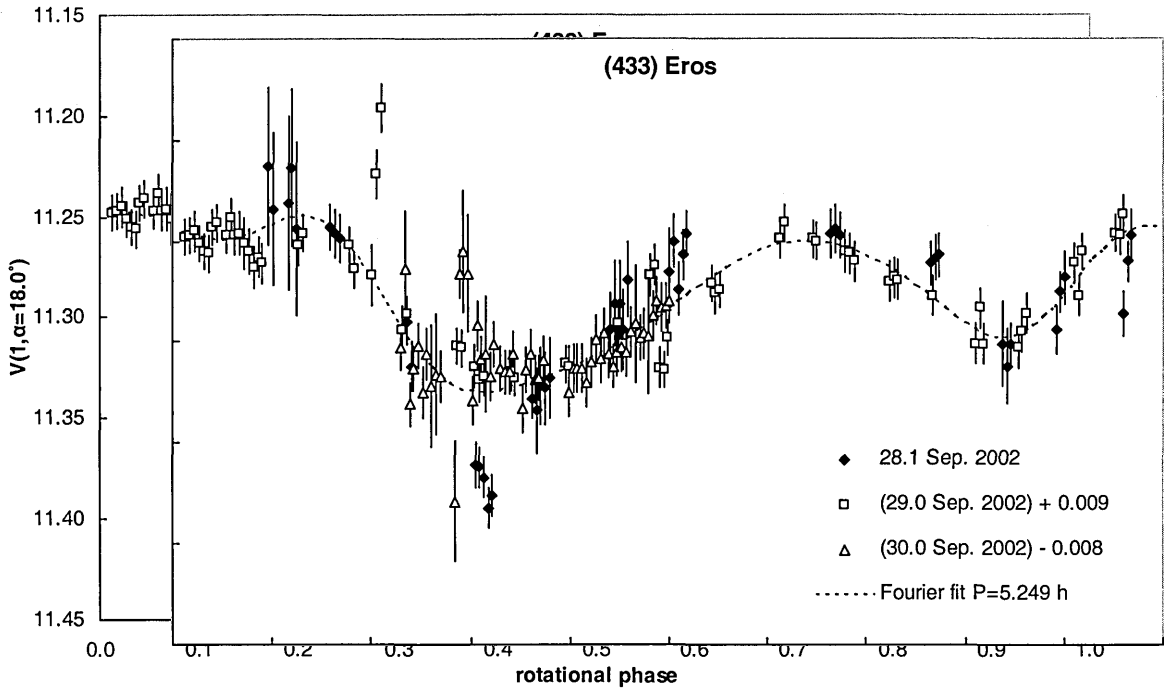


Fig. 3.33 Composite lightcurve of (433) Eros combining JKT observations on 28.1, 29.0 and 30.0 Sep. 2002, using a 6th order Fourier fit $P = 5.249 \pm 0.001$ h. Mean magnitudes adjusted to that of 28.1 Sep. 2002, $\bar{V}(\alpha = 18.0^\circ) = 11.28 \pm 0.06$ mag. The Fourier coefficients $S_1, C_1, \dots, S_6, C_6$ following Eq. 3.8 are: 0.0113, -0.017, -0.0286, -0.012, -0.0005, -0.0013, 0.0072, 0.0013, 0.0055, -0.0015, 0.0011, -0.0009. $t_0 = 0$ h 25 Sep. 2002 UT.

The difference ΔP between the synodic period P_{syn} (the time it takes Eros to complete one revolution relative to the Earth) and the sidereal period P_{sid} (the time to complete one revolution relative to the stars) is given by (Pravec *et al.*, 1996):

$$\Delta P = \pm \omega_{PAB} P_{syn}^2 \quad (3.16)$$

where ω_{PAB} is the angular velocity of the phase angle bisector (PAB) (\pm depending on rotation direction). The PAB is the direction, or position in the sky, which is the mean between the geocentric position and the heliocentric position. If you bisected the angle formed by the lines to the Sun and the Earth from the asteroid, the resultant line would be in the direction of the PAB. The geometric heliocentric J2000 longitude (L) = 357.295° and latitude (B) = 8.674° and Eros' $L = 344.797^\circ$ and $B = 22.0367^\circ$ at 0h 28 Sep. 2002 UT (from JPL Horizons). An hour later the heliocentric $L = 357.314^\circ$ and $B = 8.676^\circ$ and Eros'

$L = 344.779^\circ$ and $B = 22.0397^\circ$. Therefore the PAB changes from $L_{PAB} = 351.0462^\circ$ and $B_{PAB} = 15.3555^\circ$ to $L_{PAB} = 351.0467^\circ$ and $B_{PAB} = 15.3581^\circ$. This is about $\omega_{PAB} = 1.5 \times 10^{-5}$ rad./h. Finally we arrive at the result $\Delta P = 0.0004$ h, which is negligible, so the difference between our measured value of $P_{syn} = 5.249$ h and the true value of $P_{sid} = 5.270$ h, about 1.5 min., cannot be accounted for by this effect. This gives us a rough idea of the real uncertainty of our period measurements, which is larger than the formal uncertainty we quote that results from the residuals in the Fourier fitting. Since the main purpose of observing Eros was to test our methods, including lightcurve correction, for deriving diameters and albedos of NEAs from thermal IR observations, we used the $P = 5.249$ h solution for lightcurve correction (Section 5.6.1, Fig. 5.23 (a), Table 5.13).

The mean magnitudes are $\bar{V}_{28.1\text{Sep}}(\alpha) = 11.275 \pm 0.003$, $\bar{V}_{29.0\text{Sep}}(\alpha)^* = 11.266 \pm 0.002$ and $\bar{V}_{30.0\text{Sep}}(\alpha)^* = 11.283 \pm 0.002$ (quoting the uncertainty obtained from the residuals in the Fourier fitting and not yet including the atmospheric extinction uncertainty; the nomenclature $\bar{V}(\alpha)^*$ is explained in Section 3.8.1). The 28.1 September observations were judged to be reasonably photometric, and the fitted magnitudes of the other nights were adjusted to this night. The final uncertainty of the derived $\bar{V}(\alpha)$ is obtained from the uncertainty of the apparent magnitude of the comparison star “Ghost C”, which is based on the (negligible) standard error of the derived value (± 0.003 mag.), the Fourier fitting uncertainty given above, and the estimated atmospheric extinction uncertainty (± 0.04 mag.) Thus we obtain $\bar{V}(\alpha = 18.0^\circ) = 11.28 \pm 0.04$. Assuming $G = 0.2$ (Lagerkvist and Magnusson, 1990) gives $H_V = 10.40 \pm 0.04$ (the uncertainty assumes no inaccuracy in G). This is in reasonable agreement with Erikson *et al.* (2000).

The “peak-to-valley” lightcurve amplitude $A_{fit}(\alpha=18^\circ) = 0.06$ mag. and “manually measured” $A_{man}(18^\circ) = 0.10$ mag. This is at the lower end of the range of measured

lightcurve magnitudes for Eros. Comparing the spin axis RA and DEC from Konopliv *et al.* (2002). with Eros' latitude and longitude given above shows that the asteroid is nearly pole-on, so we should expect a small lightcurve amplitude. Adopting A_{man} , we find $A(0^\circ) = 0.06$ mag, using $m = 0.030$ in Eq. 3.15.

3.9.2 (4034) 1986 PA

(4034) 1986 PA is an O-type Apollo asteroid (Binzel *et al.*, 2004). Delbó *et al.* (2003) measured the asteroid's effective diameter $D_{eff} = 0.42 \pm 0.06$ km and its geometric albedo $p_v = 0.52 \pm 0.16$, based on an estimate of H_V from web services JPL Horizons (<http://ssd.jpl.nasa.gov/?horizons>), the Minor Planet Centre (<http://cfa-www.harvard.edu/iau/MPEph/MPEph.html>) and NeoDys (<http://newton.dm.unipi.it/cgi-bin/neoDys/neoibo>).

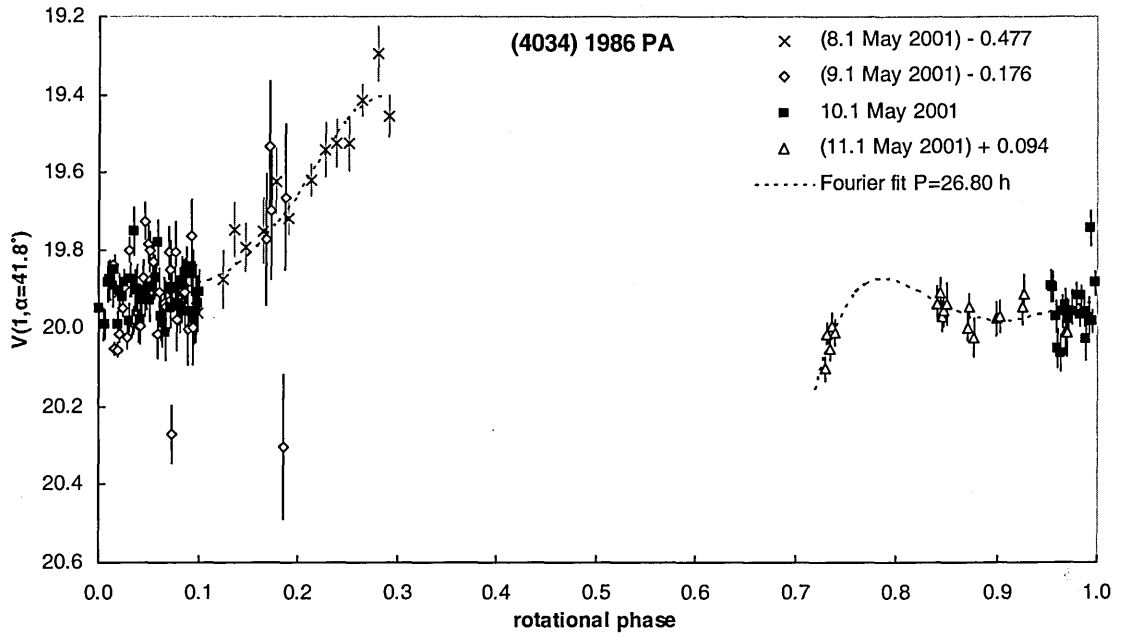
Unfortunately we are unable to find a unique composite lightcurve. Using a 4th order Fourier fit, the best five solutions are given in Table 3.4. To illustrate the difficulty of finding a solution, the $P = 26.80$, 33.06 and 38.58 h solutions are shown in Fig. 3.34 (a), (b) and (c) respectively. The magnitudes are adjusted to the data taken on the night of 9 May 2001 (10.1 May UT), judged to be the most photometric. The $P = 65.02$ h solution is approximately 2×33.06 h and 78.13 h is approximately 3×26.80 h. None of the solutions have adequate coverage at all phases, or show the classical two extrema per rotation. Also, all three solutions require a large shift in magnitude for at least one night's data. Therefore none of them are reliable. Most of the different night's observations are flat, with only 8.1 May showing an appreciable change in brightness.

Table 3.4 The 5 best Fourier fits to (4034) 1986 PA JKT May 2001 observations

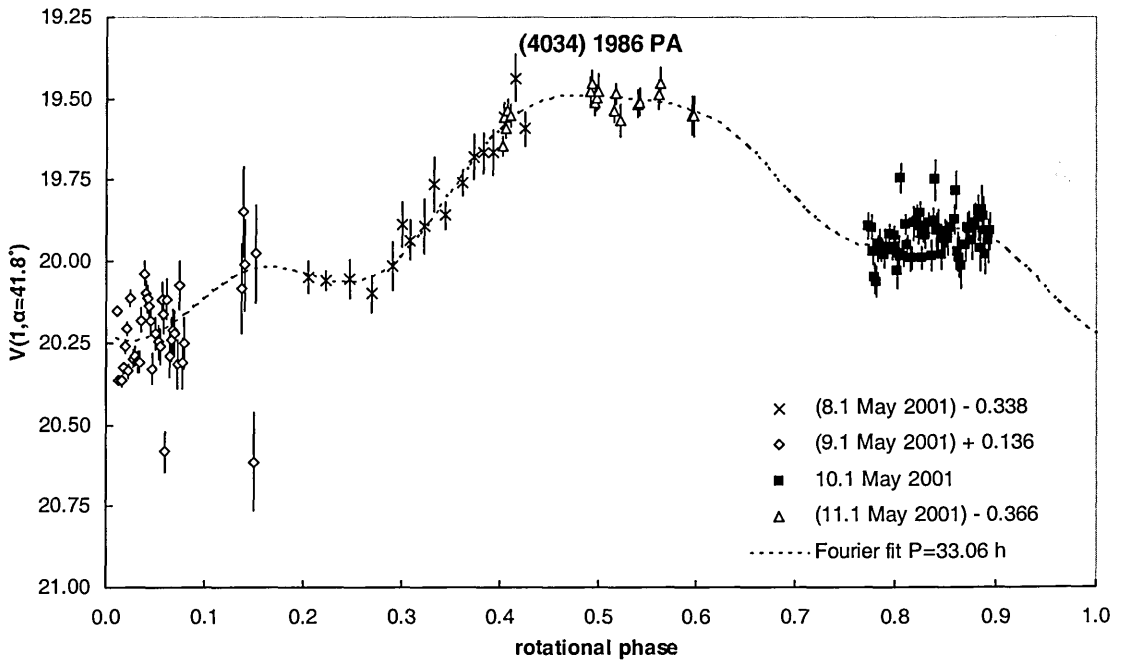
P (h)	$\Delta P(h)$
26.80	0.0049352
33.06	0.0049450
38.58	0.0049518
65.02	0.0049387
78.13	0.0049705

Fig. 3.34

(a)



(b)



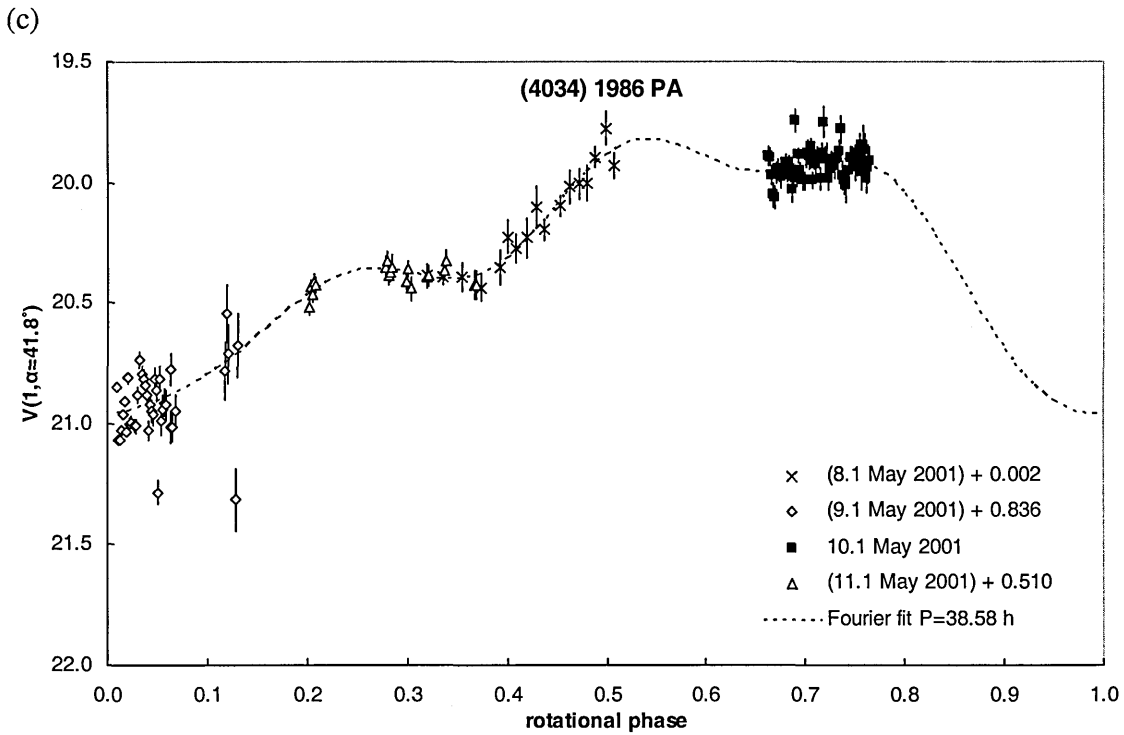


Fig. 3.34 4th order Fourier fits to (4034) 1986 PA JKT May 2001 observations. Magnitudes are adjusted to 10.1 May data. $t_0 = 0$ h, 9 May 2001 UT. (a) $P = 26.80$ h, $\bar{V}(\alpha) = 20.527 \pm 0.009$; (b) $P = 33.06$ h, $\bar{V}(\alpha) = 19.868 \pm 0.009$; (c) $P = 38.58$ h, $\bar{V}(\alpha) = 20.336 \pm 0.009$.

It appears that (4034) 1986 PA has a quite large rotation period $P > 26$ h and its lightcurve amplitude $A_{\text{man}}(41.9^\circ) > 0.6$ mag., based on the 8.1 May data. We find $A(0^\circ) > 0.3$ mag using $m = 0.018$ in Eq. 3.15.

3.9.3 (5587) 1990 SB

(5587) 1990 SB is an Sq-type Amor asteroid (Bus and Binzel, 2002). Its rotation period is 5.0522 h and it has been observed to have a range of lightcurve amplitudes 0.80-1.25 mag. (e.g. Pravec *et al.*, 1998). Delbó *et al.* (2003) measured the asteroid's effective diameter $D_{\text{eff}} = 3.57 \pm 0.54$ km and its geometric albedo $p_v = 0.32 \pm 0.10$, using a value of $H_V = 14.1 \pm 0.5$ based on quasi-simultaneous observations made by Pravec and colleagues in May 2001.

We found a rotation period $P = 5.051 \pm 0.001$ h, from a 6th order Fourier fit (Fig. 3.35), in agreement with the previous measurements of the asteroid's rotation period. Mean magnitudes are $\bar{V}_{4.9\text{May}}(\alpha) = 15.533 \pm 0.004$, $\bar{V}_{6.1\text{May}}(\alpha)^* = 15.566 \pm 0.003$ and $\bar{V}_{7.1\text{May}}(\alpha)^* = 15.619 \pm 0.003$. The magnitudes in Fig. 3.35 are adjusted to those of the night of 4 May 2001, when conditions were judged to be photometric, obtaining a mean reduced visual magnitude $\bar{V}(\alpha = 35.8^\circ) = 15.53 \pm 0.02$. The phase parameter G is unknown, so we estimate H_V by assuming an appropriate value for an S-type asteroid (Bowell *et al.*, 1989) $G = 0.25^{+0.15}_{-0.25}$, obtaining $H_V = 14.24^{+0.3}_{-0.5}$, consistent with the magnitude obtained by Pravec.

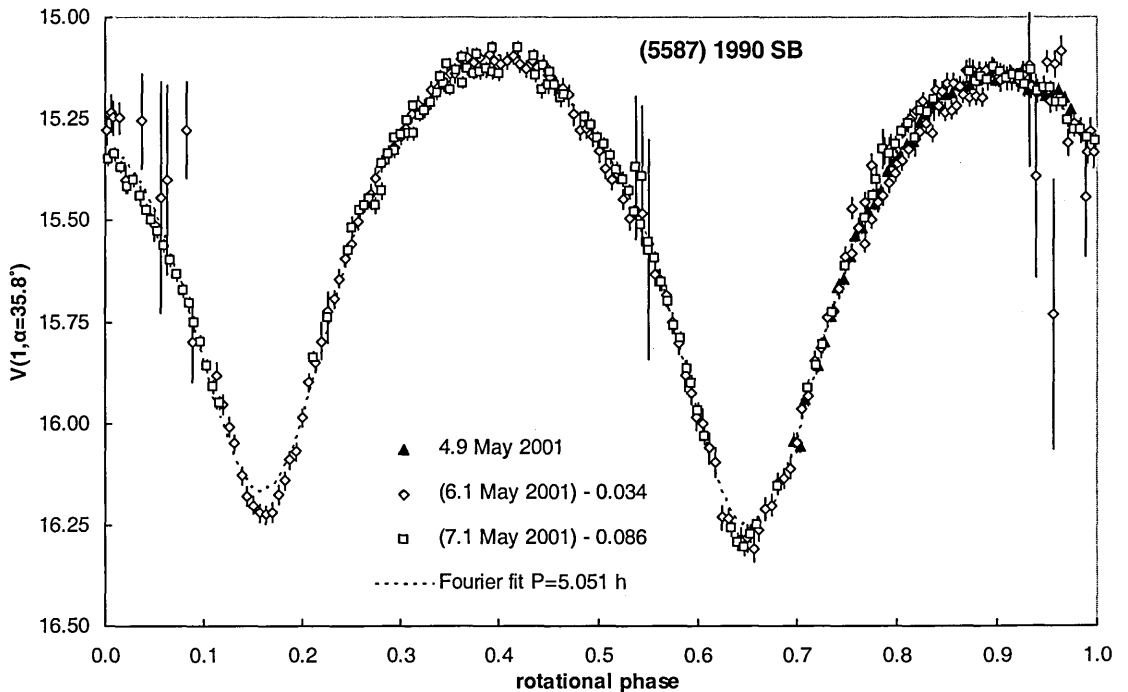


Fig. 3.35 6th order Fourier fit to (5587) 1990 SB JKT May 2001 observations, $P = 5.051 \pm 0.001$ h. Magnitudes are adjusted to 4.9 May 2001 mean reduced magnitude $\bar{V}(\alpha = 35.8^\circ) = 15.533 \pm 0.004$. $t_0 = 0\text{h } 6 \text{ May } 2001 \text{ UT}$. The Fourier coefficients $S_1, C_1, \dots, S_6, C_6$ are: $-0.0416, -0.0148, 0.4732, -0.1801, -0.0174, 0.0039, -0.0956, -0.0902, -0.0025, 0.008, -0.0159, 0.0417$.

The “peak-to-valley” lightcurve amplitude $A_{fit}(35.8^\circ) = 1.01$ mag. and the “manually measured” amplitude $A_{man}(35.8^\circ) = 1.17$ mag. Adopting A_{man} , we obtain $A(0^\circ) = 0.56$.

Assuming the asteroid is a triaxial ellipsoid with axes a , b and c ($a \geq b \geq c$) gives $a/b > 1.68$.

3.9.4 (6455) 1992 HE

(6455) 1992 HE is an S-type Apollo asteroid (Bus and Binzel, 2002). We preferred a rotation period of $P = 2.736 \pm 0.0018$ h from a 6th order Fourier fit [Fig. 3.36 (a)], despite obtaining a statistically slightly better fit of $P = 5.471 \pm 0.0017$ h [$\times 2$ multiple of the $P = 2.736$ h solution, Fig. 3.36 (b)]. This was because, if the change in brightness was due mostly to the changing surface area, reflecting sunlight as the non-spherical asteroid rotated, then we would expect two maxima and minima per rotation. Occasionally other harmonics in the Fourier fit can also dominate, for example due to a change in albedo, particularly for a low lightcurve amplitude. Observations by Pravec and colleagues (<http://sunkl.asu.cas.cz/~ppravec/neo.html>) between February and November 2002 favour $P = 5.471$ h, although do not rule out $P = 2.736$ h. They also find a changing absolute magnitude in the R-filter, $H_R = 13.80 \pm 0.1$ (March 2002) to $H_R = 13.65 \pm 0.1$ (November 2002), which they ascribe either to a change in aspect or N/S variation in albedo. They also found $G = 0.34 \pm 0.1$, and a range of lightcurve amplitudes 0.09-0.13 mag.

The main goal of our September 2002 (6455) 1992 HE observations was to provide a composite lightcurve to complement the thermal IR observations at UKIRT [Section 5.6.1 and Fig. 5.23 (b)]. Fortunately, the accuracy of the lightcurve correction does not depend on which Fourier fit is correct.

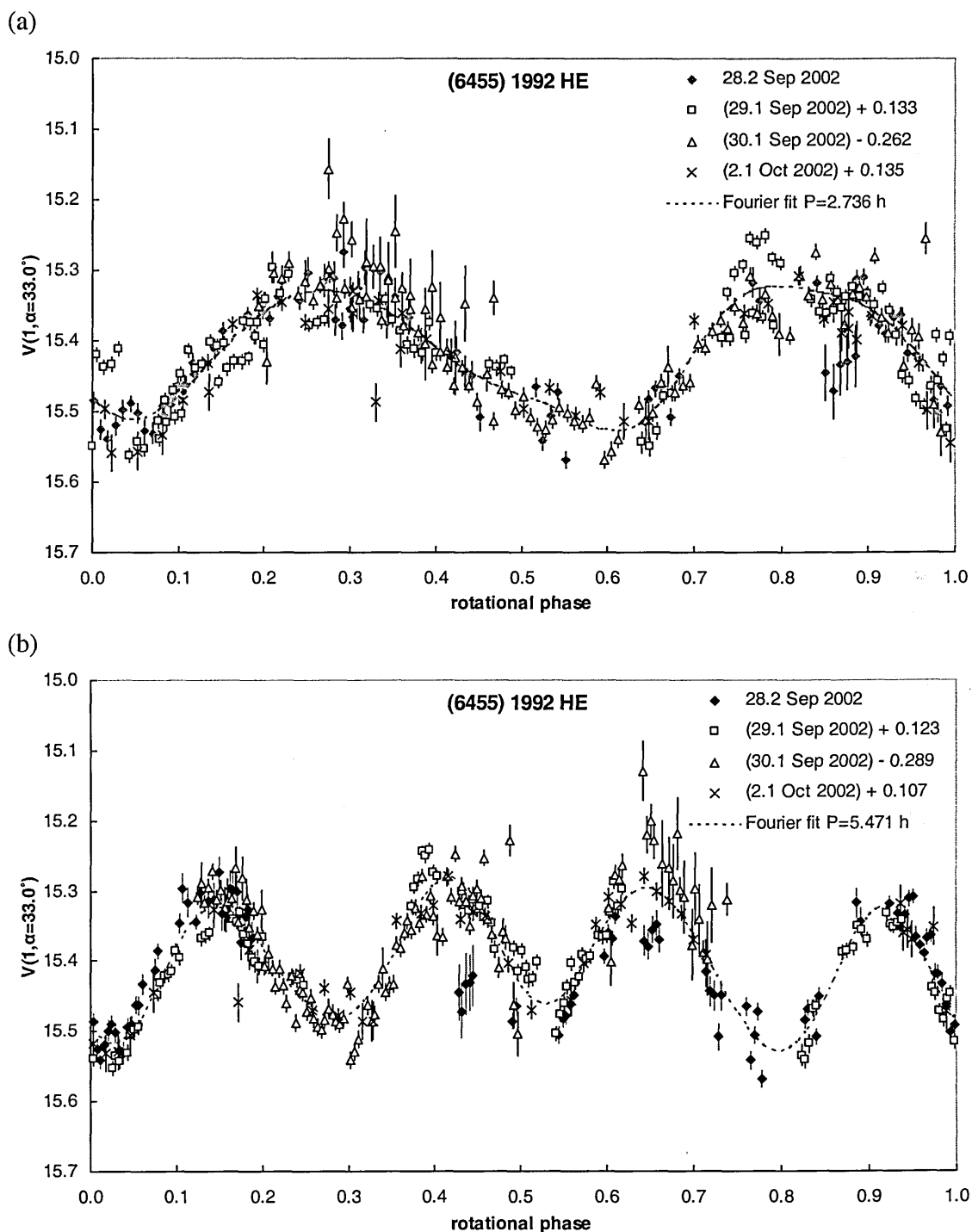


Fig. 3.36 Two possible 6th order Fourier fits for (6455) 1992 HE, JKT September 2002 observations. $t_0 = 0$ h, 25 September 2002. Magnitudes are adjusted to 28.1 September 2002 mean reduced magnitude. (a) $P = 2.736 \pm 0.0018$ and $\bar{V}(\alpha) = 15.417 \pm 0.003$; the Fourier coefficients $S_1, C_1, \dots, S_6, C_6$ are: $-0.0082, -0.0205, 0.0602, 0.0687, 0.0068, 0.019, 0.0039, -0.0079, 0.0039, -0.0014, 0.0028$. (b) $P = 5.471 \pm 0.0017$ h and $\bar{V}(\alpha) = 15.403 \pm 0.004$; the Fourier coefficients $S_1, C_1, \dots, S_6, C_6$ are: $-0.0075, 0.0284, -0.00115, -0.0148, 0.0018, -0.005, 0.0691, 0.0619, 0.0023, 0.0051, 0.0082, 0.012$.

Adopting $P = 2.736$ h (although using the other solution would make negligible difference), we obtain the following mean magnitudes: $\bar{V}_{28.2\text{Sep}}(\alpha) = 15.417 \pm 0.003$, $\bar{V}_{29.1\text{Sep}}(\alpha)^* = 15.284 \pm 0.004$, $\bar{V}_{30.1\text{Sep}}(\alpha)^* = 15.679 \pm 0.003$ and $\bar{V}_{2.1\text{Oct}}(\alpha) = 15.282 \pm 0.005$. The magnitudes in Fig. 3.36 (a) are adjusted to those of the night of 27 September 2002, when conditions were judged to be most photometric, obtaining a mean reduced visual magnitude $\bar{V}(\alpha = 33.0^\circ) = 15.42 \pm 0.04$. There may have been thin cirrus during the 27 Sep. observations, although the night was our most photometric and every effort was made to accurately calibrate the comparison stars using frames taken during clear weather (Section 3.7.4).

We derive $H_V = 14.32 \pm 0.24$. Assuming $V-R = 0.45 \pm 0.1$ (Section 3.8.2), our absolute magnitude is consistent with Pravec's. For the asteroid's lightcurve amplitudes we obtain $A_{fit} = 0.18$ and $A_{man} = 0.21$. Adopting A_{man} , and correcting to zero degree phase angle gives $A(0^\circ) = 0.11$, corresponding to $a/b > 1.10$. This lightcurve amplitude is consistent with those found by Pravec.

3.9.5 (19356) 1997 GH₃

(19356) 1997 GH₃ is an S-type Amor asteroid (Bus and Binzel, 2002). Delbó *et al.* (2003) measured an effective diameter $D_{eff} = 0.91 \pm 0.14$ km and geometric albedo $p_v = 0.34 \pm 0.10$ using a value of $H_V = 17.0$ obtained from the web services listed in Section 3.9.2. Pravec *et al.* (1998) found a rotation period $P = 6.714 \pm 0.004$ h, and lightcurve amplitudes ($\alpha = 50^\circ$) $A_{fit} = 0.60$ and $A_{man} = 0.74$.

We obtain a best 6th order Fourier fit for $P = 6.720 \pm 0.002$ (Fig. 3.37), in reasonable agreement with Pravec. The mean magnitudes $\bar{V}(\alpha)$ for 5.1 and 11.1 May are 17.530 ± 0.003 and 17.414 ± 0.004 respectively. We judged the night of 4 May 2001 to be the most photometric and adjusted the 11.1 May magnitudes accordingly in Fig. 3.37. We

obtain $\bar{V}(\alpha = 8.0^\circ) = 17.53 \pm 0.02$. Assuming $G = 0.25^{+0.15}_{-0.25}$, we derive $H_V = 17.02^{+0.09}_{-0.17}$

which indicates that the value Delbó used for radiometric diameter determination was accurate.

For the asteroid's lightcurve amplitudes we obtain $A_{fit} = 0.32$ and $A_{man} = 0.34$. Adopting A_{man} , and correcting to zero degree phase angle gives $A(0^\circ) = 0.28$, corresponding to $a/b > 1.29$. The lightcurve amplitude is smaller than that found by Pravec, although a correction of their $A_{man} = 0.74$ to zero degree phase from $\alpha = 50^\circ$ gives $A(0^\circ) = 0.30$, so it is consistent with ours.

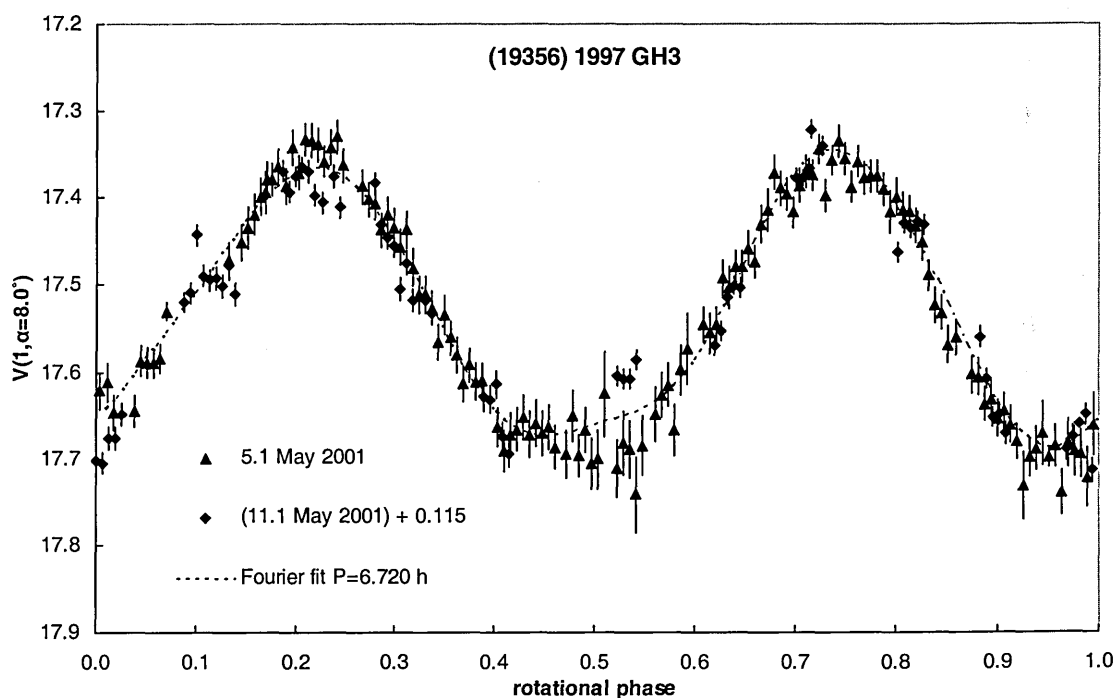


Fig. 3.37 A 6th order Fourier fit to (19356) 1997 GH₃ JKT May 2001 observations, $P = 6.270 \pm 0.002$ h. $t_0 = 0$ h, 8 May 2001. Magnitudes are adjusted to 5.1 May 2001 mean reduced magnitude $\bar{V}(\alpha) = 17.530 \pm 0.003$. Fourier coefficients $S_1, C_1, \dots, S_6, C_6$: -0.0001, -0.0179, -0.0494, 0.1508, -0.0178, 0.0109, -0.0022, -0.0181, -0.0031, 0.004, -0.0028, -0.0031.

3.9.6 1998 UO₁

1998 UO₁ is an Apollo asteroid. Pravec and colleagues have observed the asteroid in October 2004 (<http://sunkl.asu.cas.cz/~ppravec/neo.html>) and found $P = 2.90 \pm 0.02$ h and

a low lightcurve amplitude 0.04 mag. Our reduced magnitudes for the 26.2 September 2002 JKT observations (Fig. 3.19) only just cover a long enough period of time (3.2 h) to encompass the entire lightcurve. A 4th order Fourier best-fit gives a period of $P = 3.033 \pm 0.006$ h (Fig. 3.38). However, we can see that only two observations taken at the beginning (green points) overlap in rotational phase with observations taken at the end (blue points), so the period we obtain is dependent on how we mesh these few points. We therefore assign a larger uncertainty to the period to account for the possible freedom in adjusting the slope where these points lie: $P = 3.0 \pm 0.1$ h. This period is consistent with that found by Pravec.

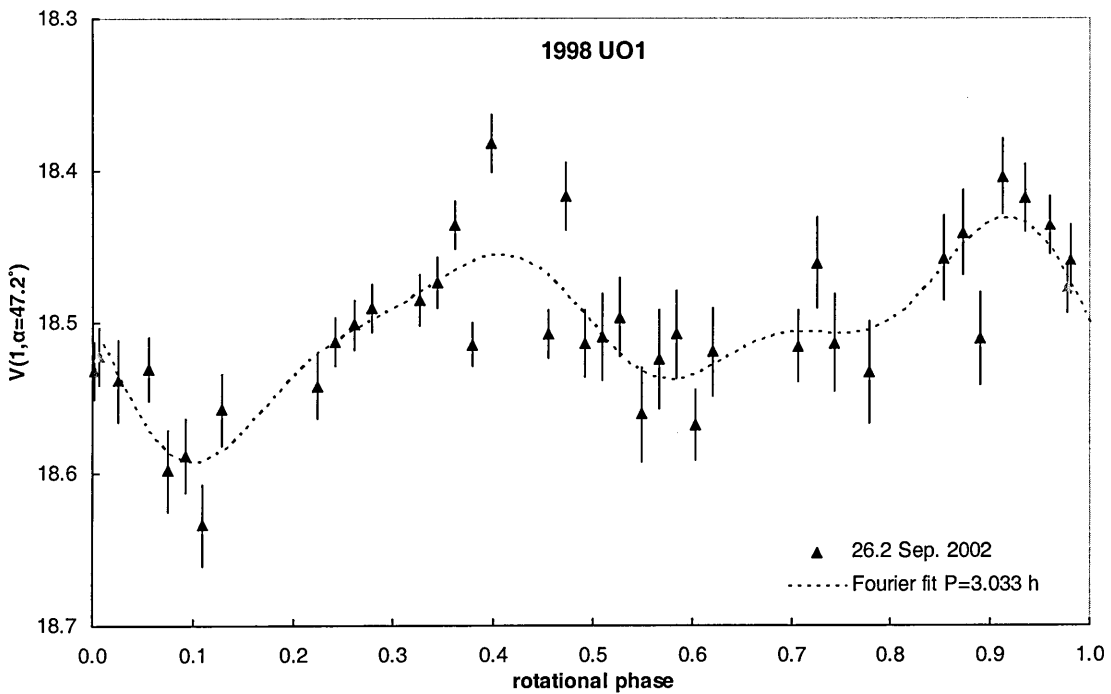


Fig. 3.38 A 4th order Fourier fit to 1998 UO₁ JKT 26.2 September 2002 observations, $P = 3.033 \pm 0.006$ h. $t_0 = 0$ h, 26 September 2002., mean reduced magnitude $\bar{V}(\alpha) = 18.506 \pm 0.006$. Fourier coefficients $S_1, C_1, \dots, S_4, C_4$: 0.0134, 0.0077, 0.0514, -0.0039, 0.0125, -0.0086, 0.0179, -0.0005. Green points were taken at the beginning of the observation and fold with the blue points taken at the end.

We derive $\bar{V}(\alpha = 47.2^\circ) = 18.51 \pm 0.04$. Assuming $G = 0.15_{-0.15}^{+0.25}$, this corresponds to $H_V = 16.7 \pm 0.4$. We obtain lightcurve amplitudes $A_{fit} = 0.1$ and $A_{man} = 0.16$. Adopting A_{man} and

correcting to zero degree phase angle gives $A(0^\circ) = 0.09$, corresponding to minimum $a/b = 1.08$.

3.9.7 (33342) 1998 WT₂₄

(33342) 1998 WT₂₄ is an E-type Aten asteroid (Lazzarin *et al.*, 2004). Radar (Zaitsev *et al.*, 2002) and polarimetry (Kiselev *et al.*, 2002) find the geometric albedo and size to be $p_v = 0.43$ and 0.42×0.33 km respectively, while Delbó (2004) has found $p_v = 0.59$, 0.35 and 0.27 and $D_{eff} = 0.34$, 0.44 and 0.50 km from thermal IR observations at the NASA-IRTF on 18, 19 and 21 December 2001 respectively. Optical observations in December 2001 by Krugly *et al.* (2002) and Pravec (<http://sunkl.asu.cas.cz/~ppravec/neo.html>) find a rotation period $P = 3.698 \pm 0.004$ h and lightcurve amplitudes ranging from 0.25-0.56 mag.

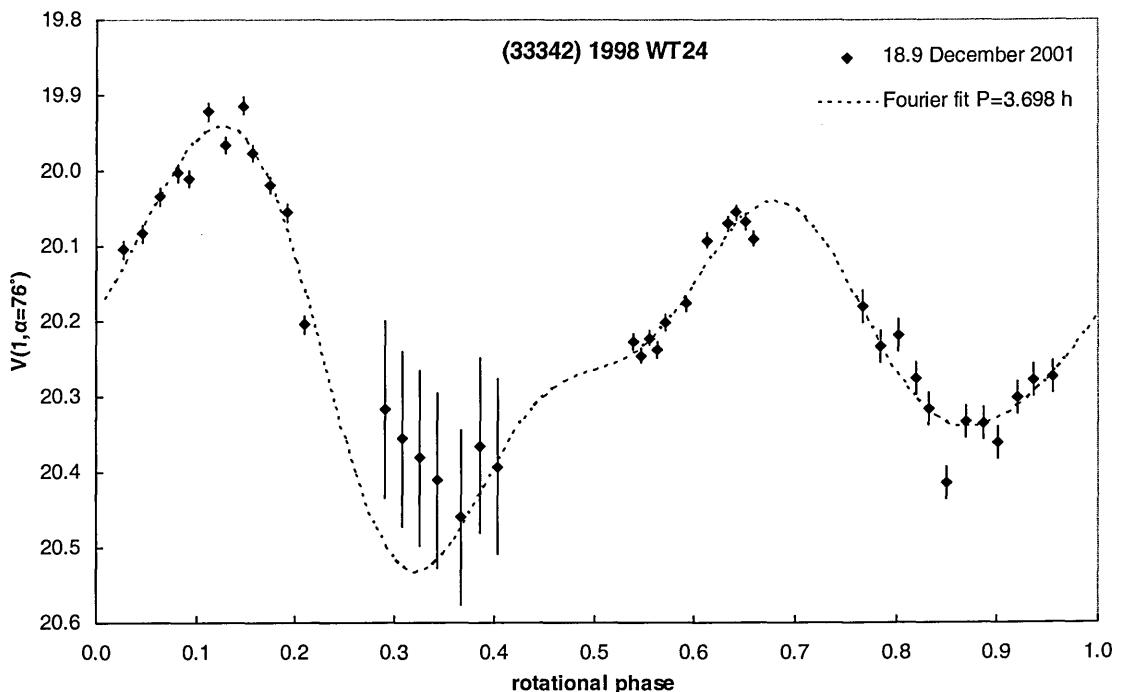


Fig. 3.39 4th order Fourier fit to (33342) 1998 WT₂₄ JKT 18 December observations, $P = 3.698 \pm 0.004$ h, $\bar{R}(\alpha) = 20.22 \pm 0.04$. $t_0 = 0h$, 18 December 2001 UT. Fourier coefficients $S_1, C_1, \dots, S_4, C_4$: 0.0458, -0.0671, -0.1889, -0.0116, -0.0612, 0.0302, 0.0444, 0.015.

Observations at the JKT had a duration of 3.5 h, which is not quite as long as the above-quoted period, so best-fit Fourier fits will give shorter periods. We can use Fourier analysis as a curve-fitting tool. A 4th order Fourier fit of $P = 3.698 \pm 0.004$ h is shown in Fig. 3.39. Clearly there are large gaps, so the reliability of the fit and the corresponding mean reduced magnitude $\bar{R}(\alpha = 76^\circ) = 20.22 \pm 0.04$ (uncertainty only estimated from the photometric calibration) is limited. However, at least one minimum and one maximum is covered, so the fitted curve's mean magnitude is probably correct to within 0.1 mag. and we can estimate the lightcurve amplitude $A_{man} = 0.40$. The amplitude is consistent with the optical observations of other authors discussed above. The correction to zero degree phase angle $A(0^\circ) = 0.17$ assuming $m = 0.018$, although we remind here of the unreliability of this correction at $\alpha > 40^\circ$, corresponding to $a/b > 1.17$. Unfortunately at such a large phase angle any estimation of H_R is very crude. Assuming $G = 0.42_{-0.20}^{+0.08}$, gives $H_R = 18.1_{-0.4}^{+0.2}$. Applying a correction of $V-R = 0.45 \pm 0.1$ obtains $H_V = 18.5_{-0.4}^{+0.2}$.

3.9.8 (25330) 1999 KV₄

(25330) 1999 KV₄ is an Apollo asteroid and has been identified as either a B- or C-type [Lazzarin *et al.* (2004), Binzel *et al.* (2004)]. Delbó *et al.* (2003) measured the asteroid's effective diameter $D_{eff} = 3.21 \pm 0.48$ km and its geometric albedo $p_v = 0.052 \pm 0.016$. Pravec (<http://sunkl.asu.cas.cz/~ppravec/neo.html>), from December 2002 observations, finds a rotation period $P = 4.919 \pm 0.004$ h and a lightcurve amplitude of 0.15 mag.

Figure 3.40 shows a 6th order Fourier fit. We obtain $P = 4.907 \pm 0.004$ h, close to Pravec's fit, despite the complex nature of the low-amplitude lightcurve. We obtain the following mean magnitudes: $\bar{V}_{8.0\text{May}}(\alpha) = 18.796 \pm 0.028$, $\bar{V}_{8.9\text{May}}(\alpha)^* = 18.735 \pm 0.054$, $\bar{V}_{10.0\text{May}}(\alpha) = 18.764 \pm 0.006$ and $\bar{V}_{11.0\text{May}}(\alpha) = 18.727 \pm 0.007$. The magnitudes in Fig.

3.40 are adjusted to those of the night of 10 May 2001, when conditions were judged to be most photometric, obtaining a mean reduced visual magnitude $\bar{V}(\alpha = 53.8^\circ) = 18.76 \pm 0.02$. Assuming $G = 0.15^{+0.25}_{-0.15}$, this corresponds to $H_V = 16.80 \pm 0.4$.

For lightcurve amplitudes, we obtain $A_{fit} = 0.06$ mag. and $A_{man} = 0.16$ mag. Adopting A_{man} and correcting to zero degree phase angle assuming $m = 0.015$, gives $A(0^\circ) = 0.09$ mag., corresponding to $a/b > 1.08$. The lightcurve amplitude is similar to that derived by Pravec.

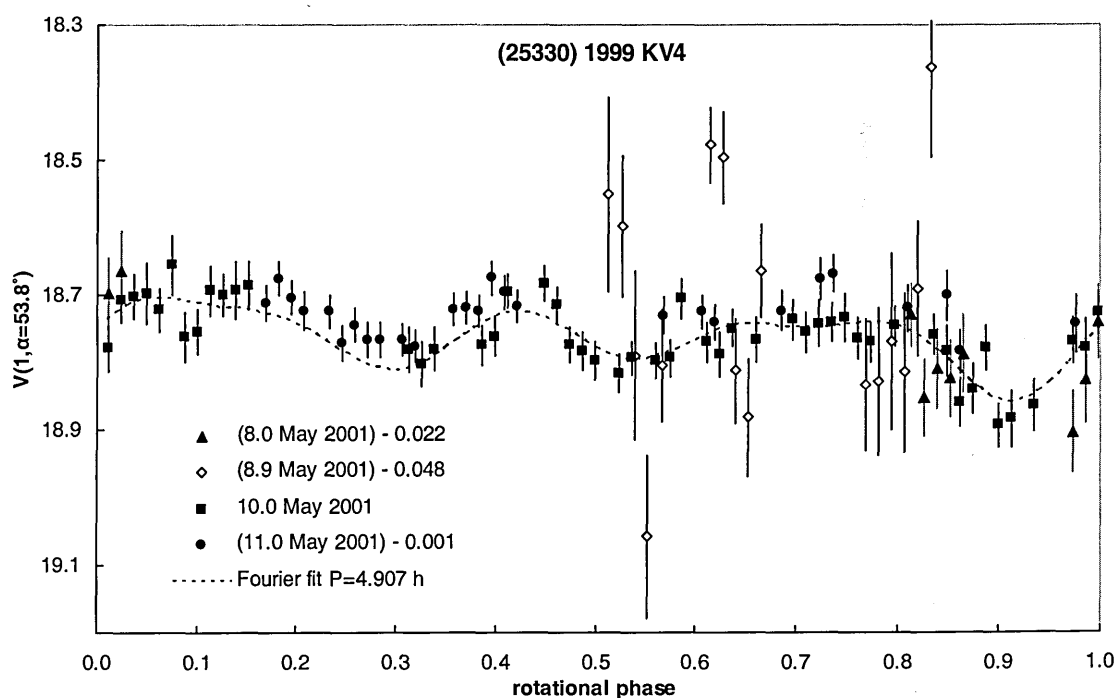


Fig. 3.40 6th order Fourier fit to (25330) 1999 KV₄ JKT May 2001 observations, $P = 4.907 \pm 0.004$. The weather on 8.9 May was cloudy. Magnitudes adjusted to $\bar{V}_{10.0\text{May}}(\alpha) = 18.764 \pm 0.006$. $t_0 = 0\text{h}, 9\text{ May } 2001\text{ UT}$. Fourier coefficients $S_1, C_1, \dots, S_6, C_6$: $-0.0096, 0.0011, -0.0286, 0.0018, -0.0412, 0.0012, 0.0001, 0.0007, -0.0102, -0.017, 0.0005, -0.0026$.

3.9.9 (53789) 2000 ED₁₀₄

(53789) 2000 ED₁₀₄ is an Amor asteroid. Optical observations by Pravec (<http://sunkl.asu.cas.cz/~ppravec/neo.html>) in September 2002 indicate that the rotation

period is about 43 h, although a number of periods are possible, and that the lightcurve amplitude > 1.1 mag.

Limited optical photometry of (53789) 2000 ED₁₀₄ obtained on the night of 1 October 2002 shows that the lightcurve amplitude $A(60.5^\circ) > 1.0$ (Fig. 3.23). Assuming $m = 0.018$, we obtain $A(0^\circ) > 0.48$, and therefore $a/b > 1.6$. We also find that the rotation period $P \gg 3.8$ h. These values are consistent with Pravec.

3.9.10 2001 SE₂₈₆

2001 SE₂₈₆ is an Amor asteroid. Optical observations by Pravec (<http://sunkl.asu.cas.cz/~ppravec/neo.html>) in December 2001 found that a period of $P = 9.323 \pm 0.002$ h is plausible, but that other periods are possible. Pravec found a lightcurve amplitude of 0.14 mag.

There are not enough observations from the limited optical photometry of 18 December to form a composite lightcurve (Fig. 3.25) although we can estimate that the lightcurve amplitude is about $A(19.2^\circ) = 0.23$. Assuming $m = 0.018$, we obtain $A(0^\circ) = 0.17$, similar to that found by Pravec. We derive $a/b > 1.2$.

3.9.11 2002 HK₁₂

2002 HK₁₂ is an Apollo asteroid. Optical observations by Pravec (<http://sunkl.asu.cas.cz/~ppravec/neo.html>) between 6.9 and 9.2 September 2002 found a period $P = 12.690 \pm 0.003$ h and a lightcurve amplitude of 1.5 mag. A 6th order Fourier fit of our September JKT observations applied with the period set to $P = 12.690$ h shows there is data missing for 0.3 of the rotational phase.

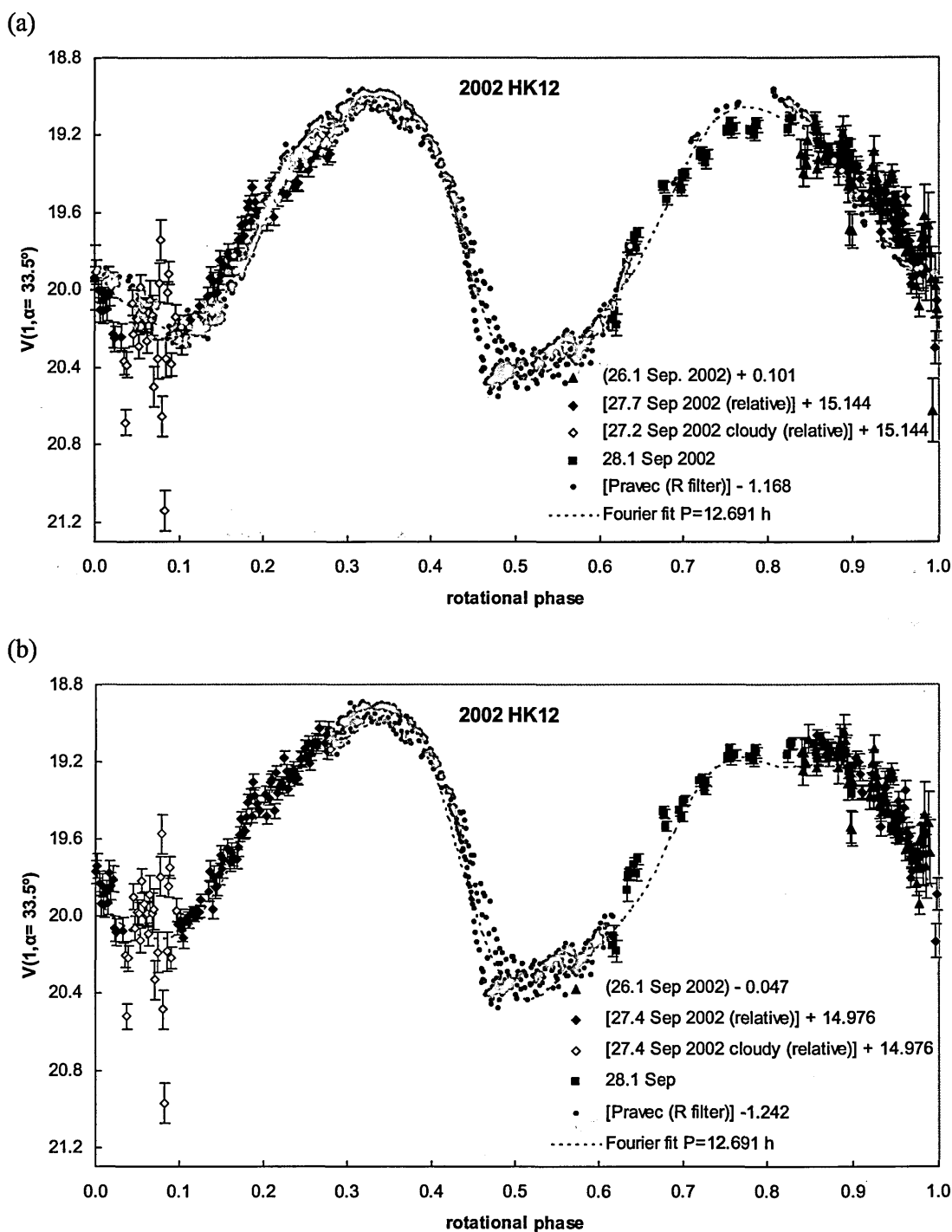


Fig. 3.41 6th order Fourier fits to 2002 HK_{12} JKT observations combined with observations by Pravec, September 2002. $t_0 = 0h$, 25 September 2002 UT. (a) Pravec data for all rotational phases, $P = 12.691 \pm 0.0028$, $\bar{V}(\alpha) = 19.659$. (b) Pravec data only at rotational phases not covered by our observations. $P = 12.691 \pm 0.0037$, $\bar{V}(\alpha) = 19.620$, Fourier coefficients $S_1, C_1, \dots, S_6, C_6$: $-0.0431, -0.1016, 0.4047, 0.4389, 0.0075, -0.1139, 0.0439, 0.0562, 0.0493, -0.0393, -0.045, 0.0419$.

We have been able to obtain Pravec's observations (Pravec, personal communications, 2003) and have combined them with ours, since both our UKIRT observations were unfortunately in this gap [Fig. 5.23 (d)]. Overlaying Pravec's complete dataset [Fig. 3.41 (a)] revealed that the lightcurve shape is slightly different, probably due to the phase-amplitude effect and/or a small change in aspect. So an alternative fit has been performed, which gives the same best-fit period, but only using Pravec's observations from the rotational phases not covered by ours [Fig. 3.41 (b)].

We obtain $P = 12.691 \pm 0.004$ h and mean magnitudes $\bar{V}_{26.0\text{Sep}}(\alpha)^* = 19.620 \pm 0.019$ and $\bar{V}_{28.1\text{Sep}}(\alpha) = 19.573 \pm 0.014$. The night of 27 September 2002 was judged to be photometric, so the magnitudes were adjusted to the 28.1 September data, obtaining $\bar{V}(\alpha = 33.5^\circ) = 19.62 \pm 0.04$. Assuming a slope parameter of $G = 0.15_{-0.15}^{+0.25}$, we derive $H_V = 17.67_{-0.3}^{+0.4}$. The lightcurve amplitude is $A_{fit} = 1.19$ and $A_{man} = 1.47$; adopting A_{man} corrects to $A(0^\circ) = 0.92$, giving limits $a/b > 2.33$.

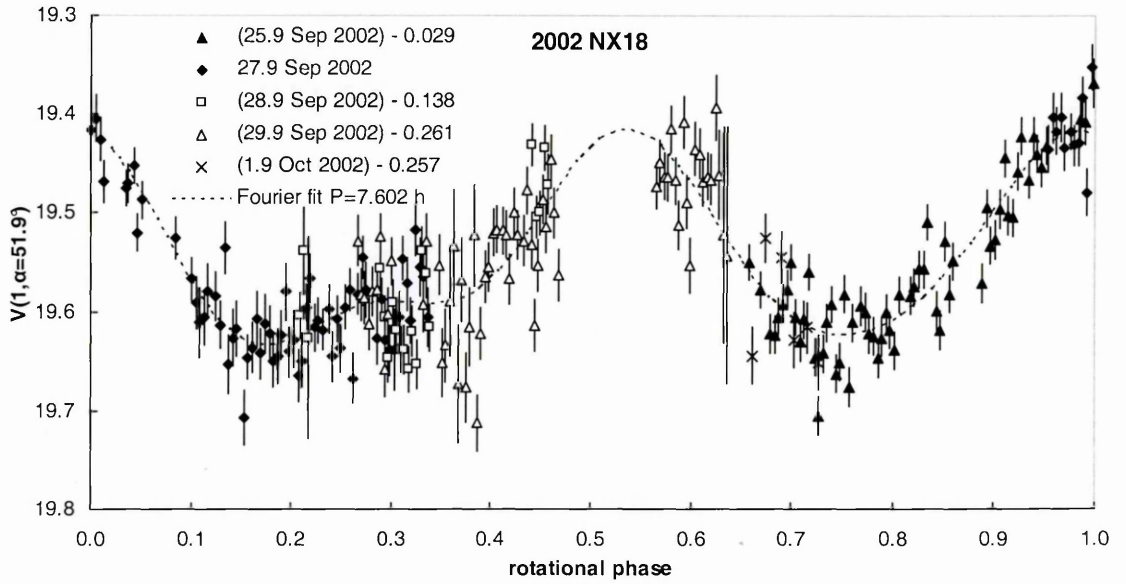
3.9.12 2002 NX₁₈

2002 NX₁₈ is an Amor asteroid. The lightcurve coverage was not adequate to produce a unique solution for the rotation period. The two best solutions are shown in Fig. 3.42 (a) and (b), obtained from 4th order Fourier fits, allowing for an arbitrary shift in mean magnitude to coincide with that of 27.9 September UT: $P = 7.602 \pm 0.002$ h and $P = 9.040 \pm 0.002$ h. Assuming the $P = 9.040$ h solution is correct, we measured a reduced visual mean magnitude $\bar{V}(\alpha = 51.9^\circ) = 19.54 \pm 0.04$ with a lightcurve amplitude $A_{man} = 0.23$ (the $P = 7.602$ h solution gives the same V with a lightcurve amplitude of 0.22) and $A_{fit} = 0.19$. A correction to zero phase assuming $m = 0.015$ gives $A(0^\circ) = 0.13$,

corresponding to $a/b > 1.13$. Assuming a slope parameter of $G = 0.15^{+0.25}_{-0.15}$ we derive

$$H_V = 17.63 \pm 0.4.$$

(a)



(b)

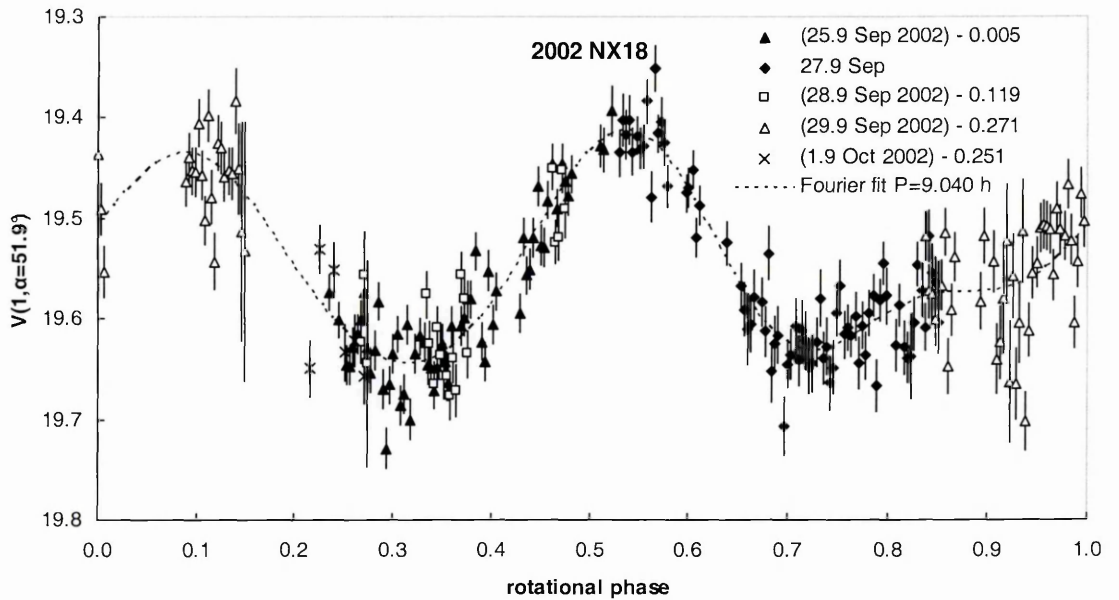


Fig. 3.42 Two possible 4th order Fourier fits for 2002 NX₁₈ JKT September 2002 observations. $t_0 = 0h$, 25 September 2002. Magnitudes are adjusted to 27.9 September 2002 mean reduced magnitude. (a) $P = 7.602 \pm 0.0023$ h; $\bar{V}(\alpha) = 19.539 \pm 0.005$, the Fourier coefficients $S_1, C_1, \dots, S_4, C_4$ are: 0.0206, 0.0047, -0.0009, -0.0928, 0.0312, -0.0108, -0.0097, -0.0191. (b) $P = 9.040 \pm 0.0022$ h; $\bar{V}(\alpha) = 19.542 \pm 0.005$, the Fourier coefficients $S_1, C_1, \dots, S_4, C_4$ are: -0.0081, -0.0004, -0.055, -0.0744, -0.001, 0.0378, -0.017, 0.0025.

3.9.13 2002 QE₁₅

2002 QE₁₅ is an Amor asteroid. Pravec (personal communication, 2003, and <http://sunkl.asu.cas.cz/~ppravec/neo.html>), from observations between 30 September and 2 October 2002, found a rotation period for 2002 QE₁₅ of 2.5811 ± 0.0001 h assuming the second harmonic in the Fourier fit is dominant, and a lightcurve amplitude of 0.08-0.10 mag. Because the lightcurve amplitude is low the period may have more than the usual two extrema per cycle, due, for example, to local topography or albedo variations on the surface, and Pravec found that a period of 3.8717 h is also possible.

Because the data mostly come from 26.9 September 2002, where there was intermittent cirrus, it is quite noisy, and hence we are unable to find a unique solution for the period with a composite lightcurve. Error bars were applied to the 26.9 September data before Fourier fitting, estimating the photon statistics uncertainty to be 0.020 mag., similar to that of the other nights. We found two solutions closest to those found by Pravec (Fig. 3.43): $P = 2.581 \pm 0.003$ h and $P = 3.870 \pm 0.003$ h. The mean magnitudes for $P = 2.581$ h are: $\bar{V}_{28.9\text{Sep}}(\alpha) = 18.348 \pm 0.005$ and $\bar{V}_{2.0\text{Oct}}(\alpha) = 18.393 \pm 0.022$; for $P = 3.870$ h they are $\bar{V}_{28.9\text{Sep}}(\alpha) = 18.348 \pm 0.006$ and $\bar{V}_{2.0\text{Oct}}(\alpha) = 18.393 \pm 0.022$. The mean magnitudes are adjusted to the night of 28 September 2002, since no standards were observed on 26 September, and only three observations were made on 1 October. However, there was intermittent cirrus on 28 September which may increase the uncertainty of the calibration. $P = 2.581$ h was a poor least-squares fit, whereas $P = 3.870$ h was among the best.

Adopting $P = 3.868 \pm 0.004$ h, we derive $V(1, \alpha = 61.7^\circ) = 18.35 \pm 0.04$ mag.; assuming $G = 0.15^{+0.25}_{-0.15}$, we obtain an H_V magnitude of $16.15^{+0.5}_{-0.4}$ which is in close agreement to the catalogued value at JPL Horizons of $H_V = 16.21$ that we used for the thermal model fitting for this asteroid. For the lightcurve amplitude, we find $A_{fit} = 0.02$ and $A_{man} = 0.11$ mag.

Adopting A_{man} , we derive $A(0^\circ) = 0.05$ mag, equivalent to $a/b > 1.05$. The lightcurve amplitude is consistent with that found by Pravec.

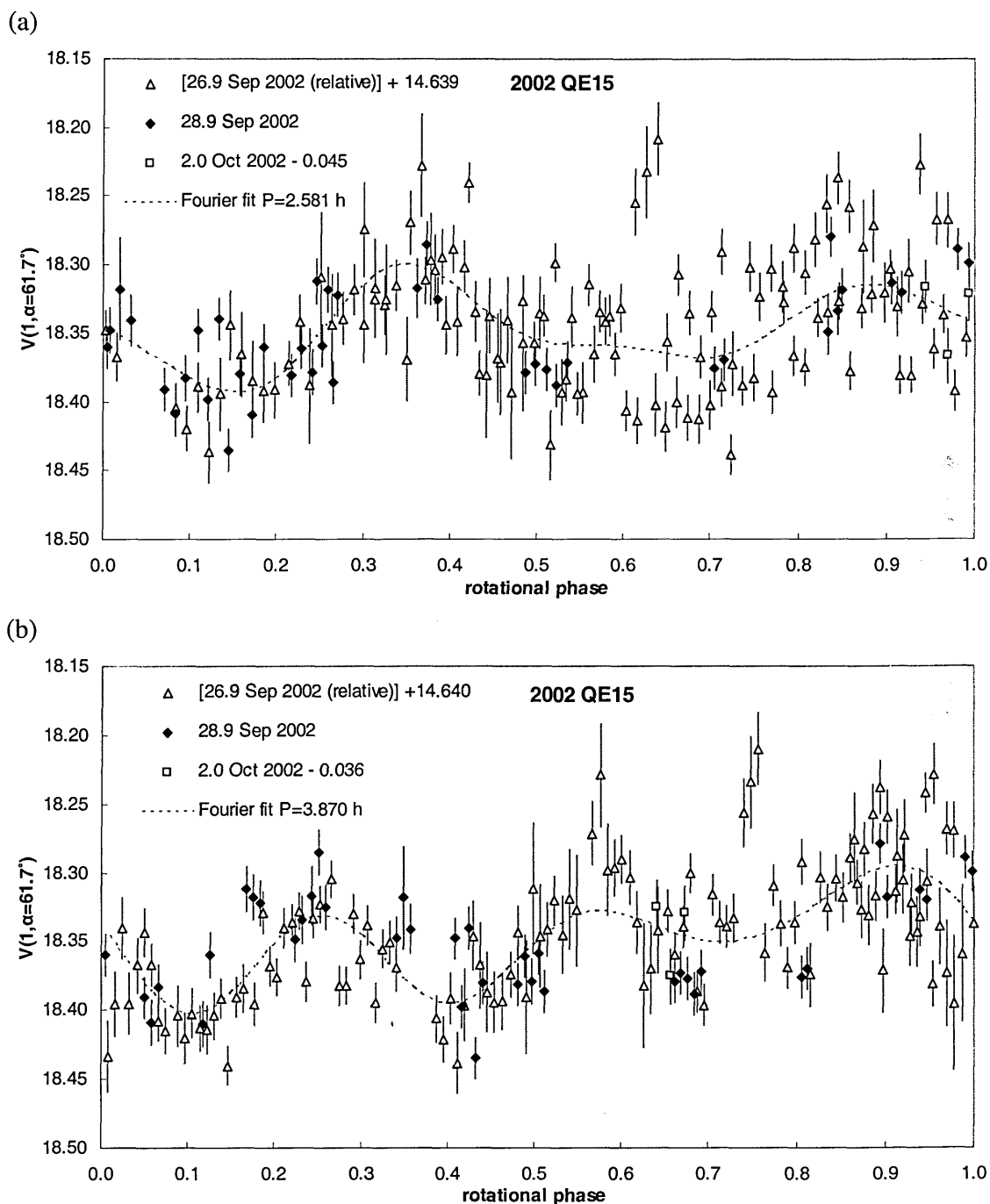


Fig. 3.43 Two possible 4th order Fourier fits for 2002 QE₁₅ JKT September/October 2002 observations. $t_0 = 0h$, 28 September 2002. Magnitudes are adjusted to 28.9 September 2002 mean reduced magnitude. (a) $P = 2.581 \pm 0.004$ h; $\bar{V}(\alpha) = 18.344 \pm 0.005$, the Fourier coefficients $S_1, C_1, \dots, S_4, C_4$ are: 0.0037, 0.013, 0.0276, -0.0057, 0.0085, -0.0114, -0.0055, 0.012. (b) $P = 3.868 \pm 0.004$ h; $\bar{V}(\alpha) = 18.352 \pm 0.004$, the Fourier coefficients $S_1, C_1, \dots, S_4, C_4$ are: 0.024, -0.0203, 0.0192, 0.014, 0.0185, 0.0002, 0.0065, -0.0197.

3.10 Summary

A summary of the results is given in Table 3.5.

Table 3.5 Summary of results of observations of near-Earth Asteroids at the JKT in May 2001, December 2001 and September 2002

Asteroid	α°	P (h)	$\bar{V}(\alpha)^a$	H_V^a	A_{fit}	A_{man}	A(0°)
(433) Eros	18.0	2.249 ± 0.001	11.28 ± 0.04	10.40 ± 0.04	0.06	0.10	0.06
(4034) 1986 PA	41.9					>0.6	>0.3
(5587) 1990 SB	35.8	5.051 ± 0.001	15.53 ± 0.02	$14.24^{+0.3}_{-0.5}$	1.01	1.17	0.56
(6455) 1992 HE	33.0	2.736 ± 0.002 or 5.471 ± 0.002	15.42 ± 0.04	14.32 ± 0.24	0.18	0.21	0.11
(19356) 1997 GH ₃	8.0	6.720 ± 0.002	17.53 ± 0.02	$17.02^{+0.09}_{-0.17}$	0.31	0.34	0.28
1998 UO ₁	47.2	3.0 ± 0.1	18.51 ± 0.04	16.7 ± 0.4	0.10	0.16	0.09
(33342) 1998 WT ₂₄	76		$\bar{R}(\alpha)=20.22 \pm 0.1$	$(H_R = 18.1)$ $H_V = 18.5^{+0.2}_{-0.4}$		0.40	0.17
(25330) 1999 KV ₄	53.8	4.907 ± 0.004	18.76 ± 0.02	16.80 ± 0.4	0.06	0.16	0.09
(53789) 2000 ED ₁₀₄	60.5	>>3.8				>1	
2001 SE ₂₈₆	19.2					≈0.2	
2002 HK ₁₂	33.5	12.691 ± 0.004	19.62 ± 0.04	$17.67^{+0.4}_{-0.3}$	1.19	1.47	0.92
2002 NX ₁₈	51.9	7.602 ± 0.002 or $9.040^b \pm 0.002$	19.54 ± 0.04	17.63 ± 0.4	0.19	0.23	0.13
2002 QE ₁₅	62.2	2.581 ± 0.004 or $3.868^b \pm 0.004$	18.35 ± 0.02	$16.15^{+0.5}_{-0.4}$	0.02	0.11	0.05

Notes. ^aUnless otherwise indicated.

^bOther periods possible.

4 Thermal Modelling of Near-Earth Asteroids

4.1 Relating the Albedo, Diameter and Absolute Magnitude

In this chapter four simple thermal models are described which can be fitted to thermal IR fluxes to derive the size and albedo of an asteroid. The size is ultimately presented as the effective diameter D_{eff} , the equivalent diameter of a perfect sphere with the same projected area as the (generally) irregularly shaped asteroid. The albedo is presented as the geometric albedo p_v , the ratio of the visual brightness to that of a perfectly diffusing ‘Lambertian’ disk of the same diameter. The bolometric Bond albedo A can be related to p_v through:

$$p_v = \frac{A}{q} \quad (4.1)$$

where q is the phase integral, related to the phase parameter G by (Bowell *et al.*, 1989):

$$q = 0.290 + 0.684 G \quad (4.2)$$

Chapter 3 explains how an asteroid’s brightness, its absolute visual magnitude H_V , is measured from observations at an optical telescope and observations made at the JKT are reported. Observations in the thermal infrared (IR) in the N (8-13 μm) and Q bands (17-25 μm) measured at the UKIRT are described in Chapter 5. For a given H_V , there is a range of possible p_v and hence D_{eff} described by (e.g. Fowler and Chillemi, 1992):

$$D_{eff} \text{ (km)} = \frac{10^{-H_V/5} 1329}{\sqrt{p_v}} \quad (4.3)$$

The H_V magnitude alone does not provide a good constraint on an asteroid’s diameter because its albedo A can lie anywhere in the range 0.02-0.7.

4.2 The Radiometric Method of Diameter Determination

The principle of the radiometric method is described in Morrison (1973) and Lebofsky and Spencer (1989), with more recent reviews by Delbó and Harris (2002) and Harris and Lagerros (2002). A representation of the energy balance at the asteroid surface is given in Fig. 4.1. The energy balance depends on the projected area and the albedo. Since the reflected solar component is proportional to A and the thermal component is proportional to $(1-A)$, simultaneous measurements of both can provide an unique D_{eff} and p_v via the radiometric method of diameter determination.

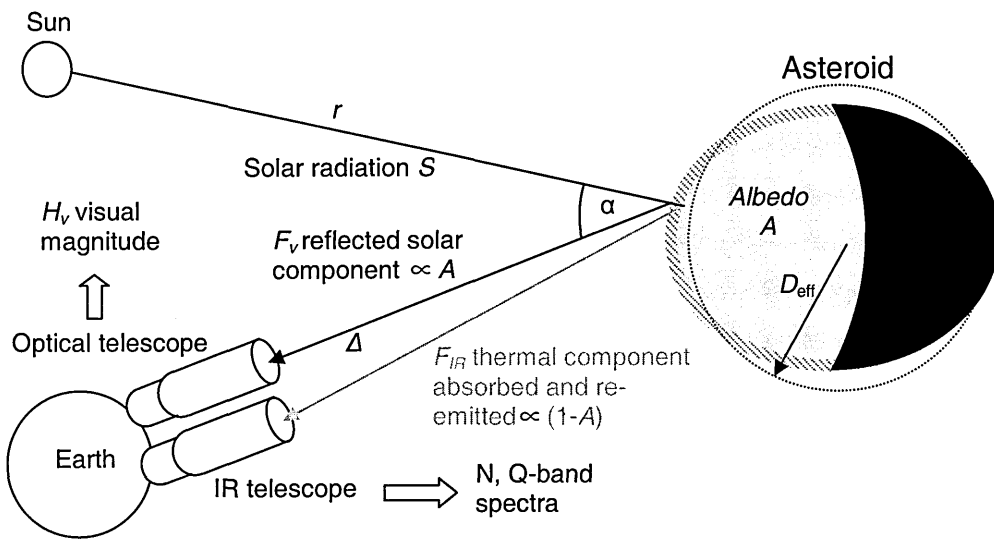


Fig. 4.1 Cartoon illustrating the reflection, absorption, and re-emission of solar radiation intercepted by an asteroid. The reflected component is observed using an optical telescope in the V filter from which the H_v magnitude is derived. The thermal component is observed using an infrared (IR) telescope in the N (8-13 μm) and Q-band (17-24 μm) windows in the atmosphere.

The temperature of a surface element dS on an asteroid is a function of the distance from the Sun r (AU), albedo A , and the angle of inclination to the solar direction ψ . The total incoming energy dF_i incident on a surface element is therefore:

$$dF_i = \frac{S_0}{r^2} \cos\psi dS \quad (4.4)$$

where $S_0 = 1374 \text{ W m}^{-2}$ is the solar flux at 1 AU. Energy that is not reflected is absorbed (dF_a) by the asteroid surface:

$$dF_a = dF_i(1 - A) \quad (4.5)$$

Further, the absorbed energy is balanced by thermal emission and energy conducted into the body of the asteroid. For a blackbody with non-unity emissivity ε , the energy emitted from the surface (depth $x = 0$) at a temperature T is:

$$dF_e = \sigma \varepsilon T_{x=0}^4 dS \quad (4.6)$$

where $\sigma = 5.670 \times 10^{-8} \text{ J K}^{-4} \text{ m}^{-2} \text{ s}^{-1}$, the Stefan-Boltzmann constant.

The energy conducted into the surface dF_c can be modelled as one dimensional heat conduction:

$$dF_c = -k \left(\frac{dT}{dx} \right)_{x=0} \quad (4.7)$$

where k is the thermal conductivity ($\text{J m}^{-1} \text{ s}^{-1} \text{ K}^{-1}$).

Unfortunately, we cannot directly measure the total radiation emitted in all directions, so a thermal model is required. We used the Standard Thermal Model (STM, Section 4.3.2), the Fast Rotating Model (FRM, Section 4.3.3) and the Near-Earth Asteroid Thermal Model (NEATM, Section 4.3.4). A Fortran program THERM was written that best-fits each thermal model to the observed fluxes. The code is given in Appendix A.

As an example, we describe the thermal model fitting to N-band (7-12.5 μm) observations made of asteroid 2002 NX₁₈ at the UKIRT on 27 September 2002 UT, the reduction of which is examined in detail in Chapter 5. The physical parameters input from a file 'param.txt' are G (if not known we assume $G = 0.15$), H_V , asteroid-Earth distance Δ (AU), r (AU), phase angle α ($^\circ$), and a fixed beaming parameter η_{spec} for the NEATM (Table 4.1). If the optical observations are quasi-simultaneous with the thermal IR observations, the composite lightcurve can be used to alter the inputted H_V to the

appropriate magnitude for the midpoint of the rotational phase of the thermal IR observation (Section 5.6.1).

Table 4.1. Input parameters in ‘param.txt’ of 2002 NX₁₈ observed on 27 September 2002 UT at UKIRT for thermal model fitting program THERM

Parameter	Value
H _v (mag.)	17.63
G	0.15
Δ (AU)	0.28065
r (AU)	1.1522
α°	51.6
η _{spec}	1.5

The observed wavelengths $\lambda_{obs}(n)$, fluxes $F_{obs}(n)$, and uncertainties $\sigma_{obs}(n)$ are input from file ‘spec.txt’, and are given in Appendix E and shown in Fig. 5.21 (n). STM, FRM, and NEATM with a fixed η are fitted for a range of p_v . If NEATM fitting with best-fit beaming parameter η is activated, a range of η is run for each value of p_v . For a given p_v , an appropriate D_{eff} is calculated from the input H_V using Eq. 4.3. So in the case where the optical observations are quasi-simultaneous, the fitted D_{eff} will be appropriate for the projected area at the time of the thermal IR observation, and not at the mean or maximum lightcurve as it is commonly presented in the literature.

The bolometric Bond albedo A is calculated from the geometric albedo p_v using Eqs. 4.1 and 4.2. Each thermal model creates a temperature (T) distribution for the visible surface of the asteroid using A , $\varepsilon = 0.9$, r , and η for the NEATM (see Section 4.3 for the appropriate equations for each model). The Planck function $B(\lambda, T)$:

$$B(\lambda, T) = \frac{2hc^2}{\lambda^5} \frac{1}{e^{\frac{hc}{\lambda kT}} - 1} \quad (4.8)$$

where Planck’s constant $h = 6.6262 \times 10^{-34}$ J s, the speed of light $c = 2.9979 \times 10^8$ m s⁻¹ and Boltzmann’s constant $k = 1.3807 \times 10^{-23}$ J K⁻¹, is numerically integrated over the visible hemisphere to provide a model IR flux $F_{mod}(n)$ for each $\lambda_{obs}(n)$ at a distance Δ .

The closeness of the fit to $F_{obs}(n)$ is found by measuring the error-weighted residual χ^2 of the fit:

$$\chi^2 = \sum_{n=1}^n \left(\frac{(F_{obs}(n) - F_{mod}(n))^2}{\sigma_{obs}^2(n)} \right) \quad (4.9)$$

If NEATM with best-fit η is being used, then χ^2 is found for a range of η until χ^2 is greater than it was for the previous value of η . The previous value was therefore the smallest residual (there is only one minimum value). For each value of p_v in the given range and step size an on-screen table is printed with D_{eff} , STM, FRM, NEATM with fixed η residuals, and NEATM with best-fit η residuals (if activated). From there a more precise range of p_v and η can be defined. The output residuals for fitting to the 27 September 2002 2002 NX₁₈ thermal IR fluxes are shown in Fig. 4.2.

When the fit is satisfactorily precise (we found the best-fit p_v for each asteroid to four decimal places, which is at least an order of magnitude more precise than necessary since the p_v model fitting uncertainty was always > 0.01 ; the best-fit η was found to three decimal places), the fit can be output for a specific p_v and thermal model. F_{mod} are found for the specific p_v at both $\lambda_{obs}(n)$ and for a defined set of wavelengths λ_{out} and output (in files 'fmodelSTM.txt', 'fmodelFRM.txt' 'fmodelNEATM.txt' and 'fmodelNEATMfit.txt' for the fits to the STM, FRM, NEATM with fixed η , and NEATM with best-fit η respectively), along with p_v , D_{eff} , χ^2 and η . For N-band observations the output wavelengths are set between 7 and 14 μm , with a step size of 0.2 μm , and for combined N and Q-band observations, between 7 and 24.5 μm , with a step size of 0.5 μm , by default. The thermal model fits to 2002 NX₁₈ 27 September 2002 are shown in Fig. 5.24 (p) and the resulting fitted p_v , D_{eff} and η in Table 5.15. Temperature profiles for each thermal model are also output (in files 'tempSTM.txt', 'tempFRM.txt', 'tempneatm.txt' and 'tempneatmfit.txt').

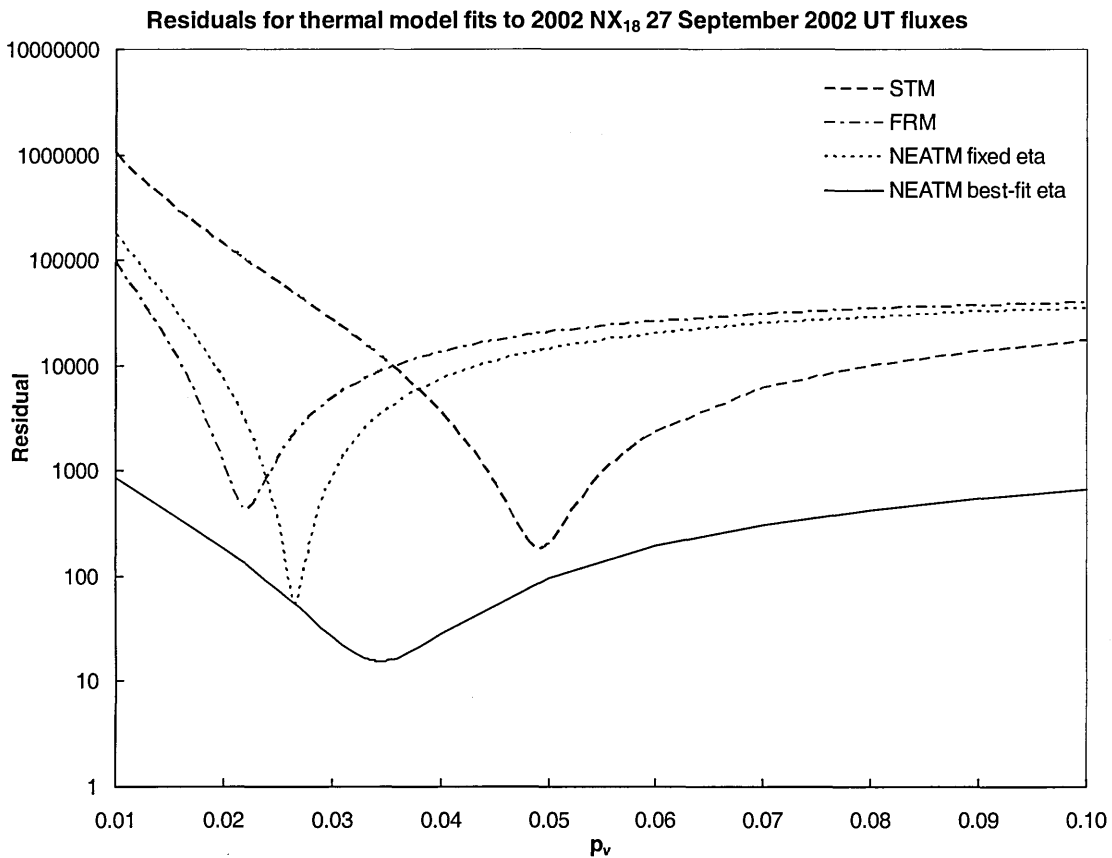


Fig. 4.2 Residuals for different thermal model fits to 2002 NX₁₈ 27 September 2002 UT thermal IR fluxes over a range of p_v . The NEATM with best-fit η curve is shallower since η is fitted for each p_v value to provide the best possible fit. However, there is still only one minimum.

4.3 Thermal Models

4.3.1 Thermophysical Models

Ideally, thermophysical models would be used which take into account the asteroid shape, thermal inertia, pole orientation, and macroscopic surface roughness. For example, Brown (1985) modelled asteroid shapes as ellipsoids and Spencer (1990) combined surface roughness with heat conduction. A model which combined these features and others was developed in a series of papers by Lagerros (1996, 1997, 1998).

A simple one dimensional thermophysical model is described below, which uses essentially the same method as Wesselink (1948). For each surface element the energy emitted by the surface F_e (Eq. 4.6) equals the energy absorbed F_a (Eq. 4.5) minus the

energy conducted into the body F_c (Eq. 4.7). If the asteroid is modelled as a smooth sphere F_a becomes:

$$F_a = \frac{S_0}{r^2} \Psi(t)(1 - A) \quad (4.10)$$

$$\Psi(t) = \cos[\theta(t)]\cos[\phi(t)]$$

$$\text{for } -\frac{\pi}{2} < \theta < +\frac{\pi}{2} \text{ and for } -\frac{\pi}{2} < \phi < +\frac{\pi}{2}$$

$$F_a = 0 \text{ for } \theta < -\frac{\pi}{2} \text{ and for } \theta > +\frac{\pi}{2}$$

where t is time (s), θ and ϕ are components of the angle between the surface normal and the subsolar direction.

Conduction is described by the 1D heat conduction equation:

$$\frac{\partial T}{\partial t} = \frac{\partial}{\partial x} \left(\frac{k}{\rho c} \frac{\partial T}{\partial x} \right) + f(x, T) \quad (4.11)$$

where $f(x, T)$ is a heat source, ρ is the density (kg m^{-3}) and c is the specific heat capacity ($\text{J kg}^{-1} \text{K}^{-1}$). For an asteroid there is no heat source, so $f(x, T) = 0$. If k , ρ and c are assumed to be constant with x and T , Eq. 4.11 reduces to:

$$\frac{\partial T}{\partial t} = \frac{k}{\rho c} \frac{\partial^2 T}{\partial x^2} \quad (4.12)$$

This is a second order linear partial differential equation with the surface boundary condition:

$$(1 - A) \frac{S_0}{r^2} \Psi(t) + k \left(\frac{dT}{dx} \right)_{x=0} - \varepsilon \sigma T_{x=0}^4 = 0 \quad (4.13)$$

If we compose the internal solution from an exponential damping term and a periodic term of the form:

$$T(x,t) = a + be^{\frac{-2\pi x}{l_s}} \cos 2\pi \left(\frac{t}{P} - \frac{x}{l_s} + \zeta \right) \quad (4.14)$$

$$l_s = \left(4\pi P \frac{k}{\rho c} \right)^{\frac{1}{2}}$$

where l_s is the thermal skin depth, P is the rotation period, and a , b and ζ are constants, then Eqs. 4.12 and 4.13 can be normalised by letting:

$$z = \frac{x}{l_s}; \quad \tau = \frac{t}{P} \quad (4.15)$$

Substituting Eq. 4.15 in Eq. 4.12 gives:

$$\frac{1}{P} \frac{\partial T}{\partial \tau} = \frac{k}{\rho c l_s^2} \frac{\partial^2 T}{\partial z^2}$$

$$\therefore \frac{\partial T}{\partial \tau} = \frac{1}{4\pi} \frac{\partial^2 T}{\partial z^2} \quad (4.16)$$

with boundary conditions:

$$(1-A) \frac{S_0}{r^2} \psi(t) + k \left(\frac{\partial T}{\partial z} \right)_{z=0} - \varepsilon \sigma T_{z=0}^4 = 0 \quad (4.17)$$

$$z \rightarrow \infty \quad \frac{\partial T}{\partial z} \rightarrow 0$$

Eq. 4.16 can be solved using finite difference equations and an iterative technique such as Newton-Raphson.

Thermophysical models are useful for understanding asteroid thermal processes, but for NEAs we rarely have sufficient thermal IR data, or any of the requisite physical parameters, and so more simple thermal models are used to derived albedos and diameters, described in Sections 4.3.2-5.

4.3.2 The Standard Thermal Model (STM)

The ‘refined’ Standard Thermal Model, as outlined in Lebofsky *et al.* (1986), considers the asteroid as a spherical non-rotating object, with a surface temperature in instantaneous equilibrium with incoming solar radiation, i.e. $F_c = 0$. Therefore $dF_a = dF_e$ (Eqs. 4.5 and 4.6) due to conservation of energy:

$$\frac{S_0(1-A)}{r^2} \cos\psi \, dS = \sigma\epsilon T^4 \, dS \tag{4.18}$$

where ψ is the angle between the normal to the surface element and the asteroid-Sun vector (and so for a spherical body can be regarded as the angle from the subsolar point). At the subsolar point $T_{max} = T(\psi = 0)$:

$$T_{max} = \left[\frac{(1-A)S_0}{r^2 \epsilon\sigma} \right]^{\frac{1}{4}} \tag{4.19}$$

It follows that:

$$\begin{aligned} T(\psi) &= T_{max} \cos^{\frac{1}{4}}\psi \text{ for } 0 \leq \psi \leq \pi/2 \\ T(\psi) &= 0 \text{ at all other } \psi \end{aligned} \tag{4.20}$$

with a temperature distribution decreasing from a maximum at the subsolar point to zero at the terminator, and no thermal emission on the night side (Fig. 4.3).

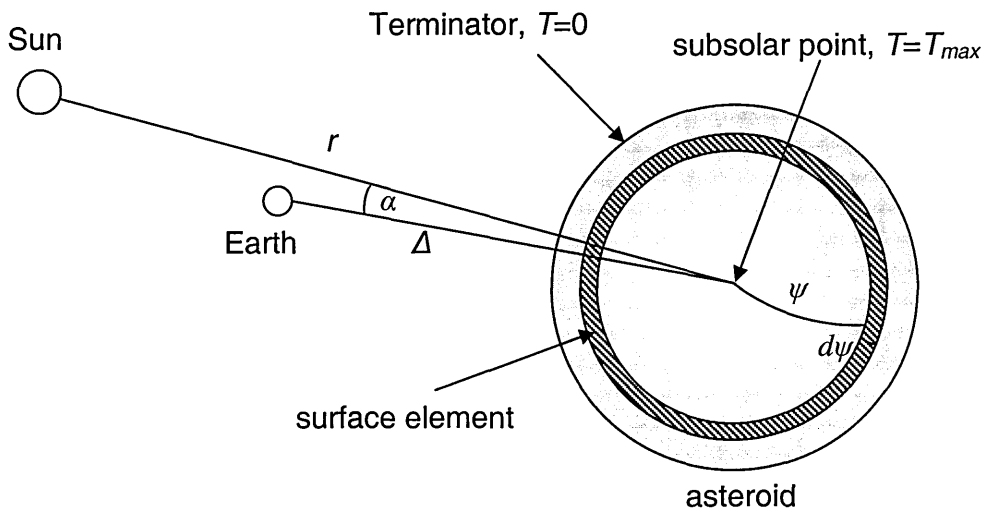


Fig. 4.3 Diagram of the Standard Thermal Model (STM) (not to scale).

The beaming parameter η was introduced to take account of enhanced sunward thermal emission due to the surface roughness. In the STM $\eta = 0.756$, calibrated from the occultation diameters of (1) Ceres and (2) Pallas, and T_{max} becomes:

$$T_{max} = \left[\frac{(1-A)S_0}{r^2 \epsilon \sigma \eta} \right]^{\frac{1}{4}} \quad (4.21)$$

Figure 4.4 shows the calculated temperature distribution of 2002 NX₁₈ on 27 September 2002 UT, for the best-fit STM $p_v = 0.049$. The model thermal IR fluxes $F_{mod}(n)$ are calculated from the temperature distribution as described in Section 4.2:

$$F_{mod}(n) = \left[\frac{\pi \epsilon D_{eff}^2}{2 \Delta^2} \int_0^{\frac{\pi}{2}} B(\lambda_{obs}(n), T(\psi)) \sin \psi \cos \psi d\psi \right] \cdot 10^{-0.4 \alpha \beta} \quad (4.22)$$

including a phase angle (α) correction $\beta_E = 0.01 \text{ mag. deg}^{-1}$, which appears to be valid out to at least $\alpha = 20^\circ$ (Lebofsky and Spencer, 1989), and has been used on main belt asteroids observed at $\alpha < 30^\circ$.

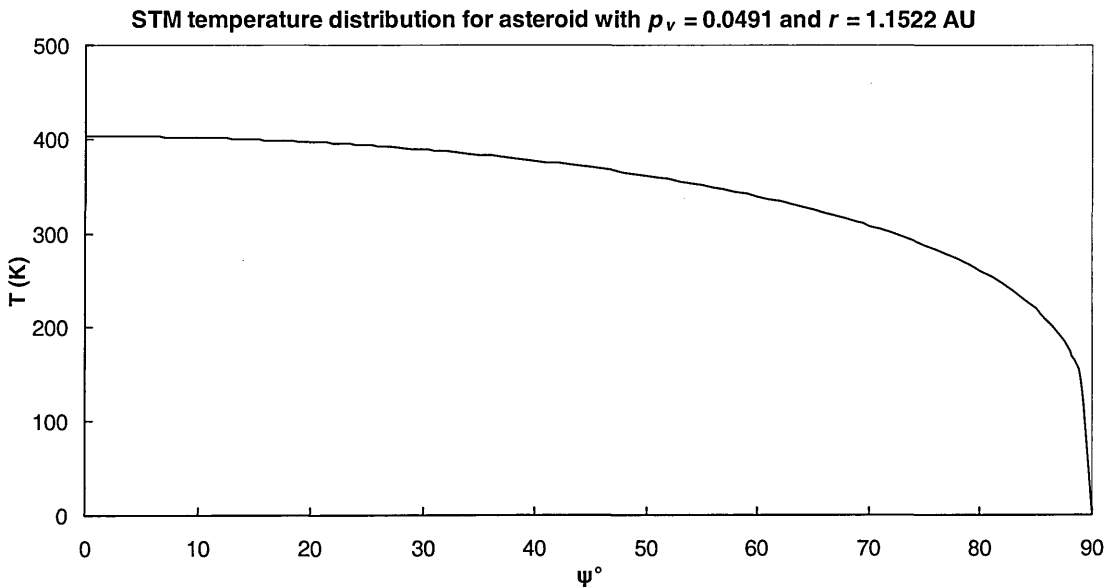


Fig. 4.4 Temperature distribution at different angles from the subsolar point using the Standard Thermal Model on observed fluxes of asteroid 2002 NX₁₈ taken at UKIRT on 27 September 2002 UT, with best-fit $p_v = 0.0491$.

The STM has been used to derive the majority of asteroid diameters and albedos, particularly those in the IRAS Survey [Tedesco *et al.*(2002b), see also Section 2.9.1]. It is suited to main belt asteroids which are more regular and observed at lower phase angles than typical NEAs.

4.3.3 The Fast Rotating Model (FRM)

The Fast Rotating Model [FRM, Lebofsky and Spencer (1989)], also known as the isothermal latitude model, applies to an asteroid that has a high thermal inertia (e.g. one with exposed bare rock) and/or fast rotation. The temperature contours of an assumed spherical asteroid, with a rotation axis at 90° to the solar direction, are smoothed out due to a combination of thermal lag and rotation which causes received solar flux at a given latitude ϕ to be re-emitted at a constant rate, without cooling as it rotates (Fig. 4.5).

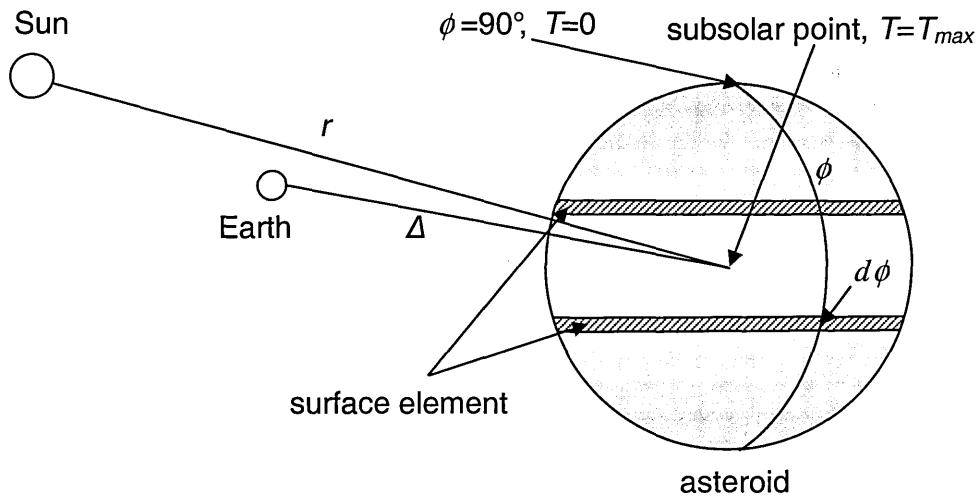


Fig. 4.5 Diagram of Fast Rotating Model (FRM) (not to scale).

Consequently the temperature distribution depends only on latitude, and the day and night side are at an equal temperature. The FRM can be regarded as the opposite extreme

to the STM. The FRM temperature distribution decreases from a maximum T_{max} at $\phi = 0^\circ$ to $T = 0$ at $\phi = 90^\circ$ following:

$$T(\phi) = T_{max} \cos^{1/4} \phi \text{ for } 0 \leq \phi \leq \pi/2 \quad (4.23)$$

T_{max} is the subsolar maximum temperature [$T(\phi = 0)$] and is given by:

$$T_{max} = \left[\frac{(1-A)S_0}{r^2 \pi \epsilon \sigma} \right]^{1/4} \quad (4.24)$$

which is the same as Eq. 4.19 with η replaced by π . Figure 4.6 shows the calculated temperature distribution of 2002 NX₁₈ on 27 September 2002 UT, for the best-fit STM $p_v = 0.022$. The model thermal IR fluxes $F_{mod}(n)$ are:

$$F_{mod}(n) = \frac{\epsilon D_{eff}^2}{\Delta^2} \int_0^{\pi/2} B(\lambda_{obs}(n), T(\phi)) \cos^2 \phi d\phi \quad (4.25)$$

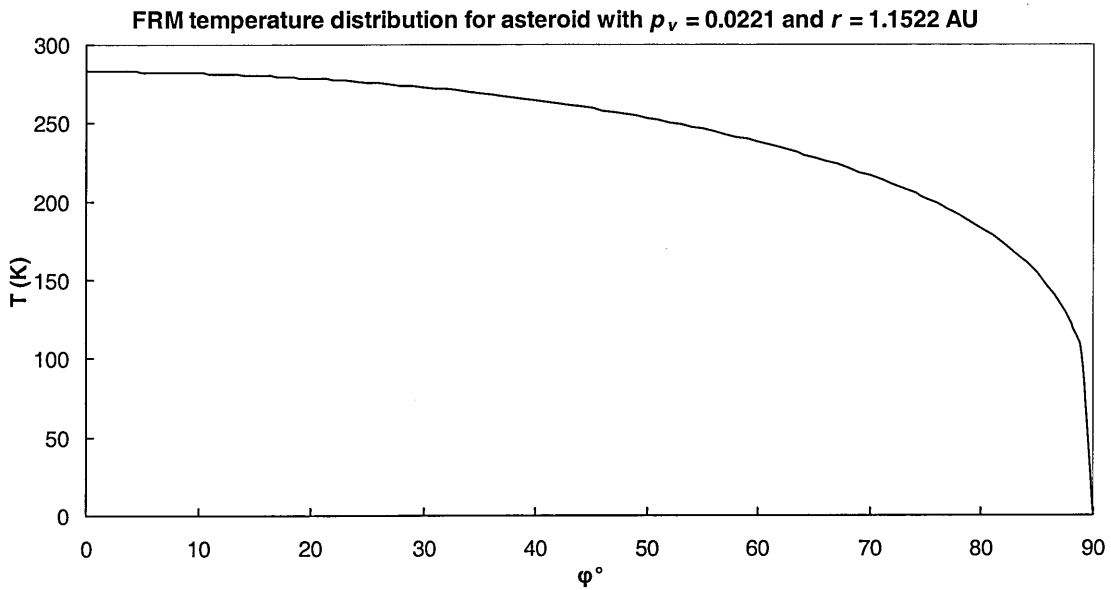


Fig. 4.6 Temperature distribution at different latitudes using the Fast Rotating Model on observed fluxes of asteroid 2002 NX₁₈ taken at UKIRT on 27 September 2002 UT, with best-fit $p_v = 0.022$.

4.3.4 The Near-Earth Asteroid Thermal Model (NEATM)

In general, the use of neither the STM nor the FRM gives accurate diameters or albedos for NEAs, since they may be observed at high phase angles, and are often smaller and more irregular than main belt asteroids. As their surfaces may be more varied, e.g. with different surface roughness or thermal inertia, the calibrated η in the STM may no longer be appropriate for NEAs, as shown by Veeder *et al.* (1989).

Harris (1998) introduced the Near-Earth Asteroid Thermal Model (NEATM) which modifies the STM in two ways. First, it allows η in Eq. 4.21 to be varied until $F_{mod}(n)$ gives a best fit to the observed thermal IR spectrum $F_{obs}(n)$ at each value of p_v , effectively forcing the model temperature distribution to show a colour temperature consistent with the apparent colour temperature implied by the data. Second, it replaces the STM phase angle correction in the same way as the projected model [e.g. Cruikshank and Jones (1977), Green (1985)], which models the asteroid as a sphere and calculates the temperature on the surface assuming Lambertian emission and zero emission on the night side. The projected model is the equivalent of the NEATM with $\eta = 1$ (i.e. with no beaming).

The temperature distribution is defined by the longitude θ and latitude ϕ on the asteroid surface, where $\theta = 0^\circ$ and $\phi = 0^\circ$ are at the subsolar point (Fig. 4.7).

$$\begin{aligned}
 T(\theta, \phi) &= 0 \text{ for } \frac{\pi}{2} \leq \theta \leq \frac{3\pi}{2} \\
 T(\theta, \phi) &= T_{\max} \cos^{\frac{1}{4}} \theta \cos^{\frac{1}{4}} \phi \text{ for } -\frac{\pi}{2} < \theta < +\frac{\pi}{2} \text{ and for } -\frac{\pi}{2} \leq \phi \leq +\frac{\pi}{2}
 \end{aligned} \tag{4.26}$$

The model fluxes $F_{mod}(n)$ are calculated by integrating $B(\lambda_n, T(\theta, \phi))$ over the portion of the asteroid surface visible to the observer:

$$F_{\text{mod}}(n) = \frac{\varepsilon D^2}{4\Delta^2} \int_{-\frac{\pi}{2}}^{+\frac{\pi}{2}} \int_{\alpha-\frac{\pi}{2}}^{+\frac{\pi}{2}} B(\lambda_n, T(\theta, \phi)) \cos^2 \phi \cos(\alpha - \theta) d\theta d\phi \tag{4.27}$$

Figure 4.8 shows the calculated temperature distribution of 2002 NX₁₈ on 27 September 2002 UT, for the best-fit NEATM $p_v = 0.034$ and best-fit $\eta = 1.18$.

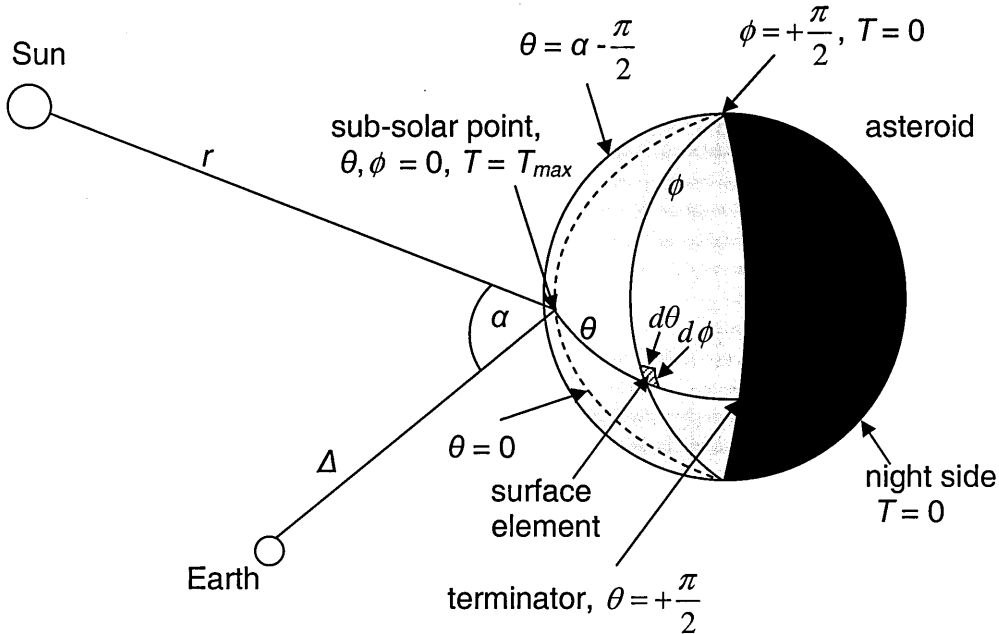
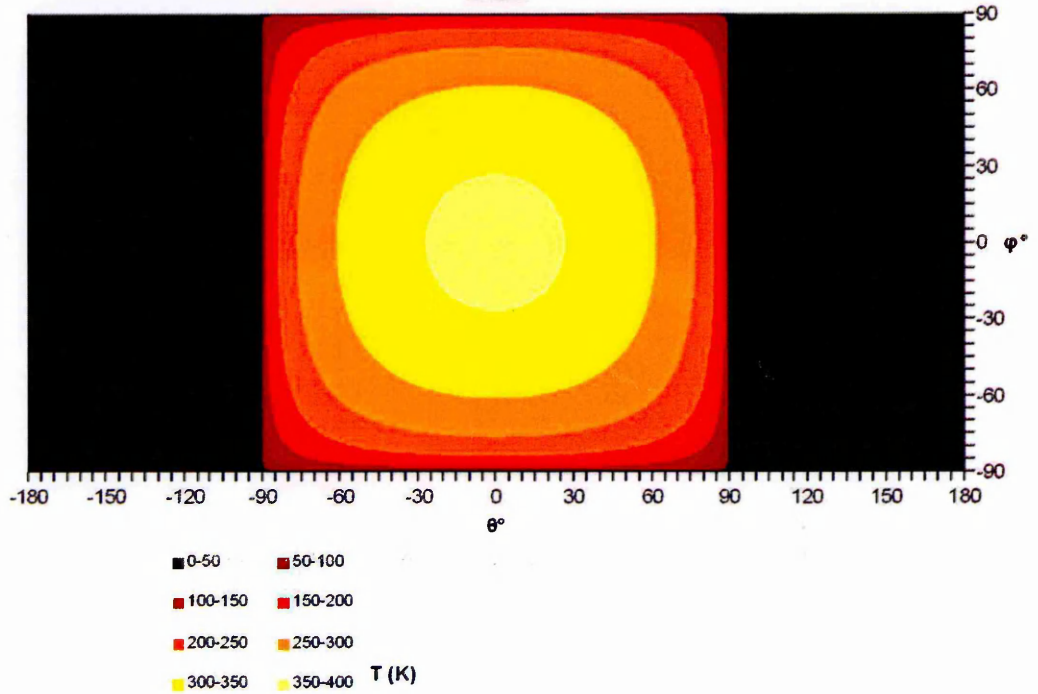


Fig. 4.7 Diagram of the Near-Earth Asteroid Thermal Model (NEATM) showing the surface visible to an observer (not to scale).

Finding an accurate η requires good wavelength sampling of the thermal continuum, ideally at least four or five filter measurements over the range 5-20 μm (e.g. observations with the Michelle instrument in imaging mode, Section 5.2). We also used η -fitting for observations over a narrower range, 8-12.5 μm , but with higher spectral resolution (Michelle instrument in spectroscopy mode, Section 5.3). Delbó *et al.* (2003) found a trend of increasing η with α , which our observations support (Fig. 5.25). From this trend, they proposed a default $\eta = 1.0$ for observations $\alpha < 45^\circ$ (equivalent to projected model) and $\eta = 1.5$ for $\alpha \geq 45^\circ$, for the case where only one or two N- and/or Q-band observations are available, or the spectral resolution is not high enough to make η -fitting sensible. So, for every asteroid, p_v and D_{eff} were found by best-fitting η and by using the appropriate default η .

(a)

NEATM temperature distribution for asteroid with $\eta = 1.184$, $p_v = 0.0344$, and $r = 1.1522$



(b)

NEATM temperature distribution for asteroid with $\eta = 1.184$, $p_v = 0.0344$, and $r = 1.1522$

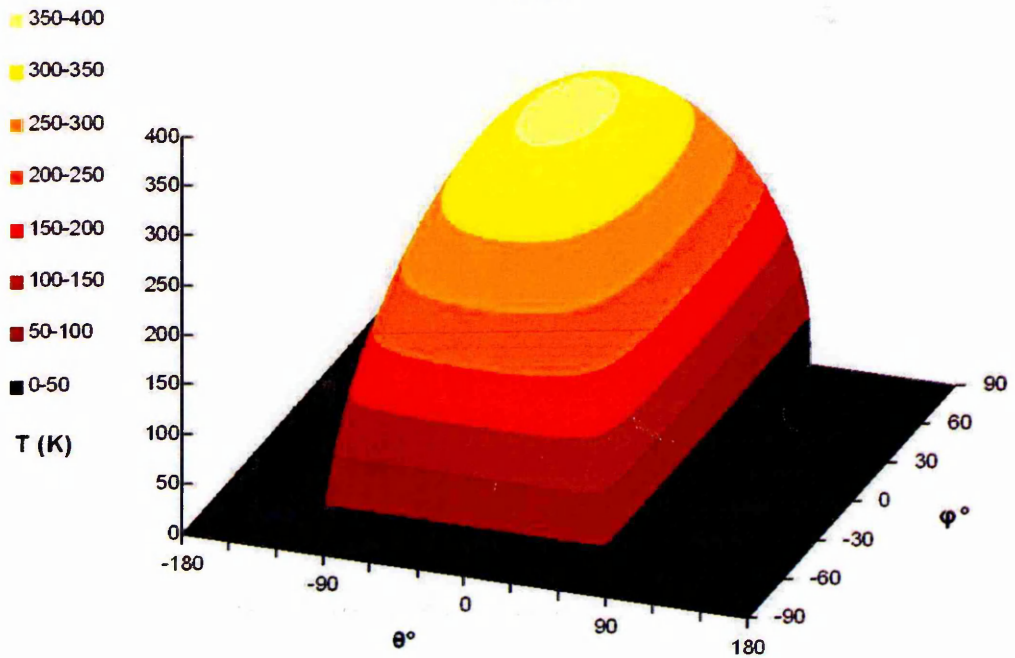


Fig. 4.8 Temperature distribution at different longitudes and latitudes (0° is subsolar point) using the NEATM on observed fluxes of asteroid 2002 NX₁₈ taken at UKIRT on 27 September 2002 UT, for best-fit $p_v = 0.034$ and $\eta = 1.18$.

4.3.5 The Modified Projected Model

The modified projected model was introduced by Green *et al.* (1985b) as an appropriate model to fit to thermal IR fluxes of NEA (3200) Phaethon, which was observed at a reasonably high phase angle (48°), and for which the STM fit badly. The model is outlined in more detail in Green (1985). It was not applied to the thermal IR fluxes given in Chapter 5, but elements of the model are combined with elements of the NEATM in Chapter 6, where a new thermal model is introduced.

Whereas the NEATM assumes that there is no night side emission, the modified projected model uses a parameter f to define the night side temperature, so that for a latitude ϕ the night side temperature is:

$$T_{\text{night}} = fT_{\text{max}} \cos^{\frac{1}{4}} \phi \quad (4.28)$$

where T_{max} is defined as in Eq. 4.19, i.e. beaming is not considered in this model. Setting $f=0$ would be the equivalent of the projected model, which is itself the equivalent of the NEATM with the beaming parameter $\eta = 1$.

Hansen (1977) has also discussed using a non-zero night side temperature distribution. Hansen ensured a smooth transition from the day side to the night side temperature by introducing a monotonically increasing function $f(\theta)$ which is 0 for $\theta = 0^\circ$ and 0.60 for $\theta \geq 90^\circ$. In Hansen's model the maximum day side temperature is not recalculated to conserve energy.

In the modified projected model, in order to conserve energy, T_{max} is replaced by a reduced maximum day side temperature T_{mod} . The day side temperature for a given latitude ϕ and longitude θ is given by

$$T_{\text{day}} = T_{\text{mod}} \cos^{\frac{1}{4}} \theta \cos^{\frac{1}{4}} \phi \quad (4.29)$$

For a particular latitude and longitude on the day side, if T_{night} is greater than T_{day} then the night side temperature takes precedence. T_{mod} is calculated by balancing the total emitted flux to that absorbed in the energy balance equation:

$$\frac{\pi D_{eff}^2 (1-A)}{4r^2} = \frac{D_{eff}^2}{2} \varepsilon \sigma \int_{-\frac{\pi}{2}}^{\frac{\pi}{2}} \int_0^{\pi} G(T_{mod}^4 \cos \theta, f^4 T_{max}^4) \cos^2 \phi d\theta d\phi \quad (4.30)$$

where $T_{mod} < T_{max}$, and $G(x, y) = x$ if $x > y$ and $G(x, y) = y$ if $x < y$, which can then be solved iteratively to give T_{mod} .

The emitted flux measured from Earth (outside the atmosphere) is calculated by integrating over the visible hemisphere longitudes and latitudes using the black-body function for each surface element:

$$F_{mod}(n) = \frac{D_{eff}^2}{2\Delta^2} \varepsilon \int_{-\frac{\pi}{2}}^{\frac{\pi}{2}} \left[\int_{\alpha-\frac{\pi}{2}}^{\frac{\pi}{2}} B\left(\lambda(n), G\left(T_{mod} \cos^{\frac{1}{4}} \theta, f T_{max}\right) \cos^{\frac{1}{4}} \phi\right) \cos(\alpha - \theta) d\theta \right. \\ \left. + \int_{\frac{\pi}{2}}^{\alpha+\frac{\pi}{2}} B\left(\lambda(n), f T_{max} \cos^{\frac{1}{4}} \phi\right) \cos(\alpha - \theta) d\theta \right] \cos^2 \phi d\phi \quad (4.31)$$

f depends on the asteroid's pole orientation, rotation, thermal inertia and shape. Green (1985) was able to vary f to provide a best-fit to Phaethon ($f = 0.65 \pm 0.02$). Green also found that $f = 0.73$ corresponded to the equivalent of the FRM for the geometry of the Phaethon observation. Using the thermophysical model described in Section 4.3.1 on an asteroid with $r = 1$ AU, a rotation period $P = 10$ h, a “dusty” surface thermal inertia $\Gamma = 40 \text{ J m}^{-2} \text{ s}^{-1/2} \text{ K}^{-1}$ (equivalent to the lunar surface) and a “bare rock” $\Gamma = 2200 \text{ J m}^{-2} \text{ s}^{-1/2} \text{ K}^{-1}$ (equivalent to granite), equatorial surface temperatures were obtained. The average night side surface temperature was ratioed with T_{max} to obtain $f = 0.43$ and $f = 0.62$ respectively. Chapter 6 will expand on this principle to determine appropriate f values for use in a new thermal model which combines the modified projected model with NEATM.

5 Thermal Infrared Observations

5.1 Introduction

In this chapter diameters and albedos for eight near-Earth asteroids (and limits for two others) are derived by combining thermal infrared observations taken using the Michelle instrument at the United Kingdom Infrared Telescope (UKIRT) with quasi-simultaneous optical observations taken at the Jacobus Kapteyn Telescope (JKT), or with catalogued visual magnitudes if necessary. Thermal IR observations using Michelle in imaging mode were taken and reduced by J. K. Davies (ATC) in March 2002; the reduction of those observations is described briefly. Thermal IR observations using Michelle in spectroscopy mode were taken by S. F. Green and myself in September 2002. The reduction process of these observations is described in detail in this chapter.

UKIRT is a 3.8 m classical cassegrain telescope with a thin primary mirror utilising an “English” yoke mounting. It is sited on Mauna Kea in Hawaii and is operated by the Joint Astronomy Centre on behalf of the UK Particle Physics and Astronomy Research Council. (More details on the telescope can be found on the Joint Astronomy Centre website at: <http://www.jach.hawaii.edu/UKIRT/telescope/description.html>.)

5.2 Using Michelle in Imaging Mode at UKIRT (March 2002)

Michelle is a mid-infrared imager/spectrometer with a SBRC Si:As 320×240-pixel array operating between 8 and 25 microns. When used in imaging mode it provides a 67.2×50.4 arcsec field of view at 0.21 arcsec/pixel. (Fuller details on the instrument can be found at: <http://www.jach.hawaii.edu/UKIRT/instruments/michelle/michelle.html>.)

Observations of asteroids (6455) 1992 HE and 1999 HF₁ were made on 22 March 2002 and 2000 GD₂ on 23 March 2002 UT, under clear skies, using the 8.8, 10.3, 12.5 and 18.5 μm filters. The observational circumstances are shown in Table 5.1. Images were

taken using the standard UKIRT imaging sequences which include nodding and chopping. The result is a final frame with four images, two positive and two negative, resulting from the sum of the chopped pairs at the first nod position, plus the second chopped pairs at the opposite nod. These images were pipeline reduced by the Observatory Reduction and Acquisition Control Data Reduction (ORAC-DR) package, developed at the Joint Astronomy Centre, which “snips” the images, inverts them as needed, and then recombines them as a single frame, one quarter of the size of the array, containing a single positive image comprising the sum of the four nod-chop positions.

Table 5.1

Observational circumstances of asteroids observed at UKIRT in March 2002 using Michelle in imaging mode

Asteroid	Time (UT)	r (AU)	Δ (AU)	α°
(6455) 1992 HE	0h, 22 March 2002	1.647	0.745	22
1999 HF ₁	0h, 22 March 2002	0.958	0.207	95
2000 GD ₂	0h, 23 March 2002	1.084	0.101	28

Notes. Ephemerides are taken from JPL Horizons.

Photometry was carried out on these images using the photometry module of the Starlink GAIA software. Apertures of 5, 8 and 13 pixels radius (equivalent to 2.1, 3.4, and 5.5 arcsecond diameters) were used to determine the flux from the object. The 13 pixel aperture includes the central spot plus the first diffraction ring. Since the background sky is removed by the chopping, it should not be necessary to subtract the sky background, but as a precaution a sky annulus of 12.5-19.0, 12.0-18.4 and 19.5-30.0 pixels for the 5, 8 and 13 pixel apertures respectively were used to remove any residual background.

Determination of the extinction and photometric calibration was done in the normal manner, similar to that done for optical observations discussed in Section 3.4.2:

$$M_{\text{inst}} = M_{\text{std}} + k_M \mathcal{X} + Z_M \quad (5.1)$$

where M_{inst} is the instrumental magnitude of the standard star observed at that wavelength, M_{std} is the apparent standard star magnitude which would be observed from above the

atmosphere, k_M is the extinction coefficient, Z_M is the zero point of the instrumental magnitude scale and χ is the airmass. Colour transformation terms are assumed to be zero; the uncertainty introduced by this assumption is negligible compared to the overall calibration uncertainty. M_{std} are shown in Table 5.2. Figures 5.1 and 5.2 show the resulting extinction plots ($M_{inst} - M_{std}$) vs. χ , the slope of which gives k_M and the y-intercept gives Z_M .

Table 5.2
Standard star magnitudes, Michelle instrument in imaging mode, 22 and 23 March 2002 UT

Star	M_{std}				Used on (dd March 2002 UT)
	8.8	10.3	12.5	18.5	
BS 1457				-3.08	
BS 2990				-1.21	22
BS 3748	-1.24	-1.30	-1.37	-1.40	22, 23
BS 4728	+2.79	+2.80	+2.80		23
BS 5340	-3.13	-3.13	-3.17	-3.20	22
BS 5793	+2.19	+2.19	+2.19		22
BS 6134	-4.53	-4.54	-4.54		22
BS 7525	-0.72	-0.80	-0.82	-0.82	22

Notes. Standard star magnitudes M_{std} were collated from the MIRAC manual, the Timmi2 website (<http://www.la.eso.org/lasilla/sciops/3p6/timmi>) and the IRTF-ISO website (http://irtfweb.ifa.hawaii.edu/IRrefdata/Catalogs/bright_standards).

The linear fit to 22 March 10.3 μm and 12.5 μm extinction plots [Fig. 5.1 (b) and (c)] exclude standard star BS 6134, which is so bright that it probably saturated the array. There is something wrong with the extinction plots for the 8.8 μm filter on 23 March [Fig. 5.2 (a)]; since there are only two points there is no way to address this but the flux calibration uncertainty for this filter is large enough to take this into account. Also note that the extinction plots for the 12.5 μm filter on 23 March [Fig. 5.2 (c)] are technically physically impossible and the assigned calibration uncertainty reflects this.

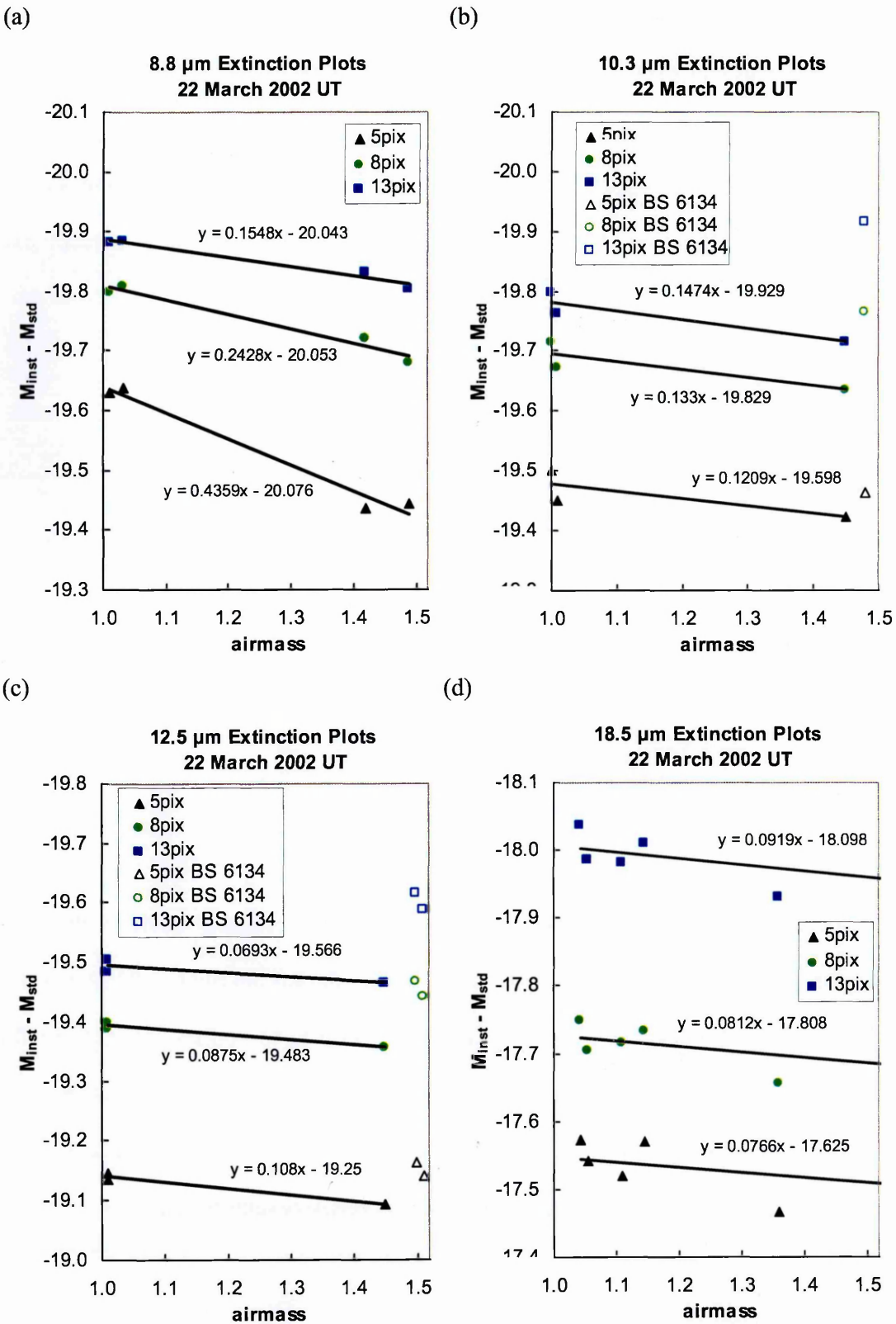


Fig. 5.1 Extinction plots ($M_{inst} - M_{std}$) versus airmass χ for UKIRT 22 March 2002 UT with Michelle in imaging mode for 8.8, 10.3, 12.5 and 18.5 μm filters. Slope and y-intercept gives atmospheric extinction k_M and zero point correction Z_M respectively.

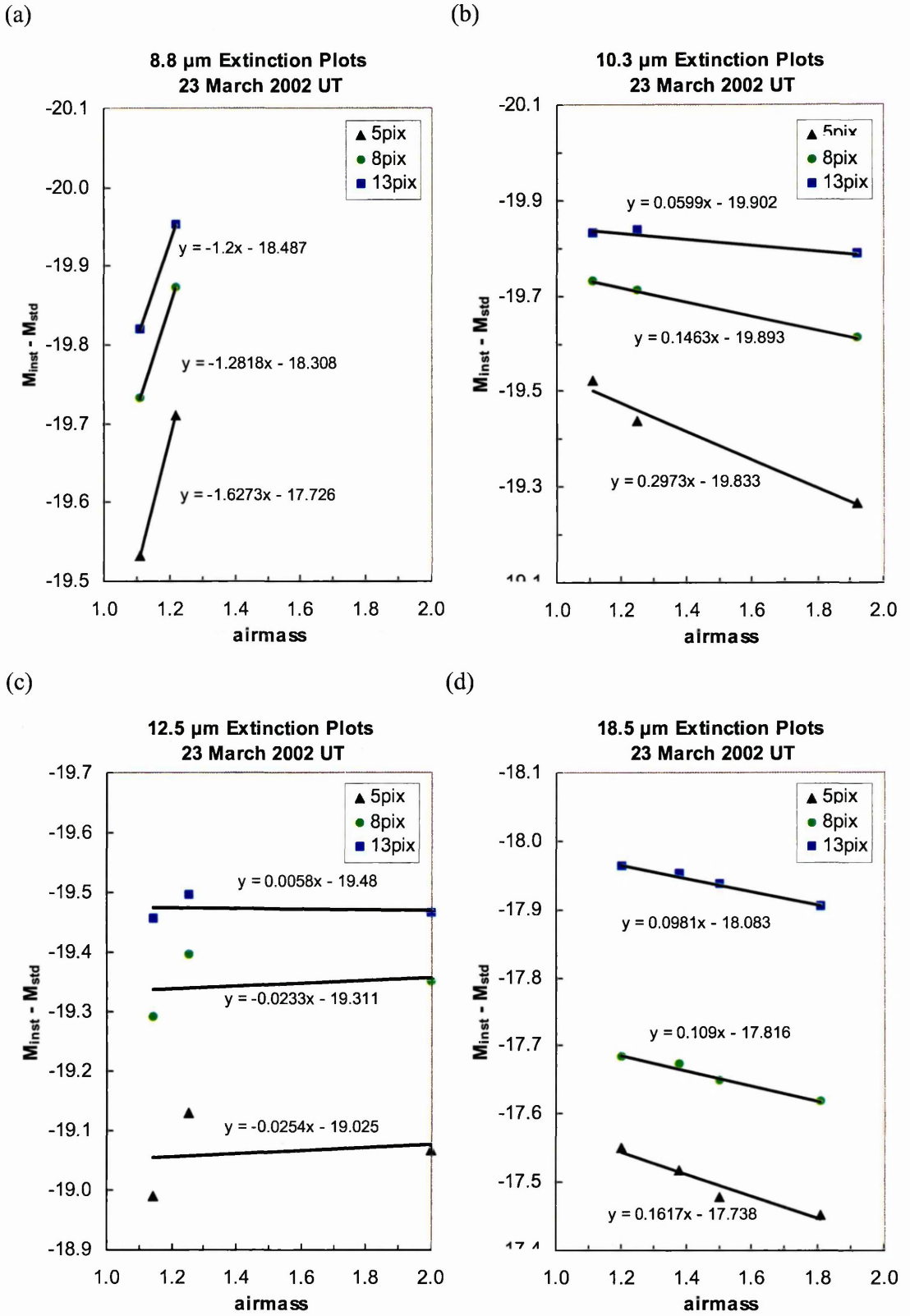


Fig. 5.2 Extinction plots ($M_{inst} - M_{std}$) versus airmass χ for UKIRT 23 March 2002 UT with Michelle in imaging mode for 8.8, 10.3, 12.5 and 18.5 μm filters. Slope and y-intercept gives atmospheric extinction k_M and zero point correction Z_M respectively.

The derived k_M and Z_M and the associated flux calibration uncertainties are shown in Table 5.3.

Table 5.3

Derived extinction coefficients k_M and zero points Z_M of the magnitude scale for the Michelle instrument in imaging mode, 22 and 23 March 2002 UT

Date	Wavelength (μm)	Aperture radius (pixels)	k	Z	\pm^a	Figure
22 March 2002 UT	8.8	5	+0.44	-20.08	0.05	Fig. 1 (a)
		8	+0.24	-20.05	0.03	
		13	+0.15	-20.04	0.02	
	10.3	5	+0.12	-19.60	0.04	(b)
		8	+0.13	-19.83	0.03	
		13	+0.15	-19.93	0.02	
	12.5	5	+0.18	-19.31	0.02	(c)
		8	+0.16	-19.54	0.02	
		13	+0.14	-19.62	0.02	
18.5	5	+0.08	-17.63	0.08	(d)	
	8	+0.08	-17.81	0.04		
	13	+0.09	-18.10	0.04		
23 March 2002 UT	8.8	5	-1.63	-17.73	0.16	Fig. 2 (a)
		8	-1.28	-18.31	0.14	
		13	-1.20	-18.49	0.14	
	10.3	5	+0.30	-19.83	0.02	(b)
		8	+0.15	-19.89	0.01	
		13	+0.06	-19.90	0.01	
	12.5	5	-0.03	-19.03	0.07	(c)
		8	-0.02	-19.31	0.05	
		13	+0.01	-19.48	0.03	
18.5	5	+0.16	-17.74	0.01	(d)	
	8	+0.11	-17.82	0.01		
	13	+0.10	-18.08	0.01		

Notes. ^a Combined uncertainty of k and Z estimated from visual inspection of Figs. 5.1 and 5.2.

The measured instrumental magnitudes M_{inst} of asteroids (6455) 1992 HE, 1999 HF₁, and 2000 GD₂ are given in Appendix B. Their relative magnitudes M_{ast} are calculated using:

$$M_{ast} = M_{inst} - k_m \chi - Z_m \quad (5.2)$$

To convert M_{ast} to asteroid fluxes F_{ast} in units of $\text{W m}^{-2} \mu\text{m}^{-1}$ we need to use the zero magnitude flux F_M for each filter (by definition the flux from the standard star Vega at the filter wavelength).

$$F_{ast} = \frac{F_M}{2.51^{M_{ast}}} \quad (5.3)$$

The values used are listed in Table 5.4.

Table 5.4

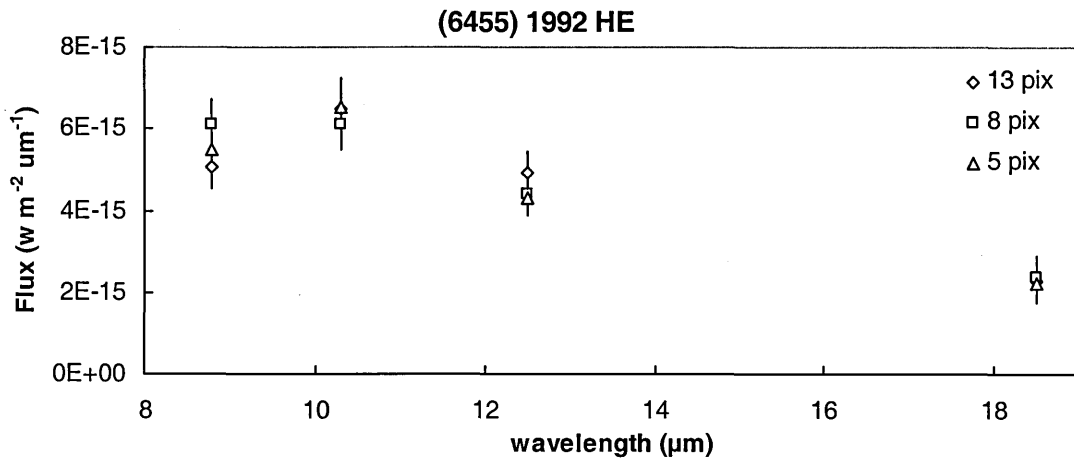
Zero magnitude fluxes used for each Michelle imaging mode filter

Wavelength (μm)	0 Mag. flux ($\text{W m}^{-2} \mu\text{m}^{-1}$)	Notes
8.8	2.1×10^{-12}	Value for 8.7 μm filter
10.3	1.09×10^{-12}	
12.5	5.07×10^{-13}	
18.5	7.80×10^{-14}	Value for Q-filter

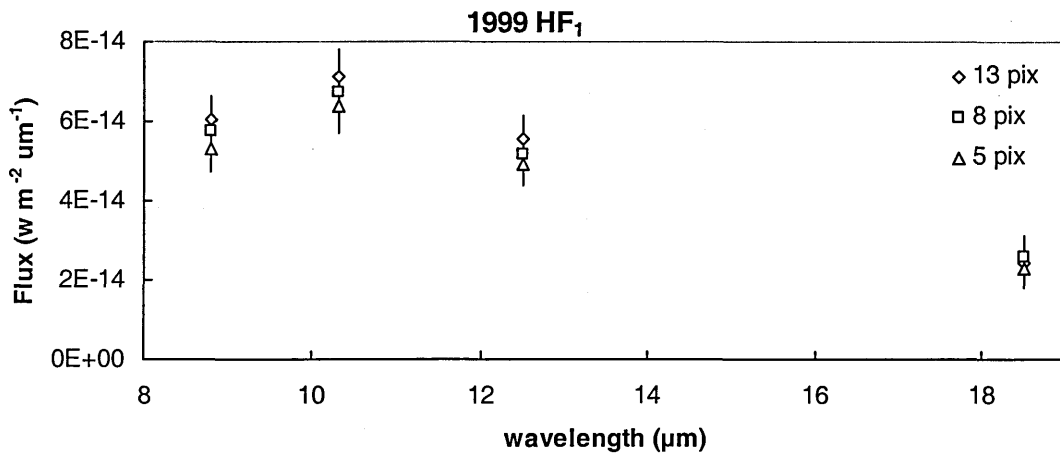
Notes. Fluxes from Beckwith *et al.* (1976) with modifications to be consistent with Tokunaga (1984).

Figure 5.3 shows the reduced apparent fluxes for the three asteroids at each wavelength and for each aperture radius. It was decided to use the 13 pixel radius aperture fluxes for thermal model fitting, because the extinction coefficients were generally most precisely defined at that aperture and because the aperture includes the central spot plus the first diffraction ring. For 2000 GD₂ the 8.8 μm flux value is not used in the thermal model fitting because of the standard star calibration problem for that filter on 23 March [Fig. 5.2 (a)]. Thermal models are fitted in Section 5.6.

(a)



(b)



(c)

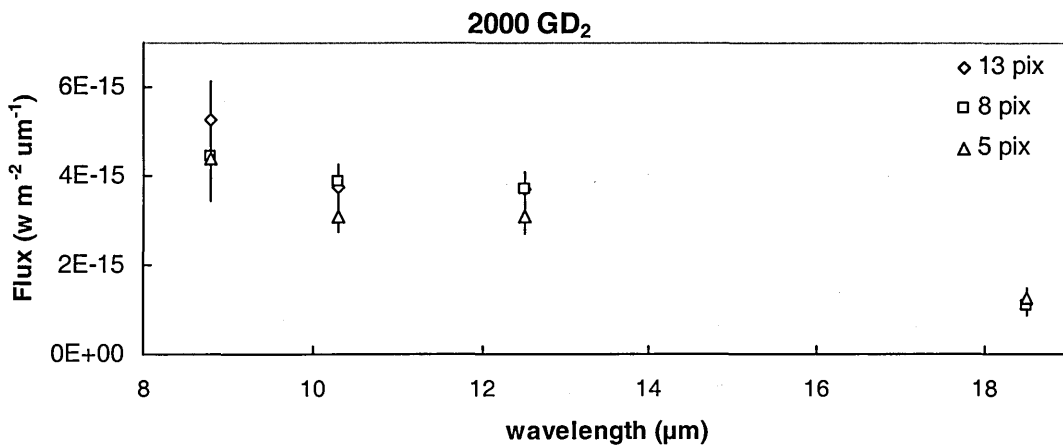


Fig. 5.3 Flux-calibrated apparent thermal IR fluxes of three asteroids observed on 22 and 23 March 2002 UT at UKIRT with the Michelle instrument in imaging mode, using 8.8, 10.3, 12.5 and 18.5 μm filters and 5, 8 and 13 pixel radius apertures. (a) (6455) 1992 HE, (b) 1999 HF₁ on 22 March; (c) 2000 GD₂ on 23 March.

5.3 Using Michelle in Spectroscopy Mode at UKIRT (September 2002)

5.3.1 Target Selection and Observation Planning

Appropriate targets need to be realistically observable at both UKIRT and JKT. Potential target asteroids for observation were selected using the “What’s Observable” webpage on JPL’s Solar System Dynamics website (<http://ssd.jpl.nasa.gov/sbwobs.cgi>). This uses all asteroids and comets listed in JPL’s DASTCOM (Database of ASTeroids and COMets). For each allocated half-night at UKIRT (between 05:00 and 16:00 26-30 September 2002 UT) two constraints were initially used: a 17th magnitude limit, since it is our experience that the JKT cannot be used to observe asteroids fainter without having to track on the asteroid (something we ideally wish to avoid doing to ease the use of comparison stars on the frame as part of flux calibration, see Section 3.5.5); a heliocentric distance limit of $\Delta = 1.5$ AU to focus on NEOs (Near-Earth Objects), with a little leeway. From the list produced, the further constraint of the object having to be between -40° and $+60^\circ$ declination (DEC) is applied, due to the limitations imposed by the observatory latitude and the UKIRT mounting. Detailed ephemerides for this list can be produced using JPL’s HORIZONS system (<http://ssd.jpl.nasa.gov/?horizons>).

The Michelle Observation Planning Applet (<http://www.jach.hawaii.edu/UKIRT/instruments/michelle/planner/msensi.htm>) calculates an optimistic estimate of the predicted sensitivity for the required Michelle spectrometry gratings, lowN and lowQ, given an estimated emissivity (15%), a typical wavelength within the grating waveband (10.5 and 20.5 μm for lowN and lowQ respectively) and the intended slit width (4 pixels). For the centre of the lowN grating (at the time of observation planning in September 2002; subsequently, estimated sensitivities have been reduced by 50%, and even these are probably over-optimistic) the flux required for a signal to noise ratio (S/N) ratio of one in

one minute (1σ 1min) given by the applet is 36 mJy and for the lowQ grating is 195 mJy. Millijanskys (mJy) can be converted to $\text{W m}^{-2} \mu\text{m}^{-1}$ via:

$$F(\text{mJy}) = 3.336 \times 10^{14} \lambda^2 F(\text{Wm}^{-2} \mu\text{m}^{-1}) \quad (5.4)$$

Rearranging Eq. 5.3 can convert these fluxes into magnitudes: $N = 7.5$ mag and $Q = 4.3$ mag assuming $F_N = 9.63 \times 10^{-13} \text{ W m}^{-2} \mu\text{m}^{-1}$ and $F_Q = 7.80 \times 10^{-14} \text{ W m}^{-2} \mu\text{m}^{-1}$ (Tokunaga, 2000). Using a crude estimate of the target asteroid's N magnitude by assuming $V-N \approx 10$, a rough estimate of the necessary observing time to achieve minimum adequate S/N is acquired. This estimate does not include overheads ($\sim 100\%$) and in practice was revealed to be several factors too optimistic, partly due to instrument performance not matching the planning applet.

Since objects with brighter apparent V are consequently higher on the priority list, this results in an observational selection effect. The larger and higher-albedo an object is, the more light reflected from its surface, resulting in a brighter visual magnitude. Therefore we are most likely to *try* to observe *large, high-albedo* objects, less likely small, high-albedo and large, low-albedo objects, and least likely small, low-albedo objects. The larger and lower-albedo an object is, the greater the absorbed and re-emitted thermal IR flux. So we are most likely to *succeed* in measuring IR flux from *large, low-albedo* objects, less from small, low-albedo and large, high-albedo objects, and least from small, high-albedo objects. Unfortunately, prior to measuring the thermal IR flux, we are unable to distinguish between high-albedo and large objects, so can prioritise only on visible brightness, presuming that more thermal flux will be received since a brighter object is more likely to be larger.

Standard and ratio stars were chosen from the list available on the UKIRT website (http://www.jach.hawaii.edu/UKIRT/astronomy/calib/spec_cal/ratio_std.html). Bright ratio stars, of spectral type K0 and earlier with smooth spectra (no SiO fundamental band) were

chosen to be close on the sky to the object and at as similar an airmass as possible.

Table 5.5 gives the standard and ratio stars selected. For simplicity, only the standard stars actually observed during the run are listed.

Table 5.5
Standard and ratio stars observed at UKIRT, 27-30 September 2002 UT

Star	Type	T_{eff} (K)	RA	Dec.	V (mag)	N (mag)	Q (mag)	Date (Sep. 2002 UT)	For Asteroid(s):
Standard^a									
BS 7001	A0	9520	18h 36m	+39°	0.0	0.00	0.00	27, 28	2002 QE ₁₅
BS 1017	F5	6440	03h 24m	+50°	1.8	0.5		28	(6455) 1992 HE
BS 1708	G8	5430	05h 12m	+06°	0.1	-1.94	-1.93	28	(6455) 1992 HE
BS 617	K2III	5010	02h 07m	+23°	2.0	-0.34	-0.85	29	
BS 7525	K3II	4785	19h 46m	+10°	2.7	-0.78	-0.82	30	2000 ED ₁₀₄ and 2002 NX ₁₈
BS 1457	K5III	4340	04h 36m	+17°	0.8	-3.03	-3.09	30	(6455) 1992 HE
Ratio									
BS 7264	F2	6890	19h 09m	-21°	2.9			27, 29	2002 NX ₁₈
BS 437	G9	5335	01h 30m	+15°	3.6			27, 28	2002 HK ₁₂
BS 8650	G8	5430	22h 42m	+30°	2.9			28, 29	(433) Eros
BS 915	G8	5430	03h 04m	+53°	2.9			28	1998 UO ₁
BS 7615	K0	5240	19h 56m	+35°	3.9			29	2000 ED ₁₀₄
BS 8414	G2	5830	22h 06m	+00°	3.0			29	1998 RO ₁
BS 1030	G6	5620	03h 25m	+09°	3.6			29, 30	(6455) 1992 HE
BS 1136	K0	5240	03h 43m	-10°	3.5			29	(6455) 1992 HE
BS 7776	F8	6200	20h 21m	-14°	3.1			30	2002 NX ₁₈

Notes. Some standard stars were also used as ratio stars. T_{eff} is effective black body temperature for the given star spectral type, taken from ORAC-DR's internal table, uncertainty approximately ± 100 K. Absolutely calibrated N- and Q-band fluxes in magnitudes are taken from Tokunaga (1984) and Rieke *et al.* (1985).

Prior to observing, the observation sequences of flats, arcs, standard stars, ratio stars, and objects are loaded as minimum schedulable blocks (MSBs) into the UKIRT Observing Tool. The coordinates (RA and DEC) of the potential standard stars and ratio stars are loaded from a database, and the asteroid coordinates are entered manually. The grating, slit width, exposure time of each coadd, number of coadds and chopping offset are all preloaded. The target observation sequence in an MSB can be repeated during the night to alter the total number of frames depending on time available. More details on the Observing Tool can be found on <http://www.jach.hawaii.edu/software/ukirtot/>.

5.3.2 Observations

Observations in the thermal infrared of eight NEAs were carried out at UKIRT on five half-nights, 26-30 September 2002 UT, using the Michelle instrument in spectroscopy mode, in which it has a resolution of 0.38 arcsec per pixel. The log sheets showing details of the exact order of observations are shown in Appendix C. A summary of the observations made of the standards, ratio stars and NEAs including the observational circumstances, instrument configuration, and notes on each asteroid are given in Tables 5.6, 5.7 and 5.8.

Apart from flat fields and bias arrays, no data were obtained on 26 September due to an equipment malfunction (the flat field plate became jammed in the IR beam). The weather on 27 September appeared to be clear with an optical depth $\tau = 0.14$, seeing 0.5". On 28 September, there was some cirrus around the horizon, mostly to the East, but clear overhead, $\tau = 0.14$, seeing 0.55". On 29 September, $\sim 5/8$ of the sky was covered with cirrus, but after about 05:45 UT it appeared to clear slightly and we began observing, concentrating on targets for which we already had some calibration. On 30 September weather appeared clear, $\tau = 0.06$.

The lowN and lowQ gratings were used, obtaining spectra in the range 7-13 μm and 17-25 μm respectively. The gratings can be set to different slit widths: on 27, 28 and 30 September a 4-pixel slit width was used to maximise the accuracy of the absolute flux calibration by ensuring that all the possible light from the ratio star was received. On 29 September a 2-pixel slit was used so as to reduce noise from the sky background due to the cirrus.

Table 5.6
Observational circumstances of standard and ratio stars observed at UKIRT and instrument configuration in September 2002 UT using Michelle in spectroscopy mode

Star	Date (UT)	Group	Start and end time (UT)	Slit width (pixels)	Grating	no. of frames	Total exp. time (s)	Start and end λ	Ratio for asteroid:	Standard?
BS 7001	27 Sep.	10	06:47:24 – 06:59:57	4	N	8	140.80	1.209 – 1.243		y
BS 7001	27 Sep.	74	08:52:07 – 09:04:44	4	N	8	140.80	1.884 – 2.025		y
BS 617	29 Sep.	208	12:13:44 – 12:19:55	2	N	4	65.52	1.004 – 1.006		y
BS 7525	30 Sep.	92	08:05:28 – 08:11:45	4	N	4	70.40	1.267 – 1.293		y
BS 8650	28 Sep.	95	09:23:35 – 09:36:07	4	N	8	140.80	1.034 – 1.045	(433) Eros	
BS 8650	29 Sep.	127	09:35:46 – 09:48:08	2	N	8	131.04	1.049 – 1.063	(433) Eros	
BS 1017	28 Sep.	144	11:15:37 – 11:28:09	4	N	8	140.80	1.280 – 1.254	(6455) 1992 HE	y
BS 1708	28 Sep.	168	12:06:46 – 12:13:06	4	N	4	70.40	1.431 – 1.405	(6455) 1992 HE	y
BS 1030	29 Sep.	147	10:16:23 – 10:22:34	2	N	4	65.52	1.399 – 1.366	(6455) 1992 HE	
BS 1136	29 Sep.	176	11:09:21 – 11:15:32	2	N	4	65.52	1.443 – 1.413	(6455) 1992 HE	
BS 1136	29 Sep.	204	12:03:48 – 12:09:59	2	N	4	65.52	1.249 – 1.235	(6455) 1992 HE	
BS 1030	30 Sep.	133	09:32:16 – 09:38:33	4	N	4	70.40	1.694 – 1.637	(6455) 1992 HE	
BS 1457	30 Sep.	153	10:15:39 – 10:21:55	4	N	4	70.40	1.903 – 1.808	(6455) 1992 HE	y
BS 1457	30 Sep.	157	10:24:35 – 10:30:53	4	Q	4	64.80	1.798 – 1.732	(6455) 1992 HE	y
BS 1457	30 Sep.	185	11:14:28 – 11:20:44	4	Q	4	64.80	1.402 – 1.368	(6455) 1992 HE	y
BS 8414	29 Sep.	75	08:06:17 – 08:12:28	2	N	4	65.52	1.066 – 1.068	1998 RO ₁	
BS 915	28 Sep.	119	10:13:15 – 10:29:46	4	N	8	140.80	1.444 – 1.393	1998 UO ₁	
BS 7615	29 Sep.	41	06:45:11 – 06:51:22	2	N	4	65.52	1.064 – 1.070	2000 ED ₁₀₄	
BS 7615	29 Sep.	61	07:25:44 – 07:51:22	2	N	4	65.52	1.119 – 1.130	2000 ED ₁₀₄	
BS 7525	30 Sep.	117	08:52:34 – 08:58:51	4	N	4	70.40	1.523 – 1.570	2000 ED ₁₀₄	y
BS 437	27 Sep.	82	09:12:48 – 09:25:21	4	N	8	140.80	1.190 – 1.153	2002 HK ₁₂	
BS 437	28 Sep.	63	08:23:08 – 08:35:40	4	N	8	140.80	1.382 – 1.318	2002 HK ₁₂	
BS 7264	27 Sep.	18	07:06:20 – 07:18:52	4	N	8	140.80	1.557 – 1.620	2002 NX ₁₈	
BS 7264	29 Sep.	9	05:44:55 – 05:57:18	2	N	8	131.04	1.351 – 1.371	2002 NX ₁₈	
BS 7525	30 Sep.	88	07:50:37 – 07:56:53	4	Q	4	64.80	1.213 – 1.234	2002 NX ₁₈	y
BS 7776	30 Sep.	113	08:44:41 – 08:50:56	4	N	4	70.40	1.621 – 1.664	2002 NX ₁₈	
BS 7001	28 Sep.	11	06:47:32 – 06:53:48	4	N	4	70.40	1.219 – 1.237	2002 QE ₁₅	y

Notes. Group number is assigned as the start frame number by ORAC-DR. ‘N’ and ‘Q’ gratings are abbreviations for ‘lowN’ and ‘lowQ’ gratings respectively. Sequence of observations can be seen more clearly in Appendix C.

Table 5.7

Observational circumstances of asteroids observed at UKIRT in September 2002 UT using Michelle in spectroscopy mode

Asteroid	Date (UT)	Start and end time (UT)	Start and end χ	r (AU)	Δ (AU)	α°
(433) Eros	28 Sep.	09:38:52 – 09:57:38	1.057 – 1.089	1.5894	0.6397	18.2
	29 Sep.	09:51:43 – 10:10:13	1.088 – 1.128	1.5867	0.6409	18.8
(6455) 1992 HE	28 Sep.	11:38:03 – 12:03:08	1.403 – 1.358	1.3555	0.44357	31.1
	29 Sep.	10:29:14 – 11:06:26	1.597 – 1.444	1.3631	0.44388	29.7
		11:28:18 – 12:00:28	1.386 – 1.334	1.3633	0.44389	29.6
	30 Sep.	09:47:08 – 10:12:14	1.787 – 1.617	1.3707	0.44454	28.3
		10:34:55 – 11:12:34	1.506 – 1.384	1.3710	0.44457	28.2
11:24:22 – 12:14:33	1.358 – 1.301	1.3713	0.44461	28.1		
(66063) 1998 RO ₁	29 Sep.	08:17:31 – 09:31:53	1.138 – 1.403	1.1245	0.1839	44.5
1998 UO ₁	28 Sep.	10:52:07 – 11:12:29	1.238 – 1.201	1.2304	0.3491	42.8
(53789) 2000 ED ₁₀₄	29 Sep.	06:55:52 – 07:14:21	1.070 – 1.097	1.0888	0.2068	60.1
	30 Sep.	09:07:06 – 09:25:52	1.510 – 1.649	1.0854	0.1991	60.2
2002 HK ₁₂	27 Sep.	09:31:08 – 10:06:26	1.275 – 1.162	1.1344	0.1658	34.6
	28 Sep.	08:40:48 – 09:18:20	1.493 – 1.299	1.1408	0.1708	33.1
2002 NX ₁₈	27 Sep.	07:32:27 – 08:47:45	1.449 – 1.839	1.1522	0.2807	51.6
	29 Sep.	06:01:04 – 06:32:04	1.339 – 1.352	1.1439	0.2760	52.9
	30 Sep.	07:11:02 – 07:48:43	1.421 – 1.541	1.1394	0.2734	53.6
08:16:55 – 08:41:55		1.683 – 1.864	1.1393	0.2734	53.6	
2002 QE ₁₅	28 Sep.	06:59:05 – 08:14:25	1.365 – 1.626	1.1311	0.4183	61.6

Notes. Ephemerides are taken from JPL Horizons. r , Δ , and α given for midpoint of observation. Sequence of observations can be seen more clearly in Appendix C.

Table 5.8
Instrument configuration and notes for asteroids observed at UKIRT in September 2002 UT using Michelle in spectroscopy mode

Asteroid	Date (UT)	Group	Slit width (pixels)	Grating	no. of frames	Total exp. (s)	Notes
(433) Eros	28 Sep.	103	4	N	12	211.20	Clear skies. Ratio star BS 8650 is a spectroscopic binary.
	29 Sep.	135	2	N	12	196.56	~5/8 cirrus. Ratio star BS 8650 is a spectroscopic binary.
(6455) 1992 HE	28 Sep.	152	4	N	16	281.60	Clear skies. 2 ratio stars were observed, BS 1017 and BS 1708 (are also standards), allows comparison with how using a different ratio star in a different part of sky affects flux calibration.
	29 Sep.	152	2	N	24	393.12	~5/8 cirrus. 2 ratio stars: BS 1030 and BS 1136.
		184	2	N	20	327.60	
	30 Sep.	137	4	N	16	281.60	Clear skies.
		161	4	Q	24	388.80	
		189	4	Q	32	518.40	
(66063) 1998 RO ₁	29 Sep.	79	2	N	48	786.24	Only object observed on 29 Sep. not also observed other night. Observed after 2000 ED ₁₀₄ (sky clear?) and before Eros (cirrus), so may be affected by cloud.
1998 UO ₁	28 Sep.	131	4	N	12	211.20	Ratio star BS 915, observed before 1998 UO ₁ . Between these observations., new flat field and arc taken since grating moved to new position, because wrong λ entered into observing tool for previously observed standard. No spectrum was seen and 1998 UO ₁ was not attempted again.
(53789) 2000 ED ₁₀₄	29 Sep.	45	2	N	12	196.56	~5/8 cirrus. Obs. obscured by cloud after frame 56, then autoguider lost lock on asteroid and locked onto a star, because asteroid in galactic plane. Obs. actually taken until frame 74. 2 more attempts on made but autoguider immediately reattached to a star.
	30 Sep.	121	4	N	12	196.56	Clear skies.
2002 HK ₁₂	27 Sep.	90	4	N	20	352.00	Clear skies, but no spectrum observed.
	28 Sep.	71	4	N	24	422.40	Clear skies, faint spectrum.
2002 NX ₁₈	27 Sep.	26	4	N	48	844.80	Clear skies.
	29 Sep.	17	2	N	20	327.60	Partial cirrus, observed till frame 40, but only usable until frame 36.
	30 Sep.	64	4	Q	24	388.80	Clear skies.
		96	4	N	16	281.60	Clear skies.
2002 QE ₁₅	28 Sep.	15	4	N	48	844.80	Clear skies.

Notes. "N" and "Q" are abbreviations for "lowN" and "lowQ" gratings respectively. Group number is assigned as the start frame number by ORAC-DR. Sequence of observations and some additional notes in Appendix C

At the start of each night, four array frames were taken, then a series of flat frames. In order to be able to flux calibrate the asteroid spectrum during data reduction, a standard star with known N- and Q-band flux was observed, several times throughout the night if possible. Either directly before or after each asteroid was observed, a ratio star was observed in order to correct for wavelength-dependent atmospheric transmission. Ephemerides for each asteroid were obtained from JPL Horizons, and the telescope was tracked at the rates provided while offset autoguiding on a nearby star.

For the lowN grating, the observing sequence for each frame, automatically coadding the exposures onto the raw frame, was run through 176 times (176 'coadds') using the 4-pixel slit, and 78 times using the 2-pixel slit. Exposure times for each coadd were 0.10 s and 0.21 s for the 4-pixel and 2-pixel slits respectively. Each object was observed for a variable number of frames, so the total exposure time for each object using the 4-pixel slit is $(0.1 \text{ s} \times 176 \text{ coadds} \times \text{no. of frames})$, and for the 2-pixel slit it is $(0.21 \text{ s} \times 78 \text{ coadds} \times \text{no. of frames})$. For the lowQ grating (only 4-pixel slit used) there were 90 coadds and the exposure time was 0.18 s, so the total exposure time was $(0.18 \text{ s} \times 90 \text{ coadds} \times \text{no. of frames})$.

5.3.3 Sky Background Thermal Emission

There is a large background thermal infrared flux from the sky that has to be removed from the observations. Chopping uses the telescope's secondary mirror to move the telescope field of view from the target to nearby sky and takes the difference. The difference between on- and off-target exposures contains spatial and spectral structure due to the combined effects of the atmosphere, the optics and the pixel to pixel variations in gain across the detector. Following the Michelle UKIRT manual (Glasse, 2001), the detected photon signal f in each pixel, assuming a model for the transport of radiation

through the atmosphere in terms of τ , as a function of on-target chop position C_1 and off-target chop position C_2 , is:

$$\begin{aligned} f(C_1) &= g(i, j) \left[S_{\text{tel}}(C_1) + S_{\text{atm}}(1 - e^{-\tau}) + S_{\text{tgt}} e^{-\tau} \right] \\ f(C_2) &= g(i, j) \left[S_{\text{tel}}(C_2) + S_{\text{atm}}(1 - e^{-\tau}) \right] \end{aligned} \quad (5.5)$$

where $g(i, j)$ is the optical efficiency or the product of the detector gain matrix with the instrument's response function, S_{tel} is the source function for the thermal emission from the telescope optics, S_{tgt} is the signal from the target object. $g(i, j)$ will vary both from pixel (on row i and column j) to pixel and more slowly with position across the entire array. We assume $g(i, j)$ is not a strong function of time.

$$S_{\text{tel}}(C) = \varepsilon_{\text{tel}} B_{\lambda}(\lambda, 275\text{K}) + \Delta S_{\text{tel}}(C) \quad (5.6)$$

where B_{λ} is the black body function for the telescope optics which are assumed to be at an ambient temperature of 275 K, λ is the wavelength, ε_{tel} is the emissivity [$\sim 3\%$, with variations across the telescope focal plane included in $g(i, j)$] and $\Delta S_{\text{tel}}(C)$ is the telescope's thermal offset as it varies from one chop position to the other.

$$S_{\text{atm}}(\alpha, \delta, \lambda) = (1 - \varepsilon_{\text{tel}}) B_{\lambda}(\lambda, T_{\text{sky}}) \quad (5.7)$$

where the continuum source function for the sky S_{atm} is approximated by a black body at a temperature T_{sky} somewhat colder than ambient which varies with RA (α), DEC (δ) and with wavelength (λ). The optical depth of the atmosphere, τ , is a strong and complicated function of wavelength and airmass Z :

$$\tau(\alpha, \delta, \lambda) = \tau_{\text{zen}}(\lambda) Z(\alpha, \delta) \quad (5.8)$$

We will label the telescope's current beam position A ; the equations for the on- and off-target signals are now:

$$\begin{aligned}
 f(A, C_1) &= g(i, j) \left[\varepsilon_{\text{tel}} B_\lambda(\lambda, 275\text{K}) + \Delta S_{\text{tel}}(C_1) + S_{\text{atm}}(1 - e^{-\tau}) + S_{\text{tgt}} e^{-\tau} \right] \\
 f(A, C_2) &= g(i, j) \left[\varepsilon_{\text{tel}} B_\lambda(\lambda, 275\text{K}) + \Delta S_{\text{tel}}(C_2) + S_{\text{atm}}(1 - e^{-\tau}) \right]
 \end{aligned} \tag{5.9}$$

and the difference between them is:

$$f_{\text{tgt}}(A) = f(A, C_1) - f(A, C_2) = g(i, j) \left[\Delta S_{\text{tel}}(C_1) - \Delta S_{\text{tel}}(C_2) + S_{\text{tgt}} e^{-\tau} \right] \tag{5.10}$$

It can be seen that the atmospheric terms cancel, and the telescope's chop position-specific thermal offset remains from the telescope's thermal emission profile. The cancellation tends to be effective as long as the chop frequency is higher than the characteristic timescale over which the sky emission changes. During an observation the telescope was chopped with an amplitude of 16'' and frequency 10 Hz (when using a 4-pixel width slit) or 4.8 Hz (2-pixel slit) in a direction along the slit. Chopping along the slit maximises the observing time on the target since the source is always being measured.

The telescope's thermal offset can be removed by nodding, whereby the chop positions of the target and the sky are swapped so that the target is placed in chop position C_2 and the sky in C_1 . The new beam-switch position is labelled B :

$$f_{\text{tgt}}(B) = f(B, C_2) - f(B, C_1) g(i, j) \left[\Delta S_{\text{tel}}(C_2) - \Delta S_{\text{tel}}(C_1) + S_{\text{tgt}} e^{-\tau} \right] \tag{5.11}$$

$$f_{\text{tgt}} = f_{\text{tgt}}(A) + f_{\text{tgt}}(B) = 2g(i, j) S_{\text{tgt}} e^{-\tau} \tag{5.12}$$

The timescale for nodding can be longer than that for chopping because its effectiveness depends on the more slowly varying parameters along the telescope's optical path.

The observing sequence is on-target, off-target, off-target, on-target so that each raw output grouped frame thus consists of four horizontal rows (several pixels wide), with off-source rows apparent as negative values on the image. The slits were carefully positioned to so that the rows avoided bad pixels on the CCD array; occasionally they were offset by up to 3 pixels in both the x- and y-axis directions to accomplish this.

Flat-fielding removes the remaining gain matrix $g(i, j)$. Flux calibration, through observation of a standard star, removes the atmospheric optical depth $e^{-\tau}$.

5.4 Data Reduction using ORAC-DR

To illustrate the data reduction process we will examine in detail the reduction of a spectrum of asteroid 2002 NX₁₈ observed on 27 September UT. ORAC-DR is a pipeline data reduction package that runs a linear series of routines written using PERL. The header file of each frame contains a call to a data reduction ‘recipe’ which runs a series of ‘primitives’. Each primitive contains a series of lines of code which perform manipulations and calculations on the content of each frame using Starlink KAPPA, FIGARO and CCDPACK commands or calls a lower-level sequence of primitives which are executed in order. There are no loops – every primitive is read once. ORAC-DR was designed for data reduction on-the-fly i.e. while observations were being taken. It deals with each frame as it arrives without behaving intelligently based on what frames it knows are coming. The complete sequence of primitives run for each frame type and in which order, with brief descriptions of each primitive’s function, are displayed in Appendix D. The rest of this section summarises the operations of these primitives, with additional explanation as required.

5.4.1 Bias Frames

The first step in the data reduction process is to reduce the dark array frames. The array frames are needed to create a bias frame for subsequent data reduction. Frames m20020927_00001.sdf to m20020927_00004.sdf (1-4) taken between 04:29 and 04:30 UT are the array frames for 27 September 2002 UT. The frame headers which identify the frame type instruct that the recipe REDUCE_BIAS is called which creates a reduced bias

frame. All raw files contain “ndf” components (Starlink data files are called ndfs for historical reasons, although their extension is *.sdf) from both beam paths A and B, multiplied by the number of chop positions (I1 and I2).

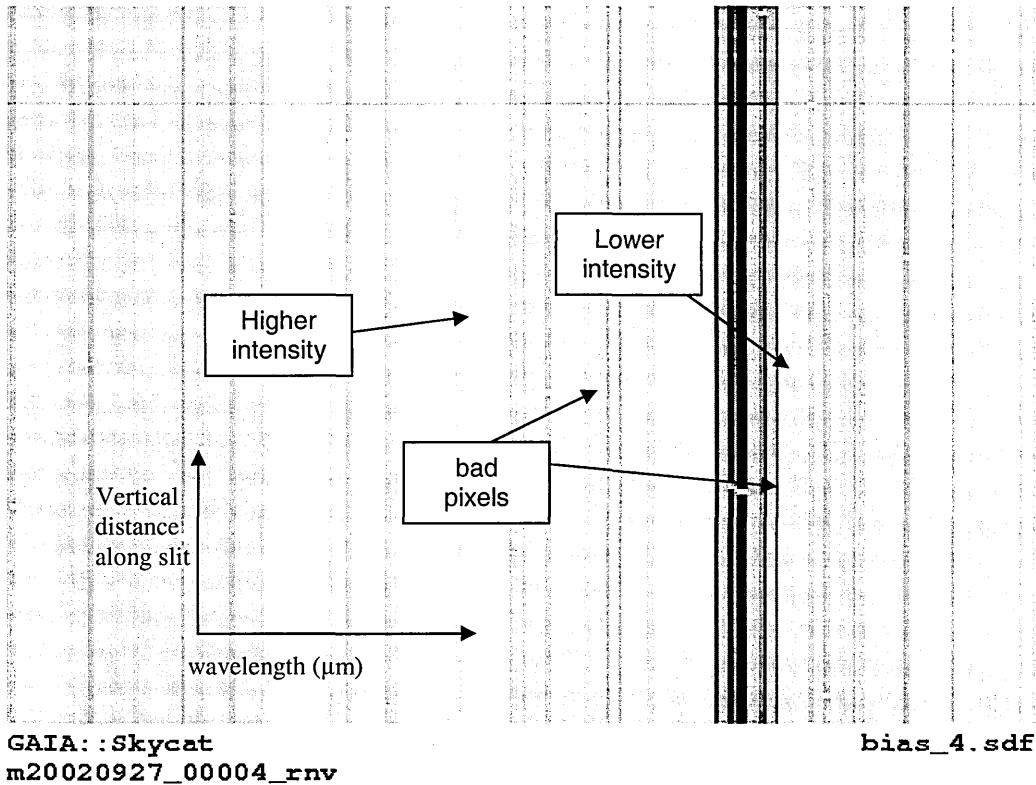


Fig. 5.4 Michelle instrument spectroscopy mode bias frame taken for 27 September 2002 UT, reduced by ORAC-DR. Every flat field, standard and object frame has this bias frame subtracted from it.

First, a sequence of primitives do various tasks including: setting the hardwire read noise to 1000 electrons and flipping the lowQ frames because the lowQ grating is installed the wrong way round in the cryostat (this problem is worked around by driving the grating angle to what would have been negative orders), determining the array sampling pattern used (1×1), the number of array reads per exposure (one) and starting a log of the frames reduced. See Appendix D for more detail. The two integrations are averaged together to create a master bias frame, and a variance array is added, adjusting the 1000 electrons read noise according to the gain, number of exposures and number of array reads per exposure.

The bias frame is filed as 'bias_1' and ORAC-DR moves onto the next frame ('bias_4' is shown in Fig. 5.4).

5.4.2 Flat Field Frames

Frames 5-7 taken between 04:43 and 04:47 UT are the flat field frames, taken using a flat-fielding plate; the frame header calls the recipe REDUCE_FLAT. There are four integrations in each frame: I1BEAMA, I1BEAMB, I2BEAMA and I2BEAMB.

First, a sequence of primitives do various tasks including: setting the hardware read noise to 1000 electrons, flipping the lowQ frames, determining the array sampling pattern used (1×2), the number of array reads per exposure (one) and starting a log of the frames reduced. The array sampling is a result of the array being read out twice per exposure to reduce noise, known as “interleaving”. See Appendix D for more detail.

A bad pixel mask is applied to each sub-image, flagging individual pixels that are known to be bad on the CCD. The read noise variance is added, the bias frame (bias_4) is subtracted and Poisson variance is added to the variance component, taking into account the gain of the detector. The two chop beam sub-frames are coadded to form a calibration frame, and the 1×2 pixel-sampling is interleaved to combine all the sub-frames into a single frame.

An approximate wavelength scale is added using the header value for the grating wavelength (the wavelength for the middle pixel along the x-axis, 320 pixels long), 10.4706 μm and 21.0279 μm for the lowN grating and the lowQ grating respectively, and the grating dispersion, 0.024046 $\mu\text{m}/\text{pixel}$ and 0.028624 $\mu\text{m}/\text{pixel}$ for the lowN grating and the lowQ grating respectively. From these values it calculates a wavelength value for each x-pixel. Unfortunately, although the grating wavelength is accurate, the grating dispersion is only close to the true value at the shortest wavelength side of the grating, and is non-

linear. As a result, the wavelength calibration by estimation can be out by as much as 0.5 microns. This has serious consequences for ORAC-DR's black body profile division of the standard stars, as described in Section 5.4.6. Correct wavelength calibration is described in Section 5.5.1.

The frame is now normalised with a black body curve. Michelle's integrating sphere (flat field plate) temperature is assumed to be 330 K, a black body spectrum based on this temperature is created (see Section 5.4.6) which is grown to the size of the image, then the flat field frame is divided by this spectrum. The image is divided by its mean pixel level, normalising it so the average pixel value is one.

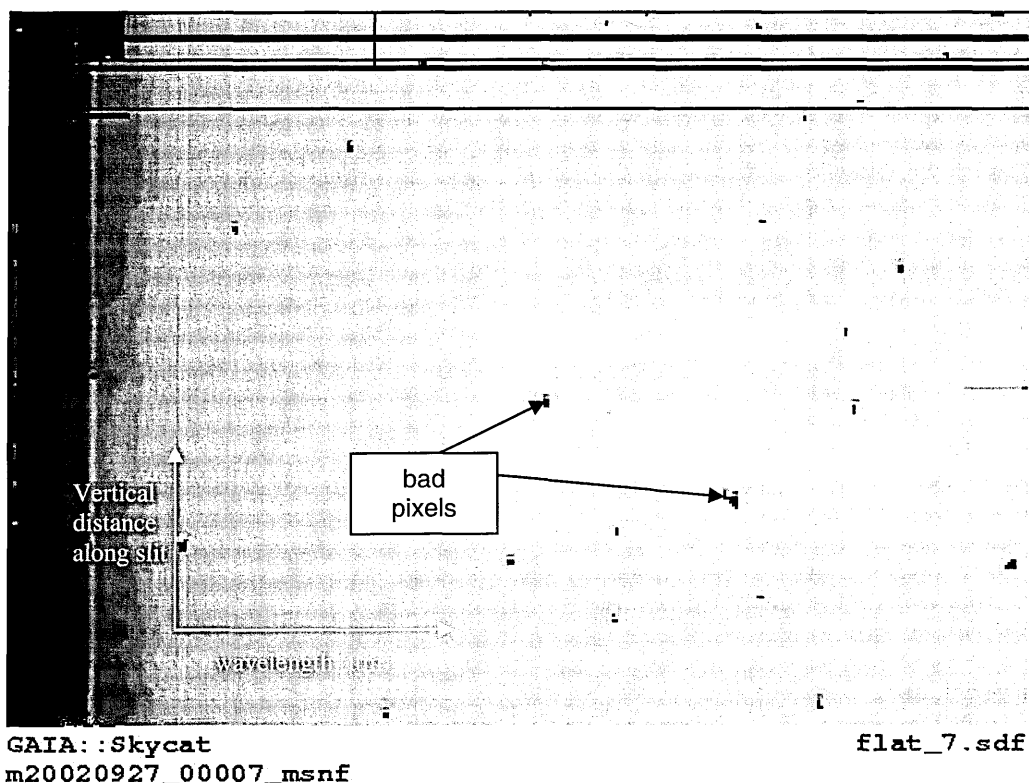


Fig. 5.5 Michelle instrument spectroscopy mode flat field frame taken for 27 September 2002 UT, reduced by ORAC-DR. Under-illuminated areas of the slit and bad pixels are masked. Whiter areas are higher intensity. Every standard and object frame is divided by this flat field frame.

Areas which are under-illuminated (less than 75% of average pixel value), at the ends of the slit generally, are masked off. Pixels which are more than 20 standard deviations

different from other pixels in a 5-pixel radius are flagged as bad. The frame is filed, and ORAC-DR proceeds to reduce frames 6 and 7 in the same way. See Fig. 5.5 for the flat field of frame 7, flat_7.sdf.

5.4.3 *Standard Star Frames*

Frames 10-17 of standard star BS 7001 (Vega) were taken on 27 September between 06:47 and 06:58 UT. Frames 18-25 of standard star BS 7264 were taken between 07:06 and 07:17 UT. Both standard stars are reduced in the same way by ORAC-DR, but both are ultimately used in different ways to flux calibrate the 2002 NX₁₈ spectrum. ORAC-DR eventually attempts to use the BS 7264 spectrum to flux calibrate the 2002 NX₁₈ spectrum because it is reduced directly before the object spectrum, so is set as the current standard; for convenience we will describe the reduction of BS 7264. See Appendix D for details of all the primitives called. By default, the m20020927_00018 frame header calls the recipe STANDARD_STAR. It is possible to force ORAC-DR to use user-defined recipes (for example STANDARD_STAR_ONE_POINT_FIVE_PIXEL_ROW_SET) and primitives. The STANDARD_STAR recipe was renamed and minor alterations were applied, causing it to call user-defined primitives, which are all themselves renamed and slightly altered versions of the default primitives. The changes made are all described later.

5.4.4 *Standard Stars: Preparing Frames for Spectrum Extraction*

The first frame in the group is used to make a sky-arc. The use of this sky-arc frame in wavelength calibration is described in Section 5.5.1. The frame is reduced in the same way as described below except that the two chop beams (beam path A and B) are coadded to form a calibration frame. By coadding the chop beams instead of subtracting them a

spectrum of the sky is obtained. Reduction on the sky-arc ceases after the frame is wavelength calibrated by estimation ('_wce'), and the frame is called 'arc_g18'.

ORAC-DR then starts reduction on the first frame again. The frame is reduced in the same way as described for flat field frames (Section 5.4.2) up until the frame is wavelength calibrated by estimation, except that instead of coadding the two chop beam sub-frames they are subtracted from each other, so that beam path B appears as negative intensity values on the image. After the 1×2 pixel-sampling is interleaved, the frame is divided by the reduced flat field frame (flat_7, Fig. 5.5). Thus, the frame has been reduced to m20020927_00018_wce (Fig. 5.6).

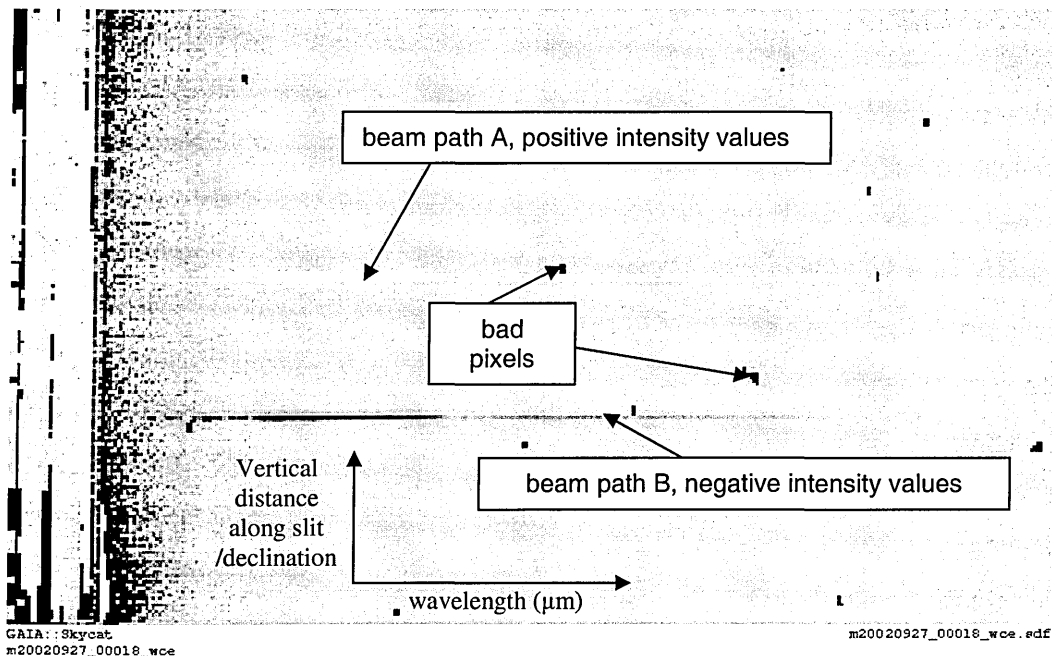


Fig. 5.6 Wavelength-calibrated-by estimation image of the first frame of standard star BS 7264 taken on 27 September 2002 UT using Michelle in spectroscopy mode and reduced by ORAC-DR. Top portion of frame is clipped, but total usable portion of slit is shown.

ORAC-DR detects that m20020927_00018 is the first in a pair. Reduction now proceeds to the second frame, m20020927_00019. The telescope was chopping at $16''$, and off-set by $8''$ declination between frames so that the observing sequence was on-target, off-target, off-target, on-target; the second frame was taken in the off-set position. In the

second frame of the pair, beam path A has negative intensity values, and beam path B has positive. m20020927_00019 is reduced to m20020927_00019_wce. This off-set frame is subtracted from m20020927_00018_wce to create a single “sky-subtracted” frame m20020927_00018_ss with four beams in the image. This is the equivalent of the operation described by Eq. 5.10. The group gm20020927_18 (Fig. 5.7) is created into which every pair up until the pair of frames 24 and 25 will be coadded. This ends the operations on single frames for this recipe; the subsequent primitives are fed the group frame.

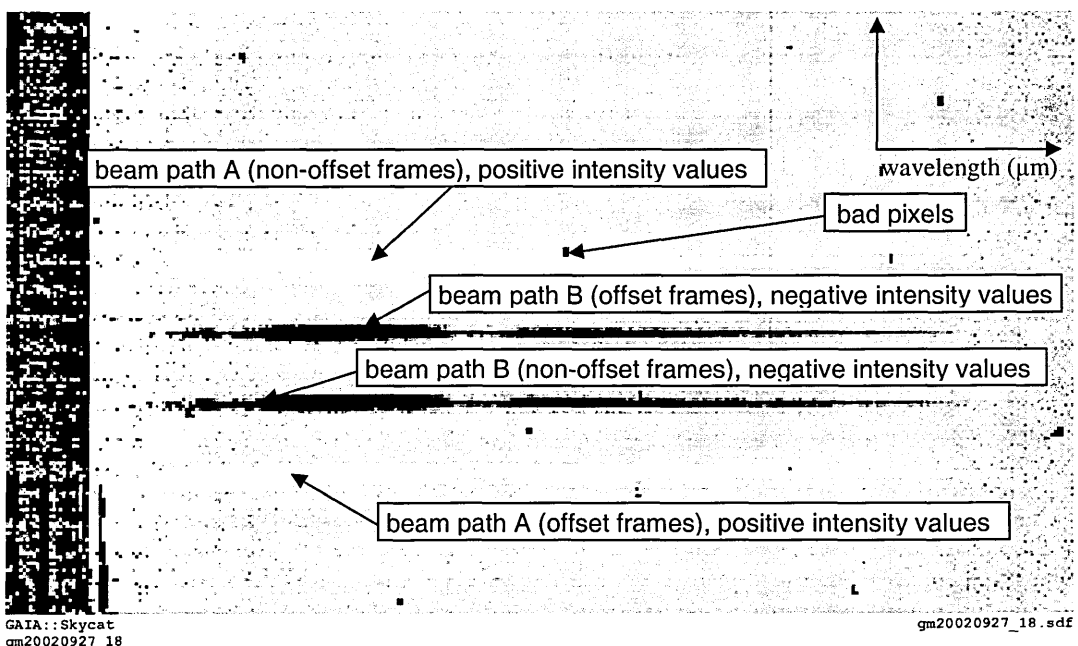


Fig. 5.7 The group frame gm20020927_18.sdf of standard star BS 7264 taken on 27 September 2002 UT using Michelle in spectroscopy mode and reduced by ORAC-DR. It is formed by coadding all 4 pairs of “sky-subtracted” frames in the observation. The second frame in a pair is subtracted from the first, so beams with positive intensity values in the second frame of a pair now have negative, and visa versa. Top portion of frames are not visible, but total usable portion of slit is shown.

5.4.5 Standard Stars: Optimum Extraction of Spectrum

The spectrum can now be extracted from the group file. The first task is to determine which rows the peak fluxes are in for each beam. We checked several different sets of pairs from different observations to check that the row centres in each ‘_ss’ frame were the same

throughout the group – i.e. that the telescope was tracking precisely. Almost no changes were found, the row centres varied by less than one pixel. Here we come to the first point where the user-defined recipe differs from the default STANDARD_STAR recipe. The default recipe calls the primitive `_EXTRACT_SPECTRA_`. In a temporary file, the primitive collapses the image along the dispersion (x) axis and runs the FIGARO routine ‘emlt’ which uses centre of moment analysis to determine line centres. This generally works well for the standard stars where the rows are bright, but for our fainter targets this routine often fails to correctly detect the rows. Instead, the modified recipe calls e.g. `_EXTRACT_SPECTRA_ONE_POINT_FIVE_PIXEL_` that collects the y-coordinates of the four rows from a calibration file. These are found by creating a mean y-profile of the group file in the Starlink program GAIA (Fig. 5.8). The row centres are defined as being in the middle of a y-pixel value, for gm20020927_18 they are: (positive beams) 43.5, 106.5; (negative beams) 64.5, 84.5.

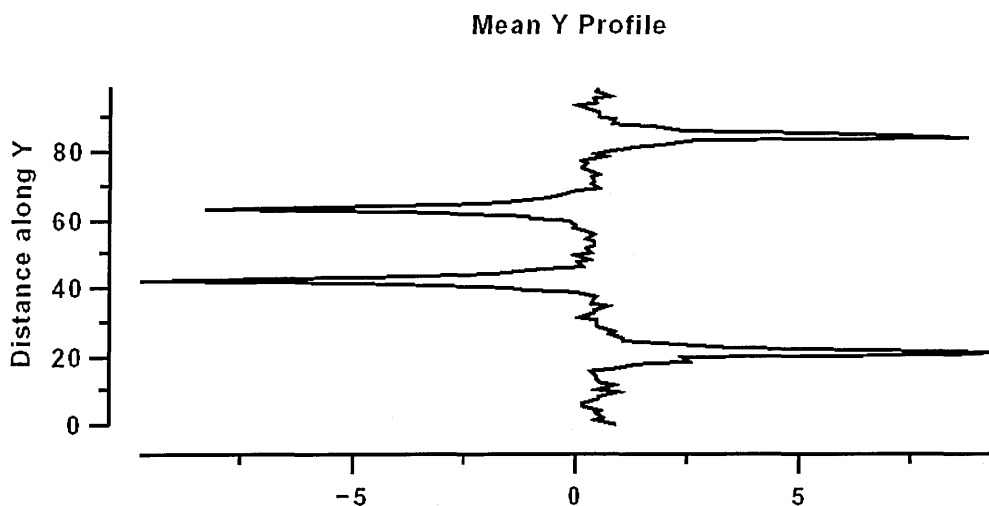


Fig. 5.8 Mean y-profile of gm20020927_18 (Fig. 5.7) from which the four row centres for optimum spectrum extraction can be determined.

The `_EXTRACT_SPECTRA_` primitive subtracts a lower and upper y-boundary from the image using the NDFPACK routine ‘ndftrace’, the FIGARO routine ‘profile’ determines a spatial image profile, then the FIGARO routine ‘optextract’ performs the

optimal extraction of the spectrum, applying the algorithm of Horne (1986) using the profile (and dividing by -1 if the beams are negative). The default recipe uses a 20 pixel diameter window for the optimum extraction. In order to achieve maximum S/N we experimented with reducing this generous diameter, as described in Section 5.4.10. For example, the recipe `STANDARD_STAR_ONE_POINT_FIVE_PIXEL_ROW_SET` uses a 3 pixel diameter (1.5 pixel radius). Since the row centres have been set to the centre of a pixel the optimal extraction window boundary is on the edge of a pixel (although 'optextract' can handle partial pixels).

The four beams are cross-correlated with the first beam ($y = 43.5$ row centre) using the FIGARO routine 'scross', which uses the Fourier cross-correlation technique (e.g. Tonry and Davis, 1979) that determines the relative shift between two spectra and computes the location of the central peak of cross-correlation. If the shift is calculated as being more than 2 pixels or the peak is at less than 60% then the shift is rejected, otherwise the beam is aligned with the first beam.

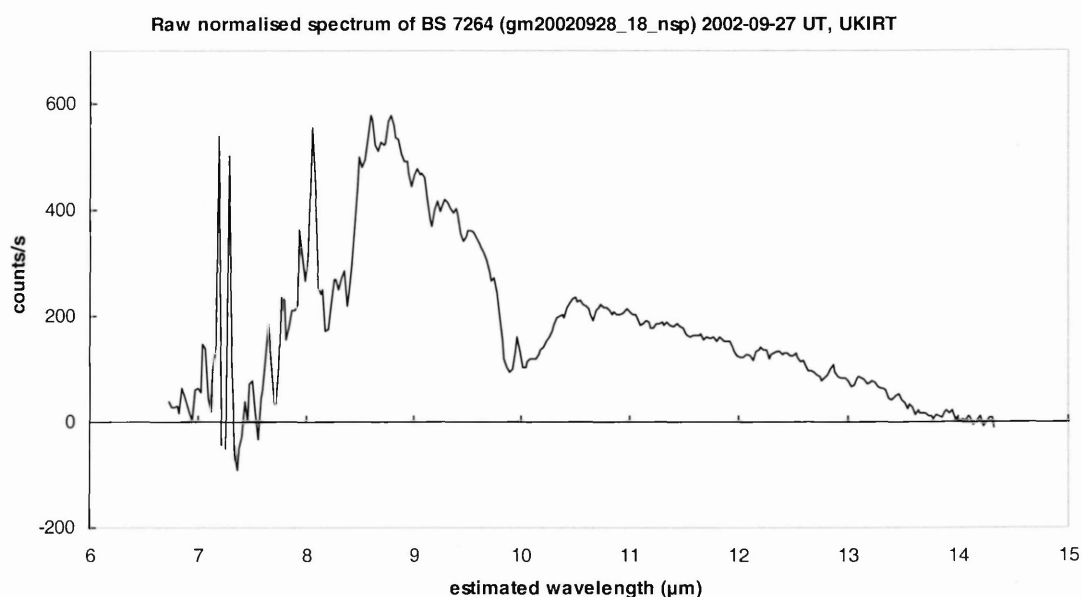


Fig. 5.9 *gm20020927_18_nsp*, the raw normalised spectrum of BS 7264 observed on 27 September 2002 UT, output by ORAC-DR using 3 pixel window diameter optimum extraction. The wavelength scale is calibrated by estimation in ORAC-DR and is inaccurate. The output from the whole grating is shown, but marked bad pixels have been removed.

The four beams are finally coadded to create one single spectrum. Since beam path B has negative intensity values, this constitutes a combination of the operations described by Eqs. 5.11 and 5.12, removing the telescope's thermal offset by adding together beams with swapped beamswitch positions. The frame is normalised to 1 s exposure time, gm2002027_18_nsp (Fig. 5.9).

5.4.6 Standard Stars: Black Body Correction

The extracted spectrum has to be divided by the black body spectral shape of the standard in order to account for the difference in shape between the standard star and object's spectrum due to their different temperatures. ORAC-DR creates a black body profile of the standard using the FIGARO routine 'bbody' (see Eq. 4.8). The temperature of the star corresponding to the star spectral type is obtained from an internal table. Temperatures for the given star spectral type are given in Table 5.5 [which are, within the uncertainty, the same as those given by Tokunaga (2000)]. The black body function is normalised to one at the grating wavelength (10.471 μm), then gm20020927_18_nsp divides by this profile. The final reduced standard star spectrum is filed as 'std_18_sp'.

Since ORAC-DR uses a wavelength scale calibrated by estimation, inaccurate by as much as 0.5 μm , the black body function division calculated for the standard star is inaccurate because it is normalised to one at the wrong pixel value, and the resulting spectral shape of the standard star is different. Section 5.5.2 demonstrates what effect this has on the flux calibrated object spectrum. Ultimately, the black body division for each standard star had to be manually calculated and performed after accurate wavelength calibration using the sky-arcs (Section 5.5.1). Therefore the operations performed by ORAC-DR on the standard star after optimum extraction are never used, and

gm20020927_18_nsp is regarded as the final product of the pipeline reduction of the standard star.

5.4.7 Object Frames: Spectrum Extraction

Frames 26-73 taken between 07:32 and 08:48 on 27 September 2002 UT are of asteroid 2002 NX₁₈. The frame header calls the recipe POINT_SOURCE. As for the standard star frames (Section 5.4.3), this is overridden and user-defined recipe POINT_SOURCE_ONE_POINT_FIVE_PIXEL_ROW_SET_ is used, which makes the same changes to the optimum spectrum extraction as described for the standard star frames. Pipeline data reduction proceeds as in Sections 5.4.4 and 5.4.5 [gm20020227_18 (Fig. 5.10); y-profiles (Fig. 5.11)], until the spectrum has been extracted and gm20020927_26_nsp (Fig. 5.12) has been formed.

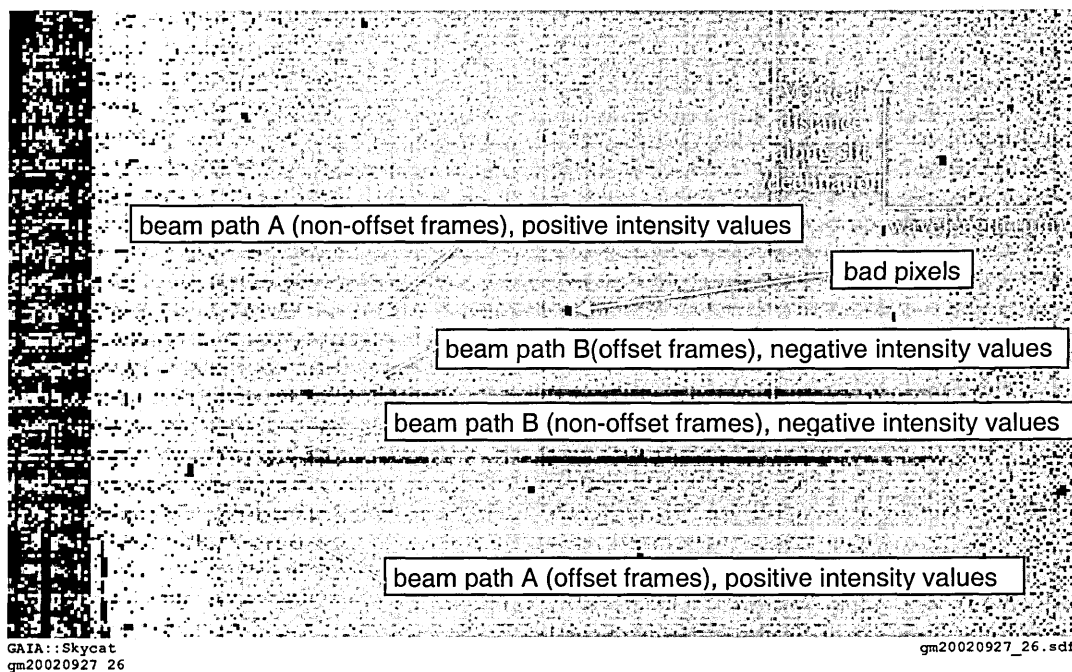


Fig. 5.10 The group frame gm20020927_26 of frames 26-73, comprising observations of 2002 NX₁₈ on 27 September 2002 UT at UKIRT using the lowN grating with the 4-pixel slit width. Note how the beams are much fainter than the previous standard star observation (Fig. 5.7). Very faintly, the electronic pickup noise can now be seen in the background as a ripple parallel to the spectra, since the contrast of the image is over a smaller range. Top portion of frame is not visible, but total usable portion of slit is shown.

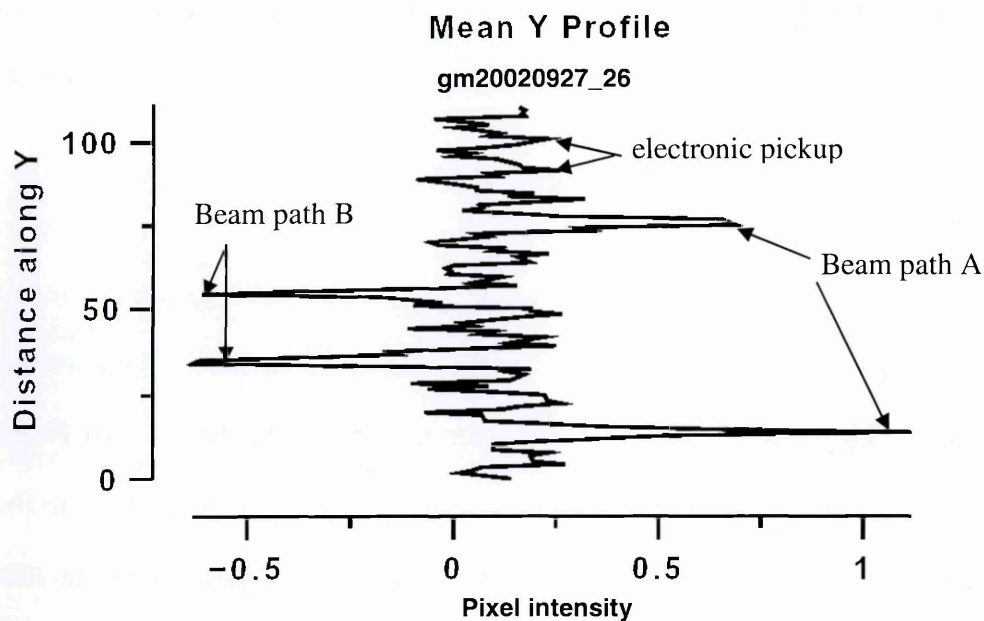


Fig. 5.11 Mean y-profile of gm20020927_26 (Fig. 5.10) from which the four row centres for optimum spectrum extraction can be determined. The electronic pickup noise can clearly be seen as a varying positive bias in intensity.

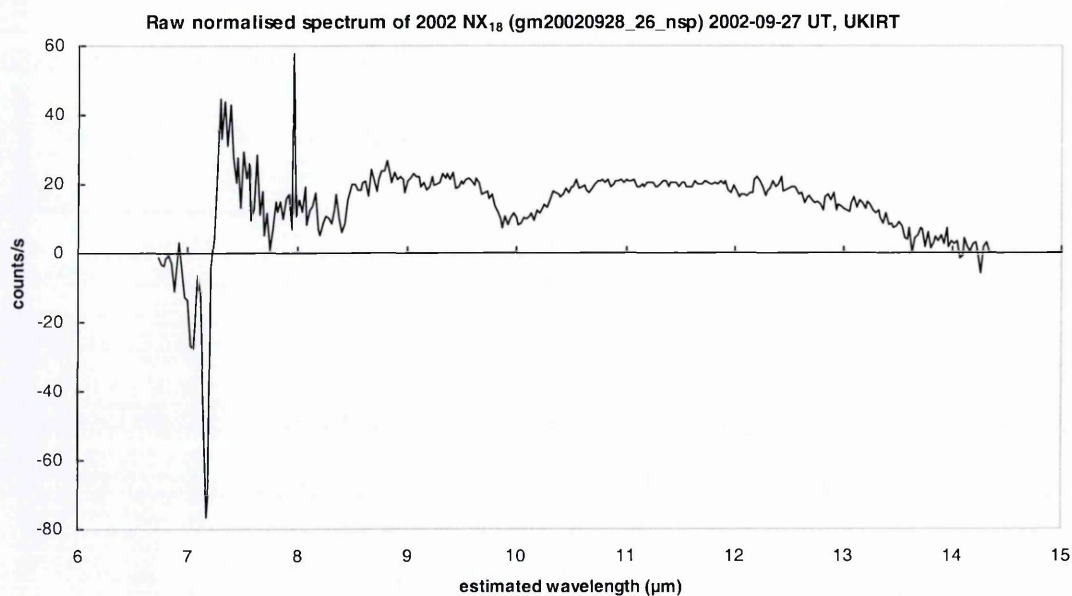


Fig. 5.12 gm20020927_26_nsp, the raw normalised spectrum of 2002 NX₁₈ observed on 27 September 2002 UT, outputted by ORAC-DR using a 3 pixel window diameter optimum extraction. Wavelength scale isvcalibrated by estimation in ORAC-DR and is inaccurate. The output from the whole grating is shown, but marked bad pixels have been removed.

The optimum extraction row centres were the same as for gm20020927_18, and in general the object row centre would rarely drift more than one pixel away from the standard star row centres, which proved useful when the object row centres were difficult to discern for the fainter objects.

5.4.8 *Electronic Pickup Noise*

There is a little understood source of noise in the array which we refer to as ‘electronic pickup’ and can be seen as a faint ripple of varying positive intensity in Figs. 5.10 and 5.11. IR arrays are generally coupled to a silicon array (a multiplexer). Each pixel from the multiplexer array is read out individually, in sequence; charge is not transferred from one pixel to another like in CCDs. Each pixel can be thought of as a capacitor; as photons are detected, charge builds up on the capacitor. The amount of charge on the capacitor can be read out at any time, without affecting the accumulated charge, referred to as non-destructive reads. A separate reset operation performs the charge removal.

Before charge accumulation begins, each pixel is reset to some initial value. Because of thermal noise it is not possible to know precisely what this initial value is from one reset operation to the next. This would introduce a fundamental uncertainty in the total charge measured if each pixel was only read once at the end of the integration period. To avoid this, Michelle performs doubly-correlated sampling, in which the array is read shortly after reset (non-destructively) and then again at the end of a specified integration period. The difference between the two readouts gives the desired counts per integration period. To lower the effect of readout noise the chip can be read several times. Averaging the successive differences reduces the effective readout noise.

When the exposure time is reduced to 0.1 s or less, Michelle is no longer able to use non-destructive reads. It may be that that this is the cause of the electronic pickup noise.

The noise is only significant in 4-pixel slit frames, where the exposure time is reduced to 0.1 s automatically in order to avoid saturating the array. When the 2-pixel slit was used on 29 September the noise is negligible. (433) Eros is bright enough that the contribution of electronic pickup is negligible. For (6455) 1992 HE we estimate the noise to be ~5%. In the case of observations of 2002 NX₁₈ observed on 27 and 30 September we estimate the uncertainty in flux calibration caused by the noise to be ~10%. For 2000 ED₁₀₄ on 30 September, and 2002 QE₁₅, the error may be as large as 30%, and for 2002 HK₁₂ up to 50%. The effect on the uncertainty in the estimation of effective diameter D_{eff} scales as the square root of the above uncertainty, but the effect on the uncertainty of η is negligible since the shape of the spectrum is not affected. For 2000 ED₁₀₄ on 30 September, 2002 HK₁₂, and 2002 QE₁₅, the electronic pickup noise is the largest contribution to the uncertainty in the flux calibration, of similar order to the thermal model uncertainties when measuring effective diameter D_{eff} and p_v . The contribution of the uncertainty in flux to the estimation of D_{eff} and p_v is described in Section 5.6.2. For our faintest object 1998 UO₁ the noise completely masks the signal, as described in Section 5.5.5.

5.4.9 Remaining ORAC-DR Processes

gm20020927_26_nsp, the raw normalised optimum extracted spectrum of 2002 NX₁₈, is the last data product of ORAC-DR that is used generally. This is due to the first remaining primitive, which divides by the reduced standard star frame std_18_sp after first attempting to cross-correlate and align the spectrum to std_18_sp, using the same criteria for the procedure as described in Section 5.4.5 (this often fails, although they are rarely misaligned by more than a pixel). The file this operation produces is gm20020227_26_dbs, and the shape is inaccurate due to the incorrect blackbody profiling which is a result of inaccurate wavelength calibration. However, when the different pixel diameter optimum

extraction was investigated (Section 5.4.10), the `_dbs` (divide by standard) frames were used because the inaccuracy of the wavelength calibration, and the consequent inaccuracy of the `_dbs` frames' shape, does not invalidate the S/N analysis of the `_dbs` frames.

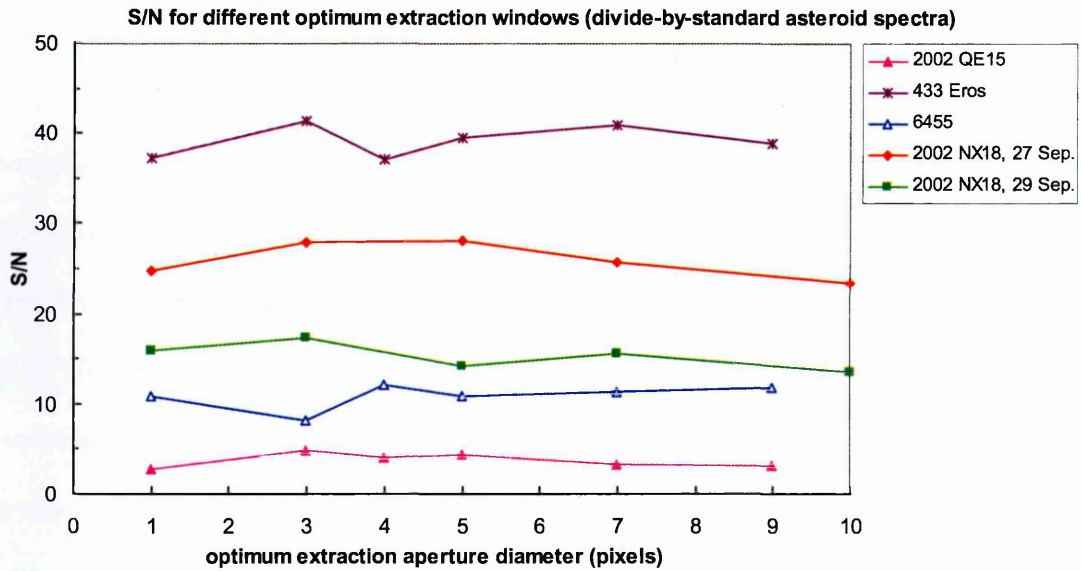
ORAC-DR fails to flux calibrate `gm20020927_26_dbs` since the flux calibration primitive is incompletely written and does not check for an N or Q standard magnitude, (producing a "Flux calibration problem – unknown waveband" warning message). Even if it was complete, however, we intend to use BS 7264 as a ratio star and BS 7001 as the standard star, and BS 7264 does not have a known N magnitude for it to be used as a standard.

5.4.10 Optimum Extraction Window Diameter Investigation

We investigated 1, 3, 4, 5, 7, 9 (or 10) pixel diameters for optimum extraction of both the appropriate ratio star and the object, ranging from the fainter sources to the brightest. We found the mean and the standard deviation (σ) of a flat part of the resulting divide-by-standard `_dbs` spectrum, 10.8 – 11.8 μm in the wavelength-calibrated-by-estimation scale, using the FIGARO routine 'istat'. The ratio of the mean to σ gives an estimate of the signal to noise (S/N) ratio (Fig. 5.13). ORAC-DR reduced standard frames (e.g. `std_11_sp`, the output from ORAC-DR's reduction of BS 7001 on 28 September 2002 UT) were investigated in the same way later on so as to include some more spectra.

Based on these results, an optimal extraction window of 3 pixels (0.64'') was found to yield the most favourable S/N. For the 30 September reduction 4 pixel (0.85'') optimum extraction windows (with the boundary between pixels becoming row centres) were used, because it was decided that the S/N was slightly better, particularly for brighter objects. The difference between the two methods, tested by checking the final flux-calibrated spectra using both windows on 30 September data, was negligible.

(a)



(b)

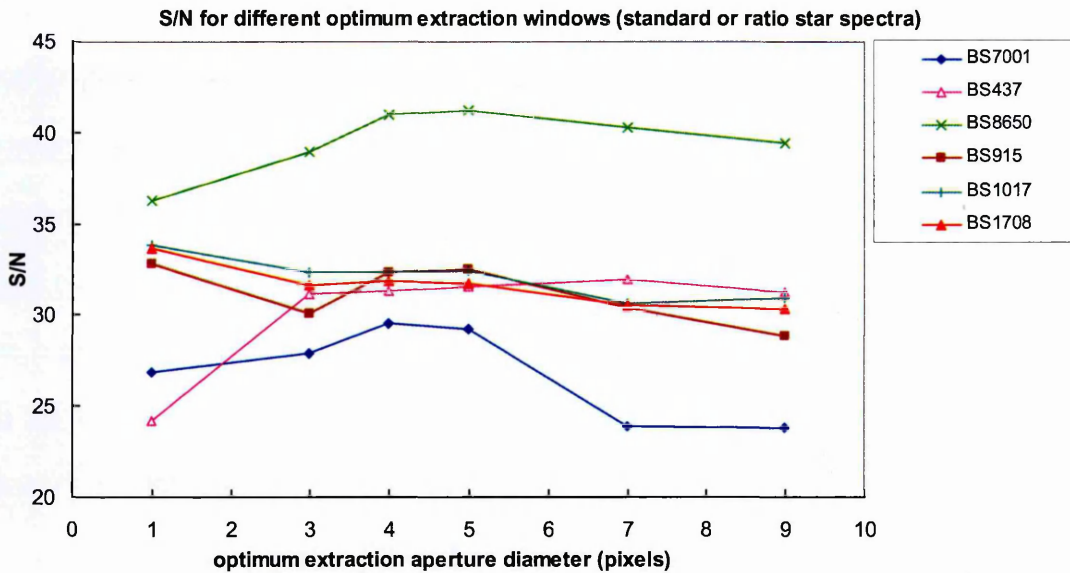


Fig. 5.13 Estimated signal-to-noise ratio (S/N) for a variety of sources ranging from the faint (2002 QE_{15}) to the bright (all the standard stars, Eros) using different optimum extraction window diameters. Our initial decision was to use a 3 pixel window diameter aperture, as this gave the best S/N for the fainter objects. Later on, the 4 pixel diameter, with row centres on the pixel edge, was investigated; we decided this gave better S/N overall, and it was subsequently used for 30 September 2002 UT data reduction. (a) S/N for asteroid spectra (`_dbs` “divide-by-standard” frames); (b) S/N for standard and ratio star spectra (`std_xx_sp` frames).

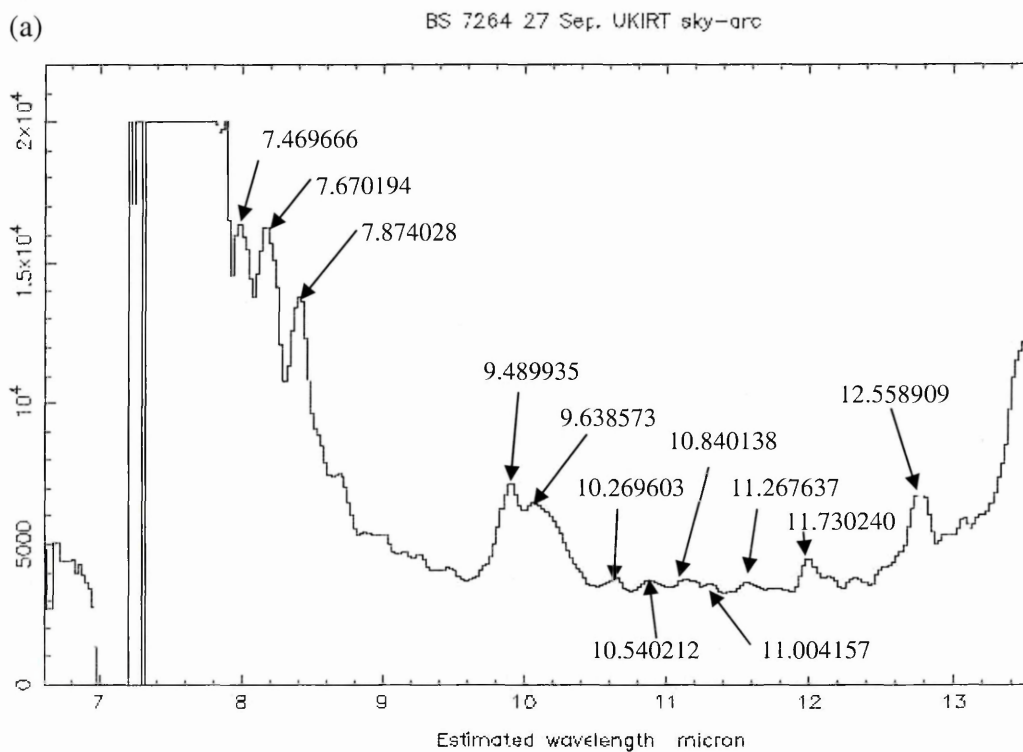
5.5 Data Reduction: from ORAC-DR to Flux-calibrated and Binned Spectra

5.5.1 Wavelength Calibration

Wavelength calibration was carried out by making use of atmospheric transmission versus wavelength graphs for Mauna Kea generated using the program IRTRANS4 with the parameters: altitude = 4200 m, airmass = 1.0, H₂O column 1.2 mm, resolving power = 3000, and were obtained from the UKIRT webpage <http://www.jach.hawaii.edu/UKIRT/astronomy/utis/atmos-index.html>.

The arc file generated by ORAC-DR for BS 7264 on 27 September, produced as described in Section 5.4.4, is arc_g18. This is collapsed to one dimension (KAPPA command 'collapse') along the dispersion (x) axis to form a 1D spectrum, and clipped to less than 20000 counts (FIGARO command 'clip', 20000 counts for all 4-pixel slit width arcs, 50000 counts was appropriate for 2 pixel slit width 29 September data) [Fig. 5.14 (a)]. An example of a Q-band sky-arc is given in Fig. 5.14 (b).

Fig. 5.14



(b)

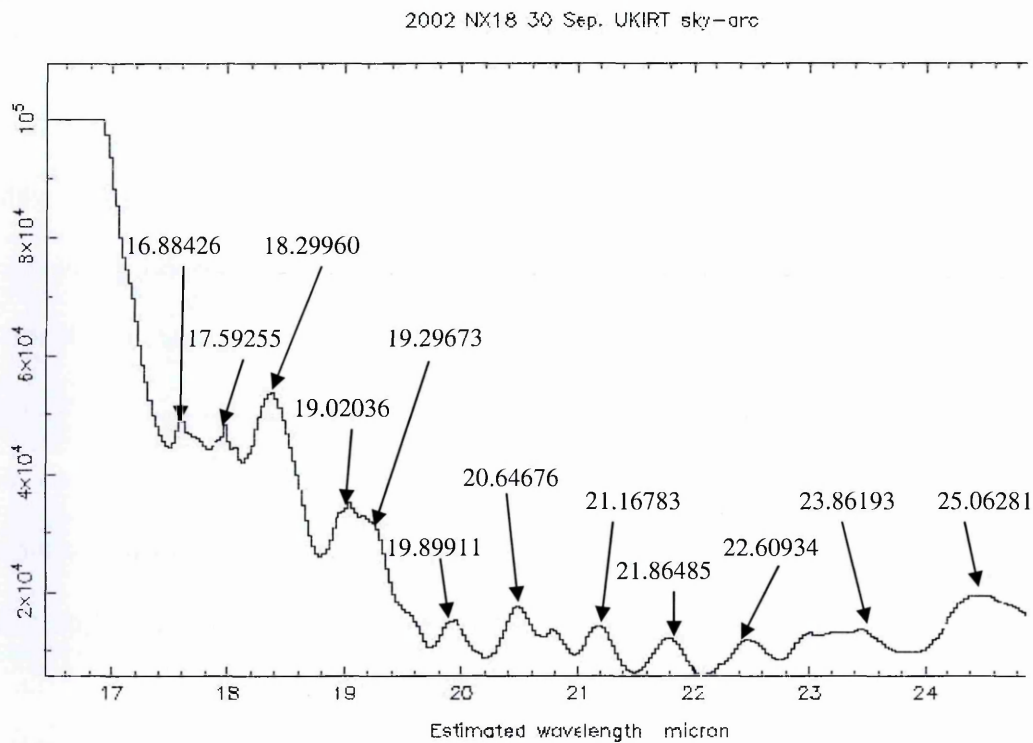
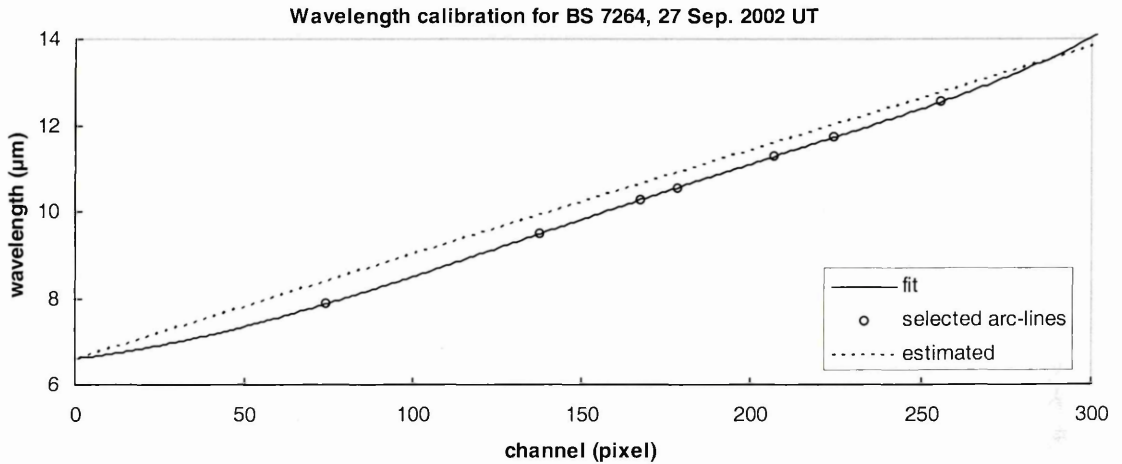


Fig. 5.14 Sky-arc spectra for: (a) N-band observation of BS 7264 on 27 September 2002 UT (*arc_g18*); (b) Q-band observation of 2002 NX₁₈ on 30 September 2002 UT (*arc_g64*). ORAC-DR incorrectly calibrates wavelengths by estimation using frame header grating positions and dispersions. The correct wavelengths associated with the peaks in the spectrum are obtained with reference to the model atmospheric transmission spectra.

The FIGARO command ‘arc’ is used to interactively fit a dispersion polynomial to the sky-arc given the correct wavelengths of the peaks in the arc from reference to the model atmospheric transmission spectrum, as marked on Fig. 5.14. Some trial-and-error is required to obtain a satisfactory fit. Sometimes it is necessary to vary the order of the polynomial fit from 3rd order to 5th order, especially if the fit is not monotonic (i.e. at some point the wavelength decreases as the x-axis increases). Sometimes we reject particular peaks if the RMS (root mean square) difference between it and the polynomial is large (indicates the peak may be incorrectly selected or has drifted from the modelled wavelength position). Not all the peaks marked in Fig. 5.14 are used, often a reliable fit is found by using five or six of the most dependable lines. Figure 5.15 shows two example

wavelength calibrations. Typical RMS difference between the selected arc-lines and the fitted polynomials is between 0.01-0.02 μm .

(a)



(b)

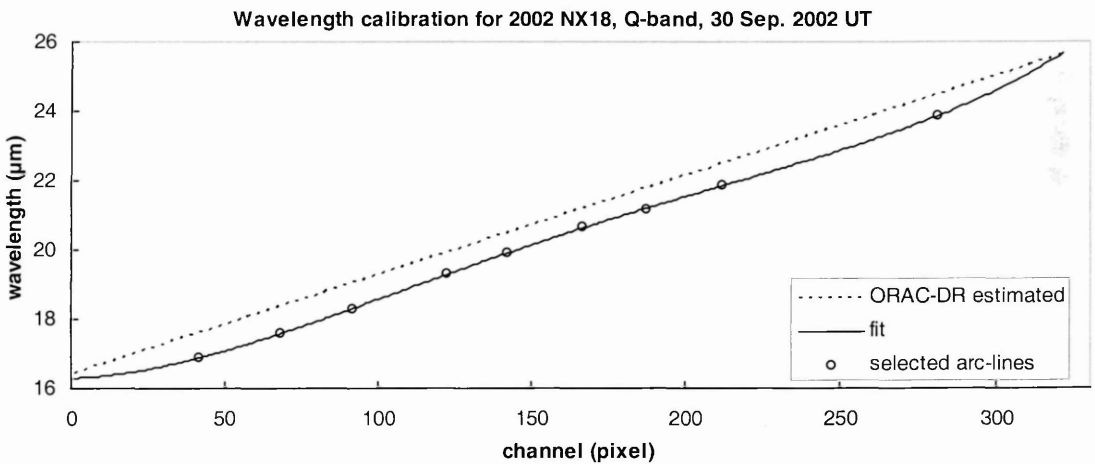


Fig. 5.15 Example wavelength calibrations, showing ORAC-DR wavelength-calibrated-by-estimation and polynomials fitted using 2 pixels FWHM for arc-line selection. (a) BS 7264 on 27 Sep. ‘arc_g18’, 3rd order polynomial fit, 0.01 μm RMS difference between fit and selected arc-lines; (b) 2002 NX₁₈ on 30 Sep., ‘arc_g64’, 4th order polynomial fit, 0.02 μm RMS difference.

The final result is a wavelength value for each dispersion (x) axis pixel that can be applied to the extracted spectrum from the associated group file.

5.5.2 Black Body Profiling of Standard Star Spectrum

Once the BS 7264 ratio star spectrum (gm20020927_18_nsp) and the BS 7001 standard star spectrum (gm20020927_10_nsp) for the 27 September 2002 UT observation of 2002 NX₁₈ have been wavelength calibrated, they can now be divided by a black body profile formed using Eq. 4.8 and the temperatures listed for each standard star in Table 5.5. The profile is normalised to one at the grating wavelength by dividing by the value of the profile for the pixel nearest to the grating wavelength (10.471 μm for N-band, 21.028 μm for Q-band).

An example of the difference in shape between the ORAC-DR black body profile, calculated using wavelengths calibrated by estimation, and the manually calculated profile after the wavelengths have been calibrated using the sky-arcs is given in Fig. 5.16: the normalised black body profile of (433) Eros ratio star BS 8650 observed on 28 September 2002 UT, calculated by both methods, between 8 and 13 μm . The manually calculated black body profile has a steeper gradient at shorter wavelengths. The main reason for the difference between the two shapes is the different pixel the profile is normalised with respect to when the wavelength calibration has been performed.

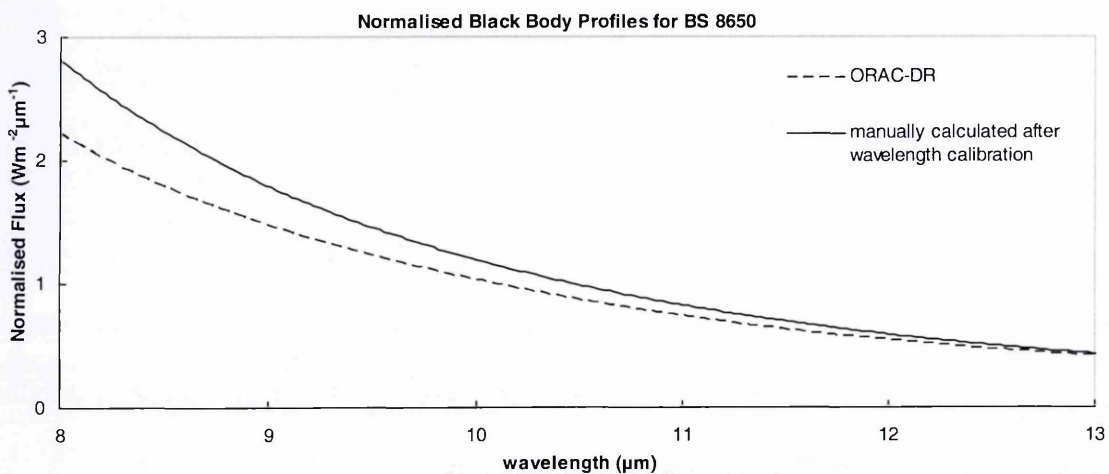


Fig. 5.16 Normalised black body profiles for (433) Eros ratio star BS 8560, calculated by ORAC-DR before wavelength calibration (dashed line) and manually calculated after wavelength calibration (solid line).

5.5.3 Flux Calibration

In the majority of objects observed in the N-band, including 2002 NX₁₈ on 27 September 2002 UT, a ratio star, whose *N* magnitude is not known but which is close on the sky to the asteroid, is observed, as well as a standard star. To flux calibrate the object spectrum the ratio star spectrum must first be flux calibrated.

Using separate ratio and standard stars instead of standard stars alone has the advantage that a ratio star for correction of atmospheric transmission could be chosen closer in the sky to the asteroid, since there were more stars to choose from, but there is additional error introduced by the need to flux calibrate the ratio star. If a standard star close enough to the object in the sky has been observed, then it can be used as the ratio star as well. For all Q-band observations standard stars were also used as ratio stars.

Table 5.9
Zero magnitude flux for Vega at given filter wavelengths and bandwidths

Filter name	$\lambda_{\text{iso}}^{\text{a}}$ (μm)	$\Delta\lambda^{\text{b}}$ (μm)	F_0 ($\text{W m}^{-2} \mu\text{m}^{-1}$)
N	10.472	5.19	9.63×10^{-13}
Q	20.130	7.8	7.18×10^{-14}

Notes. ^aThe infrared isophotal wavelengths and flux densities are taken from Table 1 of Cohen *et al.* (1992), based on the UKIRT filter set and the atmospheric absorption at Mauna Kea. The isophotal wavelength is defined by:

$$F(\lambda_{\text{iso}}) = \frac{\int F(\lambda)S(\lambda)d\lambda}{\int S(\lambda)d\lambda}$$

where $F(\lambda)$ is the flux density of Vega and $S(\lambda)$ is the (detector quantum efficiency) \times (filter transmission) \times (optical efficiency) \times (atmospheric transmission).

^bThe filter full width at half maximum.

Table 5.9 gives the zero magnitude flux for standard star Vega (BS 7001) at N- and Q-band wavelengths and bandwidths based on the UKIRT filter set, from Tokunaga (2000). From the isophotal wavelength λ_{iso} (which is the wavelength which must be assigned to the monochromatic flux density derived from a broadband measurement, equivalent to the grating wavelength) and the filter full width at half maximum $\Delta\lambda$ [$(\lambda_{\text{iso}} - 0.5\Delta\lambda)$ and

($\lambda_{iso}+0.5\Delta\lambda$)] we can assign sensible waveband ranges 7.877 – 13.069 μm for the N-band and 16.23 – 24.03 μm for the Q-band.

The absolute flux of the standard star can be calculated from its magnitude (M_{std}) given in Table 5.5 and its zero magnitude flux F_0 given in Table 5.9:

$$F_{std} = F_0 10^{\frac{M_{std}}{-2.5}} \quad (5.13)$$

An estimated correction to the airmass of the ratio star is applied:

$$F_{std}(\chi_{rat}) = F_{std} 10^{\left(\frac{(\chi_{std}-\chi_{rat})k_M}{-2.5}\right)} \quad (5.14)$$

where χ_{std} is the airmass of the standard star, χ_{rat} is the airmass of the ratio star, and k_M is the extinction coefficient. The airmass of the observation is assumed to be the average of the start and end airmasses. The median extinction for the N-band is $k_N = 0.151 \pm 0.017$ mag./airmass from the UKIRT website <http://www.jach.hawaii.edu/UKIRT/astronomy/exts.html>. The absolute flux of the ratio star is calculated from:

$$F_{rat} = F_{std}(\chi_{rat}) \frac{\int_{7.88\mu\text{m}}^{13.07\mu\text{m}} C_{rat} d\lambda}{\int_{7.88\mu\text{m}}^{13.07\mu\text{m}} C_{std} d\lambda} \quad (5.15)$$

where C_{rat} is the counts per second of the ratio star at a given wavelength (the output of gm20020927_18_nsp) and C_{std} is the counts per second of the standard star at a given wavelength (gm20020927_10_nsp) which are integrated in Eq. 5.15 over the waveband. C_{rat} and C_{std} are the counts per second before the ratio star spectrum is divided by a black body profile. For each pixel p_n :

$$\begin{aligned} \int_{7.88\mu\text{m}}^{13.07\mu\text{m}} C_{rat} d\lambda &= \sum_{n(\lambda=7.88\mu\text{m})=1}^{n(\lambda=13.07\mu\text{m})} C_{rat}(n)(\lambda(p_{n+1})-\lambda(p_n)) \\ \int_{7.88\mu\text{m}}^{13.07\mu\text{m}} C_{std} d\lambda &= \sum_{n(\lambda=7.88\mu\text{m})=1}^{n(\lambda=13.07\mu\text{m})} C_{std}(n)(\lambda(p_{n+1})-\lambda(p_n)) \end{aligned} \quad (5.16)$$

C_{rat} and C_{std} can be normalised to one at the grating wavelength (just as is done to the black body profile before dividing the counts per second spectra by it) and then multiplied by F_{rat} or F_{std} respectively to produce a flux calibrated spectrum for the ratio or standard star. Figure 5.17 shows example flux calibrated spectra for 2002 NX₁₈'s ratio and standard stars. Table 5.10 shows the calculated N-band fluxes for the ratio stars.

Example wavelength calibrated counts-per-second asteroid spectra C_{ast} are shown in Fig. 5.18. They are divided by the ratio star spectra C_{rat_dbb} (which have themselves been divided by a black body spectrum) and multiplied by the absolute flux of the ratio star F_{rat} given in Table 5.10 (or F_{std} if a standard star is also to be used as a ratio star) to give the flux calibrated asteroid spectrum $F_{ast}(\lambda)$:

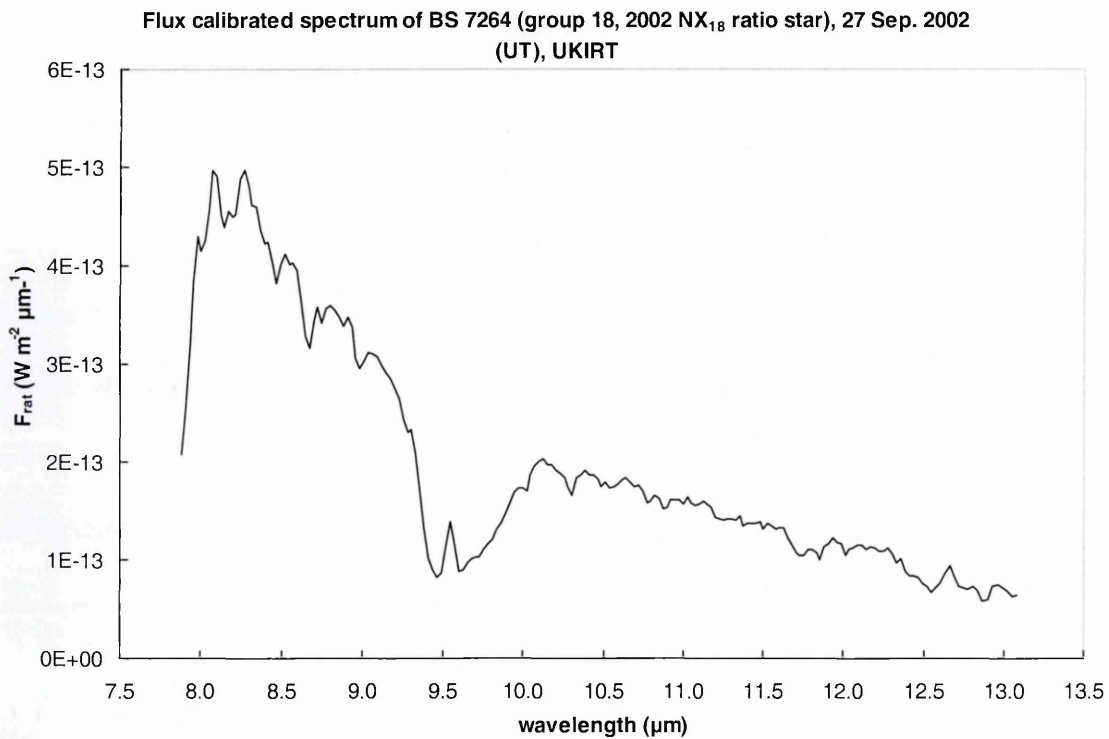
$$F_{ast}(\lambda) = F_{rat} \frac{C_{ast}(\lambda)}{C_{rat_dbb}(\lambda)} \quad (5.17)$$

Table 5.10
Calculated absolute N-band fluxes for ratio stars

Star	For asteroid:	Date	Group	Std. star used	$F_{rat} (\times 10^{-13} \text{ W m}^{-2} \mu\text{m}^{-1})$	N (mag.)
BS 8650	(433) Eros	28 Sep.	95	BS 7001	5.29	0.65
		29 Sep.	127	BS 617	4.69	0.78
BS 1030	(6455) 1992 HE	29 Sep.	147	BS 617	2.73	1.37
		30 Sep.	133	BS 1457	2.96	1.28
BS 1136	(6455) 1992 HE	29 Sep.	176	BS 617	2.94	1.29
		29 Sep.	204	BS 617	3.31	1.16
BS 8414	(66063) 1998 RO ₁	29 Sep.	75	BS 617	5.49	0.61
BS 915	1998 UO ₁	28 Sep.	119	BS 1708	4.72	0.77
BS 7615	(53789) 2000 ED ₁₀₄	29 Sep.	41	BS 617	2.68	1.39
		29 Sep.	61	BS 617	1.83	1.80
BS 437	2002 HK ₁₂	27 Sep.	82	BS 7001	2.60	1.42
		28 Sep.	63	BS 7001	2.79	1.34
BS 7264	2002 NX ₁₈	27 Sep.	18	BS 7001	1.82	1.81
		29 Sep.	9	BS 617	2.26	1.57
BS 7776	2002 NX ₁₈	30 Sep.	113	BS 7525 (grp. 117)	5.28	0.65

Note. Absolute fluxes for standard stars which were also used as ratio stars are obtained from their given N/Q magnitudes (Table 5.5), and not listed here.

(a)



(b)

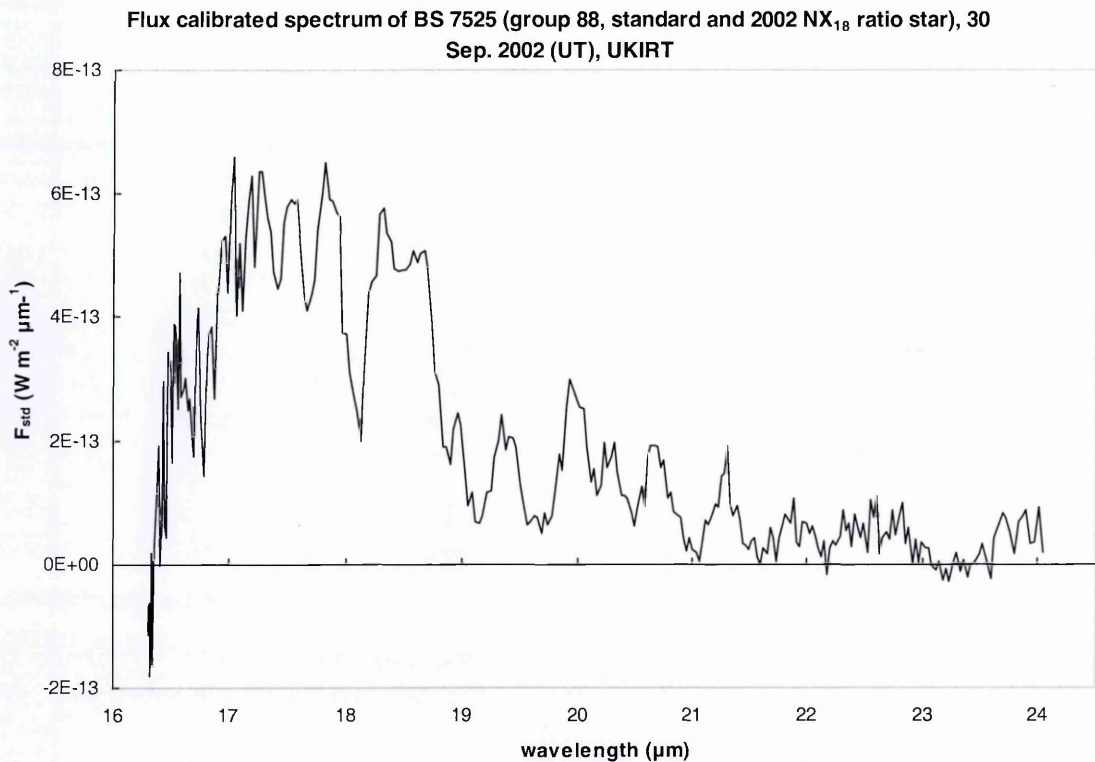
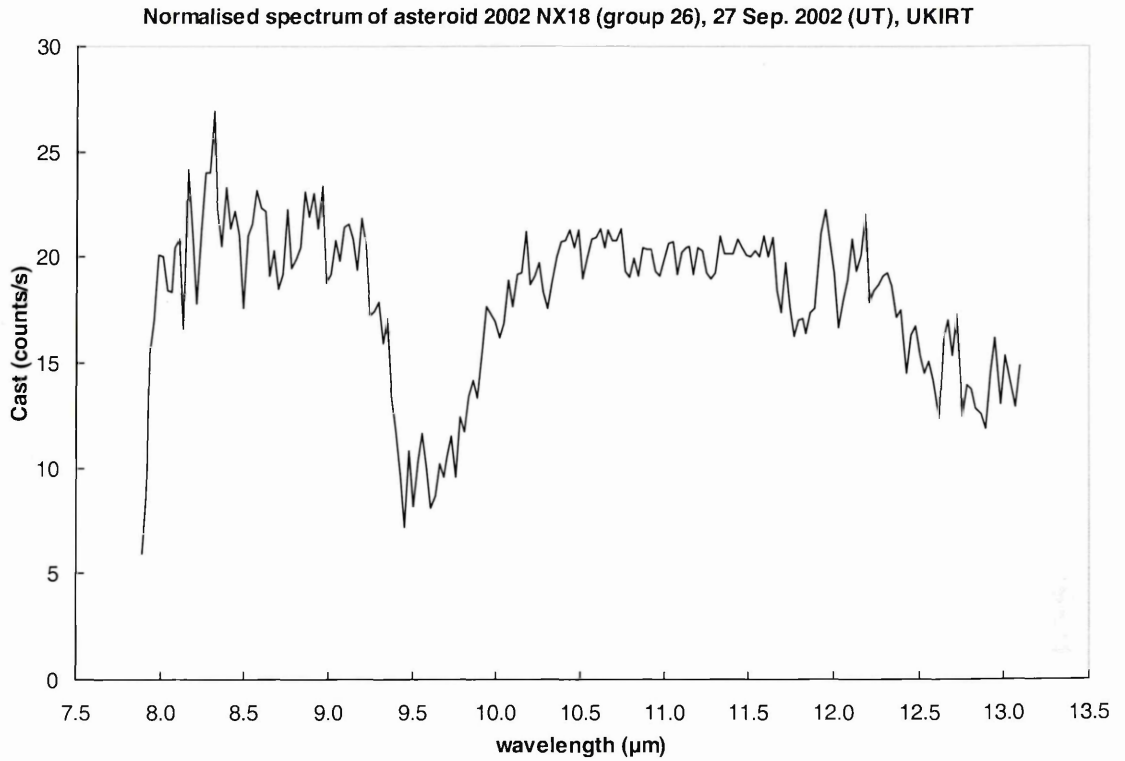


Fig. 5.17 (a) Flux-calibrated spectrum of 2002 NX_{18} ratio star BS 7264, N-band (7.08 - 13.07 μm). (b) Flux-calibrated spectrum of 2002 NX_{18} standard/ratio star BS 7525 on 30 September 2002 UT, Q-band (16.4 - 24.0 μm). Bad pixel values are removed (four or five points at start of Q-band spectrum).

(a)



(b)

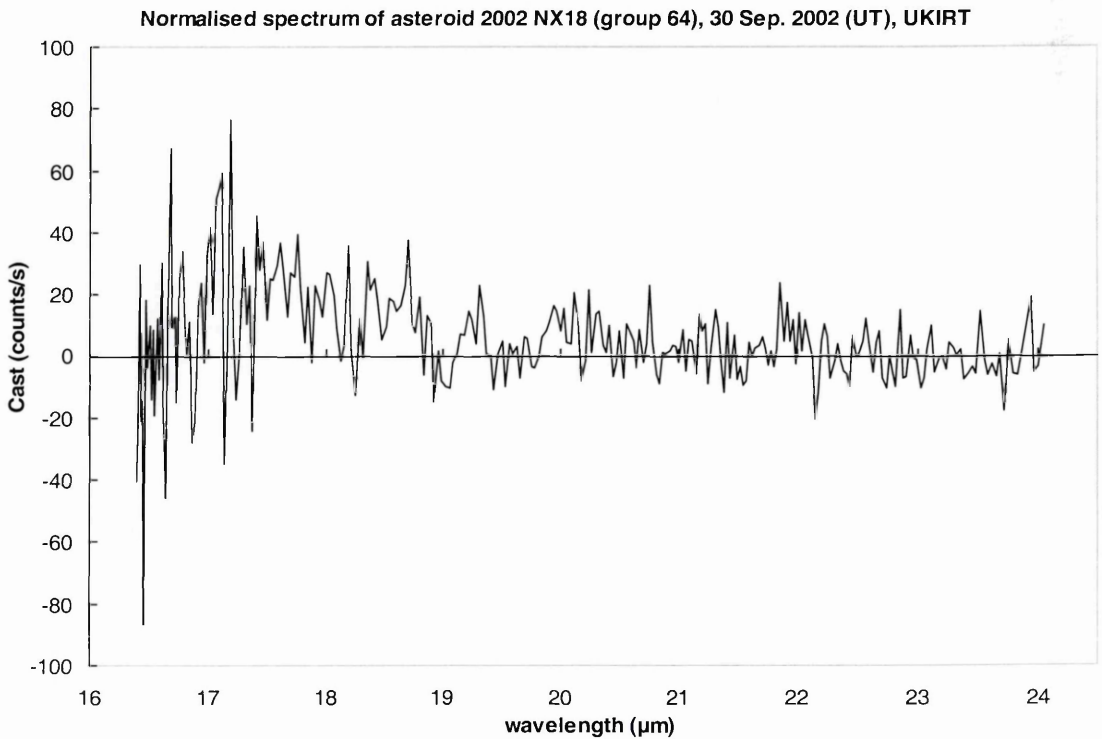


Fig. 5.18 Normalised counts-per-second spectra of 2002 NX₁₈. (a) N-band (7.08-13.0 μm), 27 September 2002 UT (gm20020927_26_nsp). (b) Q-band (16.4-24.2 μm), 30 September 2002 UT (gm20020930_64_nsp); Bad pixel values are removed (four or five points at start).

Some uncertainty in the absolute flux calibration is due to imperfectly accounting for differing atmospheric absorption between the standard star and the ratio star. The worst case was estimated by treating the bright standard star BS 7001 (Vega) (group 10, $\chi = 1.226$) observed on 27 September 2002 UT, as if it were a target asteroid, flux-calibrating it using BS 7001 observed at a much higher airmass ($\chi = 1.995$, group 74). Figure 5.19 shows the resulting flux-calibrated spectrum. An estimated correction to the airmass of the ratio star is applied using Eq. 5.14. The measured magnitude was $N = -0.24$. Compare this with its known magnitude ($N = 0.00$ mag.) and we see that the maximum uncertainty in flux calibration is about 25%.

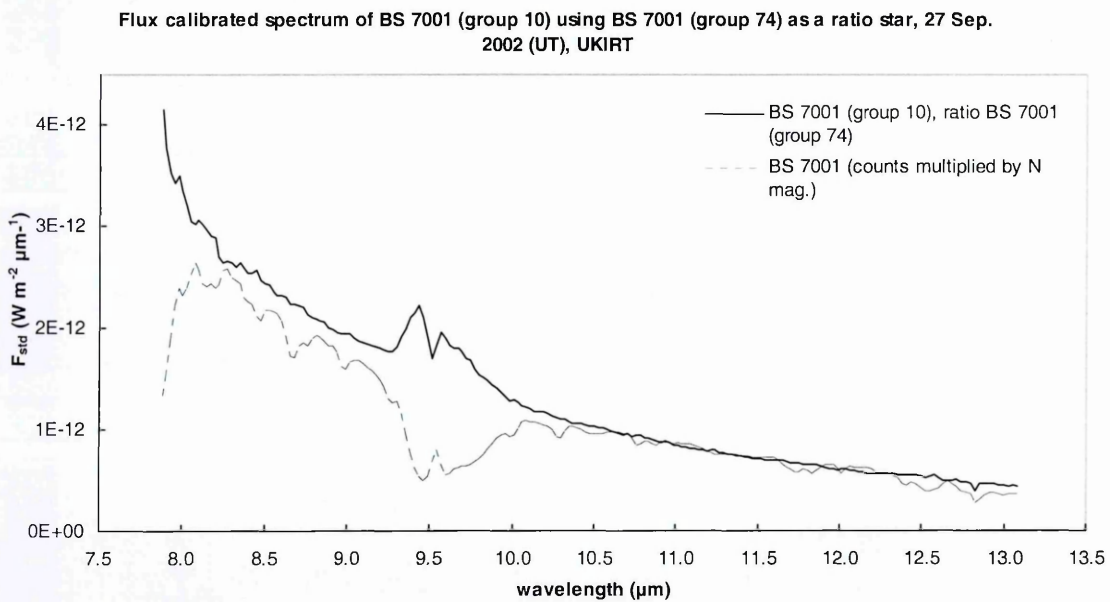


Fig. 5.19 Flux-calibrated spectrum of BS 7001 observed between 06:47 and 07:00 on 27 September 2002 UT at UKIRT (group 10) using Michelle instrument in spectroscopy mode, at an airmass of between 1.209 and 1.243. BS 7001 observed between 09:52 and 09:05 UT (group 74) at an airmass of between 1.884 and 2.025 is used as a ratio star (solid line) to flux calibrate group 10 observation. Compare with flux calibrating this standard star directly by multiplying the counts per second C_{std} by its known magnitude $N = 0.00$ ($9.63 \times 10^{-13} \text{ W m}^{-2} \mu\text{m}^{-1}$) (dashed line).

Where ratio stars' magnitudes were independently measured on different nights (Table 5.10), the difference in magnitude can provide an estimate of the typical uncertainty. Unfortunately, only in one example do we have two measurements of a ratio star on a night

not including 29 September, when there was considerable cirrus: ratio star BS 437 on 27 and 28 September. The measured magnitudes in this case are 6.8% different. Including the 29 September observations, the average difference is 14.5%, the high value due to the cloud on that night. Therefore we adopt a 7% uncertainty from this source of error, which is considerably smaller than thermal model dependent uncertainties (Section 5.6.2).

The wavelength-dependent uncertainty contributed by differing atmospheric absorption between the ratio star and the asteroid was estimated on two different nights by dividing a bright standard star's spectrum with two different ratio stars' spectra at different airmasses, then taking the ratio of the two measured fluxes for the standard star. This uncertainty will affect the shape of the spectrum, so will have an impact on the accuracy of the derived η . The results are given in Fig. 5.20. The resulting scatter at different wavelengths is due solely to the differing atmospheric absorption from using ratio stars at different airmasses and at different parts of the sky. Overall, the uncertainty was found to be between 1 and 3% for the N-band between 8-9.3 μm and 10.0-12.5 μm (the spectra from the ozone absorption band 9.3-10.0 μm was excluded) but would be smaller for our targets because the airmass differences between the asteroids and the ratio stars were smaller. For $\lambda > 12.5$ μm we found the uncertainty to be between 4 and 6%. The shape of the flux-calibrated asteroid spectrum is sensitive to this source of uncertainty. Because we are particularly interested in the shape of the spectrum, in order to measure the beaming parameter η when using the Near-Earth Asteroid Thermal Model (NEATM), we decided to exclude the measured N-band asteroid fluxes at wavelengths greater than 12.5 μm .

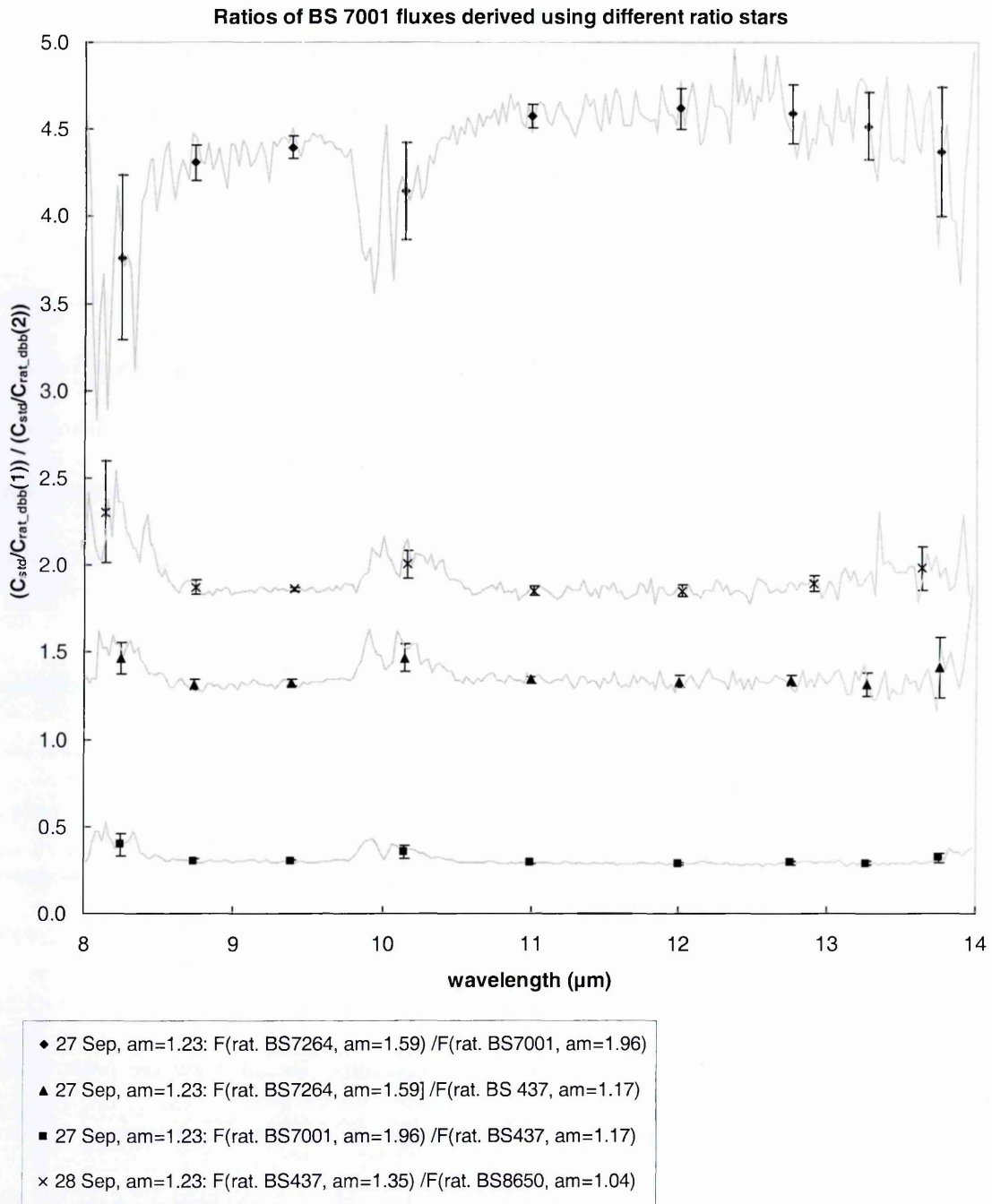


Fig. 5.20 Estimating the wavelength-dependent uncertainty due to differing atmospheric absorption between the ratio star and the asteroid, by dividing fluxes of BS 7001 found using different ratio stars.

5.5.4 Binning Spectra

The raw spectra in the N- and Q-bands covered between 8-12.5 μm and 18-25 μm respectively with a resolution of about 0.03 μm per pixel (the dispersion was non-linear as described in Section 5.5.1). A Fortran program 'spec' was written that binned the spectra to a given bin size over selected ranges. For a given bin's start wavelength λ_{start} and end wavelength λ_{end} the binned flux F_{bin} would be:

$$F_{bin} = \frac{\sum_{n(\lambda_{start})=1}^{n(\lambda_{end})} F_n (\lambda_{n+1} - \lambda_n)}{\lambda_{end} - \lambda_{start}} \quad (5.18)$$

The N-band spectra were binned over wavelength ranges varying between 0.26 μm (10 pixels) and 1.53 μm (51 pixels) depending on the data quality for that object at that wavelength. The flux measured in the atmospheric ozone absorption feature at 9.3-10 μm is excluded. The Q-band spectra were binned over wavelength ranges between 0.75 μm (25 pixels) and 1.62 μm (54 pixels). They were also binned for more accurate flux measurements between 17.4 and 18.8 μm where the best signal to noise ratio is obtained due to low atmospheric absorption. 'spec' also measures the standard error over the bin range to provide an uncertainty for the binned fluxes.

Figure 5.21 shows the flux-calibrated asteroid spectra. The binned thermal infrared fluxes, the bin size in pixels, and the standard error for each flux-calibrated spectrum can be found in Appendix E.

Fig. 5.21

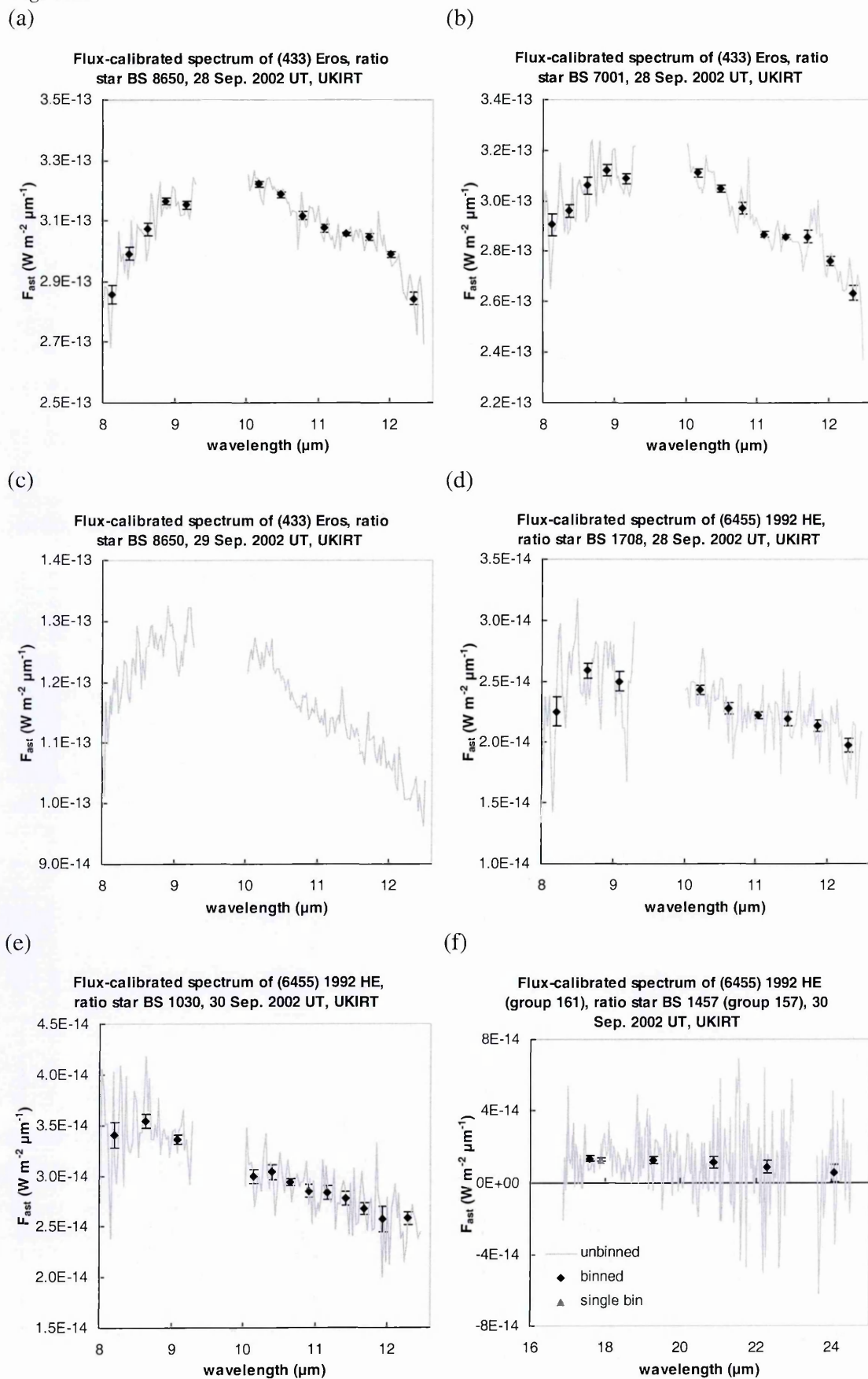
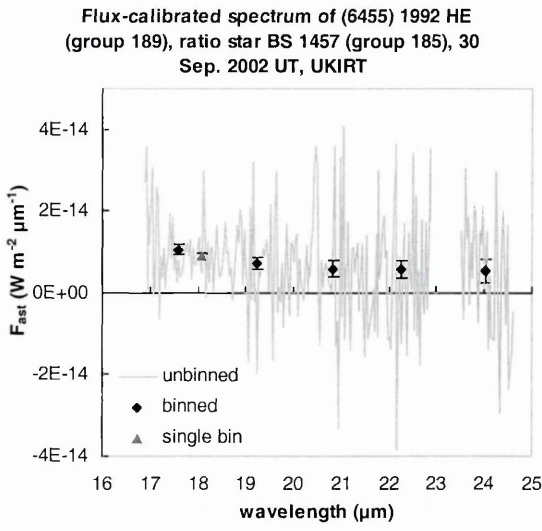
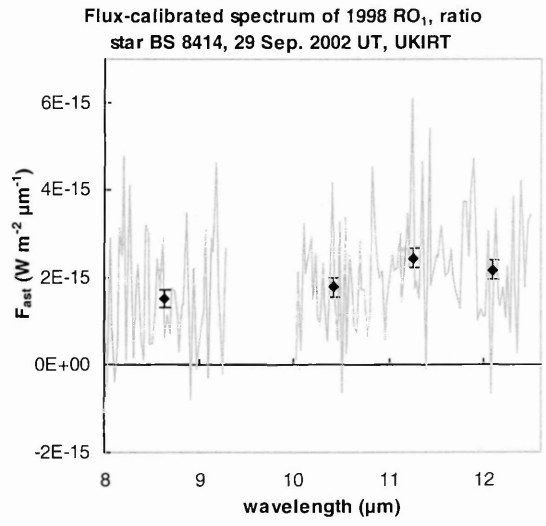


Fig. 5.21 continued.

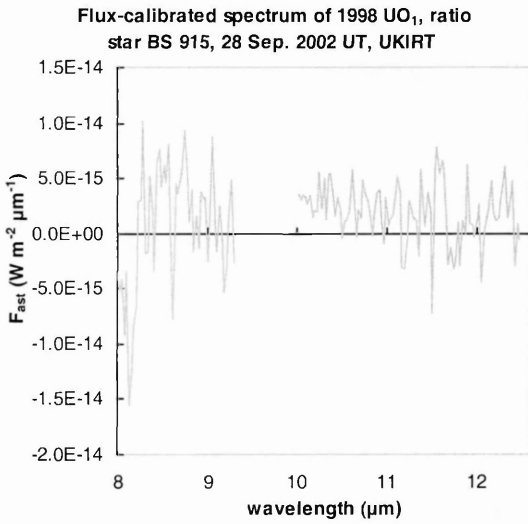
(g)



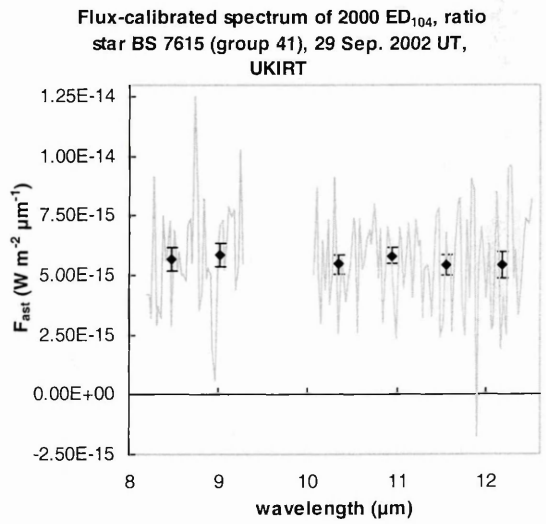
(h)



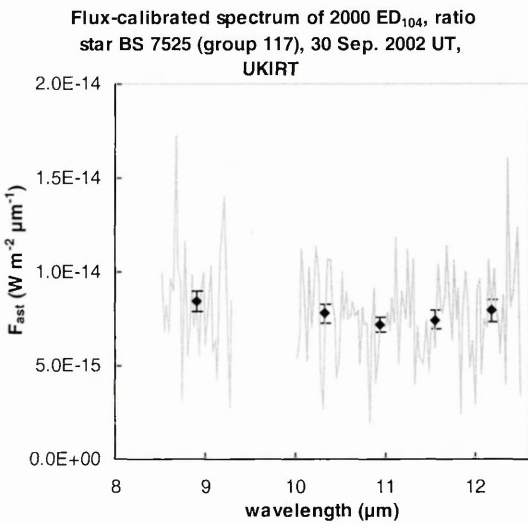
(i)



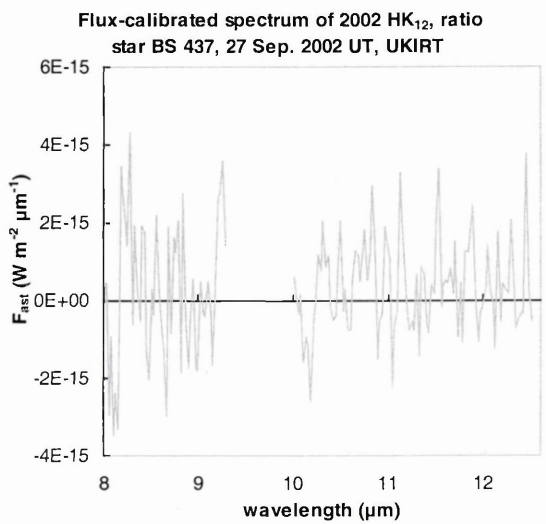
(j)



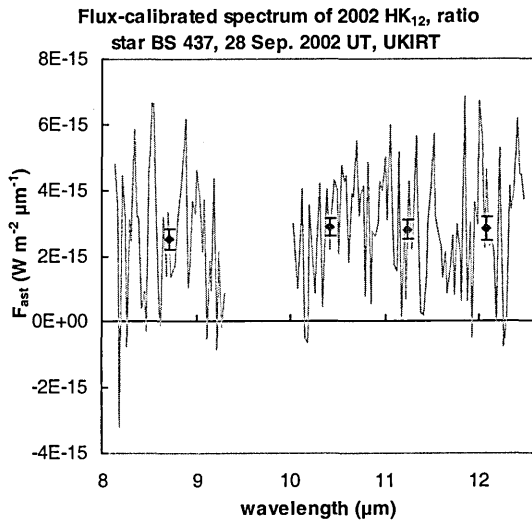
(k)



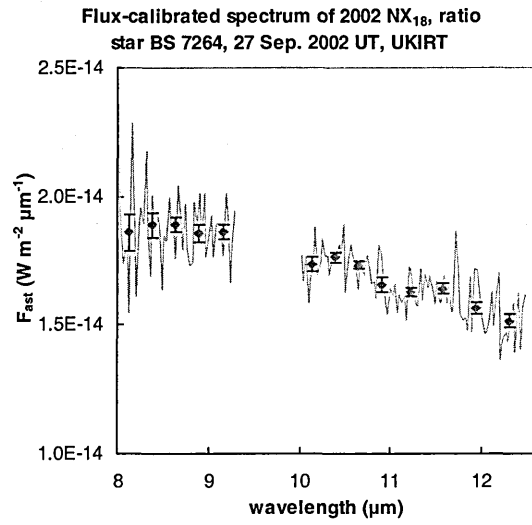
(l)



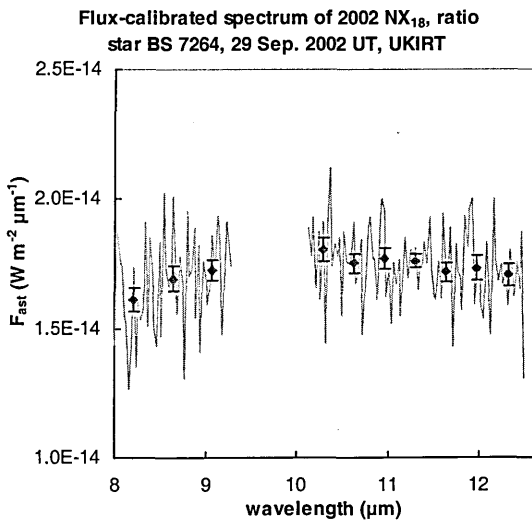
(m)



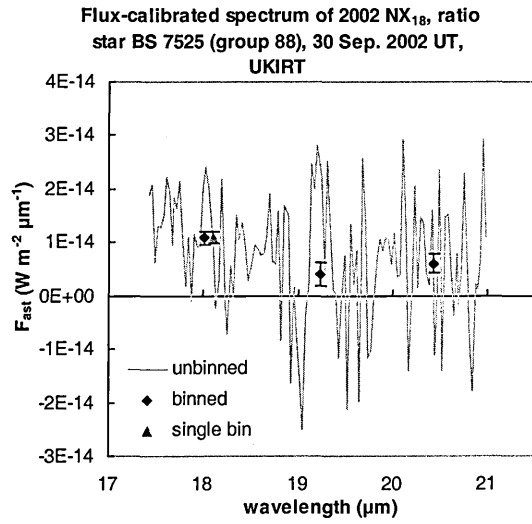
(n)



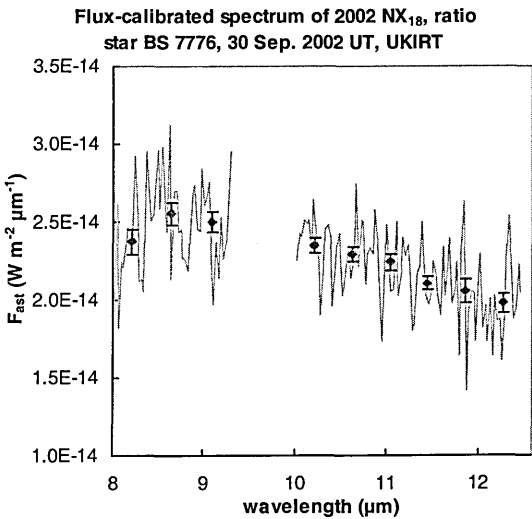
(o)



(p)



(q)



(r)

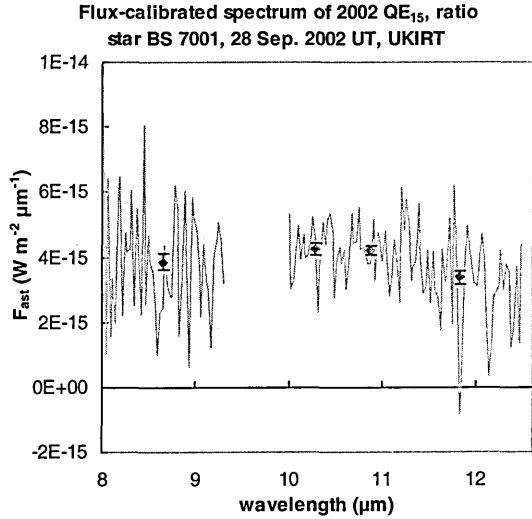


Fig. 5.21 (Previous 3 pages). Flux-calibrated spectra of asteroids observed 27-30 September 2002 UT at UKIRT using the Michelle instrument in spectroscopy mode (grey solid lines). N-band spectra are 8.0-12.5 μm with the ozone absorption feature at 9.3-10.0 μm excluded. In a few noisy cases the spectra start slightly after 8.0 μm , up until 8.5 μm . Binned fluxes are also shown (diamonds); error bars represent the standard error; data are given in Appendix E. For Q-band spectra, there is also a single binned flux value for the most noise-free region between 17.4 and 18.8 μm (triangles). In the cases of 1998 UO₁ observed on 28 September (i) and 2002 HK₁₂ on 27 September (l) no spectrum was found in the group images, and the noise spectrum shown is extracted from the same rows in the group image that the ratio star spectrum was extracted from.

5.5.5 Notes on Individual Objects

(433) Eros

There was some concern over the choice of ratio star BS 8650, because it is known to be a binary, and hence its temperature profile may not have a similar spectral shape to that of the Sun. Standard star BS 7001 (Vega) was used to directly flux calibrate the 28 September 2002 UT spectrum [Fig. 5.21 (b)], as well as using BS 8650 [Fig. 5.21 (a)], in order to compare the resulting best-fit η found when fitting thermal models (Section 5.6.3).

The flux measured on the 29 September [Fig. 5.21 (c)] is much lower (estimated N mag. of 2.31 as opposed to 1.26), despite Eros having a flat visual lightcurve at the time (lightcurve amplitude ~ 0.10 mag., Section 3.9.1). This is probably due to cirrus on 29 September, which resulted in much lower normalised asteroid flux. The 29 September spectrum is therefore not binned, since it is not instructive to fit thermal models to these data.

(6455) 1992 HE

The 28 September 2002 UT observations of (6455) 1992 HE give an estimated N mag. of 4.20 (with BS 1017 as ratio star) and 4.07 (with BS 1708 as ratio star). The BS 1708 flux-calibrated spectrum [Fig. 5.21 (d)] was chosen for binning, simply because it followed the default sequence of observing a ratio star before the object. Like (433) Eros, (6455)

1992 HE has much lower flux-calibrated N-band spectra on 29 September 2002 UT despite having a low visual lightcurve amplitude (~ 0.2 mag., Section 3.9.4), and so the spectra were not binned. (6455) 1992 HE was observed on 30 September, and both BS 1030 and BS 1457 were used as ratio stars. Since the ratio star BS 1030 was observed at a closer airmass than the standard star BS 1457 [(6455) 1992 HE $\chi = 1.70$; BS 1030 $\chi = 1.67$; BS 1457 $\chi = 1.86$] the flux-calibrated spectrum obtained using BS 1030 as a ratio star was binned for thermal model fitting [Fig. 5.21 (e)].

(6455) 1992 HE is one of two asteroids observed in the Q-band, on 30 September [Fig. 5.21 (f) and (g)]. The flux-calibrated spectra are binned between 16.9 and 24.5 μm , excluding a particularly noisy portion due to water absorption in the atmosphere between 23.0 μm and 23.6 μm .

(66063) 1998 RO₁

(66063) 1998 RO₁ is the only asteroid with a flux-calibrated asteroid spectrum observed on 29 September [Fig. 5.21 (h)], when there was known to be cirrus, that was not observed on other nights. The uncertainty in the fluxes must therefore be increased. We can estimate the percentage increase in uncertainty by calculating the average difference in N-band fluxes for asteroids observed on 29 September and also on other nights: (433) Eros, (6455) 1992 HE, (53789) 2000 ED₁₀₄, 2002 NX₁₈, using the magnitudes given in Appendix E (converted to $\text{W m}^{-2} \mu\text{m}^{-1}$). The percentage differences for these objects are, respectively: 163%, 126%, 66%, 20%. The average difference in N-band fluxes between 29 September and another night is 94%. The uncertainty in the thermal model fits to the 1998 RO₁ fluxes must take this flux uncertainty into account.

1998 UO₁

No spectrum was found to be extracted from the 1998 UO₁ group file (gm20020928_131). Since the asteroid spectrum was not clearly seen, a 3 pixel diameter optimum extraction was performed on the same rows as the spectrum was extracted from the accompanying ratio star [Fig. 5.21 (i)]. Limits on the maximum D_{eff} and minimum p_v can be estimated from the amplitude of the noise. However, since it is not known what rows to extract the spectrum from, the noise is dominated by electronic pickup (Section 5.4.8). We optimally extracted a spectrum using row centres -8 to +8 pixels around the same row centres used to extract the ratio star (positive beams: 45.5, 108.5; negative beams: 66.5, 87.5). The resulting variation in N-band flux is seen in Fig. 5.22. The amplitude of the variation in flux due to this noise is found to be 3.43×10^{-15} W m⁻² μm⁻¹. This noise estimate will be used to estimate D_{eff} and p_v limits in Section 5.6.6.

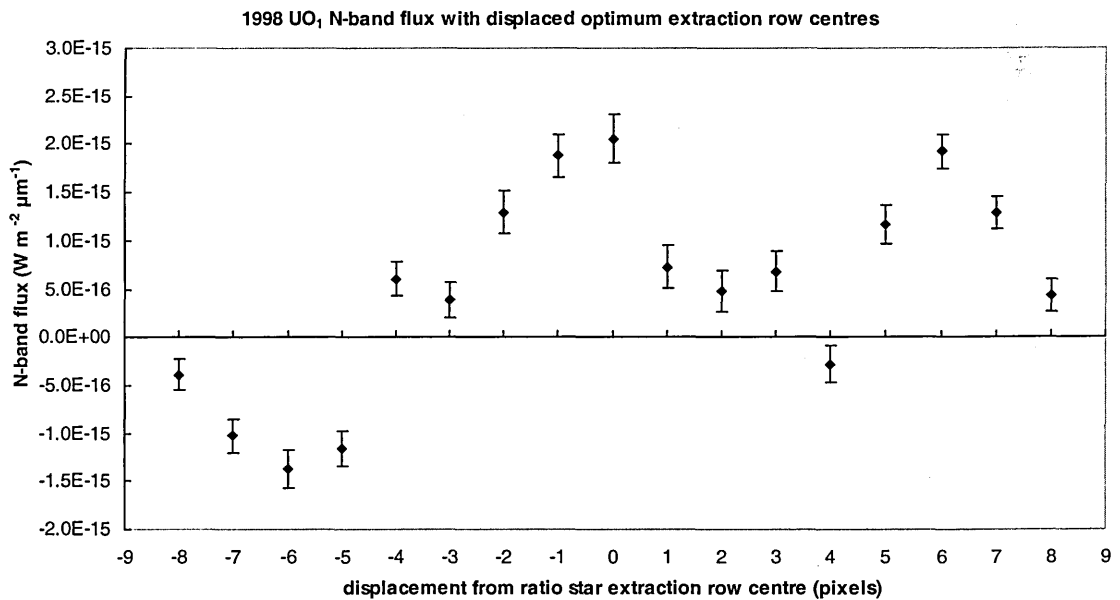


Fig. 5.22 N-band flux of asteroid 1998 UO₁ with different optimum extraction row centres, displaced from the row centres used to extract the ratio star (BS 915) spectrum. The amplitude gives an indication of the electronic pickup noise.

(53789) 2000 ED₁₀₄

For the 29 September 2002 UT observation of (53789) 2000 ED₁₀₄ [Fig. 5.21 (j)], we needed to test where cirrus starts to affect the observation; as described in Section 5.3.2, our notes indicated this occurred around frame 56. We determined which frames were useable by increasing the number of frames reduced by one pair each time until the S/N decreased in the next ORAC-DR output _dbs spectrum, measuring the S/N using the same method as described for determining optimum extraction row centres in Section 5.4.5. Table 5.11 shows the results, from which we conclude that the S/N begins to decrease after frame 56, so the (53789) 2000 ED₁₀₄ spectrum was extracted from frames 45-56. The flux-calibrated spectra using ratio star BS 7615 (group 41 and group 61) were similar, the former is binned by default, since the ratio star is observed just previous to the asteroid.

Table 5.11

Estimates of signal-to-noise ratio (S/N) for 29 September 2002 UT observations of (53789) 2000 ED₁₀₄ using increasing frame ranges to determine where cirrus affects the observation

Frame range	Measured between 10.8 and 11.8 μm (estimated wavelength)		
	Mean	σ	Est. S/N
45 – 52	1.4968	0.6160	2.4
45 – 54	1.5172	0.5656	2.7
45 – 56	1.7346	0.5016	3.5
45 – 58	1.5097	0.4748	3.2
45 – 60	1.5448	0.4638	3.3

2002 HK₁₂

For the 27 September 2002 UT observation of 2002 HK₁₂ no spectrum was found to extract from the group file (gm20020927_90). As for 1998 UO₁, a 3 pixel diameter optimum extraction was performed on the same rows as the spectrum was extracted from the accompanying ratio star [Fig. 5.21 (l)]. The quasi-simultaneous visual composite lightcurve of 2002 HK₁₂ measured at the JKT (Section 3.9.11) indicates a rotational phase of 0.56 at the midpoint of the observation, near lightcurve minimum [Fig. 5.23 (d)]. This

represents an $H_V = 18.89_{-0.3}^{+0.4}$ at the phase angle $\alpha = 34.6^\circ$, assuming a phase parameter $G = 0.15_{-0.15}^{+0.25}$, compared to the midpoint rotational phase of the 28 September UKIRT observation of 0.38, near lightcurve maximum, which indicates $H_V = 17.67_{-0.3}^{+0.4}$. Therefore 2002 HK₁₂ was over 1 magnitude dimmer on 27 September (though H_V is uncertain due to an unknown G , the phase correction will be almost the same on each night, so the lightcurve amplitude difference is accurate), which explains why we were unable to detect any thermal IR flux.

The 28 September 2002 observation of 2002 HK₁₂ [Fig. 5.21 (m)] did successfully measure thermal IR flux from 2002 HK₁₂, finding an estimated N mag. of 6.30. The uncertainty is increased considerably by the electronic pickup noise, as described in Section 5.4.8. We assign an additional 50% uncertainty to the flux-calibrated binned fluxes [although not relative to each other, hence this uncertainty is not included in the error bars of the binned fluxes in Fig. 5.21 (m)].

2002 NX₁₈

The 27, 29 and 30 September 2002 UT observations of 2002 NX₁₈ [Fig. 5.21 (n), (o) and (q)] give estimated N mag. of 4.36, 4.38 and 4.04 respectively. Cirrus was known to have begun to affect the 29 September observation as described in Section 5.3.2. As for (53789) 2000 ED₁₀₄, we determined which frames were useable by increasing the number of frames reduced by one pair each time until the S/N decreased in the next ORAC-DR output `_dbs` spectrum, measuring the S/N using the same method as described for determining optimum extraction row centres in Section 5.4.5. Table 5.12 shows the results, from which we conclude that the S/N begins to decrease after frame 36, and so the 2002 NX₁₈ spectrum was extracted from frames 17-36.

Table 5.12

Estimates of signal-to-noise ratio (S/N) for 29 September 2002 UT observations of 2002 NX₁₈ using increasing frame ranges to determine where cirrus affects the observation

Frame range	Measured between 10.8 and 11.8 μm (estimated wavelength)		
	Mean	σ	Est. S/N
17 – 36	5.801	0.375	15
17 – 38	5.443	0.403	14
17 – 40	6.723	0.387	17 ^a

Notes. ^aAlthough frame range 17 – 40 has the best S/N, there is a sudden change in gradient in the 17 – 40 μm spectrum and an anomalous group of points near 12 μm , that suggests that cirrus is increasing the noise there despite what our estimate suggests.

2002 NX₁₈ was observed in the Q-band on 30 September [Fig. 5.21 (p)]. The flux-calibrated spectrum is binned between 17.4 and 21.0 μm .

2002 QE₁₅

The 28 September 2002 UT observation of 2002 QE₁₅ [Fig. 5.21 (r)] gives an estimated N mag. of 6.01. The uncertainty is increased considerably by the electronic pickup noise, as described in Section 5.4.8. We assign an additional 30% uncertainty to the flux-calibrated binned fluxes.

5.6 Thermal Model Fitting of Infrared Fluxes

5.6.1 Using Optical Observations

Chapter 4 explains how thermal infrared (IR) fluxes can be fitted with thermal models to measure an asteroid's effective diameter D_{eff} (the diameter the asteroid would have if it were a perfect sphere) and geometric albedo p_v using the absolute visual magnitude H_V . These three parameters can be related, as explained in Section 4.1, using (e.g. Fowler and Chillemi, 1992):

$$D_{\text{eff}} (\text{km}) = 10^{-H_V/5} 1329 / \sqrt{p_v} \quad (5.19)$$

For (433) Eros, (6455) 1992 HE, 1998 UO₁ and 2002 HK₁₂ appropriate absolute visual magnitudes H_V corresponding to the midpoint of the thermal IR observations can be used

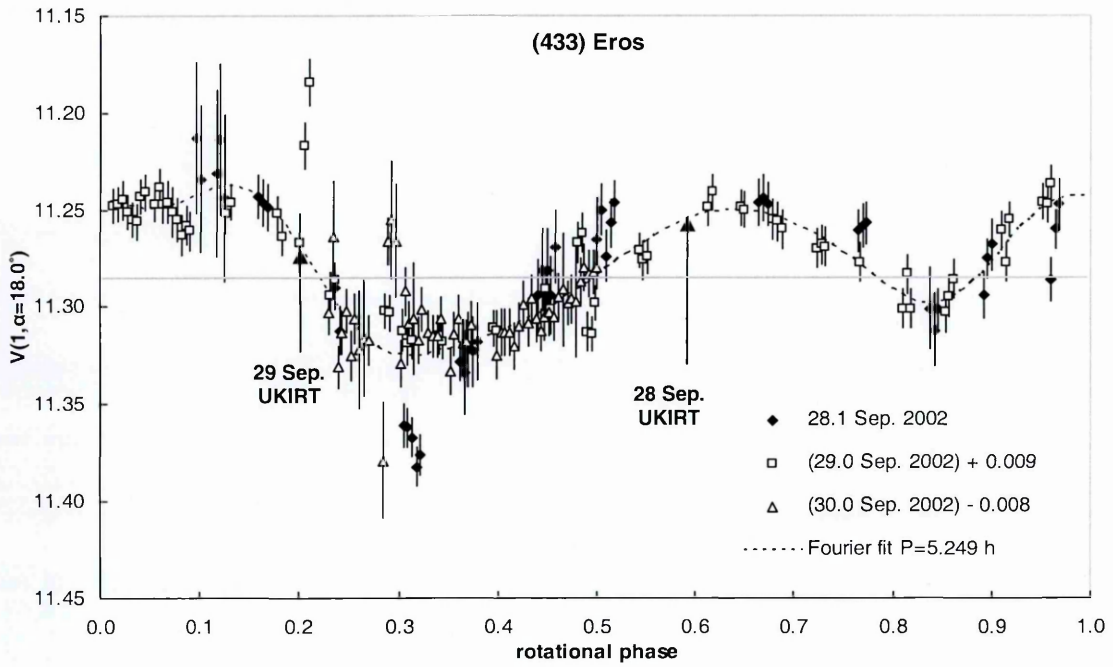
in the thermal model fitting, using composite visual lightcurves derived in Chapter 3 from Jacobus Kapteyn Telescope (JKT) observations (Fig. 5.23). The rotational phases corresponding to the start, end, and midpoint of the thermal IR observations of these asteroids are given in Table 5.13, along with the appropriate derived H_V magnitude.

The main purpose behind observing Eros was to test our methods, including lightcurve correction, for deriving diameters and albedos of NEAs. In Section 3.9.1 we estimate that our rotation period solution for Eros, $P = 2.249$ h, is 1.5 min too short. Assuming that all period solutions are of similar uncertainty, this will have negligible effect on the uncertainty of the lightcurve correction.

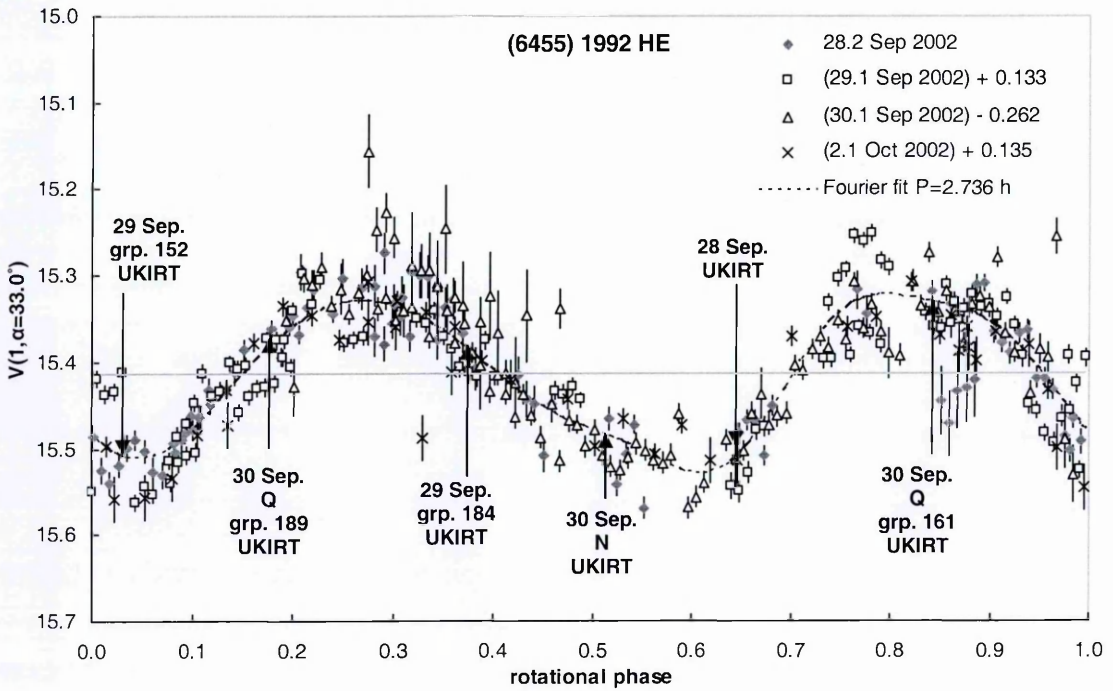
The rotational phase of the 28 September UKIRT observation of 2002 HK₁₂ is not covered by our optical observations, but we were able to extrapolate the correct magnitude by combining our composite lightcurve with observations by Petr Pravec (Section 3.9.11). For 2002 NX₁₈, the lightcurve coverage was not adequate to produce a unique solution for the rotation period P . Figure 5.23 (e) and (f) shows the two best solutions, 4th order Fourier fits $P = 7.602 \pm 0.002$ h and $P = 9.040 \pm 0.002$ h. The 2002 NX₁₈ JKT observations were able to provide a mean $H_V = 17.63 \pm 0.4$ for the thermal model fitting. The uncertainty in our knowledge of H_V for this object is dominated by our lack of knowledge of the phase parameter G and the high phase angle of observation ($\alpha = 52^\circ$), and not by our inability to produce a unique composite lightcurve, since the lightcurve amplitude is small (0.22 for $P = 7.602$ h, 0.23 for $P = 9.040$ h). Combining 2002 NX₁₈ N-band and Q-band observations without lightcurve correction will have a small effect on the uncertainty compared to the uncertainty of the calculated standard error on the binned fluxes represented by their error bars.

Fig. 5.23

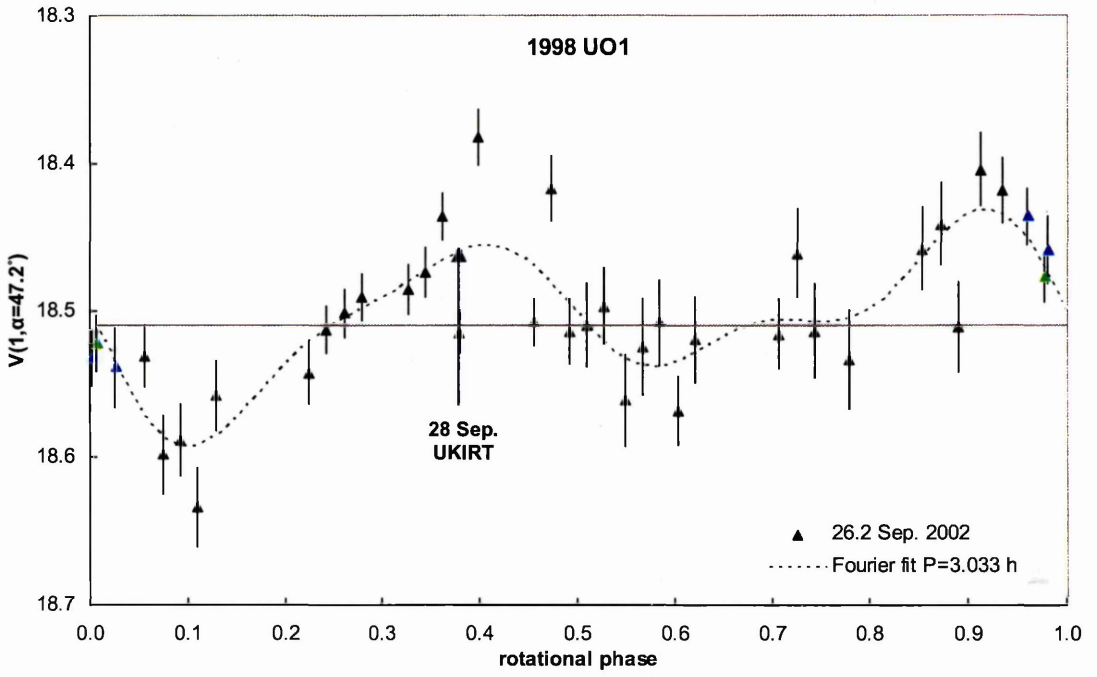
(a)



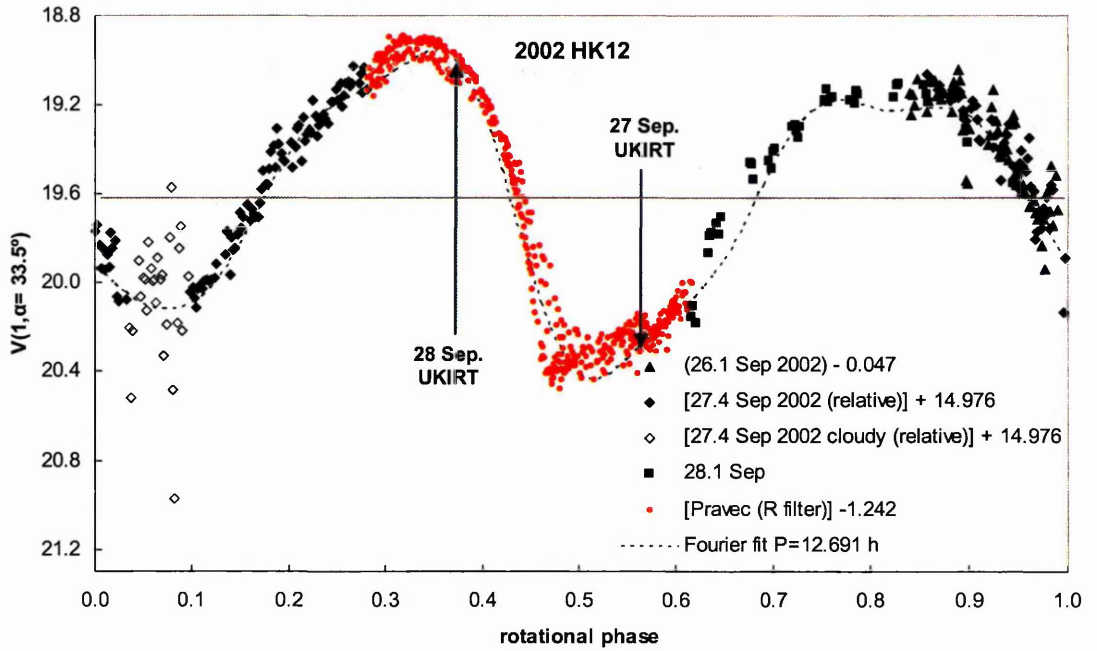
(b)



(c)



(d)



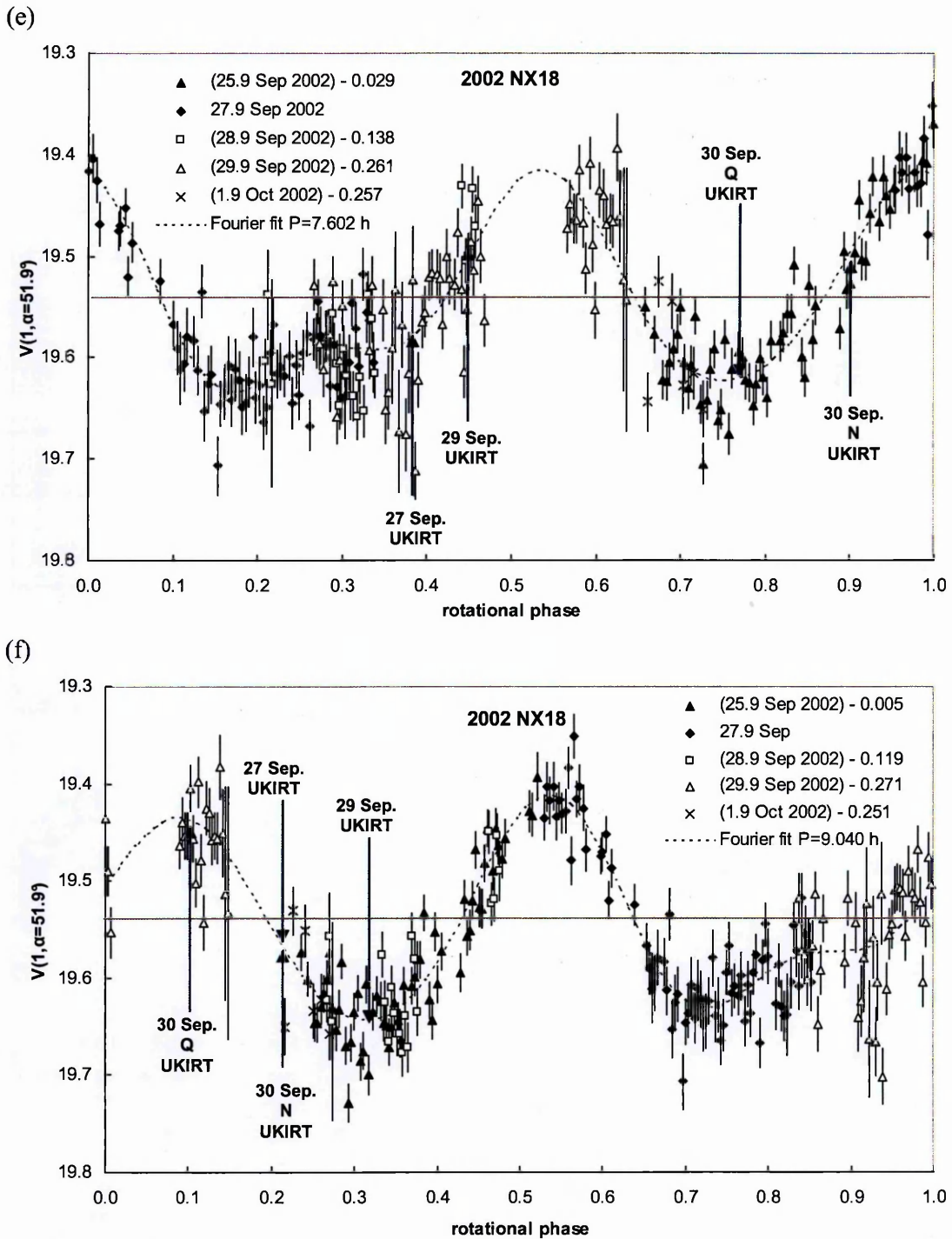


Fig. 5.23 Reduced composite visual lightcurves. Grey horizontal line marks mean visual magnitude. Arrows point to the rotational phase at the midpoint of the UKIRT thermal IR observations. t_0 is 0h 25 September 2002 UT. (a) (433) Eros with a fit of 5.249 h; (b) (6455) 1992 HE with a fit of 2.736 h; (c) 1998 UO₁ with a Fourier fit of 3.033 h. (d) 2002 HK₁₂ with a Fourier fit of 12.691 h. The 27 and 28 September UKIRT observations are near lightcurve minimum and maximum respectively; (e) 2002 NX₁₈ with a Fourier fit of 7.602 h; (f) 2002 NX₁₈ with a Fourier fit of 9.040 h. For both 2002 NX₁₈ solutions, the 27 and 29 September UKIRT observations are on the same hemisphere.

Table 5.13
Rotational phases and H_V magnitude of asteroids at time of UKIRT observations

Asteroid	Date	Group	Time (UT)	Grating	Fourier fit P (h)	Rotational phase of UKIRT obs.			H_V (mag.)	H_V err. (mag)
						start	midpoint	end		
(433) Eros	28 Sep.	103	09:39 – 09:58	N	5.249	0.555	0.585	0.615	10.32	± 0.04
	29 Sep.	135	09:52 – 10:10	N		0.168	0.197	0.227	10.34	
(6455) 1992 HE	28 Sep.	152	11:38 – 12:03	N	2.736	0.568	0.644	0.721	14.32	± 0.24
	29 Sep.	152	10:29 – 11:06	N		0.921	0.034	0.147	14.41	
		184	11:28 – 12:00	N		0.281	0.379	0.477	14.29	
	30 Sep.	137	09:47 – 10:12	N		0.436	0.513	0.589	14.38	
		161	10:35 – 11:13	Q		0.727	0.842	0.957	14.23	
		189	11:24 – 12:15	Q		0.029	0.181	0.334	14.28	
1998 UO ₁	28 Sep.	131	10:52 – 11:12	N	3.033	0.322	0.378	0.434	16.66	± 0.4
2002 HK ₁₂	27 Sep.	90	09:31 – 10:06	N	12.691	0.532	0.555	0.579	18.89	+0.38, -0.31
	28 Sep.	71	08:41 – 09:18	N		0.357	0.382	0.407	17.67	
2002 NX ₁₈	27 Sep.	26	07:32 – 08:48	N	7.602	0.306	0.389	0.471	17.66	± 0.4
	29 Sep.	17	06:01 – 06:32	N		0.420	0.454	0.488	17.58	
	30 Sep.	64	07:11 – 07:49	Q		0.730	0.772	0.813	17.71	
		96	08:17 – 08:42	N		0.875	0.902	0.923	17.58	
2002 NX ₁₈	27 Sep.	26	07:32 – 08:48	N	9.040	0.144	0.213	0.283	17.65	
	29 Sep.	17	06:01 – 06:32	N		0.285	0.314	0.342	17.73	
	30 Sep.	64	07:11 – 07:49	Q		0.069	0.104	0.138	17.52	
		96	08:17 – 08:42	N		0.190	0.214	0.237	17.63	

Notes. ‘N’ and ‘Q’ are abbreviations for lowN and lowQ gratings respectively.

For (6455) 1992 HE, the Q-band thermal IR fluxes of 30 September 2002 UT can be lightcurve corrected to the N-band observations (Table 5.14). This amounts to an assumption that the thermal IR and optical lightcurves coincide.

Table 5.14

Lightcurve correcting (6455) 1992 HE 30 September 2002 UT lowQ grating observations to rotational phase of lowN grating observation

Group 161						
		H_V at time of lowN observation (mag.):		14.38		
		H_V at time of lowQ observation (mag.):		14.23		
		Difference (mag.):		+ 0.15		
Wavelength (μm)	$F_{\text{ast}} (\times 10^{-14})$ $\text{W m}^{-2} \mu\text{m}^{-1}$	Q (mag.)	lc. corrected Q (mag.)	lc. corrected $F_{\text{ast}} (\times 10^{-14})$ $\text{W m}^{-2} \mu\text{m}^{-1}$	Error ($\times 10^{-15}$) $\text{W m}^{-2} \mu\text{m}^{-1}$	
17.580	1.35	1.82	1.97	1.17	1.59	
19.252	1.28	1.88	2.03	1.11	1.85	
20.869	1.14	2.00	2.15	0.994	3.20	
22.294	0.881	2.28	2.43	0.767	3.65	
24.052	0.520	2.85	3.00	0.453	5.01	
single flux bin between 17.4 and 18.8 μm :						
Wavelength (μm)	$F_{\text{ast}} (\times 10^{-14})$ $\text{W m}^{-2} \mu\text{m}^{-1}$	Q (mag.)	lc. corrected Q (mag.)	lc. corrected $F_{\text{ast}} (\times 10^{-14})$ $\text{W m}^{-2} \mu\text{m}^{-1}$	Error ($\times 10^{-15}$) $\text{W m}^{-2} \mu\text{m}^{-1}$	
17.877	1.27	1.88	2.03	1.10	1.10	
Group 189						
		H_V at time of lowN observation (mag.):		14.38		
		H_V at time of lowQ observation (mag.):		14.28		
		Difference (mag.):		+ 0.10		
Wavelength (μm)	$F_{\text{ast}} (\times 10^{-15})$ $\text{W m}^{-2} \mu\text{m}^{-1}$	Q (mag.)	lc. corrected Q (mag.)	lc. corrected $F_{\text{ast}} (\times 10^{-15})$ $\text{W m}^{-2} \mu\text{m}^{-1}$	Error ($\times 10^{-15}$) $\text{W m}^{-2} \mu\text{m}^{-1}$	
17.594	10.5	2.09	2.19	9.59	1.19	
19.235	7.04	2.52	2.62	6.42	1.42	
20.825	5.77	2.74	2.84	5.27	1.93	
22.255	5.72	2.75	2.85	5.22	2.31	
24.039	5.47	2.80	2.90	4.99	2.85	
single flux bin between 17.4 and 18.8 μm :						
Wavelength (μm)	$F_{\text{ast}} (\times 10^{-15})$ $\text{W m}^{-2} \mu\text{m}^{-1}$	Q (mag.)	lc. corrected Q (mag.)	lc. corrected $F_{\text{ast}} (\times 10^{-15})$ $\text{W m}^{-2} \mu\text{m}^{-1}$	Error ($\times 10^{-16}$) $\text{W m}^{-2} \mu\text{m}^{-1}$	
18.089	8.94	2.26	2.36	8.15	7.57	

For 1999 HF₁ we used a mean $H_V = 14.60 \pm 0.5$ supplied by Petr Pravec (personal communication, 2003). For 1998 UO₁ we measured $H_V = 16.66 \pm 0.4$. We were unable to find a unique period for 2002 QE₁₅ (Section 3.9.13). 2002 QE₁₅ had a small lightcurve

amplitude of 0.11 mag. and we derived a mean H_V magnitude of $16.15^{+0.5}_{-0.4}$ which is in close agreement to the HORIZONS value of $H_V = 16.21$ that we used for thermal fitting. For (66063) 1999 RO₁, (53789) 2000 ED₁₀₄ and 2000 GD₂ we used catalogued values of H_V from JPL's HORIZONS system (<http://ssd.jpl.nasa.gov/?horizons>). Limited relative optical photometry of (53789) 2000 ED₁₀₄ obtained on October 1 shows that the lightcurve amplitude is >1 magnitude and that P is $\gg 3.8$ hours.

5.6.2 Results

The Standard Thermal Model (STM), Fast Rotating Model (FRM), and Near-Earth Asteroid Thermal Model (NEATM), using both a default beaming parameter η and a best-fit η , are best-fitted to the thermal IR fluxes using the method described in Chapter 4 to derive effective diameters D_{eff} and p_v . The fits are shown in Fig. 5.24. The results are given in Table 5.15, as well as the H_V magnitude used.

Fig. 5.24
(a)

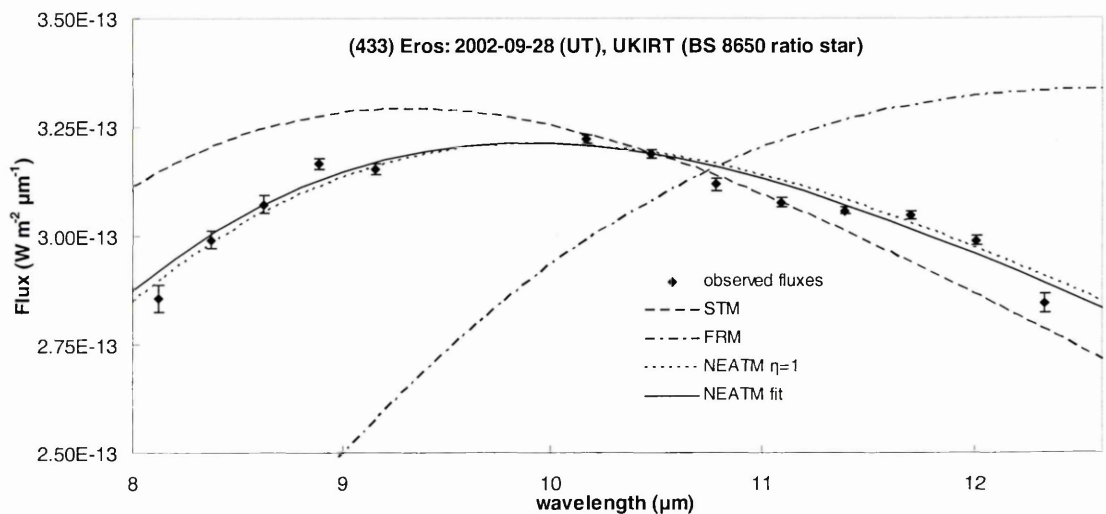
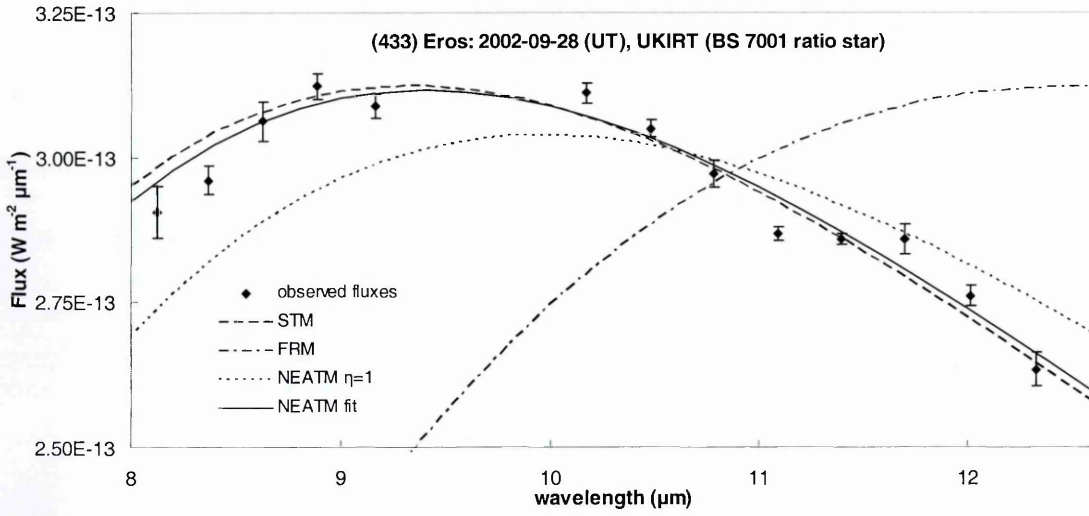
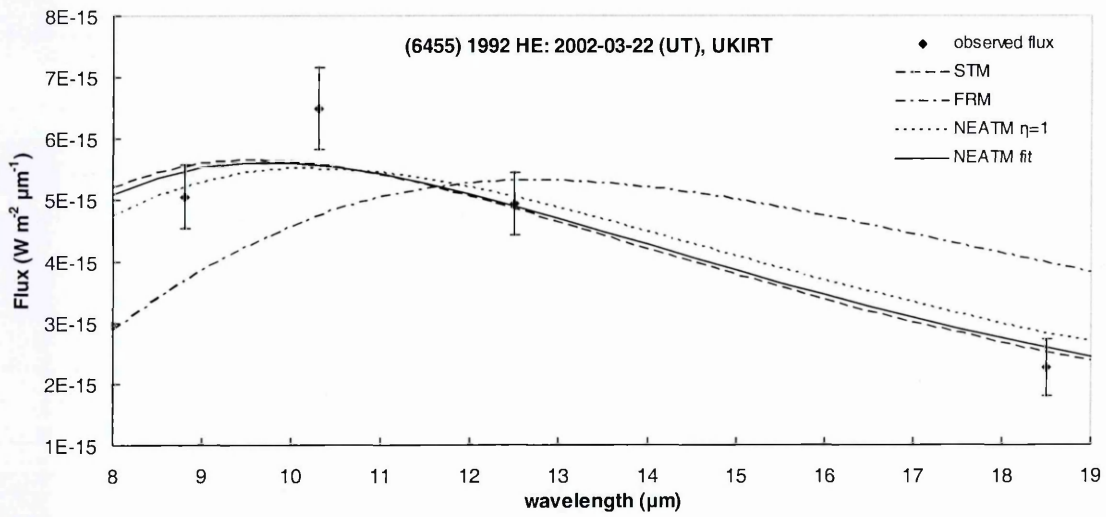


Fig. 5.24 continued.

(b)



(c)



(d)

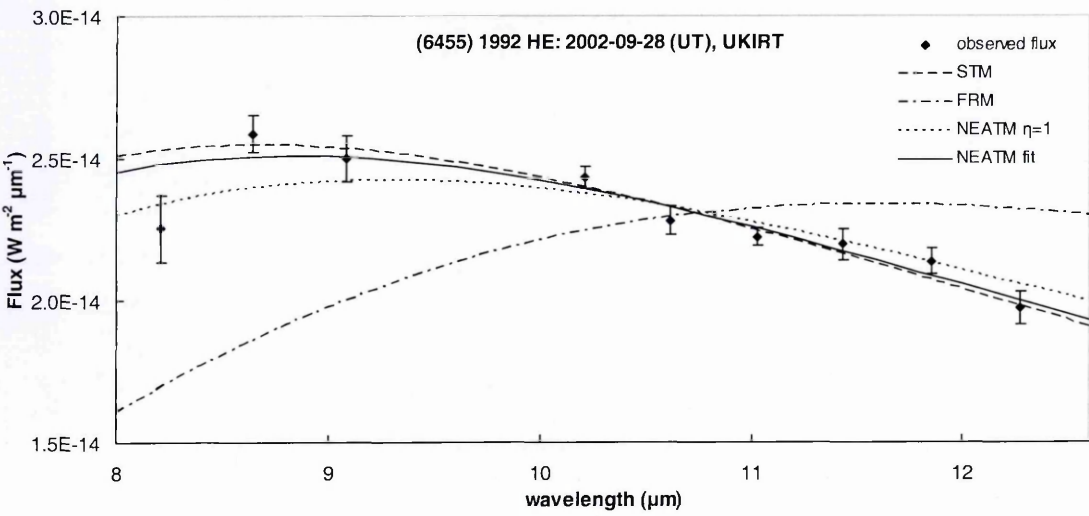
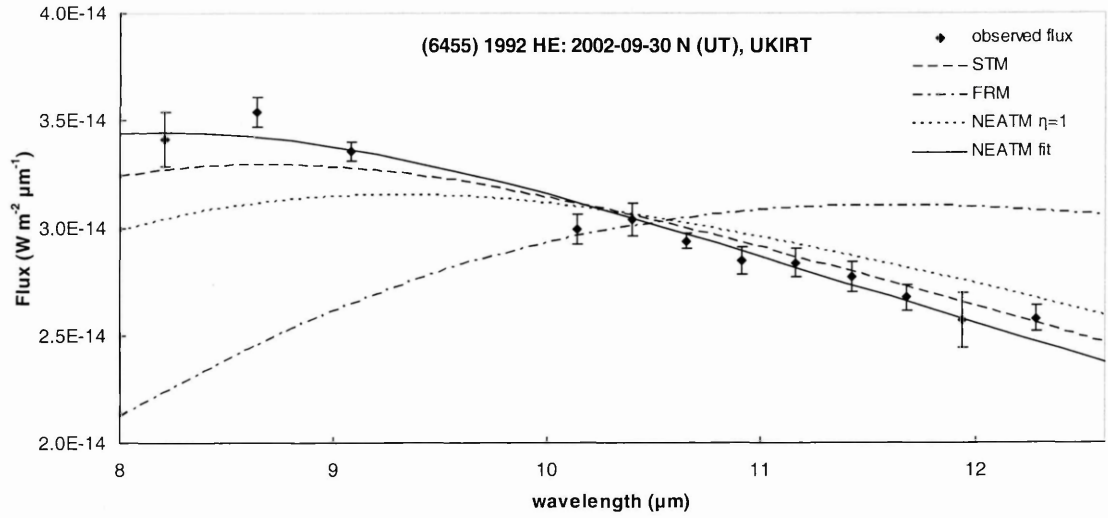
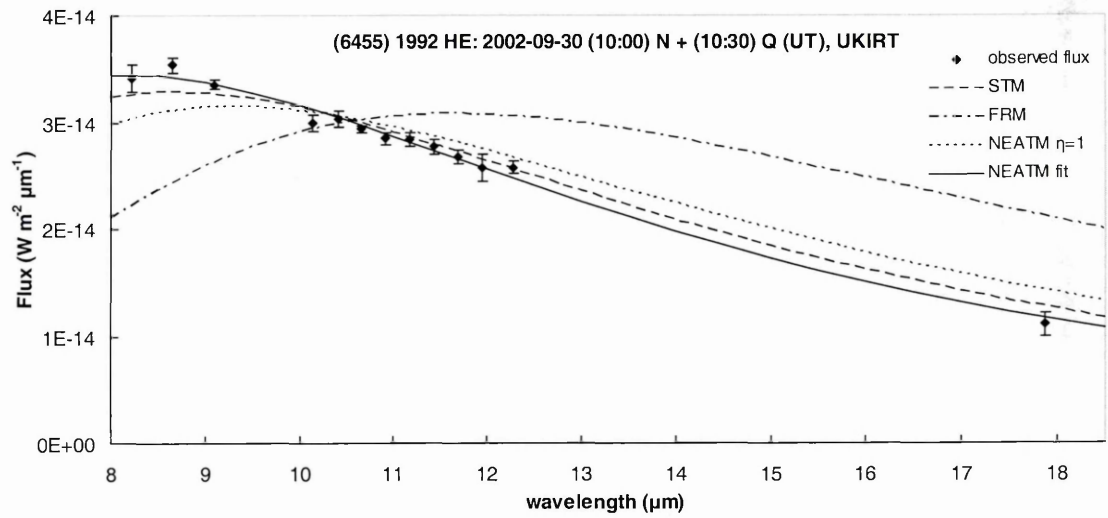


Fig. 5.24 continued.

(e)



(f)



(g)

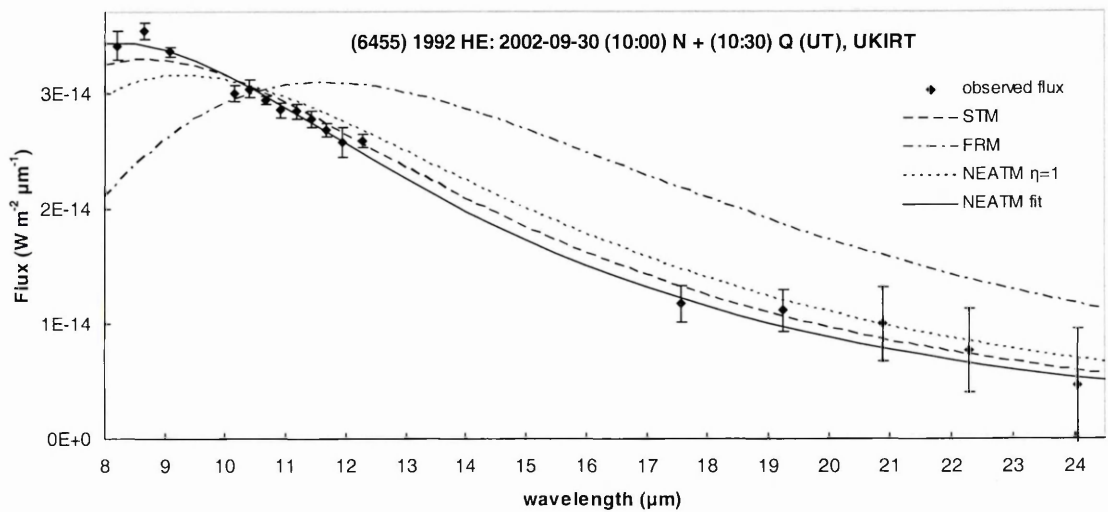
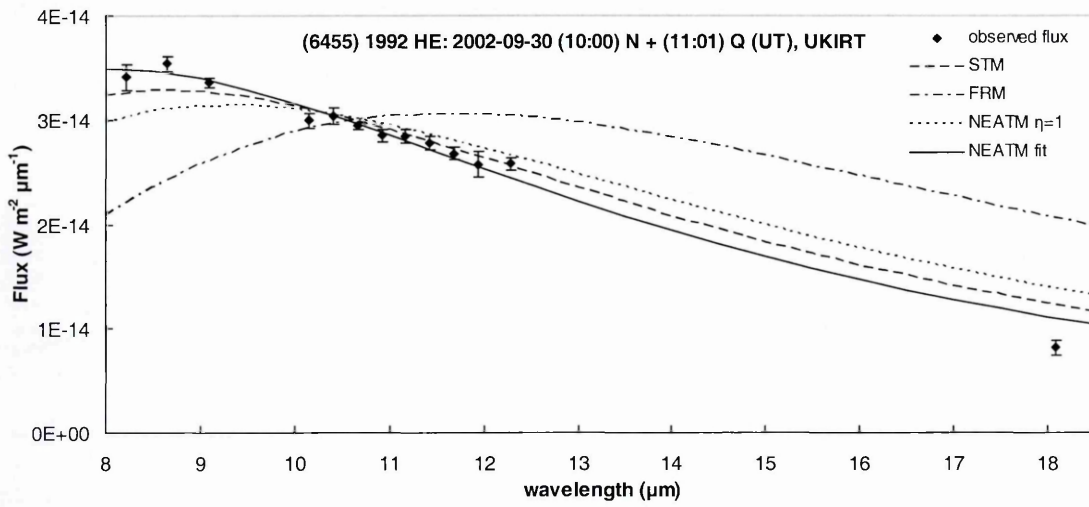
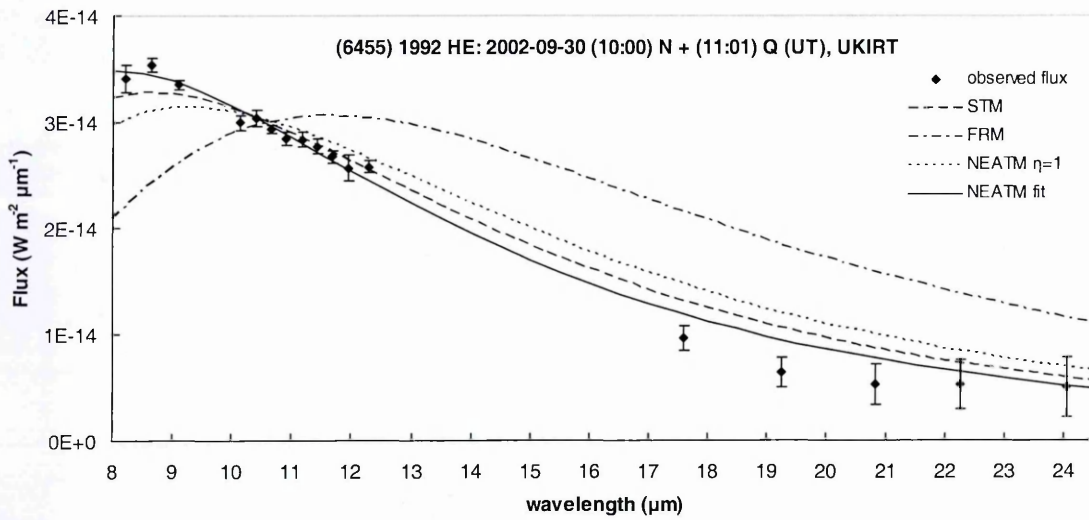


Fig. 5.24 continued.

(h)



(i)



(j)

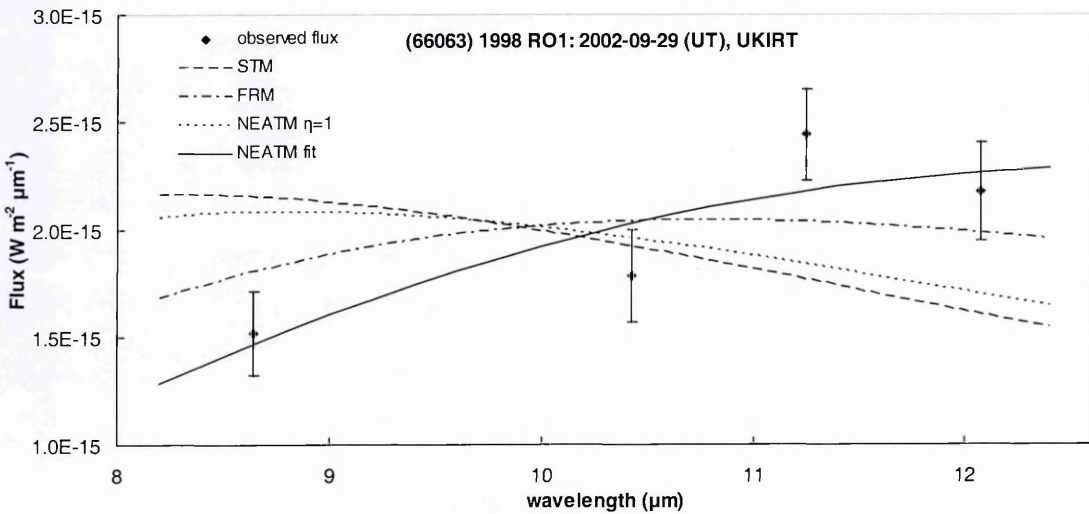
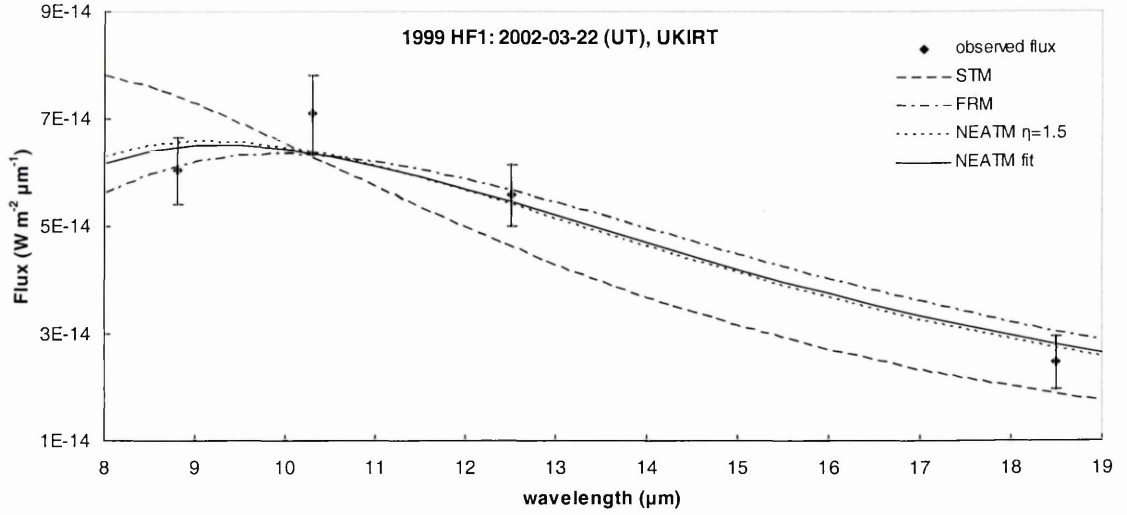
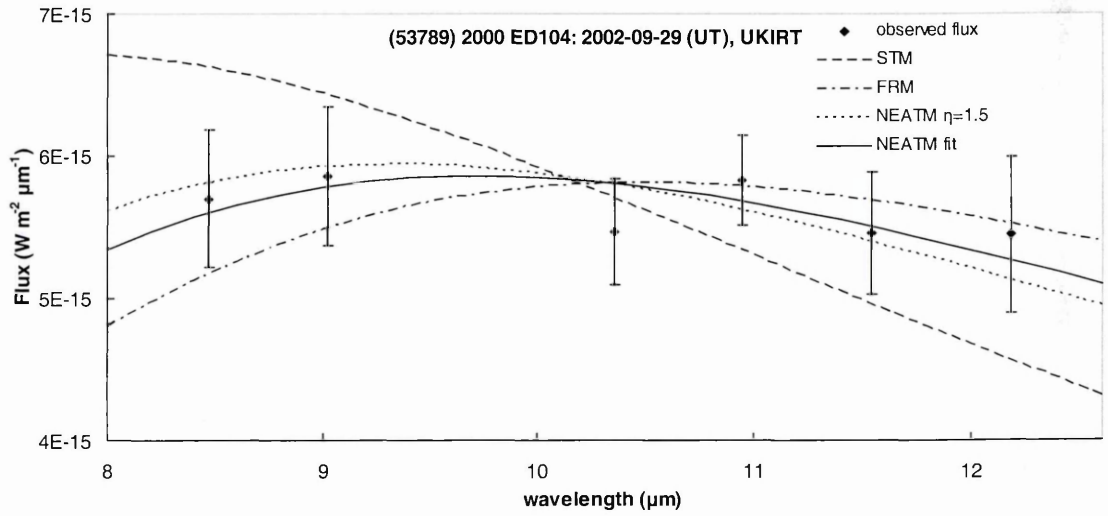


Fig. 5.24 continued.

(k)



(l)



(m)

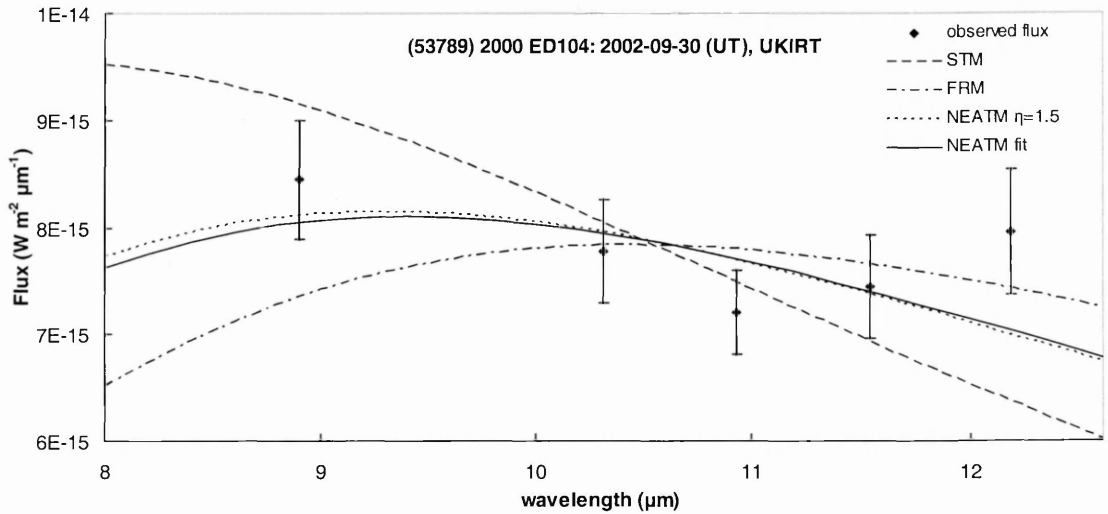
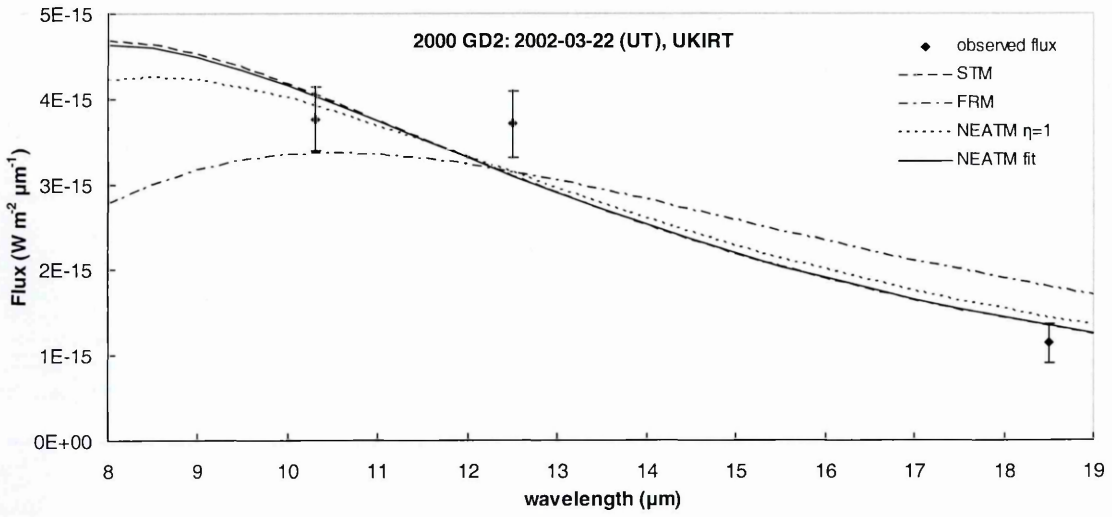
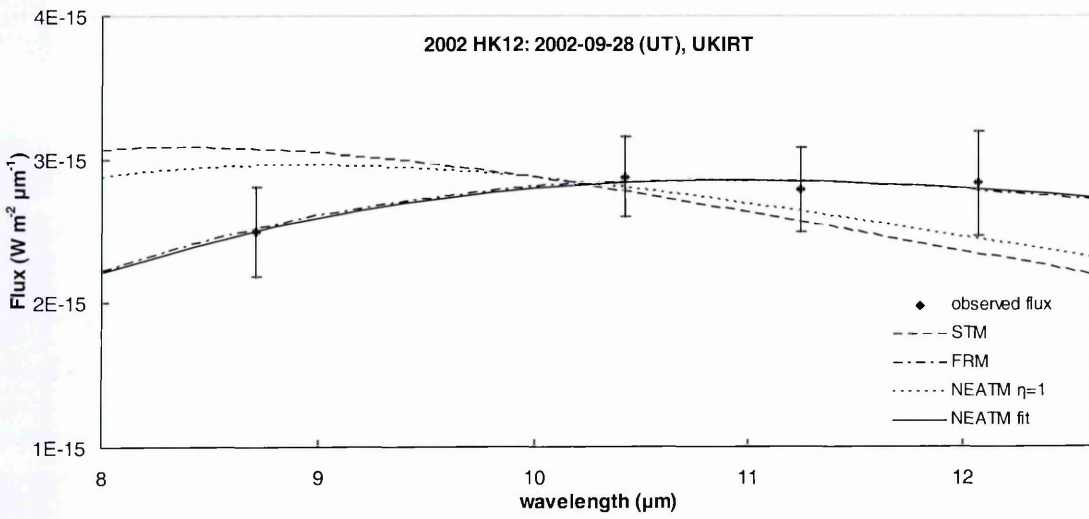


Fig. 5.24 continued.

(n)



(o)



(p)

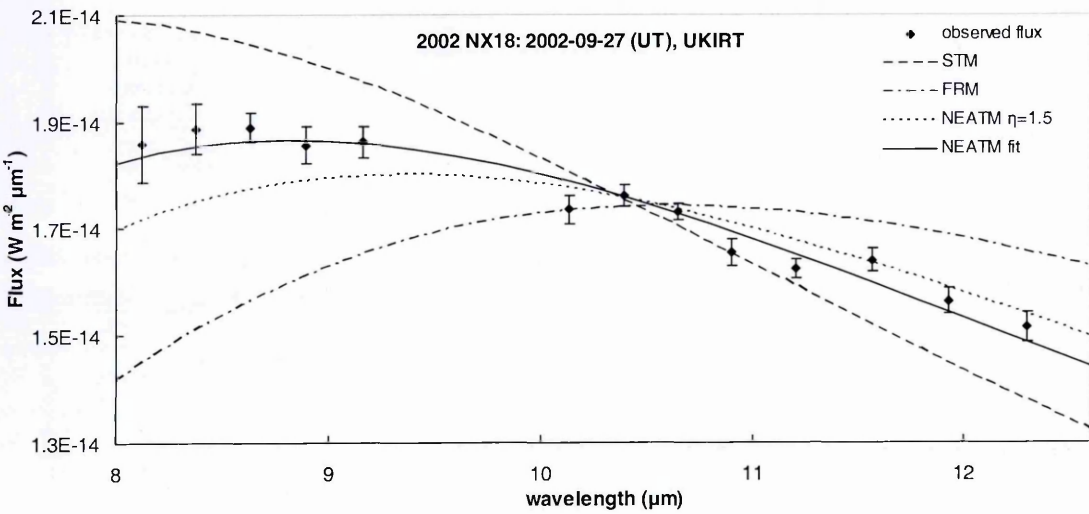
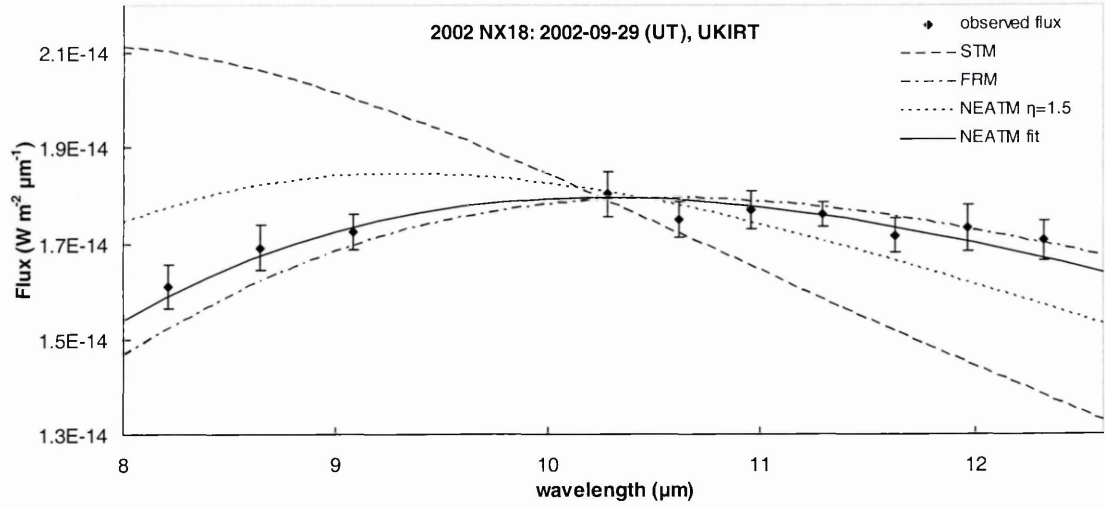
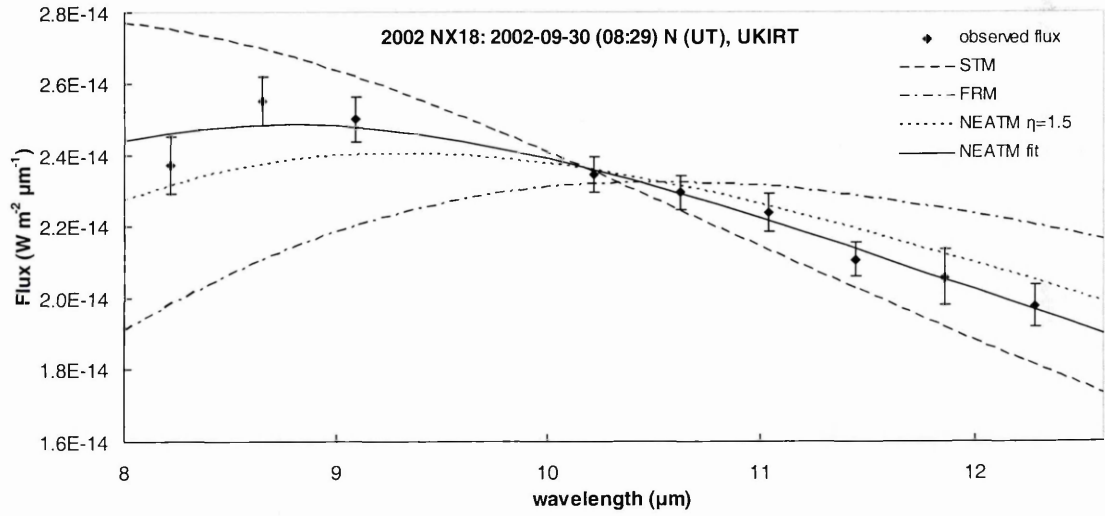


Fig. 5.24 continued.

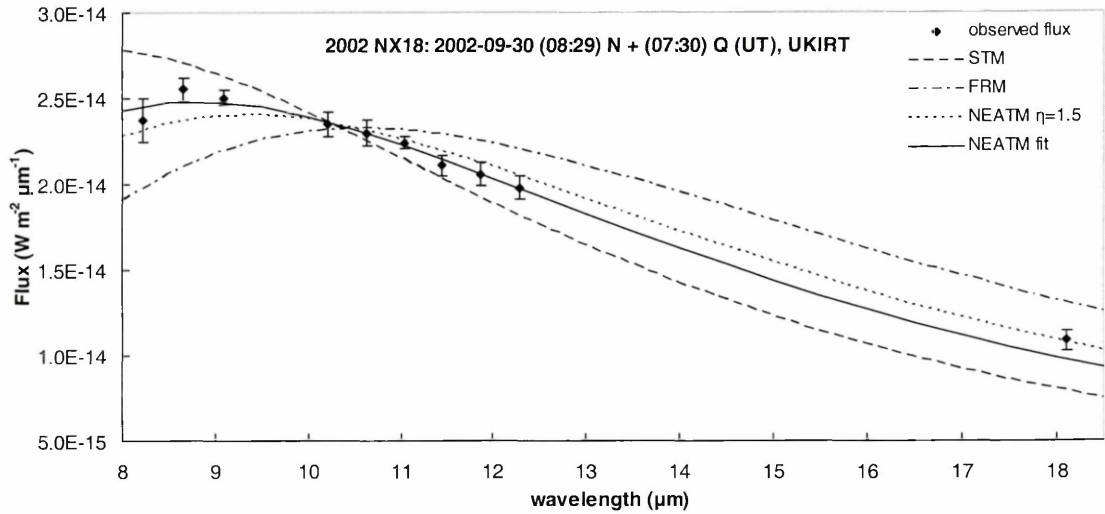
(q)



(r)



(s)



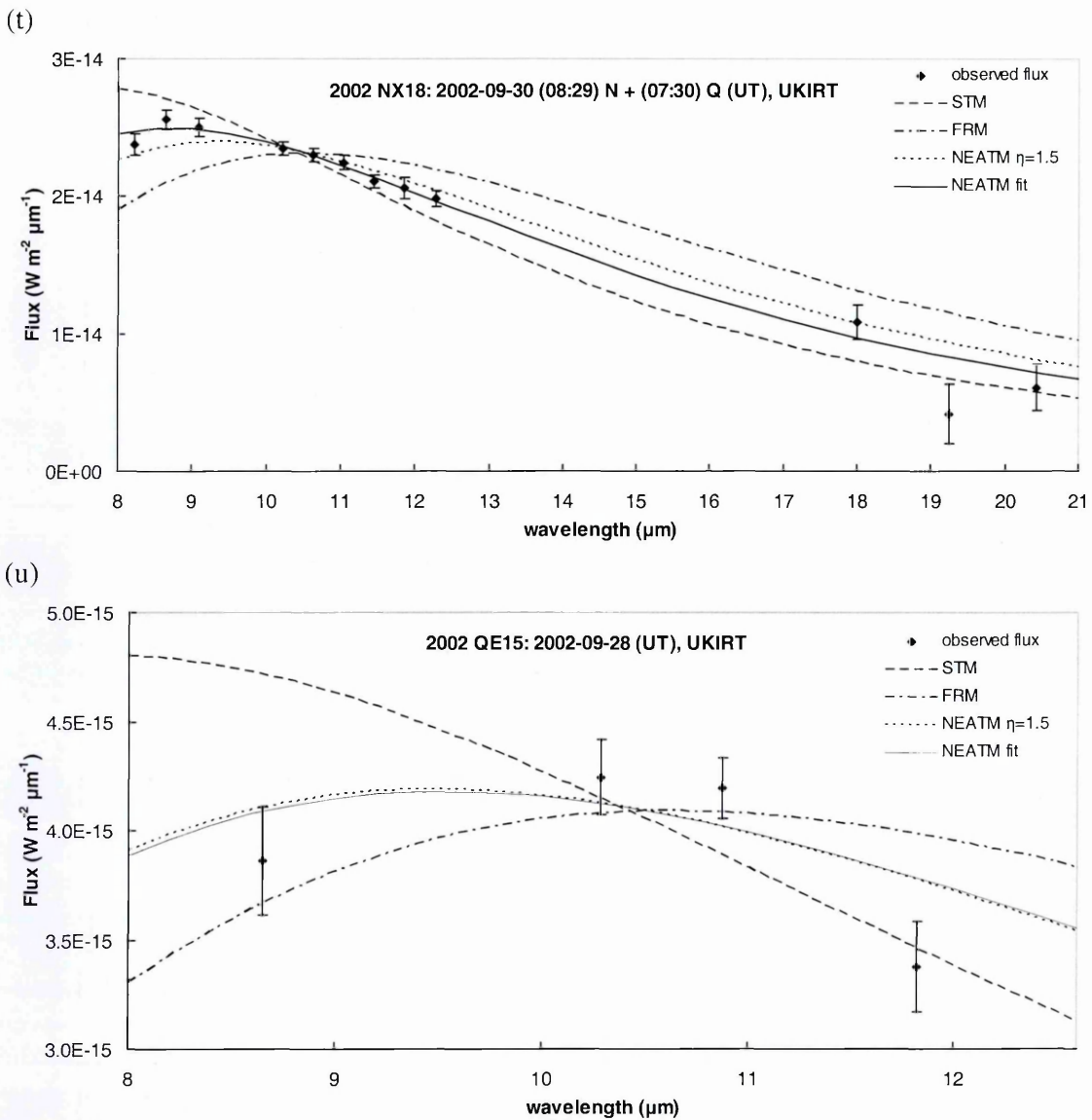


Fig. 5.24 Standard Thermal Model (STM, long-dashed line), Fast Rotating Model (FRM, dash-dot line), Near-Earth Asteroid Thermal Model with default η (NEATM, dotted line) and NEATM with best-fit η (solid line) fits to calibrated binned Michelle spectra using lowN and lowQ gratings (September UKIRT observations) and reduced broadband observations using Michelle in imaging mode (March UKIRT observations). The weighted best fits are those that minimise $\Sigma[F_{obs}(n) - F_{mod}(n)]/\sigma(n)^2$ where $F_{obs}(n)$ are the observed apparent fluxes, $F_{mod}(n)$ are the model fluxes at that wavelength, and $\sigma(n)$ are the statistical uncertainties in the binned fluxes, resulting in a unique diameter and albedo for a given H_V magnitude. The derived D_{eff} and p_v are listed in Table 5.15, as well as the H_V magnitude used, the best-fit η for each object, and the default η for those spectra based upon their phase angle (Section 5.8.1). The Q spectra for (6455) 1992 HE taken in September are lightcurve corrected to the time of the N-band observation, assuming the thermal and visual lightcurves correspond.

Object /Date	STM		FRM		NEATM Default η			NEATM Fitted/chosen η			H_V (mag)	α°	Fig. Comments 5.24
	P_V	D_{eff} (km)	χ^2	η	P_V	D_{eff} (km)	χ^2	η	P_V	D_{eff} (km)			
(53789)											17.10		Mean mag. from JPL Horizons, err. ± 0.5 mag., 1 mag. lc. amp.
2000 ED₁₀₄													
2002-09-29	0.41	0.79	11.9	1.5	0.21	1.10	2.91	1.80	0.18	1.18	1.25	60 (l)	
2002-09-30	0.32	0.89	11.0	1.5	0.17	1.22	7.17	1.57	0.17	1.23	4.76	60 (m)	
2000 GD₂													Mean mag. from JPL Horizons, err. ± 0.5 mag.
2002-03-23	0.49	0.29	3.76	1.0	0.24	0.41	11.5	0.74	0.56	0.27	3.78	28 (n)	
2002 HK₁₂													1.5 mag. lc. amp
2002-09-28	0.72	0.46	5.92	1.0	0.31	0.70	0.0773	2.75	0.24	0.80	0.0734	17.67 33 (o)	Rot. phase = 0.38, H_V value used see 7.4.1
2002 NX₁₈													
2002-09-27	0.049	1.79	183	1.5	0.022	2.66	436	1.18	0.034	2.13	15.5	52 (p)	
2002-09-29	0.051	1.76	414	1.5	0.023	2.63	9.82	2.19	0.017	3.02	3.07	53 (q)	Cirrus on 29 Sep.
2002-09-30	0.040	1.99	49.2	1.5	0.018	2.95	49.2	1.17	0.028	2.38	3.02	54 (r)	N only
	0.040	1.99	56.6	1.5	0.018	2.95	130	1.19	0.027	2.40	4.11	(s)	N + 1Q, not lc. corr. but lc. amp. = 0.3 mag.
2002 QE₁₅													
2002-09-28	0.30	1.39	16.9	1.5	0.018	2.94	147	1.16	0.028	2.37	8.04	(t)	Mean mag. from JPL Horizons, err. ± 0.5 mag.
2002-09-28	0.30	1.39	16.9	1.5	0.15	1.94	10.9	1.53	0.15	1.94	6.71	62 (u)	

Notes. Unless otherwise indicated, effective diameters and albedos are based on thermal model fits to 8-12.5 μm N-band data (Fig. 5.24). H_V magnitudes given on "object" rows are mean visual magnitudes, from JKT observations described in Chapter 4 in the case of (433) Eros, 2002 HK₁₂ and 2002 NX₁₈ or as described in the notes column. If H_V magnitude is left blank on the "date" rows, the mean H_V magnitude was used in the thermal fitting. In the cases of the September UKIRT observations of (433) Eros, (6455) 1992 HE, and 2002 HK₁₂, the rotational phases are known, and the corresponding H_V magnitudes used in the thermal fit are given on the "date" row. Values in bold are averaged for each object to provide the adopted P_V and D_{eff} , Table 5.17. The calculation of the fit residual χ^2 is explained in Section 4.2 and in the caption for Fig. 5.24. The smaller the fit residual the better the fit, but this comparison can only be made between different fits to the same data, i.e. between residuals on the same row.

The uncertainty in the model fitting appropriateness typically dominates the uncertainty in the flux calibration and the scatter due to atmospheric absorption discussed in Section 5.5.3. Comparison with other sources such as radar shows that it is generally less than 15% in diameter and 30% in albedo for the NEATM (Harris, 1998). In the cases of 2002 QE₁₅ and 2002 HK₁₂, the observational uncertainties are of the same order of magnitude as the uncertainty due to model-fitting because of the electronic pickup problem. For (66063) 1998 RO₁ the uncertainty is even greater due to the possible cirrus during the observation. For these asteroids, the uncertainty in the adopted result is calculated from the change in the albedo and diameter from the NEATM fit obtained at either end of the possible range of calibrated fluxes, combined with the model fitting uncertainty. For (53789) 2000 ED₁₀₄ the uncertainty in the adopted result reflects a large H_V uncertainty estimated at ± 0.5 due to a large lightcurve amplitude of greater than 1 mag. For 1999 HF₁ the uncertainty is bounded by the NEATM and FRM fits.

Many previous derivations of albedo and diameter using NEATM fitting have used measurements over the range 4-20 μm from instruments such as the Keck I/Long Wave Spectrometer (e.g. Delbó *et al.*, 2003) or non-simultaneous narrow-band photometry (e.g. Harris *et al.*, 1998). Although the Michelle spectra, in both the Q- and the N-band, are able to produce higher spectral resolution in the ranges covered, there are no data at wavelengths shorter than 8 μm . The greater the wavelength range available the more accurately the shape of the thermal infrared spectra can be fitted and the models are particularly sensitive in the 5 μm (M-band) region. Where only N-band data for an object are available, the accuracy of the NEATM fitted η is hard to gauge, since there are not generally enough results to judge the reproducibility. In the cases of asteroids (433) Eros, (6455) 1992 HE and 2002 NX₁₈ where N- and Q-band data are available, and/or there is high spectral resolution in the 7-12.5 μm region and where closely reproduced best-fit η are

found on different nights, the NEATM fitted η are certainly reliable enough to use the uncertainties associated with the model discussed above.

For 1999 HF₁, (53789) 2000 ED₁₀₄, 2002 NX₁₈ and 2002 QE₁₅ the accuracy of the measured diameters and albedos are dominated by the uncertainty in their corresponding H_V magnitude, due to a combination of optical observations at high phase angle and an unknown phase parameter. A change of H_V by +0.3 magnitudes produces a change in modelled diameter of $\sim -15\%$ and modelled geometric albedo of $\sim +30\%$. In the future, when knowledge of these objects' visual magnitude, and/or phase parameter improves, the albedo and diameter can be updated using the helpful expressions given by Harris and Harris (1997). An assumed value of $G = 0.15$ is used for all the thermal model fitting, except for (433) Eros and (6455) 1992 HE where values derived from observations are $G = 0.20$ and $G = 0.34$ respectively.

5.6.3 (433) Eros

We observed (433) Eros in order to test the accuracy of Michelle thermal IR measurements by comparing derived effective diameters D_{eff} and geometric albedos p_v with those obtained by previous groundbased measurements and by the NEAR-Shoemaker spacecraft. Figure 5.24 (a) and (b) shows the thermal model fits to (433) Eros 28 September 2002 UT N-band spectrum using ratio star BS 8650 and BS 7001 (Vega) as ratio stars respectively. Since BS 7001 is a standard star, flux-calibration can be done directly. However, BS 7001 was at a different airmass and different part of the sky from Eros, while BS 8650 was closer (Tables 5.5, 5.6 and 5.7). Therefore the two spectra can be regarded as an evaluation of the effect on the accuracy of η by flux-calibrating a ratio star rather than flux-calibrating with a standard directly.

The NEATM fit to the Fig. 5.24 (a) and (b) spectra gives $\eta = 0.95$ and $\eta = 0.75$ respectively. Previous observations of (433) Eros thermal IR spectra have been made by Lebofsky and Rieke (1979) and by Harris and Davies (1999), and fitted to the NEATM by Harris (1998) and Harris and Davies (1999). A summary of these observations is given in Table 5.16. The NEAR-Shoemaker mission measured a triaxial ellipsoid diameter of $34.4 \times 11.2 \times 11.2$ km and estimates of its p_v averaged 0.25 ± 0.05 (Veverka *et al.*, 2000). The Fig. 5.24 (a) spectrum, using BS 8650 as a ratio star, gives a similar best-fit η , and hence the shape of the spectrum is similar to these previously published results, suggesting this method is the best one and is producing spectra with accurate shapes.

Table 5.16
Previously published NEATM fits to (433) Eros

Diameter	p_v	η	H_V (mag.)	α°	Reference
23.6 (lc max.)	0.20	1.05	10.47 (lc max.)	10	Harris (1998)
23.6 (lc max.)	0.21	1.07	10.47 (lc max.)	31	Harris and Davies (1999)
14.3 (lc min.)	0.22	1.15	11.50 (lc min.)	10	Harris and Davies (1999)

Notes. Table adapted from Delbó *et al.* (2003)

Our optical and thermal infrared observations were made almost pole-on (Section 3.9.1), hence the low lightcurve amplitude [Fig. 5.23 (a)]. As a result, our optical observations produced a composite lightcurve with a mean $H_V = 10.40$, which is almost at lightcurve maximum, hence we derive a similar diameter $D_{eff} = 23.31 \pm 3.5$ km. Our derived $p_v = 0.24 \pm 0.07$ is in agreement with ground-based measurements and with NEAR-Shoemaker, within the uncertainties. It is interesting that groundbased measurements of the albedo of (433) Eros are consistently lower than NEAR-Shoemaker's.

Since (433) Eros is nearly pole-on, it might be expected that our derived η would be slightly less than that previously measured since any increase in η due to significant thermal inertia transporting thermal IR radiation onto the unobserved night-side of the asteroid would be missing, so it is interesting to note that this is the case. However, it is not

possible at present to be sure of the accuracy of the measurement of η , and so the lower measured value may be coincidental.

5.6.4 (6455) 1992 HE

It was particularly useful to observe (6455) 1992 HE because the derived D_{eff} and p_v can be compared with those obtained by fitting the March 2002 thermal IR fluxes [Fig. 5.3 (a)] using the Michelle instrument in imaging mode. Figure 5.24 (c) shows the thermal model fits to (6455) 1992 HE March 2002 infrared photometry. Figure 5.24 (d) and (e) show fits to N-band spectra from 28 and 30 September respectively. Figure 5.24 (f) and (g) show the 30 September N-band spectrum combined with the group 161 (midpoint 10:30 UT) Q-band spectrum for a single binned value, and binned over a wider range as described in Section 5.5.4. Figure 5.24 (h) and (i) show the same 30 September N-band spectrum combined with the group 189 Q-band spectrum taken at 11:01 UT. The Q-band spectra are lightcurve corrected to the magnitude of the asteroid at the time of the N-band spectrum, assuming that the thermal infrared and visual lightcurves coincide (Section 5.6.1). The thermal model fits for the March 2002 infrared photometry [Fig. 5.24 (c)] are in excellent agreement with those for the September 28 thermal infrared N-band spectrum [Fig. 5.24 (d)], indicating that these two techniques are consistent with each other.

Lightcurve correction of 30 September Q-band data placed the first (10:30 UT) Q-band spectrum very close to the NEATM best-fit η curve [Fig. 5.24 (f) and (g), solid line], indicating that the absolute flux calibration was good enough to combine results from the two filters. The second Q-band spectrum [Fig. 5.24 (h) and (i)] has lower fluxes. The NEATM fit shown in Fig. 5.24 (g) was chosen as the 30 September contribution to calculating the adopted p_v and D_{eff} because the 10:30 UT Q-band spectrum is most

consistent with the N-band spectrum, and it is taken closer in time than the 11:01 UT spectrum.

The 22 March and 28 September spectra [Fig 5.24 (c) and (d), solid line] both have very similar best-fit beaming parameters $\eta = 0.80$ and $\eta = 0.79$ respectively. But the 30 September spectrum has $\eta = 0.57$ [Fig 5.24 (f)-(i), solid line]. We have checked the calibration carefully, for example by trying different ratio stars, but the discrepancy remains. It could be that the weather, such as very light cirrus, affected the shape of the spectrum through wavelength-dependent absorption. However, the derived p_v and D_{eff} for 30 September ($p_v = 0.27$, $D_{eff} = 3.43$ km) is very close to that derived for 22 March ($p_v = 0.28$, $D_{eff} = 3.43$ km) whereas if we set $\eta = 0.80$, the NEATM fit for 30 September has $p_v = 0.20$ and $D_{eff} = 4.00$ km which is less consistent (although still within the 30% and 15% uncertainty for p_v and D_{eff} respectively). Delbó *et al.* (2003) found a conservative $\pm 20\%$ uncertainty for a measurement of η based on the reproducibility of η for those objects for which more than one measurement is available; the fitted beaming parameters are a little outside those limits (± 0.16). It is possible that it is a genuine effect, and that the beaming parameter varies on different parts of the asteroid due to changing surface characteristics, such as the extent of regolith or surface roughness, that affect the thermal inertia or emission. The midpoint of the 28 September *N* spectrum was at rotational phase 0.51, with reference to Fig. 5.23 (b), whereas for 30 September it was at rotational phase 0.64.

All of the model fits to (6455) 1992 HE thermal IR spectra show that the FRM (dash-dot line) is not a good fit and the STM (dashed line) is an excellent fit. The adopted results are $p_v = 0.26 \pm 0.08$ and effective diameter $D_{eff} = 3.55 \pm 0.53$ km at the mean visual magnitude, $D_{eff} = 3.73 \pm 0.56$ km at lightcurve maximum. The NEATM best-fit $\eta = 0.72$ (solid line) is very close to the STM value $\eta = 0.756$. A low near-STM beaming parameter

even at a moderate phase angle ($\alpha = 22^\circ, 30^\circ$) suggests considerable beaming in the sunward direction due to surface roughness. Since we have found that (6455) 1992 HE is a relatively fast rotator (assuming that the $P = 2.736$ h period is correct, although the inference is still valid for $P = 5.471$ h) if it had any significant thermal inertia the beaming parameter would be greater than one (see Section 5.8.2). This indicates that (6455) 1992 HE has low thermal inertia, implying a “dusty” regolith-covered surface. The value of $p_v = 0.26$ is consistent with its S-class taxonomic designation (Bus and Binzel, 2002).

5.6.5 (66063) 1998 RO₁

Aten asteroid (66063) 1998 RO₁ has been observed by Pravec *et al.* (2006) on every September 2002-2004 and found to be a binary asteroid based on lightcurve characteristics, with a rotation period of the primary $P = 2.492$ h and the secondary orbiting the primary in 14.5 h. A lightcurve amplitude of 0.13-0.16 mag. was also observed, suggesting the primary is nearly spherical, while observations suggested that the secondary is an elongated body. Pravec *et al.* found the ratio of the secondary diameter (D_s) to the primary (D_p) to be $D_s/D_p = 0.48 \pm 0.03$ based on an occultation event in September 2002.

Due to the possible cirrus in the 29 September observation [Fig. 5.24 (j)] which resulted in an uncertain flux calibration (Section 5.5.5) we can only roughly constrain the derived $p_v > 0.3$, however the range of possible diameters has $D_{eff} = 0.45^{+0.16}_{-0.13}$ km using the NEATM fit with default $\eta = 1$, since the (physically unlikely) best-fit $\eta = 5.91$ is probably due to cirrus affecting the shape of the spectrum. From the limit on p_v , (66063) 1998 RO₁ is not a low albedo asteroid, and unlikely to have taxonomic classes B, C, D or P. If the combined observed surface area of the binary system is equal to that of a disc of diameter D_{eff} , then $D_p^2 + D_s^2 = D_{eff}^2$ if both components have the same albedo. From these assumptions, we derive $D_p = 0.41^{+0.15}_{-0.12}$ km and $D_s = 0.19^{+0.08}_{-0.06}$ km.

5.6.6 1998 UO₁

An estimate of the electronic pickup noise (Section 5.4.8) is the amplitude of the N-band flux from the displaced optimum row extraction centres seen in Fig. 5.22. This can be put into the thermal models to give limits of p_v and D_{eff} (i.e. a single binned flux of $3.43 \times 10^{-15} \text{ W m}^{-2} \mu\text{m}^{-1}$ at $10.47 \mu\text{m}$). Using the output of NEATM with default $\eta = 1.0$, and using $H_V = 16.66 \pm 0.4$ (Section 5.6.1) we obtain $p_v > 0.29$ and $D_{eff} < 1.15 \text{ km}$. At the mean visual magnitude $H_V = 16.7 \pm 0.4$ we obtain $D_{eff} < 1.13 \text{ km}$. From the limit on p_v , 1998 UO₁ is not a low albedo asteroid, and unlikely to have taxonomic classes B, C, D or P.

5.6.7 1999 HF₁

Figure 5.24 (k) shows the thermal model fits for the 22 March thermal infrared photometry. We have no lightcurve correction for the observations, but the lightcurve amplitude is relatively small, < 0.23 (Pravec, personal communication, 2003). The STM (dashed line) is not a good fit; this is not surprising since the STM phase correction is not reliable at the observed phase angle $\alpha = 91^\circ$. The FRM (dash-dot line) is better, but the NEATM with default $\eta = 1.5$ (dotted line) and fitted $\eta = 1.61$ (solid line) are both good fits. The NEATM is not generally reliable at such high phase angles (Chapter 6); since the phase correction assumes zero emission on the night side, any body with significant thermal inertia will find the phase correction is not an adequate approximation at high phase angles. The adopted solution estimates p_v and D_{eff} by taking the average of the FRM and NEATM fits: $p_v = 0.18 \pm 0.07$, $D_{eff} = 3.73_{-0.5}^{+1.0} \text{ km}$ at the mean visual magnitude, $D_{eff} < 3.84_{-0.5}^{+1.0} \text{ km}$ at lightcurve maximum (from the limit of the lightcurve amplitude). 1999 HF₁ is a binary asteroid based on lightcurve characteristics [Pravec *et al.* (2002a) and Pravec *et al.* (2006)]; the effect of this on thermal model fitting and the relative contribution of each component to observed fluxes is unknown. Pravec *et al.* (2006) found

the ratio of the secondary diameter (D_s) to the primary (D_p) to be $D_s/D_p = 0.23 \pm 0.03$ based on an occultation event in March 2002. Using the same assumptions as for (66063) 1998 RO₁ (Section 5.6.5), we derive $D_p = 3.64^{+1.00}_{-0.51}$ km and $D_s = 0.84^{+0.35}_{-0.20}$ km. Pravec *et al.* found that 1999 HF₁ belongs to the X-type taxonomic class as defined by Bus and Binzel (2002), i.e. it is spectrally degenerate and is either an E, M, or a P-type asteroid. From our estimated p_v , we can say that the spectrally dominant component is not a P-type, but it could still be either an E or an M-type.

5.6.8 (53789) 2000 ED₁₀₄

Figure 5.24 (l) and (m) show thermal fits to 29 September and 30 September N-band spectra respectively. Although there was cirrus on the second half of 29 September, resulting in noisy data for asteroids (6455) 1992 HE and (433) Eros, early observations made of (53789) 2000 ED₁₀₄ and 2002 NX₁₈, when the weather was clearer, agree with observations on other nights.

The STM (dashed line) is not a good fit, perhaps due to the high phase angle of observation. The NEATM with default $\eta = 1.5$ (dotted line) gives a better fit than the FRM (dash-dot line). The thermal infrared flux was close to the detection threshold, hence the spectral resolution is low, and consequently the fitted η is rather uncertain. Since the lightcurve amplitude is greater than 1 mag., the difference in measured albedo and diameter between 29 September and 30 September, based on a value of the visual magnitude derived from the catalogued $H_V = 17.10 \pm 0.5$, can be attributed to the changing brightness (and therefore projected area, i.e. the assumption that the object is a sphere is not reasonable). The adopted $p_v = 0.18^{+0.11}_{-0.06}$ is an intermediate albedo consistent with taxonomic classes such as S, M, Q, R and V. $D_{eff} = 1.21 \pm 0.2$ km at the mean visual magnitude.

5.6.9 2000 GD₂

2000 GD₂ is an Sq-type asteroid (Binzel *et al.*, 2004). Figure 5.24 (n) shows the thermal model fits to the March 2002 UT Michelle imaging mode data. The NEATM fit is less certain due the missing 8.8 μm point (Section 5.2). The STM is an excellent fit and accordingly the best-fit $\eta = 0.74$. The adopted results are $p_v = 0.56 \pm 0.17$ and $D_{\text{eff}} = 0.27 \pm 0.04$ km, making 2000 GD₂ the smallest asteroid we observed. The measured albedo is the highest albedo measured for an S-type NEA, to date. This result is placed in context in Section 5.8.1.

5.6.10 2002 HK₁₂

Figure 5.24 (o) shows the thermal model fits to the 28 September N-band spectrum. The STM (dashed line) and NEATM with default $\eta = 1.0$ (dotted line) do not fit well. The NEATM fit (solid line) has an unusually high beaming parameter $\eta = 2.75$, and is a similar shape to the FRM (dash-dot line); both fit the spectrum well. The high beaming parameter at a moderate phase angle ($\alpha = 33^\circ$) and good fit of the FRM suggests that 2002 HK₁₂ may have a surface with significant thermal inertia, such as bare rock (Section 5.8.2). The adopted $p_v = 0.24^{+0.25}_{-0.11}$ is an intermediate albedo consistent with taxonomic classes such as S, M, Q, R and V. $D_{\text{eff}} = 0.62 \pm 0.2$ km at the mean visual magnitude.

5.6.11 2002 NX₁₈

Figure 5.24 (p), (q) and (r) show thermal fits to N-band spectra on 27, 29, and 30 September respectively. The spectra on all three nights are of high spectral resolution, binned over 0.25 μm wavebands on 27 and 29 September, and over 0.27 μm wavebands (for the lowN grating) on 30 September. Figure 5.24 (s) and (t) show thermal fits to the 30

September N-band spectrum combined with the Q-band spectrum taken on the same night, binned as a single value and over a larger wavelength range as described in Section 5.5.4.

The STM (dashed line) does not fit well, as would be expected given the large phase angle of observation ($\alpha = 53^\circ$). The FRM (dash-dot line) fits badly on 27 September [Fig. 5.24 (p)] and 30 September [Fig. 5.24 (r), (s) and (t)], but fits well on 29 September [Fig. 5.24 (q)]. The $\eta = 1.18$ fit for NEATM on 27 September is in very close agreement with $\eta = 1.16$ on 30 September. We regard the NEATM with fitted η as reliable on 27 September and 30 September, and hence these fits were used to calculate the adopted p_v and D_{eff} . The 29 September NEATM fit has a much higher beaming parameter $\eta = 2.19$. The weather later in the night on 29 September was affected by cirrus, so it is possible that the wavelength-dependent calibration with the standard star affected the shape of the spectrum more than is typical due to differing atmospheric absorption at different wavelengths. We regard the NEATM fit on 29 September as being unreliable.

Because we do not have a unique solution for the rotation period of 2000 NX₁₈ it was not possible to lightcurve correct the Q-band to the N-band data. The visual observations were used to supply the mean H_V magnitude used in the thermal model fits. As can be seen in Fig. 5.23 (e) and (f) the lightcurve amplitude is 0.23, which is not large, so the error in p_v and D_{eff} is dominated by the model-fitting. It is possible that the higher beaming parameter measured on 29 September is due to differing thermal properties at different parts of the asteroid surface. However, if either of the two most likely solutions for the rotation period ($P = 7.602$ h and $P = 9.040$ h) are correct then the observations on 27 September and 29 September are on the same hemisphere (for $P = 7.602$ h, rotational phase 0.39 and 0.49 on 27 and 29 September respectively; for $P = 9.040$ h, rotational phase 0.21 and 0.34). The adopted $p_v = 0.031 \pm 0.009$ is a low albedo consistent with taxonomic

classes such as B, C, D or P. $D_{eff} = 2.24 \pm 0.3$ km at the mean visual magnitude, $D_{eff} = 2.40 \pm 0.3$ km at lightcurve maximum.

5.6.12 2002 QE₁₅

Figure 5.24 (u) shows the thermal model fits to the 28 September N-band spectrum. None of the thermal models fit well because of large scatter due to the low thermal flux. The best-fit NEATM has a beaming parameter of $\eta = 1.53$. For the other asteroids we adopt an estimate of the uncertainty in measurement of η at 20% based on the reproducibility for those objects for which there is more than one measurement from independent data sets. For 2002 QE₁₅, because of the large scatter, we increase the uncertainty to 50%.

Delbó (2004) measured $p_v = 0.24 \pm 0.07$ and $D_{eff} = 1.49 \pm 0.2$ km using a default $\eta = 1.5$ at a phase angle of 50° , from observations in November 2002 at the European Southern Observatory. Our adopted $p_v = 0.15^{+0.08}_{-0.06}$ and $D_{eff} = 1.94 \pm 0.4$ km at the mean visual magnitude. Our measured albedo is slightly lower than Delbó's, although their uncertainties overlap.

5.7 Summary

We have derived the geometric albedos of eight NEAs and the effective diameters [all given at mean visual magnitude, except for (433) Eros] of nine NEAs, fitting the STM, FRM, NEATM (with a default beaming parameter η appropriate to the phase angle of observation and with a best-fit η) to thermal infrared photometry and spectrophotometry. Table 5.17 gives the adopted results, the final result arrived at in the discussions about each individual object above; for those objects where multiple spectra are available [(6455) 1992 HE, (53789) 2000 ED₁₀₄ and 2002 NX₁₈], this is an average of the reliable spectra

shown in bold in Table 5.15, while for the other objects, where there was only one spectrum, it is simply the NEATM fit for that object (except 1999 HF₁).

Table 5.17

Adopted results of derived effective diameters D_{eff} , geometric albedos p_v , and beaming parameters η

Asteroid	Mean H_V	Adopted results				α°	η		Tax. Class
		p_v		D_{eff} (km)					
(433) Eros	10.64	0.24	± 0.07	23.31	± 3.5	18	0.95	± 0.19	S
(6455) 1992 HE	14.32	0.26	± 0.08	3.55	± 0.5	22	0.79	± 0.16	S
						29	0.68	± 0.14	
(66063) 1998 RO ₁	17.97	>0.30		0.45	+ 0.16 - 0.13	45			
				$D_p = 0.41$	+0.15 -0.12				
				$D_s = 0.19$	+0.08 -0.06				
1998 UO ₁	16.4	>0.29		<1.13		43			
1999 HF ₁	14.60	0.18	± 0.07	3.73	+ 1.0 - 0.5	91	1.61	± 0.32	X
				$D_p = 3.64$	+1.0 -0.5				
				$D_s = 0.84$	+0.4 -0.2				
(53789) 2000 ED ₁₀₄	17.10	0.18	+ 0.12 - 0.08	1.21	± 0.2	60	1.69	± 0.34	
2000 GD ₂	19.11	0.56	± 0.17	0.27	± 0.04	28	0.74	± 0.15	Sq
2002 HK ₁₂	18.22	0.24	+ 0.25 - 0.11	0.62	± 0.2	33	2.75	± 0.55	
2002 NX ₁₈	17.63	0.031	± 0.009	2.24	± 0.3	53	1.17	± 0.23	
2002 QE ₁₅	16.21	0.15	+ 0.08 - 0.06	1.94	± 0.4	62	1.53	± 0.77	S

Notes. Uncertainties of p_v and D_{eff} calculated as described in Section 5.6.2. D_{eff} is given at mean H_V and is simply calculated from the derived p_v , using Eq. 5.19. Where there is more than one measurement of η [(6455) 1992 HE and 2002 NX₁₈] during the September UKIRT observations, these are averaged, and the associated average α is given. Uncertainty of η is estimated conservatively at 20% based on the reproducibility for those objects [in this chapter and the other reliable spectra used in Fig. 5.25, see Delbó *et al.* (2003)] where more than one spectrum is available, except for 2002 QE₁₅, where a 50% uncertainty is applied (Section 5.6.12). For the binary asteroids (66063) 1998 RO₁ and 1999 HF₁ the diameters for the primary (D_p) and secondary (D_s) components are also given.

5.8 Discussion

5.8.1 Integration with Previous NEATM Fits to Thermal IR Fluxes

Delbó (2004) used the NEATM (and STM, FRM) to derive effective diameters D_{eff} and geometric albedos p_v for 32 NEAs. Delbó also compiled together the results from all previous NEATM fits to NEAs to produce a database of 47 objects in total. Several NEAs have been observed more than once, so that the database had 67 diameters/albedos in total.

Including our 8 new objects and 14 new observations brings the total to 55 objects and 81 datasets.

Many datasets were observations of a broadband N magnitude, or at only one or two wavelengths, and so for these objects the NEATM was used with default beaming parameters η . For early NEATM fits, $\eta = 1.2$ at all phase angle α was used, as suggested by Harris (1998). After Delbó *et al.* (2003), $\eta = 1.0$ for $\alpha < 45^\circ$ and $\eta = 1.5$ for $\alpha \geq 45^\circ$ was adopted, as a consequence of the found linear trend of increasing η with α .

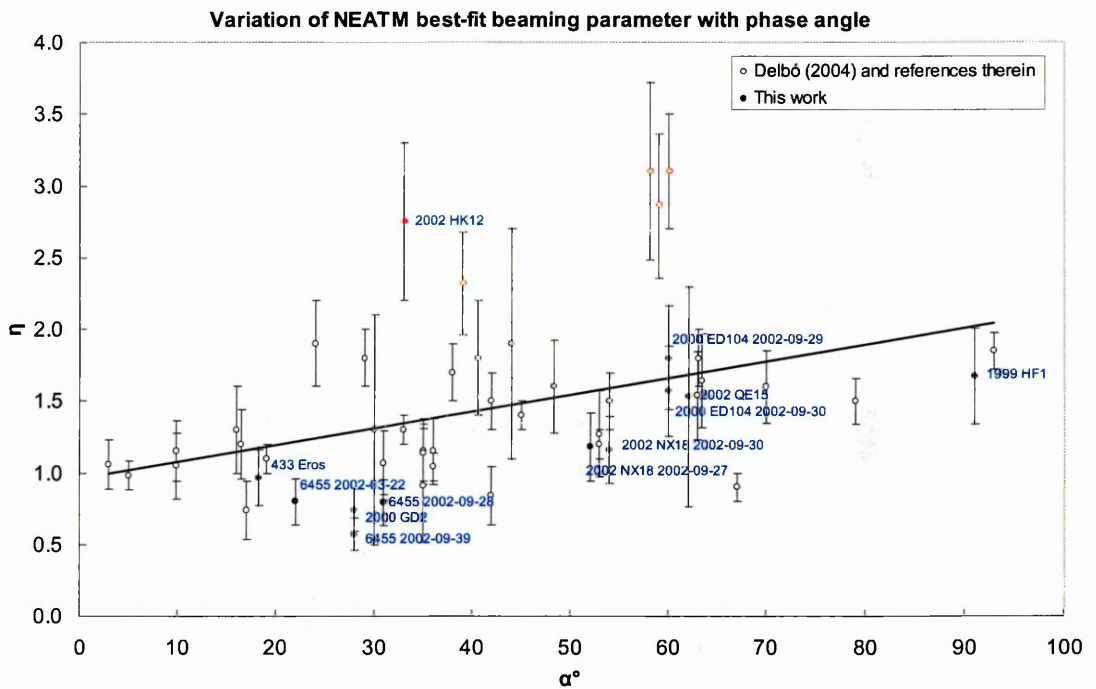


Fig. 5.25 The relationship between phase angle (α) and fitted beaming parameters (η). (Open circles) are from Delbó (2004) and references therein; (filled circles) are derived in this chapter and given in Table 5.15. The line shows a linear fit including all objects: $\eta = 0.012\alpha + 0.96$. Delbó (2004) found a linear fit $\eta = (0.011 \pm 0.002)\alpha + (0.92 \pm 0.07)$, which Delbó suggests can be used to derive a default η for a given α ; our added points have not altered the fit significantly. The scatter of η is partly due to variation of the asteroids' thermal inertia, rotation period, spin axis and shape, but also due to the evening/morning effect (see Sections 6.4.1 and 6.4.3). The red points are those marked as anomalous by Delbó *et al.* (2003) and Wolters *et al.* (2005).

Overall, 23 objects in the database had a measured η , which is the equivalent of a measurement of the asteroid's surface temperature. There were 39 separate observations

with measurements of η in total. Figure 5.25 shows the trend of increasing η with α , including our 8 objects and 12 new observations where η was measured [including (433) Eros, which was already observed several times already] bringing the total to 30 objects and the number of separate observations to 51.

Delbó *et al.* (2003) and Delbó (2004) found a possible trend of increasing albedo with decreasing diameter for S-type NEAs, and interpreted it as evidence for space weathering, with younger, fresher surfaces having higher albedos (Section 2.4.5). We include Q-types also, and for (433) Eros and (25143) Itokawa we use spacecraft diameters and albedos. Our results for (6455) 1992 HE and 2000 GD₂ are consistent with this trend (Fig. 5.26). We obtain a Pearson's correlation coefficient (for $\log p_v$ vs. $\log D_{eff}$) of $r = -0.74$ with the probability that $r = 0$ (obtained by performing a t-test) of $p < 0.001$

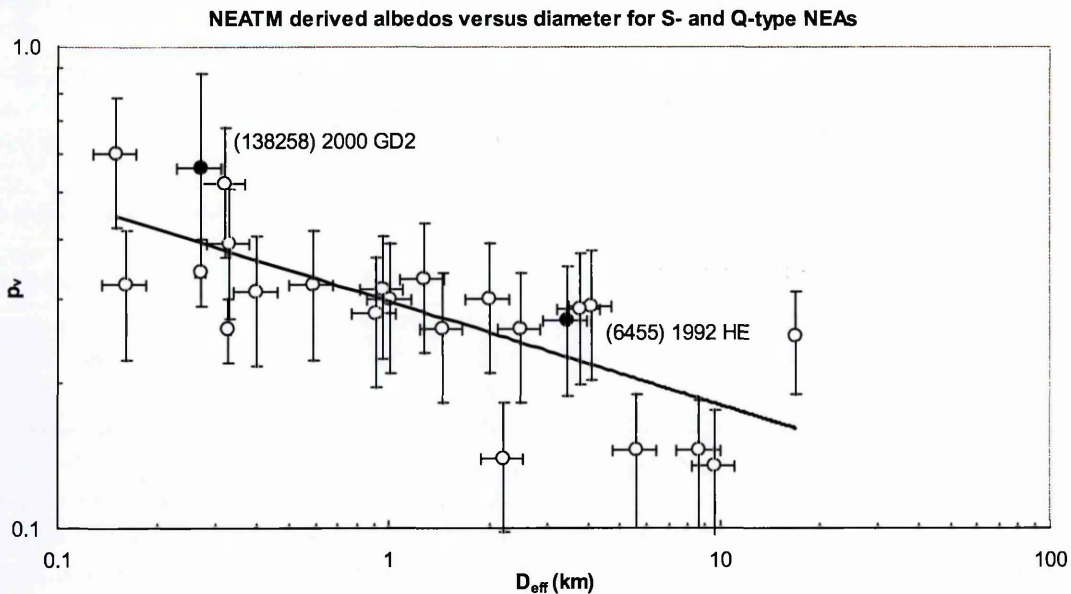


Fig. 5.26 Plot of the geometric visible albedo versus diameter derived by NEATM for S-type and Q-type NEAs using data from Delbó (2004) and references therein (open circles), with multiple datasets for objects averaged. Our data for (6455) 1992 HE and 2000 GD₂ is overlaid (filled circles).

2000 GD₂ has the highest albedo ($p_v = 0.56 \pm 0.17$) ever derived for an S-type NEA [with the following exception: Harris (1998) measured $p_v = 0.63$ for (6489) Golevka based

on a single broadband N mag. from Mottola *et al.* (1997) and using a default $\eta = 1.2$, an inappropriate value for the phase angle $\alpha = 89^\circ$; subsequent observations by Delbó (2004) found $p_v = 0.39$]. The correlation of 2000 GD₂'s albedo with its small diameter ($D_{eff} = 0.27 \pm 0.04$ km) suggests that the trend is real.

5.8.2 The Beaming Parameter

The trend of increasing η with α given in Fig. 5.25 has a physical explanation. NEATM allows the beaming parameter to be adjusted to fit the apparent colour temperature implied by the spectra. At low phase angles, for large main-belt asteroids with a low thermal inertia, typically covered with a mature dusty regolith, the beaming parameter will be less than one as there is enhanced emission in the sunward direction due to surface roughness. Hence the STM gives good fits with $\eta = 0.756$. At mid to high phase angles, the beaming parameter will be higher: for energy to be conserved, the apparent colour temperature is lower because there is “missing” thermal flux being sent in the sunward direction. The resulting modelled temperature distribution is an apparent temperature, partly due to the beaming effect enhancing or reducing the observed thermal flux depending on the phase angle of observation, and not necessarily enhancing/reducing the actual surface temperature to that which is modelled.

Objects with a higher thermal inertia, such as a bare rock surface, cause η to increase, as the temperature distribution is smoothed around the body of the asteroid due to a combination of thermal lag and rotation. In this case, the increase of η is entirely due to a real difference in the temperature profile of the asteroid: the maximum temperature is lower, and there is more flux at longer wavelengths due to the cooler asteroid surface. The NEATM finds the best-fit η based on the observations, irrespective of whether η is a result of significant thermal inertia, phase angle dependent beaming, or both. One interpretation

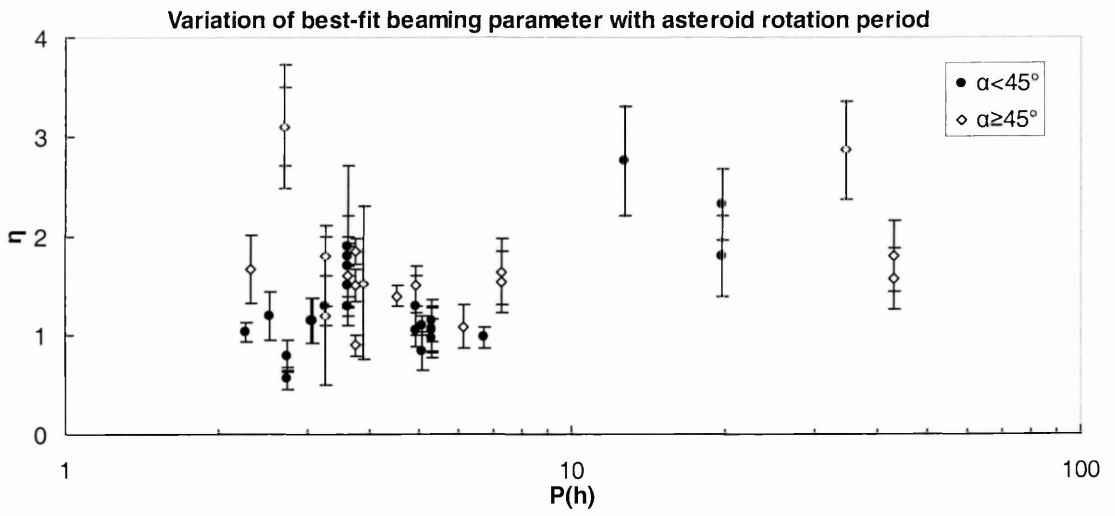
of the fact that many NEAs appear to have a value of $\eta > 1$ is that beaming due to roughness may be less than that of other solar system bodies, and that, due to high thermal inertia and/or fast rotation rates, the temperature distributions around the body are smoothed and there is significant thermal emission on the night side.

Higher thermal inertia and rotation should cause η to increase. To check if a trend is apparent, a graph of η versus rotation period P was produced [Fig. 5.27 (a)]. No trend is found: this is likely because any effect is masked by variations of η with phase angle and with thermal inertia. We also checked for a trend with D_{eff} [Fig. 5.27 (b) and (c)] since it is conceivable that smaller diameter asteroids might retain less regolith and hence have higher surface thermal inertia. Again, no trend is apparent.

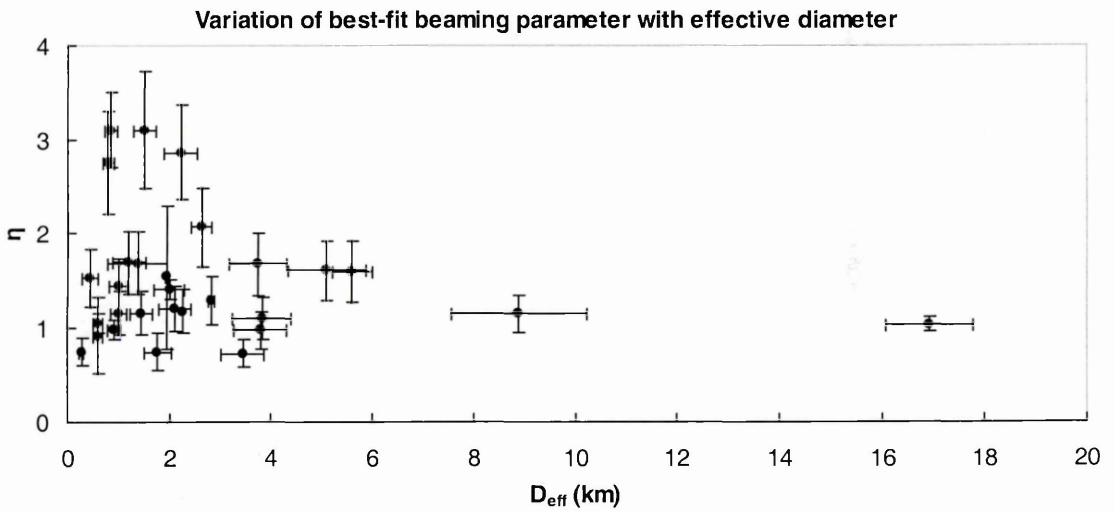
These graphs were also produced for just the S- and Q-type NEAs. No trend was found with rotation period or with effective diameter plotted over all size ranges [Fig. 5.27 (d)]. Figure 5.27 (e) shows η versus diameter for S- and Q-type NEAs below 2.3 km, including and not including the possibly anomalous object 1999 NC₄₃. With 1999 NC₄₃, we obtain a Pearson's linear correlation coefficient of $r = 0.91$, with a probability that $r = 0$ of $p = 0.01$. Without 1999 NC₄₃ we obtain $r = 0.93$, with a probability that $r = 0$ of $p = 0.02$. Therefore there is a possible trend of increasing η with diameter. This trend is unexpected. If smaller diameter NEAs had higher surface thermal inertia then we might expect decreasing η with diameter. One possible explanation for this trend is that, for observations at higher phase angles the NEATM overestimates diameters (significantly at approximately $\alpha > 45^\circ$, Table 6.1), while η also increases with phase angle. However, in Fig. 5.27 (e) we can see that only one NEA was observed at a high phase angle. We also plotted p_v versus η for S- and Q-type asteroids [Fig. 5.27 (f) and (g)], and there may be a possible trend of decreasing η with increasing p_v for asteroids below 2.3 km diameter, although the correlation is lower [$r = -0.76$ and $p(r=0) = 0.077$].

Fig. 5.27

(a)



(b)



(c)

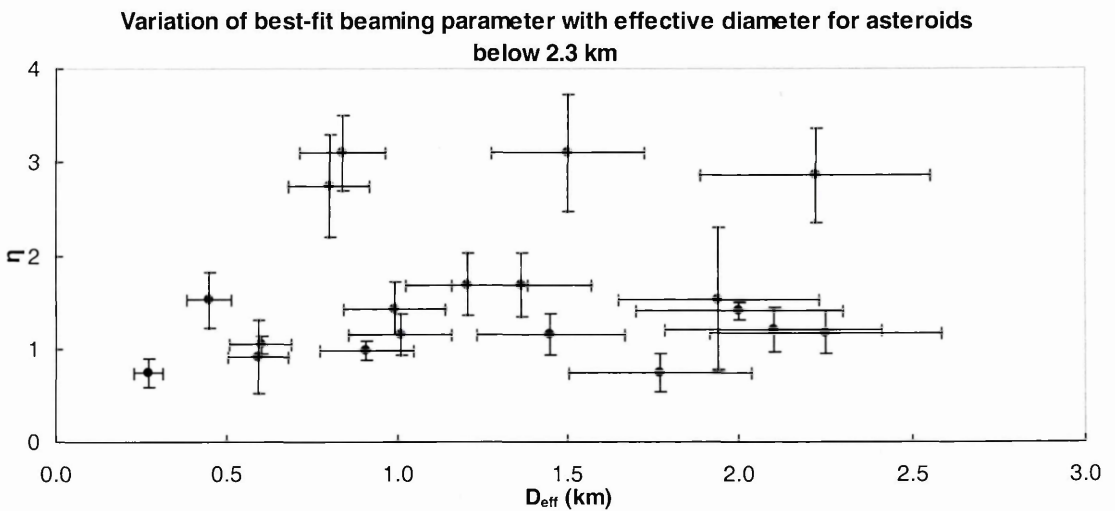
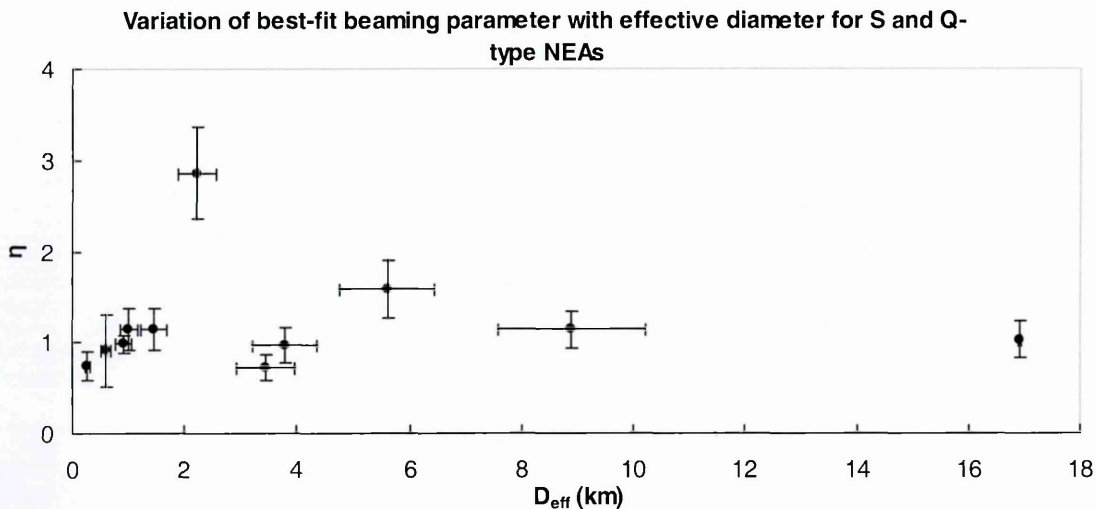
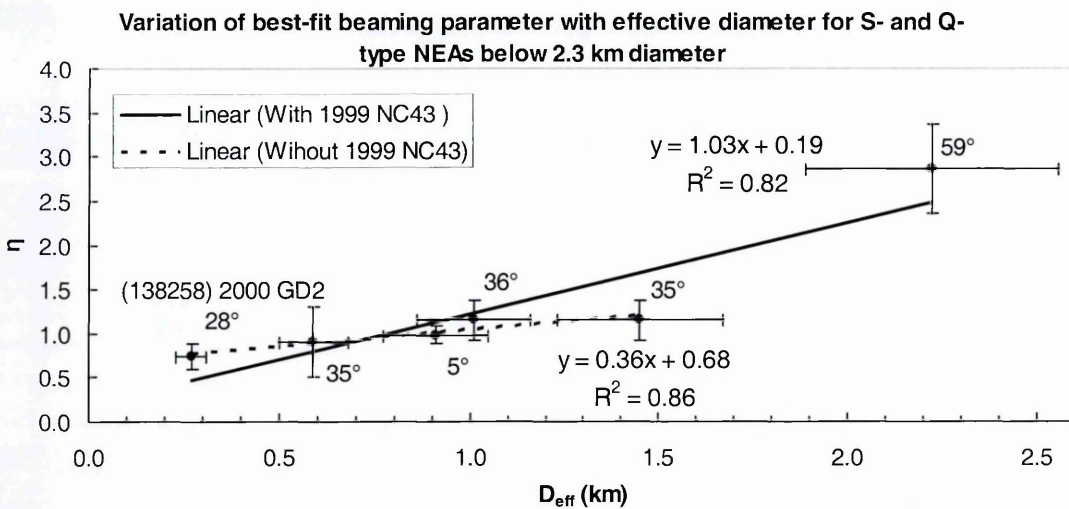


Fig. 5.27 continued.

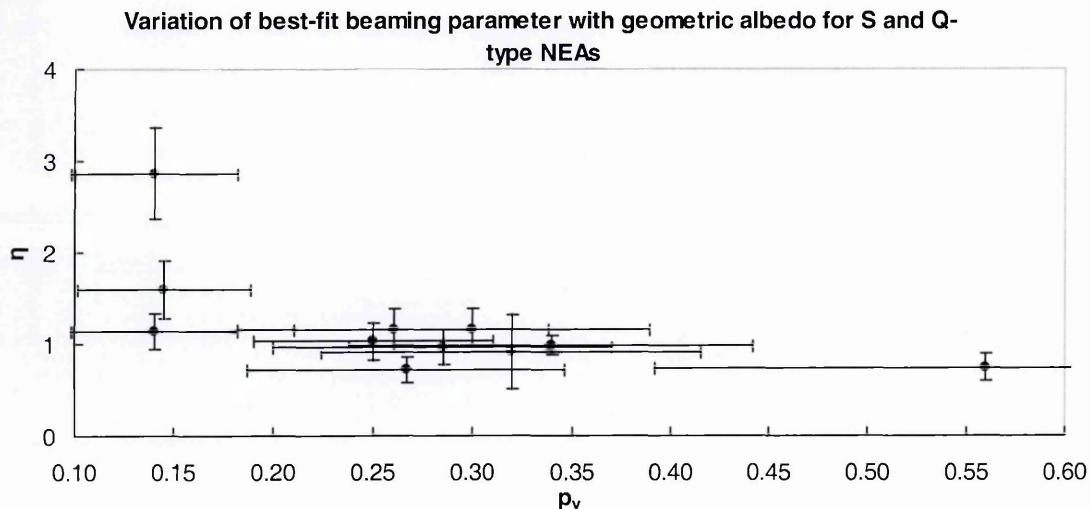
(d)



(e)



(f)



(g)

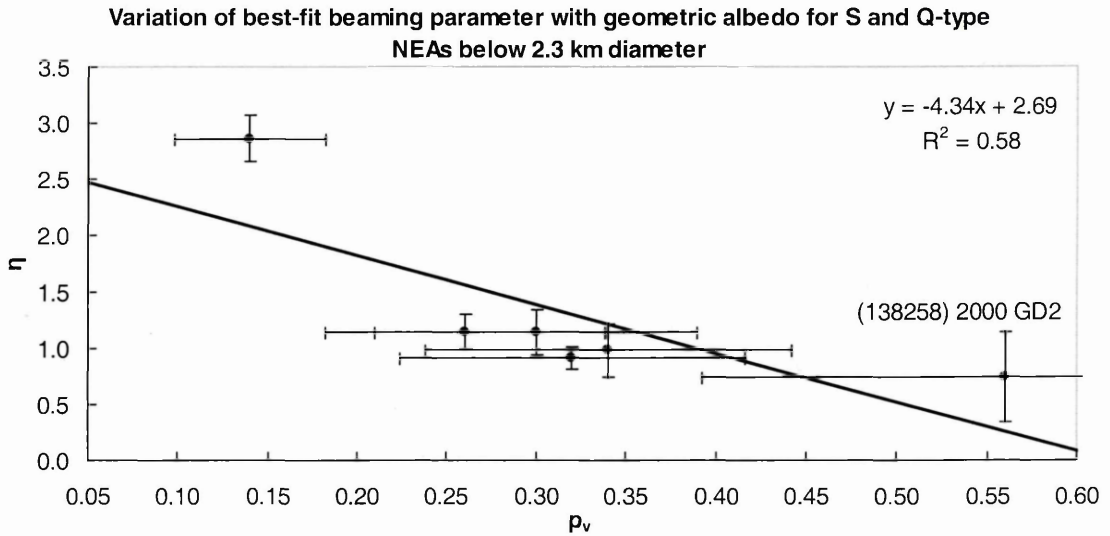


Fig. 5.27 (a) Variation of NEATM best-fit beaming parameter η with: (a) rotation period $P(h)$; (b) effective diameter D_{eff} (km); (c) effective diameter below 2.3 km (no trend found even if possibly anomalous points above $\eta = 2$ are excluded); (d) effective diameter for S- and Q-type asteroids; (e) effective diameter for S- and Q-type asteroids below 2.3 km with data labels showing phase angle; (f) geometric albedo for S- and Q-type asteroids; (g) geometric albedo for S- and Q-type asteroids below 2.3 km diameter. In (b)-(g) objects for which there is more than one observation have their values averaged.

It may be important that the trend of increasing beaming parameter with diameter is only apparent for S- and Q-type NEAs. It is possible that this trend is related in some way to the trend of decreasing albedo for increasing diameters for S- and Q-type NEAs (Fig. 5.26) interpreted as evidence for space weathering. Smaller NEAs are thought to have younger surfaces (i.e. the time since they were catastrophically disrupted from their parent body is shorter than for larger bodies, see also Section 2.4.5). A speculative explanation for increasing beaming parameter with diameter is that something about the process of space weathering (one theory is theory is sputtering of iron-bearing silicates by the impact of the solar wind, cosmic rays and possibly micrometeorite impacts, producing nanophase iron) is changing the asteroid's surface to in such a way as to increase the beaming parameter: either by decreasing surface roughness or by increasing thermal inertia.

An exception in the η - α plot (Fig. 5.25) is 2002 HK₁₂, which appears to join a group of four other anomalous objects. Like these objects, the FRM for 2002 HK₁₂ is also a good fit. Using the relation derived by Spencer *et al.* (1989), a rough estimate of the surface thermal inertia from measured values of η can be obtained (Section 2.7). For example, Harris *et al.* (1998) found high values for some smaller near-Earth asteroids that are characteristic of pure rock. The η -value found for 2002 HK₁₂ of 2.75 indicates an unrealistically high surface thermal inertia $>5000 \text{ J m}^{-2} \text{ s}^{-1/2} \text{ K}^{-1}$. An explanation of η -values purely in terms of thermal inertia and surface roughness is probably an oversimplification.

Delbó *et al.* (2003) pointed out the disconcerting fact that no high- η objects are observed at moderate or low phase angles. The 2002 HK₁₂ point is at a lower phase angle than the other high- η objects. Delbó *et al.* suggest two different explanations, beyond the fact that a statistically significant number of objects have not yet been observed. (i) Two of the high- η objects are known to be binaries. Near-Earth binaries may have unusually rough surfaces, because of possible disruption of the rubble piles from which they are thought to be constituted, when passing close to a planet (Section 2.8). As a result they would have a high degree of beaming in the sunward direction due to surface roughness, and consequently a lower apparent temperature distribution at high phase angles. (ii) NEAs can often be elongated, so shape or shadowing effects may be more pronounced at high phase angles (Section 7.2.5). 2002 HK₁₂ could be an example of (ii), since it has a lightcurve amplitude of 1.5 magnitudes, indicating that it is a highly elongated asteroid.

With the current wide scatter in measured beaming parameters at high phase angle, the use of a default $\eta = 1.5$ could be unsafe, although it is interesting that in the cases for 1999 HF₁ which is a binary asteroid, and for (53789) 2000 ED₁₀₄ which has a large lightcurve amplitude and is therefore presumably very elongated, they both fit well on the

trend shown in Fig. 5.25. The situation may be clarified when there is a greater dataset of NEAs observed in the thermal infrared at several different phase angles.

The NEATM phase correction models the asteroid as a smooth sphere, assuming Lambertian emission, and calculates the thermal flux from the sunlit portion visible to the observer only, thereby assuming zero emission from the night side. Objects with significant thermal inertia will have non-negligible thermal emission on their night side; at higher phase angles the effect of omitting the night side emission will be more significant. By assuming zero emission, all the observed thermal flux has to come from the sunlit side. To account for the low colour temperature of the observed thermal flux, higher best-fit values of η are found. This may contribute to the general trend of increasing η with higher phase angles as well as to the high beaming parameters of the anomalous objects. If the thermal emission on the night side was included in the model, as in the modified projected model (Section 4.3.5), then this might lead to clarification of the effects on η at high phase angle and the physical interpretation of best-fit beaming parameters. Chapter 6 assesses the inaccuracies of the NEATM due to not including thermal emission on the night side and introduces the Night Emission Simulated Thermal Model (NESTM) which combines features of the NEATM and the modified projected model.

6 The Night Emission Simulated Thermal Model

6.1 Introduction

6.1.1 Implications of Previous Studies of NEAs Using the NEATM

The trend of increasing beaming parameter η with phase angle α , using all available NEATM fits to thermal IR fluxes from NEAs, is given in Fig. 5.25, and discussed in Section 5.8. Delbó (2004) points out that their sample contained only one object with high beaming parameter at a low phase angle, (2100) Ra-Shalom ($\eta = 2.3$, $\alpha = 39^\circ$), which suggests that objects with high thermal inertia, i.e. regolith-free surfaces, are uncommon among the NEA population. Our measurement of 2002 HK₁₂ ($\eta = 2.75$, $\alpha = 33^\circ$) adds one more object, but this observation still seems valid.

Delbó observes: “One of the crucial issues concerning the reliability of the NEATM is to assess the error incurred by ignoring thermal emission from the night side. Ignoring the night side flux causes the resulting diameter to be overestimated and the albedo consequently underestimated. If such an error had played a major role, one would expect to see a trend of decreasing albedos with increasing phase angle. Results of this work indicate that this is not the case up to $\alpha \sim 60^\circ$.” However, the default model uncertainty in the measurement of p_v is 30% and the sample size is still small.

The degree to which the surface of an asteroid responds to changes in insolation can be characterised by the thermal parameter Θ , which combines the rotation rate $\omega = 2\pi/P$, the surface thermal inertia Γ and the STM maximum temperature T_{max} (Spencer *et al.*, 1989):

$$\Theta = \frac{\Gamma\sqrt{\omega}}{\varepsilon\sigma T_{max}^3} \quad (6.1)$$

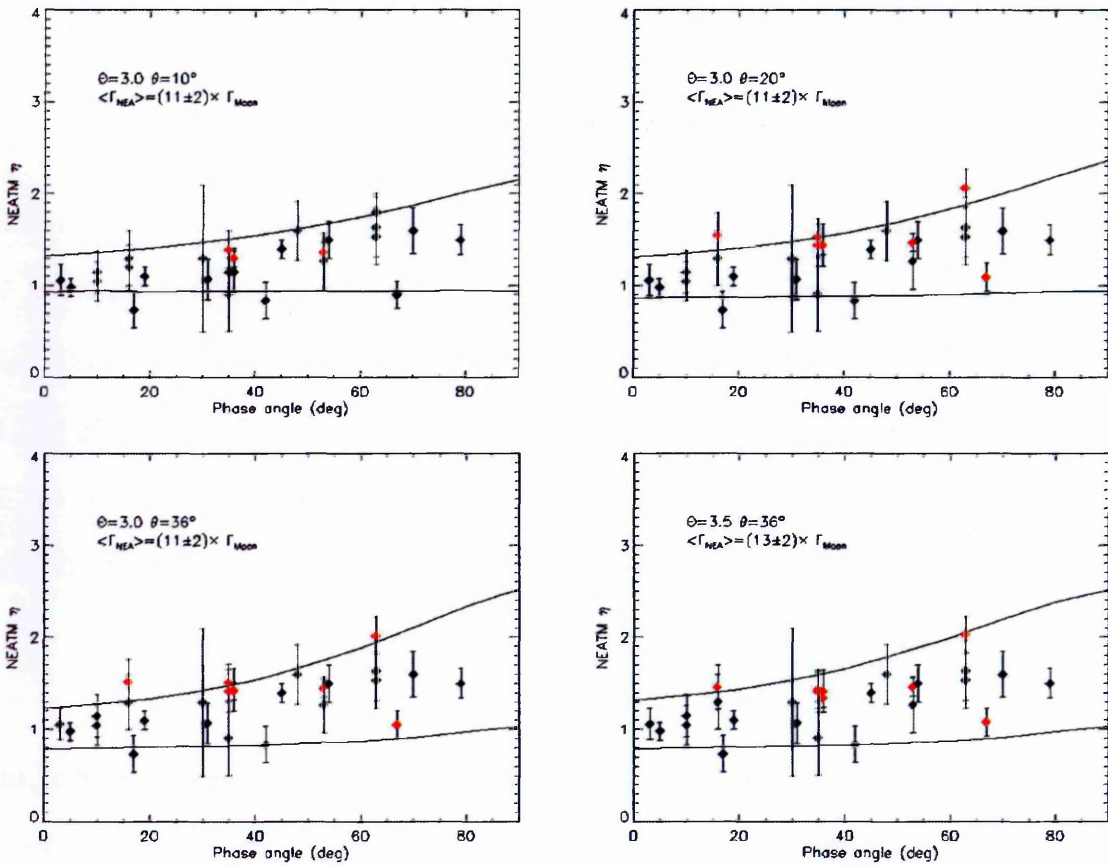


Fig. 6.1 Limiting curves, reproduced from Delbó (2004), which fit the observed α - η distribution for different thermal parameters Θ and surface roughness $\bar{\theta}$. The lower limit is represented by a curve calculated for $\Theta = 0$, a range of $\bar{\theta}$ and for the absolute value of $|\alpha|$: $\eta(|\alpha|, \Theta = 0, \bar{\theta})$. The phase angle is considered to be positive if the observer is centred on the asteroid's "afternoon" side and negative on the "morning" side; for $\Theta = 0$, the surface temperature distribution is symmetrical with respect to the subsolar point, and so for this curve it is not important whether α is positive or negative. The upper limit is found by taking the curve that an observer would find by always viewing the morning hemisphere of the asteroid with a rotational axis perpendicular to the plane containing the Sun and the Earth: the "morning curve" $\eta(-|\alpha|, \Theta, \bar{\theta})$. Data points where η has been corrected to a mean rotation period of 6 hours are shown in red colours.

Using a thermophysical model similar to that described in Section 4.3.1, but which also models macroscopic surface roughness $\bar{\theta}$ (Section 7.2.4), Delbó (2004) found that for a given value of thermal parameter Θ and $\bar{\theta}$, the possible derived η -values are delimited by two curves in the η - α plane, depending on the orientation of the asteroid with respect to its illumination. An asteroid with nonzero surface thermal inertia will be hotter on the

afternoon side (defined as $+\alpha$) and cooler on the morning side ($-\alpha$). The consequent scatter of the η -values is referred to as the “evening/morning” effect. Delbó best-fit these curves to the observed η - α distribution (i.e. Fig. 5.25) and found the range of Θ that fit reasonably to be 2.8-3.5 (Fig. 6.1). Assuming that all NEAs enclosed by the curves in Fig. 6.1 have the same thermal parameter, Delbó found a best-fit average surface thermal inertia $\Gamma = 550 \pm 100 \text{ J m}^{-2} \text{ s}^{-1/2} \text{ K}^{-1}$ (see also Section 2.7).

Using their thermophysical model, Delbó (2004) was able to assess the accuracy of the NEATM for a range of α , Θ and $\bar{\theta}$, with the asteroids observed on both the morning and afternoon side. Delbó found that for $\eta > 1.5$, the NEATM is likely to underestimate the albedo and consequently overestimate the diameter, the error being the result of ignoring thermal emission from the night side. The accuracies derived indicated that the NEATM gives reliable results for an NEA if its thermal parameter is in the range $0.1 \leq \Theta \leq 5$ and the phase angle $|\alpha| < 60^\circ$.

6.1.2 Introducing the NESTM

In this chapter we introduce a new thermal model that combines features of the modified projected model (Section 4.3.5) and the NEATM (Section 4.3.4): the Night Emission Simulated Thermal Model (NESTM). The NESTM applies an iso-latitudinal night side temperature that is a fraction f of the maximum day side temperature when $\eta = 1$ (T_{max}). The fraction depends on the asteroid’s thermal parameter Θ . We relate f to Θ in Section 6.3 by using the simple thermophysical model discussed in Section 4.3.1.

The NESTM requires an input of an assumed surface thermal inertia Γ and an asteroid rotation period P . As we do not generally know the surface thermal inertia of an NEA, we study four different versions of the NESTM corresponding to different Γ . In Section 6.4, we attempt to assess the reliability of the four versions of the NESTM at different phase

angles by fitting them to simulated thermal IR fluxes from asteroids with different applied surface thermal inertias, their synthetic temperature arrays produced using the simple thermophysical model. From analysing the results, we can recommend which version of NESTM to use as a default. Finally in Section 6.5, we compare derived NESTM diameters with diameters of NEAs derived from radar observations, and contrast this with a similar analysis using NEATM.

6.2 NESTM Operation

In this chapter we refer to the NEATM maximum day side temperature as T_{fit} , as opposed to T_{max} in Chapter 4:

$$T_{fit} = \left[\frac{S_0(1-A)}{\eta \epsilon \sigma r^2} \right]^{\frac{1}{4}} \quad (6.2)$$

where S_0 is the solar flux at 1 AU = 1374 W m⁻², A is the bolometric Bond albedo, ϵ is the emissivity (assumed $\epsilon = 0.9$), σ is the Stefan-Boltzmann constant and r is the Sun-asteroid distance (AU). T_{max} is defined as the maximum temperature in the projected model, i.e. the NEATM with $\eta = 1$:

$$T_{max} = \left[\frac{S_0(1-A)}{\epsilon \sigma r^2} \right]^{\frac{1}{4}} \quad (6.3)$$

A Fortran program THERME (Appendix F) was written that runs the NESTM using an input file containing wavelengths $\lambda_{obs}(n)$, fluxes $F_{obs}(n)$ and errors $\sigma_{obs}(n)$, a parameter file providing an absolute visual magnitude H_V , a phase parameter G , Sun-asteroid distance r (AU), Earth-asteroid distance Δ (AU), phase angle α , thermal inertia Γ and rotation period P . As explained in Section 6.4, the NESTM was run for four different values of Γ : 40, 200, 550 and 2200 J m⁻² s^{-1/2} K⁻¹. If P is not known, it is assumed to be 5 h, which is the average rotation period of an NEA (Binzel *et al.*, 2002).

As for the NEATM, the NESTM goes through a range of p_v , then for each p_v a range of η , and generates a surface temperature array. For every p_v , an effective diameter D_{eff} is found using Eq. 4.3 and the input H_V . The model thermal IR fluxes $F_{mod}(n)$ are generated for each λ_{obs} , integrating over the surface using the Planck function (Eqs. 4.27, 4.8). For each p_v and η the error-weighted residual χ^2 is found, and the best-fit p_v has the smallest residual.

As in the modified projected model, a parameter f is used to define the night side temperature, so that for a latitude ϕ the night side temperature T_{night} is:

$$T_{night} = fT_{max} \cos^{\frac{1}{4}} \phi \quad (6.4)$$

Since the degree to which the surface of an asteroid can respond to changes in insolation is characterised by the thermal parameter Θ (Eq. 6.1), the f parameter is a function of Θ . Clearly, since Θ is dependent on T_{max} , we must recalculate the asteroid's thermal parameter for every p_v , so THERME is run with a look-up table with an appropriate f for any given small range of thermal parameter. We describe this table and how it was generated in Section 6.3. Θ is much more strongly dependent on Γ and P than p_v , such that the appropriate f does not typically change by more than 0.02 as a range of p_v is run through, and so it would be an acceptable simplification to run the model with a fixed f parameter for the whole range of p_v if required.

The beaming parameter η is applied to the day side, so that the maximum day side temperature T_{fit} is:

$$T_{fit} = \frac{T_{max}}{\eta^{\frac{1}{4}}} \quad (6.5)$$

The major departure from the modified projected model here is that a modified maximum day side temperature T_{mod} is no longer iteratively calculated using the energy balance Eq. 4.30. Instead the beaming parameter η is best-fitted, effectively measuring the real day

side temperature from the observed thermal IR fluxes. This makes the model considerably simpler than the modified projected model.

As for the NEATM the asteroid is treated as a Lambertian sphere:

$$T_{day} = T_{fit} \cos^{\frac{1}{4}} \theta \cos^{\frac{1}{4}} \phi \quad (6.6)$$

where θ is the longitude. Like the modified projected model, if $T_{night} > T_{day}$ at any point on the day side then T_{night} is used. The emitted flux measured from Earth (outside the atmosphere) $F_{mod}(n)$ is thus:

$$F_{mod}(n) = \frac{D_{eff}^2}{2\Delta^2} \varepsilon \int_{-\frac{\pi}{2}}^{\frac{\pi}{2}} \left[\int_{\alpha-\frac{\pi}{2}}^{\frac{\pi}{2}} B \left(\lambda(n), G \left(T_{fit} \cos^{\frac{1}{4}} \theta, fT_{max} \right) \cos^{\frac{1}{4}} \phi \right) \cos(\alpha - \theta) d\theta \right. \\ \left. + \int_{\frac{\pi}{2}}^{\alpha+\frac{\pi}{2}} B \left(\lambda(n), fT_{max} \cos^{\frac{1}{4}} \phi \right) \cos(\alpha - \theta) d\theta \right] \cos^2 \phi d\phi \quad (6.7)$$

where $G(x, y) = x$ if $x > y$ and $G(x, y) = y$ if $x < y$.

6.3 Defining an Appropriate f Parameter

Applying a night side constant temperature profile as a latitude-dependent fraction f of T_{max} is just an approximation of the effect that a body with significant thermal inertia would have on the temperature profile. In reality the temperature on the night side would slowly cool from the day side temperature. We can model the temperature for the night side for an asteroid with a given Γ , P , A , and r using the simple thermophysical model described in Section 4.3.1.

The thermophysical model was run for an asteroid with bolometric Bond albedo $A = 0.2$ at a distance from the Sun of $r = 1$ AU and at thermal inertias $\Gamma = 40, 550$ and 2200 $\text{J m}^{-2} \text{s}^{-1/2} \text{K}^{-1}$: representing a “dusty” Γ approximately equivalent to that of the lunar surface, the “average” NEA Γ found by Delbó (2004), and a “bare rock” Γ equivalent to that of granite. It was run for rotation periods $P = 1, 2, 3, 4, 5, 6, 8, 10, 12, 15, 20, 25, 30,$

40, 50, 60, 80, 100 h. An average NEA rotation period is 5 h (Binzel *et al.*, 2002). Code for the thermophysical model was written by S. F. Green. The model assumes that the pole orientation is 90° and that the asteroid is spherical. Other parameters used in the model are the maximum skin depth $z_{max} = 2.0$ and the number of steps over z_{max} $n(z) = 60$. The accuracy of the temperature found for each surface element $T_{acc} = 0.05$ K and each surface element goes through $n_{rev} = 300$ rotations. It produces equatorial surface temperatures only. Example temperatures curves are shown in Fig. 6.2.

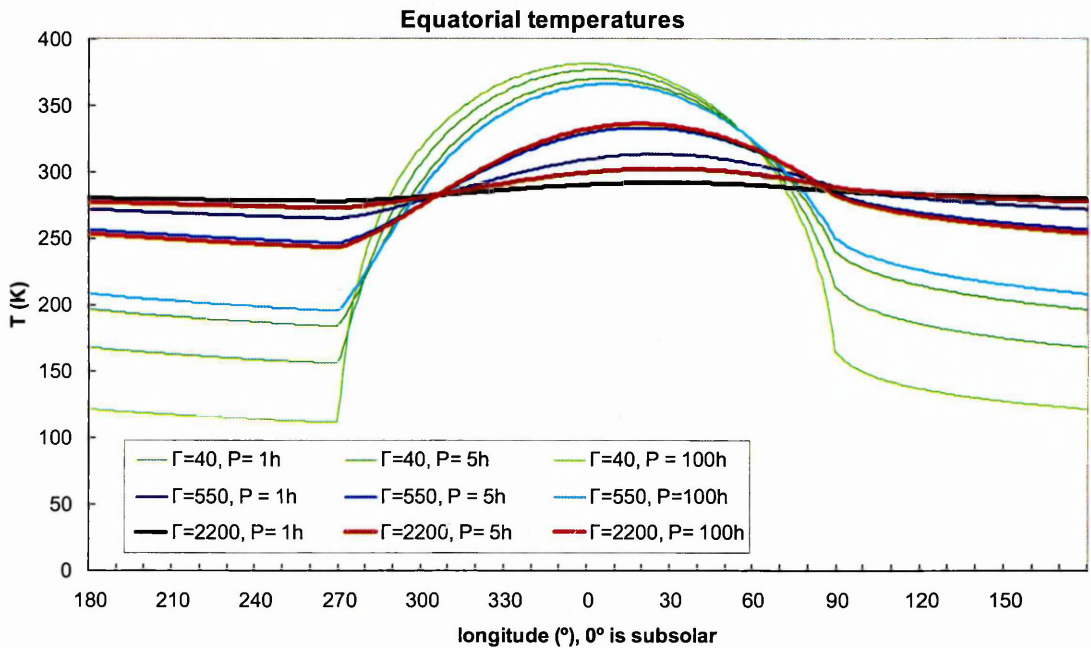


Fig. 6.2 Equatorial temperatures produced by the thermophysical model run for an asteroid at $r = 1$ AU, with $A = 0.2$.

The average night side temperature $\bar{T}(90^\circ \geq \theta \geq 270^\circ)$ is found for each plot, from which we can derive f , having found T_{max} following Eq. 6.3:

$$f = \frac{\bar{T}(90^\circ \geq \theta \geq 270^\circ)}{T_{max}} \tag{6.8}$$

We can relate these f parameters to the thermal parameter Θ through Eq. 6.1, and hence have an appropriate value to use for any heliocentric distance, rotation period and albedo in

the NESTM. The variation of f with Θ is given in Fig. 6.3, and the resulting look-up table is given in Appendix G.

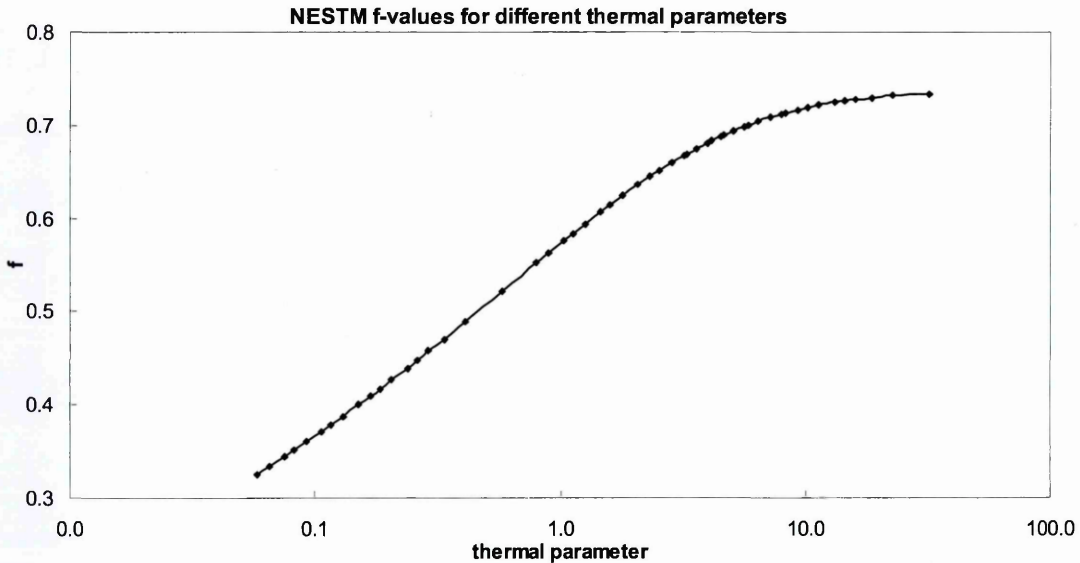


Fig. 6.3 f parameters for different thermal parameters Θ found by ratioing night side equatorial surface temperatures, produced using the thermophysical model, to T_{max} .

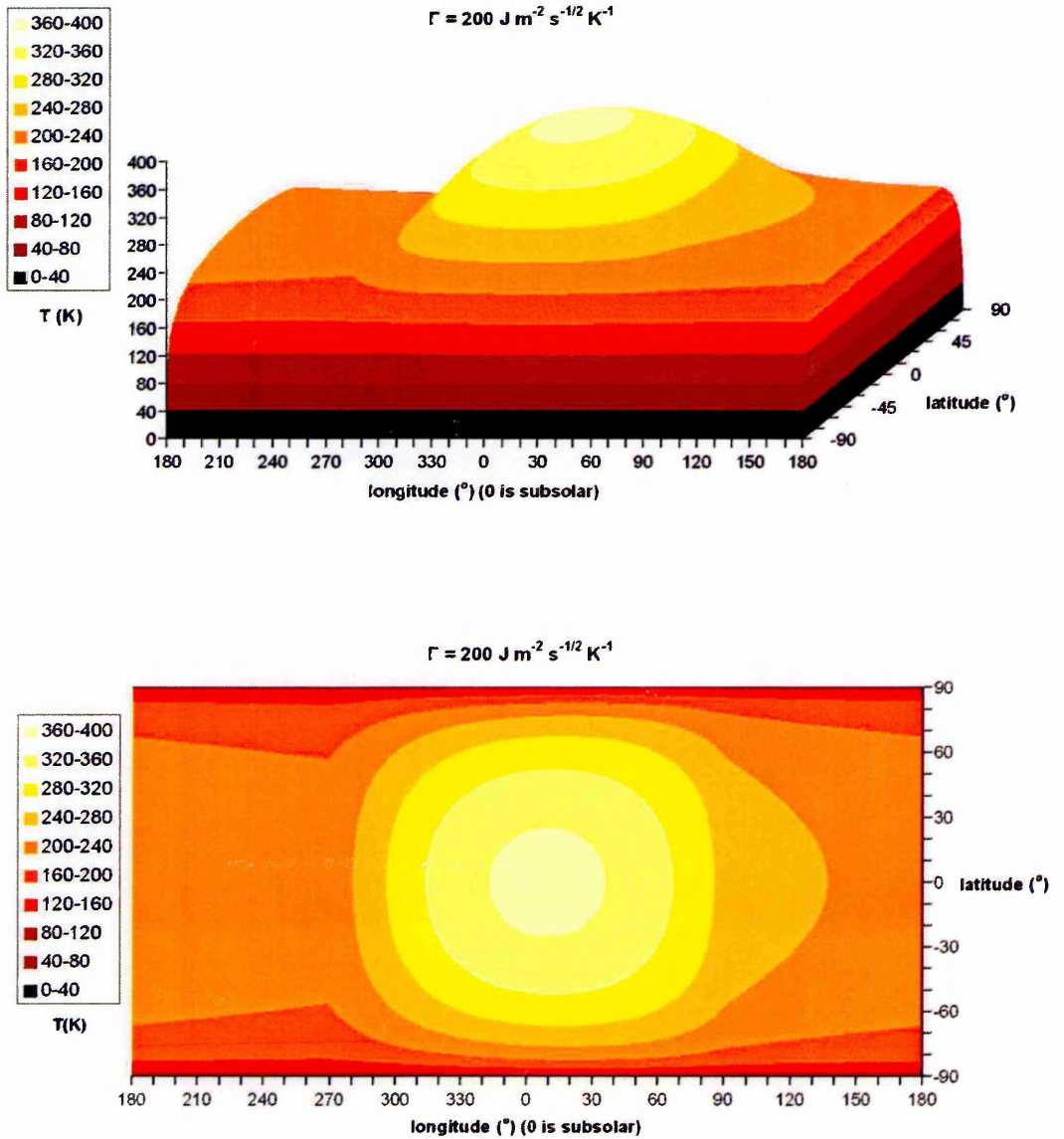
6.4 Testing the NESTM

6.4.1 Model Testing Method

The NESTM was tested by creating temperature arrays of a test asteroid using the thermophysical model. S. F. Green's Fortran code for the thermophysical model was altered to produce temperatures for surface elements at different latitudes ϕ as well as different longitudes θ at 1° intervals. We used an asteroid with parameters $p_v = 0.25$, $r = 1$ AU, $P = 5$ h, and $\Gamma = 40, 200, 550$ and 2200 $\text{J m}^{-2} \text{s}^{-1/2} \text{K}^{-1}$. A surface thermal inertia of $\Gamma = 200$ $\text{J m}^{-2} \text{s}^{-1/2} \text{K}^{-1}$ is similar to those that have been derived for a small number of NEAs (four, to date; Section 2.7). Assigning a phase parameter $G = 0.15$, the asteroid's albedo is equivalent to $A = 0.09815$. Following Eq. 6.1, the asteroid's surface has thermal parameter $\Theta = 0.238, 1.190, 3.273$ and 13.094 respectively. $z_{max} = 2.0$, $n(z) = 60$, $T_{acc} = 0.05$ K and $n_{revs} = 300$ (except for $\Gamma = 2200$ $\text{J m}^{-2} \text{s}^{-1/2} \text{K}^{-1}$ where $n_{revs} = 1000$ was used because $T_{acc} > 0.05$ K after 300 revolutions in this case). The resulting temperature array

for $\Gamma = 200 \text{ J m}^{-2} \text{ s}^{-1/2} \text{ K}^{-1}$ and the equatorial temperatures for all four cases are shown in Fig. 6.4.

Fig. 6.4
(a)



(b)

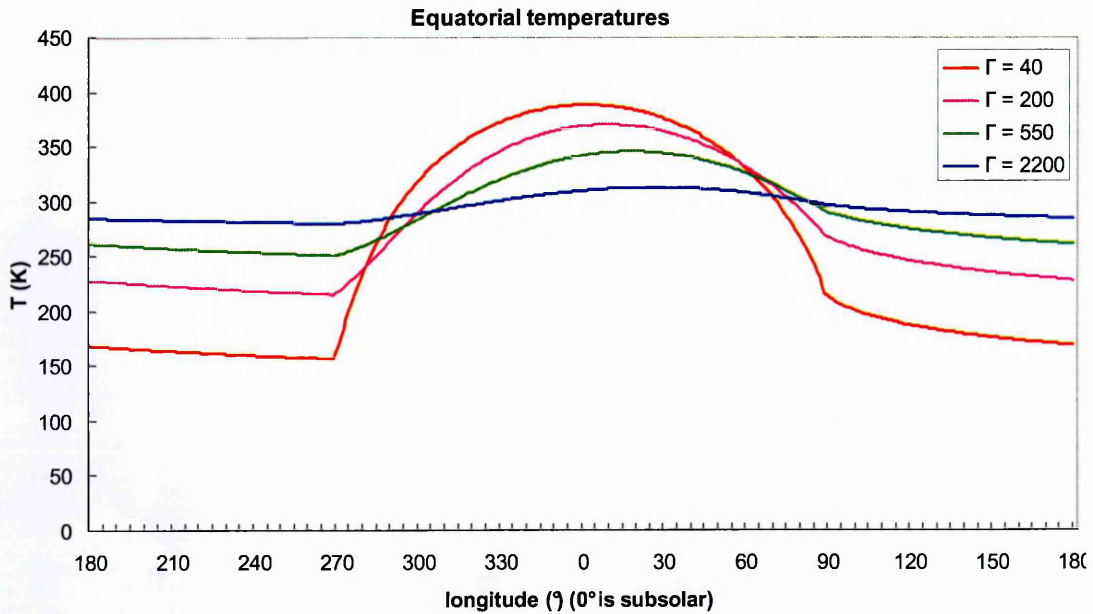


Fig. 6.4 Surface temperatures for the thermophysical model run with $A = 0.09815$, $P = 5h$, $r = 1$ AU: (a) $\Gamma = 200$, (b) equatorial surface temperatures. As the surface thermal inertia increases, the maximum day side temperature decreases and the night side temperature increases.

To contrast the different models, the NESTM temperature array produced by setting $p_v = 0.25$, $r = 1$ AU, $P = 5$ h and $\Gamma = 200 \text{ J m}^{-2} \text{ s}^{-1/2} \text{ K}^{-1}$, and the NEATM temperature array produced by setting $p_v = 0.25$ and $r = 1$ AU is shown in Fig. 6.5. Figure 6.5 (c) shows the NEATM and NESTM equatorial temperatures, when run with $\Gamma = 40, 200, 550$, and $2200 \text{ J m}^{-2} \text{ s}^{-1/2} \text{ K}^{-1}$. η is set to 1 in all cases.

Fig. 6.5
(a)

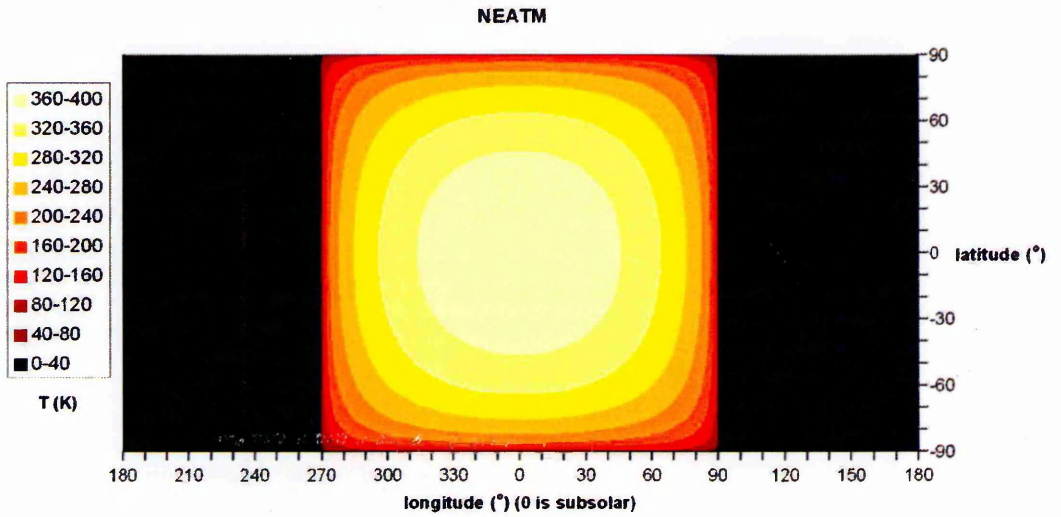
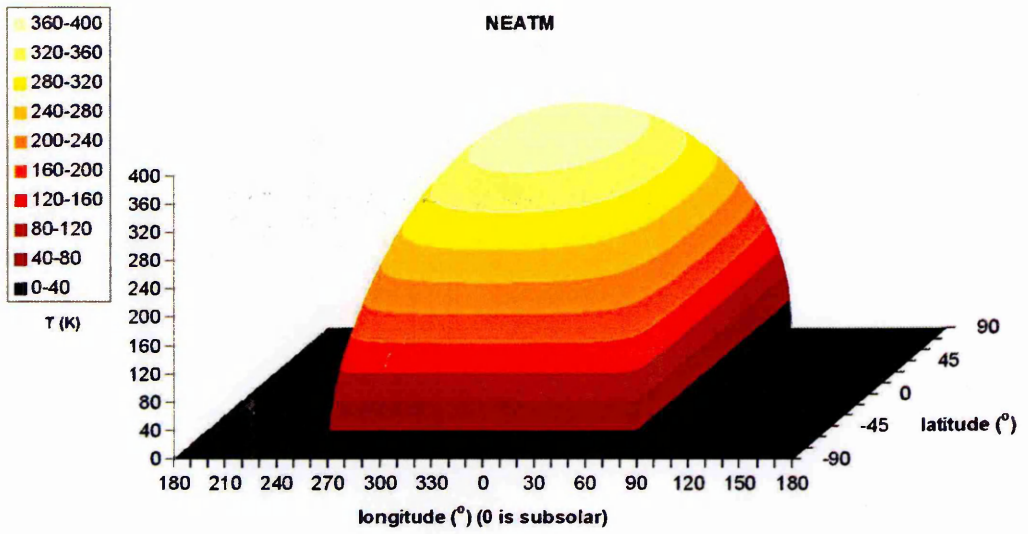
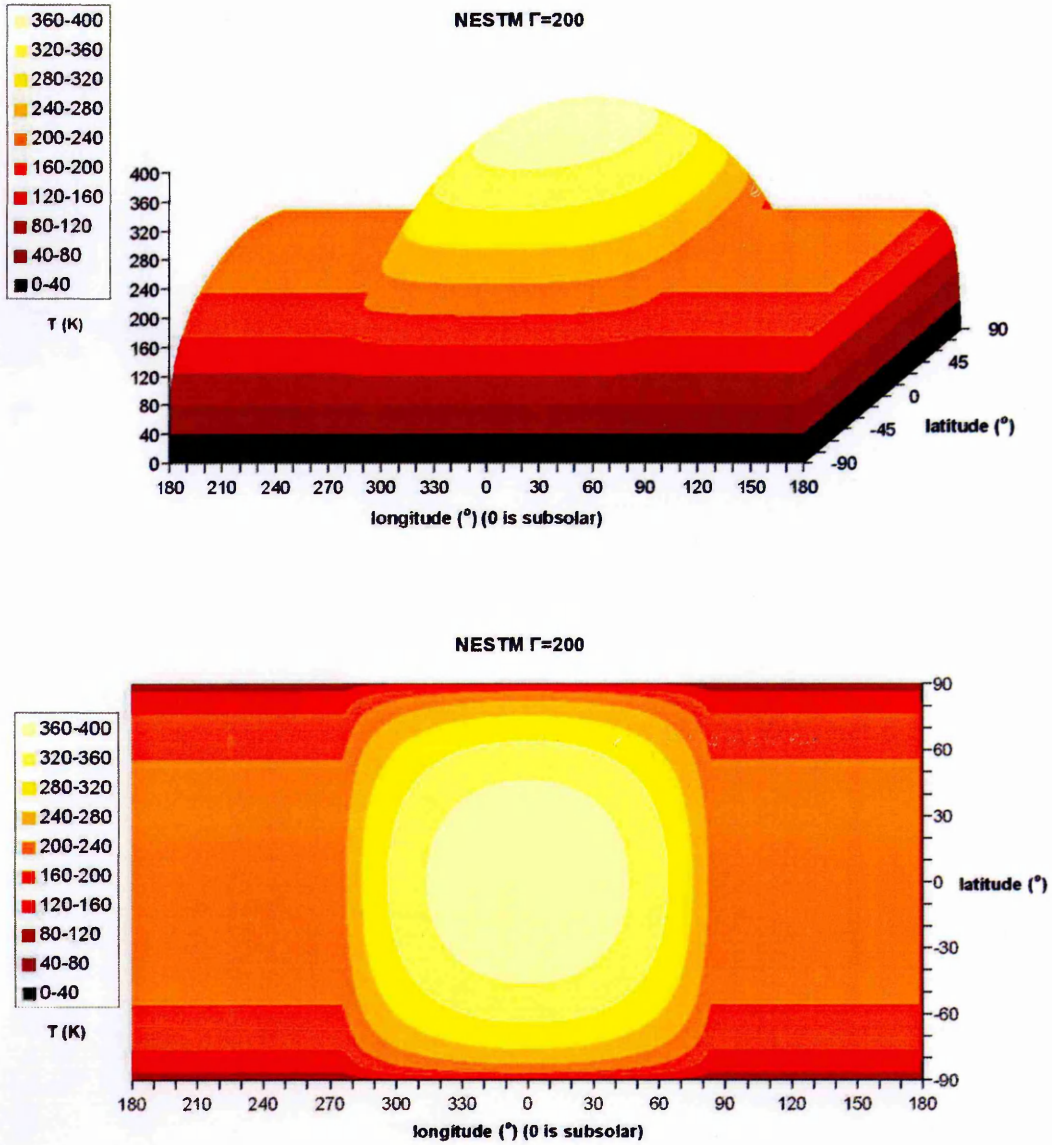


Fig. 6.5 continued.
(b)



(c)

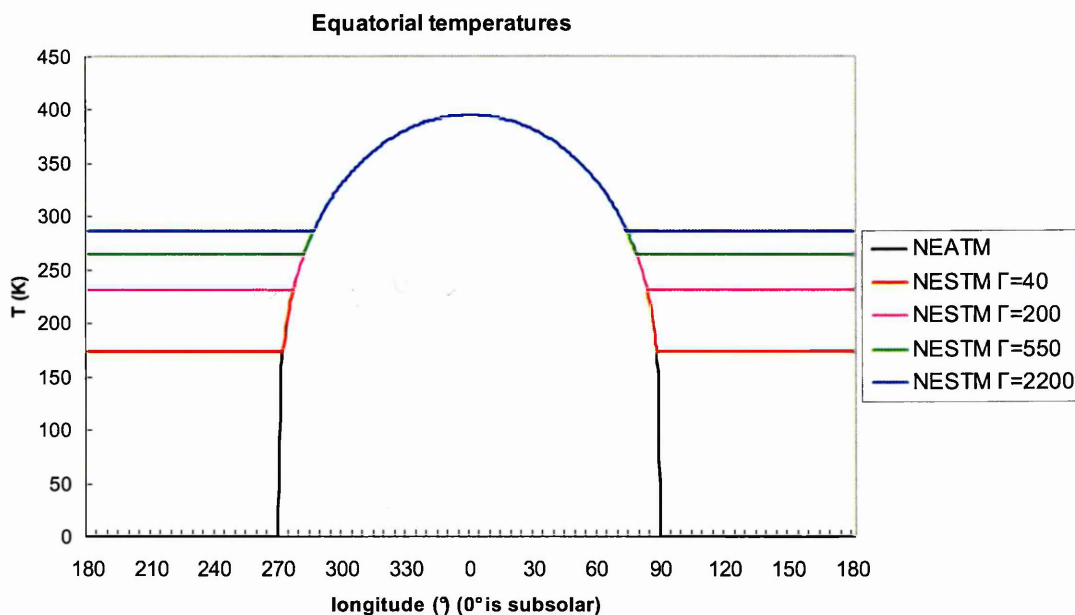


Fig. 6.5 Temperature profiles at different longitudes θ and latitudes ϕ produced by the NEATM and NESTM for an asteroid with $p_v = 0.25$, $G = 0.15$, $r = 1.0$ AU. (a) The NEATM: it can be seen that there is zero emission on the night side; (b) NESTM with $P = 5$ h, $\Gamma = 200 \text{ J m}^{-2} \text{ s}^{-1/2} \text{ K}^{-1}$: for a given latitude there is a constant temperature on the night side. (c) Equatorial temperatures for NEATM and NESTM with four different thermal inertias $\Gamma = 40, 200, 550$ and $2200 \text{ J m}^{-2} \text{ s}^{-1/2} \text{ K}^{-1}$ and $P = 5$ h. These correspond to asteroids with thermal parameter $\Theta = 0.238, 1.190, 3.273$ and 13.094 respectively. The appropriate f parameters are obtained from a look-up table plotted in Fig. 6.4 and are $f = 0.439, 0.584, 0.669$ and 0.725 respectively. Since η is set to 1 in all cases, the day side temperatures are identical except for the last 16° longitude at equatorial latitudes, where the NESTM night side temperature for that latitude is greater than the calculated day side temperature.

A Fortran program “tempread” was written that reads in the temperature arrays and forms synthetic thermal IR fluxes $F_{obs}(n)$, depending on the assigned parameters: asteroid diameter D_{eff} , Earth-asteroid distance Δ (AU), phase angle α , “instrument” wavelengths $\lambda_{obs}(n)$. The λ_{obs} are set at filter wavelengths equivalent to a range of narrow-band filters used by the Keck-1 Long Wavelength Spectrograph, which are ideal for sampling a wide range of wavelengths at a high spectral resolution: 4.8, 8.0, 8.9, 10.7, 11.7, 12.5 and 20.0 μm , i.e. one M- and Q-band measurement and five N-band measurements. The asteroid diameter D_{eff} was set to 1.0 km, and $\Delta = 0.2$ AU. The output flux is determined

from the temperature array by integrating the black body function over the visible surface, i.e. over all latitudes, and for the 180° of longitude in the temperature array that would be visible depending on the phase angle (c.f. Eq. 4.27 where not all visible longitudes were integrated, since the night side emission was assumed to be zero):

$$F_{obs}(n) = \frac{\epsilon D_{eff}^2}{4\Delta^2} \int_{-\frac{\pi}{2}}^{\frac{\pi}{2}} \int_{\alpha-\frac{\pi}{2}}^{\alpha+\frac{\pi}{2}} B(\lambda_n, T(\theta, \phi)) \cos^2 \phi \cos(\alpha - \theta) d\theta d\phi \quad (6.9)$$

The phase angle was varied for each asteroid and was set to: $\alpha = 0^\circ, \pm 30^\circ, \pm 45^\circ, \pm 60^\circ, \pm 75^\circ, \pm 90^\circ, \pm 105^\circ, \pm 120^\circ$. The resulting thermal IR fluxes at $10.7 \mu\text{m}$ for each simulated surface are given in Fig. 6.6. The direction of the phase angle, i.e. whether the cooler morning side of the asteroid or the warmer afternoon side is being observed, is important. If we input negative α in Eq. 6.9 we can obtain a second set of results for the cooler morning side.

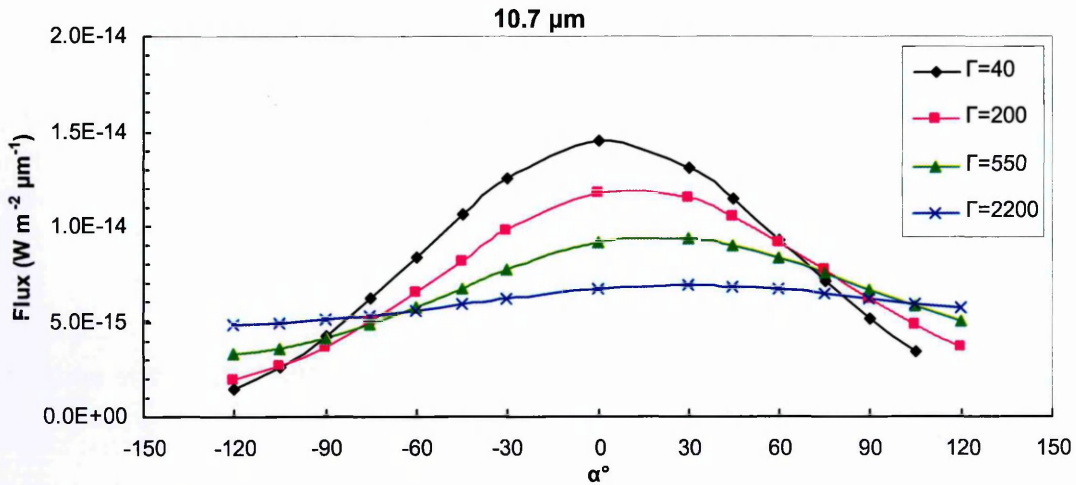


Fig. 6.6 Synthetic thermal IR fluxes at $10.7 \mu\text{m}$ for thermophysical model-derived surface temperatures simulating an asteroid with $r = 1.0 \text{ AU}$, $P = 5 \text{ h}$ and 4 different thermal inertias Γ , “observed” at a range of different phase angles on the afternoon side ($+\alpha$) and on the morning side ($-\alpha$). Note how for $\Gamma = 550$ and $\Gamma = 2200 \text{ J m}^{-2} \text{ s}^{-1/2} \text{ K}^{-1}$ the $\alpha = +30^\circ$ fluxes are actually higher than at $\alpha = 0^\circ$ due to thermal lag (c.f. Fig. 6.4).

The NEATM and NESTM with Γ set to 40, 200, 550 and $2200 \text{ J m}^{-2} \text{ s}^{-1/2} \text{ K}^{-1}$ (which from now on we will refer to as NESTM40, NESTM200, NESTM550 and NESTM2200

respectively), and with P set to 5 h, were best-fitted to the thermal IR fluxes. H_V was set to 17.12277 consistent with the test asteroid's 1 km diameter, following Eq. 4.3 (so we assume perfect precision in the optical observations).

6.4.2 Derived Diameters

The derived effective diameters D_{eff} are shown in Fig. 6.7. The f parameters used for the different NESTM setups varied only slightly from those given in the caption for Fig. 6.5, as the best-fit p_v altered. The NEATM relative errors from the true diameter are consistent with the results of Delbó (2004). Table 6.1 summarises the derived accuracies. When analysing the results, we were interested in answering two questions. First, at what phase angles does NESTM offer significantly greater accuracy than NEATM? Second, what is the best version of NESTM to use? Different cases are discussed below.

$\Gamma = 40 \text{ J m}^{-2} \text{ s}^{-1/2} \text{ K}^{-1}$ surface, afternoon side

The NEATM gives satisfactory accuracies since this surface is close to being in instantaneous equilibrium. For surfaces observed on the afternoon side, sometimes a NESTM with a simulated surface thermal inertia higher than that modelled by the thermophysical model gives the best fits. For the $\Gamma = 40 \text{ J m}^{-2} \text{ s}^{-1/2} \text{ K}^{-1}$ surface, the NESTM200 gives the best fit for $\alpha < 75^\circ$, better than the NESTM40. This is because NESTM applies an average night side temperature (e.g. Fig. 6.5), but for the asteroid surface modelled by the thermophysical model (and for true asteroid surfaces) the temperature gradually decreases from the day side temperature (higher than the average night side temperature) to a temperature lower than the average at $\theta = 270^\circ$ (e.g. Fig. 6.4), when observing the afternoon side. As α increases, the warmer limb of the night side becomes visible at first, and so a NESTM version where a higher temperature is applied to

the night side gives a p_v and D_{eff} closer to the true value. If true NEA surfaces have a low thermal inertia similar to the lunar surface then the best of the five compared models is NESTM200 for an asteroid observed on the afternoon side.

Fig. 6.7 (a)

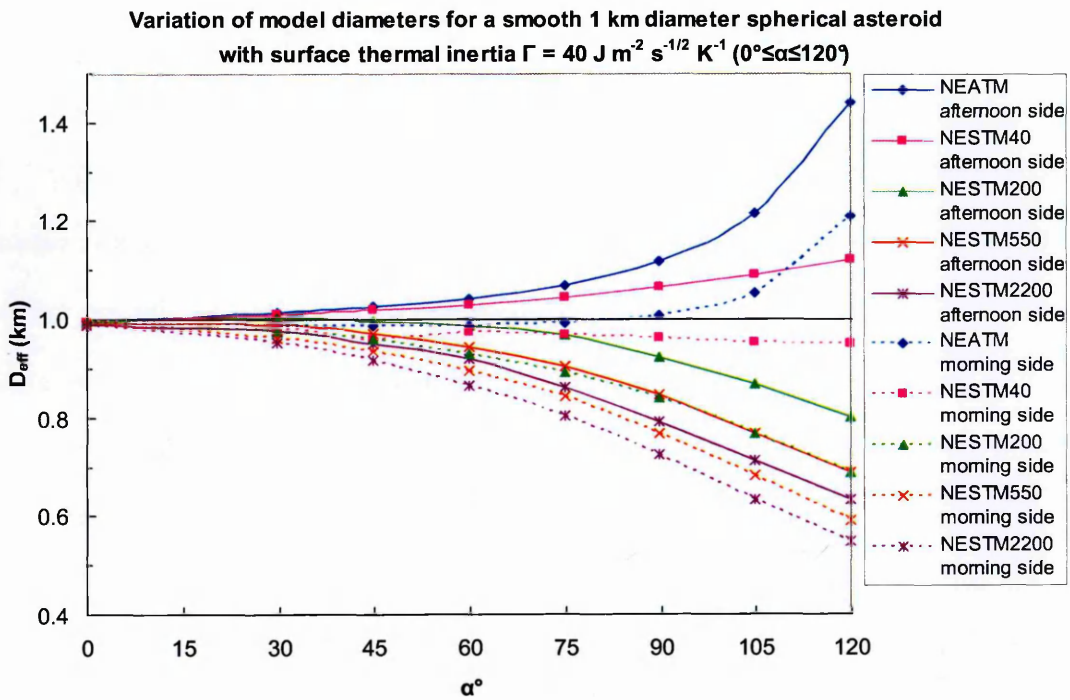
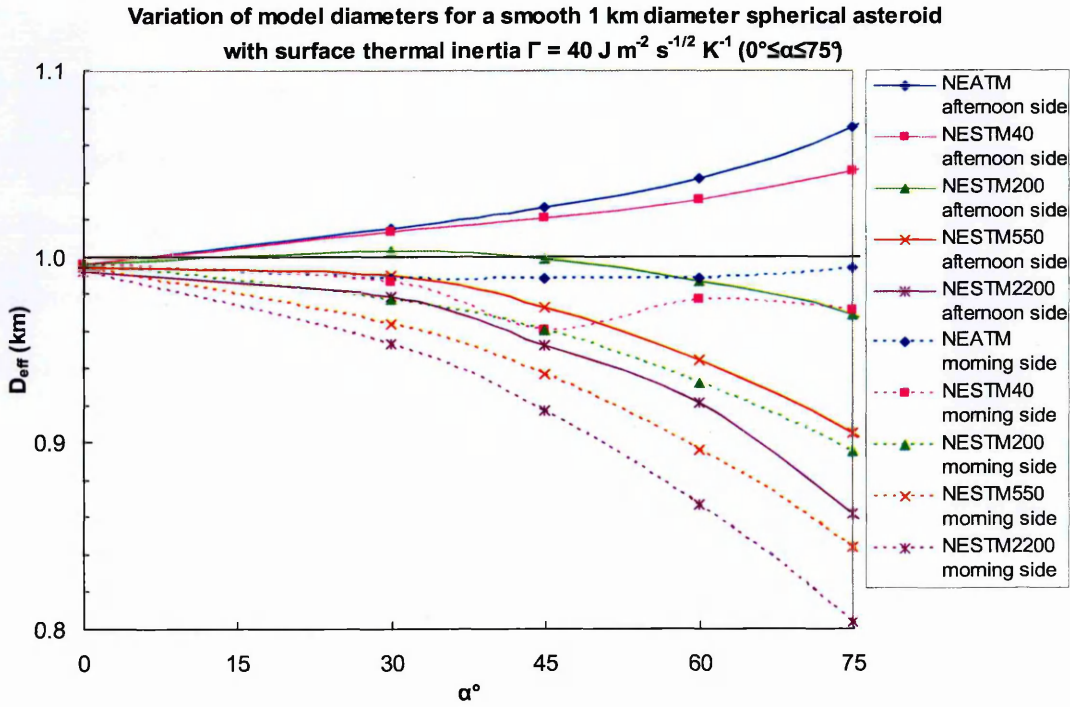


Fig. 6.7 continued.
(b)

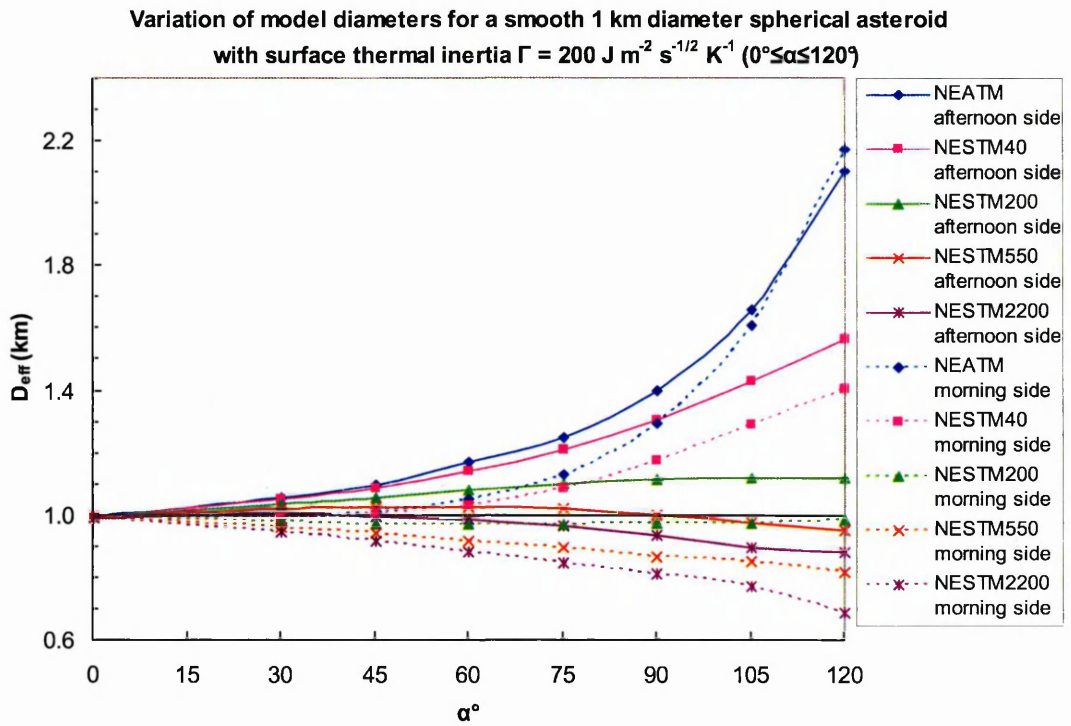
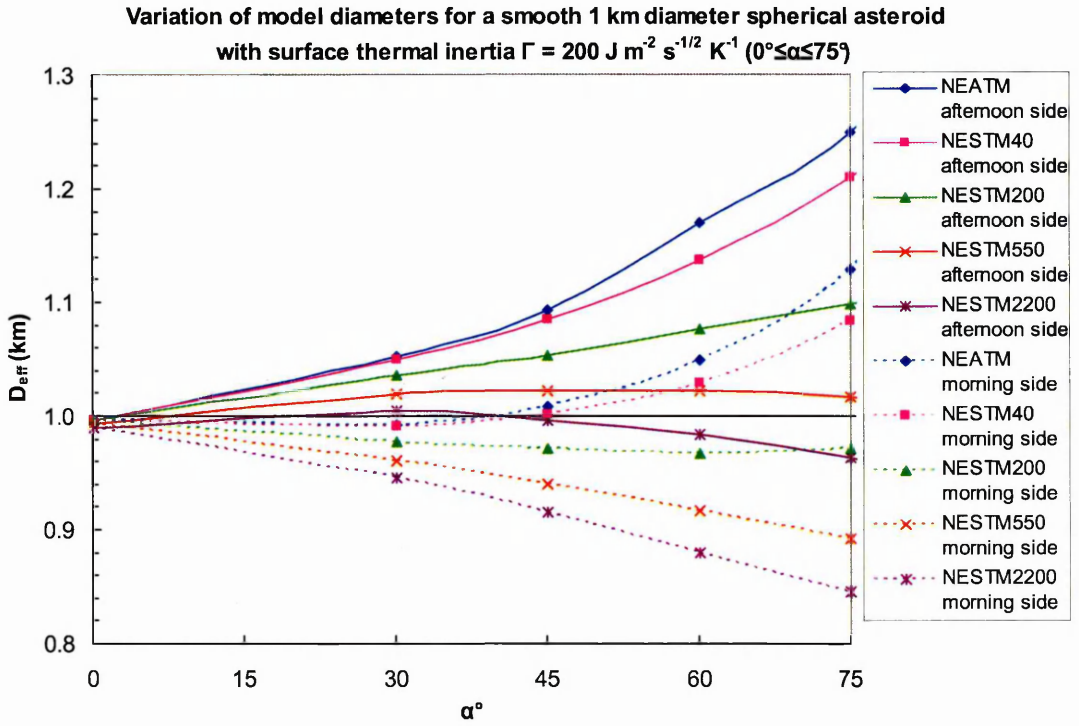
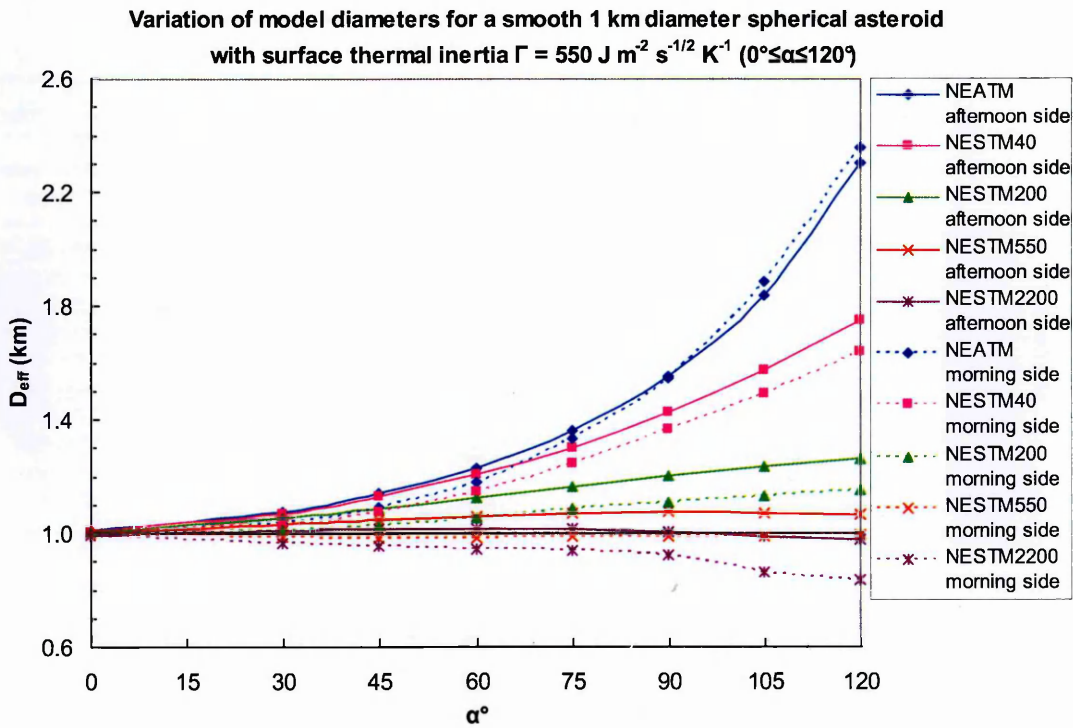
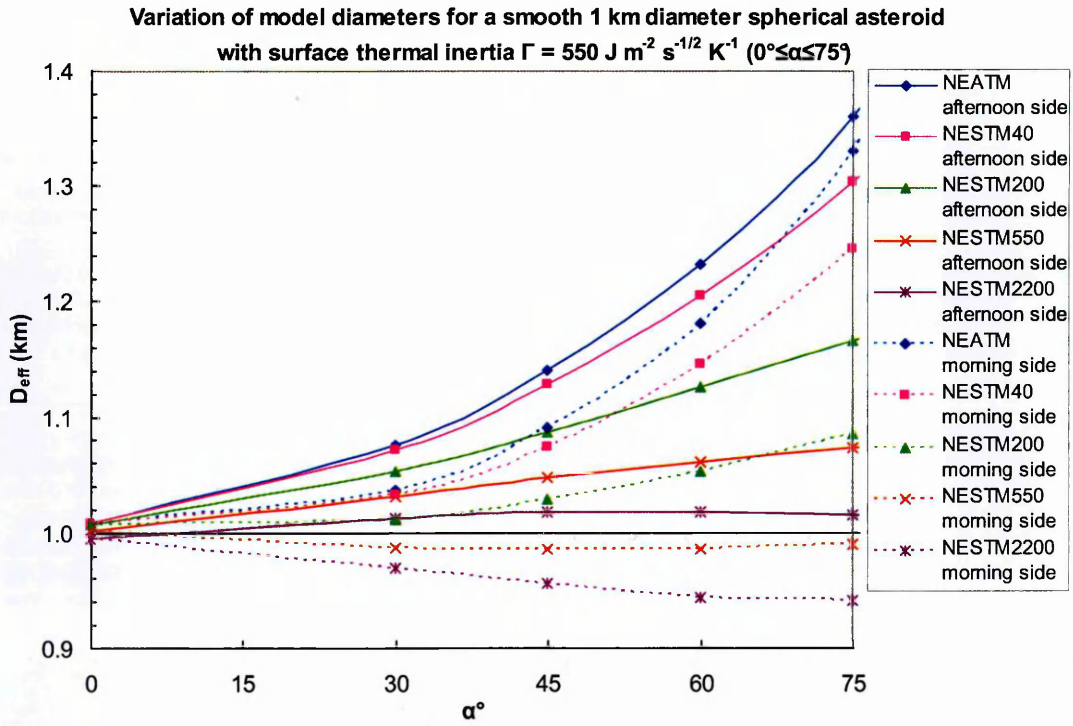


Fig. 6.7 continued.
(c)



(d)

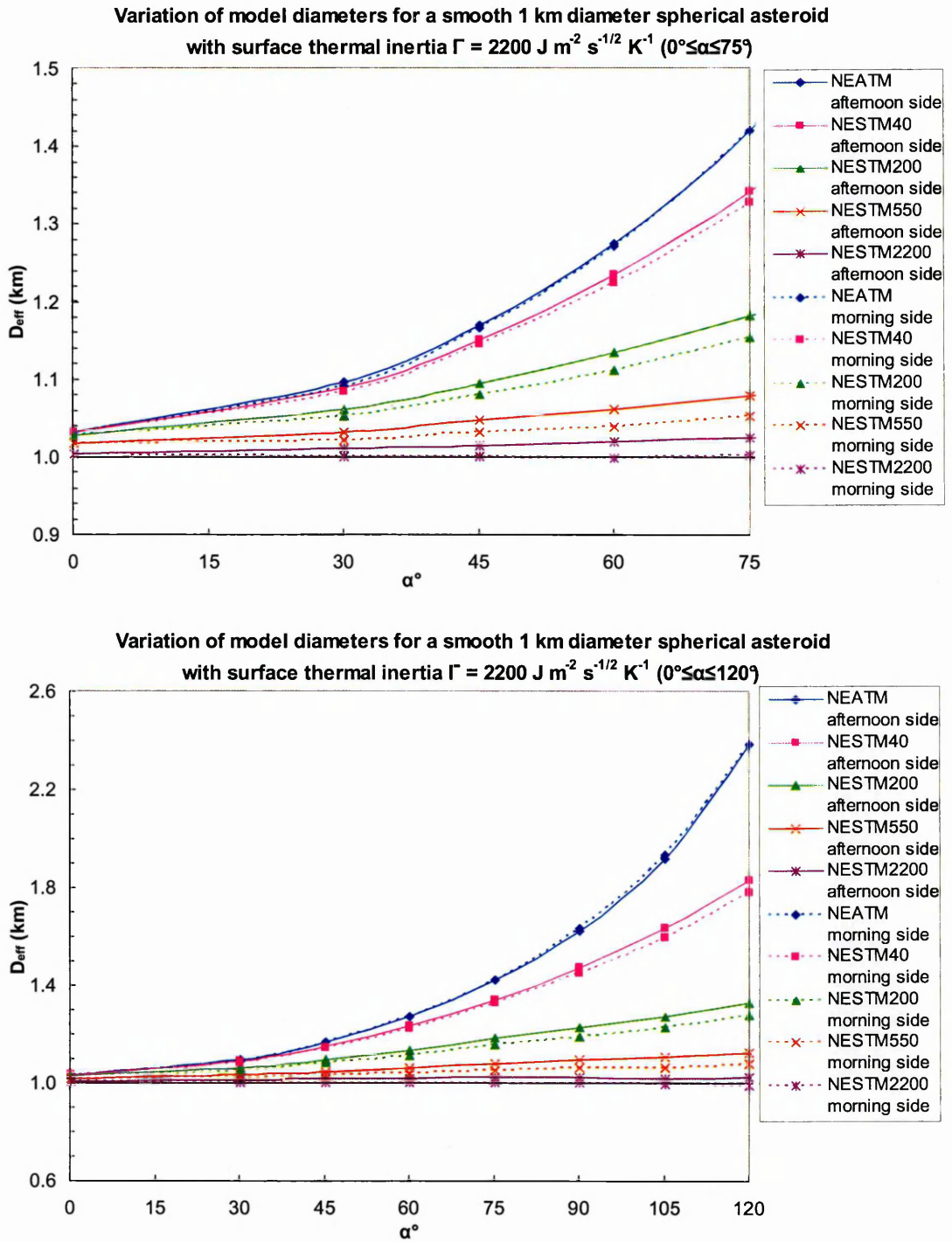


Fig. 6.7 Variation of model diameters with phase angle, observed on the afternoon side (solid lines) and the morning side (dotted lines), fitting to thermophysical model-derived thermal IR fluxes for an asteroid with $p_v = 0.25$, $D_{\text{eff}} = 1.0 \text{ km}$, $P = 5 \text{ h}$ at $r = 1.0 \text{ AU}$. The NEATM and NESTM assuming four different surface thermal inertias $\Gamma = 40, 200, 550$ and $2200 \text{ J m}^{-2} \text{ s}^{-1/2} \text{ K}^{-1}$ are fitted (resulting in applying $f \approx 0.439, 0.584, 0.669$ and 0.725 respectively, although f varies depending on the best-fit p_v). Asteroid surface with (a) $\Gamma = 40$, (b) $\Gamma = 200$, (c) $\Gamma = 550$, (d) $\Gamma = 2200 \text{ J m}^{-2} \text{ s}^{-1/2} \text{ K}^{-1}$.

Table 6.1 Summary table with the acceptability of fits of NEATM, NESTM40, NESTM200, NESTM550 and NESTM2200 to four different asteroid surfaces, thermophysically modelled with $\Gamma = 40, 200, 550$ and $2200 \text{ J m}^{-2} \text{ s}^{-1/2} \text{ K}^{-1}$

Model	$\alpha \leq 45^\circ$		$45^\circ < \alpha \leq 60^\circ$		$60^\circ < \alpha \leq 75^\circ$		$75^\circ < \alpha \leq 90^\circ$		$90^\circ < \alpha \leq 105^\circ$		$105^\circ < \alpha \leq 120^\circ$	
	a	m	a	m	a	m	a	m	a	m	a	m
$\Gamma = 40 \text{ J m}^{-2} \text{ s}^{-1/2} \text{ K}^{-1}$ surface												
NEATM	Y	Y	Y	Y	y	Y	~	Y	~	y	n	~
NESTM40	Y	Y	Y	Y	Y	Y	y	Y	y	Y	~	Y
NESTM200	Y	Y	Y	y	Y	~	y	~	~	~	~	n
NESTM550	Y	y	y	~	y	~	~	~	~	n	n	n
NESTM2200	Y	y	y	~	~	~	~	~	~	n	n	n
$\Gamma = 200 \text{ J m}^{-2} \text{ s}^{-1/2} \text{ K}^{-1}$ surface												
NEATM	y	Y	~	Y	~	~	n	~	N	N	N	N
NESTM40	y	Y	~	Y	~	y	n	~	n	~	N	n
NESTM200	y	Y	y	Y	y	Y	~	Y	~	Y	~	Y
NESTM550	Y	y	Y	y	Y	~	Y	~	Y	~	y	~
NESTM2200	Y	y	Y	~	Y	~	y	~	~	~	~	n
$\Gamma = 550 \text{ J m}^{-2} \text{ s}^{-1/2} \text{ K}^{-1}$ surface												
NEATM	~	y	~	~	n	n	N	N	N	N	N	N
NESTM40	~	y	~	~	n	~	n	n	N	n	N	N
NESTM200	y	Y	~	y	~	y	~	~	~	~	~	~
NESTM550	Y	Y	y	Y	y	Y	y	Y	y	Y	y	Y
NESTM2200	Y	Y	Y	y	Y	y	Y	y	Y	~	Y	~
$\Gamma = 2200 \text{ J m}^{-2} \text{ s}^{-1/2} \text{ K}^{-1}$ surface												
NEATM	~	~	~	~	n	n	N	N	N	N	N	N
NESTM40	~	~	~	~	n	n	n	n	N	N	N	N
NESTM200	y	y	~	~	~	~	~	~	~	~	n	~
NESTM550	Y	Y	y	Y	y	y	y	y	~	y	~	y
NESTM2200	Y	Y	Y	Y	Y	Y	Y	Y	Y	Y	Y	Y

Notes:

m = morning side

a = afternoon side

Y = fit stays better than 5% accurate.

y = fit stays better than 10% accurate

~ = fit is between 10% and 30% accurate

n = fit becomes worse than 30% accurate

N = fit becomes worse than 50% accurate

$\Gamma = 40 \text{ J m}^{-2} \text{ s}^{-1/2} \text{ K}^{-1}$ surface, morning side

The NEATM gives its best result. In fact it is more accurate than all versions of NESTM for $\alpha < 90^\circ$. So, if an asteroid has a lunar-like surface thermal inertia, NEATM would be the best model to adopt when observing the morning side. This is because the exposed night side is cooled down, so simulating its temperature to be the average of the

night side applies too high a temperature. Unfortunately we do not generally know the direction of an NEA's spin axis, and therefore do not know whether we are observing the afternoon or the morning side.

$\Gamma = 200 \text{ J m}^{-2} \text{ s}^{-1/2} \text{ K}^{-1}$ surface, afternoon side

The NESTM2200 results are closest to the true value until $\alpha > 60^\circ$, at which point too much of the night side has simulated too high a temperature and the diameter becomes increasingly underestimated. The NESTM550 results are fascinating: they are the second closest until $\alpha > 60^\circ$, increasingly (but only slightly) overestimating diameter, peaking between $\alpha = 45^\circ$ and $\alpha = 60^\circ$. Then its behaviour changes and the overestimation of the diameter begins to decrease until $\Delta D_{eff}(\alpha=90^\circ) = 0\%$ after which the diameter is then slightly underestimated ($\Delta D_{eff}(\alpha=120^\circ) = -5\%$). This behaviour can be explained by the initial segments of the night side being slightly warmer than that modelled by NESTM, but by $\alpha = 90^\circ$ cooler portions are visible, approximately matching the constant temperature applied. So for an $\Gamma = 200 \text{ J m}^{-2} \text{ s}^{-1/2} \text{ K}^{-1}$ asteroid surface observed on the afternoon side at low phase angles, NESTM2200 gives the closest results, but for consistent closeness to the true diameter the NESTM550 is preferred.

$\Gamma = 200 \text{ J m}^{-2} \text{ s}^{-1/2} \text{ K}^{-1}$ surface, morning side

The NEATM outperforms all but the NESTM40 for $\alpha < 45^\circ$, then increases its overestimation of diameter so that NESTM200 is more accurate from $\alpha = 60^\circ$ onwards. The NESTM200 results are interesting to compare to the NESTM550 results for the afternoon side. NESTM200 first underestimates the diameter, peaking at $\alpha=60^\circ$, then the underestimation decreases as the average exposed night side temperature becomes closer to

that approximated. So for the $\Gamma = 200 \text{ J m}^{-2} \text{ s}^{-1/2} \text{ K}^{-1}$ surface observed on the morning side the NESTM200 is the best model.

$\Gamma = 550 \text{ J m}^{-2} \text{ s}^{-1/2} \text{ K}^{-1}$ surface

The NEATM is the least accurate. On the afternoon side, the NESTM2200 gives results closest to the true value, gradually increasing its diameter overestimation until $\alpha=60^\circ$, at which point the trend is reversed. So if an asteroid surface had an $\Gamma = 550 \text{ J m}^{-2} \text{ s}^{-1/2} \text{ K}^{-1}$ surface then the NESTM2200 would be preferred. These are unexpected results. The NESTM2200 model was supposed to model an “extreme” case of a bare rock surface, but here we find that it provides the best results for an “average” NEA surface when the asteroid is observed on the afternoon side.

On the morning side, the NESTM550 is the most accurate, underestimating the diameter by 1% at all phase angles. However, the NESTM200 is a considerable improvement on the NEATM.

Conclusions

After analysing the results of this test I would not recommend adopting the NESTM550 model as the default. First, we have no idea what the thermal inertia of most NEAs is, but those that have been measured (Section 2.7) are closer to $\Gamma = 200 \text{ J m}^{-2} \text{ s}^{-1/2} \text{ K}^{-1}$ on average. The estimation of $550 \pm 100 \text{ J m}^{-2} \text{ s}^{-1/2} \text{ K}^{-1}$ by Delbó (2004) could be described as speculative, since a large range of curves give reasonable fits, and the position of the limiting curves depend on a handful of observations (Fig. 6.1). The relatively high estimate seems to contradict Delbó’s result that the STM gives good fits to thermal IR fluxes at low phase angles, since we would expect lower maximum day side temperatures.

Second, even if the average NEA did have $\Gamma = 550 \text{ J m}^{-2} \text{ s}^{-1/2} \text{ K}^{-1}$, this means that approximately half of the NEA population are likely to have $\Gamma < 550 \text{ J m}^{-2} \text{ s}^{-1/2} \text{ K}^{-1}$.

Whatever default model we adopt should be as accurate as the NEATM for all realistic asteroids. We find that this is not true for NESTM550 or NESTM2200 if the asteroid is observed on the morning side. NESTM200 provides more accurate diameters than the NEATM for all asteroids with $\Gamma \geq 40 \text{ J m}^{-2} \text{ s}^{-1/2} \text{ K}^{-1}$ when observed on the afternoon side. If the asteroid is observed on the morning side, then the NEATM provides a better result for a $\Gamma = 40 \text{ J m}^{-2} \text{ s}^{-1/2} \text{ K}^{-1}$ surface when $\alpha < 90^\circ$, and also for a $\Gamma = 200 \text{ J m}^{-2} \text{ s}^{-1/2} \text{ K}^{-1}$ surface when $\alpha < 45^\circ$. However in the latter case, both NEATM and NESTM200 provide good accuracy (e.g. at $\alpha = 45^\circ$ NEATM $\Delta D_{eff} = +1\%$, NESTM200 $\Delta D_{eff} = -3\%$). We assume that most NEAs have a thermal inertia in the range $200 \leq \Gamma \leq 2200 \text{ J m}^{-2} \text{ s}^{-1/2} \text{ K}^{-1}$ and adopt NESTM200 as the default model. If it is discovered that a typical NEA has a lunar-like surface thermal inertia then the NEATM would be the preferred model.

The above analysis assumes the extreme case of the pole orientation at 90° to the solar direction. In this geometry the effects of significant thermal inertia are at their greatest. If the spin axis was pointing towards the Sun, then no part of the day side is rotated onto the night side, there is no emission on the night side, and the NEATM or the STM are the appropriate models. In between, there is a gradation between the two cases. This further supports an adoption of NESTM200 as the default, since, even if a typical NEA has a higher thermal inertia, NESTM200's simulated night side temperatures will be closer to the true night side temperature profile of an asteroid with a spin axis less than 90° to the solar direction.

In Section 6.5 we compare NESTM with NEATM fits and radar diameters for real asteroids. We calculate the NESTM fits using all four versions, to see if we can measure an

improvement in accuracy over the NEATM, and which model offers the best improvement, if any.

6.4.3 Derived Beaming Parameters

Delbó (2004) has done a thorough study of the effect of different thermal inertias and surface roughness $\bar{\theta}$ on NEATM-derived η -values with different phase angle. First Delbó examines the results for a smooth ($\bar{\theta} = 0$) NEA, which is equivalent to our thermophysical model. Like our model, the subsolar latitude is always assumed to be zero. The results are reproduced in Fig. 6.8.

NEATM η -value as a function of the phase angle

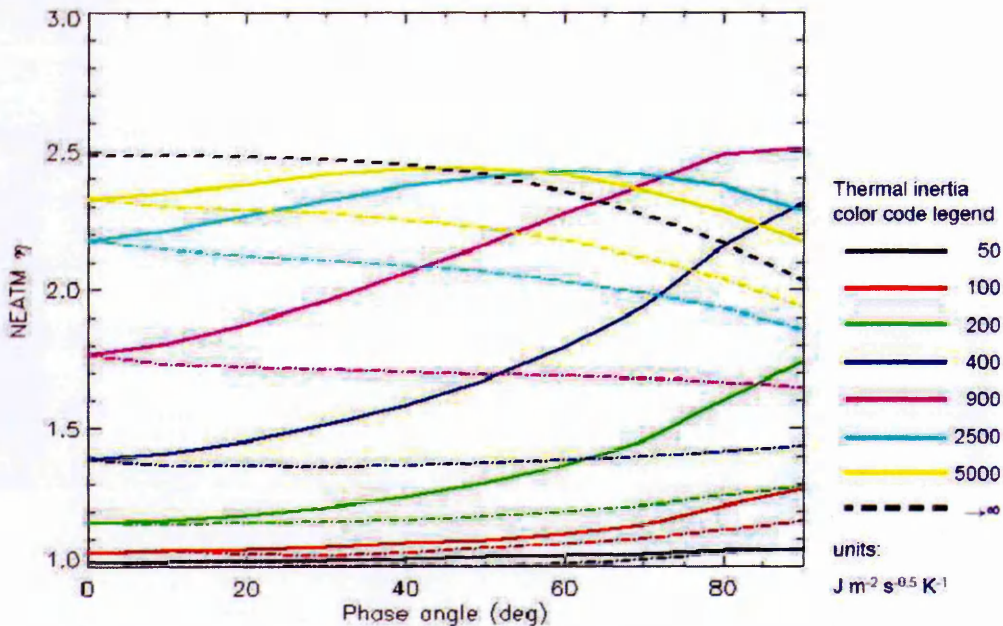


Fig. 6.8 Figure reproduced from Delbó (2004) showing the variation of the NEATM η -values at different phase angles for a smooth ($\bar{\theta} = 0$) asteroid surface, modelled with a thermophysical model assuming various thermal inertias and $P = 6$ h. Continuous curves refer to those η -values derived by observing the morning side of the asteroid. Dashed-dotted curves are derived from observing the afternoon side.

For $\Theta < 0.5$ (our $\Gamma = 40 \text{ J m}^{-2} \text{ s}^{-1/2} \text{ K}^{-1}$ asteroid surface has $\Theta = 0.238$) Delbó finds $\eta < 1.3$ for $\alpha < 90^\circ$. For both the morning and afternoon curves, η increases, and no large variations of η are seen when the morning rather than the afternoon hemisphere is observed. But for $\Theta > 1.0$ (e.g. our $\Gamma = 200 \text{ J m}^{-2} \text{ s}^{-1/2} \text{ K}^{-1}$ asteroid surface has $\Theta = 1.190$), variations between the morning and afternoon curves become apparent. The afternoon curves are flatter and for lower Θ , η will tend to slightly increase with α ; and for greater Θ (c.f. our $\Gamma = 2200 \text{ J m}^{-2} \text{ s}^{-1/2} \text{ K}^{-1}$ asteroid surface with $\Theta = 13.094$), η will tend to decrease with α . In contrast, for the morning curves, η increases rapidly with α . Including different surface roughness had the overall effect of increasing η at higher phase angles irrespective of whether the morning or afternoon hemisphere was being observed.

We can compare Delbó's results with our own, for the NEATM. Figure 6.9 shows the variation of beaming parameter η with phase angle α for NEATM, NESTM40, NESTM200, NESTM550 and NESTM2200 for all four simulated surfaces. The NEATM-derived η are consistent with Delbó's.

Fig. 5.25 showed the measured trend of increasing η with α , which we speculated was partly due to disregarding thermal emission from the night side. We can see that as the simulated surface increases in thermal inertia, so the η -value at zero phase angle increases. The η -values are larger than in Fig. 6.8. This is because we have not included beaming (i.e. surface roughness) in our model which would decrease η at low phase angles and increase it at large phase angles. We would expect beaming to affect the NEATM and NESTM in the same manner since they both best-fit η , and beaming would alter the day side temperature profile. As the surface type increases in thermal inertia, the maximum day side temperature becomes reduced compared to T_{max} , conserving energy as more thermal flux comes from the night side. In the modified projected model this reduced maximum day

side temperature T_{mod} was calculated (Section 4.3.5) but in the NEATM and NESTM the observed temperature is effectively measured. As a result the best-fit η increases.

Fig. 6.9 (a)

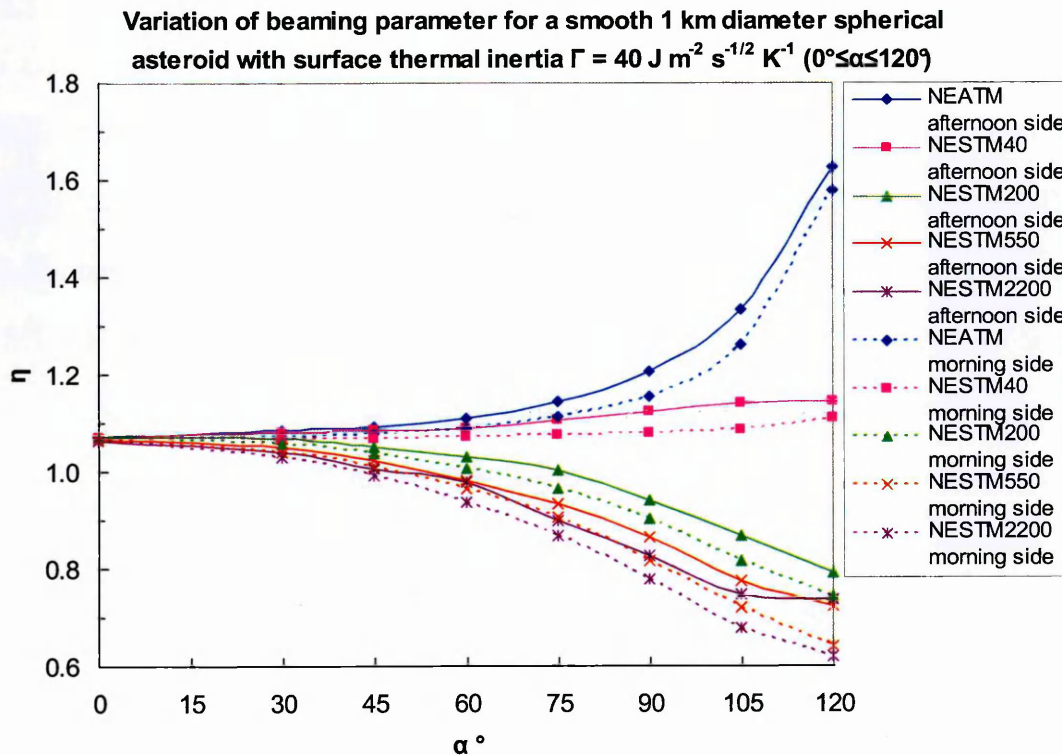
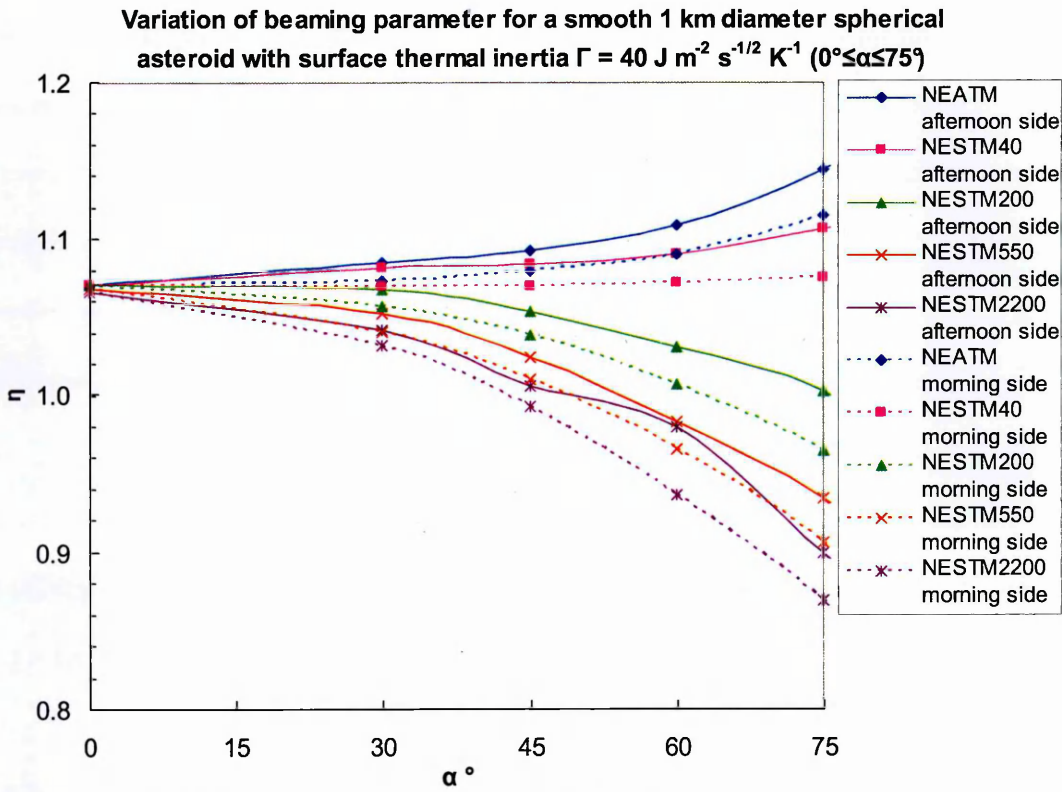


Fig. 6.9 continued.
(b)

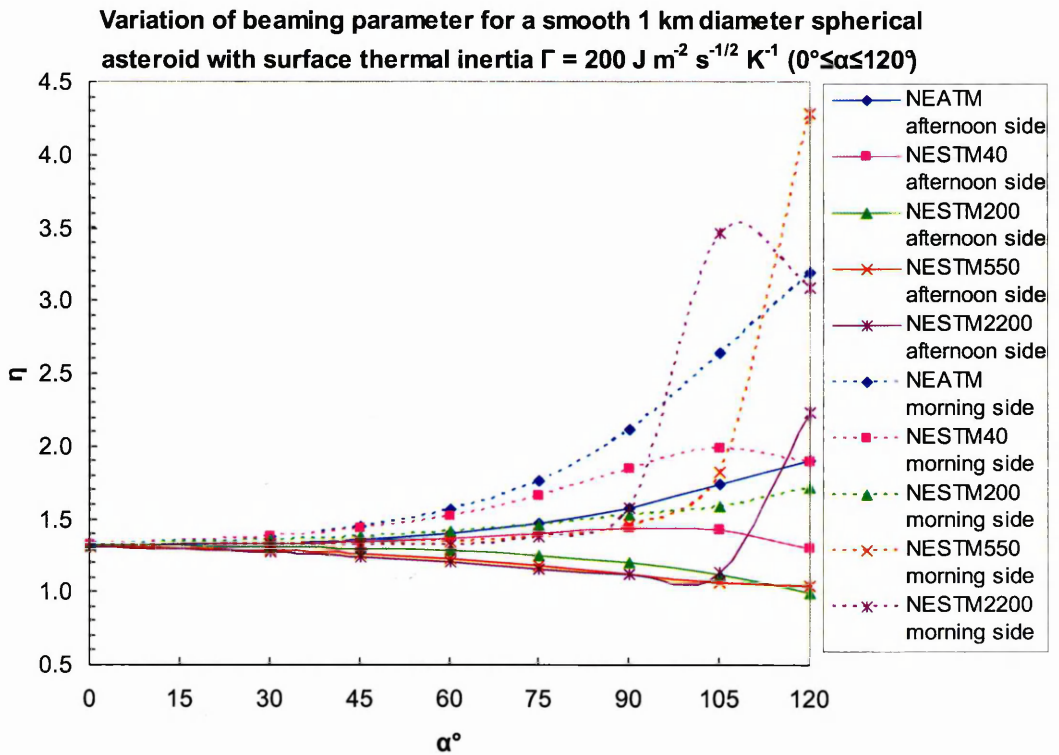
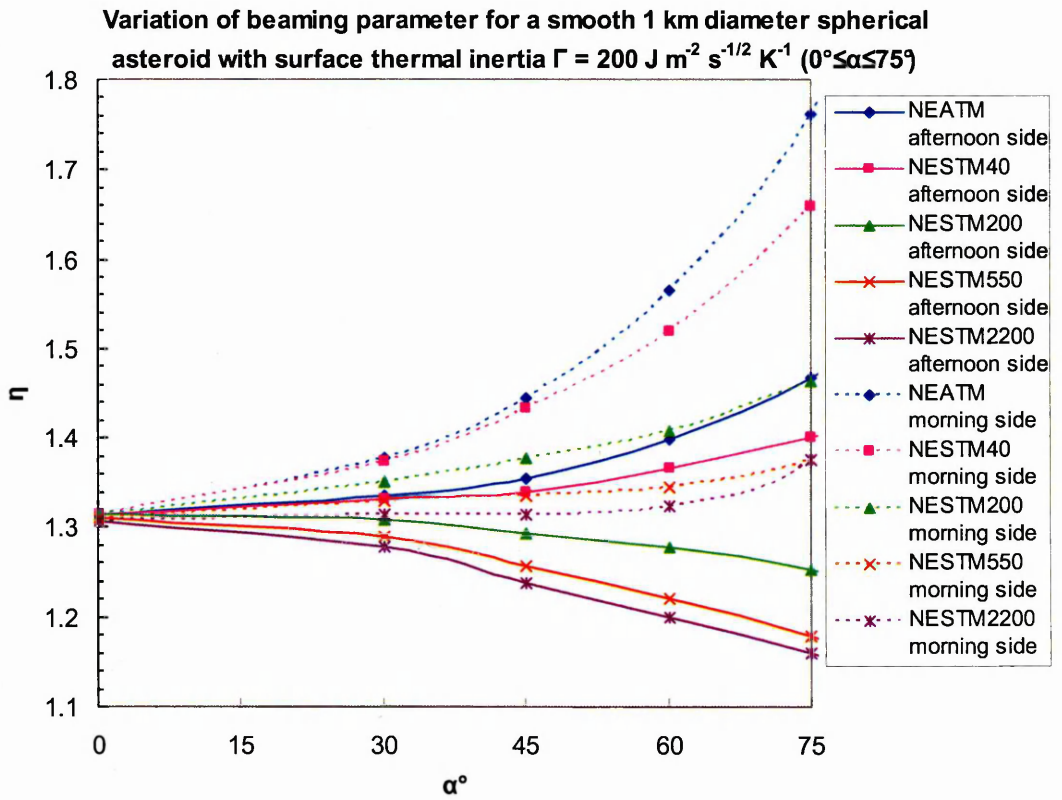


Fig. 6.9 continued.
(c)

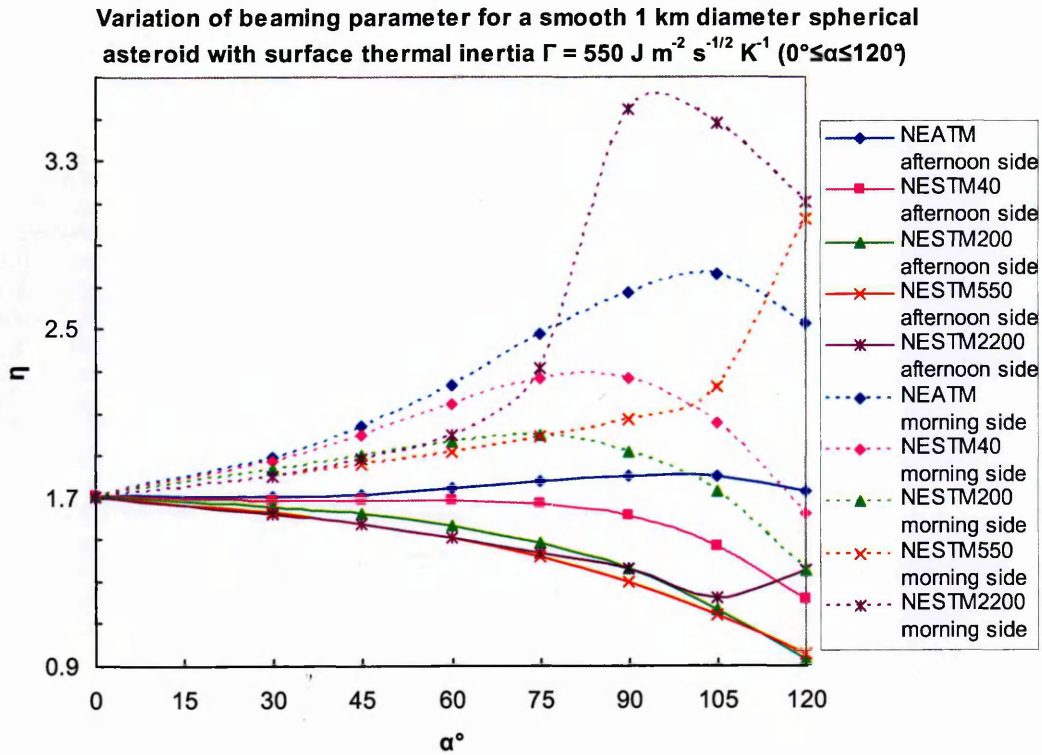
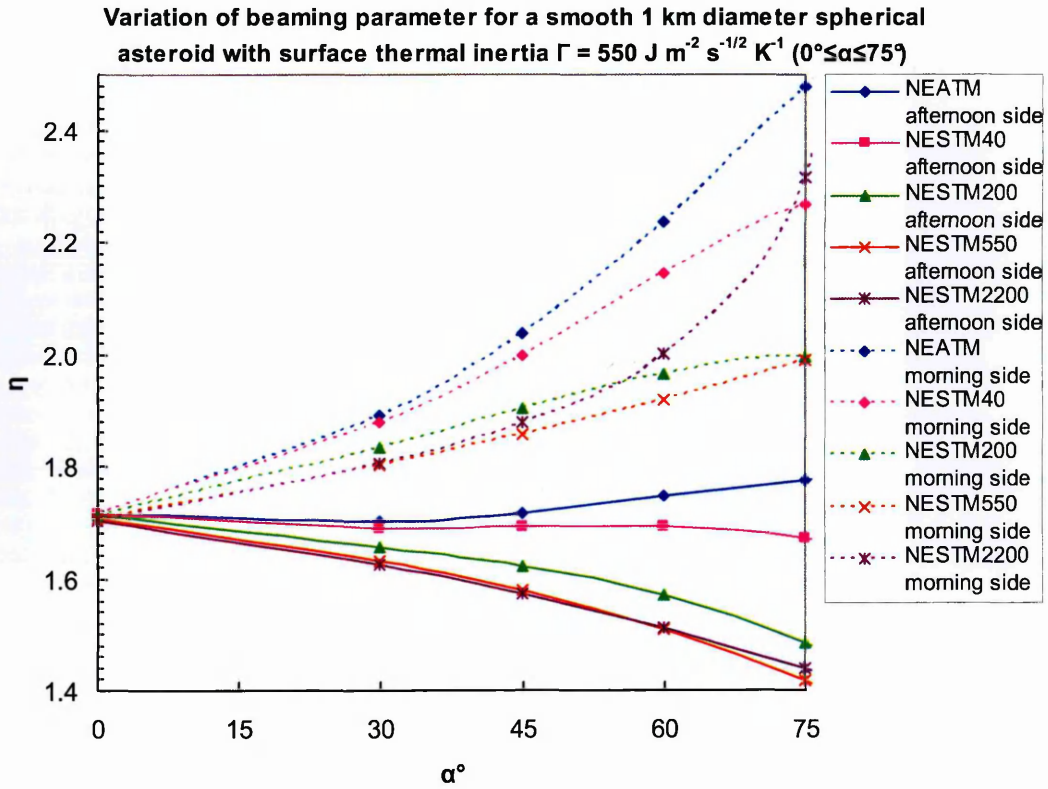


Fig. 6.9 continued.
(d)

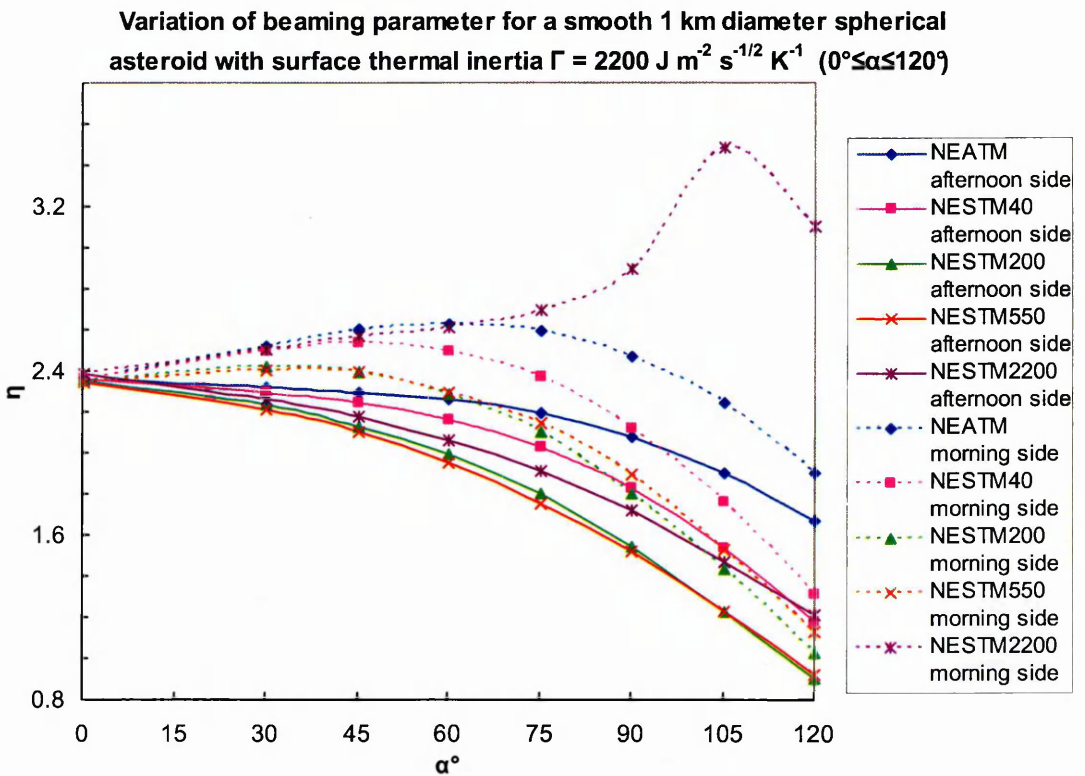
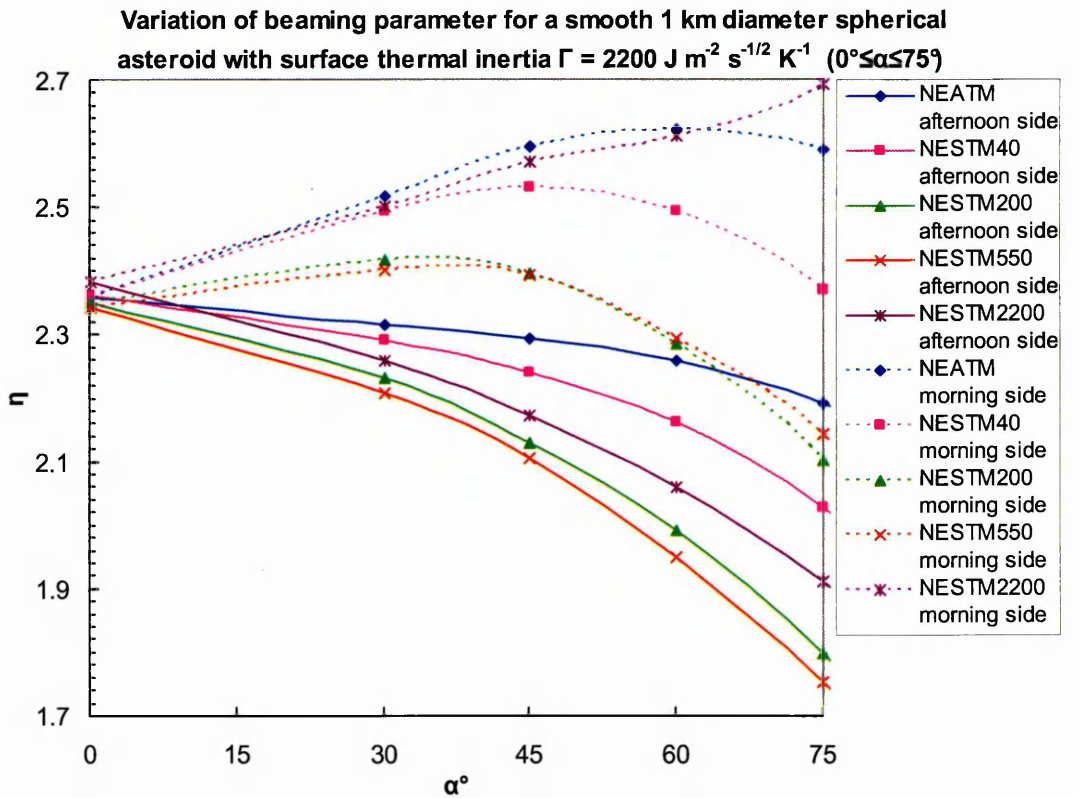


Fig. 6.9 (Previous 4 pages.) Variation of model best-fit beaming parameters η at different phase angles α , fitting to thermophysical model-derived thermal IR fluxes for an asteroid with $p_v = 0.25$, $D_{\text{eff}} = 1.0$ km, $P = 5$ h at $r = 1.0$ AU. Asteroid is "observed" on the afternoon side (solid lines) and the morning side (dotted lines). The NEATM and NESTM assuming four different surface thermal inertias are fitted ($\Gamma = 40, 200, 550$ and 2200 $\text{J m}^{-2} \text{s}^{-1/2} \text{K}^{-1}$, resulting in using f parameters of approximately 0.439, 0.584, 0.669 and 0.725 respectively, although f varies depending on the best-fit p_v). Asteroid surface with (a) $\Gamma = 40$, (b) $\Gamma = 200$, (c) $\Gamma = 550$, (d) $\Gamma = 2200$ $\text{J m}^{-2} \text{s}^{-1/2} \text{K}^{-1}$.

Different cases are discussed below.

$\Gamma = 40 \text{ J m}^{-2} \text{s}^{-1/2} \text{K}^{-1}$ surface ($\Theta = 0.238$)

The NESTM40-derived η -values are nearly flat, increasing gradually from $\eta = 1.07$ to $\eta = 1.15$. Therefore including appropriate thermal emission on the night side has the effect of flattening the increase of η . If beaming were included in the model, the η -values would still increase as there would be enhanced thermal emission in the sunward direction, which would decrease at larger phase angle. For the higher NESTMs, η decreases with α . More thermal flux on the night side increases thermal emission at longer wavelengths, and so where there is a model-introduced excess of thermal flux from cooler surface elements, the best-fit beaming parameter becomes <1 to best-fit to the observed higher colour temperature.

$\Gamma = 200 \text{ J m}^{-2} \text{s}^{-1/2} \text{K}^{-1}$ surface ($\Theta = 1.170$)

For the afternoon side, the NESTM40-derived η -values stay fairly flat. The NESTM200 and NESTM550 η -values both decrease with α . We might have expected the NESTM200 η -values to stay flatter since this model is the closest to producing the correct flux on the night side, but the behaviour of the best-fit η is more complex. While the NEATM was inaccurate in not introducing thermal flux, NESTM forces a particular amount of thermal flux from the night side. The more night side flux is introduced the less

the fitted maximum day side temperature T_{fit} has to be reduced in order to account for the fact that the observed day side temperature is lower than T_{max} . The NESTM2200 η -values also decrease until $\alpha = 90^\circ$ and then the behaviour becomes quite curious. The best-fit η -values increase slightly ($\eta(\alpha=105^\circ) = 1.14$) and then dramatically ($\eta(\alpha=120^\circ) = 2.23$). This behaviour does not seem to especially affect the accuracy of the fitted ($\Delta D_{eff} = -12\%$) which is closer to the true value than for NEATM and NESTM40 and as close as NESTM200. At such a high phase angle, there are many more surface elements from both the night side and the day side with temperatures replaced by $fT_{max} \cos^{1/4} \phi$ (because it was higher), than there are elements fitted by η , and so an isothermal latitude model (e.g. the FRM) begins to fit the observed fluxes better.

Conclusions

Including appropriate thermal emission on the night side has the effect of flattening the increase of η . For simulated surfaces with a lunar-like surface thermal inertia, where there is a model-introduced excess of thermal flux from cooler surface elements, the best-fit beaming parameter can become <1 , best-fitting to the observed higher colour temperature. When applying a NESTM that assumes too high a surface thermal inertia, the derived best-fit η can be very large at high α , and its behaviour can be quite complex. It is therefore not appropriate to use NESTM-derived best-fit η for physical interpretation of asteroid surfaces, e.g. to estimate the true surface thermal inertia.

6.5 NESTM Compared with NEATM and Radar Diameters for NEAs

We intend to derive NESTM diameters using NESTM40, NESTM200, NESTM550 and NESTM2200 for all NEAs with diameters measured using radar for which thermal IR fluxes are also available. At present, 7 out of the 22 thermal IR datasets remain unfitted (5

of which are for (5381) Sekhmet), because we have not yet been able to obtain the appropriate lightcurve corrected fluxes, or do not have copies of the fluxes at all. Delbó (2004) performed a similar analysis to test the NEATM, using NEATM fits from various sources [not including the NEATM fit for (433) Eros from this work]. We compare our results with those obtained for the NEATM.

Tables 6.4 and 6.5 show the resulting p_v and D_{eff} , as well as those obtained by radar and from NEATM fits. Tables 6.2 and 6.3 shows the observational circumstances, appropriate input model parameters and references to the original data sources. Where the uncertainty is not given in the original source for the radar diameter an uncertainty of 10% is assumed.

Figure 6.10 (a) shows the variation of the relative error $(D_{radiometry} - D_{radar})/D_{radar}$ with phase angle α , and (b) with radar diameter D_{radar} . The formal uncertainty of the relative diameter error σ_{rel_D} is:

$$\sigma_{rel_D} = \sqrt{\left(\frac{0.15D_{radiometry}}{D_{radar}}\right)^2 + \left(\frac{\sigma_{D_{radar}} D_{radiometry}}{D_{radar}^2}\right)^2} \quad (6.10)$$

Delbó found no clear trend with either α or D_{radar} for NEATM, and we see no trend with NESTM either.

Delbó found a mean relative error of +8% between the two complete sets of data (i.e. without the seven missing datasets, which are not shown in Table 6.3 or in Fig. 6.10) and a root-mean-square (RMS) fractional difference between the NEATM and radar diameters of 20%. To estimate the uncertainty of the mean relative error, Delbó fit a Gaussian function to the relative error distribution with standard deviation $\sigma = 0.17$ and a mean value $x_0 = 0.08$. The uncertainty of the mean is $\sigma/\sqrt{N} = 0.04$, so the mean relative error is +8% \pm 4%. This indicates that there is a systematic error between the radar and the NEATM diameters.

Table 6.2
Original data sources for NEAs for which radar diameters and thermal IR fluxes are available

Asteroid	Thermal IR flux source	Date of obs. yyyy-mm-dd	NEATM fit source if different	Period (if known) source ^a	Radar diameter source
(433) Eros	Lebofsky and Rieke (1979) Harris and Davies (1999) this work	1975-01-17 1998-06-27 2002-09-28	Harris and Davies (1999)	e.g. Campa (1938)	Harris and Lagerros (2002) ^b
(1566) Icarus	Veeder <i>et al.</i> (1989)	1987-06-23	Harris (1998)	e.g. Miner and Young (1969)	Pettengill <i>et al.</i> (1969)
(1580) Betulia	Lebofsky <i>et al.</i> (1978) Delbó (2004) ^c	1976-05-23 2002-06-02	Harris (1998)	e.g. Lagerkvist (1977)	Pettengill <i>et al.</i> (1979)
(1620) Geographos	Veeder <i>et al.</i> (1989)	1983-03-11	Harris (1998)	e.g. Magnusson <i>et al.</i> (1996)	Ostro <i>et al.</i> (1996)
(1627) Ivar	Veeder <i>et al.</i> (1989) Delbó <i>et al.</i> (2003) ^d	1985-07-10 2000-03-06	Harris (1998)	e.g. Harris and Young (1985)	Ostro <i>et al.</i> (1990)
(1685) Toro	Veeder <i>et al.</i> (1989)	1981-03-12	Harris (1998)	e.g. Dunlap <i>et al.</i> (1973)	Ostro <i>et al.</i> (1983)
(1862) Apollo	Lebofsky <i>et al.</i> (1981)	1980-11-26	Harris (1998)	e.g. Harris <i>et al.</i> (1987)	Goldstein <i>et al.</i> (1981)
(2100) Ra-Shalom	Harris <i>et al.</i> (1998)	1997-08-31		e.g. Ostro <i>et al.</i> (1984)	Ostro <i>et al.</i> (1984)
(2100) Ra-Shalom	Delbó <i>et al.</i> (2003) ^d	2000-08-21			
(5381) Sekhmet	^c	2003-05-12 → 2003-05-16	Delbó (2004)	Delbó (2004)	Nolan <i>et al.</i> (2003)
(6178) 1986 DA	Tedesco and Gradie (1987)	2003-06-02	Delbó (2004)		
(6489) Golevka	Mottola <i>et al.</i> (1997) Delbó (2004) ^c	1986-04-22 1995-06-16 2003-05-15	Harris and Lagerros (2002) Harris (1998)	e.g. Wisniewski (1987) e.g. Mottola <i>et al.</i> (1997)	Ostro <i>et al.</i> (1991) Hudson <i>et al.</i> (2000)
(33342) 1998 WT ₂₄	Delbó (2004) Delbó (2004)	2001-12-02 2001-12-18 → 2001-12-21		Delbó (2004)	Zaitsev <i>et al.</i> (2002)

Notes. ^aFor more sources, and for more references to the physical properties of each asteroid: <http://earn.dlr.de/nea/database.htm>

^bUsed spacecraft diameter.

^cFluxes not yet obtained.

^dLightcurve-corrected fluxes (Delbó, private communication, 2004).

Table 6.3
Observational circumstances, NESTM input parameters and notes for NEAs for which radar diameters and thermal IR fluxes are available

Asteroid	Date of obs. yyyy-mm-dd	H _v	G	r (AU)	Δ (AU)	α°	P (h)	Tax. type	Notes
(433) Eros	1975-01-17	11.5	0.32	1.134	0.153	9.9	5.270	S	Lightcurve minimum; spacecraft $p_r = 0.25 \pm 0.06$ (Veverka <i>et al.</i> , 2000).
	1975-01-17	10.47	0.32	1.134	0.153	9.9			Lightcurve maximum; H , G as used by Harris and Davies (1999).
	1998-06-27	10.47	0.32	1.619	0.804	30.9			Lightcurve maximum. H , G as used by Harris and Davies (1999).
	2002-09-28	10.64	0.20	1.589	0.640	18.2			Lightcurve corrected. G from Lagerkvist and Magnusson (1990).
(1566) Icarus	1987-06-23	16.3	0.09	0.993	0.166	93	2.273	S	H , G as used by Harris (1998) assuming lightcurve maximum and using brightest measured mag. in Veeder <i>et al.</i> (1989). Delbó (2004) did not include this object when calculating/plotting the relative error due to the large error in radar diameter.
(1580) Betulia	1976-05-23	14.58	0.18	1.140	0.130	10	6.132	C	H , G as used by Harris (1998); Pettengill <i>et al.</i> (1979) found radar diameter > 5.4 km, we assume same radar diameter as Delbó (2004).
(1620) Geographos	1983-03-11	15.09	0.31	1.070	0.095	34	5.223	S	H , G as used by Harris (1998) assuming lightcurve maximum and using brightest measured mag. in Veeder <i>et al.</i> (1989); Ostro <i>et al.</i> (1996) found radar diameter < 3.0 km, we assume same radar diameter as Delbó (2004).
(1627) Ivar	1985-07-10	12.9	0.25	1.124	0.202	53	4.795	S	H , G as used by Harris (1998) assuming lightcurve maximum and using brightest measured mag. in Veeder <i>et al.</i> (1989).
(1685) Toro	2000-03-06	12.87	0.25	2.057	1.073	5			H , G as used by Harris (1998) assuming lightcurve maximum and using brightest measured mag. in Veeder <i>et al.</i> (1989).
	1981-03-12	13.9	0.07	1.668	0.738	18	10.196	S	
(1862) Apollo	1980-11-26	16.27	0.23	1.105	0.148	35	3.065	Q	Lightcurve corrected as described in Harris (1998)
(2100) Ra-Shalom	1997-08-31	15.9	0.12	1.195	0.264	40.6	19.800	Xc	Lightcurve maximum; Ostro <i>et al.</i> (1984) found radar diameter to be > 3.0 km, we assume same diameter as Delbó (2004)
(2100) Ra-Shalom	2000-08-21	16.11	0.12	1.175	0.222	39			H , G as used by Harris <i>et al.</i> (1998)
(6178) 1986 DA	1986-04-22	15.94	0.25	1.179	0.211	31.4	3.58	M	Delbó (2004) did not include this object in his radar diameter list.
(6489) Golevka	1995-06-16	18.82	0.14	1.016	0.051	88.8	6.026	S	Delbó (2004) did not include this fit when calculating/plotting the relative error, it gives a very different p_r from his other fit for this object; we exclude it also.
(33342) 1998 WT ₂₄	2001-12-02	18.54	0.40	1.015	0.062	60	3.723	E	G value as appropriate for an E-type asteroid; not lightcurve corrected, lightcurve amplitude = 0.2.
	2001-12-18			0.990	0.016	67			
	2001-12-19			0.987	0.020	79			
	2001-12-21			0.982	0.028	93			

Table 6.4
NEATM, NESTM40 and NESTM200 derived p_v , D_{eff} , and η , f parameters used, and radar diameters and albedos for NEAs for which radar diameters and thermal IR fluxes are available

Asteroid	Date of obs. yyyy-mm-dd	NEATM			Radar			NESTM40			NESTM200					
		α°	p_v	D_{eff} (km)	η^a	p_v	D (km)	\pm^b (km)	p_v^c	D_{eff} (km)	η^a	f	p_v^c	D_{eff} (km)	η^a	f
(433) Eros	1975-01-17	9.9	0.22	14.3	1.15	0.22	14.1	0.2	0.219	14.23	1.11	0.457	0.220	14.20	1.11	0.607
	1975-01-17	9.9	0.20	23.6	1.05	0.28	20.06	0.2	0.209	23.41	1.01	0.457	0.210	23.36	1.01	0.607
	1998-06-27	30.9	0.21	23.6	1.07	0.28	20.06	0.2	0.212	23.25	1.03	0.489	0.220	22.82	1.00	0.644
	2002-09-28	18.2	0.18	23.33	0.97	0.28	20.06	0.2	0.181	23.26	0.96	0.489	0.183	23.14	0.96	0.644
(1566) Icarus	1987-06-23	93	0.33	1.27	(1.2)	0.09	2.5	1.5	0.347	1.24	(1.2)	0.470	0.424	1.12	(1.2)	0.624
(1580) Betulia	1976-05-23	10	0.17	3.9	(1.2)	0.06	6		0.166	3.96	(1.2)	0.447	0.166	3.96	(1.2)	0.594
(1620) Geographos	1983-03-11	34	0.26	2.5	(1.2)	0.07	2.56		0.260	2.50	(1.2)	0.447	0.263	2.49	(1.2)	0.594
(1627) Ivar	1985-07-10	53	0.12	10.2	(1.2)	0.17	8.5	3	0.118	10.18	(1.2)	0.457	0.123	9.97	(1.2)	0.607
	2000-03-06	5	0.15	9.12	(1.0)	0.17	8.5	3	0.156	8.97	(1.0)	0.552	0.157	8.94	(1.0)	0.675
(1685) Toro	1981-03-12	18	0.29	4.1	(1.2)	0.43	3.3	0.9	0.292	4.08	(1.2)	0.470	0.293	4.07	(1.2)	0.624
(1862) Apollo	1980-11-26	35	0.26	1.45	1.15	0.38	1.2		0.278	1.40	1.01	0.470	0.289	1.38	1.07	0.624
(2100) Ra-Shalom	1997-08-31	40.6	0.13	2.48	1.80	0.11	2.4		0.130	2.44	1.76	0.400	0.138	2.36	1.69	0.552
(2100) Ra-Shalom	2000-08-21	39	0.083	2.79	2.32	0.11	2.4		0.085	2.73	2.30	0.400	0.091	2.64	2.22	0.552
(6178) 1986 DA	1986-04-22	31.4	0.17	2.1	(1.0)	0.14	2.3	0.6	0.165	2.12	(1.0)	0.470	0.167	2.11	(1.0)	0.624
(6489) Golevka	1995-06-16	88.8	0.63	0.29	(1.2)	0.15	0.53	0.03	0.634	0.29	(1.2)	0.447	0.708	0.27	(1.2)	0.594
(33342) 1998 WT ₂₄	2001-12-02	60	0.50	0.37	(1.5)	0.4	0.41		0.520	0.36	(1.5)	0.470	0.550	0.35	(1.5)	0.624
	2001-12-18	67	0.59	0.34	0.9	0.4	0.41		0.651	0.32	0.80	0.470	0.745	0.30	0.66	0.624
	2001-12-19	79	0.35	0.44	1.5	0.4	0.41		0.447	0.39	1.17	0.457	0.563	0.35	0.94	0.615
	2001-12-21	93	0.27	0.50	1.85	0.4	0.41		0.342	0.45	1.51	0.457	0.507	0.37	1.12	0.615

Notes. ^a η -values in brackets are the default η used and are not best-fitted, due to their only being one or two flux values, or for other reasons explained in the NEATM fit source (Table 6.2).

^bIf not given in literature, uncertainty is assumed to be 10%.

^c p_v values for NESTM are give to three decimal places to allow comparison between close results from different versions of NESTM. As for the NEATM, the uncertainty in p_v , D_{eff} and η is assumed to be 30%, 15% and 20% respectively.

Table 6.5
NEATM, NESTM550 and NESTM2200 derived p_v , D_{eff} and η , f parameters used, and radar diameters and albedos for NEAs for which radar diameters and thermal IR fluxes are available

Asteroid	Date of obs. yyyy-mm-dd	NEATM			Radar			NESTM550			NESTM2200					
		α°	p_v	D_{eff} (km)	η^a	p_v	D (km)	\pm^b (km)	p_v^c	D_{eff} (km)	η^a	f	p_v^c	D_{eff} (km)	η^a	f
(433) Eros	1975-01-17	9.9	0.22	14.3	1.15	0.22	14.1	0.2	0.222	14.14	1.10	0.681	0.223	14.10	1.10	0.728
	1975-01-17	9.9	0.20	23.6	1.05	0.28	20.06	0.2	0.211	23.30	1.01	0.681	0.213	23.19	1.00	0.728
	1998-06-27	30.9	0.21	23.6	1.07	0.28	20.06	0.2	0.225	23.56	0.99	0.704	0.227	22.47	0.99	0.732
	2002-09-28	18.2	0.18	23.34	0.93	0.28	20.06	0.2	0.185	23.01	0.95	0.704	0.186	22.95	0.95	0.732
(1566) Icarus	1987-06-23	93	0.33	1.27	(1.2)	0.09	2.5	1.5	0.500	1.03	(1.2)	0.694	0.554	0.98	(1.2)	0.732
(1580) Betulia	1976-05-23	10	0.17	3.9	(1.2)	0.06	6		0.167	3.95	(1.2)	0.675	0.168	3.93	(1.2)	0.726
(1620) Geographos	1983-03-11	34	0.26	2.5	(1.2)	0.07	2.56		0.268	2.46	(1.2)	0.675	0.274	2.44	(1.2)	0.726
(1627) Ivar	1985-07-10	53	0.12	10.2	(1.2)	0.17	8.5	3	0.129	9.73	(1.2)	0.681	0.135	9.51	(1.2)	0.728
	2000-03-06	5	0.15	9.12	(1.0)	0.17	8.5	3	0.157	8.94	(1.0)	0.716	0.157	8.94	(1.0)	0.733
(1685) Toro	1981-03-12	18	0.29	4.1	(1.2)	0.43	3.3	0.9	0.295	4.06	(1.2)	0.694	0.297	4.05	(1.2)	0.730
(1862) Apollo	1980-11-26	35	0.26	1.45	1.15	0.38	1.2		0.299	1.35	1.05	0.694	0.305	1.34	1.04	0.730
(2100) Ra-Shalom	1997-08-31	40.6	0.13	2.48	1.80	0.11	2.4		0.146	2.30	1.66	0.636	0.154	2.24	1.67	0.713
(2100) Ra-Shalom	2000-08-21	39	0.083	2.79	2.32	0.11	2.4		0.097	2.56	2.19	0.636	0.103	2.48	2.27	0.712
(6178) 1986 DA	1986-04-22	31.4	0.17	2.1	(1.0)	0.14	2.3	0.6	0.169	2.10	(1.0)	0.694	0.171	2.08	(1.0)	0.730
(6489) Golevka	1995-06-16	88.8	0.63	0.29	(1.2)	0.15	0.53	0.03	0.803	0.26	(1.2)	0.675	0.889	0.24	(1.2)	0.728
(33342) 1998 WT ₂₄	2001-12-02	60	0.50	0.37	(1.5)	0.4	0.41		0.580	0.34	(1.5)	0.689	0.608	0.33	(1.5)	0.730
	2001-12-18	67	0.59	0.34	0.9	0.4	0.41		0.805	0.29	0.60	0.699	0.833	0.29	0.57	0.732
	2001-12-19	79	0.35	0.44	1.5	0.4	0.41		0.627	0.33	0.86	0.689	0.662	0.32	0.83	0.730
	2001-12-21	93	0.27	0.50	1.85	0.4	0.41		0.598	0.34	1.02	0.689	0.648	0.32	1.00	0.730

Notes. ^a η -values in brackets are the default η used, and are not best-fitted, due to their only being one or two flux values, or for other reasons explained in the NEATM fit source (Table 6.2).

^bIf not given in literature, uncertainty is assumed to be 10%.

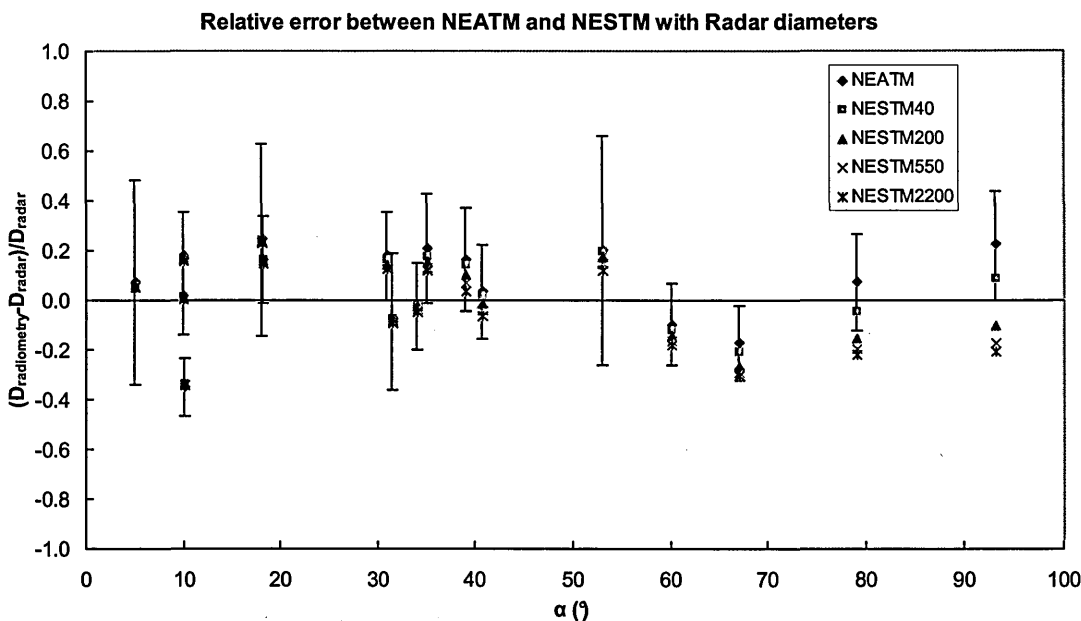
^c p_v values for NESTM are given to three decimal places to allow comparison between close results from different versions of NESTM. As for the NEATM, the uncertainty in p_v , D_{eff} and η is assumed to be 30%, 15% and 20% respectively.

Fig. 6.10 (c) shows a histogram of the relative error distribution for both NEATM and NESTM. The mean relative errors and RMS fractional difference are given in Table 6.6. Using our incomplete dataset the mean relative error between the NEATM diameters and the radar diameters changes to +6%. For NESTM200 the mean relative error is 0%, so this version of NESTM appears to most effectively remove bias between radar and radiometric diameters. However, we note that radar diameters themselves will have uncertainties which may be systematic: for more detail on the radar astronomy of asteroids, see Section 2.4.6 and references therein.

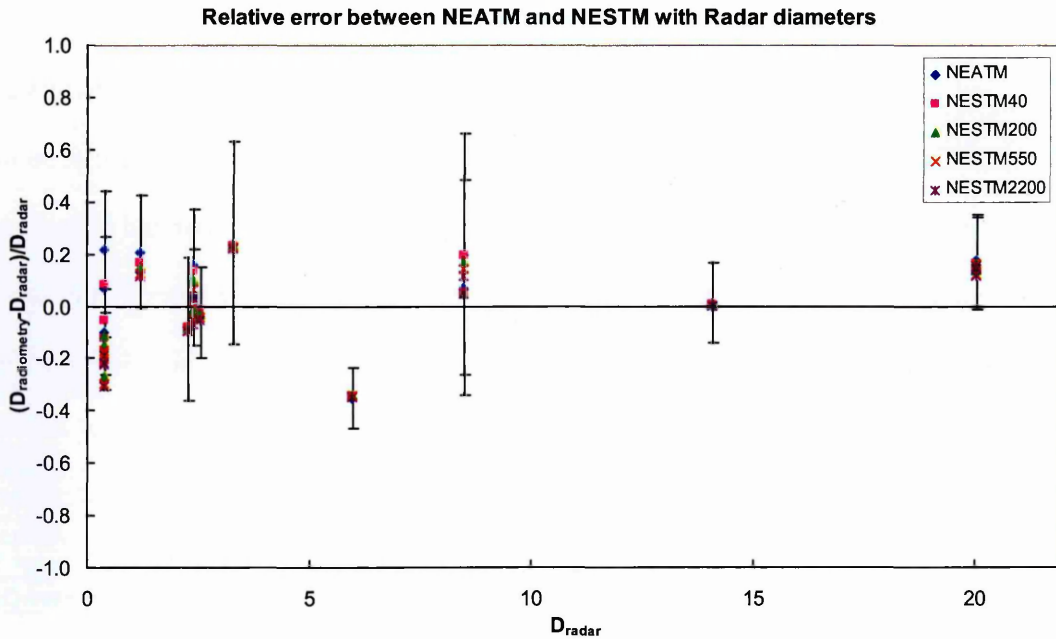
Table 6.6 Mean relative error and RMS fractional difference between radiometrically-derived diameters, using NEATM and NESTM, and radar derived diameters

Model	Mean Relative Error (%)	RMS Fractional difference (%)
NEATM	+6	15
NESTM40	+3	13
NESTM200	0	14
NESTM550	-2	14
NESTM2200	-3	14

Fig. 6.10 (a)



(b)



(c)

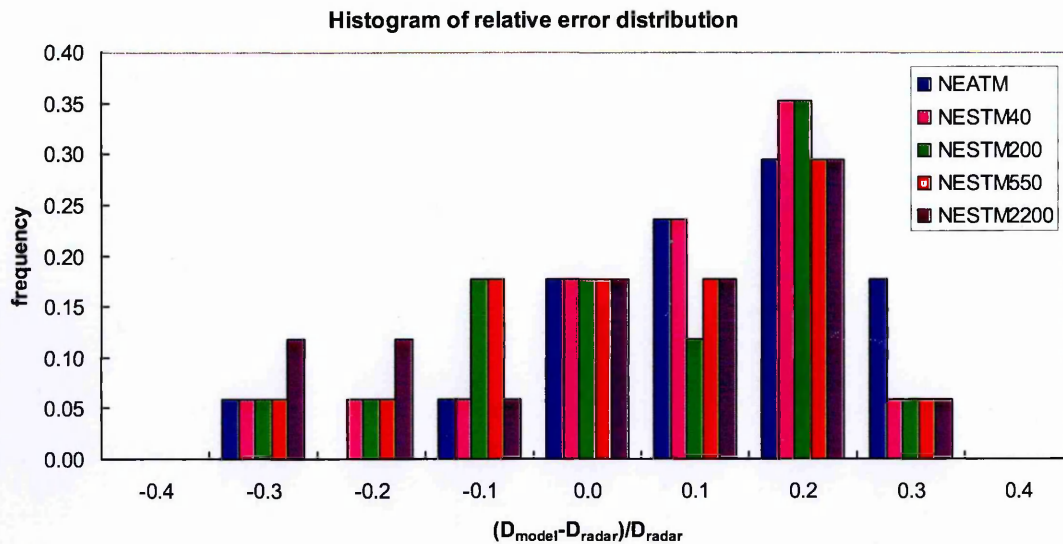


Fig. 6.10 Comparison of NEATM and NESTM relative error distribution with radar diameters. (a) Relative error variation with phase angle α , error bars only included for NEATM for clarity, and are the same size for NESTM; (b) relative error variation with radar diameter D_{radar} , error bars as for (a); (c) histogram of relative error distribution. Note the positive bias for NEATM ($+0.08 \pm 0.04$). There are more frequently smaller diameters for NESTM compared to radar.

Of particular note are the NESTM fits to observations of (33342) 1998 WT₂₄, which were reported by Delbó (2004). (33342) 1998 WT₂₄ was observed at a range of high phase angles: 60°, 67°, 79° and 93°, and NEATM fits seemed to have a systematic trend of increasing D_{eff} and η , and a corresponding decreasing p_v , with phase angle. Using NESTM reduces this trend, although it needs NESTM2200 to (mostly) remove it. This could indicate that (33342) 1998 WT₂₄ has a high surface thermal inertia; on the other hand, it is an elongated object – from radar measurements it has dimensions of 0.42×0.33 km as well as a significant lightcurve amplitude (Section 3.9.7). It is possible that shape effects are responsible for the changing η -values and corresponding values of D_{eff} and p_v (Section 7.2.5).

6.6 Conclusions

Disregarding the thermal flux from the night side decreases the accuracy of the NEATM, which overestimates the asteroid's diameter and underestimates its albedo as the phase angle increases. By simulating asteroid surfaces using a simple thermophysical model we have been able to estimate the extent of this inaccuracy. For example, for asteroids with rotation period $P = 5$ h observed at $r = 1$ AU at $\alpha = 60^\circ$ observed on the afternoon side with surface thermal inertias $\Gamma = 40, 200, 550$ and $2200 \text{ J m}^{-2} \text{ s}^{-1/2} \text{ K}^{-1}$ their diameters are +4%, +17%, +23% and +27% inaccurate respectively (on top of any other inaccuracy due to asteroid shape, uncertainty in H_V etc.). However, for the same set of asteroids observed on the morning side their diameters are -1%, +5%, +18% and +27% inaccurate respectively, so the NEATM is more accurate for asteroids observed on the morning side than it is for the afternoon side.

The NESTM is a modification of NEATM which applies a temperature to the night side that is a latitude-dependent fraction f of the maximum day side temperature when

$\eta = 1$, i.e. $T_{\text{night}} = fT_{\text{max}} \cos^{1/4} \phi$. The f parameter depends on the asteroid's thermal parameter Θ , which in turn depends on the assumed surface thermal inertia of the asteroid and its rotation period. Four different versions of NESTM were studied where the thermal inertia is assumed to be $\Gamma = 40, 200, 550$ and $2200 \text{ J m}^{-2} \text{ s}^{-1/2} \text{ K}^{-1}$, referred to as NESTM40, NESTM200, NESTM550 and NESTM2200 respectively.

The NESTM reduces the inaccuracy of diameter and albedo estimation for a wide range of different simulated asteroid surfaces. However, where the NESTM applies too high a night side temperature, which is most likely to happen for an asteroid observed on the morning side, it will underestimate the diameter (and consequently overestimate the albedo). In some circumstances, it can underestimate the diameter by a greater percentage than NEATM will overestimate it. The NESTM200 produces the most improved accuracy in diameter estimation over the greatest range of asteroid surfaces. For example, for asteroids observed on the afternoon side with rotation period $P = 5$ h, at a heliocentric distance $r = 1$ AU at $\alpha = 60^\circ$ with surface thermal inertias $\Gamma = 40, 200, 550$ and $2200 \text{ J m}^{-2} \text{ s}^{-1/2} \text{ K}^{-1}$, their diameters are -6%, +2%, +6% and +14% inaccurate respectively. For the same asteroids observed on the morning side their diameters are -7%, -3%, +5% and +11% inaccurate respectively.

We have shown that the NESTM produces diameters significantly closer to radar-derived diameters, with the NEATM systematic bias of overestimating diameters eradicated by NESTM200. We suggest adopting the NESTM200 as the default NESTM. Alternatively to inputting a thermal inertia and rotation period into NESTM to derive a unique f parameter from a look-up table, it would be adequate to use $f = 0.6$ as a default.

7 Conclusions and Future Work

7.1 Conclusions

7.1.1 Optical Observations

Optical observations at the JKT in May 2001, December 2001 and September/October 2002 have measured physical properties of 13 NEAs. By creating composite lightcurves using Fourier fits, six rotation periods have been obtained unambiguously, and three more with other periods possible. 10 mean magnitudes $\bar{V}(\alpha)$ [or in one case $\bar{R}(\alpha)$] have been derived. From these, three absolute magnitudes H_V have been measured fairly precisely (i.e. with known phase parameter G or at low phase angle), while seven other H_V are estimated. The lightcurve amplitudes of 10 asteroids have been derived and reduced to 0° phase angle and two have had limits estimated. The physical properties measured are given in Table 3.5.

The main purpose of the September 2002 JKT observations was to support the UKIRT thermal IR observations. From the optical observations at the JKT we were able to lightcurve correct the thermal IR fluxes of (433) Eros, (6455) 1992 HE, 1998 UO₁ and 2002 HK₁₂ and establish that 2002 NX₁₈ and 2002 QE₁₅ had low lightcurve amplitudes, making the lack of lightcurve correction an unimportant contribution to the uncertainty.

7.1.2 Thermal Infrared Observations

Thermal IR observations in March and September 2002 of 10 NEAs at the UKIRT using the Michelle instrument have been made. The geometric albedo (p_v) and beaming parameter (η , effectively a measurement of the surface temperature) of seven objects, and the effective diameters (D_{eff}) of eight objects previously unobserved in the thermal IR, have been measured by fitting the NEATM, principally, to the fluxes. Also (433) Eros was observed, and limits in p_v of two objects and D_{eff} of one object were determined. Some

objects were observed several times, providing 14 datasets of thermal IR fluxes, with an estimated 67 available previous to this work. As of 8 August 2005, this brings the total number of NEOs with known p_v and D_{eff} (measured by thermal radiometry, radar or spacecraft) to about 78 (http://earn.dlr.de/nea/table1_new.html) and the number of NEOs with measured η to 30. This work is a significant contribution statistically to the physical characterisation of NEOs: it increases the number of NEOs with measured diameters by about 11%. The measured η are consistent with the linear η - α relation found by Delbó (2004) (Fig. 5.25). Some of the derived parameters are discussed below. The full results are given in Table 5.17.

The derived albedos for the S-type NEAs observed [(433) Eros, (6455) 1992 HE, 2000 GD₂) are consistent with the trend of increasing albedo with decreasing diameter reported by Delbó (2004) (Fig. 5.26, where we include Q-type asteroids also). Particularly interesting is the result for 2000 GD₂. It has $p_v = 0.56 \pm 0.17$, $D_{eff} = 0.27 \pm 0.04$ with a best-fit $\eta = 0.74$ at $\alpha = 28^\circ$. It is the highest albedo yet measured for an S-type NEA (disregarding a result for Golevka, see Section 5.8.1). Additionally, we have discovered a possible trend of increasing η with diameter for S- and Q-type asteroids below 2.3 km [Fig. 5.27 (e)].

(433) Eros was found to have $D_{eff} = 23.31 \pm 3.5$ km at lightcurve maximum and $p_v = 0.24 \pm 0.07$, consistent with previous thermal IR observations and NEAR-Shoemaker results, validating our experimental setup and data reduction process. We measured $\eta = 0.95 \pm 0.19$ at $\alpha = 18^\circ$, while previous η have ranged between 1.05-1.15. The estimate in the uncertainty of η is crude, so we cannot be sure that the difference is not significant. It may be, since (433) Eros was observed pole-on, that we are seeing the effects of less thermal emission being carried to the night side, although this is speculative.

(6455) 1992 HE has $D_{eff} = 3.55 \pm 0.5$ km and $p_v = 0.26 \pm 0.08$, consistent with its S class. $\eta = 0.80$ at 22° measured in March 2002 and an average $\eta = 0.68$ in September 2002. The low η , coupled with a bad fit for the FRM and probable relatively fast rotation rate, indicates that it is a low surface thermal inertia, extended-regolith, “dusty” object.

(66063) 1998 RO₁ probably had cirrus affecting the observation; as a result of the increased uncertainty, only limits were obtained for the albedo. $p_v > 0.30$ and $D_{eff} = 0.45^{+0.16}_{-0.13}$ km, using a NEATM fit with default $\eta = 1$. (66063) 1998 RO₁ is a binary asteroid, and the derived diameters of its primary (D_p) and secondary components (D_s) are $D_p = 0.41^{+0.15}_{-0.12}$ km and $D_s = 0.19^{+0.08}_{-0.06}$ km.

It is not possible to clarify which model is to be preferred for X-type (i.e. E, M or P-type) 1999 HF₁, since NEATM may not be reliable at the high phase angle of observation ($\alpha = 91^\circ$). The albedo is estimated as an average of the FRM and NEATM fits: $p_v = 0.19 \pm 0.07$ and $D_{eff} = 3.73^{+1.0}_{-0.5}$ km. The measured p_v indicates it is not a P-type. 1999 HF₁ is a binary asteroid and we derived $D_p = 3.64^{+1.00}_{-0.51}$ km and $D_s = 0.84^{+0.35}_{-0.20}$ km.

2002 HK₁₂ has a moderate albedo $p_v = 0.24^{+0.25}_{-0.11}$, $D_{eff} = 0.62 \pm 0.2$ km, and an anomalously high best-fit $\eta = 2.75$ at $\alpha = 33^\circ$ (c.f. Fig. 5.25), indicating an unrealistically high surface thermal inertia $>5000 \text{ J m}^{-2} \text{ s}^{-1/2} \text{ K}^{-1}$, such as a bare rock surface. The FRM was also a good fit. An explanation of η -values purely in terms of thermal inertia and surface roughness is probably an oversimplification.

2002 NX₁₈ has an unusually low albedo $p_v = 0.031 \pm 0.009$ and $D_{eff} = 2.24 \pm 0.3$ km, with an average fitted $\eta = 1.18$ at $\alpha = 53^\circ$.

7.1.3 Night Emission Simulated Thermal Model

Disregarding the thermal flux from the night side decreases the accuracy of the NEATM as the phase angle increases, which overestimates the asteroid's diameter and underestimates its albedo. The NESTM is a modified NEATM that applies a temperature to the night side that is a latitude-dependent fraction f of the maximum day side temperature when $\eta = 1$, i.e. $T_{\text{night}} = fT_{\text{max}} \cos^{1/4} \phi$. The f parameter depends on the asteroid's thermal parameter Θ , which in turn is a function of the assumed surface thermal inertia of the asteroid and its rotation period.

We found that NESTM reduces the inaccuracy of diameter and albedo measurements for a wide range of different simulated asteroid surfaces (Table 6.1, Fig. 6.7). However, when the NESTM applies too high a night side temperature it will underestimate the diameter. The version of NESTM which assumes a surface thermal inertia of $200 \text{ J m}^{-2} \text{ s}^{-1/2} \text{ K}^{-1}$ (NESTM200) produces the most improved accuracy in diameter estimation over the greatest range of asteroid surfaces. We have shown that NESTM-derived diameters are significantly closer to radar-derived diameters compared to a similar analysis for NEATM. The NEATM systematic bias of overestimating diameters is eradicated by NESTM200. An acceptable approximation to NESTM200 is to use $f = 0.6$. We suggest adopting NESTM200 as a default model when observing at $\alpha > 45^\circ$.

7.2 Future Work

7.2.1 Optical Observations

There are R and I-filter frames for 2002 NX₁₈, (6455) 1992 HE, (53789) 2000 ED₁₀₄, 2002 HK₁₂ and 2002 QE₁₅ taken on the night of 1 October 2002. Initially the calibration for that night indicated that the conditions were not photometric, and therefore it was not considered worthwhile reducing the frames. A re-evaluation suggests that assessment may be too harsh; cirrus may have been affecting the high airmass (near-horizon) observations between 22:24 and 22:54 UT (Fig. 7.1). The calibration of the standards in the I-filter are still affected by cirrus, but after a complete reduction of all the night's *V* frames, we know that any cirrus was probably sparse and temporary.

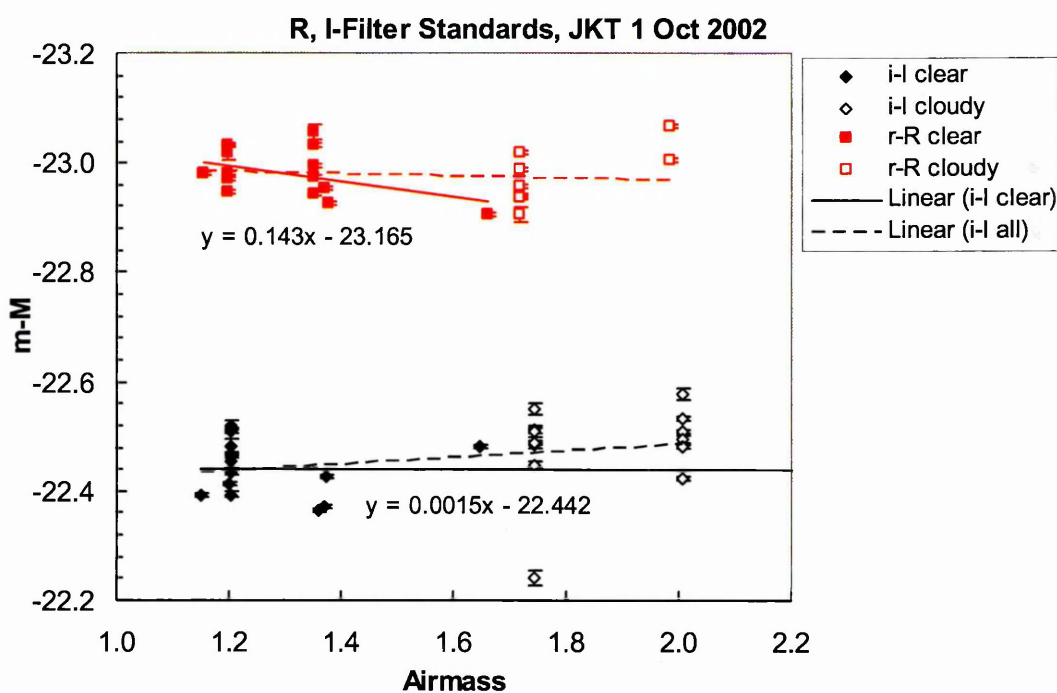


Fig. 7.1 Extinction plots for standards (R and I-filter) on JKT 1 October 2002, re-evaluated to exclude high airmass observations taken between 22:24 and 22:54 UT, that were probably affected by cirrus. Equations given for clearer weather linear fits (solid lines).

The new extinction plots can be used to reduce the R and I-filter frames, and from these we can obtain *V-I* and *V-R* colour indices for the asteroids. Measuring the colour indices of an asteroid can provide clues to the mineralogy and the asteroid's taxonomic

class (Bowell and Lumme, 1979). A recent survey of optical colours of NEOs can be found in Dandy *et al.* (2003).

There are unreduced JKT runs: September 2001 and April 2002. The amount of data unreduced is roughly equal to 50% of that presented in this work. The April 2002 observations also include observations of (6455) 1992 HE, and 1999 HF₁. Reducing these observations is a high priority since it may help interpret the optical and thermal IR observations in this thesis. Particularly, the rotation period of (6455) 1992 HE is ambiguous (Section 3.9.4), while 1999 HF₁ is a binary asteroid. A complete list of the asteroids to be reduced is given in Table 7.1.

Table 7.1 NEOs observed at the JKT in September 2001 and April 2002, to be reduced

Date (UT)	Object	No. of frames
09/10 Sep. 2001	(5587) 1990 SB	211
11/12 Sep. 2001	Comet C/Loneos (2001 OG ₁₀₈)	172
13/14 Sep. 2001	(5587) 1990 SB	75
	Comet C/Loneos (2001 OG ₁₀₈)	159
14/15 Sep. 2001	(5587) 1990 SB	77
	Comet C/Loneos (2001 OG ₁₀₈)	47
15/16 Sep. 2001	(5587) 1990 SB	130
	Comet C/Loneos (2001 OG ₁₀₈)	95
20/21 Apr. 2002	(10199) Chariklo	6
	(6455) 1992 HE	175
21/22 Apr. 2002	(4660) Nereus	25
	1999 HF ₁	137
	(6134) 1990 RA ₅	12
25/26 Apr. 2002	1999 HF ₁	320
26/27 Apr. 2002	Comet C/Loneos (2001 OG ₁₀₈)	13
	1999 HF ₁	285
27/28 Apr. 2002	(4660) Nereus	16
	(6455) 1992 HE	174
	1999 HF ₁	118
28/29 Apr. 2002	Comet C/Loneos (2001 OG ₁₀₈)	14
	(4660) Nereus	16
	(6455) 1992 HE	24
	(31669) 1999 JT ₆	70
	(89355) 2001 VS ₇₈	20
	1999 HF ₁	43
29/30 April 2002	Comet C/Loneos (2001 OG ₁₀₈)	15
	(4660) Nereus	12
	(31669) 1999 JT ₆	140
	1999 HF ₁	69

7.2.2 Fitting More Thermal IR Fluxes with NESTM

Chapter 6 introduced the NESTM and applied it to a dataset of thermal IR fluxes for NEAs which have radar diameters available (Table 6.2). At the present time, we have not yet obtained the thermal IR fluxes for six datasets: five of (5381) Sekhmet and one of (6489) Golevka. It is a priority to obtain the (5381) Sekhmet dataset, since it is the second NEA to be observed at a fairly wide range of phase angles (24° - 44°) after (33342) 1998 WT₂₄, the NESTM fits for which were intriguing (Section 6.5). Additionally we need the lightcurve corrected fluxes of (1580) Betulia. All seven NEATM fits are reported by Delbó (2004).

Previous to this work, the total number of NEAs observed in the thermal IR was 47 objects, with 67 datasets of thermal IR fluxes in total. The derived p_v and D_{eff} from STM, FRM and NEATM fits were compiled in a single database by Delbó (2004). Including our 8 new objects and 14 new observations brings the total to 55 objects and 81 datasets. For single broadband N-band and Q-band fluxes [often reported as magnitudes, e.g. by Veeder *et al.* (1989)] or for poor quality datasets, default values of η were used (Section 5.8.1), best guesses based on a few fits. Previous to Delbó *et al.* (2003), $\eta = 1.2$ was used, as suggested by Harris (1998). Delbó *et al.* (2003) suggested using $\eta = 1.0$ for $\alpha < 45^\circ$ and $\eta = 1.5$ for $\alpha \geq 45^\circ$. With a fairly well-defined η - α linear relation, first reported by Delbó *et al.* (2003), updated by Delbó (2004) and not significantly altered by this work (Fig. 5.24, Section 5.8.1), a unique η for any given α can be obtained. Including the objects in this work, the η - α linear fit is:

$$\eta = 0.012\alpha + 0.96 \quad (7.1)$$

A straightforward, but relatively time consuming task, is to collect together all the original papers with reported thermal IR observations of NEAs, and create a single database of fluxes in units of ($\text{W m}^{-2} \mu\text{m}^{-1}$) or (mJy). Since many monochromatic

measurements were given in magnitudes, these would therefore need to be converted using the zero magnitude flux of the observed standard stars given in the original source.

Careful attention also needs to be paid to the appropriate H_V that should be used for the geometry of the observation. Sometimes the mean magnitude must be assumed, since there were no quasi-simultaneous optical observations. If this is the case, then some idea of the uncertainty this will contribute can be given by reporting measured lightcurve amplitudes, if any are known. Sometimes the asteroid can be considered to be near lightcurve minimum or maximum. The asteroid may have been better observed optically at a later date, and new updated values of H_V can then be used to improve the fits. If quasi-simultaneous optical observations were made, then the lightcurve-corrected thermal IR fluxes must be obtained, if they were made over a significant period of time (and fitted with the mean H_V). Otherwise, they can be fitted with the appropriate H_V for the time of the observation. Sometimes, only the non-lightcurve corrected fluxes were reported, or the fluxes were not given at all, in which case we have to obtain the data directly from the original authors. To complete the resource, the phase parameter G (if known), the phase angle α , the asteroid-Sun distance r (AU) and asteroid-Earth distance Δ (AU) at the time of the observation would also need to be compiled.

We will initially concentrate on completing this database for all datasets of high enough quality that a best-fit η can be found. Including the observations in this work, the number of these is 30 objects (50 datasets). Since we have adopted NESTM200 as the default, we would fit this to these objects to define the equivalent relation for NESTM. Figure 7.2 shows the limited progress made so far, obtained for the few asteroids with radar diameter and thermal IR datasets at a range of wavelengths (Tables 6.4 and 6.5, objects for which η is not given in brackets). It is hoped that the gradient will be shallower, since the physical explanation for the relation is partly due to neglecting thermal emission

on the night side, and partly due to beaming. Optimistically, we might hope for an insight into the relative strengths these two effects have on η by the change in the gradient. It is possible that the appropriate relation would no longer be linear. Whatever the outcome, we would need to acquire an η - α relation, equivalent to that found for the NEATM, for the NESTM.

Earlier NEATM fits made using default values of η need to be re-derived using η acquired from Eq. 7.1. It would be interesting to see what effect this has on the comparison of NEATM diameters with those made by radar, especially since many of those were made using default η . Does this increase or reduce the bias? Also, does an improvement in the precision of NEATM reveal any hidden biases in the derived albedos? A plot of p_v against α appears to show no trend, which Delbó interprets as indicating that NEATM is reliable for $\alpha < 60^\circ$. The NESTM comparison with radar diameters would also have to be re-evaluated, using the new default values of η for NESTM. Finally, the NESTM would be fitted to the entire database.

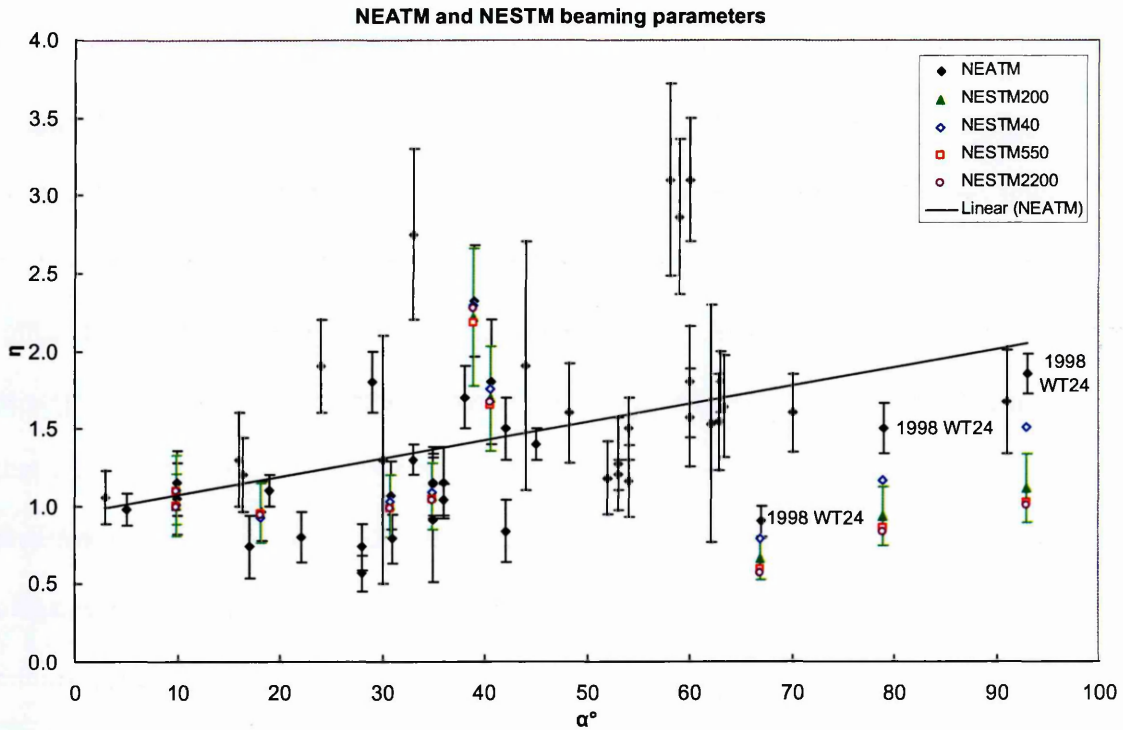


Fig. 7.2 Best-fit beaming parameters η versus phase angle α for asteroids fitted with NEATM and the few asteroids fitted with NESTM. Error bars are plotted for NEATM and NESTM200 only, for clarity.

7.2.3 Improving the NESTM

An early version of the NESTM separated the beaming parameter into two components (β and γ). γ was the contribution to η from night side emission, and so β (the “separated-beaming parameter”) was defined by:

$$\eta = \beta\gamma \quad (7.2)$$

The day side temperatures T_{day} were divided by η , while the night side temperatures T_{night} by β (since it does not make sense to divide the night side temperatures by a component of the beaming parameter that represents the reduction in temperature due to including emission on the night side). γ (and hence β since η is best-fitted) was calculated from the ratio of the modified projected model’s (Section 4.3.5) T_{mod} and T_{max} :

$$\eta = \left(\frac{T_{max}}{T_{mod}} \right)^4 \quad (7.3)$$

This version of the model, although it had been successfully tested on one or two objects, was simplified into the version described in Section 6.2 because the early version was considered confusing and needlessly complex. It arguably does not make sense to fit a beaming parameter to the night side, since surely there is no beaming on the night side.

But η (and hence β) is a beaming parameter in name only and could more accurately be referred to as a calibration parameter. We best-fit η to the observed temperature profile of the asteroid, effectively measuring the surface temperature. Using our current NESTM, this observed temperature profile can only be applied to the day side. If the calculated night side temperature, an iso-latitudinal fraction of the maximum day side temperature (which can be thought of as a damped-down FRM), gives a higher temperature at any latitude on the day side longitudes, it replaces the day side temperature. If we choose too high a f parameter, it could “swamp” the day side temperatures if the best-fit η indicate a cool surface. Essentially, NESTM forces a certain minimum temperature, no matter what we observe.

By allowing the night side component to be fitted by η also, we can avoid this problem. It is perhaps unnecessary to separate η into β and γ and then have to define a T_{mod} for every p_v , since we want to keep NESTM a simple thermal model. An experimental alteration to our current NESTM would be to divide the night side by η also, i.e. replace T_{max} with T_{fit} in Eq. 6.7. It would be interesting to see if this removes the bizarre behaviour of best-fit η at high phase angles in some circumstances when testing NESTM (Fig. 6.9). Also, by allowing the applied night side temperatures to be altered by the observed temperature profile, it might compensate somewhat if the assumed surface thermal inertia is significantly different from the actual surface.

7.2.4 *Improving the Thermophysical Model*

Delbó (2004) tested the NEATM by using a more sophisticated model that included surface roughness. Using a variant of the model developed by Spencer *et al.* (1989) and Spencer (1990), the asteroid surface was divided up into triangular elements, each of which contained a crater of defined slope. The model took account of the effect of shadowing, heating by sunlight multiply scattered within the crater, and self-heating by re-absorption of thermal radiation from other parts of the crater. By not including surface roughness, we derived unrealistically high η when testing NESTM. However, Delbó was trying to achieve a different goal, which was to produce a database of physically realistic η -values for a range of surface roughness and thermal parameters. In testing the NESTM, we wanted to evaluate different types of NESTM to decide on a default by comparing derived diameter accuracies. For that goal, using a simpler thermophysical model was felt to be the appropriate tool. It would be helpful to trial a similar thermophysical model to check whether the derived diameter accuracies, and differences between the models, are changed when we include surface roughness.

7.2.5 *Ellipsoid Approximation Thermal Model (EATM)*

The principle behind NESTM was: although we do not know how much thermal emission there is on the night side of an NEA, it is not the best solution to assume it is zero. It is better to estimate an average temperature and apply it. What we have found is that the assumption of zero thermal emission on the night side does not significantly affect the measurement of the diameter compared to other uncertainties below about 45° phase angle.

Probably the biggest unevaluated parameter that affects the measured surface temperature of NEAs from disk-integrated measurements (i.e. η) is an NEA's shape.

Although asteroid shapes have been modelled as ellipsoids (e.g. Brown, 1985), such models have not been employed on NEAs in general, because we do not know their shapes.

However we can attempt to overcome this problem, using the same principle as when developing the NESTM. Just because we do not know what shape an NEA has, that does not mean it is the best solution to assume it is spherical. The Ellipsoid Approximation Thermal Model (EATM) would model an NEA as an ellipsoid and η would be best-fit. If lightcurve amplitudes are available, these would be used to assume an ellipsoid shape for an NEA. Of course, lightcurve amplitudes only provide a minimum axis ratio, assuming a 90° pole orientation. But our model will assume a 90° pole orientation anyway, since again this is generally not known for an NEA. If a lightcurve amplitude is not known, then EATM will assume an $a:b$ ratio of 1.3 calculated from the average NEO reduced lightcurve amplitude 0.29 (Binzel *et al.*, 2002) using Eq. 3.14. The model could be tested and compared with NEATM and NESTM by generating synthetic fluxes using a thermophysical model that modelled an asteroid with a range of ellipsoid shapes, initially with zero surface thermal inertia, and later with a range of thermal inertias.

EATM could be applied to our database of thermal IR fluxes, compared with radar diameters, and its effect on the η - α relation evaluated. An interesting immediate test case would be to apply it to (33342) 1998 WT₂₄, for which we have an approximation of its shape from radar (0.42×0.33 km, Section 3.9.7) and observations at a range of high phase angles (Section 6.5). I would speculate that EATM will have a more dramatic effect on derived D_{eff} and p_v than the NESTM did, and may significantly improve the accuracy of our modelling. It could be combined with NESTM, e.g. we could assume an average night side temperature as a iso-latitudinal fraction $f = 0.6$ of the day side.

Taking the concept further, we could develop a model that assumes a sensible average surface roughness for NEAs (e.g. estimated from the 6 NEOs in Table 4 in Binzel *et al.* (2002), $\bar{\theta} = 21^\circ$) and combine that with the other features, for an all-encompassing model which would be continually refined as our knowledge of typical and specific physical properties of NEA surfaces improves from groundbased and spacecraft observations.

7.2.6 Further Thermal IR Observations

For the time being, the NEATM appears to be an adequate tool for the measurement of diameters and albedos of NEAs. However, there is currently no dedicated program within the UK for thermal IR observations of NEAs, or perhaps even an appropriate instrument since Michelle was taken off UKIRT on 1 October 2002. International efforts, principally by A.W. Harris and colleagues at DLR, are rapidly outpaced by the discovery rate of NEAs (Section 2.10).

If I was to have the opportunity to make further observations, then I would concentrate on several different goals, although since the number of NEAs measured is still small, any object is valuable. First, observe the same NEA at a large range of phase angles, to evaluate NEATM and NESTM, and other thermal models. An object that makes a close pass to the Earth is a good candidate, since it will rapidly change phase angle and will be bright. Do this for a number of objects, with known shape and, ideally, other surface characteristics well-defined; although to measure the surface thermal inertia without resorting to the thermal models you are trying to evaluate perhaps requires a spacecraft encounter. However, knowledge of an asteroid's taxonomic type would be valuable, and it is possible to estimate surface grain density from radar and optical polarimetry (Binzel *et al.*, 2002). Second, concentrate on small objects with diameters less than 1 km ($H_V > 17$), since there is a bias against observing them (Section 5.3.1), and hence de-biased estimates

of the NEA size distribution are size-limited (Stuart and Binzel, 2004). Third, concentrate on objects with known taxonomic types, particularly ones that are typically dark (e.g. D-type) for which we have few measured albedos, and X-types, since approximately 30% of NEAs are X-types and they degenerate into E, M and P-types in order of decreasing albedo (Sections 2.4.4 and 2.10).

References

- Alvarez, L. W., Alvarez, W., Asaro, F. and Michel, H. V. 1980. Extraterrestrial Cause for the Cretaceous Tertiary Extinction. *Science* 208, 1095-1108.
- Barucci, M. A., Cruikshank, D. P., Mottola, S. and Lazzarin, M. 2002. Physical properties of Trojan and Centaur asteroids. In: W. F. Bottke, A. Cellino, P. Paolicchi and R. P. Binzel (Eds.), *Asteroids III*, University of Arizona Press, Tucson, pp. 273-288.
- Beatty, J. K. 2001. NEAR Falls for Eros. *Sky and Telescope* May, 34-37.
- Becker, L., Poreda, R. J., Hunt, A. G., Bunch, T. E. and Rampino, M. 2001. Impact Event at the Permian-Triassic Boundary: Evidence from Extraterrestrial Noble Gases in Fullerenes. *Science* 291, 1530-1534.
- Beckwith, S., Evans, N. J., Becklin, E. E. and Neugebauer, G. 1976. Infrared observations of Monoceros R2. *Astrophys. J.* 208, 390-396.
- Belton, M. J. S., Chapman, C. R., Klaasen, K. P., Harch, A. P., Thomas, P. C., Veverka, J., McEwen, A. S. and Pappalardo, R. T. 1996. Galileo's Encounter with 243 Ida: an Overview of the Imaging Experiment. *Icarus* 120, 1-19.
- Bendjoya, P. and Zappalà, V. 2002. Asteroid Family Identification. In: W. F. Bottke, A. Cellino, P. Paolicchi and R. P. Binzel (Eds.), *Asteroids III*, The University of Arizona Press, Tucson, pp. 613-618.
- Benner, L. A. M., Ostro, S. J., Giorgini, J. D., Jurgens, R. F., Mitchell, D. L., Rose, R., Rosema, K. D., Slade, M. A., Winkler, R., Yeomans, D. K., Campbell, D. B., Chandler, J. F. and Shapiro, I. I. 1997. Radar detection of near-Earth asteroids 2062 Aten, 2101 Adonis, 3103 Eger, 4544 Xanthus, and 1992 QN. *Icarus* 130, 296-312.
- Binzel, R. P., Farinella, P., Zappalà, V. and Cellino, A. 1989. Asteroid Rotation Rates: Distributions and Statistics. In: R. P. Binzel, T. Gehrels and M. S. Matthews (Eds.), *Asteroids II*, University of Arizona Press, Tucson, pp. 416-441.
- Binzel, R. P., Xu, S., Bus, S. J. and Bowell, E. 1992. Origins for the near-Earth asteroids. *Science* 257, 779-782.
- Binzel, R. P., Gaffey, M. J., Thomas, P. C., Zellner, B. H., Storrs, A. D. and Wells, E. N. 1997. Geologic Mapping of Vesta from 1994 Hubble Space Telescope Images. *Icarus* 128, 95-103.
- Binzel, R. P., Lupishko, D. F., Di Martino, M., Whiteley, R. J. and Hahn, G. J. 2002. Physical properties of near-Earth objects. In: W. F. Bottke, A. Cellino, P. Paolicchi and R. P. Binzel (Eds.), *Asteroids III*, University of Arizona Press, Tucson, pp. 251-271.
- Binzel, R. P., Rivkin, A. S., Stuart, J. S., Harris, A. W., Bus, S. J. and Burbine, T. H. 2004. Observed spectral properties of near-Earth objects: results for population distribution, source regions, and space weathering processes. *Icarus* 170, 259-294.
- Bottke, W. F. and Melosh, H. J. 1996a. The formation of asteroid satellites and doublet craters by planetary tidal forces. *Nature* 381, 51-53.
- Bottke, W. F. and Melosh, H. J. 1996b. Binary Asteroids and the Formation of Doublet Craters. *Icarus* 124, 372-391.
- Bottke, W. F., Morbidelli, A., Jedicke, R., Petit, J. M., Levison, H. F., Michel, P. and Neeb, T. S. 2002a. Debaised orbital and magnitude distribution of the near-Earth objects. *Icarus* 156, 399-433.
- Bottke, W. F., Vokrouhlický, D., Rubincam, D. P. and Brož, M. 2002b. The effect of Yarkovsky thermal forces on the dynamical evolution of asteroids and meteoroids. In: W. F. Bottke, A. Cellino, P. Paolicchi and R. P. Binzel (Eds.), *Asteroids III*, The University of Arizona Press, Tucson, pp. 395-408.
- Bottke, W. F., William F., Durda, D. D., Nesvorný, D., Jedicke, R., Morbidelli, A., Vokrouhlický, D. and Levison, H. F. 2006. Linking the collisional history of the main asteroid belt to its dynamical excitation and depletion. *Icarus* 183, 235-236.
- Bowell, E. and Lumme, K. 1979. Colorimetry and Magnitudes of Asteroids. In: T. Gehrels (Eds.), *Asteroids*, Univ. of Arizona Press, Tucson, pp. 132-169.
- Bowell, E., Hapke, B., Domingue, D., Lumme, K., Peltoniemi, J. and Harris, A. W. 1989. Application of photometric models to asteroids. In: R. P. Binzel, T. Gehrels and M. S. Matthews (Eds.), *Asteroids II*, The University of Arizona Press, Tucson, pp. 524-556.
- Britt, D. T., Yeomans, D. K., Housen, K. and Consolmagno, G. 2002. Asteroid Density, Porosity, and Structure. In: W. F. Bottke, A. Cellino, P. Paolicchi and R. P. Binzel (Eds.), *Asteroids III*, University of Arizona Press, Tucson, pp. 485-500.
- Brown, M. E., Trujillo, C. A. and Rabinowitz, D. 2005. 2003 EL61, 2003 UB313, and 2005 FY9. IAU Circular No. 8577.
- Brown, R. H. 1985. Ellipsoidal geometry in asteroid thermal models: the standard radiometric model. *Icarus* 64, 53-63.

- Bus, S. J. 1999. Compositional structure in the asteroid belt: results of a spectroscopic survey. Ph.D. thesis, Massachusetts Institute of Technology, Cambridge.
- Bus, S. J. and Binzel, R. P. 2002. Phase II of the Small Main-Belt Asteroid Spectroscopic Survey. *Icarus* 158, 146-177.
- Bus, S. J., Vilas, F. and Barucci, M. A. 2002. Visible-wavelength spectroscopy of asteroids. In: W. F. Bottke, A. Cellino, P. Paolicchi and R. P. Binzel (Eds.), *Asteroids III*, The University of Arizona Press, Tucson, pp. 169-182.
- Caldwell, J. 1975. Ultraviolet observations of small bodies in the solar system by OAO-2. *Icarus* 25, 384-396.
- Campa, M. 1938. Rotation Period of 433 Eros. *Mem. Soc. Astron. Ital.* 11, 285-301.
- Cellino, A., Bus, S. J., Doressoundiram, A. and Lazzaro, D. 2002a. Spectroscopic Properties of Asteroid Families. In: W. F. Bottke, A. Cellino, P. Paolicchi and R. P. Binzel (Eds.), *Asteroids III*, The University of Arizona Press, Tucson, pp. 633-643.
- Cellino, A., Zappalà, V. and Tedesco, E. F. 2002b. Near-Earth objects: origins and need of physical characterization. *Meteoritics and Planetary Science* 37, 1965-1974.
- Chapman, C. R. and Morrison, D. 1994. Impacts on the Earth by asteroids and comets: assessing the hazard. *Nature* 367, 33-39.
- Cheng, A. F. 2002. Near Earth Asteroid Rendezvous: Mission Summary. In: W. F. Bottke, A. Cellino, P. Paolicchi and R. P. Binzel (Eds.), *Asteroids III*, The University of Arizona Press, Tucson, pp. 351-366.
- Chesley, S. R., Orbit estimation and potential impact detection for near-Earth asteroids (abstract). *Asteroids, Comets, Meteors, 2005*, Rio de Janeiro. p. 57.
- Chyba, C. F., Thomas, P. J. and Zahnle, K. J. 1993. The 1908 Tunguska explosion - Atmospheric disruption of a stony asteroid. *Nature* 361, 40-44.
- Clark, B. E., Veverka, J., Helfenstein, P., Thomas, P. C., Bell, J. F., Harch, A., Robinson, M. S., Murchie, S. L., McFadden, L. A. and Chapman, C. R. 1999. NEAR Photometry of Asteroid 253 Mathilde. *Icarus* 140, 53-65.
- Clark, B. E., Hapke, B., Pieters, C. and Britt, D. 2002. Asteroid space weathering and regolith evolution. In: W. F. Bottke, A. Cellino, P. Paolicchi and R. P. Binzel (Eds.), *Asteroids III*, The University of Arizona Press, Tucson, pp. 585-599.
- Cohen, M., Walker, R. G., Barlow, M. J. and Deacon, J. R. 1992. Spectral Irradiance Calibration in the Infrared .I. Ground- Based and Iras Broad-Band Calibrations. *Astron. J.* 104, 1650-1657.
- Cohen, M., Witteborn, F. C., Roush, T., Bregman, J. and Wooden, D. 1998. Spectral Irradiance Calibration in the Infrared. VIII. 5-14 Micron Spectroscopy of the Asteroids Ceres, Vesta, and Pallas. *Astron. J.* 115, 1671-1679.
- Cruikshank, D. P. and Jones, T. J. 1977. The diameter and albedo of asteroid 1976 AA. *Icarus* 31, 427-429.
- Cruikshank, D. P., Tholen, D. J., Hartmann, W. K., Bell, J. F. and Brown, R. H. 1991. Three basaltic Earth-approaching asteroids and the source of the basaltic meteorites. *Icarus* 89, 1-13.
- Culler, T. S., Becker, T. A., Muller, R. A. and Renne, P. R. 2000. Lunar Impact History from $^{40}\text{Ar}/^{39}\text{Ar}$ Dating of Glass Spherules. *Science* 287, 1785-1788.
- D'Abramo, G., Harris, A. W., Boattini, A., Werner, S. C., Harris, A. W. and Valsecchi, G. B. 2001. A simple probabilistic model to estimate the population of near-Earth asteroids. *Icarus* 153, 214-217.
- Dandy, C. L., Fitzsimmons, A. and Collander-Brown, S. J. 2003. Optical colors of 56 near-Earth objects: trends with size and orbit. *Icarus* 163, 363-373.
- Davis, D. R., Durda, D. D., Marzari, F., Campo Bagatin, A. and Gil-Hutton, R. 2002. Collisional Evolution of Small-Body Populations. In: W. F. Bottke, A. Cellino, P. Paolicchi and R. P. Binzel (Eds.), *Asteroids III*, The University of Arizona Press, Tucson, pp. 545-558.
- Delbó, M. and Harris, A. W. 2002. Physical properties of near-Earth asteroids from thermal infrared observations and thermal modeling. *Meteoritics and Planetary Science* 37, 1929-1936.
- Delbó, M., Harris, A. W., Binzel, R. P., Pravec, P. and Davies, J. K. 2003. Keck observations of near-Earth asteroids in the thermal infrared. *Icarus* 166, 116-130.
- Delbó, M. 2004. The nature of near-Earth asteroids from the study of their thermal infrared emission. Ph.D. thesis, Freie Universität, Berlin.
- Dohnanyi, J. S. 1969. Collisional model of asteroids and their debris. *Journal of Geophysical Research* 74, 2431-2554.
- Dotto, E., Barucci, M. A., Müller, T. G., Storrs, A. D. and Tanga, P. 2002. Observations from Orbiting Platforms. In: W. F. Bottke, A. Cellino, P. Paolicchi and R. P. Binzel (Eds.), *Asteroids III*, The University of Arizona Press, Tucson, pp. 219-234.
- Dunlap, J. L., Gehrels, T. and Howes, M. L. 1973. Minor planets and related objects. IX. Photometry and polarimetry of (1685) Toro. *Astron. J.* 78, 491-501.

- Erikson, A., Mottola, S., Lagerros, J. S. V., Lindgren, M., Piironen, J., Oja, T., Hahn, G., Lagerkvist, C.-I., Harris, A. W., Nathues, A. and Neukem, G. 2000. The Near-Earth Object Follow-up Program. *Icarus* 147, 487-497.
- Farinella, P., Vokrouhlický, D. and Hartmann, W. K. 1998. Meteorite Delivery via Yarkovsky Orbital Drift. *Icarus* 132, 378-387.
- Farinella, P. and Vokrouhlický, D. 1999. Semimajor axis mobility of asteroidal fragments. *Science* 283, 1507-1510.
- Farquhar, R., Kawaguchi, J., Russell, C., Schwehm, G., Veverka, J. and Yeomans, D. K. 2002. Spacecraft Exploration of Asteroids: The 2001 Perspective. In: W. F. Bottke, A. Cellino, P. Paolicchi and R. P. Binzel (Eds.), *Asteroids III*, The University of Arizona Press, Tucson, pp. 367-376.
- Fitzsimmons, A., Measuring the YORP effect. The Royal Astronomical Society National Astronomy Meeting, 2004, Milton Keynes, UK. p. 177.
- Fowler, J. W. and Chillemi, J. R. 1992. IRAS asteroid data processing. In: (Eds.), *The IRAS Minor Planet Survey*, Phillips Laboratory, Hanscom AF Base, M. A., pp. 17-43.
- Gaffey, M. J., The Abundance of Metal on S-Asteroid Surfaces: Indications from IRAS 12 and 25 Micron Flux Ratios. *Lunar Planet. Sci. Conf. XX*, 1989, pp. 321-322.
- Gaffey, M. J., Reed, K. L. and Kelley, M. S. 1992. Relationship of E-type Apollo asteroid 3103 (1982 BB) to the enstatite achondrite meteorites and the Hungaria asteroids. *Icarus* 100, 95-109.
- Gaffey, M. J., Bell, J. F., Brown, R. H., Burbine, T. H., Piatek, J. L., Reed, K. L. and Chaky, D. A. 1993. Mineralogical variations within the S-type asteroid class. *Icarus* 106, 573-602.
- Gaffey, M. J., Cloutis, E. A., Kelley, M. S. and Reed, K. L. 2002. Mineralogy of asteroids. In: W. F. Bottke, A. Cellino, P. Paolicchi and R. P. Binzel (Eds.), *Asteroids III*, The University of Arizona Press, Tucson, pp. 183-204.
- Glasse, A. 2001. Michelle on UKIRT: The User Manual. http://www.jach.hawaii.edu/JACdocs/UKIRT/michelle/michelle_atc/user/ocdd/ocdd.html
- Goldstein, R. M., Jurgens, R. F. and Yeomans, D. K. 1981. Radar observations of Apollo. *Icarus* 126, 450-454.
- Gradie, J. C. and Tedesco, E. F. 1982. Compositional structure of the asteroid belt. *Science* 216, 1405-1407.
- Gradie, J. C., Chapman, C. R. and Tedesco, E. F. 1989. Distribution of taxonomic classes and the compositional structure of the asteroid belt. In: R. P. Binzel, T. Gehrels and M. S. Matthews (Eds.), *Asteroids II*, University of Arizona Press, Tucson, pp. 316-335.
- Green, S. F. 1985. Infrared observations and thermal emission models of asteroids. Ph.D. thesis, University of Leicester, Leicester.
- Green, S. F., Eaton, N., Meadows, A. J., Davies, J. K. and Stewart, B. C. 1985a. The detection of fast-moving asteroids and comets by IRAS. *Icarus* 64, 517-527.
- Green, S. F., Meadows, A. J. and Davies, J. K. 1985b. Infrared observations of the extinct cometary candidate minor planet (3200) 1983TB. *Monthly Notices of the Royal Astronomical Society* 214, 29P-35P.
- Green, S. F. and McBride, N., Photometry Techniques - Report of Splinter Meeting. ESO Workshop, 1998, Garching, Germany. pp. 57-60.
- Hansen, O. L. 1977. An Explication of the Radiometric Method for Size and Albedo Determination. *Icarus* 31, 456-482.
- Harris, A. W. and Young, J. W. 1985. Photometric Results for Earth Approaching Asteroids. *B. A. A. S.* 17, 726.
- Harris, A. W., Young, J. W., Goguen, J., Hammel, H. B., Hahn, G., Tedesco, E. F. and Tholen, D. J. 1987. Photoelectric lightcurves of the asteroid 1862 Apollo. *Icarus* 70, 246-256.
- Harris, A. W. and Lupishko, D. F. 1989. Photometric Lightcurve Observations and Reduction Techniques. In: Binzel R P, Gehrels T and Matthews M S (Eds.), *Asteroids II*, The University of Arizona Press, Tucson, pp. 39-53.
- Harris, A. W., The rotation rates of very small asteroids: evidence for "rubble pile" structure (abstract). *Lunar and Planetary Science XXVII*, 1996, Lunar and Planetary Science, Houston. pp. 493-494.
- Harris, A. W. and Harris, A. W. 1997. On the revision of radiometric albedos and diameters. *Icarus* 126, 450-454.
- Harris, A. W. 1998. A Thermal Model for Near-Earth Asteroids. *Icarus* 131, 291-301.
- Harris, A. W., Davies, J. K. and Green, S. F. 1998. Thermal infrared spectrophotometry of the near-Earth asteroids 2100 Ra-Shalom and 1991 EE. *Icarus* 135, 441-450.
- Harris, A. W. and Davies, J. K. 1999. Physical Characteristics of near-Earth asteroids from thermal infrared spectrophotometry. *Icarus* 142, 464-475.

- Harris, A. W., Delbó, M., Binzel, R. P., Davies, J. K., Roberts, J., Tholen, D. J. and Whiteley, R. J. 2001. Visible to Thermal-Infrared Spectrophotometry of a Possible Inactive Cometary Nucleus. *Icarus* 153, 332-337.
- Harris, A. W. 2002. On the slow rotation of asteroids. *Icarus* 156, 184-190.
- Harris, A. W. and Lagerros, J. S. V. 2002. Asteroids in the Thermal Infrared. In: W. F. Bottke, A. Cellino, P. Paolicchi and R. P. Binzel (Eds.), *Asteroids III*, The University of Arizona Press, Tucson, pp. 205-218.
- Harris, A. W., Mueller, M., Delbo, M. and Bus, S. J. 2005. The surface properties of small asteroids: Peculiar Betulia - A case study. *Icarus*, 179, 95-108.
- Hartmann, W. K. and Tholen, D. J. 1990. Comet nuclei and Trojan asteroids: a new link and possible mechanism for comet splitting. *Icarus* 86, 448-454.
- Hechler, M. 1997. ROSETTA Mission Design. *Adv. Space Res.* 19, 127-136.
- Hirayama, K. 1918. Groups of asteroids probably of common origin. *Astron. J.* 31, 185-188.
- Horne, K. 1986. An Optimal Extraction Algorithm for CCD Spectroscopy. *Publ. Astron. Soc. Pac.* 98, 609-617.
- Hudson, R. S., Ostro, S. J., Jurgens, R. F., Rosema, K. D., Giorgini, J. D., Winkler, R., Rose, R., Choate, D., Cormier, R. A., Franck, C. R., Frye, R., Howard, D., Kelley, D., Littlefair, R., Slade, M. A., Benner, L. A. M., Thomas, M. L., Mitchell, D. L., Chodas, P. W., Yeomans, D. K., Scheeres, D. J., Palmer, P., Zaitsev, A., Koyama, Y., Nakamura, A., Harris, A. W. and Meshkov, M. N. 2000. Radar Observations and Physical Model of Asteroid 6489 Golevka. *Icarus* 148, 37-51.
- Kaasalainen, M., Mottola, S. and Fulchignoni, M. 2002. Asteroid Models from Disk-integrated Data. In: W. F. Bottke, A. Cellino, P. Paolicchi and R. P. Binzel (Eds.), *Asteroids III*, University of Arizona Press, Tucson, pp. 139-150.
- Kiselev, N. N., Rosenbush, V. K., Jockers, K., Velichko, F. P., Shakhovskoj, N. M., Efimov, Y. S., Lupishko, D. F. and Rumyantsev, V. V., Polarimetry of near-Earth asteroid 33342 (1998 WT24): synthetic phase angle dependence of polarization for the E-type asteroids. *Asteroids, Comets, Meteors - ACM 2002*, 2002, Berlin, Germany. pp. 883-886.
- Konopliv, A. S., Miller, J. K., Owen, W. M., Yeomans, D. K. and Giorgini, J. D. 2002. A Global Solution for the Gravity Field, Rotation, Landmarks, and Ephemeris of Eros. *Icarus* 160, 289-299.
- Krugly, Y. N., Belskaya, I. N., Chiorny, V. G., Shevchenko, V. G. and Gaftonyuk, N. M., CCD Photometry of Near-Earth Asteroids in 2001. *Asteroids, Comets, Meteors - ACM 2002*, 2002, Berlin, Germany. pp. 883-886.
- Lagerkvist, C. I. 1977. A Photographic Lightcurve of the Amor Asteroid 1580 Betulia. *Icarus* 32, 233-234.
- Lagerkvist, C.-I. and Magnusson, P. 1990. Analysis of asteroid lightcurves. II. Phase curves in a generalised HG-system. *Astron. Astrophys. Suppl. Ser.* 86, 119-165.
- Lagerros, J. S. V. 1996. Thermal physics of asteroids I: Effects of shape, heat conduction and beaming. *Astronomy and Astrophysics* 310, 1011-1020.
- Lagerros, J. S. V. 1997. Thermal physics of asteroids III. Irregular shapes and albedo variegations. *Astronomy and Astrophysics* 325, 1226-1236.
- Lagerros, J. S. V. 1998. Thermal physics of asteroids IV. Thermal infrared beaming. *Astronomy and Astrophysics* 332, 1123-1132.
- Landis, R. R., Stern, A. S., Wood, C. A. and Storrs, A. D., Observations of 1 Ceres with HST Faint Object Camera (Abstract No. 1937). *Lunar Planet. Sci. Conf. XXIX*, 1998.
- Landolt, A. U. 1992. UBVR photometric standard stars in the magnitude range 11.5 < V < 16.0 around the celestial equator. *The Astronomical Journal* 104, 340-491.
- Lazzarin, M., Marchi, S., Barucci, M. A., Martino, M. D. and Barbieri, C. 2004. Visible and near-infrared spectroscopic investigation of near-Earth objects at ESO: first results. *Icarus* 169, 373-384.
- Lebofsky, L. A., Veeder, G. J., Lebofsky, M. J. and Matson, D. L. 1978. Visual and Radiometric Photometry of 1580 Betulia. *Icarus* 35, 336-343.
- Lebofsky, L. A. and Rieke, G. H. 1979. Thermal properties of 433 Eros. *Icarus* 40, 297-308.
- Lebofsky, L. A., Veeder, G. J., Rieke, G. H., Lebofsky, L. A., Matson, D. L., Kowal, C., Wynn-Williams, C. G. and Becklin, E. E. 1981. The Albedo and Diameter of 1862 Apollo. *Icarus* 48, 335-338.
- Lebofsky, L. A., Sykes, M. V., Tedesco, E. F., Veeder, G. J., Matson, D. L., Brown, R. H., Gradie, J. C., Feierberg, M. A. and Rudy, R. J. 1986. A refined "standard" thermal model for asteroids based on observations of 1 Ceres and 2 Pallas. *Icarus* 68, 239-251.
- Lebofsky, L. A. and Spencer, J. R. 1989. Radiometry and thermal modeling of asteroids. In: R. P. Binzel, T. Gehrels and M. S. Matthews (Eds.), *Asteroids II*, Univ. of Arizona Press, Tucson, pp. 128-147.
- Love, S. G. and Ahrens, T. J. 1996. Catastrophic impacts on gravity dominated asteroids. *Icarus* 124, 141-155.

- Lupishko, D. F. and Di Martino, M. 1998. Physical properties of near-Earth asteroids. *Planetary and Space Sciences* 46, 47-74.
- Luu, J. X. and Jewitt, D. C. 1989. On the relative number of C types and S types among near-Earth asteroids. *Astron. J.* 98, 1905-1911.
- Luu, J. X. 1994. Comets disguised as asteroids. *Publ. Astron. Soc. Pacific* 106, 425-435.
- Magnusson, P., Barucci, M. A., Drummond, J. D., Lumme, K., Ostro, S. J., Surdej, J., Taylor, R. C. and Zappalà, V. 1989. Determination of Pole Orientations and Shapes of Asteroids. In: R. P. Binzel, T. Gehrels and M. S. Matthews (Eds.), *Asteroids II*, The University of Arizona Press, Tucson, pp. 66-97.
- Magnusson, P., Dahlgren, M., Barucci, M. A., Jorda, L., Binzel, R. P., Slivan, S. M., Blanco, C., Riccioli, D., Buratti, B. J., Colas, F., Berthier, J., de Angelis, G., di Martino, M., Dotto, E., Drummond, J. D., Fink, U., Hicks, M., Grundy, W., Wisniewski, W., Gaftonyuk, N. M., Geyer, E. H., Bauer, T., Hoffmann, M., Ivanova, V., Komitov, B., Donchev, Z., Denchev, P., Krugly, Y. N., Velichko, F. P., Chiorny, V. G., Lupishko, D. F., Shevchenko, V. G., Kwiatkowski, T., Kryszczynska, A., Lahulla, J. F., Licandro, J., Mendez, O., Mottola, S., Erikson, A., Ostro, S. J., Pravec, P., Pych, W., Tholen, D. J., Whiteley, R., Wild, W. J., Wolf, M. and Sarounova, L. 1996. Photometric Observations and Modeling of Asteroid 1620 Geographos. *Icarus* 123, 227-244.
- Marchis, F., Descamps, P., Hestroffer, D. and Berthier, J. 2005. Discovery of the triple asteroid system 87 Sylvia. *Nature* 436, 822-824.
- Margot, J. L., Nolan, M. C., Benner, L. A. M., Ostro, S. J., Jurgens, R. F., Slade, M. A., Giorgini, J. D. and Campbell, D. B. 2000. Satellites of Minor Planets. IAU Circular No. 7503.
- Margot, J. L., Nolan, M. C., Benner, L. A. M., Ostro, S. J., Jurgens, R. F., Giorgini, J. D., Slade, M. A. and Campbell, D. B. 2002. Binary Asteroids in the Near-Earth Object Population. *Science* 296, 1445-1448.
- Marsden, B. G. and Williams, G. V. 1999. *Catalogue of Cometary Orbits*, 13th edition. IAU Central Bureau for Astronomical Telegrams and Minor Planet Center, 127.
- McCoy, T. J., Burbine, T. H., McFadden, L. A., Starr, R. D., Gaffey, M. J., Nittler, L. R., Evans, L. G., Izenberg, N., Lucey, P., Trombka, J. I., Bell, J. F. I., Clark, B. E., Clark, P. E., Squyres, S. W., Chapman, C. R., Boynton, W. V. and Veeverka, J. 2001. The composition of 433 Eros: a mineralogical-chemical synthesis. *Meteoritics & Planet. Sci.* 36, 1661-1672.
- McFadden, L. A., Gaffey, M. J. and McCord, T. B. 1984. Mineralogical-petrological characterization of near-Earth asteroids. *Icarus* 59, 25-40.
- McFadden, L. A., Tholen, D. J. and Veeder, G. J. 1989. Physical properties of Aten, Apollo and Amor asteroids. In: R. P. Binzel, T. Gehrels and M. S. Matthews (Eds.), *Asteroids II*, University of Arizona Press, Tucson, pp. 442-467.
- Melosh, H. J., Schneider, N. M., Zahnle, K. J. and Latham, D. 1990. Ignition of global wildfires at the Cretaceous/Tertiary boundary. *Nature* 343, 251-254.
- Merline, W. J., Close, L. M., Dumas, C., Shelton, J. C., Ménard, F., Chapman, C. R. and Slater, D. C. 2000. Discovery of companions to asteroids 762 Pulcova and 90 Antiope by direct imaging. *Bull. Am. Astron. Soc.* 32, 1309.
- Merline, W. J., Weidenschilling, S. J., Durda, D. D., Margot, J., Pravec, P. and Storrs, A. D. 2002. Asteroids do have satellites. In: W. F. Bottke, A. Cellino, P. Paolicchi and R. P. Binzel (Eds.), *Asteroids III*, The University of Arizona Press, Tucson, pp. 289-312.
- Michel, P., Farinella, P. and Froeschlé, C. 1998. Dynamics of Eros. *Astron. J.* 116, 2023-2031.
- Michel, P., Zappalà, V., Cellino, A. and Tanga, P. 2000. Estimated abundance of Atens and asteroids evolving on orbits between Earth and Sun. *Icarus* 143, 421-424.
- Milani, A., Carpino, M., Hahn, G. and Nobili, A. M. 1989. Dynamics of planet-crossing asteroids: Classes of orbital behaviour: Project SPACEGUARD. *Icarus* 78, 212-269.
- Miner, E. and Young, J. 1969. Photometric Determination of the Rotation Period of 1566 Icarus. *Icarus* 10, 436-440.
- Mitchell, D. L., Hudson, R. S., Ostro, S. J. and Rosema, K. D. 1998. Shape of asteroid 433 Eros from inversion of Goldstone radar doppler spectra. *Icarus* 131, 4-14.
- Morbidelli, A. and Nesvorný, D. 1999. Numerous weak resonances drive asteroids toward terrestrial planets orbits. *Icarus* 139, 295-308.
- Morbidelli, A., Bottke, W., F., Froeschlé, C. and Michel, P. 2002. Origin and Evolution of Near-Earth Objects. In: W. F. Bottke, A. Cellino, P. Paolicchi and R. P. Binzel (Eds.), *Asteroids III*, The University of Arizona Press, Tucson, pp. 409-422.
- Morrison, D. 1973. Determination of radii of satellites and asteroids from radiometry and photometry. *Icarus* 19, 1-14.

- Morrison, D., Harris, A. W., Sommer, G., Chapman, C. R. and Carusi, A. 2002. Dealing with the impact hazard. In: W. F. Bottke, A. Cellino, P. Paolicchi and R. P. Binzel (Eds.), *Asteroids III*, University of Arizona Press, Tucson, pp. 739-754.
- Mottola, S., Erikson, A., Harris, A. W., Hahn, G., Neukum, G., Buie, M. W., Sears, W. D., Harris, A. W., Tholen, D. J., Whiteley, R. J., Magnusson, P., Piironen, J., Kwiatkowski, T., Borczyk, W., Howell, E. S., Hicks, M. D., Fevig, R., Krugly, Y. N., Velichko, F. P., Chiorny, V. G., Gaftonyuk, N. M., Di Martino, M., Pravec, P., Šarounová, L., Wolf, M., Worman, W., Davies, J. K., Schober, H.-J. and Pych, W. 1997. Physical model of near-Earth asteroid 6489 Golevka (1991 JX) from optical and infrared observations. *Astron. J.* 114, 1234-1245.
- Mueller, M., Delbó, M., Di Martino, M., Harris, A. W., Kaasalainen, M. and Bus, S. J., Indications for regolith on Itokawa from thermal-infrared observations. ASP Conference Series. Submitted for publication., 2005.
- Müller, T. G. and Lagerros, J. S. V. 1998. Asteroids as far-infrared photometric standards for ISOPHOT. *Astron. Astrophys.* 338, 340-352.
- Nelson, R. M., Rayman, M. D., Varghese, P. and Lehman, D. H. 2001. The Deep Space One encounter with the comet Borrelly. *Bull Am. Astron. Soc.* 33, 1087.
- Newburn, R. L., Duxbury, T. C., Hanner, M., Semenov, B. V., Hirst, E. E., Bhat, R. S., Bhaskaran, S., Wang, T.-C. M., Tsou, P., Brownlee, D. E., Chevront, A. R., Gingerich, D. E., Bollendonk, G. R., Vellinga, J. M., Parham, K. A. and Mumaw, S. J. 2003. Phase curve and albedo of asteroid 5535 Annefrank. *Journal of Geophysical Research (Planets)* 108k, 3-1.
- Nolan, M., Howell, E. S., Rivkin, A. S. and Neish, C. D. 2003. (5381) Sekhmet. I.A.U. Circular No. 8163.
- Ostro, S. J., Campbell, D. B. and Shapiro, I. I. 1983. Radar observations of asteroid 1685 Toro. *Astron. J.* 88, 565-576.
- Ostro, S. J., Harris, A. W., Campbell, D. B., Shapiro, I. I. and Young, J. W. 1984. Radar and photoelectric observations of asteroid 2100 Ra-Shalom. *Icarus* 60, 391-403.
- Ostro, S. J., Campbell, D. B., Hine, A. A., Shapiro, I. I., Chandler, J. F., Werner, C. L. and Rosema, K. D. 1990. Radar images of asteroid 1627 Ivar. *Astron. J.* 99, 2012-2018.
- Ostro, S. J., Campbell, D. B., Chandler, J. F., Hine, A. A., Hudson, R. S., Rosema, K. D. and Shapiro, I. I. 1991. Asteroid 1986 DA: Radar evidence for a metallic composition. *Science* 252, 1399-1404.
- Ostro, S. J., Jurgens, R. F., Rosema, K. D., Hudson, R. S., Giorgini, J. D., Winkler, R., Yeomans, D. K., Choate, D., Rose, R., Slade, M. A., Howard, S. D., Scheeres, D. J. and Mitchell, D. L. 1996. Radar observations of asteroid 1620 Geographos. *Icarus* 121, 46-66.
- Ostro, S. J., Pravec, P., Benner, L. A. M., Hudson, R. S., Šarounová, L., Hicks, M. D., Rabinowitz, D. L., Scotti, J. V., Tholen, D. J., Wolf, M., Jurgens, R. F., Thomas, M. L., Giorgini, J. D., Chodas, P. W., Yeomans, D. K., Rose, R., Frye, R., Rosema, K. D., Winkler, R. and Slade, M. A. 1999. Radar and optical observations of asteroid 1998 KY₂₆. *Science* 285, 557-559.
- Ostro, S. J., Margot, J.-L., Nolan, M. C., Benner, L. A. M., Jurgens, R. F. and Giorgini, J. D. 2000. 2000 DP₁₀₇. IAU Circular No. 7496.
- Ostro, S. J., Hudson, R. S., Benner, L. A. M., Giorgini, J. D., Magri, C., Margot, J. and Nolan, M. C. 2002. Asteroid Radar Astronomy. In: W. F. Bottke, A. Cellino, P. Paolicchi and R. P. Binzel (Eds.), *Asteroids III*, The University of Arizona Press, Tucson, Arizona, pp. 151-168.
- Parker, J. W., Stern, S. A., Thomas, P. C., Festou, M. C., Merline, W. J., Young, E. F., Binzel, R. P. and Lebofsky, L. A. 2002. Analysis of the First Disk-resolved Images of Ceres from Ultraviolet Observations with the Hubble Space Telescope. *Astron. J.* 123, 549-557.
- Peebles, C. 2000. *Asteroids: A History*. Smithsonian Institution Press, Washington and London.
- Pettengill, G. H., Shapiro, I. I., Ash, M. E., P., I. R., Rainville, L. P., Smith, W. B. and Stone, M. L. 1969. Radar observations of Icarus. *Icarus* 10, 432-435.
- Pettengill, G. H., Ostro, S. J., Shapiro, I. I., Marsden, B. G. and Campbell, D. B. 1979. Radar observations of 1580 Betulia. *Icarus* 40, 350-354.
- Petit, J. M., Chambers, J., Franklin, F. and Nagasawa, M. 2002. Primordial Excitation and Depletion of the Main Belt. In: W. F. Bottke, A. Cellino, P. Paolicchi and R. P. Binzel (Eds.), *Asteroids III*, University of Arizona Press, Tucson, pp. 711-723.
- Pope, K. O. 2002. Impact dust not the cause of the Cretaceous-Tertiary mass extinction. *Geology* 30, 99-102.
- Pravec, P., Šarounová, L. and Wolf, M. 1996. Lightcurves of 7 Near-Earth Asteroids. *Icarus* 124, 471-482.
- Pravec, P. and Hahn, G. 1997. Two-Period Lightcurve of 1994 AW₁: Indication of a Binary Asteroid? *Icarus* 127, 431-440.
- Pravec, P., Wolf, M. and Šarounová, L. 1998. Lightcurves of 26 Near-Earth Asteroids. *Icarus* 136, 124-153.
- Pravec, P., Wolf, M. and Šarounová, L., How many binaries are there among near-Earth asteroids? IAU Colloquium No. 173, *Evolution and Source Regions of Asteroids and Comets*, 1999, Tatranská Lomnica. pp. 159-162.

- Pravec, P. and Harris, A. W. 2000. Fast and slow rotation of asteroids. *Icarus* 148, 12-20.
- Pravec, P., Hergenrother, C., Whiteley, R. J., Šarounová, L., Kušnirák, P. and Wolf, M. 2000. Fast rotating asteroids 1999 TY₂, 1999 SF₁₀, 1998 WB₂. *Icarus* 147, 477-486.
- Pravec, P. and Kušnirák, P. 2001. 2001 OE₈₄. IAU Circular No. 7735.
- Pravec, P., Šarounová, L., Hicks, M., Rabinowitz, D., Wolf, M., Scheirich, P. and Krugly, Y. 2002a. Two periods of 1999 HF₁ - another binary NEA candidate. *Icarus* 158, 276-280.
- Pravec, P., Harris, A. W. and Michalowski, T. 2002b. Asteroid Rotations. In: W. F. Bottke, A. Cellino, P. Paolicchi and R. P. Binzel (Eds.), *Asteroids III*, The University of Arizona Press, Tucson, Arizona, pp. 113-122.
- Pravec, P., Scheirich, P., Kušnirák, P., Šarounová, L., Mottola, S., Hahn, G., Brown, P., Esquerdo, G., Naiser, N., Krzeminski, Z., Pray, D. P., Warner, B. D., Harris, A. W., Nolan, M. C., Howell, E. S., Benner, L. A. M., Margot, J.-L., Galád, A., Holliday, W., Hicks, M. D., Krugly, Yu. N., Tholen, D., Whiteley, R., Marchis, F., DeGraff, D. R., Grauer, A., Larson, S., Velichko, F. P., Cooney Jr., W. R., Stephens, R., Zhu, J., Kirsch, K., Dyvig, R., Snyder, L., Reddy, V., Moore, S., Gajdoš, Š, Világi, J., Masi, G., Higgins, D., Funkhouser, G., Knight, B., Slivan, S., Behrend, R., Grenon, M., Burki, G., Roy, R., Demeautis, C., Matter, D., Waelchli, N., Revaz, Y., Klotz, A., Rieugné, M., Thierry, P., Cotrez, V., Brunetto, L. and Kober, G. 2006. Photometric survey of binary near-Earth asteroids. *Icarus* 181, 63-93.
- Rabinowitz, D., Helin, E., Lawrence, K. and Pravdo, S. 2000. A reduced estimate of the number of kilometre-sized near-Earth asteroids. *Nature* 403, 165-166.
- Richardson, D. C., Bottke, W. F. and Love, S. G. 1998. Tidal distortion and disruption of Earth-crossing asteroids. *Icarus* 134, 47-76.
- Richardson, D. C., Leinhardt, Z. M., Melosh, H. J., Bottke, W. F. and Asphaug, E. 2002. Gravitational aggregates: evidence and evolution. In: W. F. Bottke, A. Cellino, P. Paolicchi and R. P. Binzel (Eds.), *Asteroids III*, The University of Arizona Press, Tucson, pp. 501-516.
- Rieke, G. H., Lebofsky, M. J. and Low, F. J. 1985. An Absolute Photometric System at 10-Micron and 20-Micron. *Astron. J.* 90, 900-906.
- Rubincam, D. P. 2000. Radiative Spin-up and Spin-down of Small Asteroids. *Icarus* 148, 2-11.
- Russell, C. T., Raymond, C. A., Fraschetti, T. C., Rayman, M. D., McCarthy, J. and Grandfield, A., Dawn mission to minor planets 1 Ceres and 4 Vesta: status report (abstract). *Asteroids, Comets, Meteors*, 2005, Rio de Janeiro, Brazil. p. 29.
- Russell, H. N. 1906. On the light-variations of asteroids and satellites. *Astrophys. J.* 24, 1-18.
- Scheeres, D. J., Ostro, S. J., Werner, R. A., Asphaug, E. and Hudson, R. S. 2000. Effects of gravitational interactions on asteroid spin states. *Icarus* 147, 106-118.
- Scheeres, D. J., Benner, L. A. M., Ostro, S. J., Rossi, A., Marzari, F. and Washabaugh, P. 2005. Abrupt alteration of Asteroid 2004 MN₄'s spin state during its 2029 Earth flyby. *Icarus* 178, 281-283.
- Sharpton, V. L., Dalrymple, G. B., Marin, L. E., Ryder, G., Schuraytz, B. C. and Urrutia-Fucugauchi, J. 1992. New links between the Chicxulub impact structure and the Cretaceous/Tertiary boundary. *Nature* 359, 819-821.
- Shevchenko, V. G. and Mohamed, R. A. 2005. Spacecraft Exploration of Asteroids. *Solar Syst. Res.* 39, 73-81.
- Shoemaker, E. M., Williams, J. G., Helin, E. F. and Wolf, R. F. 1979. Earth-crossing asteroids: orbital classes, collision rates with Earth, and origin. In: T. Gehrels (Ed.), *Asteroids*, University of Arizona Press, Tucson, pp. 253-282.
- Spencer, J. R., Lebofsky, L. A. and Sykes, M. V. 1989. Systematic biases in radiometric diameter interpretations. *Icarus* 78, 337-354.
- Spencer, J. R. 1990. A rough-surface thermophysical model for airless planets. *Icarus* 83, 27-38.
- Stokes, G. H., Evans, J. B., Vigh, H. E. M., Shelly, F. C. and Pearce, E. C. 2000. Lincoln near-Earth asteroid program (LINEAR). *Icarus* 148, 21-28.
- Stokes, G. H., Evans, J. B. and Larson, S. M. 2002. Near-Earth asteroid search programs. In: W. F. Bottke, A. Cellino, P. Paolicchi and R. P. Binzel (Eds.), *Asteroids III*, The University of Arizona Press, Tucson, pp. 45-54.
- Stuart, J. S. 2001. A near-Earth asteroid population estimate from the LINEAR survey. *Science* 294, 1691-1693.
- Stuart, J. S. and Binzel, R. P. 2004. Bias-corrected population, size distribution, and impact hazard for the near-Earth objects. *Icarus* 170, 295-311.
- Sullivan, R. J., Thomas, P. C., Murchie, S. L. and Robinson, M. S. 2002. Asteroid Geology from Galileo and NEAR Shoemaker Data. In: W. F. Bottke, A. Cellino, P. Paolicchi and R. P. Binzel (Eds.), *Asteroids III*, The University of Arizona Press, Tucson, pp. 331-350.

- Swisher, C. C. I., Grajales-Nishimura, J. M., Montanari, A., Margolis, S. V., Claeys, P., Alvarez, W., Renne, P., Cedillo-Pardo, E., Mauresse, F. J.-M., Curtis, G. H., Smit, J. and McWilliams, M. O. 1992. Coeval $^{40}\text{Ar}/^{39}\text{Ar}$ ages of 65.0 million years ago from Chicxulub crater melt rock and Cretaceous-Tertiary boundary tektites. *Science* 257, 954-958.
- Tedesco, E. F. and Gradie, J. 1987. Discovery of M class objects among the near-Earth asteroid population. *Astron. J.* 93, 738-746.
- Tedesco, E. F., Egan, M. P. and Price, S. D. 2002a. The Midcourse Space Experiment Infrared Minor Planet Survey. *Astron. J.* 124, 583-591.
- Tedesco, E. F., Noah, P. V., Noah, M. and Price, S. D. 2002b. The Supplemental IRAS Minor Planet Survey. *The Astronomical Journal* 123, 1056-1085.
- Tholen, D. J. 1984. Asteroid taxonomy from cluster analysis of photometry. Ph.D. thesis, University of Arizona, Tucson.
- Tholen, D. J. 1989. Asteroid Taxonomic Classifications. In: R. P. Binzel, T. Gehrels and M. S. Matthews (Eds.), *Asteroids II*, The University of Arizona Press, Tucson, pp. 1139-1150.
- Thomas, P. C., Veverka, J., Bell, J. F., Clark, B. E., Carcich, B., Joseph, J., Robinson, M., McFadden, L. A., Malin, M. C., Chapman, C. R., Merline, W. and Murchie, S. 1999. Mathilde: Size, Shape, and Geology. *Icarus* 140, 17-27.
- Tokunaga, A. T. 1984. A re-evaluation of the 20- μm magnitude system. *Astron. J.* 89, 172-175.
- Tokunaga, A. T. 2000. Infrared Astronomy. In: A. N. Cox (Ed.), *Allen's Astrophysical Quantities*, The Athlone Press, Los Alamos, pp. 143-167.
- Tonry, J. and Davis, M. 1979. A Survey of Galaxy Redshifts. I. Data Reduction Techniques. *Astron. J.* 84, 1511-1525.
- Toon, O. B., Zahnle, K., Morrison, D., Turco, R. P. and Covey, C. 1997. Environmental perturbations caused by the impacts of asteroids and comets. *Reviews of Geophysics* 35, 41-78.
- Trombka, J., Squyres, S., Bruckner, J., Boynton, W., Reedy, R., McCoy, T., Gorenstein, P., Evans, L., Arnold, J., Starr, R., Nittler, L., Murphy, M., Mikheeva, I., McNutt, R., McClanahan, T., McCartney, E., Goldsten, J., Gold, R., Floyd, S., Clark, P., Burbine, T., Bhangoo, J., Bailey, S. and Pataev, M. 2000. The elemental composition of asteroid 433 Eros: results of the NEAR-Shoemaker X-ray spectrometer. *Science* 289, 2101-2105.
- Veeder, G. J., Hanner, M. S., Matson, D. L., Tedesco, E. F., Lebofsky, L. A. and Tokunaga, A. T. 1989. Radiometry of near-Earth asteroids. *Astron. J.* 97, 1211-1219.
- Veverka, J., Belton, M., Klaasen, K. and Chapman, C. 1994. Galileo's Encounter with 951 Gaspra: Overview. *Icarus* 107, 2-17.
- Veverka, J., Thomas, P., Harch, A., Clark, B., Bell, J. F., Carcich, B., Joseph, J., Murchie, S., Izenberg, N., Chapman, C., Merline, W., Malin, M., McFadden, L. and Robinson, M. 1999. NEAR Encounter with Asteroid 253 Mathilde: Overview. *Icarus* 140, 3-16.
- Veverka, J., Robinson, M., Thomas, P., Murchie, S., Bell III, J. F., Izenberg, N., Chapman, C., Harch, A., Bell, M., Carcich, B., Cheng, A., Clark, B., Domingue, D., Dunham, D., Farquhar, R., Gaffey, M. J., Hawkins, E., Joseph, J., Kirk, R., Li, H., Lucey, P., Malin, M., Martin, P., McFadden, L., Merline, W. J., Miller, J. K., Owen, W. M., Peterson, C., Prockter, L., Warren, J., Wellnitz, D., Williams, B. G. and Yeomans, D. K. 2000. NEAR at Eros: Imaging and Spectral Results. *Science* 289, 2088-2097.
- Vokrouhlický, D. and Farinella, P. 2000. Efficient delivery of meteorites to the Earth from a wide range of asteroid parent bodies. *Nature* 407, 606-608.
- Weidenschilling, S. J., Paolicchi, P. and Zappalà, V. 1989. Do asteroids have satellites? In: R. P. Binzel, T. Gehrels and M. S. Matthews (Eds.), *Asteroids II*, Univ. of Arizona Press, Tucson, pp. 643-658.
- Werner, S. C., Harris, A. W., Neukum, G. and Ivanov, B. A. 2002. The near-Earth asteroid size-frequency distribution: a snapshot of the lunar impactor size-frequency distribution. *Icarus* 156, 287-290.
- Wesselink, A. J. 1948. Heat conductivity and nature of lunar surface material. *Bull. Ast. Inst.* 10, 351.
- Wisniewski, W. Z. 1987. Photometry of six radar target asteroids. *Icarus* 70, 566-572.
- Wolters, S. D., Green, S. F., McBride, N. and Davies, J. K. 2005. Optical and thermal infrared observations of six near-Earth asteroids in 2002. *Icarus* 175, 92-110.
- Yeomans, D. K., Barriot, J.-P., Dunham, D. W., Farquhar, R. W., Giorgini, J. D., Helfrich, C. E., Konopliv, A. S., McAdams, J. V., Miller, J. K., Owen, W. M., Jr., Scheeres, D. J., Synnott, S. P. and Williams, B. G. 1997. Estimating the Mass of Asteroid 253 Mathilde from Tracking Data During the NEAR Flyby. *Science* 278, 2106.
- Yeomans, D. K., Antreasian, P. G., J.-P., B., Chesley, S. R., Dunham, D. W., Farquhar, R. W., Giorgini, J. D., Helfrich, C. E., Konopliv, A. S., McAdams, J. V., Miller, J. K., Owen, W. M. J., Scheeres, D. J., Thomas, P. C., Veverka, J. and Williams, B. G. 2000. Radio science results during the NEAR-Shoemaker spacecraft rendezvous with Eros. *Science* 289, 2085-2088.

- Young, A. T. 1976. Atmospheric Extinction. In: M. L. Meeks (Eds.), *Meth. Exp. Phys.*, Vol. 12A, Optical and Infrared, Academic Press, New York, pp. 123-180.
- Zaitsev, A., Di Martino, M., Konovalenko, A. A., Montebugnoli, S., Ignatov, S. P., Kolyuka, Y. F., Nabatov, A. S., Falkovich, I. S., Gavrik, A. L., Gavrik, Y. A., Bortolotti, C., Cattani, A., Maccaferri, A., Maccaferri, G., Roma, M., Delbó, M. and Saba, L., Radar Detection of NEA 33342 (1998 WT24) with Evpatoria=>Medicina System at 6 cm. *Asteroids, Comets, Meteors - ACM 2002*, 2002, Berlin, Germany. pp. 883-886.
- Zappalà, V., Cellino, A., Barucci, M. A., Fulchignoni, M. and Lupishko, D. F. 1990. An analysis of the amplitude-phase relationship among asteroids. *Astron. Astrophys.* 231, 548-560.
- Zappalà, V., Cellino, A., A., D. O. and Paolicchi, P. 2002. Physical and Dynamical Properties of Asteroid Families. In: W. Bottke, F., A. Cellino, P. Paolicchi and R. P. Binzel (Eds.), *Asteroids III*, The University of Arizona Press, Tucson, pp. 619-631.
- Zellner, B. 1976. Physical properties of asteroid 433 Eros. *Icarus* 28, 149-153.
- Zellner, B. 1979. Asteroid taxonomy and the distribution of the compositional types. In: T. Gehrels (Ed.), *Asteroids*, The University of Arizona Press, Tucson, pp. 783-806.
- Zellner, B., Tholen, D. J. and Tedesco, E. F. 1985. The eight-color asteroid survey: results for 589 minor planets. *Icarus* 61, 335-416.
- Zellner, B. H., Albrecht, R., Binzel, R. P., Gaffey, M. J., Thomas, P. C., Storrs, A. D. and Wells, E. N. 1997. Hubble Space Telescope Images of Asteroid 4 Vesta in 1994. *Icarus* 128, 83-87.
- Zuber, M. T., Smith, D. E., Cheng, A. F., Garvin, J. B., Aharonson, O., Cole, T. D., Dunn, P. J., Guo, Y., Lemoine, F. G., Neumann, G. A., Rowlands, D. D. and Torrence, M. H. 2000. The Shape of 433 Eros from the NEAR-Shoemaker Laser Rangefinder. *Science* 289, 2097-2101.

Appendix A. Fortran 90 Code for Thermal Model Fitting Program THERM

```

! THERM.f90                2005-03-02                Stephen Wolters
!
!
!
!
!
!*****
! PROGRAM: THERM
!
!   PURPOSE: Calculates Standard Thermal Model, Fast Rotating Model, Projected Model and
!   Near Earth Asteroid Thermal Model flux, from a set of wavelengths and for a range of
!   values of pv, from an input of H, G, delta, r, alpha. For each value of pv it
!   compares the model flux with the observed flux at each wavelength, calculating the fit.
!   Then, it outputs the model flux at a specific pv.
!*****

      program THERM

      implicit none

      real*8 g, h, pv, pvstart, pvend, pvstep, q, bigA, epsilon, eta, s0, stef, &
         au, r, delta, diameter, tmax, psirad, dps, thetarad, dtheta, phirad, dphi, &
         consta, constb, fbit, fmod, pi, bigT(2000), wavelength(100), flux(100), err(100), &
         fmodstm(100), fmodfrm(100), fmodproj(100), fmodneatm(100), oldfmodneatm(100), &
         alpha, alphaspec, planck, bigTproj(361,181), resstm, resfrm, resproj, resneatm, &
         etastart, etaend, etastep, oldres, pvspec, etastm, etaspec, waveoutstart, &
         waveoutend, waveoutstep, waveout(1000), wavel, fstmout(1000), ffrmout(1000), &
         fprojout(1000), fneatmout(1000), dang, beststmpv, bestfrmvp, bestprojpv, &
         bestneatmpv, oldresstm, oldresfrm, oldresproj, oldresneatm, newpvstart, newpvend, &
         newpvstep, newetastart, newetastep

      character pvquery, neatmquery, modelquery, outwavequery, etaquery
      integer i, j, k, n, m, beststmfound, bestfrmfound, bestprojfound, bestneatmfound, &
         stmoutrange, frmoutrange, projoutrange, neatmoutrange

!      define constants emmissivity, beaming parameter, pi,
!      solar flux at 1AU, Stefan-Boltzmann constant, distance 1AU (km)

      epsilon=0.9
      etastm=0.756
      pi=4.0e+00*atan(1.0e+00)
      s0=1374.0e+00
      stef=5.670512e-08
      au=1.49597870671e+08

!      specify range of pv and specific pv

      pvstart=0.20
      pvend=0.30
      pvstep=0.01
      pvspec=0.16

!      specify range of eta and step size for NEATM

```

```

etastart=0.8
etaend=3
etastep=0.01
etaspec=1

! specify initial output model for specific pv

modelquery="1"

! specify output wavelength range and stepsize for output flux in microns

waveoutstart=4
waveoutend=23
waveoutstep=0.5

! angle steplength in radians

dang= 1*(pi/180)
write (*,(" Angle step size = ",f4.1," deg")) dang/(pi/180)

! steplength of psi, theta, phi in radians

dpsi = dang
dtheta = dang
dphi = dang

! open file 'param.txt' containing
! H, G, delta= Earth-Sun distance (AU), r = Asteroid-Sun distance (AU), alpha
! (phase angle, degrees). use H value corresponding to V(1,alpha) from composite
! lightcurve from JKT data, which is then run through phasecor using the value
! of G supplied below to correct to V(1,0).

open (1, file='param.txt', status='unknown')
read (1,*) g
read (1,*) h
read (1,*) delta
read (1,*) r
read (1,*) alpha
read (1,*) etaspec
close (1)

alpharad = alpha*(pi/180)

! inform user

1 format (" g = ",f4.2)
2 format (" h = ",f6.3)
3 format (" delta = ",f6.3)
4 format (" r = ",f6.3)
5 format (" alpha = ", f4.1)
6 format (" NEATM fixed eta = ", f4.2)

print *, " "
print *, "Opened file param.txt"
print *, " "
write(*,1) g
write(*,2) h
write(*,3) delta
write(*,4) r
write(*,5) alpha

```

```

write(*,6) etaspec

!   Open file spec.txt containing observed spectrum
!   and read in wavelengths and fluxes
!   n is number of rows

open (2,file='spec.txt',status='unknown')

do 10 i=1,100

        read(2,*,end=99) wavelength(i), flux(i), err(i)
        wavelength(i) = wavelength(i)*1e-06
        n=n+1

10 continue

99      close(2)

!       Inform user

        print *, " "
        print *, "Opened file spec.txt, read wavelengths, fluxes and errors."

!       calculate phase integral q from value of G
        q=0.290 + 0.684*g

!       do you want to run the models over a pv range?
600     print *, " "
        print *, "Press:"
        print *, "(1) if you want to run over a range of pv"
        write(*,(" (2) to output model flux at a specific pv -> "\))
        read (*, '(A1)') pvquery

        if (pvquery.eq."2") GOTO 1000

500     open (12,file="residual.txt")

        print *, " "
        print *, "Current pv range is:"
        print *, " "
        write (*,(' start = ', f6.4)) pvstart
        write (*,(' end   = ', f6.4)) pvend
        write (*,(' step = ', f6.4)) pvstep
        print *, " "
        print *, "Press:"
        print *, "ENTER to use current pv range"
        print *, "(1) to change pv range"
        write(*,(' (2) to change pv step -> "\))
        read (*, '(A1)') pvquery
        print *, " "

        if (pvquery.eq."1") then

                write(*,(' start: "\))
                read (*, '(f6.4)') pvstart
                write(*,(' end: "\))
                read (*, '(f6.4)') pvend
                GOTO 500

        end if

```

```

if (pvquery.eq."2") then

    write*,'(" step: "\)
    read (*, '(f6.4)') pvstep
    GOTO 500

end if

! do you want to run NEATM with eta-fitting

write*,'(" Enter (y) if you want to run NEATM with eta fit (will take long time) &
or press ENTER: "\)
read (*, '(A1)') neatmquery

    if (neatmquery.eq."y") then

501        print *, " "
            print *, "eta range and step size are:"
            write (*, '((" start = ", f5.3)') etastart
            write (*, '((" end = ", f5.3)') etaend
            write (*, '((" step = ", f6.4)') etastep
            print *, " "
            print *, "(1) change eta range"
            print *, "(2) change eta step size"
            write (*, '((" ENTER to use current values ->")')
            read(*, '(a1)') etaquery

            if (etaquery.eq."1") then

                write (*, '((" start = "\)
                read (*, '(f5.3)') etastart
                write (*, '((" end = "\)
                read (*, '(f5.3)') etaend
                GOTO 501

            end if

            if (etaquery.eq."2") then

                write (*, '((" step = "\)
                read (*, '(f6.4)') etastep
                GOTO 501

            end if

        end if

    end if

! *****
! run models over the range of pv
! *****

beststmfound = 0
bestfrmfound = 0
bestprojfound = 0
bestneatmfound = 0

stmoutrange=0
frmoutrange=0
projoutrange=0

```

```

neatmoutrange=0

print *, " "
print *, "          SUM(((Fobs(n)-Fmod(n))/err_obs(n))^2) [min is best fit]"
print *, "          NEATM"
7  format('pv',5x, 'D(km)', 2x 'STM', 10x, 'FRM', 10x, 'fixed', 8x,'best-fit',&
5x,'eta')
write(*,7)
write (12,*) " "
write (12,*)"          NEATM"
write (12,7)

do 20 pv = pvstart, pvend, pvstep

!          calculate bolometric albedo A from q and geometric albedo pv
bigA=q*pv

!          calculate diameter from inputted H and pv values
diameter = (1329/sqrt(pv))*10**(-h/5)

!          STM

!          calculate maximum temperature
tmax = (((1.0-bigA)*s0)/(etastm*epsilon*stef*r**r))**0.25

!          calculate total flux Fmod seen at Earth by integrating over theta, the angular distance
!          from the subsolar point. that is add up rectangles of area dtheta (1 degree) * Fmod(theta)

!          calculate the temperature at different values of psi, the angular distance from
!          the subsolar point

i=1

do 30 psirad = 0, pi/2, dpsi

    bigT(i) = tmax * (cos(psirad))**0.25
    if (psirad.GT.(pi/2)-(dpsi/2)) bigT(i)=0
    i=i+1

30  continue

!          calculate flux for each wavelength using planck function

do 40 i=1,n

    fmod = 0
    j=1

    do 50 psirad = 0, pi/2, dpsi

        fbit = ((pi * epsilon * diameter * diameter)/(2*delta * delta * au * au))&
        * planck(bigT(j), wavelength(i)) * sin(psirad) * cos(psirad) * dpsi
        fmod = fmod + fbit
        j=j+1

50  continue

!          phase angle correction now

```

```

fmod = fmod * 10**(-0.4*alpha*0.01)
fmodstm(i)=fmod

40      continue

!      FRM
!      replacement of pi for beta in tmax calculation
!      flux calculated over latitude, so different equation there

tmax = (((1-bigA)*s0)/(pi*epsilon*stef*r*r))**0.25

i=1

do 60 psirad = 0, pi/2, dpsid

    bigT(i) = tmax * (cos(psirad))**0.25
    if (psirad.GT.(pi/2)-(dpsid/2)) bigT(i)=0
    i=i+1

60      continue

!      calculate frm fluxes for each wavelength using planck function

do 70 i=1,n

    fmod = 0
    j=1

    do 80 psirad = 0, pi/2, dpsid

        fbit = ((epsilon * diameter * diameter) / (delta * delta * au * au))&
        * planck(bigT(j), wavelength(i)) * cos(psirad) * cos(psirad) * dpsid
        fmod = fmod + fbit
        j=j+1

80      continue

    fmodfrm(i) = fmod

70      continue

!      NEATM specific eta Model
!
!      As STM but allows for phase effects in a more complex way. As phase angles
!      increase the temperature contours gradually disappear around the limb. Allows
!      a set beaming parameter to be used

!      etaspec instead of etastm here

tmax = (((1-bigA)*s0)/(etaspec*epsilon*stef*r*r))**0.25

!      now calculate temperature as function of longitude (thetarad) and latitude (phirad)
!      at one degree intervals, for fraction that is sunlit
!      ie. from (-90 + alpha) -> +90 longitude, and -90 -> +90 latitude

thetarad = alphaspec - pi/2
i=1

do while(thetarad.LE.((pi/2)+(dtheta/2)))

```

```

j=1
do 100 phirad = -pi/2, +pi/2, dphi
    bigTproj(i,j) = tmax * (cos(thetarad)**0.25 * (cos(phirad))**0.25
    if (phirad.LE.-pi/2) bigTproj(i,j)=0
    if (phirad.GT.(pi/2)-(dphi/2)) bigTproj(i,j)=0
    if (thetarad.GE.pi/2) bigTproj(i,j)=0
    if (thetarad.le.-pi/2) bigTproj(i,j)=0
    j=j+1
100    continue

    thetarad = alpharad - pi/2 + i * dtheta
    i=i+1

end do

! this is the flux calculation using the planck calculated for a specific wavelength
! integrates over surface elements dphi and dtheta

do 110 i=1,n

    thetarad = alpharad - pi/2
    fmod = 0
    j=1

    do while (thetarad.LT.((pi/2)+(dtheta/2)))

        k=1

        do 120 phirad = -pi/2, +pi/2, dphi

            fbit = ((epsilon * diameter * diameter) / (4 * delta * delta * au*&
            au))* planck(bigTproj(j,k),wavelength(i)) * cos(phirad) * &
            cos(phirad) * cos (alpharad-thetarad) * dphi * dtheta

            fmod = fmod + fbit
            k=k+1

120    continue

            thetarad = alpharad - pi/2 + j * dtheta
            j=j+1

        end do

        fmodproj(i)=fmod

110    continue

! Check to see if NEATM eta fitting is on

if (neatmquery.NE."y") GOTO 2000

! NEATM eta fit
! Now beaming parameter eta is varied to give a
! best fit to the data

```

```

!           initialise some values

oldres = 100

do 130 eta=etastart,etaend,etastep

        tmax = (((1-bigA)*s0)/(eta*epsilon*stef*r*r))**0.25

!           now calculate temperature as function of longitude (thetarad) and latitude (phirad)
!           at one degree intervals, for fraction that is sunlit
!           ie. from (-90 + alpha) -> +90 longitude, and -90 -> +90 latitude

thetarad = alpharad - pi/2
i=1

do while(thetarad.LE.((pi/2)+(dtheta/2)))

        j=1

        do 140 phirad = -pi/2, +pi/2, dphi

                bigTproj(i,j) = tmax * (cos(thetarad))**0.25 * (cos(phirad))**0.25
                if (phirad.LE.-pi/2) bigTproj(i,j)=0
                if (phirad.GT.(pi/2)-(dphi/2)) bigTproj(i,j)=0
                if (thetarad.GE.pi/2) bigTproj(i,j)=0
                if (thetarad.LE.-pi/2) bigTproj(i,j)=0
                j=j+1

140        continue

        thetarad = alpharad - pi/2 + i * dtheta
        i=i+1

end do

!           this is the flux calculation using the planck calculated for a specific wavelength
!           integrates over surface elements dphi and dtheta

do 150 i=1,n

        thetarad = alpharad - pi/2
        fmod = 0
        j=1

        do while (thetarad.LT.((pi/2)+(dtheta/2)))

                k=1

                do 160 phirad = -pi/2, +pi/2, dphi

                        fbit = ((epsilon * diameter * diameter) / (4 * delta * delta*au * &
                                au))* planck(bigTproj(j,k),wavelength(i)) * cos(phirad) * &
                                cos(phirad) * cos (alpharad-thetarad) * dphi * dtheta

                        fmod = fmod + fbit
                        k=k+1

160                continue

                thetarad = alpharad - pi/2 + j * dtheta

```

```

        j=j+1
    end do

    fmodneatm(i)=fmod

150    continue

!    calculate the fit for this value of eta

        resneatm = 0

        do 170 i=1,n

            resneatm = resneatm + ((flux(i)-fmodneatm(i))/err(i))* &
                ((flux(i)-fmodneatm(i))/err(i))

170    continue

!    compare the fit with the one calculated before it; if its bigger then
!    well done, the last set of fmodneatm were the best fit at this value of pv

        if (resneatm.GT.oldres) THEN

            if (eta.GT.etastart) GOTO 3000

        end if

        oldres=resneatm

!    store a back-up of these fmodneatm values

        do 175 i=1,n

            oldfmodneatm(i) = fmodneatm(i)

175    continue

130    continue

!    so correct fmodneatm was the one before, and so was eta

3000    do 180 i=1,n

        fmodneatm(i) = oldfmodneatm(i)

180    continue

        if (eta.GT.etastart) eta=eta-etastep

!    remember that i am looping over a range of pv values here, so for this value of pv
!    lets measure the fit of the model; do this by calculating
!    SUM((F(obs)-F(mod)/err(obs))^2), minimum value = best fit!

2000    resstm = 0
        resfrm = 0
        resproj = 0
        resneatm = 0

        do 190 i=1,n

```

```

resstm = resstm + ((flux(i)-fmodstm(i))/err(i))* ((flux(i)-fmodstm(i))/err(i))
resfrm = resfrm + ((flux(i)-fmodfrm(i))/err(i))*((flux(i)-fmodfrm(i))/err(i))
resproj = resproj + ((flux(i)-fmodproj(i))/err(i))*((flux(i)-fmodproj(i)) &
/err(i))
if (neatmquery.EQ."y") resneatm = resneatm + ((flux(i)-fmodneatm(i))/err(i)) &
* ((flux(i)-fmodneatm(i))/err(i))

190      continue

8      format (f6.4, f7.3, e13.6, e13.6, e13.6, e13.6, f6.3)
if (neatmquery.EQ."y") write (*,8) pv, diameter, resstm, resfrm, resproj,&
resneatm, eta
if (neatmquery.EQ."y") write (12,8) pv, diameter, resstm, resfrm, resproj,&
resneatm, eta
if (neatmquery.NE."y") write (*,8) pv, diameter, resstm, resfrm, resproj
if (neatmquery.NE."y") write (12,8) pv, diameter, resstm, resfrm, resproj

!      if this isn't the start of the pv run, compare residuals to the one before
!      if its bigger for the first time then well done!! the last pv value was the
!      best-fit.

!      check for the seocond pv value in the range if the residuals are increasing
!      if they are the best-fit pv is at a lower pv than this range, need to recognise
!      this

if (pv.EQ.(pvstart+pvstep)) then

    if (resstm.GT.oldresstm) stmoutrange=1
    if (resfrm.GT.oldresfrm) frmoutrange=1
    if (resproj.GT.oldresproj) projoutrange=1
    if ((neatmquery.eq."y").and.(resneatm.GT.oldresneatm)) neatmoutrange=1

end if

if (pv.GT.pvstart) then

    if ((beststmfound.eq.0).and.(resstm.GT.oldresstm).and.(stmoutrange.ne.1)) then

        beststmpv = pv - pvstep
        beststmfound = 1

    end if

    if ((bestfrmfound.eq.0).and.(resfrm.GT.oldresfrm).and.(frmoutrange.ne.1)) then

        bestfrmpv = pv - pvstep
        bestfrmfound = 1

    end if

    if ((bestprojfound.eq.0).and.(resproj.GT.oldresproj).and.(projoutrange.ne.1)) then

        bestprojpv = pv - pvstep
        bestprojfound = 1

    end if

    if ((neatmquery.eq."y").and.(bestneatmfound.eq.0).and.(resneatm.GT. &
oldresneatm).and.(neatmoutrange.ne.1)) then

```

```

bestneatmpv = pv - pvstep
bestneatmfound = 1
newpvstart=pv - 2*pvstep
newpvend=pv
newpvstep=0.1*pvstep
newetastart=eta
if (etastep.gt.0.0001) newetastep=etastep*0.1

end if

end if

! store these residual values for comparison with next loop run

if (beststmfound.eq.0) oldresstm=resstm
if (bestfrmfound.eq.0) oldresfrm=resfrm
if (bestprojfound.eq.0) oldresproj=resproj
if ((neatmquery.EQ."y").and.(bestneatmfound.eq.0)) oldresneatm=resneatm

20 continue

print *, " "
if (beststmfound.eq.1) write (*,(' best-fit STM pv= ", f6.4)') beststmpv
if (beststmfound.eq.1) write (12,(' best-fit STM pv= ", f6.4)') beststmpv

if (bestfrmfound.eq.1) write (*,(' best-fit FRM pv= ", f6.4)') bestfrmpv
if (bestfrmfound.eq.1) write (12,(' best-fit FRM pv= ", f6.4)') bestfrmpv

if (bestprojfound.eq.1) write (*,(' best-fit NEATM pv with fixed eta = ", f6.4)') &
bestprojpv
if (bestprojfound.eq.1) write (12,(' best-fit NEATM pv with fixed eta = ", f6.4)') &
bestprojpv

if (bestneatmfound.eq.1) write (*,(' best-fit NEATM pv with best-fit eta = ", f6.4) &
') bestneatmpv
if (bestneatmfound.eq.1) write (12,(' best-fit NEATM pv with best-fit eta = ", f6.4) &
') bestneatmpv

if (bestneatmfound.eq.1) then

pvstart=newpvstart
pvend=newpvend
pvstep=newpvstep
etastart=newetastart
etastep=newetastep

end if

GOTO 600

close (12)

!*****
! run models for the specific pv value
!*****

1000 pv=pvspec

! calculate diameter from inputted H and pv values

```

```

diameter = (1329/sqrt(pv))*10**(-h/5)

!   inform user

9   format (" pv = ",f6.4)
11  format (" Deff = ",f6.2," km")

    print *, " "
    print *, "Current pv and diameter are:"
    write(*,9) pv
    write(*,11) diameter

!   put etastep back up

    etastep = 0.001

!   inform user

    print *, " "
    print *, "Output wavelength range:"
    write (*,(" start = ",f6.3," um")) waveoutstart
    write (*,(" end = ",f6.3," um")) waveoutend
    write (*,(" step = ",f6.3," um")) waveoutstep
    print *, " "

!   pick model or adjust wavelength range (rare), go back to pv ranges, or quit

    print *, "Would you like to change pv, output model flux,"
    print *, "or adjust output wavelength range and stepsize?"
    print *, " "
    print *, "(1) change pv"
    print *, "(2) STM"
    print *, "(3) FRM"
    print *, "(4) NEATM with fixed eta"
    print *, "(5) NEATM with eta best-fitted"
    print *, "(6) adjust output wavelength range or stepsize"
    print *, "(7) run models over a pv range"
    write (*,(" Press (q) to quit: \"\"))
    read (*,("A1")) modelquery
    print *, " "

    if (modelquery.eq."1") then

        print *, "Press:"
        print *, "(1) enter manual pv"

        if (beststmfound.eq.1) write (*,(" (2) use STM best fit pv (" ,f6.4,")") &
            beststmpv

        if (bestfrmfound.eq.1) write (*,(" (3) use FRM best fit pv (" ,f6.4,")") &
            bestfrmpv

        if (bestprojfound.eq.1) write (*,(" (4) use NEATM (fixed eta) best fit pv &
            (" ,f6.4,")") bestprojpv

        if (bestneatmfound.eq.1) write (*,(" (5) use NEATM (best fit eta) best fit pv &
            (" ,f6.4,")") bestneatmpv

```

```

write (*,(' ->\''))
read (*,(a1)) pvquery
if (pvquery.eq."1") then
    write (*,('Enter new pv: \''))
    read (*,(f6.4)) pvspec
end if

if (pvquery.eq."2") pvspec=beststmpv
if (pvquery.eq."3") pvspec=bestfrmpv
if (pvquery.eq."4") pvspec=bestprojpv
if (pvquery.eq."5") pvspec=bestneatmpv
GOTO 1000

end if

! calculate bolometric albedo A from q and geometric albedo pv now that pv is set
bigA=q*pv

if (modelquery.eq."6") then

    print *, "Press (1) to adjust output wavelength range"
    write (*,(' Press (2) to adjust output wavelength step size: \''))
    read (*,(A1)) outwavequery
    print *, " "

    if (outwavequery.eq."1") then

        write (*,(' start = \''))
        read (*,(f6.3)) waveoutstart
        write (*,(' end = \''))
        read (*,(f6.3)) waveoutend

    end if

    if (outwavequery.eq."2") then

        write (*,(' step = \''))
        read (*,(f6.3)) waveoutstep

    end if

    GOTO 1000

end if

! wavelength output range is agreed on now so lets generate output arrays
i=1

do 191 wavel=waveoutstart,(waveoutend+waveoutstep/2),waveoutstep

    waveout(i)=wavel*1e-06
    i=i+1

191 continue

```

```

! m is number of output wavelengths for later loops

      m=i-1

      if (modelquery.eq."2") GOTO 800
      if (modelquery.eq."3") GOTO 900
      if (modelquery.eq."4") GOTO 1100
      if (modelquery.eq."5") then
700    print *,"eta range and step size are:"
        write (*,(' start = ",f5.3)') etastart
        write (*,(' end = ", f5.3)') etaend
        write (*,(' step = ", f6.4)') etastep
        print *, " "
        print *, "Press (1) to change eta range"
        print *, "Press (2) to change eta step size"
        write (*,(' Press ENTER to use current values ->"))')
        read(*,(a1)) etaquery

          if (etaquery.eq."1") then

            write (*,(' start = "))')
            read (*,(f5.3)) etastart
            write (*,(' end = "))')
            read (*,(f5.3)) etaend
            GOTO 700

          end if

          if (etaquery.eq."2") then

            write (*,(' step = "))')
            read (*,(f6.4)) etastep
            GOTO 700

          end if

          print *, " "

          GOTO 1200

      end if

      if (modelquery.eq."7") GOTO 500
      if (modelquery.eq."q") GOTO 1300

! STM

!   calculate maximum temperature

800  tmax = (((1.0-bigA)*s0)/(etastm*epsilon*stef*r*r))**0.25

!   calculate total flux Fmod seen at Earth by integrating over theta, the angular
!   distance from the subsolar point. that is add up rectangles of area
!   dtheta (1 degree) * Fmod(theta)

!   open file to write temperatures to

```

```

!       these format expressions are used in FRM, projected, and NEATM model as well

12      format(T5,'angle/deg', T20, 'temp/K')
13      format(f15.8, f15.8)
14      format(T5,'long/deg', T20, 'lat/deg', T35, 'temp/K')
15      format(f15.8, f15.8, f15.8)

       open (3, file = 'tempSTM.txt')
       write (3,12)

!       calculate the temperature at different values of psi, the angular distance from the
!       subsolar point

       i=1

       do 200 psirad = 0, pi/2, dpsid

           bigT(i) = tmax * (cos(psirad))**0.25
           if (psirad.GT.(pi/2)-(dpsid/2)) bigT(i)=0
           write(3,13) psirad/(pi/180), bigT(i)
           i=i+1

200      continue

       close (3)

!       inform user

       write (*,(' STM maximum temperature is ', f6.2, " K")) tmax
       print *, "The temperature variation with angular distance from the subsolar point"
       print *, "is written to tempSTM.txt."
       print *, " "

!       calculate STM flux for each input wavelength using planck function

       do 210 i=1,n

           fmod = 0
           j=1

           do 220 psirad = 0, pi/2, dpsid

               fbit = ((pi * epsilon * diameter * diameter) / (2 * delta * delta * au * au))&
                   * planck(bigT(j), wavelength(i)) * sin(psirad) * cos(psirad) * dpsid
               fmod = fmod + fbit
               j=j+1

220      continue

!       phase angle correction now

       fmod = fmod * 10**(-0.4*alpha*0.01)
       fmodstm(i)=fmod

210      continue

!       lets measure the fit of the model; do this by calculating
!       SUM((F(obs)-F(mod)/err(obs))^2)

       resstm = 0

```

```

do 211 i=1,n
    resstm = resstm + ((flux(i)-fmodstm(i))/err(i))* ((flux(i)-fmodstm(i))/err(i))
211 continue
! lets generate output fluxes for the output wavelengths
do 212 i= 1,m
    fmod = 0
    j=1
    do 213 psirad = 0, pi/2, dpsci
        fbit = ((pi * epsilon * diameter * diameter) / (2 * delta * delta * au * au))&
            * planck(bigT(j), waveout(i)) * sin(psirad) * cos(psirad) * dpsci
        fmod = fmod + fbit
        j=j+1
213 continue
! phase angle correction now
    fmod = fmod * 10**(-0.4*alpha*0.01)
    fstmout(i)=fmod
212 continue
! now make file fmodelstm.txt
    open (7,file='fmodelstm.txt',status='unknown')
16    format (2x,'wavel(um)',3x,'flux(Wm^-2um^-1)',5x,'error',7x,'STM flux(Wm^-2um^-1)')
17    format (f11.4, 4x, e14.8, 2x, e14.8, 2x, e14.8)
18    format (2x,'wavel(um)',3x,'STM flux(Wm^-2um^-1)')
19    format (f11.4, 4x, e14.8)

    write (7,*) "Asteroid with:"
    write (7,*) " "
    write(7,1) g
    write(7,2) h
    write (7,*)" "
    write (7,(" pv = ",f6.4)) pv
    write (7,(" Deff = ",f4.2," km")) diameter
    write (7,*)" "
    write(7,3) delta
    write(7,4) r
    write(7,5) alpha
    write (7,*)" "
    write (7,("STM fit is: ",e9.3)) resstm
    write (7,*)" "
    write (7,16)

    do 214 i=1,n

        write(7,17) wavelength(i)/1e-06, flux(i), err(i), fmodstm(i)
214 continue

```

```

write (7, *) " "
write (7,18)

do 215 i=1,m

                write(7,19) waveout(i)/1e-06, fstmout(i)

215             continue

close(7)

!             inform user

write (*, '(' STM fit residual = ',e9.3)') resstm
print *, "For the given parameters, the STM fluxes are written to fmodelstm.txt"
GOTO 1000

! FRM

!             Same as STM except for replacement of pi for eta in tmax calculation
!             and different equation for flux (psi now representing latitude)

900 tmax = (((1-bigA)*s0)/(pi*epsilon*stef*r*r))**0.25

open (4, file = 'tempFRM.txt')
write(4,12)

i=1

do 230 psirad = 0, pi/2, dpsi

                bigT(i) = tmax * (cos(psirad))**0.25
                if (psirad.GT.(pi/2)-(dpsi/2)) bigT(i)=0
                write(4,13) psirad/(pi/180), bigT(i)
                i=i+1

230             continue

close(4)

!             inform user

write (*, '(' FRM maximum temperature is ',f6.2, " K"') tmax
print *, "The temperature variation with angular distance from the subsolar point"
print *, "is written to tempFRM.txt."
print *, " "

!             calculate frm fluxes for each input wavelength using planck function

do 240 i=1,n

                fmod = 0
                j=1

                do 250 psirad = 0, pi/2, dpsi

                        fbit = ((epsilon * diameter * diameter) / (delta * delta * au * au))&
                                * planck(bigT(j), wavelength(i)) * cos(psirad) * cos(psirad) * dpsi
                        fmod = fmod + fbit

```

```

                j=j+1
250      continue

            fmodfrm(i) = fmod

240 continue

!      lets measure the fit of the model; do this by calculating
!      SUM((F(obs)-F(mod)/err(obs))^2)

    resfrm = 0

    do 251 i=1,n

        resfrm = resfrm + ((flux(i)-fmodfrm(i))/err(i))* ((flux(i)-fmodfrm(i))/err(i))

251      continue

!      calculate frm fluxes for each output wavelength using planck function

    do 252 i=1,m

        fmod = 0
        j=1

        do 253 psirad = 0, pi/2, dpsirad

            fbit = ((epsilon * diameter * diameter) / (delta * delta * au * au)) &
                * planck(bigT(j), waveout(i)) * cos(psirad) * cos(psirad) * dpsirad
            fmod = fmod + fbit
            j=j+1

253      continue

        ffrmout(i) = fmod

252 continue

! now make file fmodelfrm.txt

    open (8,file='fmodelfrm.txt',status='unknown')
    write (8,*) "Asteroid with:"
    write (8,*) " "
    write(8,1) g
    write(8,2) h
    write (8,*) " "
    write (8,("pv = ",f6.4)) pv
    write (8,("Deff = ",f4.2," km")) diameter
    write (8,*) " "
    write(8,3) delta
    write(8,4) r
    write(8,5) alpha
    write (8,*) " "
    write (8,("FRM fit is: ",e9.3)) resfrm
    write (8,*) " "
    write (8,(2x,"wavel(um)",3x,"flux(Wm^-2um^-1)",5x,"error",7x,"FRM flux(Wm^-2um^-1)"&
    ))

```

```

do 254 i=1,n
    write(8,17) wavelength(i)/1e-06, flux(i), err(i), fmodfrm(i)
254    continue

    write (8,*) " "
    write (8,'(2x,"wavel(um)",3x,"FRM flux(Wm^-2um^-1)')')

    do 255 i=1,m

        write(8,19) waveout(i)/1e-06, ffrmout(i)
255    continue

    close(8)

!    inform user

    write (*, (" FRM fit residual = ",e9.3)) resfrm
    print *, "For the given parameters, the FRM fluxes are written to fmodelfrm.txt"
    GOTO 1000

!    NEATM with set eta
!
!    As STM but allows for phase effects in a more complex way. As phase angles increase
!    the temperature contours gradually disappear around the limb
!    and beaming parameter can now be set

!    etaspec instead of etastm

1100 tmax = (((1-bigA)*s0)/(etaspec*epsilon*stef*r*r))**0.25

!    now calculate temperature as function of longitude (thetarad) and latitude (phirad)
!    at one degree intervals, for fraction that is sunlit
!    ie. from (-90 + alpha) -> +90 longitude, and -90 -> +90 latitude
!    also output to file

    open (5, file = 'tempneatm.txt')

!    indicate table layout

    write(5,*) "      lat/deg"
    write(5,*) "long/deg  temp/K"
    write(5,*) " "

!    produce a 7 space gap before latitude table heading begins

    write(5,('      "\))

!    write latitude headings

    do      256 phirad = -pi/2,+pi/2+dphi/2, dphi

        write(5,'(f7.2)\') phirad/(pi/180)

256 continue

!    go to new line

```

```

        write(5,*) " "
!       generate temperatures and print them
        i=1
        do 259 thetarad = -pi, +pi, dtheta
!           print longitude heading
            write(5,(f7.2\)) thetarad/(pi/180)
            j=1
            do 260 phirad = -pi/2,pi/2+dphi/2,dphi
                if (thetarad.LE.-pi/2) bigTproj(i,j) = 0
                if ((thetarad.GT.-pi/2).and.(thetarad.LT.pi/2)) bigTproj(i,j) = tmax *&
                    (cos(thetarad))**0.25 * (cos(phirad))**0.25
                if (thetarad.GT.pi/2-dphi/2) bigTproj(i,j)=0
                if (phirad.LE.-pi/2) bigTproj(i,j)=0
                if (phirad.GT.(pi/2)-(dphi/2)) bigTproj(i,j)=0
!           write temperature
                if (phirad.lt.+pi/2-dphi/2) write(5,(f7.2\)) bigTproj(i,j)
!           for final temperature at that latitude require that next output will be on new line
                if (phirad.gt.pi/2-dphi/2) write(5,(f7.2\)) bigTproj(i,j)
                j=j+1
260        continue
            i=i+1
259    continue
! inform user
        write (*,(" NEATM with eta = ",f5.3," maximum temperature is ", f6.2, " K.)) &
            etaspec,tmax
        print *, "The temperature variation with angular distance from the subsolar point"
        print *, "is written to tempneatm.txt."
        print *, " "
!       calculate neatm fluxes for each input wavelength using planck function
!       integrates over surface elements dphi and dtheta
        do 270 i=1,n
!           thetarad = alphasad - pi/2
            fmod = 0
            j=1
!           do while (thetarad.LT.((pi/2)+(dtheta/2)))
            do 279 thetarad = - pi/2 + alphasad , +pi/2, dtheta

```

```

k=1

do 280 phirad = -pi/2, +pi/2, dphi

    fbit = ((epsilon * diameter * diameter) / (4 * delta * delta * au * &
    au))* planck(bigTproj(j,k),wavelength(i)) * cos(phirad) * &
    cos(phirad) * cos (alpharad-thetarad) * dphi * dtheta

    fmod = fmod + fbit
    k=k+1

280      continue

!      thetarad = alpharad - pi/2 + j * dtheta
      j=j+1

!      end do
279      continue

      fmodproj(i)=fmod

270  continue

!      lets measure the fit of the model; do this by calculating
!      SUM((F(obs)-F(mod)/err(obs))^2)

      resproj = 0

      do 281 i=1,n

          resproj = resproj + ((flux(i)-fmodproj(i))/err(i))* ((flux(i)-fmodproj(i))/err(i))

281  continue

!      calculate neatm fluxes for each output wavelength using planck function
!      integrates over surface elements dphi and dtheta

      do 282 i=1,m

          thetarad = alpharad - pi/2
          fmod = 0
          j=1

          do while (thetarad.LT.((pi/2)+(dtheta/2)))

              k=1

              do 283 phirad = -pi/2, +pi/2, dphi

                  fbit = ((epsilon * diameter * diameter) / (4 * delta * delta * au * &
                  au))* planck(bigTproj(j,k),waveout(i)) * cos(phirad) * &
                  cos(phirad) * cos (alpharad-thetarad) * dphi * dtheta

                  fmod = fmod + fbit
                  k=k+1

283      continue

          thetarad = alpharad - pi/2 + j * dtheta
          j=j+1

```

```

        end do

        fprojout(i)=fmod

282    continue

! now make file fmodelneatm.txt

    open (9,file='fmodelneatm.txt',status='unknown')
    write (9,*) "Asteroid with:"
    write (9,*) " "
    write(9,1) g
    write(9,2) h
    write (9,*)" "
    write (9,('pv = ",f6.4)') pv
    write (9,('Deff = ",f4.2," km")) diameter
    write (9,*)" "
    write (9,('eta = ",f5.3)') etaspec
    write (9,*)" "
    write(9,3) delta
    write(9,4) r
    write(9,5) alpha
    write (9,*)" "
    write (9,('NEATM fit is: ",e9.3)') resproj
    write (9,*)" "
    write (9,(2x,"wavel(um)",3x,"flux(Wm^-2um^-1)",5x,"error",7x,"NEATM flux(Wm^-2um^-1)"&
    ))

        do 284 i=1,n

                write(9,17) wavelength(i)/1e-06, flux(i), err(i), fmodproj(i)

284    continue

    write (9,*)" "
    write (9,(2x,"wavel(um)",3x,"NEATM flux(Wm^-2um^-1)"))

    do 285 i=1,m

                write(9,19) waveout(i)/1e-06, fprojout(i)

285    continue

    close(9)

!    inform user

    write (*, (' NEATM fit residual = ",e9.3)') resproj
    print *, "For the given parameters, the NEATM fluxes are written to fmodelneatm.txt"
    GOTO 1000

!    NEATM
!    now beaming parameter eta is varied to give a
!    best fit to the data

!    initialise some values

1200 oldres = 100

```

```

do 290 eta=etastart,etaend,etastep

      tmax = (((1-bigA)*s0)/(eta*epsilon*stef*r*r))**0.25

!      now calculate temperature as function of longitude (thetarad) and latitude (phirad)
!      at one degree intervals, for fraction that is sunlit
!      ie. from (-90 + alpha) -> +90 longitude, and -90 -> +90 latitude

      thetarad = alpharad - pi/2

      i=1

      do while(thetarad.LE.pi/2)

          j=1

          do 300 phirad=-pi/2,pi/2,dphi

              bigTproj(i,j) = tmax * (cos(thetarad))**0.25 * (cos(phirad))**0.25
              if (phirad.LE.-pi/2) bigTproj(i,j)=0
              if (phirad.GT.(pi/2)-(dphi/2)) bigTproj(i,j)=0
              if (thetarad.GE.pi/2) bigTproj(i,j)=0
              if (thetarad.LE.-pi/2) bigTproj(i,j)=0
              j=j+1

300          continue

          thetarad = alpharad - pi/2 + i * dtheta
          i=i+1

      end do

!      this is the flux calculation for the input wavelengths using the planck function
!      integrates over surface elements dphi and dtheta

      do 310 i=1,n

          thetarad = alpharad - pi/2
          fmod = 0
          j=1

          do while (thetarad.LT.((pi/2)+(dtheta/2)))

              k=1

              do 320 phirad=-pi/2,pi/2,dphi

                  fbit = ((epsilon * diameter * diameter) / (4 * delta * delta*au* &
                  au))* planck(bigTproj(j,k),wavelength(i)) * cos(phirad) * &
                  cos(phirad) * cos (alpharad-thetarad) * dphi * dtheta

                  fmod = fmod + fbit
                  k=k+1

320              continue

          thetarad = alpharad - pi/2 + j * dtheta
          j=j+1

      end do

```

```

                fmodneatm(i)=fmod
!               store a back-up of these fmodneatm values
                oldfmodneatm(i) = fmodneatm(i)
310            continue
!               calculate the fit SUM(F(obs)-F(mod)/err(obs))^2 for this value of eta
                resneatm = 0
                do 330 i=1,n
                    resneatm = resneatm + ((flux(i)-fmodneatm(i))/err(i))* &
                        ((flux(i)-fmodneatm(i))/err(i))
330            continue
!               compare the fit with the one calculated before it if its bigger then well done
!               the last set of fmodneatm were the best fit at this value of pv
                if (resneatm.GT.oldres) THEN
                    if(eta.GT.etastart) GOTO 5000
                end if
                oldres=resneatm
290 continue
! so correct fmodneatm was the one before, and so was eta
5000 do 340 i=1,n
                fmodneatm(i) = oldfmodneatm(i)
340 continue
if (eta.GT.etastart) eta=eta-etastep
                resneatm=oldres
! inform user
                write (*,(' NEATM best fit eta is ', f5.3)) eta
                write (*,(' NEATM maximum temperature is ', f6.2, ' K')) tmax
!               i've already calculated the neatm fit while finding the right eta
!               now we have found the best eta, lets regenerate the tempatures for
!               output to file
                tmax = (((1-bigA)*s0)/(eta*epsilon*stef*r**r))**0.25
!               now calculate temperature as function of longitude (thetarad) and latitude (phirad)
!               at one degree intervals, for fraction that is sunlit

```

```

!       ie. from (-90 + alpha) -> +90 longitude, and -90 -> +90 latitude
       open (10, file = 'tempneatmfit.txt')

!       indicate table layout

       write(10,*) "      lat/deg"
       write(10,*) "long/deg  temp/K"
       write(10,*) " "

!       produce a 7 space gap before latitude table heading begins

       write(10,('      '\))

!       write latitude headings

       do      338 phirad = -pi/2,+pi/2+dphi/2, dphi
               write(10,(f7.2\)) phirad/(pi/180)

338 continue

!       go to new line

               write(10,*) " "

!       generate temperatures and print them

       i=1

       do 339 thetarad = -pi, +pi, dtheta

!           print longitude heading

               write(10,(f7.2\)) thetarad/(pi/180)

               j=1

               do 341 phirad = -pi/2,pi/2+dphi/2,dphi

                       if (thetarad.LE.-pi/2) bigTproj(i,j) = 0
                       if ((thetarad.GT.-pi/2).and.(thetarad.LT.pi/2)) bigTproj(i,j) = tmax *&
                                   (cos(thetarad)**0.25 * (cos(phirad))**0.25
                       if (thetarad.GT.pi/2-dphi/2) bigTproj(i,j)=0
                       if (phirad.LE.-pi/2) bigTproj(i,j)=0
                       if (phirad.GT.(pi/2)-(dphi/2)) bigTproj(i,j)=0

!                       write temperature

                                   if (phirad.lt.+pi/2-dphi/2) write(10,(f7.2\)) bigTproj(i,j)

!                       for final temperature at that latitude require that next output will be on new line

                                   if (phirad.gt.pi/2-dphi/2) write(10,(f7.2\)) bigTproj(i,j)

                                   j=j+1

341          continue

               i=i+1

```

339 continue

close (10)

!
! need to integrate the above bigTproj into the flux calculation below but for now
! recalculate it the way the flux calculation wants to read it in

thetarad = alphasad - pi/2
i=1

do while(thetarad.LE,pi/2)

j=1

do 346 phirad = -pi/2,pi/2,dphi

bigTproj(i,j) = tmax * (cos(thetarad))**0.25 * (cos(phirad))**0.25
if (phirad.LE.-pi/2) bigTproj(i,j)=0
if (phirad.GE.pi/2) bigTproj(i,j)=0
if (thetarad.GE.pi/2) bigTproj(i,j)=0
if (thetarad.LE.-pi/2) bigTproj(i,j)=0
j=j+1

346 continue

thetarad = alphasad - pi/2 + i * dtheta
i=i+1

end do

!
! this is the flux calculation for the output wavelengths using the planck function
! integrates over surface elements dphi and dtheta

do 342 i=1,m

thetarad = alphasad - pi/2
fmod = 0
j=1

do while (thetarad.LT.((pi/2)+(dtheta)))

k=1

do 343 phirad=-pi/2,pi/2,dphi

fbit = ((epsilon * diameter * diameter) / (4 * delta * delta*au* &
au))* planck(bigTproj(j,k),waveout(i)) * cos(phirad) * &
cos(phirad) * cos (alphasad-thetarad) * dphi * dtheta

fmod = fmod + fbit
k=k+1

343 continue

thetarad = alphasad - pi/2 + j * dtheta
j=j+1

end do

```

                                fneatmout(i)=fmod
342                                continue

! now make file fmodelneatmfit.txt

    open (11,file='fmodelneatmfit.txt',status='unknown')
    write (11,*) "Asteroid with:"
    write (11,*) " "
    write(11,1) g
    write(11,2) h
    write (11,*) " "
    write (11,('pv = ",f6.4)') pv
    write (11,('Deff = ",f4.2," km")) diameter
    write (11,*) " "
    write (11,('eta = ",f5.3)') eta
    write(11,3) delta
    write(11,4) r
    write(11,5) alpha
    write (11,*) " "
    write (11,('NEATM fit is: ",e9.3)') resneatm
    write (11,*) " "
    write (11,('2x,"wavel(um)",3x,"flux(Wm^-2um^-1)",5x,"error",7x,"NEATM flux(Wm^-2um^-1)"&
    ))

                                do 244 i=1,n

                                        write(11,17) wavelength(i)/1e-06, flux(i), err(i), fmodneatm(i)
244                                continue

    write (11,*) " "
    write (11,('2x,"wavel(um)",3x,"NEATM flux(Wm^-2um^-1)'))

    do 245 i=1,m

                                write(11,19) waveout(i)/1e-06, fneatmout(i)
245                                continue

    close(11)

    write (*, ('" NEATM fit residual = ",e9.3)') resneatm
    print *, "For the given parameters, the NEATM fluxes are written to fmodelneatmfit.txt"

    GOTO 1000

1300 end program THERM

! This is my planck function. It calculates the spectral radiance for a given wavelength
! and maximum temperature

    real*8 FUNCTION planck (bigT, wavelength)

    real*8 consta, constb, bigT, wavelength

    planck = 0

    consta = 1.191044d-16

```

```
constb = 1.438769d-02
```

```
planck = dble((((consta/wavelength**5)*(dexp(constb/(wavelength*bigT))-1)**-1))
```

```
! to convert to units of W m^-2 um^-1:
```

```
planck = planck * 1d-06
```

```
return
```

```
end
```

Appendix B. Thermal IR Fluxes (March 2002)

Asteroid instrumental magnitudes M_{inst} and apparent magnitudes M_{ast} observed at UKIRT on 22 March 2002 and 23 March 2002 UT using Michelle in imaging mode

Asteroid	λ (μm)	χ	M_{ast} [for aperture radius (pixels)]:			F_{ast} ($\times 10^{-15} \text{ W m}^{-2} \mu\text{m}^{-1}$) [for aperture radius (pixels)]:			Uncertainty ($\times 10^{-15} \text{ W m}^{-2} \mu\text{m}^{-1}$) ^a		
			5	8	13	5	8	13	5	8	13
			22 March 2002								
(6455) 1992 HE	8.8	1.07	6.46	6.35	6.55	5.50	6.11	5.06	0.6	0.6	0.5
	10.3	1.02	5.56	5.63	5.57	6.54	6.11	6.49	0.7	0.6	0.7
	12.5	1.03	5.17	5.15	5.03	4.33	4.42	5.94	0.4	0.4	0.5
	18.5	1.26	3.87	3.79	3.84	2.21	2.39	2.27	0.5	0.5	0.5
1999 HF ₁	8.8	2.06	4.00	3.91	3.86	53.1	57.6	60.3	6	6	6
	10.3	1.45	3.09	3.03	2.97	63.7	67.3	71.0	7	7	7
	12.5	1.83	2.54	2.48	2.40	49.1	51.5	55.7	5	5	6
	18.5	1.90	1.33	1.20	1.25	23.0	25.9	24.6	5	5	5
23 March 2002											
2000 GD ₂	8.8	1.17	6.72	6.71	6.52	4.38	4.43	5.27	0.8	1	0.9
	10.3	1.70	6.38	6.13	6.16	3.07	3.86	3.76	0.3	0.4	0.4
	12.5	1.23	5.39	5.35	5.35	3.07	3.68	3.70	0.4	0.4	0.4
	18.5	1.34	4.50	4.64	4.59	1.24	1.09	1.14	0.2	0.2	0.2

Notes. ^aFlux calibration uncertainty based on combination of uncertainty due to extinction and an estimated 10% uncertainty for N-band filters (8.8, 10.3, 12.5 μm filters) and 20% for Q-band (18.5 μm).

Appendix C. September 2002 UKIRT Log Sheets

Word processed transcription of handwritten log-sheets (with additional footnotes) produced during September 2002 UKIRT observations. These were the main tool in deciphering the purpose of each group during data reduction.

MICHELLE – UNITED KINGDOM INFRARED TELESCOPE, MAUNA KEA, HAWAII – MICHELLE

UT Date: 27/09/02..... Observers: Simon Green + Stephen Wolters

OBS/GRP NO.	UT TIME	OBJECT NAME	IMAGER /SPEC	λ OR FILTER	GRATING /ORDER	EXP (sec)	CO-ADDS	SAMP-LING	SLIT WID.	POSN ANG.	SEC(z)	CHOP THROW	CHOP ANG.	NOTES
1	4:30	Array tests	imaging	Blank	LowN	0.01	624	1x1						
5-7	4:40	Flats ^a	spec.	NBlock	LowN	0.1	176	1x2	4	-0.456		16.01	0.0	
8	4:55	BS7001	spec.	NBlock	LowN									Failed ^b
8-9	6:30	BS7001	spec.	NBlock	LowN	0.1	176	1x2	4	-0.456		16.01		Vega
10-17 ^c	6:40	BS7001	''	''	''	''	''	''	''	''	1.21	''	''	''
18-25	7:02	BS7264	''	''	''	''	''	''	''	''	1.56	''	''	NX18 ratio star
26-73	7:35	2002 NX18	spec.	NBlock	LowN	0.1	176	1x2	4	-0.456	1.46	''	''	2002 NX18
74-91	8:50	BS7001	''	''	''	''	''	''	''	''	1.84	''	''	Vega, high AM
82-89	9:07	BS437	''	''	''	''	''	''	''	''	1.22	''	''	HK12 ratio star
90-109	9:33	2002 HK12	''	''	''	''	''	''	''	''	1.29	''	''	2002 HK12
110	10:10	Flat												BS7615

^aSet on Vega (with dome closed) at am ~1.0 for flat and arc.

^bProblems with X-head on autoguider.

^cOffset x = 2.8, y = -2.2 to get onto good pixels.

MICHELLE – UNITED KINGDOM INFRARED TELESCOPE, MAUNA KEA, HAWAII – MICHELLE

UT Date: 28/09/02 Observers: Simon Green + Stephen Wolters

OBS/GRP NO.	UT TIME	OBJECT NAME	IMAGER /SPEC	λ OR FILTER	GRATING /ORDER	EXP (sec)	CO-ADDS	SAMP-LING	SLIT WID.	POSN ANG.	SEC (z)	CHOP THROW	CHOP ANG.	NOTES
1-4	05:50 ^a	Array	imaging	blank		0.01	624							
5-7	05:56	Flats	spec	NBlock	LowN	0.1	176	1x2	4	-0.456	1.11	16.01	0.0	Just flats, arc missing
8-9	6:00	Flats												failing to get arc
10	6:30	Arc	spec	WCalLowN	LowN	0.1	176	1x2	4	-0.456	1.17	16.01	0.0	arc working
11-14 ^b	6:50	BS7001	''	NBlock							1.20		''	Vega
15-62	7:00	2002 QE15	''	''							1.36		''	
63-70 ^c	8:25	BS437	''	''							1.43		''	2002 HK12 ratio star
71-94	8:40	2002 HK12 ^d	''	''						''	1.51		''	aborted halfway, no signal?
95-102 ^e	9:25	BS 8650	''	''							1.03		''	Eros ratio star
103-114	9:40	433 Eros	''	''							1.06		''	
115-118	10:03	BS617 ^e	''	''							1.14		''	Standard → wrong wavelength
119-126	10:15	BS915	''	''							1.46		''	1998 UOI ratio star
127-130	10:35	Flats and Arc	''	''							1.38		''	Had to retake so ORAC will read BS915
131-143	10:53	1998 UOI	''	''						''	1.24		''	
144-151	11:16	BS1017	''	''						''	1.28		''	6455 ratio star
152-167	11:40	6455	''	''						''	1.41		''	
168-171	12:08	BS1708 ^f	''	''						''	1.45		''	Standard

Notes. ^aUnable to observe previously, since phones broken, network down, and orac-om not working. ^bOffset (3.0, -2.2). ^cOffset (2.6, 0.5). ^dCan't see it, even though it was guiding easily. ^eObserving tool had set this observation to wrong wavelength. As a result grating was moved. This group is not useable, and for ORAC-DR to be able to reduce the subsequent observation, we have to retake the flats and arc for the new position. Although BS 915 was observed before the new flats, they can still be used to reduce it. ^fCan also be used as ratio star for (6455) 1992 HE.

MICHELLE – UNITED KINGDOM INFRARED TELESCOPE, MAUNA KEA, HAWAII – MICHELLE

UT Date: 29/09/02..... Observers: Simon Green + Stephen Wolters

OBS/GRP NO.	UT TIME	OBJECT NAME	IMAGER /SPEC	λ OR FILTER	GRATING /ORDER	EXP (sec)	CO-ADDS	SAMP-LING	SLIT WID.	POSN ANG.	SEC (z)	CHOP THROW	CHOP ANG.	NOTES
1-4	4:15	Array test	imaging	Blank	LowN	0.01	624							
5-7	4:22	Flats	spec	NBlock	LowN	0.21	78	1x2	2	-0.456	1.06	16.01	0.0	
8-16	5:36	BS7264	"								1.34		"	cloudy, output test
17-40	6:02	2002 NX18	"								1.34		"	clouds at frame 36? So stop at break.
41-44	6:47	BS7615	"								1.06		"	ED104 ratio star
45-60	6:57	2000 ED104 ^a	"											lost between frames 52-56, after that a star
61-64	7:33	BS7615	"								1.11			
65-66	7:43	2000 ED104	"								1.15			attached to star again
67-74	7:50	"	"								1.16			last frame (74) in a star again
75-78	8:08	BS8414	"								1.07		"	1998 ROI ratio star
79-126	8:19	1998 ROI	"								1.13		"	
127-134	9:38	BS8650	"								1.05		"	Eros ratio star
135-146	9:53	433 Eros	"								1.08		"	
147-151	10:17	BS1030	"								1.43		"	6455 ratio star
152-175	10:31	6455	"								1.49		"	
176-179	11:11	BS1136	"								1.44		"	another 6455 ratio star
180-183	11:20	BS617 ^b	"								1.01		"	standard – wrong λ
184-203	11:30	6455	"								1.38		"	need flat for new grating posn
204-207	12:00	BS1136	"								1.01		"	
208-211	12:15	BS617	"								1.00		"	standard – correct λ
212-214	12:25	Flats	"								1.01		"	

Notes. ^aClearer of cloud now, but asteroid near galactic plane, autoguiding keeps locking onto stars. ^bAs last night, object with wrong grating position.

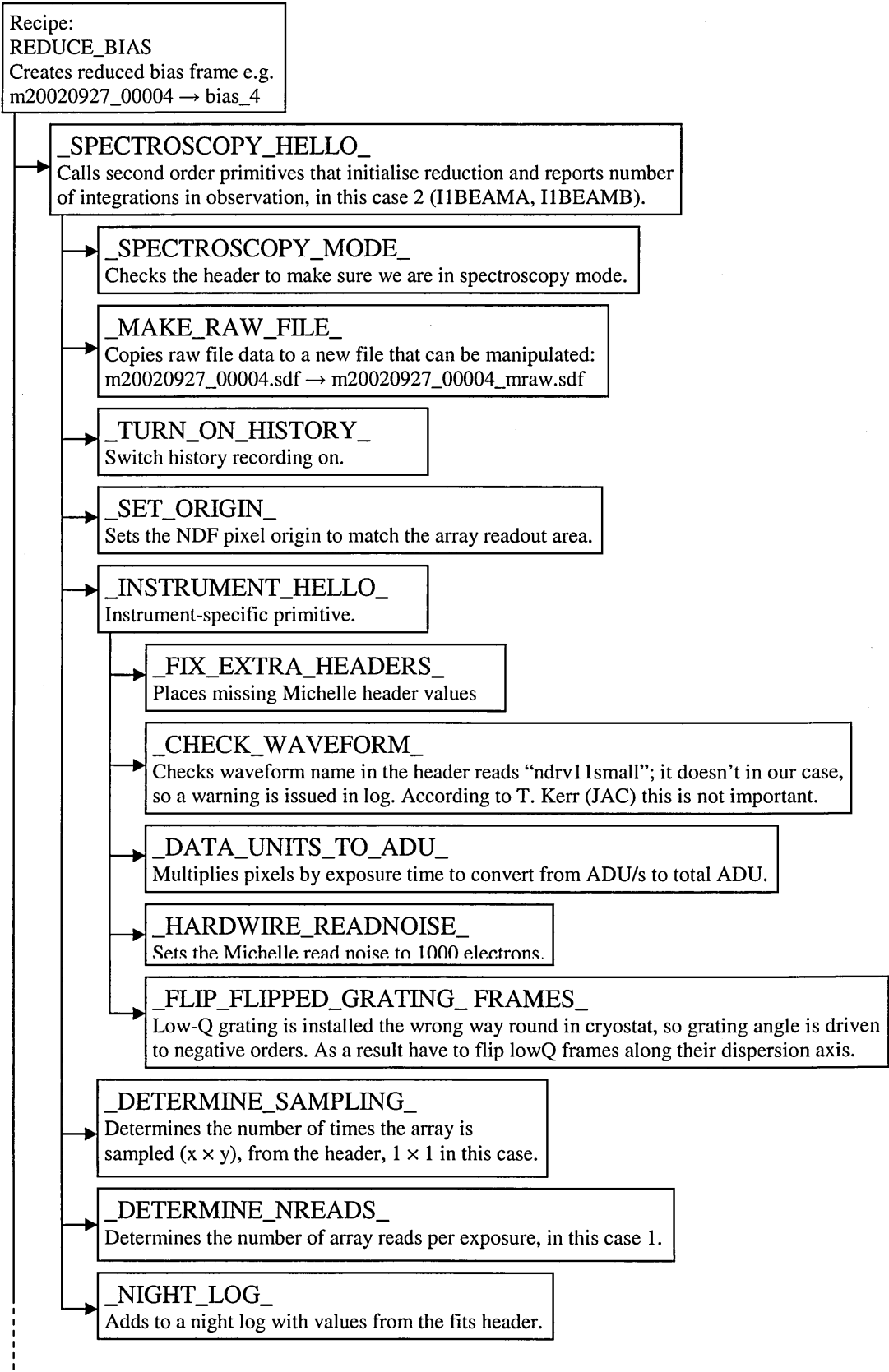
MICHELLE – UNITED KINGDOM INFRARED TELESCOPE, MAUNA KEA, HAWAII – MICHELLE

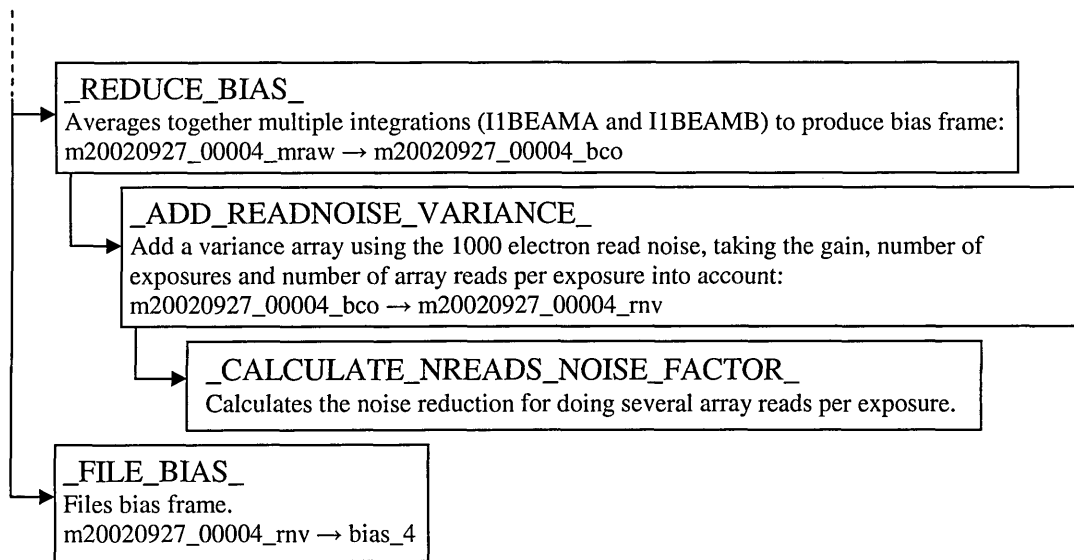
UT Date: 30/09/02..... Observers: Simon Green + Stephen Walters

OBS/GRP NO.	UT TIME	OBJECT NAME	IMAGER /SPEC	λ OR FILTER	GRATING /ORDER	EXP (sec)	CO-ADDS	SAMP-LING	SLIT WID.	POSN ANG.	SEC (z)	CHOP THROW	CHOP ANG.	NOTES
1-4	4:10	Array	imaging	Blank		0.01	624				1.00			
5	4:16	Flat N	spec	NBlock	MedN1	0.1	176	1x2	4	-0.456	1.06	16.01	0.0	wrong grating
6-8	4:24	Flat N	spec	NBlock	LowN	0.1	176	1x2	4	-0.456	1.06	16.01	0.0	
9-11	4:31	''								''	1.74	''	''	dec at -20
12-14	4:38	''								''	1.74	''	''	''
15-17	4:46	Flat Q	spec	QBlock	LowQ	0.18	90	''	''	-0.768	1.78	''	''	setting side
18-20	4:52	''								''	1.75	''	''	rising side
21-23	4:59	''								''	1.07	''	''	''
24-27	5:45	BS6705	''							''	1.28	''	''	standard (Offset N)
28-35		BS7264	''							''	1.38	''	''	NX18 ratio peak
36-38	6:12	BS7264	''							''	1.41	''	''	(unable to peak-up) using nominal offset
39-62	6:30	2002 NX18	''							''	1.35	''	''	NOT OFFSET using offset N-filter
63	7:10	nothing	''							''	1.42	''	''	not on target
64-87 ^a	7:12	2002 NX18	''							''	1.42	''	''	''
88-91	7:52	BS7525	''							''	1.21	''	''	standard + ratio, using nominal offset
92-95	8:07	BS7525	''	NBlock	LowN	0.1	176	''	''	-0.456	1.27	''	''	''
96-112	8:18	2002 NX18	''							''	1.68	''	''	''
113-116	8:47	BS7776	''							''	1.62	''	''	NX18 ratio star
117-120	8:54	BS7525	''							''	1.53	''	''	ED104 standard + ratio
121-132	9:09	2000 ED104	''							''	1.51	''	''	''
133-136	9:34	BS1030	''							''	1.69	''	''	6455 ratio star
137-152	9:48	6455	''							''	1.79	''	''	''

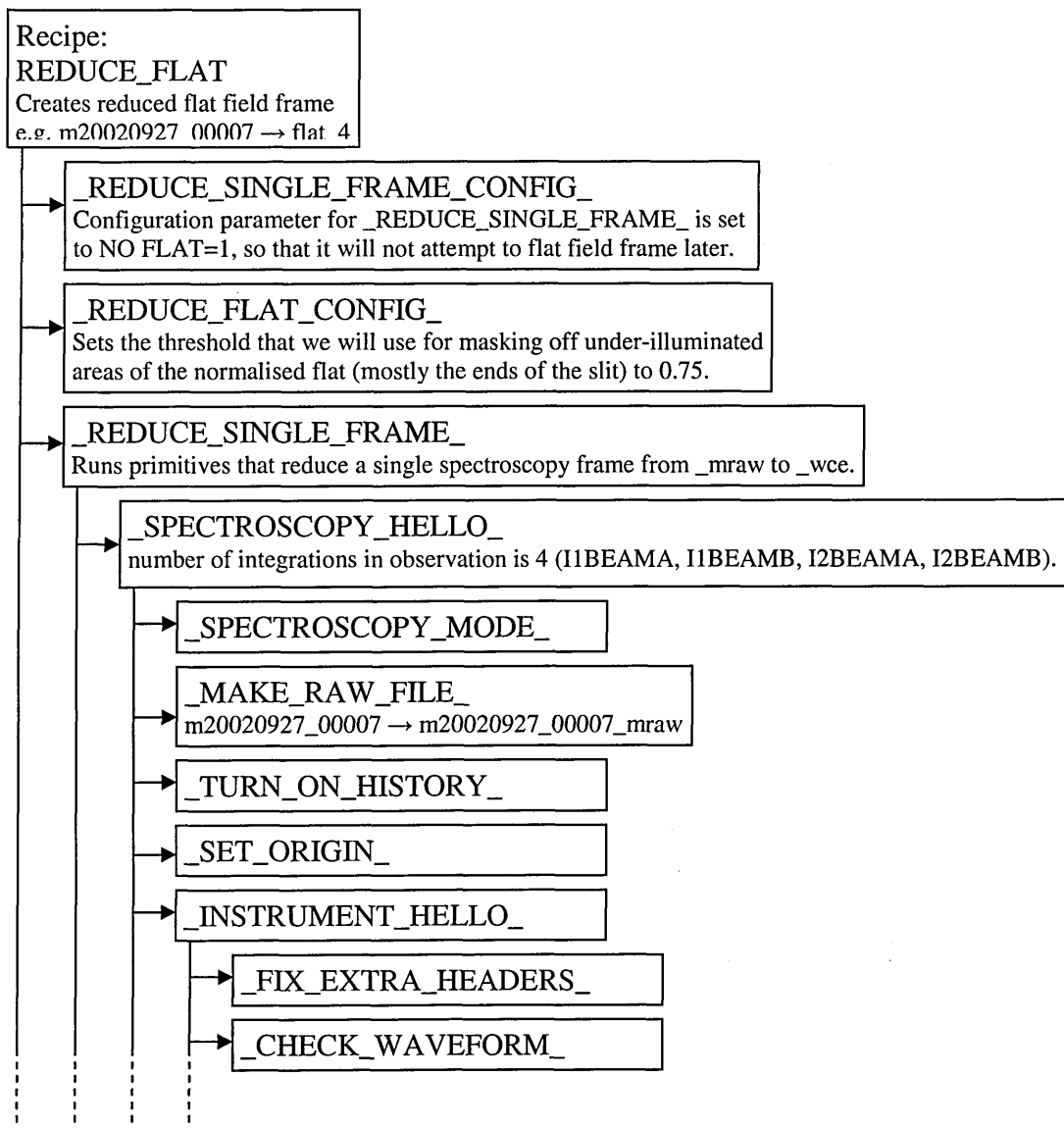
Appendix D. ORAC-DR Primitives Flowchart

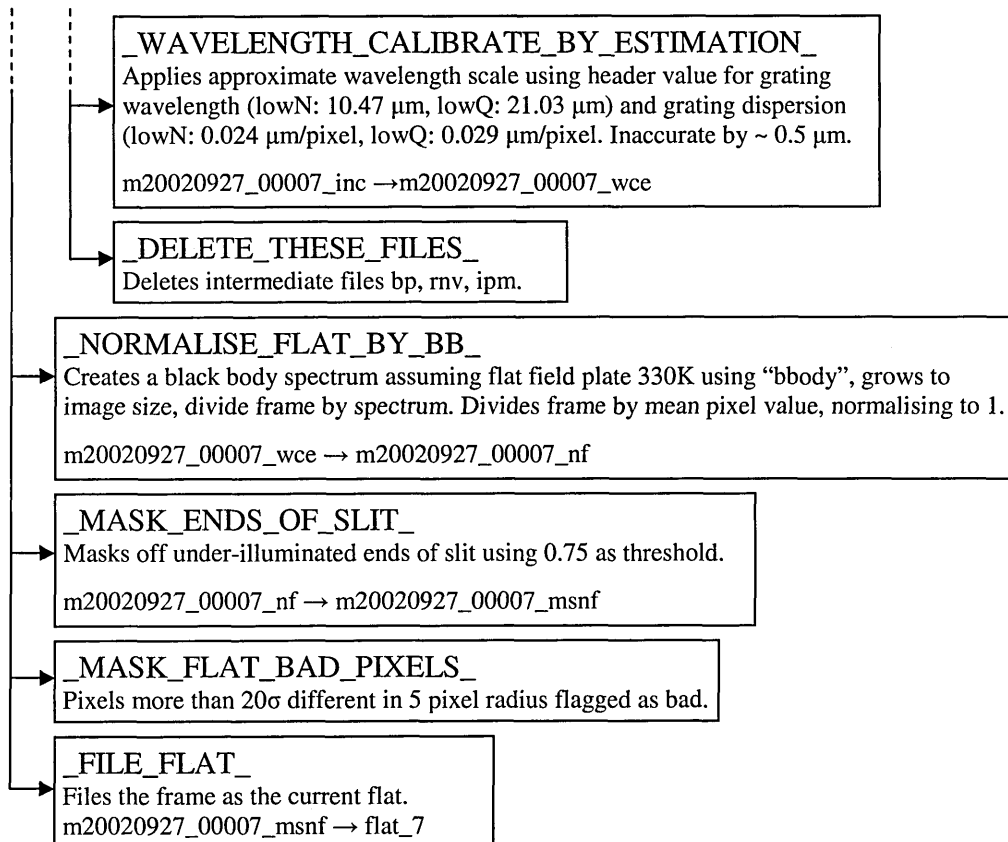
Array Frame



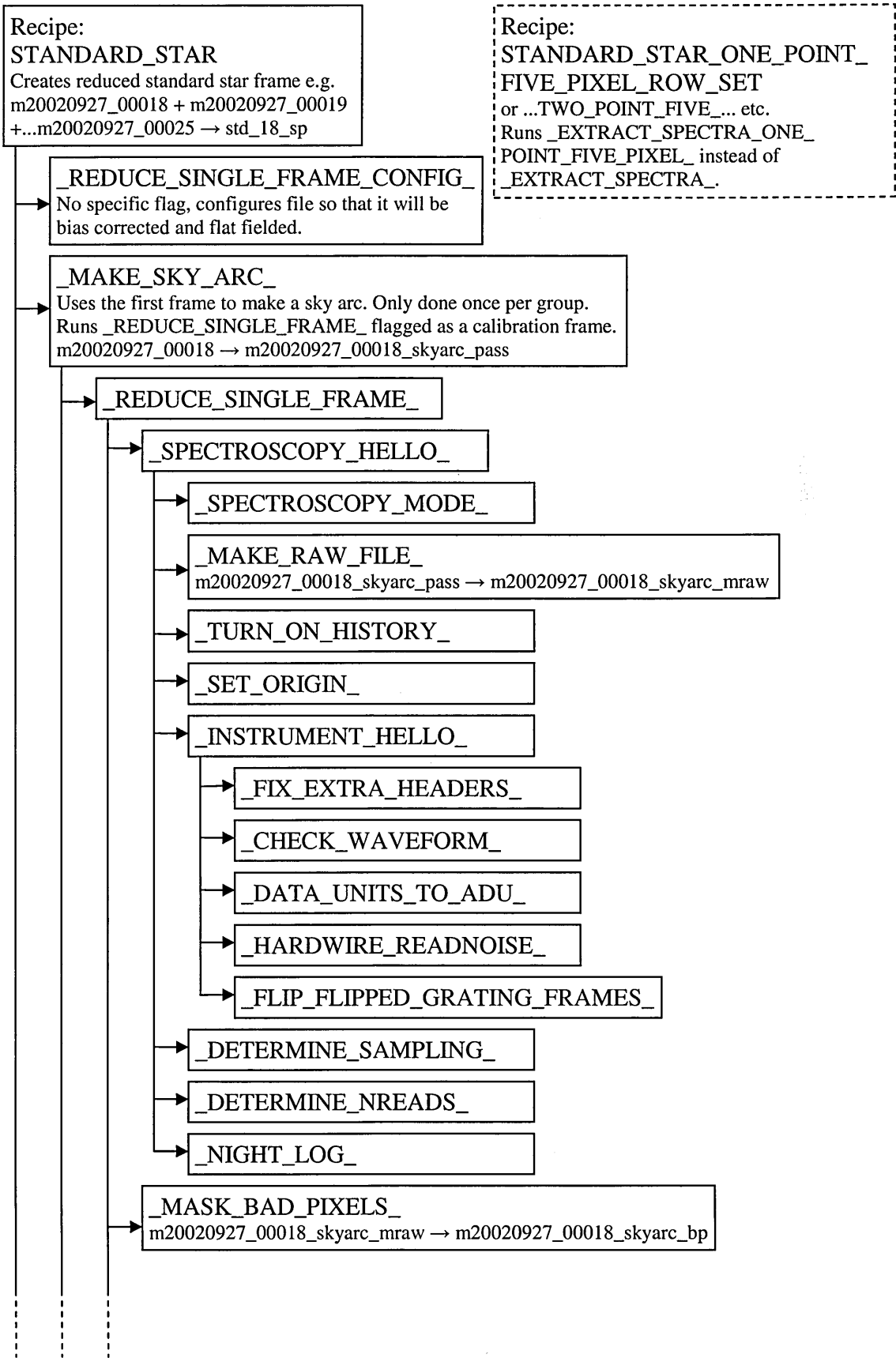


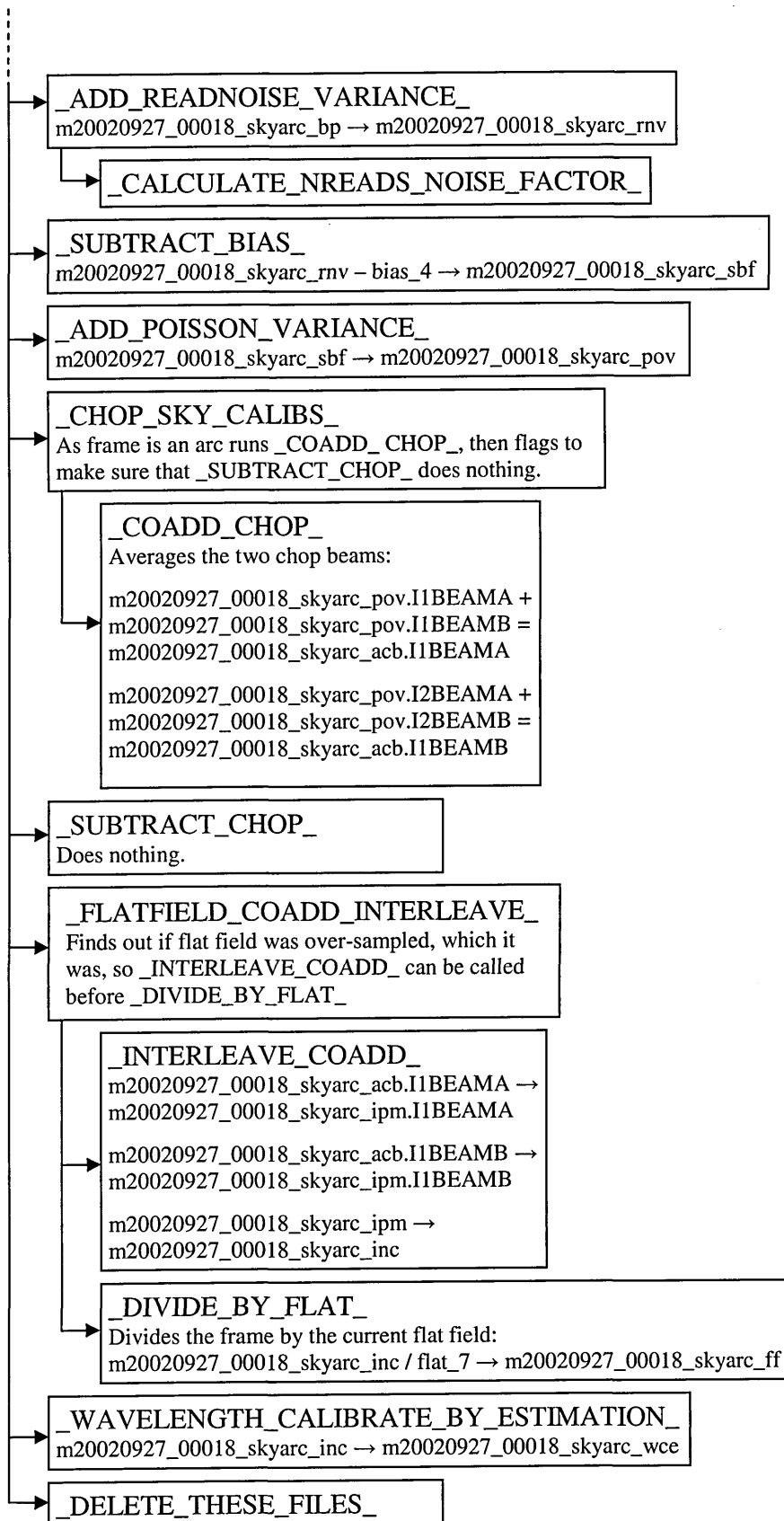
Flat Frame

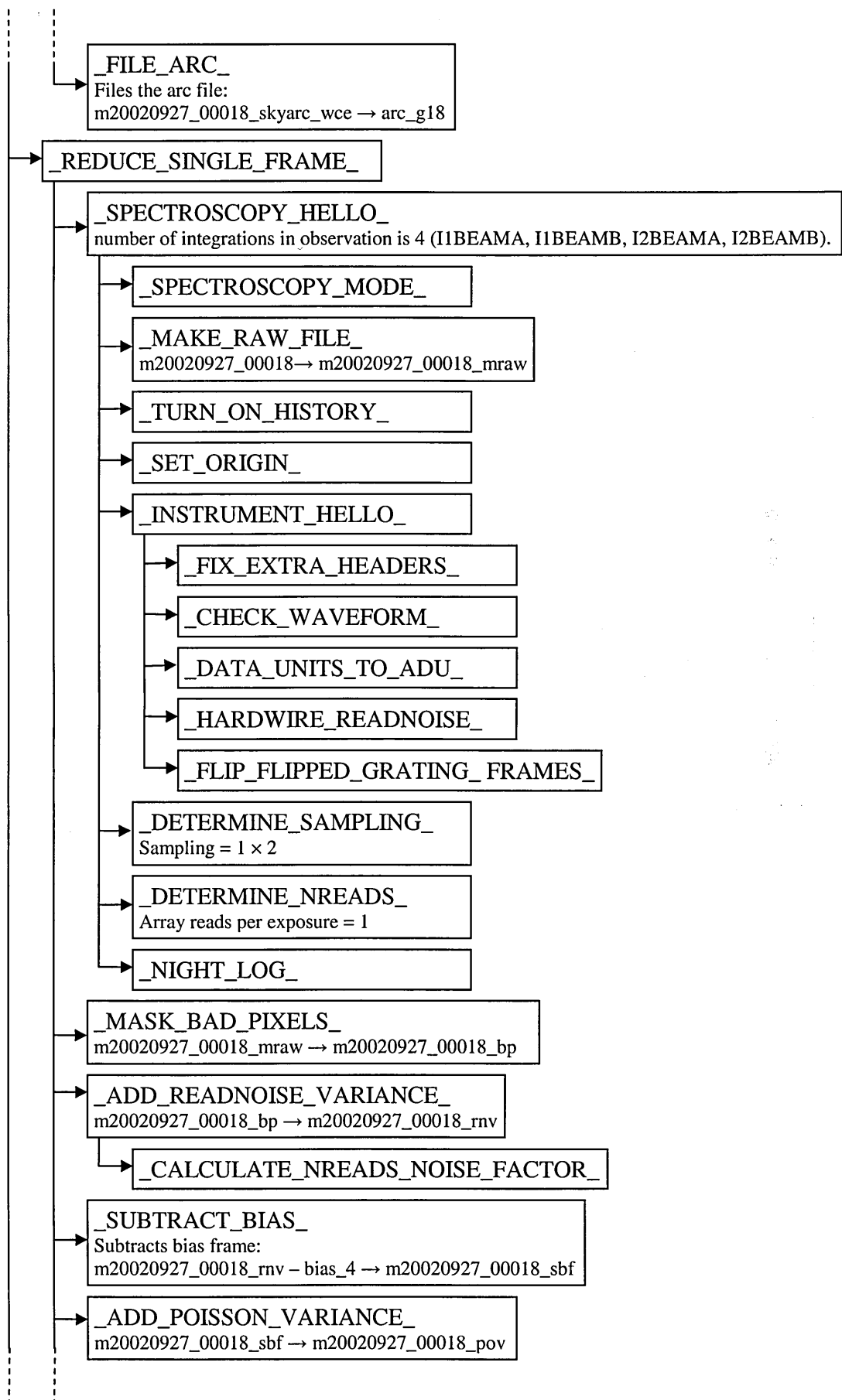


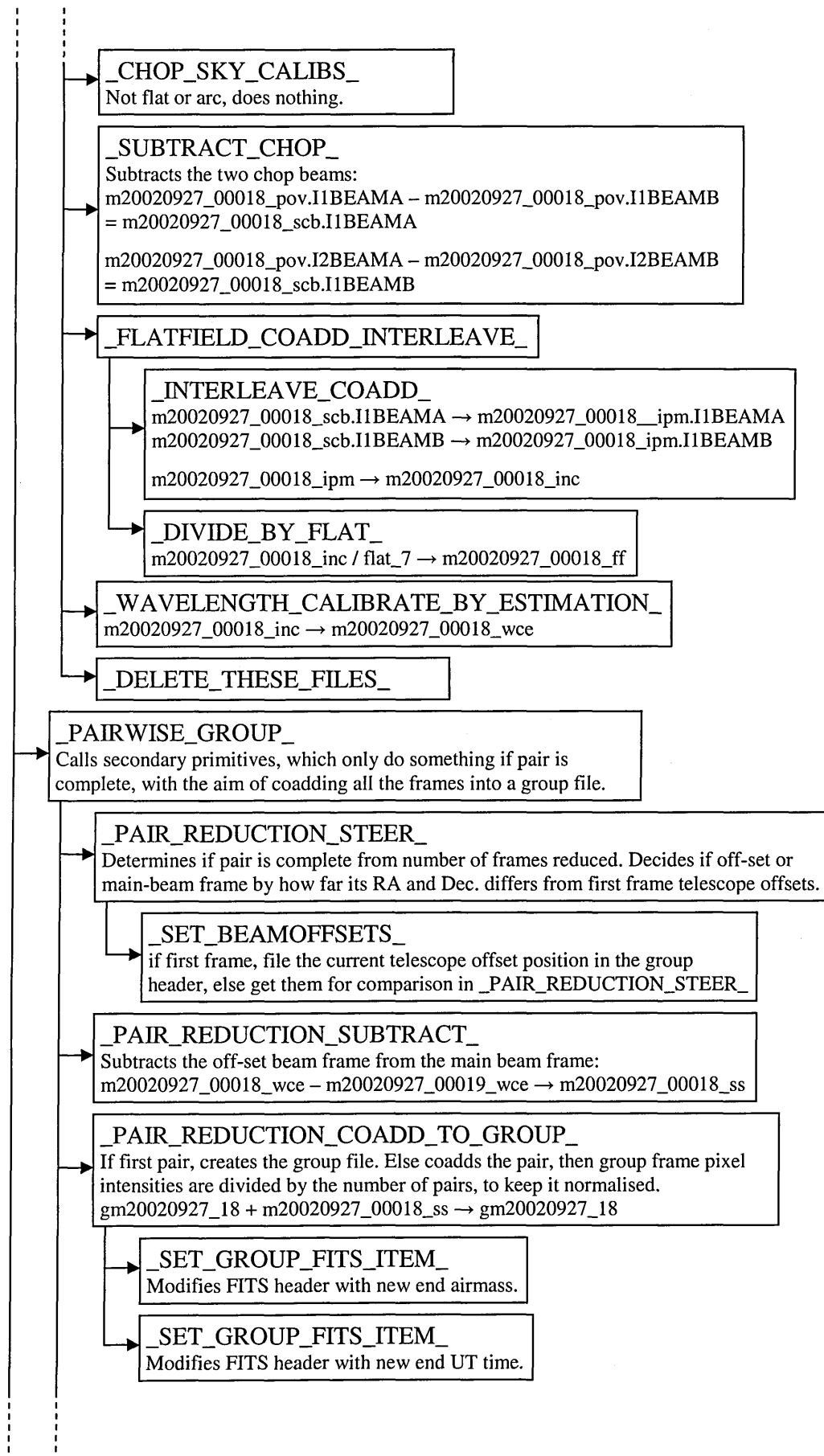


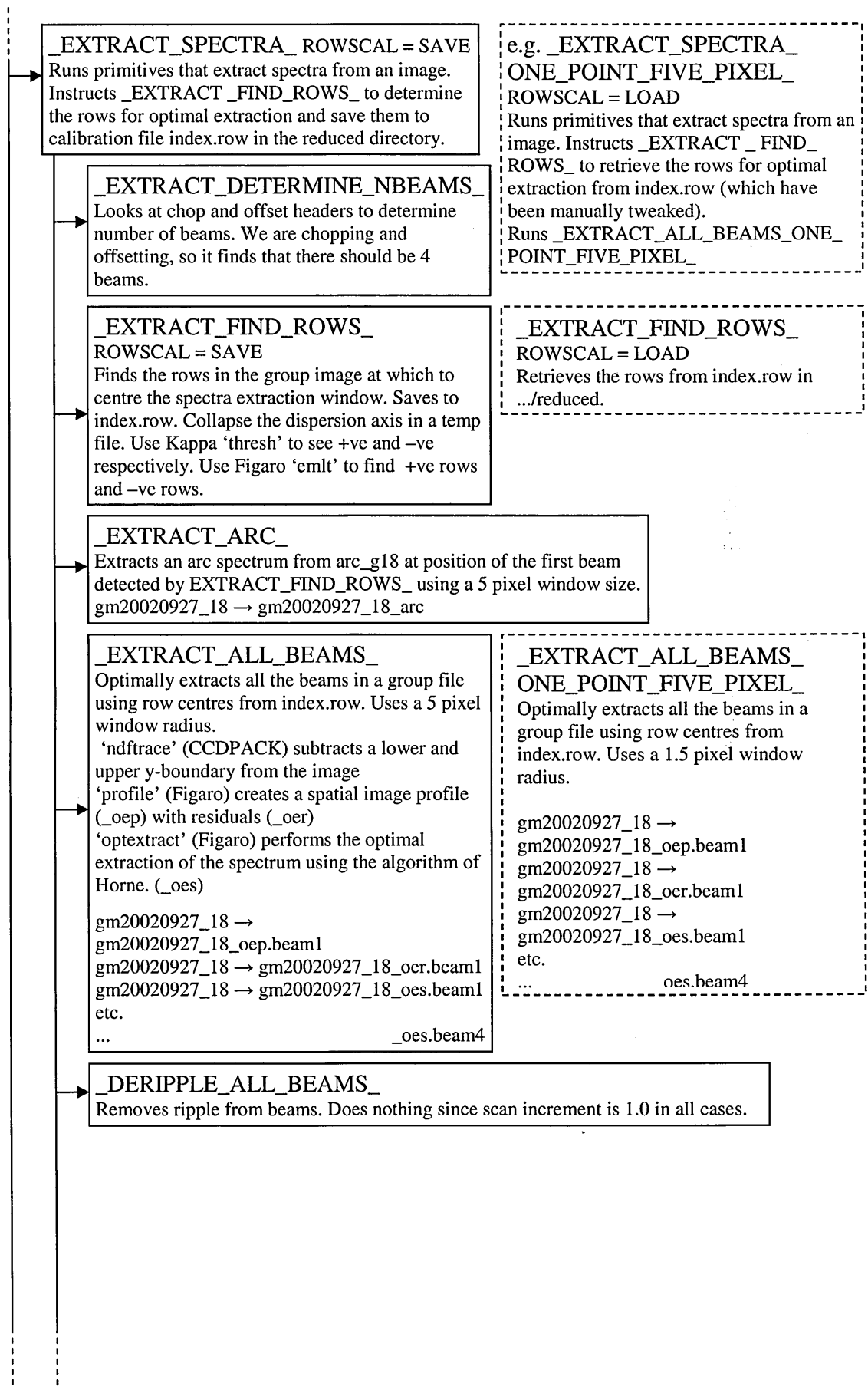
Standard Star Frame

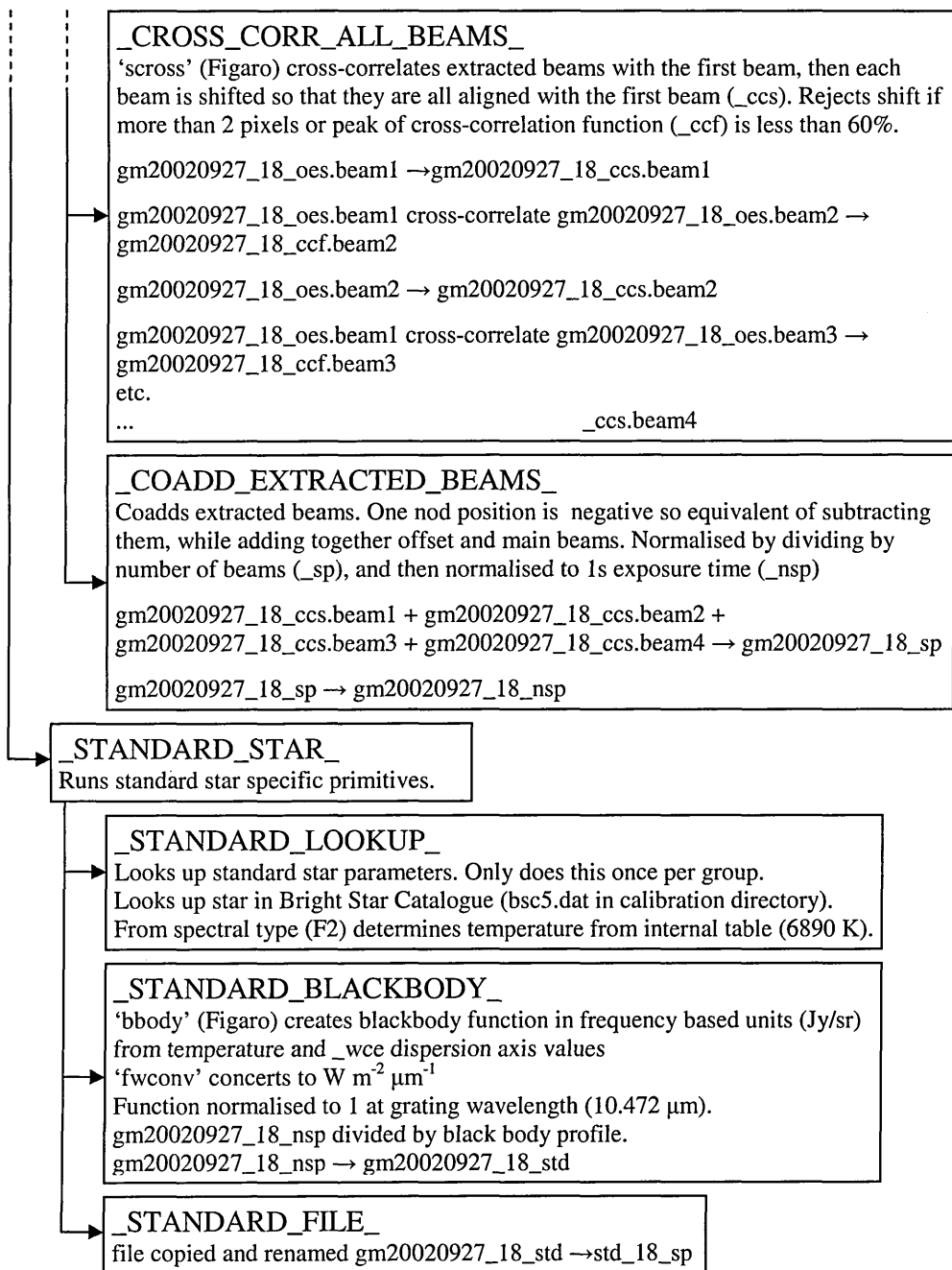




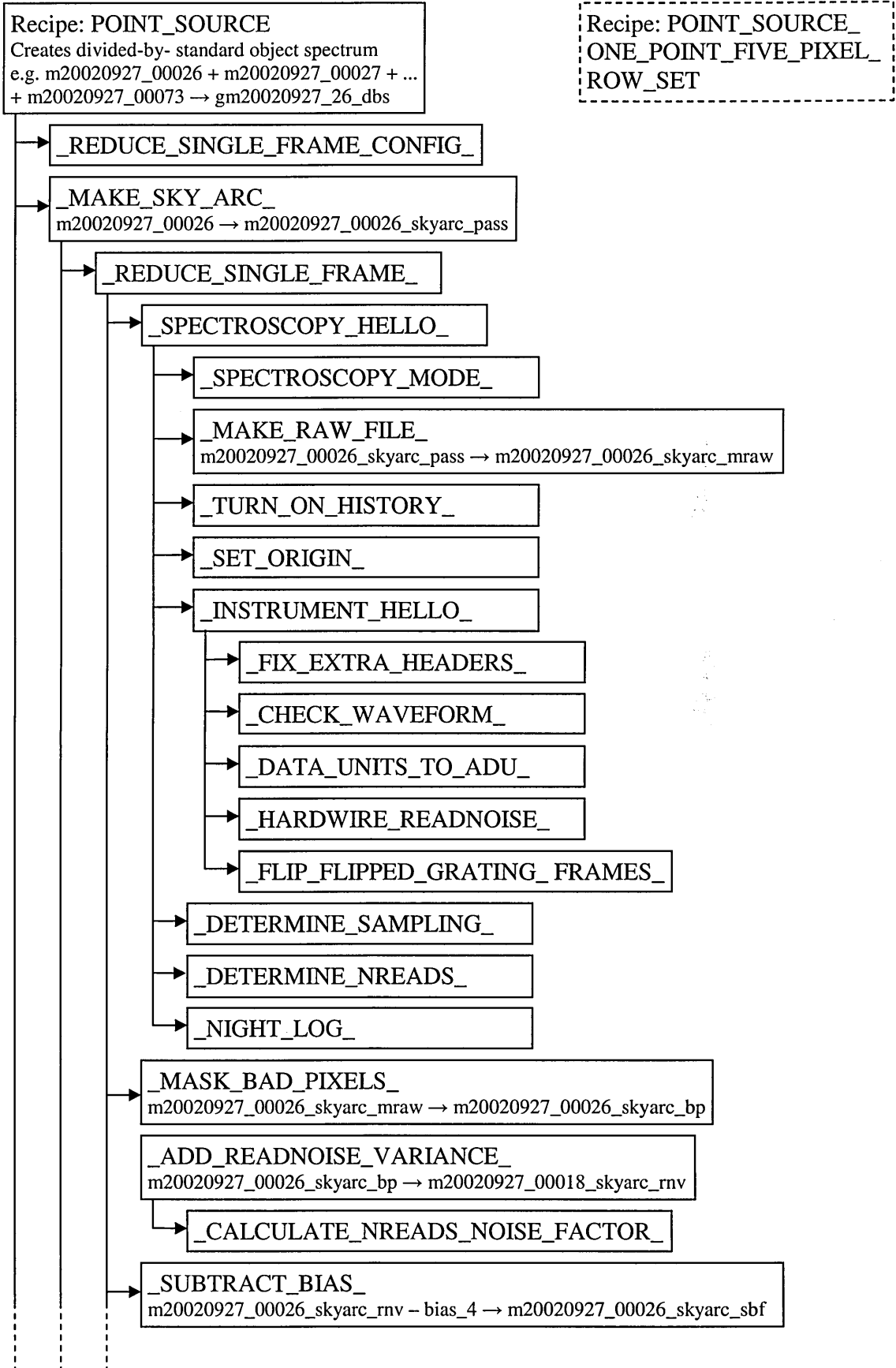


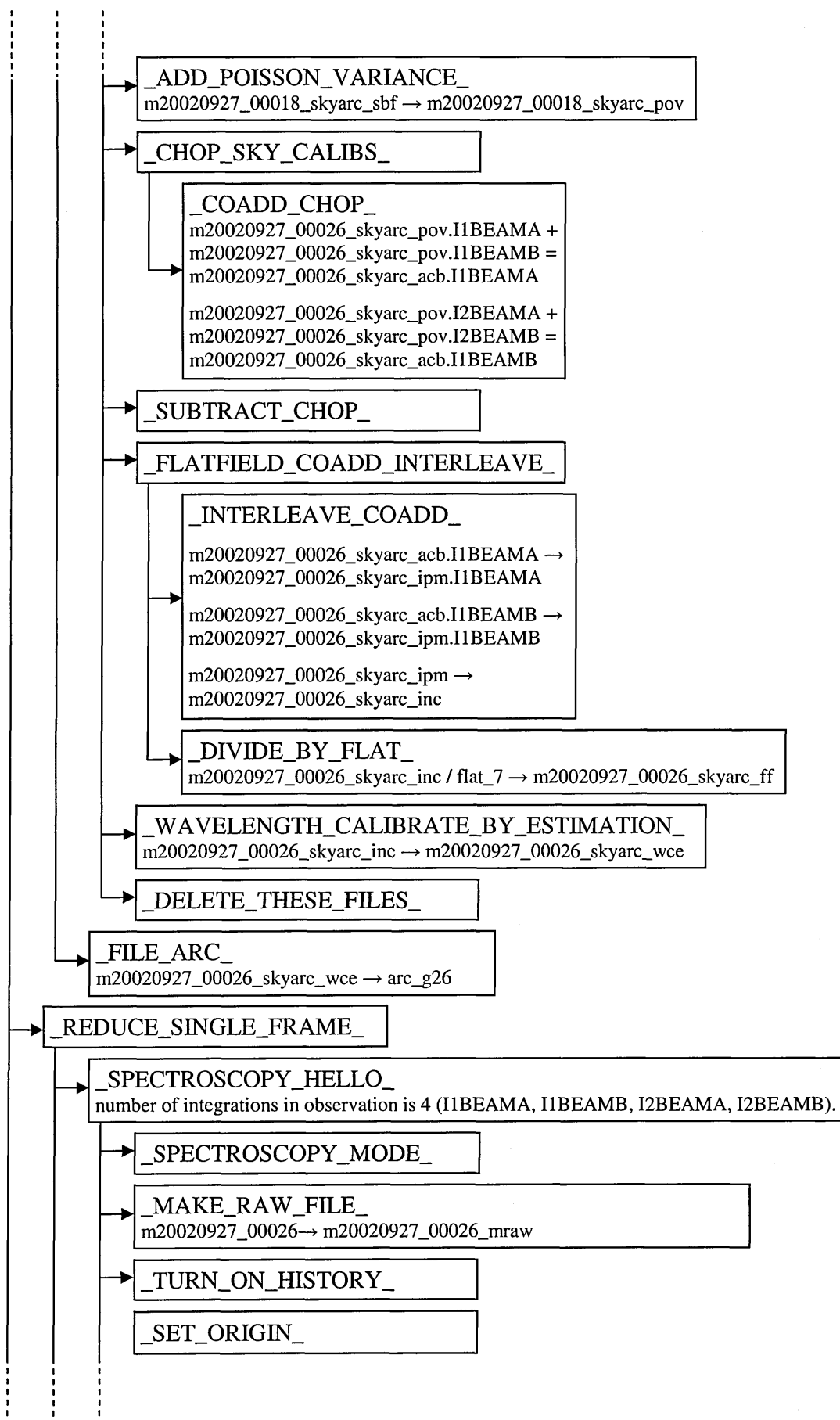


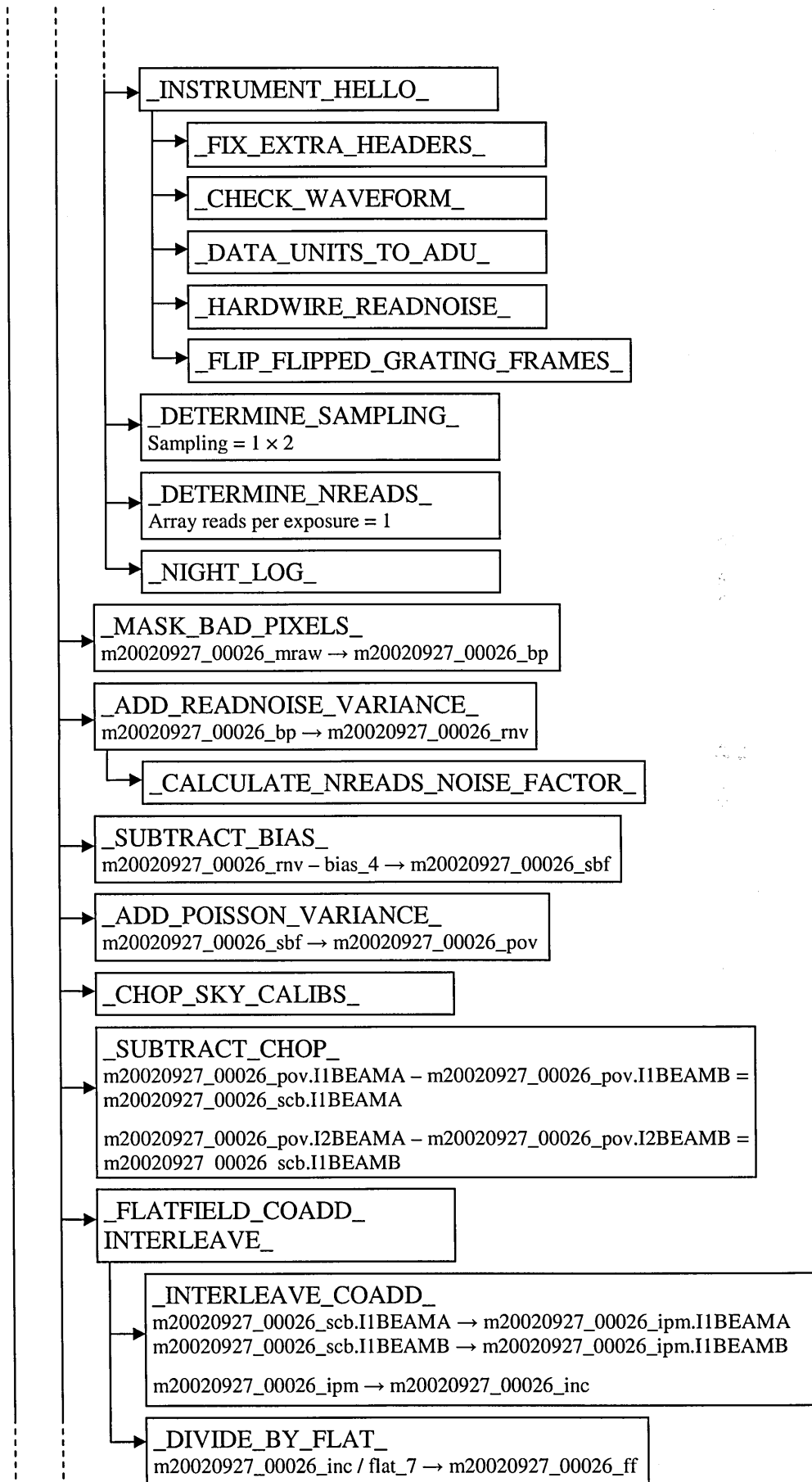


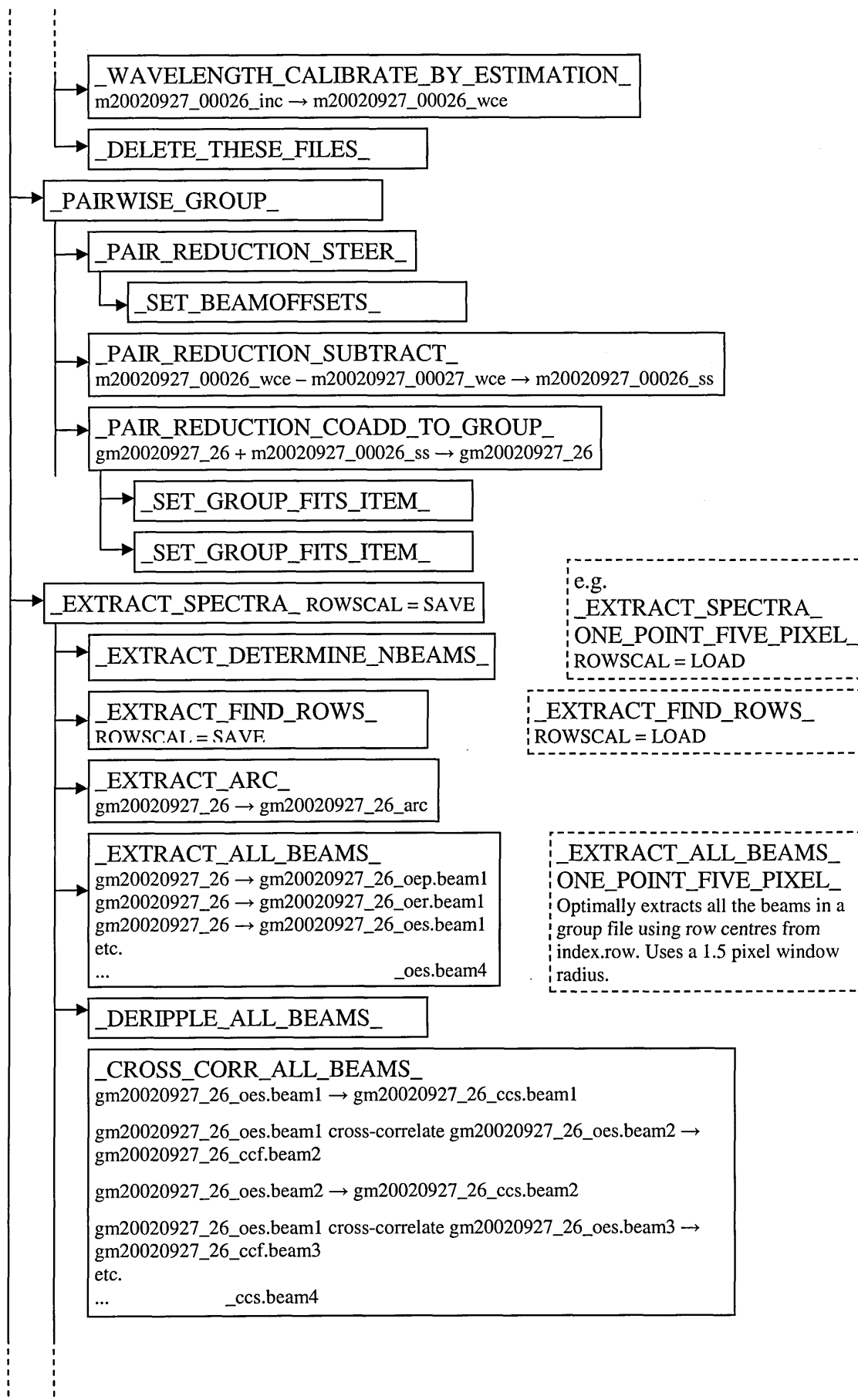


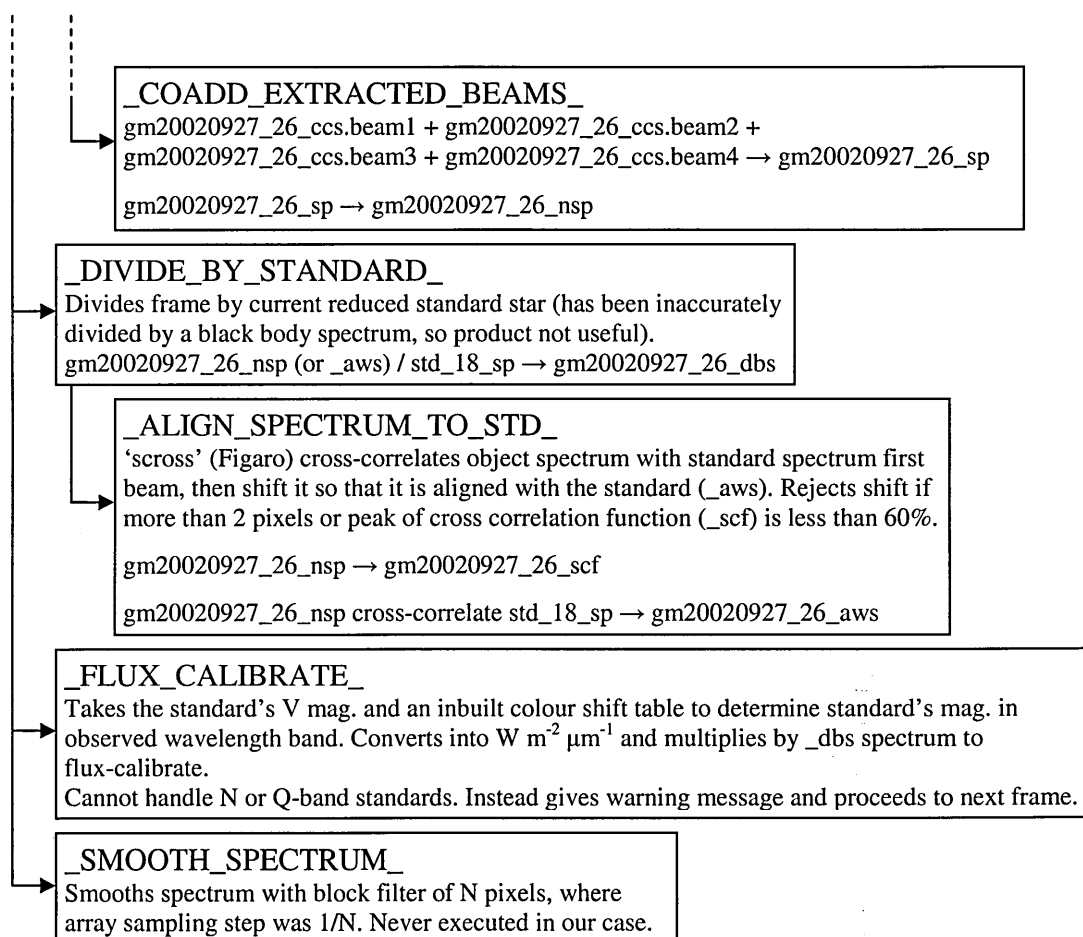
Object Frame











Appendix E. Thermal IR Fluxes (September 2002)

Estimated N magnitudes, flux-calibrated and binned asteroid fluxes observed in September 2002 (UT) at UKIRT using Michelle in spectroscopy mode

Asteroid: (433) Eros
Date: 28 Sep.
Ratio star: BS 8650
Est. asteroid N mag. 1.26
Fig. 5.21 (a)

Wavelength (μm)	F_{ast} ($\times 10^{-13} \text{ W m}^{-2} \mu\text{m}^{-1}$)	Standard error ($\times 10^{-15} \text{ W m}^{-2} \mu\text{m}^{-1}$)	Bin size (pixels)
8.120	2.86	3.17	10
8.369	2.99	1.95	10
8.625	3.07	2.16	10
8.884	3.17	1.18	10
9.159	3.15	1.33	11
10.166	3.22	0.967	12
10.476	3.19	0.888	12
10.783	3.12	1.36	12
11.088	3.08	1.22	12
11.393	3.06	0.662	12
11.700	3.05	1.03	12
12.011	2.99	1.07	12
12.329	2.84	2.10	12

Asteroid: (433) Eros
Date: 28 Sep.
Ratio star: BS 7001
Est. asteroid N mag. 1.28
Fig. 5.21 (b)

Wavelength (μm)	F_{ast} ($\times 10^{-13} \text{ W m}^{-2} \mu\text{m}^{-1}$)	Standard error ($\times 10^{-15} \text{ W m}^{-2} \mu\text{m}^{-1}$)	Bin size (pixels)
8.120	2.91	4.45	10
8.369	2.96	2.53	10
8.625	3.06	3.47	10
8.884	3.12	2.21	10
9.159	3.09	2.02	11
10.166	3.11	1.68	12
10.476	3.05	1.50	12
10.783	2.97	2.27	12
11.088	2.87	1.13	12
11.393	2.86	0.933	12
11.700	2.86	2.56	12
12.011	2.76	1.74	12
12.329	2.63	2.99	12

Asteroid: (6455) 1992 HE
Date: 28 Sep.
Ratio star: BS 1708
Est. asteroid N mag. 4.07
Fig. 5.21 (d)

Wavelength (μm)	F_{ast} ($\times 10^{-14} \text{ W m}^{-2} \mu\text{m}^{-1}$)	Standard error ($\times 10^{-16} \text{ W m}^{-2} \mu\text{m}^{-1}$)	Bin size (pixels)
8.208	2.25	11.6	17
8.643	2.59	6.30	17
9.082	2.50	8.02	17
10.205	2.43	3.92	16
10.616	2.28	4.92	16
11.026	2.22	3.11	16
11.437	2.20	5.66	16
11.853	2.14	4.52	16
12.276	1.97	5.64	16

Asteroid: (6455) 1992 HE
Date: 30 Sep.
Ratio star: BS 1030
Est. asteroid N mag. 3.75
Fig. 5.21 (e)

Wavelength (μm)	F_{ast} ($\times 10^{-14} \text{ W m}^{-2} \mu\text{m}^{-1}$)	Standard error ($\times 10^{-16} \text{ W m}^{-2} \mu\text{m}^{-1}$)	Bin size (pixels)
8.210	3.41	12.6	17
8.640	3.54	6.84	17
9.082	3.36	4.42	17
10.141	2.99	7.10	10
10.399	3.04	7.60	10
10.657	2.94	3.55	10
10.912	2.85	6.18	10
11.167	2.84	6.73	10
11.422	2.77	6.82	10
11.677	2.68	6.09	10
11.935	2.57	12.6	10
12.276	2.58	5.83	16

Asteroid: (6455) 1992 HE (group 161)
Date: 30 Sep.
Ratio star: BS 1457 (group 157)
Est. asteroid Q mag. 1.80
Fig. 5.21 (f)

Wavelength (μm)	F_{ast} ($\times 10^{-14} \text{ W m}^{-2} \mu\text{m}^{-1}$)	Standard error ($\times 10^{-15} \text{ W m}^{-2} \mu\text{m}^{-1}$)	Bin size (pixels)
17.580	1.35	1.59	54
19.252	1.28	1.85	54
20.869	1.14	3.20	54
22.294	0.881	3.65	52
24.052	0.520	5.01	25

single flux bin between 17.4 and 18.8 μm :

Wavelength (μm)	F_{ast} ($\times 10^{-14} \text{ W m}^{-2} \mu\text{m}^{-1}$)	Standard error ($\times 10^{-15} \text{ W m}^{-2} \mu\text{m}^{-1}$)	Bin size (pixels)
17.877	1.27	1.10	60

Asteroid: (6455) 1992 HE (group 189)**Date:** 30 Sep.**Ratio star:** BS 1457 (group 185)**Est. asteroid Q mag.** 2.19**Fig. 5.21** (g)

Wavelength (μm)	F_{ast} ($\times 10^{-15} \text{ W m}^{-2} \mu\text{m}^{-1}$)	Standard error ($\times 10^{-15} \text{ W m}^{-2} \mu\text{m}^{-1}$)	Bin size (pixels)
17.594	10.5	1.19	53
19.235	7.04	1.42	53
20.825	5.77	1.93	53
22.255	5.72	2.31	47
24.039	5.47	2.85	30

single flux bin between 17.4 and 18.8 μm :

Wavelength (μm)	F_{ast} ($\times 10^{-15} \text{ W m}^{-2} \mu\text{m}^{-1}$)	Standard error ($\times 10^{-16} \text{ W m}^{-2} \mu\text{m}^{-1}$)	Bin size (pixels)
18.089	8.94	7.57	60

Asteroid: (66063) 1998 RO₁**Date:** 29 Sep.**Ratio star:** BS 8414**Est. asteroid N mag.** 6.75**Fig. 5.21** (h)

Wavelength (μm)	F_{ast} ($\times 10^{-15} \text{ W m}^{-2} \mu\text{m}^{-1}$)	Standard error ($\times 10^{-16} \text{ W m}^{-2} \mu\text{m}^{-1}$)	Bin size (pixels)
8.641	1.52	1.96	51
10.421	1.78	2.15	32
11.249	2.44	2.11	32
12.081	2.18	2.28	32

Asteroid: (53789) 2000 ED₁₀₄**Date:** 29 Sep.**Ratio star:** BS 7615 (group 41)**Est. asteroid N mag.** 5.68**Fig. 5.21** (j)

Wavelength (μm)	F_{ast} ($\times 10^{-15} \text{ W m}^{-2} \mu\text{m}^{-1}$)	Standard error ($\times 10^{-16} \text{ W m}^{-2} \mu\text{m}^{-1}$)	Bin size (pixels)
8.471	5.70	4.85	22
9.021	5.86	4.91	21
10.355	5.47	3.73	23
10.945	5.83	3.16	23
11.543	5.46	4.28	23
12.177	5.45	5.52	24

Asteroid: (53789) 2000 ED₁₀₄
Date: 30 Sep.
Ratio star: BS 7525 (group 117)
Est. asteroid N mag. 5.12
Fig. 5.21 (k)

Wavelength (μm)	F_{ast} ($\times 10^{-15} \text{ W m}^{-2} \mu\text{m}^{-1}$)	Standard error ($\times 10^{-16} \text{ W m}^{-2} \mu\text{m}^{-1}$)	Bin size (pixels)
8.904	8.45	5.53	31
10.317	7.77	4.82	24
10.932	7.21	3.94	24
11.544	7.45	4.83	24
12.180	7.96	5.84	25

Asteroid: 2002 HK₁₂
Date: 28 Sep.
Ratio star: BS 437
Est. asteroid N mag. 6.30
Fig. 5.21 (m)

Wavelength (μm)	F_{ast} ($\times 10^{-15} \text{ W m}^{-2} \mu\text{m}^{-1}$)	Standard error ($\times 10^{-16} \text{ W m}^{-2} \mu\text{m}^{-1}$)	Bin size (pixels)
8.715	2.49	3.15	46
10.424	2.87	2.80	32
11.241	2.79	2.89	32
12.067	2.83	3.64	32

Asteroid: 2002 NX₁₈
Date: 27 Sep.
Ratio star: BS 7264
Est. asteroid N mag. 4.36
Fig. 5.21 (n)

Wavelength (μm)	F_{ast} ($\times 10^{-14} \text{ W m}^{-2}$)	Standard error ($\times 10^{-16} \text{ W m}^{-2} \mu\text{m}^{-1}$)	Bin size (pixels)
8.123	1.86	7.07	10
8.374	1.89	4.75	10
8.630	1.89	2.83	10
8.888	1.86	3.44	10
9.161	1.86	2.96	11
10.134	1.74	2.63	10
10.391	1.76	2.14	10
10.647	1.73	1.50	10
10.903	1.66	2.60	10
11.210	1.63	1.76	14
11.568	1.64	2.16	14
11.931	1.57	2.48	14
12.301	1.52	2.71	14

Asteroid: 2002 NX₁₈
Date: 29 Sep.
Ratio star: BS 7264
Est. asteroid N mag. 4.38
Fig. 5.21 (o)

Wavelength (μm)	F_{ast} ($\times 10^{-14} \text{ W m}^{-2}$)	Standard error ($\times 10^{-16} \text{ W m}^{-2} \mu\text{m}^{-1}$)	Bin size (pixels)
8.210	1.61	4.46	17
8.643	1.69	4.82	17
9.077	1.72	3.82	17
10.283	1.80	4.68	13
10.617	1.75	3.64	13
10.952	1.77	4.00	13
11.289	1.76	2.62	13
11.626	1.72	3.67	13
11.964	1.73	4.75	13
12.318	1.71	4.17	14

Asteroid: 2002 NX₁₈
Date: 30 Sep.
Ratio star: BS 7525 (group 88)
Est. asteroid Q mag. 2.02
Fig. 5.21 (p)

Wavelength (μm)	F_{ast} ($\times 10^{-15} \text{ W m}^{-2}$)	Standard error ($\times 10^{-15} \text{ W m}^{-2} \mu\text{m}^{-1}$)	Bin size (pixels)
18.007	10.8	1.23	39
19.241	4.14	2.16	39
20.432	6.08	1.69	39

single flux bin between 17.4 and 18.8 μm :

Wavelength (μm)	F_{ast} ($\times 10^{-14} \text{ W m}^{-2}$)	Standard error ($\times 10^{-15} \text{ W m}^{-2} \mu\text{m}^{-1}$)	Bin size (pixels)
18.102	1.08	1.10E-15	45

Asteroid: 2002 NX₁₈
Date: 30 Sep.
Ratio star: BS 7776
Est. asteroid N mag. 4.04
Fig. 5.21 (q)

Wavelength (μm)	F_{ast} ($\times 10^{-14} \text{ W m}^{-2}$)	Standard error ($\times 10^{-16} \text{ W m}^{-2} \mu\text{m}^{-1}$)	Bin size (pixels)
8.216	2.37	8.06	17
8.648	2.55	6.87	17
9.087	2.50	6.40	17
10.215	2.35	4.96	16
10.627	2.30	4.62	16
11.038	2.24	5.29	16
11.449	2.11	4.66	16
11.862	2.06	7.70	16
12.280	1.98	5.91	16

Asteroid: 2002 QE₁₅
Date: 28 Sep.
Ratio star: BS 7001
Est. asteroid N mag. 6.01
Fig. 5.21 (r)

Wavelength (μm)	F_{ast} ($\times 10^{-15} \text{ W m}^{-2}$)	Standard error ($\times 10^{-16} \text{ W m}^{-2} \mu\text{m}^{-1}$)	Bin size (pixels)
8.652	3.86	2.49	51
10.284	4.25	1.74	23
10.873	4.19	1.41	23
11.823	3.38	2.06	51

Appendix F: NESTM Fortran 90 Code

```

! therme.f90                Stephen Wolters        2005-02-15
!
!*****
!
! PROGRAM: therme
!
!   PURPOSE: Calculates Night Emission Simulated Thermal Model from a set of wavelengths
! and for a range of values of pv, from an input of H, G, delta, r, alpha, thermal inertia, rotation period
! For each value of pv it compares the model flux with the observed flux at each wavelength, calculating
! the fit by using an appropriate f parameter from a look-up table
!   Then, it outputs the model flux at a specific pv.
!
!*****

program therme

implicit none

real*8 g, h, pv, pvstart, pvend, pvstep, q, bigA, epsilon, eta, s0, stef, &
      au, r, delta, diameter, tmax, psirad, dps, thetarad, dtheta, phirad, dphi, &
      consta, constb, fbit, fmod, pi, wavelength(100), flux(100), err(100), &
      fmodarray(100), alpha, alphaspec, planck, bigT(181,181), res, pvspec, &
      etaspec, waveoutstart, waveoutend, waveoutstep, waveout(1000), wavel, &
      fmodout(1000), dang, bestfitpv, oldres, f, tmod, tmodstart, tmodend, &
      maxtol, enbal, enbalbit, enbalmid, tmodlow, tmodhigh, &
      tmodmid, etastart, etaend, etastep, tfit, bestfiteta, oldeta, &
      oldfmodarray(100), lowres, bigTout(181,361), P, thermal_inertia, thermal_parameter, &
      thermal_parameter_lookup(100), flookup(100), beta, newpvstart, newpvend, newetastart, &
      newetastep, newpvstep

character pvquery, modelquery, outwavequery
integer i, j, k, n, m, x, pvoutrange, bestfitpvfound, definerangedone

!   define constants emmissivity, beaming parameter, pi,
!   solar flux at 1AU, Stefan-Boltzmann constant, distance 1AU (km)
!   and set projected model eta=1

epsilon=0.9
pi=4.0e+00*atan(1.0e+00)
s0=1374.0e+00
stef=5.670512e-08
au=1.49597870671e+08
etaspec = 1.0

!   specify range of pv and specific pv

pvstart=0.15
pvend=0.40
pvstep=0.01
pvspec=0.16

!   specify range of eta and step size

etastart=0.9
etaend=3.0
etastep=0.01

```

```

!       initialise a default option
       modelquery="1"

!       specify output wavelength range and stepsize for output flux in microns

       waveoutstart=4.0
       waveoutend=25.0
       waveoutstep=0.5

! angle steplength in radians

       dang= 1*(pi/180)
!       write (*,(" Angle step size = ",f4.1," deg")) dang/(pi/180)

!       steplength of psi, theta, phi in radians

       dpsi = dang
       dtheta = dang
       dphi = dang

!       open file 'param.txt' containing
!       H, G, delta= Earth-Sun distance (AU), r = Asteroid-Sun distance (AU), alpha
!       (phase angle, degrees). use H value corresponding to V(1,alpha) from composite
!       lightcurve from JKT data, which is then run through phasecor using the value
!       of G supplied below to correct to V(1,0).
!       P = sidereal rotation period, P and thermal inertia used to calculate thermal parameter
!       for each value of pv

       open (1, file='param.txt', status='unknown')
       read (1,*) g
       read (1,*) h
       read (1,*) delta
       read (1,*) r
       read (1,*) alpha
       read (1,*) P
       read (1,*) thermal_inertia
       close (1)

       alphasrad = alpha*(pi/180)

!       inform user

       print *, " "
       print *, "Opened file param.txt"
       print *, " "
       write(*,(' G = ',f4.2)) g
       write(*,(' H = ',f6.3)) h
       write(*,(' delta = ',f6.3)) delta
       write(*,(' r = ',f6.3)) r
       write(*,(' alpha = ',f5.1)) alpha
       write(*,(' P = ',f7.3," h")) P
       write(*,(' thermal inertia = ',f5.0)) thermal_inertia

!       Open file spec.txt containing observed spectrum
!       and read in wavelengths and fluxes
!       n is number of rows

       open (2,file='spec.txt',status='unknown')

```

```

do 10 i=1,100

    read(2,*,end=99) wavelength(i), flux(i), err(i)
    wavelength(i) = wavelength(i)*1e-06
    n=n+1

10 continue

99    close(2)

!    inform user

    print *, " "
    print *, "Opened file spec.txt, read wavelengths, fluxes and errors."

!    read in f-value look-up table
!    x is number of rows

    open (7, file='lookup.txt',status='unknown')
    x=0

    do 11 i = 1,100

        read (7,*,end=98) thermal_parameter_lookup(i), flookup(i)
        x=x+1

11    continue

98    close(7)

!    calculate phase integral q from value of G

    q=0.290 + 0.684*g

!    do you want to run the models over a pv range or at a specific pv?

1000 print *, " "
    print *, "Press:"
    print *, "(1) if you want to run Night Emission Simulated Thermal Model over a"
    print *, "range of pv and eta."
    write(*, '(2) to output model flux at a specific pv and eta -> "\)')
    read (*, '(A1)') pvquery

    if (pvquery.eq."2") GOTO 5000    ! go to specific pv section

!    if pvquery=1 or anything other than 2 it continues on

2000 open (5,file='residual.txt')
    print *, " "
    print *, "Current pv and eta range is:"    ! tell us what the range is
    print *, " "
    write (*, '(pv start = ', f6.4)') pvstart
    write (*, '(pv end   = ', f6.4)') pvend
    write (*, '(pv step  = ', f6.4)') pvstep
    print *, " "
    write (*, '(eta start = ', f6.4)') etastart
    write (*, '(eta end   = ', f6.4)') etaend
    write (*, '(eta step  = ', f6.4)') etastep
    print *, " "

```

```

print *, "Press:"
print *, "ENTER to use current pv and eta range"
print *, "(1) to change pv range and step"
write(*, '( " (2) to change eta range and step -> "\)')
read (*, '(A1)') pvquery
print *, " "

if (pvquery.eq."1") then    ! enter new pv range

    write(*, '( " start: "\)')
    read (*, '(f6.4)') pvstart
    write(*, '( " end: "\)')
    read (*, '(f6.4)') pvend
    write(*, '( " step: "\)')
    read (*, '(f6.4)') pvstep
    GOTO 2000

end if

if (pvquery.eq."2") then    ! enter new eta range

    write(*, '( " start: "\)')
    read (*, '(f6.4)') etastart
    write(*, '( " end: "\)')
    read (*, '(f6.4)') etaend
    write(*, '( " step: "\)')
    read (*, '(f6.4)') etastep
    GOTO 2000

end if

! *****
! run model over the range of pv
! *****

! initialise best pv checking variable
pvoutrange=0

print *, " "          !print table header
print *, "residual = SUM(((Fn(obs)-Fn(mod))/errn(obs))^2) [min is best fit]"
print *, " "
print *, "                thermal"

write (*, '( "pv", 6x, "D(km)", 1x, "residual", 5x, "Tmax", 3x, "Tfit", &
           4x, "eta", 3x, "parameter", 3x, "f")')
write (5, *) " residual = SUM(((Fn(obs)-Fn(mod))/errn(obs))^2) [min is best fit]"
write (5, *) " "
write (5, *) "                thermal"
write (5, '( "pv", 6x, "D(km)", 1x, "residual", 5x, "Tmax", 3x, "Tfit", &
           4x, "eta", 3x, "parameter", 3x, "f")')

do 20 pv = pvstart, pvend, pvstep    !run over pv range

!           calculate bolometric albedo A from q and geometric albedo pv
bigA=q*pv

!           calculate diameter from inputted H and pv values
diameter = (1329/sqrt(pv))*10**(-h/5)

```

```

!       calculate tmax and tmod from etaspec=1
!       tmax is projected model maximum T
!       tmod is modified projected model maximum T after night side emission is included

tmax = (((1-bigA)*s0)/(etaspec*epsilon*stef*r*r))*0.25

!       calculate thermal parameter

thermal_parameter = thermal_inertia*sqrt(2*pi/(P*3600))/(epsilon*stef*tmax**3)

!       find f-value for this thermal parameter from flookup arrays

do 30 i=1,x

    if ((i.eq.1).and.(thermal_parameter.lt.((thermal_parameter_lookup(i)+&
        thermal_parameter_lookup(i+1))/2))) then

        f=flookup(i)
        goto 4000

    end if

    if (i.eq.x) then

        f=flookup(i)
        goto 4000

    end if

    if ((i.gt.1).and.(thermal_parameter.lt.((thermal_parameter_lookup(i)+&
        thermal_parameter_lookup(i+1))/2)).and.(thermal_parameter.ge.&
        ((thermal_parameter_lookup(i-1)+thermal_parameter_lookup(i))/2)))

then

        f=flookup(i)
        goto 4000

    end if

30      continue

!       code that finds an iterative solution for Tmod from the energy balance
!       will use bisection method

!       define range and tolerance (ie. how close to true solution it must be)
!
!31      tmodlow = 1
!          tmodhigh = tmax
!          maxtol = 0.01
!
!       if range is less than tolerance then have accurately enough got tmod
!
!3000  enbal=0
!          tmodmid = (tmodhigh + tmodlow)/2
!
!          if ((tmodhigh-tmodlow).lt.maxtol) then
!
!              tmod = tmodmid
!              GOTO 4000
!
!

```

```

!      end if
!
!      enbal=0
!
!      calculate energy balance at midpoint between tmodhigh and tmodlow from SFG thesis 3.42
!
!      do 70 phirad = -pi/2+dphi/2, +pi/2, dphi
!
!          do 80 thetarad = dtheta/2, pi, dtheta
!
!              if ((tmodmid**4 * cos(thetarad)).gt.((f*tmax)**4)) enbalbit = tmodmid**4 &
!                  * cos(thetarad) * cos(phirad) * cos(phirad) * dtheta * dphi
!
!              if ((tmodmid**4 * cos(thetarad)).lt.((f*tmax)**4)) enbalbit = (f*tmax)**4 * &
!                  cos(phirad) * cos(phirad) * dtheta * dphi
!
!              enbal = enbal + enbalbit
!
!80          continue
!
!70      continue
!
!      enbalmid = 2 * epsilon * stef * enbal - (pi * (1 - bigA) * s0)/(r*r)
!
!      if midpoint greater than zero, correct solution lies between enballow and enbalmid
!      tmodhigh then becomes the old tmodmid, and iteration continues
!
!      if (enbalmid.ge.0) tmodhigh = tmodmid
!
!      if midpoint less than zero, correct solution lies between enbalhigh and enbalmid
!      tmodlow then becomes the old tmodmid, and iteration continues
!
!      if (enbalmid.lt.0) tmodlow = tmodmid
!
!      GOTO 3000
!
!      have found Tmod, the maximum temp with modified projected (ie. eta=1), energy balances
!
!      now want Tmax that results from best-fit eta, find by running
!      over eta range, call it Tfit
!
!      Tfit = Tmax/(eta^0.25)
!
!      in modified projected model night side temperature was f * Tmax cos(phi)^0.25
!      we will continue to define night side temperature same way
4000 do 21 eta = etastart, etaend, etastep !   run over eta range
!
!          tfit = tmax/eta**0.25
!
!      0 latitude and longitude is defined as the subsolar point, which is alpha degrees away
!      from the centre of the hemisphere visible to the observer
!      now calculate temperature as function of longitude (thetarad) and latitude (phirad)
!      at one degree intervals, from -90 -> +90 latitude, and from
!      (-90 + alpha) -> +90 latitude (sunlit portion), and from 90 -> (90 + alpha)
!      (night portion) for hemisphere visible to observer
!
!      generate temperature array, running through -90 -> +90 latitude
i=1

```

```

do 90 phirad = -pi/2, pi/2, dphi

!         go from -90 + alpha to +90 longitude (dayside portion visible)
!         if Tfit*cos(theta)^0.25 > fTmax then
!             T = Tmod*cos(theta)^0.25*cos(phi)^0.25
!         if Tfit*cos(theta)^0.25 < fTmax then
!             T = fTmax*cos(phi)^0.25 (ie. nightside dominant)

j=1

do 100 thetarad = -pi/2 + alphasad, +pi/2, dtheta

        if ((tfit*(cos(thetarad)**0.25)).gt.(f*tmax)) bigT(i,j) = &
            tfit*cos(thetarad)**0.25*cos(phirad)**0.25
        if ((tfit*(cos(thetarad)**0.25)).le.(f*tmax)) bigT(i,j) = &
            f*tmax*cos(phirad)**0.25

!         set -90 and +90 latitude to zero to avoid negative values

        if (phirad.LE.-pi/2) bigT(i,j)=0
        if (phirad.GE.pi/2) bigT(i,j)=0

        j=j+1
100      continue

!         go from +90 -> +90+alpha longitude (nightside portion visible)

do 110 thetarad = +pi/2 + dtheta, alphasad+pi/2, dtheta

        bigT(i,j) = f*tmax*cos(phirad)**0.25

!         set -90 and +90 latitude to zero to avoid negative values

        if (phirad.LE.-pi/2) bigT(i,j)=0
        if (phirad.GE.pi/2) bigT(i,j)=0

        j=j+1
110      continue

i=i+1
90      continue

!         calculate NESTM fluxes for each input wavelength using planck function
!         integrates over surface elements dphi and dtheta using pre-built temperature array
!         same as for modified projected model

do 120 i=1,n

        fmod = 0
        j=1

!         run over -90 -> +90 latitude

do 130 phirad = - pi/2, +pi/2, dphi

        k=1

```

```

!      run over -pi/2 + alpha -> + pi/2 + alpha longitude (ie. visible hemisphere longitudes)

      do 140 thetarad = -pi/2 + alphasad, +pi/2 + alphasad, dtheta

          fbit = ((epsilon * diameter * diameter) / (4 * delta * delta * au * au)) &
                * planck(bigT(j,k), wavelength(i)) * cos(phirad) * cos(phirad) &
                * cos(alphasad-thetarad) * dphi * dtheta

          fmod = fmod + fbit
          k=k+1

140      continue

          j=j+1

130      continue

      fmodarray(i)=fmod

120      continue

!      for this value of eta
!      lets measure the fit of the model; do this by calculating
!      SUM((F(obs)-F(mod)/err(obs))^2), minimum value = best fit!

      res = 0

      do 150 i=1,n

          res = res + ((flux(i)-fmodarray(i))/err(i))*((flux(i)-fmodarray(i)) &
                /err(i))

150      continue

!      compare the fit with the one calculated before it; if its bigger then
!      well done, the last set of fmodarray were the best fit at this value of pv

      if ((res.gt.oldres).and.(eta.gt.etastart)) GOTO 3001
      oldres=res

!      store a back-up of these fmodarray values

      do 151 i=1,n

          oldfmodarray(i) = fmodarray(i)

151      continue

21      continue

!      so correct fmodarrays were the previous values, and so was eta
!      (so need to recalc tfit) and res

3001 do 152 i=1,n

          fmodarray(i) = oldfmodarray(i)

152 continue

```

```

if (eta.gt.etastart) then
    eta=eta-etastep
    tfit = (((1-bigA)*s0)/(eta*epsilon*stef*r*r))**0.25
!    beta = (tmod/tfit)**4

end if

res=oldres

!    display values in table

    write (*,'(f6.4, f7.3, e13.6, f7.2, f7.2, f7.3, f8.4,3x, f5.3)') &
        pv, diameter, res, tmax, tfit, eta, thermal_parameter, f

    write (5,'(f6.4, f7.3, e13.6, f7.2, f7.2, f7.3, f8.4,3x, f5.3)') &
        pv, diameter, res, tmax, tfit, eta, thermal_parameter, f

!    if this is the start of the pv run, place pv value and residual into best-fit
!    pv holder, and lowest residual holder

    if (pv.eq.pvstart) then

        bestfitpv=pv
        lowres=res

    end if

!    if this isn't the start of the pv run, compare residuals to the held values
!    if its smaller then replace holder

    if ((pv.ne.pvstart).and.(pv.lt.pvend-pvstep/2).and.(res.lt.lowres)) then

        bestfitpv=pv
        bestfiteta=eta
        lowres=res
        bestfitpvfound=1

    end if

!    if res now gets bigger then this is probably the turning point, can define
!    a suggested start and end eta and pv

    if ((bestfitpvfound.eq.1).and.(res.gt.lowres).and.(definerangedone.ne.1)) then

        newpvstart = pv - 2*pvstep
        newpvend = pv
        newpvstep = 0.1*pvstep
        newetastart=eta
        if (etastep.gt.0.0001) newetastep = 0.1*etastep
        definerangedone=1

    end if

!    if this is the end of the pv run and the residual is still smaller than the held
!    value then best-fit pv is out of range

    if ((pv.gt.pvend-pvstep/2).and.(res.lt.lowres)) then

        pvoutrange=1

```

```

        bestfitpvfound=0

    end if

!       if at the end of the pv run the held pv value is pvstart, then the best-fit pv
!       value is out of range

        if ((pv.gt.pvpend-pvstep/2).and.(bestfitpv.eq.pvstart)) then

            pvoutrange=1
            bestfitpvfound=0

        end if

20    continue

    print *, " "
    if (pvoutrange.ne.1) write (*,(' best-fit pv = ', f6.4)) bestfitpv
    if (pvoutrange.ne.1) write (*,(' best-fit eta = ', f6.4)) bestfiteta

    write (5,*) " "
    if (pvoutrange.ne.1) write (5,(' best-fit pv = ', f6.4)) bestfitpv
    if (pvoutrange.ne.1) write (5,(' best-fit eta = ', f6.4)) bestfiteta
    write (5,*) " "

!       at the end of the pv run it is safe to replace pvstart, pvend, pvstep, and
!       etastart and etastep

        if (bestfitpvfound.eq.1) then

            pvstart=newpvstart
            pvend=newpvend
            pvstep=newpvstep
            etastart=newetastart
            etastep=newetastep
            definerangedone=0

        end if

GOTO 1000

!*****
! run model for the specific pv value
!*****

5000 if (bestfitpvfound.eq.1) then !options start at 5001

        pv=bestfitpv
        eta=bestfiteta

    end if

    if (bestfitpvfound.eq.0) then

        pv=pvspec
        eta=etaspec

    end if

```

```

!      calculate diameter from inputted H and pv values
5001  diameter = (1329/sqrt(pv))*10**(-h/5)      !second time through options start here
!      inform user what is the pv set to?

      print *, " "
      print *, "Current pv and diameter are:"
      write (*,(' pv = ",f6.4)") pv
      write (*,(' Deff = ",f6.2," km")) diameter
      print *, " "
      write (*,(' eta = ",f6.4)") eta

!      inform user of output wavelength range

      print *, " "
      print *, "Output wavelength range:"
      write (*,(' start = ",f6.3," um")) waveoutstart
      write (*,(' end = ",f6.3," um")) waveoutend
      write (*,(' step = ",f6.3," um")) waveoutstep
      print *, " "

!      pick model or adjust wavelength range (rare), go back to pv ranges, or quit

      print *, "Would you like to change pv, output model flux,"
      print *, "or adjust output wavelength range and stepsize?"
      print *, " "
      print *, "(1) change pv"
      print *, "(2) change eta"
      print *, "(3) Night Emission Simulated Thermal Model (NESTM)"
      print *, "(4) adjust output wavelength range or stepsize"
      print *, "(5) run models over a pv range"
      write (*,(' " Press (q) to quit: "\'))
      read (*,('A1')) modelquery
      print *, " "

      if (modelquery.eq."1") then ! they wish to change pv

          write (*,('Enter new pv: "\')) ! enter your own pv
          read (*,('f6.4')) pv
          GOTO 5001      !go back to options

      end if

      if (modelquery.eq."2") then ! they wish to change eta

          write (*,('Enter new eta: "\')) ! enter your own eta
          read (*,('f6.4')) eta
          GOTO 5001      !go back to options

      end if

!      calculate bolometric albedo A from q and geometric albedo pv now that pv is set

      bigA=q*pv

      if (modelquery.eq."4") then ! you wish to change wavelength range or step size

          print *, "Press (1) to adjust output wavelength range"
          print *, "Press (2) to adjust output wavelength step size"

```

```

write (*,(' Press (3) for alternative standard range (7.0um->14.0um, 0.2um step: "\)')
read (*,(A1)) outwavequery
print *, " "

if (outwavequery.eq."1") then ! you wish to change wavelength range

    write (*,(' start = "\)')
    read (*,(f6.3)) waveoutstart
    write (*,(' end = "\)')
    read (*,(f6.3)) waveoutend

end if

if (outwavequery.eq."2") then ! you wish to change wavelength step size

    write (*,(' step = "\)')
    read (*,(f6.3)) waveoutstep

end if

if (outwavequery.eq."3") then ! you wish to change standard set-up

    waveoutstart=7.0
    waveoutend=14.0
    waveoutstep=0.2

end if

GOTO 5001

end if

! wavelength output range is agreed on now so lets generate output arrays

i=1

do 160 wavel=waveoutstart,(waveoutend+waveoutstep/2),waveoutstep

    waveout(i)=wavel*1e-06
    i=i+1

160 continue

! m is number of output wavelengths for later loops

m=i-1

if (modelquery.eq."3") GOTO 6000! go to NESTM
if (modelquery.eq."5") GOTO 2000! go back to looping pv ranges
if (modelquery.eq."q") GOTO 9000! go to END PROGRAM

!
! Night Emission Simulated Thermal Model
!

6000 print *, "Tmod/K Precision"

! calculate tmax and tmod from etaspec=1
! tmax is projected model maximum T
! tmod is modified projected model maximum T after night side emission is included

```

```

tmax = (((1-bigA)*s0)/(etaspec*epsilon*stef*r*r))**0.25
!
! calculate thermal parameter
thermal_parameter = thermal_inertia*sqrt(2*pi/(P*3600))/(epsilon*stef*tmax**3)
!
! find f-value for this thermal parameter from flookup arrays
      do 161 i=1,x
          if ((i.eq.1).and.(thermal_parameter.lt.((thermal_parameter_lookup(i)+&
              thermal_parameter_lookup(i+1))/2))) then
              f=flookup(i)
              goto 162
          end if
          if (i.eq.x) then
              f=flookup(i)
              goto 162
          end if
          if ((i.gt.1).and.(thermal_parameter.lt.((thermal_parameter_lookup(i)+&
              thermal_parameter_lookup(i+1))/2)).and.(thermal_parameter.ge.&
              ((thermal_parameter_lookup(i-1)+thermal_parameter_lookup(i))/2)))
then
              f=flookup(i)
              goto 162
          end if
161      continue
!
! write code that finds an iterative solution for Tmod from the energy balance
! will use bisection method
!
! define range and tolerance (ie. how close to true solution it must be)
162  tmodlow = 1
      tmodhigh = tmax
      maxtol = 0.01
!
! if range is less than tolerance then have accurately enough got tmod
7000 enbal=0
      tmodmid = (tmodhigh + tmodlow)/2
      write (*,'(" ",f6.2,8x,f8.4)') tmodmid, (tmodhigh-tmodlow)/2
      if ((tmodhigh-tmodlow).lt.maxtol) then
          tmod = tmodmid
          GOTO 8000
      end if

```

```

! calculate energy balance at midpoint between tmodhigh and tmodlow, from SFG thesis page 3.42
do 210 phirad = -pi/2+dphi/2, +pi/2, dphi
    do 220 thetarad = dtheta/2, pi, dtheta
        if ((tmodmid**4 * cos(thetarad)).gt.((f*tmax)**4)) enbalbit = tmodmid**4 &
            * cos(thetarad) * cos(phirad) * cos(phirad) * dtheta * dphi

        if ((tmodmid**4 * cos(thetarad)).lt.((f*tmax)**4)) enbalbit = (f*tmax)**4 * &
            cos(phirad) * cos(phirad) * dtheta * dphi

        enbal = enbal + enbalbit
220    continue
210    continue

enbalmid = 2 * epsilon * stef * enbal - (pi * (1 - bigA) * s0)/(r*r)

! if midpoint greater than zero, correct solution lies between enballow and enbalmid
! tmodhigh then becomes the old tmodmid, and iteration continues

if (enbalmid.ge.0) tmodhigh = tmodmid

! if midpoint less than zero, correct solution lies between enbalhigh and enbalmid
! tmodlow then becomes the old tmodmid, and iteration continues

if (enbalmid.lt.0) tmodlow = tmodmid

GOTO 7000

!
! have found Tmod, the maximum temp with modified projected (ie. eta=1), energy balances

! now want Tmax that results from best-fit eta
! over eta range, call it Tfit
!
! Tfit = Tmax/(eta^0.25)

! in modified projected model night side temperature was f * Tmax cos(phi)^0.25
! we want night side temperature to be defined same way

8000 tfit = tmax/eta**0.25

! beta is beaming parameter after maximum day side temperature is recalculated

beta = (tmod/tfit)**4

! 0 latitude and longitude is defined as the subsolar point, which is alpha degrees away
! from the centre of the hemisphere visible to the observer
! now calculate temperature as function of longitude (thetarad) and latitude (phirad)
! at one degree intervals, from -90 -> +90 latitude, and from
! (-90 + alpha) -> +90 latitude (sunlit portion), and from 90 -> (90 + alpha)
! (night portion) for hemisphere visible to observer

! generate temperature array, running through -90 -> +90 latitude

i=1

```

```

do 230 phirad = -pi/2, pi/2, dphi

!           go from -90 + alpha to +90 longitude (dayside portion visible)
!           if Tfit*cos(theta)^0.25 > f*Tmax then
!               T = Tfit*cos(theta)^0.25*cos(phi)^0.25
!           if Tfit*cos(theta)^0.25 < f*Tmax then
!               T = f*Tmax*cos(phi)^0.25 (ie. nightside dominant)

j=1

do 240 thetarad = -pi/2 + alphasad, +pi/2, dtheta

    if ((tfit*(cos(thetarad)**0.25)).gt.(f*tmax)) bigT(i,j) = &
        tfit*cos(thetarad)**0.25*cos(phirad)**0.25
    if ((tfit*(cos(thetarad)**0.25)).lt.(f*tmax)) bigT(i,j) = &
        f*tmax*cos(phirad)**0.25

!           prevent negative number

    if (thetarad.gt.pi/2) bigT(i,j) = f*tmax*cos(phirad)**0.25

!           set -90 and +90 latitude to zero to avoid negative values

    if (phirad.LE.-pi/2) bigT(i,j)=0
    if (phirad.GE.pi/2) bigT(i,j)=0

    j=j+1

240      continue

!           go from +90 -> +90+alpha longitude (nightside portion visible)

do 250 thetarad = +pi/2 + dtheta, alphasad+pi/2, dtheta

    bigT(i,j) = f*tmax*cos(phirad)**0.25

!           set -90 and +90 latitude to zero to avoid negative values

    if (phirad.LE.-pi/2) bigT(i,j)=0
    if (phirad.GE.pi/2) bigT(i,j)=0

    j=j+1

250      continue

i=i+1

230      continue

!           calculate temperature's again this time over whole asteroid surface to
!           output to file

!           open file

    open(3,file='tempnestm.txt')

!           inform of calculated temperatures

write (3,(' projected model maximum temperature is ', f6.2, ' K.)) tmax
write (3,(' modified projected model maximum temperature is ', f6.2, ' K.)) tmod

```

```

write (3,(' Night Emission Simulated Model maximum temperature is ', f6.2, ' K.)) &
      tfit
write (3,*) " "

! indicate table layout

write(3,*) "          long/deg"
write(3,*) "lat/deg      temp/K"
write(3,*) " "

! produce a 7 space gap before longitude table heading begins

write(3,('      '\))

i=1

do 251 phirad = -pi/2, pi/2, dphi

!         go from -180 to -90 longitude (first nightside portion)

      j=1

      do 252 thetarad = -pi, -pi/2, dtheta

          bigTout(i,j) = f*tmax*cos(phirad)**0.25

!         set -90 and +90 latitude to zero to avoid negative values

          if (phirad.LE.-pi/2) bigTout(i,j)=0
          if (phirad.GE.pi/2) bigTout(i,j)=0

!         write longitude table headings

          if (i.eq.1) write(3,('f7.2\')) thetarad/(pi/180)
          j=j+1

252      continue

!         go from -90 to +90 longitude (dayside portion)
!         if Tfit*cos(theta)^0.25 > f*Tmax then
!             T = Tfit*cos(theta)^0.25*cos(phi)^0.25
!         if Tfit*cos(theta)^0.25 < f*Tmax then
!             T = f_alb*Tmax*gamma^0.25*cos(phi)^0.25 (ie. nightside dominant)

      do 253 thetarad = -pi/2 +dtheta, +pi/2, dtheta

          if ((tfit*(cos(thetarad)**0.25)).gt.(f*tmax)) bigTout(i,j) = &
            tfit*cos(thetarad)**0.25*cos(phirad)**0.25
          if ((tfit*(cos(thetarad)**0.25)).lt.(f*tmax)) bigTout(i,j) = &
            f*tmax*cos(phirad)**0.25

!         prevent negative number

          if (thetarad.gt.pi/2) bigTout(i,j) = f*tmax*cos(phirad)**0.25

!         set -90 and +90 latitude to zero to avoid negative values

          if (phirad.LE.-pi/2) bigTout(i,j)=0
          if (phirad.GE.pi/2) bigTout(i,j)=0

```

```

!           write the longitude table headings

           if (i.eq.1) write(3,'(f7.2\)' ) thetarad/(pi/180)
           j=j+1

253         continue

!           go from +90 -> +180 longitude (second nightside portion)

           do 254 thetarad = +pi/2 + dtheta, +pi, dtheta

               bigTout(i,j) = f*tmax*cos(phirad)**0.25

!           set -90 and +90 latitude to zero to avoid negative values

           if (phirad.LE.-pi/2) bigTout(i,j)=0
           if (phirad.GE.pi/2) bigTout(i,j)=0

!           continue to write longitude table headings

           if ((i.eq.1).and.(thetarad.lt.+pi-dtheta/2)) write(3,'(f7.2\)' ) &
               thetarad/(pi/180)

!           for final longitude table heading require that next output will be on new line

           if ((i.eq.1).and.(thetarad.gt.pi-dtheta/2)) write(3,'(f7.2)' ) &
               thetarad/(pi/180)

           j=j+1

254         continue

           i=i+1

251         continue

!           output temperature array

           phirad=-pi/2

           do 255 i=1,181,1

!           print latitude heading

               write(3,'(f7.2\)' ) phirad/(pi/180)

               do 256 j=1,361,1

                   write(3,'(f7.2\)' ) bigTout(i,j)

256                 continue

!                 begin a new line

                   write(3,*) " "
                   phirad = phirad + dphi

255                 continue

```

```

close (3)

! output actual surface temperatures now, that is temperature's without beaming, as in
! modified projected model, convert from NESTM output T

open (6,file='temp_nestm_surface.txt')

! inform of calculated temperatures

write (6,(' projected model maximum temperature is ", f6.2, " K.)) tmax
write (6,(' modified projected model maximum temperature is ", f6.2, " K.)) tmod
write (6,(' Night Emission Simulated Model maximum temperature is ", f6.2, " K.)) &
      tfit
write (6,*) " "

! indicate table layout

write(6,*) "          long/deg"
write(6,*) "lat/deg      temp/K"
write(6,*) " "

! produce a 7 space gap before longitude table heading begins

write(6,('      "\'))

i=1

do 257 phirad = -pi/2, pi/2, dphi

!          go from -180 to -90 longitude (first nightside portion)
!          temp same as NESTM apparent

      j=1

      do 258 thetarad = -pi, -pi/2, dtheta

!          write longitude table headings

          if (i.eq.1) write(6,(f7.2\)) thetarad/(pi/180)
          j=j+1

258      continue

!          go from -90 to +90 longitude (dayside portion)
!          Temp either nightside, which is same, or dayside, so remove eta

      do 259 thetarad = -pi/2 +dtheta, +pi/2, dtheta

          if ((tfit*(cos(thetarad)**0.25)).gt.(f*tmax)) bigTout(i,j) = &
              bigTout(i,j)/eta**0.25

!          write the longitude table headings

          if (i.eq.1) write(6,(f7.2\)) thetarad/(pi/180)
          j=j+1

259      continue

!          go from +90 -> +180 longitude (second nightside portion)

```

```

!           Temp same as NESTM apparent
           do 260 thetarad = +pi/2 + dtheta, +pi, dtheta

!           continue to write longitude table headings
           if ((i.eq.1).and.(thetarad.lt.+pi-dtheta/2)) write(6,'(f7.2\)' ) &
               thetarad/(pi/180)

!           for final longitude table heading require that next output will be on new line
           if ((i.eq.1).and.(thetarad.gt.pi-dtheta/2)) write(6,'(f7.2\)' ) &
               thetarad/(pi/180)

           j=j+1
260          continue

           i=i+1
257          continue

!           output temperature array
           phirad=-pi/2

           do 261 i=1,181,1

!           print latitude heading
               write(6,'(f7.2\)' ) phirad/(pi/180)

               do 262 j=1,361,1

                   write(6,'(f7.2\)' ) bigTout(i,j)
262              continue

!              begin a new line
                   write(6,*) " "
                   phirad=phirad + dphi

261          continue

           close(6)

! inform user
           print *, " "
           write (*,('(" projected model maximum temperature is ", f6.2, " K.")) tmax
           write (*,('(" modified projected model maximum temperature is ", f6.2, " K.")) tmod
           write (*,('(" Night Emission Simulated Thermal Model maximum temperature is ", &
               f6.2, "K.")) tfit
           print *, " "
           print *, "The surface temperature distribution is written to temp_nestm_surface.txt"
           print *, " "
           print *, "The apparent temperature distribution altered by the beaming parameter is"
           print *, "written to tempnestm.txt."
           print *, " "

```

```

! calculate NESTM fluxes for each input wavelength using planck function
! integrates over surface elements dphi and dtheta, from SFG thesis 3.42
! using pre-built temperature array

do 280 i=1,n
    fmod = 0
    j=1
! run over -90 -> +90 latitude
    do 290 phirad = - pi/2, +pi/2, dphi
        k=1
! run over -pi/2 + alpha -> + pi/2 + alpha longitude (ie. visible hemisphere longitudes)
        do 300 thetarad = -pi/2 + alpharad, +pi/2 + alpharad, dtheta
            fbit = ((epsilon * diameter * diameter) / (4 * delta * delta * au * au)) &
                * planck(bigT(j,k), wavelength(i)) * cos(phirad) * cos(phirad) &
                * cos(alpharad-thetarad) * dphi * dtheta

            fmod = fmod + fbit
            k=k+1
300            continue
                j=j+1
290        continue
    fmodarray(i)=fmod
280    continue
! lets measure the fit of the model; do this by calculating
! SUM((F(obs)-F(mod)/err(obs))^2)
res = 0
do 310 i=1,n
    res = res + ((flux(i)-fmodarray(i))/err(i))* ((flux(i)-fmodarray(i))/err(i))
310    continue
! calculate NESTM fluxes for each output wavelength using planck function
! integrates over surface elements dphi and dtheta
do 320 i=1,m
    fmod = 0
    j=1
    do 330 phirad = - pi/2, +pi/2, dphi
        k=1

```

```

do 340 thetarad = -pi/2 + alphasad, +pi/2 + alphasad, dtheta

      fbit = ((epsilon * diameter * diameter) / (4 * delta * delta * au * au)) &
             * planck(bigT(j,k), waveout(i)) * cos(phirad) * cos(phirad) &
             * cos(alphasad-thetarad) * dphi * dtheta

      fmod = fmod + fbit
      k=k+1

340      continue

      j=j+1

330      continue

      fmodout(i)=fmod

320      continue

! now make file fmodelnestm.txt

      open (4,file='fmodelnestm.txt',status='unknown')
      write (4,*) "Asteroid with:"
      write (4,*) " "
      write(4,(' G = ",f4.2)') g
      write(4,(' H = ",f6.3)') h
      write (4,*) " "
      write (4,('pv = ",f6.4)') pv
      write (4,('Deff = ",f4.2," km"')) diameter
      write (4,*) " "
      write (4,('thermal inertia = ",f5.0)') thermal_inertia
      write (4,('P = ",f7.3," h"')) P
      write (4,('thermal parameter = ",f7.3)') thermal_parameter
      write (4,('f = ",f7.3)') f
      write (4,*) " "
      write (4,('Tmax = ",f6.2)') tmax
      write (4,('Tmod = ",f6.2)') tmod
      write (4,('Tfit = ",f6.2)') tfit
      write (4,*) " "
      write (4,('eta = ",f6.4)') eta
      write (4,('beta = ",f5.3)') beta
      write (4,*) " "
      write(4,(' delta = ",f6.3)') delta
      write(4,(' r = ",f6.3)') r
      write(4,(' alpha = ", f5.1)') alpha
      write (4,*) " "
      write (4,('NESTM fit is: ",e9.3)') res
      write (4,*) " "
      write (4,(2x,"wavel(um)",3x,"flux(Wm^-2um^-1)",5x,"error",7x,"NESTM flux(Wm^-2um^-1)"&
      ))

      do 350 i=1,n

            write(4,('f11.4, 4x, e14.8, 2x, e14.8, 2x, e14.8)') wavelength(i)/1e-06, &
            flux(i), err(i), fmodarray(i)

350      continue

      write (4,*) " "

```

```

write (4,(2x,"wavel(um)",3x,"NESTM flux(Wm^-2um^-1)"))
do 360 i=1,m
    write (4,(f11.4, 4x, e14.8)) waveout(i)/1e-06, fmodout(i)
360    continue
close(4)
!    inform user
write (*, '( " pv = ",f6.4)') pv
write (*, '( " eta = ",f6.4)') eta
write (*, '( " NESTM fit residual = ",e9.3)') res
print *, "For the given parameters, the NESTM fluxes are written"
print *, "to fmodelnestm.txt"
GOTO 5001
9000 close(5)
end program therme
! This is my planck function. It calculates the spectral radiance for a given wavelength
! and maximum temperature
real*8 FUNCTION planck (bigT, wavelength)
real*8 consta, constb, bigT, wavelength
planck = 0
consta = 1.191044d-16
constb = 1.438769d-02
planck = dble((((consta/wavelength**5)*(dexp(constb/(wavelength*bigT))-1)**-1))
! to convert to units of W m^-2 um^-1:
planck = planck * 1d-06
return

```

Appendix G. Look-up Table for f Parameter

Thermal parameter Θ	f parameter	Thermal parameter Θ	f parameter
0.058	0.326	10.129	0.719
0.065	0.334	11.325	0.722
0.075	0.345	13.077	0.725
0.082	0.351	14.325	0.726
0.092	0.360	16.016	0.728
0.106	0.371	18.494	0.730
0.116	0.379	22.650	0.732
0.130	0.388	32.032	0.733
0.150	0.400		
0.168	0.409		
0.184	0.417		
0.206	0.426		
0.238	0.439		
0.260	0.447		
0.291	0.457		
0.336	0.470		
0.412	0.489		
0.582	0.522		
0.801	0.552		
0.895	0.562		
1.034	0.576		
1.133	0.584		
1.266	0.594		
1.462	0.607		
1.602	0.615		
1.791	0.624		
2.068	0.636		
2.312	0.644		
2.532	0.651		
2.831	0.659		
3.203	0.668		
3.269	0.669		
3.581	0.675		
3.581	0.675		
4.004	0.681		
4.135	0.683		
4.530	0.688		
4.623	0.689		
5.065	0.694		
5.663	0.699		
5.848	0.700		
6.406	0.704		
7.163	0.708		
8.008	0.712		
8.271	0.713		
9.247	0.716		